

**PURDUE UNIVERSITY**  
**GRADUATE SCHOOL**  
**Thesis/Dissertation Acceptance**

This is to certify that the thesis/dissertation prepared

By Tom Marquis Lawrence

Entitled

CHACTERIZATION AND MEASUREMENT OF HYBRID GAS JOURNAL BEARINGS

For the degree of Doctor of Philosophy

Is approved by the final examining committee:

Marvin Kemple

Chair

Hassan Akay

Ricardo Decca

Charles Krousgrill

Yogesh Joglekar

Horia Petrache

To the best of my knowledge and as understood by the student in the *Research Integrity and Copyright Disclaimer (Graduate School Form 20)*, this thesis/dissertation adheres to the provisions of Purdue University's "Policy on Integrity in Research" and the use of copyrighted material.

Approved by Major Professor(s): Kemple

Approved by: Ricardo Decca

Head of the Graduate Program

11/10/2011

Date

**PURDUE UNIVERSITY  
GRADUATE SCHOOL**

**Research Integrity and Copyright Disclaimer**

Title of Thesis/Dissertation:

Characterization and Measurement of Hybrid Gas Journal Bearings

For the degree of Doctor of Philosophy

I certify that in the preparation of this thesis, I have observed the provisions of *Purdue University Executive Memorandum No. C-22, September 6, 1991, Policy on Integrity in Research*.\*

Further, I certify that this work is free of plagiarism and all materials appearing in this thesis/dissertation have been properly quoted and attributed.

I certify that all copyrighted material incorporated into this thesis/dissertation is in compliance with the United States' copyright law and that I have received written permission from the copyright owners for my use of their work, which is beyond the scope of the law. I agree to indemnify and save harmless Purdue University from any and all claims that may be asserted or that may arise from any copyright violation.

Tom Marquis Lawrence

\_\_\_\_\_  
Printed Name and Signature of Candidate

11/19/11

\_\_\_\_\_  
Date (month/day/year)

\*Located at [http://www.purdue.edu/policies/pages/teach\\_res\\_outreach/c\\_22.html](http://www.purdue.edu/policies/pages/teach_res_outreach/c_22.html)

CHARACTERIZATION AND MEASUREMENT OF HYBRID GAS JOURNAL  
BEARINGS

A Dissertation  
Submitted to the Faculty  
of  
Purdue University  
by  
Tom Marquis Lawrence

In Partial Fulfillment of the  
Requirements for the Degree  
of  
Doctor of Philosophy

December 2011  
Purdue University  
Indianapolis, Indiana

To my beautiful and patient wife. When I first told you that I wanted to undertake this adventure I was very afraid that you would think that I was crazy. But instead you encouraged the folly.-You stood by me, supported me, and helped me in every way. We will never get back the afternoons, weekends, evenings that I spent away from you in my studies. My only prayer is that we together will be rewarded for your sacrifice.

I also need to mention our family and friends. They too lost something by my extended absence. Let us hope there is enough time to make it up.

## ACKNOWLEDGEMENTS

When I first considered this marvelous adventure, I spoke first to Professor Marvin Kemple to ask his advice. To his credit, he tried in every humane way to talk me out of it. Having failed in that, he never failed me again as he became my advisor, mentor, and friend.

I also would like to thank my thesis committee that had to endure my “painful” presentations and read my epic thesis. Without your help and recommendations it would have been much less than it is.

I would also like to acknowledge the U.S. Army Research Development and Engineering Command who provided a portion of the funding supporting the work contained herein under contract W911W6-06-C-0058.

## TABLE OF CONTENTS

	Page
ABSTRACT .....	viii
CHAPTER 1. INTRODUCTION AND BACKGROUND .....	1
1.1. Overview.....	1
1.2. The Journey.....	5
1.2.1. Beginnings Of The Journey - A Map To The Cross Roads.....	5
1.2.2. The Cross Roads.....	6
1.2.3. Stuck at the Cross Roads - Extendibility of CFD Experiment Results .....	14
1.3. Crossing the Road - a New Approach .....	16
1.3.1. CFD Microscope Examination of the Development of Pressure Waves .....	16
1.3.2. Examination of Mass Addition Compensation .....	19
1.3.3. $W/pA$ vs $h-c$ Scans to Study Hydrostatic Gas Journal Bearings .....	21
1.3.4. Determination of the Maximum Attainable Hydrostatic Bearing Efficiency .....	23
1.3.5. Complex Shape of the Hydrostatic Radial Deflection Versus Load Capacity Curve and the “Near Surface Effect” or Static Instability Region ...	24
1.3.6. Back to Extendibility and Similitude .....	25
1.3.7. Examination of the Near Surface Effect with the CFD Microscope.....	27
1.4. Summary, and Scope of the Work Presented.....	30
1.5. Bearing Geometry .....	34
CHAPTER 2. GAS BEARING TESTING .....	38
2.1. Test Methods.....	38
2.1.1. Gas Bearing Test Stand .....	38
2.1.2. Method for Measurement of Mass Addition, Volumetric Flow, and Permeability.....	47
2.1.3. Static Flight Height Versus Load Testing.....	53
2.2. Static Bearing Test Results .....	56
2.2.1. Some Terminology Used in Testing.....	56
2.2.2. Prototype Bearings and Shafts Tested .....	59
2.2.3. Test Results.....	63
2.2.4. Observations, Conclusions, and Discussion of the Results.....	66
CHAPTER 3. THE CFD LABORATORY .....	78
3.1. Overall Computational Scheme .....	78

	Page
3.2. Dimensionless, Quasi Linear, Flux Isolated Reynolds Equation.....	82
3.2.1. Consolidated Reynolds Equation.....	84
3.2.2. Flux Isolated Reynold's Equation .....	87
3.2.3. Discretization and Solution of the Reynolds Equation .....	89
3.3. CFD Methods for Fixed Displacement Hydrostatic Bearings.....	94
3.3.1. CFD Method .....	94
3.3.2. Pressure Solution Examples and Integration of Net Hydrodynamic Force .....	97
3.3.3. Sweeping Experiments by Flight Height .....	108
3.3.4. Effect of Increasing Grid Resolution .....	110
3.3.5. Effect of Increasing the Sweep Increment .....	111
3.3.6. Mapping in the $h$ - $c$ Plane .....	112
3.4. CFD Methods for Fixed Displacement Hydrodynamic and Hybrid Bearings.....	119
CHAPTER 4. CFD RESULTS.....	123
4.1. Hydrostatic Bearing Gap Pressure Distributions.....	123
4.2. Replication of Prototype Bearing Static Tests.....	126
4.3. Comparison of CFD Calculation to Test Results .....	133
4.3.1. Mass Addition .....	135
4.3.2. Load Capacity $W/pA$ vs. $H$ .....	138
4.4. Comparison of Porous Liner and Feedhole Static Bearings .....	142
4.4.1. Resultant $h$ - $c$ Plane Scans .....	142
4.4.2. Introduction and Definition of Bearing Load Efficiency .....	162
4.4.3. Summary of $W/pa$ vs $h$ - $c$ Scan Results .....	165
4.5. Using The CFD Microscope for Further Study of the Near Surface Effect .....	169
4.6. Hydrodynamic Bearing Results .....	182
4.6.1. Theoretical Expectations - Sommerfeld Long Bearing Solution.....	182
4.6.2. CFD Hydrodynamic Bearing Results .....	185
4.6.3. Hydrodynamic Bearings Under the CFD Microscope .....	189
4.7. Feedhole Hybrid Bearings Results .....	210
4.8. Porous Liner Hybrid Bearing Results.....	222
4.8.1. Overall Results .....	222
4.8.2. Examination Under the CFD Microscope and Characterization.....	224
4.9. Comparison of Hydrodynamic, Hybrid Feedhole, and Hybrid Porous Liner Bearings.....	231
4.9.1. Hydrodynamic Force and Attitude Angle .....	231
4.9.2. Comments on Stability.....	236
4.10. Comparison of Hybrid Bearings to Hydrostatic Bearing Superimposed on a Dynamic Bearing .....	240
4.11. The Metaphysics of Gas Bearings (Dimensionless Analysis) .....	243
4.11.1. "Standard" Dimensionless Variables in the Reynolds Equation.....	245

	Page
4.11.2. Dimensionless Time and the Hydrodynamic Bearing Equation .....	245
4.11.3. Dimensionless Time and the Hydrostatic and Hybrid Bearing Equations .....	247
4.11.4. Metaphysics of Mass Addition used in this Thesis.....	250
4.11.5. <i>Kmeas</i> .....	254
4.11.6. An Ontologically Meaningful Dimensionless Mass Compensation Number.....	255
4.11.7. A Re-Examination of Non-Dimensionalizing the Reynolds Equation .....	260
CHAPTER 5. CONCLUSIONS, HYPOTHESIS, AND DISCUSSION .....	268
5.1. Conclusions and Hypothesis from Analytical Work.....	268
5.2. Conclusions from Testing .....	271
5.3. Conclusions from CFD Experiments.....	272
5.3.1. Overall CFD Conclusions .....	272
5.3.2. Static (Hydrostatic) Testing Conclusions .....	272
5.3.3. Rotating Bearings .....	278
5.3.4. Pressure Wave Development.....	282
5.4. Examination Of Local Dimensionless Dynamic Similitude Numbers .....	292
5.4.1. Mach Number of the Shaft Surface .....	294
5.4.2. Knudsen Number.....	295
5.4.3. Reynolds Number, Taylor Number, Bearing Speed and Laminar Flow .....	299
5.4.4. Overall .....	306
5.4.5. Final Comments on Speed Limits.....	307
5.5. Summary Conclusions.....	311
CHAPTER 6. FUTURE AND CONTINUING WORK.....	321
6.1. Future Analytical Work.....	321
6.2. Future Testing .....	323
6.2.1. Further Static Tests .....	323
6.2.2. Dynamic Testing.....	324
6.3. Future CFD Work .....	325
6.3.1. Static Bearing Studies .....	325
6.3.2. Rotating Bearings .....	326
LIST OF SYMBOLS.....	328
REFERENCES .....	331
APPENDICES	
Appendix A Derivation And Discretization Of Reynolds Equation For Hybrid Gas Journal Bearing.....	341
A.1. Summary.....	341
A.2. Continuity of a Fluid Element in the Bearing Gap.....	344
A.3. Dimensionless Version.....	357
Appendix B Discretizations of the Reynolds Equation .....	363
B.1. Substitution of Q for $P^2$ .....	363



	Page
B.2. Discretization by Term.....	365
B.3. Reynolds Equation .....	367
B.4. Residual Error Tests .....	368
Appendix C Observations On Poiseuille Flow .....	372
C.1. Flow through a Channel.....	372
C.2. Application to Mass Addition .....	375
Appendix D Graphical Presentation of Experimental Data.....	378
D.1. $W/pA$ vs $h$ .....	378
D.2. $W/pA$ vs $H$ .....	381
D.3. $W/pA$ vs modified $H$ .....	384
D.4. Volumetric Flow vs Pressure by Load.....	385
D.5. Bearing Flow Rates vs Pressure and Clearance.....	390
D.6. Mass Flow Rate vs $(Pop)^2$ .....	404
D.7. Stiffness Factor $s(h)$ vs $h$ .....	411
D.8. Curve Fitting of Stiffness Factor.....	416
D.9. Summary Tables.....	419
Appendix E Literature Search Outline Of Gas Journal Bearing Progress ....	420
E.1. Conformal gas journal bearings .....	420
E.2. Hybrid, hydrodynamic, grooved, and noncircular gas journal bearings.....	423
E.3. Hydrostatic bearings .....	430
VITA .....	432

## ABSTRACT

Lawrence, Tom Marquis. Ph.D., Purdue University, December 2011.  
Characterization and Performance of Hybrid Gas Journal Bearings. Major  
Professor: Marvin Kemple.

This thesis concentrates on the study of hybrid gas journal bearings (bearings with externally pressurized mass addition). It differs from most work in that it goes back to “basics” to explore the hydrodynamic phenomena in the bearing gap. The thesis compares geometrically identical bearings with 2 configurations of external pressurization, porous liners where mass-addition compensation is varied by varying the liner’s permeability, and bushings with 2 rows of 6 feedholes where the mass-addition compensation is varied by the feedhole diameter. Experimentally, prototype bearings with mass-addition compensation that spans 2 orders of magnitude with differing clearances are built and their aerostatic properties and mass addition characteristics are thoroughly tested. The fundamental equations for compressible, laminar, Poiseuille flow are used to suggest how the mass flow “compensation” should be mathematically modeled. This is back-checked against the experimental mass flow measurements and is used to determine a mass-addition compensation parameter (called  $K_{meas}$ ) for each prototype bushing. In so doing, the methodology of modeling and measuring the mass addition in a hybrid gas bearing is re-examined and an innovative, practical, and simple method is found that makes it possible to make an “apples-to-apples” comparison between different configurations of external pressurization. This mass addition model is used in conjunction with the Reynolds equation to perform theory-based numerical analysis of virtual hybrid gas journal bearings (CFD experiments). The first CFD experiments performed

use virtual bearings modeled to be identical to the experimental prototypes and replicate the experimental work. The results are compared and the CFD model is validated. The ontological significance of appropriate dimensionless similitude parameters is re-examined and a, previously lacking, complete set of similitude factors is found for hybrid bearings. A new practical method is developed to study in unprecedented detail the aerostatic component of the hybrid bearings. It is used to definitively compare the feedhole bearings to the porous liner bearings. The hydrostatic bearing efficiency (HBE) is defined and it is determined that the maximum achievable hydrostatic bearing efficiency (MAHBE) is determined solely by the bearing's mass addition configuration. The MAHBE of the porous liner bearings is determined to be over 5 times that of the feedhole bearings. The method also presents a means to tune the  $K_{meas}$  to the clearance to achieve the MAHBE as well as giving a complete mapping of the hitherto misunderstood complex shapes of aerostatic load versus radial deflection curves. This method also rediscovers the obscure phenomenon of static instability which is called in this thesis the "near surface effect" and appears to be the first work to present a practical method to predict the range of static instability and quantify its resultant stiffness fall-off. It determines that porous liner type bearings are not subject to the phenomenon which appears for feedhole type bearings when the clearance exceeds a critical value relative to its mass-addition compensation. The standing pressure waves of hydrostatic and hybrid bearings with the 2 configurations of external pressurization as well as a geometrically identical hydrodynamic bearing are studied in detail under the methodology of the "CFD microscope". This method is used to characterize and identify the development, growth, and movement of the pressure wave extrema with increased hydrodynamic action (either increasing speed or increasing eccentricity). This method is also used to determine the "cause" of the "near surface effect". A gedanken experiment is performed based on these results which indicates that a bearing with a "stronger aerostatic strength" component should be more stable than one with a low aerostatic strength component. Numerical instability "speed

limits” are found that are also related to the hydrostatic strength of the bearing. The local conditions in the standing waves are characterized in terms of their local Mach number, Knudsen number, Reynolds number, and Taylor Number. It is concluded that low eccentricity bearing whirl can be attributed to the off load-line orientation of the bearing load force caused by the overlay of the hydrodynamic bearing standing wave onto the hydrostatic bearing wave of the hybrid bearing, whereas it is hypothesized that aperiodic and random self-excited vibration which occurs at high eccentricity, as reported in the literature, is probably due to shock waves, turbulence, near surface effect, and slip at local areas of the standing wave.

## CHAPTER 1. INTRODUCTION AND BACKGROUND

### 1.1. Overview

The research done in this thesis arose from a need to design a bearing capable of operating at speeds on the order of magnitude of 100,000 RPM and at ambient conditions of up to 400°C. This is consistent with the trends in advanced rotating devices which are for faster, smaller, more robust devices. These trends are enabled or (forgive the pun) “supported” by gas bearings which offer a high temperature, lubrication-free, very low friction, no-wear alternative to “traditional” contact bearings.

The concept of a journal bearing where a shaft (journal) is supported by a closely fitting bushing with a “lubricating” fluid in the bearing gap (volume between the OD of the shaft and ID of the bushing) is a very old one. However, theoretical study of the hydrodynamics of how lubricating films “support” sliding surfaces does not appear until the first half of the 20<sup>th</sup> century with the emergence of tribology as a “new” technological discipline. Typically journal bearings relied on filling the bearing gap with an incompressible lubricant (oil or water) but it was also known that theoretically, at least, a compressible fluid could be used. For example if air is used as the lubricating fluid, our atmosphere becomes a vast reservoir of lubricant so that a gas (air) bearing can be considered “lubrication free”. Also it known that the torsional drag of a journal bearing is proportional to the lubricating fluid’s viscosity. Since air has a viscosity on the order of magnitude of 1/10,000<sup>th</sup> that of oils, a gas bearing by comparison would be virtually frictionless. Unfortunately, the load bearing pressure established by the

hydrodynamic action within the bearing gap of the lubricating fluid is also proportional to its viscosity. And thus until the latter half of the 20<sup>th</sup> century the concept of a gas bearing was viewed as something of a curiosity and not thought to have practical application. The study of hydrodynamic gas journal bearings was taken up in earnest circa the 1960's with the advent of the computer and broad use of numerical analysis. Since then, air bearings are widely used and appear, in fact, to be the only practical bearing alternative in very high speed devices. Gas journal bearings are generally semi-empirically custom designed for specific applications with the underlying design detail being considered highly proprietary. Globally, different universities and research centers support gas bearing programs which produce a high volume of published academic work.

Thus, if one needs a gas journal bearing there is little alternative but to start a program joining in the adventure of learning how gas journal bearings work, that is, to join in the yet incomplete study of the gas dynamic phenomena in the bearing gap, starting with, of course, what is currently known of the phenomena. This thesis concentrates on the study of hybrid gas journal bearings (bearings with externally pressurized mass addition). In particular it goes back to basics to study the 'aerostatic' component of the gas dynamics (caused by the external pressurization) in the bearing gap and how it combines with the rotational hydrodynamic action in the bearing gap to produce the interaction force between the shaft and the bushing that is commonly called the load bearing capacity. The purely hydrostatic gas journal bearing is an interesting and important topic all unto itself that has, in the opinion of this writer, been too long neglected. This thesis introduces a new methodology to characterize hydrostatic journal bearings. It uses this method to examine the much misunderstood complex relationship between the radial deflection and the aerostatic load capacity of the hydrostatic bearing. New knowledge is added to the relationship between mass addition compensation and the bearing clearance and their effect on the

aerostatic load bearing capacity and stiffness. This method also enables the “tuning” of the clearance to the mass addition compensation to achieve optimum aerostatic load capacity. It is demonstrated that this method predicts the conditions for the onset of a static instability region, predicts its range, and quantifies the expected stiffness fall off. In order to gain a more fundamental causal knowledge of the complexities of the gas dynamics within the bearing gap and their affect on the load bearing force, the thesis introduces another technique of examining the pressure wave in the bearing gap in detail (dubbed the CFD microscope). This method is used to determine the “cause” of the so-called static instability region in terms of the pressure wave development. This thesis also presents the most thorough and detailed (found to date) examination and characterization of the development of the pressure waves for the hydrodynamic bearing, hydrostatic bearing, and hybrid bearings with porous liner type and feedhole type mass addition configurations. It examines the extent to which the hybrid pressure waves can be viewed in terms of a hydrodynamic pressure wave being superimposed on the hydrostatic pressure wave as well as the extent that the hybrid bearing force can be predicted by the vector addition of the aerostatic bearing force and the hydrodynamic bearing force. A practical method is demonstrated to express mass addition compensation in an “apples-to-apples” way between different external pressurization configurations and an ontologically meaningful dimensionless similitude factor is determined for the mass addition compensation. This leads to what is felt to be the first apples-to-apples comparison between a feedhole configuration and a porous liner configuration. It is found that the hybrid porous liner configuration has significantly higher load capacity than a comparable hydrodynamic bearing or a hybrid bearing with a feedhole configuration due to its high aerostatic component.

Mostly, it is felt that this thesis provides a much needed fundamental re-examination of the hybrid gas journal bearing that can be used as a foundation

for further studies correlating hybrid bearing “performance” to the gas dynamics within the bearing gap.



## 1.2. The Journey

### 1.2.1. Beginnings Of The Journey - A Map To The Cross Roads

Several efforts were started in parallel to accomplish our objectives. On the empirical side, a test rig was designed and built along with prototype gas journal bearings designed to have externally pressurized mass addition into the bearing gap through either a porous bushing or through feedholes in the bushing (Chapter 2). Simultaneously, on-going literature searches were performed to seek information about the progress in gas journal bearings from commercial sources, experimental studies, and theory-based numerical analysis (computational fluid dynamics CFD). A summary of the literature search is presented in Appendix E. And lastly, based largely on the information of the literature search, software was written to predict the performance of gas journal bearings using theory-based numerical calculations or, in other words, to perform “CFD experiments” (Chapter 3).

The empirical effort resulted in a thorough study of the mass addition characteristics and bearing load capacity versus radial deflection for the prototype bearings being operated at varying levels of external pressurization (operating pressure) and bearing clearances in a hydrostatic mode (non-rotating). The complete results are in sections 2.2 and Appendix D. On the computational side, CFD calculations were made to predict the performance of virtual gas journal bearings which were mathematically modeled to be identical to the prototype bearings. CFD numerical experiments were run to replicate the actual experiments performed on the prototype bearings. The numerical results were found to be in good agreement with the experimental results and it was concluded that the CFD numerical methodology had thus been “validated” (sections 4.2 and 4.3).

### 1.2.2. The Cross Roads

What was the next step? Logically it would be to apply all the knowledge gained in the previous steps (empirical experimentation, CFD experimentation, and literature search - commercial and academic) to provide the guidance for postulating the design of a bearing that would meet the (ever changing) requirements of an application. On the other hand, synergistically, often the application design can also be modified to accommodate optimization of bearing performance. So that application design also needs fundamental gas bearing knowledge. It was at this point that a crossroads was reached.

The test rig and developed software provide the capability to perform both empirical and CFD experiments on specific bearing designs. But how can these capabilities be used to optimize the design of an actual bearing application? The CFD methodology can at best be described as numerical experimentation (hence the term CFD experiments is used in this thesis). They provide no optimization capability aside from costly trial and error. In other words, while the effort to that point had produced much general “information” about gas journal bearings, it produced little “causal” knowledge as to why one type of bearing might have better performance under some operating conditions than a different bearing. Questions presented themselves. What is the role of the bearing clearance? Is it better or worse to have more or less restrictive mass addition (compensation)? Are porous liners always better than feedhole bearings? What is the role of the bearing aerostatic characteristics in its hybrid performance? Is stronger aerostatic stiffness good or bad?

The literature review indicated that a fair assessment of the “progress of gas journal bearings” could be summarized as follows. The modern study of gas journal bearings started in the 1950’s with the advent of the computer and its application to theory-based numerical analysis. The “early explorers” started

their investigations using both empirical experimentation and theory-based numerical analysis on the subject of quasi-static hydrodynamic or “self-acting” gas journal bearings (rotating with no pressurized mass addition). These early explorers sought to understand the aerodynamic phenomenon that occurs in the bearing gap of a rotating journal bearing that creates a pressure wave that generates a net interactive force between the bearing’s shaft and its bushing when radial displacement occurs. This early work discovered that quasi-static solutions of the pressure distribution in the bearing gap found by solving the Reynolds equation for isothermal, laminar, compressible, viscous, 2-dimensional flow matched experimental data in terms of load capacity. Some of these early works featured pressure mappings and cross section contours of the pressure distributions indicating how the hydrodynamic pressure wave developed based on increasing speed and/or increased radial deflection [1][2][3]. Integrating this pressure distribution about the bearing gap resulted in the net hydrodynamic interaction force that is most often called the “bearing load capacity”. Unfortunately, due to the lack of computational power, these pressure distribution mappings and contours describing the hydrodynamic pressure wave development in these early works was “sketchy” and often hand drawn. Solving the quasi-static load bearing capacity is an incomplete description of the hydrodynamic gas journal bearing’s performance as it was well known that these bearings are subject to self-excited instabilities. Marsh [4] is generally credited with developing a theory-based computational method for predicting the onset speed of the most common fractional speed whirl instability circa 1965. Marsh [4] showed that the transient term of the Reynolds equation must be included in rotor dynamic calculations. Marsh showed that assuming that the shaft center follows a circular orbit enables making a local linearization to the pressure field for small dynamic motions which can be used to determine the speed of the onset of whirl instability of a rotor in a fixed gravitational field (the standard assumption).

From this point forwards, it can be generalized that papers reporting results of theory-based numerical analysis or CFD experiments had a distinct template which is:

- 1) Statement of the Reynolds equation and some description of the numerical technique used to solve the bearing gap pressure distribution.
- 2) Discussion of the methodology used to perform rotor dynamic analysis predicting the stable operating zones of the bearing.
- 3) Presentation of the results in terms of dimensionless parameters.
- 4) And, finally, some conclusions based on the results.

In our literature search no evidence was found of anyone going back and “examining”, for example, the detail of the shape and development of the pressure wave within the bearing gap even though vastly improved modern computing power makes this possible. In the CFD experimentation template the emphasis is on rotor dynamic analysis which uses only the integrated interactive bearing force. In this thesis we use the CFD microscope to examine in detail the characteristics and development of the underlying pressure wave in the bearing gap.

In the 1970's CFD experimental work expanded to include “hybrid” gas journal bearings where external pressurization is applied to the bearing gap by either feedholes through the bushing or the use of a porous liner for the bushing. From the literature search, hybrid bearings are first introduced in Powell's [1] 1970 *Review of the progress of gas lubrication*. In it he states, “In considering the static load capacity of externally pressurized gas journal bearings all flow is assumed to be pressure induced and surface velocity effects are neglected. This condition occurs in practice when the shaft is stationary. The load capacity and stiffness of the stationary bearing are called the ‘aerostatic’ load capacity and stiffness and they can be simply measured by applying load to the stationary shaft and measuring the resulting radial deflection. Rotation of the shaft modifies the gas flow in the bearing clearance and the resulting pressure changes affect

the load capacity and stiffness of the bearing. When the velocity effects become significant the bearing is said to be operating in a hybrid mode and bearings designed to operate in this mode are called hybrid bearings.” Powell further summarizes his 1964 experimental work of the operation of a hybrid bearing (mass addition configuration is not mentioned) that, “It was shown that as the shaft accelerated under conditions of constant radial load the shaft centre moved progressively to positions of lower eccentricity and out of line of the applied load.”

The quasi-static Reynolds equation for a purely hydrostatic gas journal bearing is, in general, more difficult to solve than the case of the hydrodynamic bearing as it is dependent on the method of external pressurization applied to the bearing gap. Both equations contain a Poiseuille flow term for flow in the axial direction. For the rotating hydrodynamic bearing a relatively straight forwards Couette flow term is added for flow in the radial direction based on the no slip difference in surface speeds between the rotating shaft and the bushing. The combination of these terms results in a non-linear equation and the dimensionless statement of this equation results in the dimensionless bearing number  $\Lambda$  which is often called the dimensionless speed and is proportional to the shaft rotation speed.

For hydrostatic bearings an additional mass addition term is required based on the mode of external pressurization (porous liner or feedhole). This results in simultaneous differential equations occurring for the “restricted” or compensated flow between the high pressure reservoir used for external pressurization and the bearing gap. For porous liner type mass addition it is fairly universal to assume Darcy flow whereas differing lines of semi-empirical orifice flow theory are used for feedhole bearings. The dimensionless form of these terms creates another “bearing number” for the external pressurization. For the porous liner type hybrid bearings this bearing number is proportional to the porous liner material’s permeability and inversely proportional to the liner thickness. For feedhole fed bearings this bearing number is proportional to the feedhole radius and various

semi-empirical “discharge coefficients”. For porous liner bearings the mass addition term is applied to every element in the bearing gap whereas for feedhole bearings the mass addition is considered a point source and is applied only to the elements corresponding to the configured feedhole locations. Unlike the universally accepted bearing number,  $\Lambda$ , corresponding to the shaft rotation speed, there is no universally used dimensionless mass addition parameter for either porous liner bearings or feedholes. And when these terms are combined with the axial flow Poiseuille term, they form a challenging non-linear differential equation. A comparison is made of these mass addition terms in Appendix E.2.

The template used for the theory-based numerical analysis of hybrid journal bearings is the same CFD experiment template just described except that the additional mass addition term is tacked onto the Reynolds equations creating both a speed bearing number and a compensation related (mass addition) bearing number. The published results and observations seldom however either vary or state the compensation bearing number. If one can solve this combined Reynolds equation for the hybrid bearing then, one of course can solve the Reynolds equation for the hydrostatic case when the rotational bearing number is zero. However, in the literature search Z-S Liu et al.’s 2009 paper [5] and Y.S. Chen et al.’s 2010 work [6], are the only theory-based numerical works found that present the pressure distribution mapping and development of the hydrostatic pressure wave form or examine the radial displacement versus radial load capacity for the hydrostatic bearing. Both of these papers use 2 rows of 8 feedholes for external pressurization.

Overall papers from the late 1960’s to present, are mostly very long on rotor dynamics and almost never examine the nature and development of the pressure wave in the bearing gap which is implicit in their solutions and is the prime mover behind all the rotor dynamics. C-C Wang and C-K Chen [7] in their 2003 work, *Bifurcation analysis of externally pressurized porous gas journal bearings*, site in

the introduction a 1978 Holmes work as possibly being the first paper to deal with aperiodic behavior in journal bearings which Wang and Chen characterizes as follows: "In this work it is concluded that moderate levels of unbalance and a high eccentricity ratio led to aperiodic response at speeds above a certain threshold value. This aperiodic behavior was not the classic light load instability, which is characterized by a half-speed component and moderate eccentricity." Wang and Chen in their introduction review a continuum of experimental work previous to their 2003 paper that reports periodic, subperiodic, and chaotic motion of short hydrodynamic bearings. Wang and Chen then site their own previous work in 2001 as presenting the bifurcation analysis of a rigid rotor supported by a gas-film bearing as showing the "existence of a complex dynamic behavior comprising the periodic and subharmonic response of the rotor centre."

In their 2003 work they then perform bifurcation analysis of a gravity loaded externally pressurized porous gas journal bearing. Again in their introduction they express their interest in extending their bifurcation analysis methodology to analyzing externally pressurized bearings. They state "It is known that the main advantages of an externally pressurized bearing are high load and stiffness, even at zero speed. When the effect of speed is taken into account in the analysis, the bearing will have improved load and stiffness". And thus they proceed doing bifurcation analysis based on the bearing gap pressure solutions from the dimensionless Reynolds equation with an additional mass addition term based on Darcy flow of the air through the porous bushing. Their results are perhaps best summarized in their abstract where they state: "The analysis reveals a complex behavior comprising periodic and quasi-static responses of the rotor centre. This paper shows how the dynamic behavior of systems of this type varies with changes in rotor mass, squeeze number, and bearing number." (No mention is made of the assumed dimensionless porous mass addition number they used which is based on the porous liner permeability.) "The results of this

study contribute to a further understanding of the non-linear dynamics of gas-lubricated, externally pressurized, porous rotor-bearing systems.”

Thus one can make several observations about “the progress of gas journal bearings” as seen from the perspective of theory-based numerical analysis. The early work presented the template of using the dimensionless Reynolds equation for quasi-static pressure solutions to determine the net hydrodynamic interaction force between the bushing and the shaft which is then used as the basis for rotor dynamic analysis of various bearing systems under gravitational load and to determine the stable operating ranges of a particular bearing system. This technique which can only be generalized as a CFD experimentation technique is then applied to various bearing configurations. For hydrodynamic bearings it is applied to different bushing shapes, shaft grooves, etc. with stability analysis for a specific application such as for rigid rotors, flexible rotors, rigidly mounted bearings and flexibly mounted bearings, etc. This CFD experimental template is also applied to hybrid bearings having both rotation and external pressurization through either feedholes or porous liners. The experimental work however, shows that rotor dynamics is increasingly more complicated than that found by rotor dynamic analysis based on the assumptions of periodic motion. And hence the CFD experimentalists improve the stability analysis techniques in the CFD experimental template to mirror the more complicated rotor dynamics found in experimental work. Much of the CFD experimental work from about 2001 onwards, can be viewed as a “redo” of earlier CFD experiments on various bearing configurations using improved rotor dynamic techniques (notably the orbit technique or bifurcation) [7], [8], [9], [10], [11], [12],[13], [14].

In later works spawned mostly by micro gas turbine development programs, it will be seen in certain circumstances namely very short, high speed bearings that the bearing performance predicted by CFD experiments failed to match experimental results. These later CFD method failures were not the result of the



rotor dynamic analysis but rather were founded in the gas dynamics within the bearing gap. The CFD template's quasi-static pressure solutions are based on the Reynolds equation using the assumptions of isothermal, laminar, no-slip-flow. In several cases [15] (2005) and [16] (2010) the deviations are attributed to slip-flow regimes within the bearing gap and are "corrected" by adding slip-flow corrections to the Reynolds equation. The possible need for slip-flow modifications is mentioned by Powell [1] as early as 1970 but the need to apply these corrections does not emerge in the literature search until 2005. In 2008 Teo et al. [17] attribute unexplained self-excited vibrations of very short hybrid gas bearings with axial external pressurization to the bearing gap to the Lomakin effect which is micro bursts of vorticity and is known to exist for short seals (invalidating in this case the laminar flow assumption).

### 1.2.3. Stuck at the Cross Roads - Extendibility of CFD Experiment Results

This brings us back to the cross roads. Most of the theory-based numerical work can be described as CFD experiments reporting load capability and stability ranges for a long list of different bearings in different bearing application configurations (rigid rotor, flexible rotor, two identical rigidly mounted gas bearings, etc.) How extendable are these results? What causal knowledge was gained by these experiments? How can we apply this knowledge? What do we really know?

The value of experimental (empirical or computational) results is greatly enhanced if they are presented in the context of a *complete set* of ontologically meaningful dimensionless variables and similitude parameters that makes their results extendable to a whole class of bearings sharing the same similitude parameters. The Wang and Chen [7] work on bifurcation analysis of a porous liner was described. In this work the results were presented in terms of varying the dimensionless speed  $\Lambda$  and the dimensionless squeeze term  $\sigma$ , but the results were also given in terms of the dimensional rotor mass in kilograms. In the Reynolds equation they pose a dimensionless mass addition factor  $\Lambda_p$  which is based on the porous liner's permeability and presumably all of their results are dependent on their specific (unstated) choice of  $\Lambda_p$ .

The most troubling aspects of these results (and similar work) are their presentation of mass addition and use of the eccentricity ratio,  $\varepsilon$ , as an apparently extendable independent variable without regard to a specific clearance. In section 4.4 it will be seen that the hydrostatic bearing efficiency which is the dimensionless load of a hybrid bearing is very dependent on tuning the clearance to the dimensional mass addition parameter. How then can we extend the results for a specific hybrid bearing CFD experiment which uses a

specific clearance and mass addition parameter (particularly since it is often the case that the values of these critical parameters are not stated)?

This topic is taken up in detail in section 4.11, *The metaphysics of gas bearings (dimensionless analysis)*, and in sections C.3 and B.3.4. The results of these sections conclude, in short, that the bearing number (dimensionless speed)  $\Lambda$ , the eccentricity ratio  $\varepsilon$ , along with the slenderness ratio  $L/D$  are in fact a complete set of ontologically meaningful dimensionless similitude parameters for *purely self acting hydrodynamic journal bearings*. However, when the evolution of theory-based numerical analysis and CFD experimentation is applied to hybrid bearings and a mass addition term was tacked onto the Reynolds equation, the similitude was lost. In Appendix C.3 the similitude metaphysics of all of the hybrid CFD experimental work in the literature search was examined and the conclusion was reached that all of the hybrid bearing results and their conclusions can only be taken in their weakest sense and cannot in general be thought to be extendable. Which brings us back to our cross roads. What do we actually know about hybrid gas journal bearings?

For example, commentary in some of the work implies that it is generally known that porous hybrid bearings have higher load capacities than orifice compensated hybrid bearings and that increased aerostatic stiffness improves stability and performance. Do we know this? In the only work found in the literature search that actually compares a porous liner hybrid bearing to different configurations of feedholes for a geometrically similar hybrid journal bearings, the results [18] indicate a mixed outcome with 5-row (of eight feedhole) orifice fed bearings outperforming porous liner bearings and vice-versa in terms of stability depending on the mass addition terms used. No results are presented for load capacity.

### 1.3. Crossing the Road - a New Approach

Thus, at this juncture a new approach was taken to studying hybrid gas journal bearings. Rather than continue the trial and error pattern of running CFD experiments on different specific bearing configurations with weak results caused by dubious extendibility, the decision was made to utilize the developed CFD capability to run CFD experiments and use the CFD microscope to reestablish an understanding of the underlying fundamental hydrodynamic phenomena in the bearing gap.

#### 1.3.1. CFD Microscope Examination of the Development of Pressure Waves

The early explorers of gas journal bearings took considerable effort to examine the shape of the hydrodynamic pressure wave to understand the underlying “causes” as to why and how the net hydrodynamic interaction force between the shaft and the bearing not only increased with speed but changed in attitude angle (angle to the load line) with increased speed. The results at this CFD microscope level were sketchy. As far as can be determined (excepting reference [5]), virtually no effort has been made to describe or characterize the hydrostatic pressure wave or the combined hybrid pressure wave. This thesis corrects this. Section 4.6.2 and 4.6.3 present results for the development of the hydrodynamic pressure wave. Section 4.7 presents the pressure wave development of hydrostatic and hybrid bearing with feedhole mass addition while section 4.8.2 presents the pressure development for hydrostatic and hybrid bearings with porous liner mass addition. In each case the characteristic pressure wave extrema points are identified and their intensity and shift in location are determined as functions of radial deflection, rotation speed and mass addition parameter. These are thoroughly discussed in section 5.3.4. To our

knowledge this approach is unique to this thesis and provides the most thorough examination thus far found.

This is important given that experimental work has found that rotor dynamics are very complicated with aperiodic and random vibration. What is the underlying cause of these self-excited vibrations? Advanced rotor dynamic stability theory has helped identify the ranges of stable operation (generally in terms of speed and rotor mass) but what is the underlying cause of these instabilities? References have already been mentioned where the cause of discrepancies between empirical experimental results and CFD experimental prediction has been attributed to local conditions within the pressure wave (bearing gap height and local pressure) which cause conditions such as rarefied gas conditions or bursts of vorticity that invalidate the template assumptions of no-slip, laminar flow in the Reynolds equation. It seems very likely that that the development of the extrema in the pressure waves would be a good predictor indicating the conditions when “chaotic” or unstable conditions would be expected. For example, it was observed that for the hydrodynamic bearing that two sub-atmospheric pressure lobes develop at an angular location slightly downstream from the location of the minimum bearing gap (minimum flight height). Increasing the hydrodynamic “action” by either decreasing the minimum flight height (increasing the eccentricity) or increasing the rotation speed causes these lobes to become increasingly more sub-atmospheric to and move in their axial locations toward the ends of the bearing where the pressure is atmospheric. How sub-atmospheric and how close to the ends of the bearing can these pressure minima reach before the “real life” situation would resolve itself with bursts of vorticity as in the Lomakin effect? In general the question that begs to be asked is, “How intense can these local wave extrema become before something ‘has to give’ in terms of the underlying no-slip, laminar flow assumptions?” When might these local conditions result in self-excited vibration due to shock waves or turbulence? When might the local conditions reduce the

bearing load capacity and stiffness due to slip-flow? (A discussion of the local conditions found and what they mean in terms of local Knudsen number, Reynolds number, Taylor number and Mach number is contained in section 5.4). Thus it is seen that this type of approach is an important first step in understanding gas bearing performance from a causal approach based on gas dynamics theory.

### 1.3.2. Examination of Mass Addition Compensation

Another way in which this “at the cross roads” approach differs from the standard template is its re-examination of ontologically meaningful similitude parameters concerning gas journal bearings with external pressurization. This thesis is one of very few works that both measures and predicts mass addition to the gas journal bearings. Virtually all the standard template CFD experiments use disparate theory-based mass-addition factors for feedhole mass addition and porous liner mass addition and seldom present any mass flow results. Experimental data in terms of mass flow is also very sparse. Appendix C explores the theoretical expectations of mass addition versus the pressure difference between a high pressure reservoir and a low pressure reservoir for viscous, laminar, compressible flow (Poiseuille flow) through a narrow channel. We find that it is reasonable to expect a linear relationship between the difference of the square of the pressures ( $P_{high}^2 - P_{Low}^2$ ) and the mass flow rate. In section 2.2.3 this expectation is used to re-examine the empirical mass addition test data for the prototype feedhole and porous liner bearings tested and it was found that the mass addition data for both the feedhole and porous liner bearings was, in fact, well modeled by a linear dimensional mass addition factor (called *Kmeas* in this thesis) over a broad range of pressure differences. The conformance of the mass-addition data to a linear relationship using a constant *Kmeas* for each prototype bushing is tabulated and graphed in Appendix D.6 and the *Kmeas* factors are summarized in figures 2-21 and 2-22.

This was important for two reasons. Firstly, use of *Kmeas* as the mass addition compensation factor appears to be the first time that a practical parameter is used that makes possible an actual apples-to-apples comparison between different modes of mass addition such as porous liners and feedholes. Only one other work (Su and Lie [18]) found in the literature search attempts this. Their presented results and conclusions are very weak and are purely in the nature of

CFD experimental data observations for different specific bearings and the porous liner bearings and feedhole bearings use completely different mass addition parameters leaving the reader with no basis for directly comparing them.

The second reason is that *Kmeas* completely linearizes the Reynolds equation for hydrostatic bearings with the substitution  $Q=P^2$ . This makes it numerically economical to generate pressure wave solutions over a broad range of parameters. As was mentioned, only two papers ([5] and [6]) provide information on the development and shape the hydrostatic pressure wave and that information is sparse. And both of those examples deal only with feedhole bearings with 2 rows of 8 feedholes. Sections 4.1 through 4.5 present the form of the hydrostatic pressure waves for porous liner and feedhole externally pressurized bearings and how these pressure waves develop as the radial displacement is increased. This is not only important in its own right but is important as a similar analysis is made for purely hydrodynamic bearings in section 4.6 so that a basis is established to compare how the wave form for a hybrid bearings can be seen as an overlay of the hydrodynamic wave form onto the hydrostatic wave form as is done in sections 4.9 and 4.10. In the literature only one other relatively new paper (2009) by Zhang and Xu [5] attempts such a separation. While their paper deals only with a feedhole hybrid bearing with two rows of 8 feedholes it has very similar results to those presented in this thesis for feedhole bearings with two rows of six feedholes.



### 1.3.3. $W/pA$ vs $h-c$ Scans to Study Hydrostatic Gas Journal Bearings

Our work with purely hydrostatic bearings is important in that there does not appear to be any previous work doing a detailed study on the load capacity versus radial deflection characteristics of hydrostatic journal bearings. Reading between the lines in discussions of hybrid bearings one finds that there apparently are many misconceptions about this relationship. The relationship is either assumed to be linear or non-linear with bearing stiffness increasing at small flight heights and falling off at large flight heights. In fact, the work presented in this thesis demonstrates that this relationship can take a variety of forms. (This is discussed in detail in section 4.2.) The most surprising result was that for feedhole bearings the maximum load capacity often does not occur when the bearing is grounded (at zero flight height or bearing gap height) but occurs at a small flight height and decreases rather than increases with increased radial displacement. This surprising, non-intuitive result, was thought, while writing this thesis, to be a “new discovery” and was labeled the “near surface effect” in section 4.2.

The linearization of the hydrostatic Reynolds equation and the postulation of a mass addition compensation factor applicable to both feedhole bearings and porous liner bearings ( $K_{meas}$ ) was put to good use to develop a new methodology called  $W/pA$  versus  $h-c$  scans. In these “scans” approximately 400 CFD experiments are performed for a hydrostatic bearing configuration at different fixed values of  $K_{meas}$  and operating pressure (pressure of the high pressure reservoir used for external pressurization) by varying the bearing clearance, and radial deflection (eccentricity, minimum flight height, minimum bearing gap etc.). Each pressure solution was then integrated to determine the load capacity,  $W$ , for the bearing at the experiment’s value of clearance, eccentricity, mass addition compensation factor ( $K_{meas}$ ) and operating pressure. A dimensionless load capacity  $W/pA$  is created by dividing the load capacity by

the product of the nominal bearing area ( $LxD$ ) and the operating pressure. This is an often used common sense approach for the dimensionless load capacity as it is intuited that either increasing the bearing area or the operating pressure would increase the load capacity. In section 4.4.2., however, a stronger statement is made where it is shown that for a hydrostatic bearing  $pA$  is the maximum load capacity possible and thus  $W/pA$  is actually the hydrostatic bearing load efficiency. When the 400  $W/pA$  data points are used to create an interpolated surface in the plane of the minimum flight height versus bearing clearance ( $h-c$  plane), the result is a graphic that illustrates the hydrostatic bearing performance over a broad range of operational possibilities.

This is important because as far as can be told from the literature search and discussions with several air bearing manufacturers there is no knowledge of the relationships between the bearing clearance, the mass addition compensation, and the hydrostatic bearing load capacity and stiffness (although there is a great deal of interest in this topic).

#### 1.3.4. Determination of the Maximum Attainable Hydrostatic Bearing Efficiency

***mass addition configuration = maximum attainable hydrostatic bearing efficiency***

***attaining maximum hydrostatic bearing efficiency = tuning mass-addition compensation to clearance***

The results presented in sections 4.4.1 to 3 were surprising and meaningful. They showed that a hydrostatic bearing of a particular external pressurization configuration (such as 2 rows of 6 feedholes or a porous liner) with a specific  $L/D$  ratio, operating pressure, and mass addition compensation factor has a specific maximum achievable bearing efficiency that depends only on the bearing clearance. Moreover if the mass addition compensation factor is increased, the value of the maximum achievable bearing efficiency is unaffected but that the bearing clearance must be increased to achieve it. This means that there is no clearance value nor any mass compensation factor value that optimizes the bearing performance but rather that the optimization requires the right combination of clearance and mass addition compensation (tuning the mass addition compensation to the clearance or vice versa). Further, the results demonstrate that the value of the maximum achievable bearing efficiency is dependent only on the bearing's mass addition configuration. And thus it is possible to make quantifiable conclusions and comparisons about the maximum achievable bearing efficiency of different mass addition configurations. For example, in this thesis it was concluded that the maximum achievable bearing efficiency for a porous liner bearing with  $L/D$  of 2.67 and operating pressure of 100 psig is 0.39 while for a feedhole bearing of 2 rows of 6 feedholes it is only 0.072. (These results are summarized and discussed in section 4.4.3).

### 1.3.5. Complex Shape of the Hydrostatic Radial Deflection Versus Load Capacity Curve and the “Near Surface Effect” or Static Instability Region

Examining the shape of the  $W/pA$  surface in the  $h-c$  plane explains the variations in the shape of the curves of dimensionless load versus eccentricity ratio. Each such curve is a cross section of the  $W/pA$  surface taken at a specific clearance and a specific mass compensation so the shape of the curve depends on where the cross section is taken. It also gives clues as to the mysterious “near surface effect”. The maximum achievable bearing efficiency for porous liner bearings is always located somewhere where the minimum flight height is zero (so that the bearing is grounded) while for the feedhole bearings it is located at coordinate in the  $h-c$  plane where the minimum flight height ( $h$ ) is greater than zero. Again, it is found that this non-zero value of minimum flight height increases as optimized combination values of mass addition compensation and clearance are increased. Thus again, whether or whether not a load versus eccentricity curve will demonstrate the near surface effect depends on the mass addition compensation and clearance for which the curve represents.

### 1.3.6. Back to Extendibility and Similitude

The knowledge gained thus far, naturally brings in to question the value and extendibility of template CFD experiments regarding hybrid bearings. A prime example would be the paper of Su and Lie [18] which is the only work found that attempts to compare porous liner hybrid bearings to feedhole hybrid bearings performance over a range of “feeding” parameters where a different feeding parameter is used for the feedhole bearings than is used for the porous liner bearing and the bearing clearance is presumably kept constant but not stated. The paper’s results are presented in dimensionless threshold load capacities for whirl instability for ranges of dimensionless speeds and different values of the orifice feeding parameter and the porous feeding parameters. The threshold load capacities are based on stiffness and damping coefficients of which (we now know) the hydrostatic load capacity is a large contributor. How do we interpret or extend these results without knowing the mass addition parameters that correspond to the maximum achievable hydrostatic bearing efficiency? In section 4.9.2, a gedanken experiment is presented that gives credence to the intuition implied in some papers that a stronger hydrostatic component of load capacity increases bearing stability. The Su and Lie paper [18] concludes that in some ranges of the orifice feeding parameters that the porous hybrid bearing is more stable while in other ranges the 5 row of 8 feedhole hybrid bearing is more stable. Could it be that the work is an elaborate trial and error experiment into hydrostatic bearing efficiencies resulting from varying mismatched mass addition parameters against a constant but unstated clearance?

In section 4.11 *The metaphysics of gas bearings (dimensionless analysis)*, the dimensionless Reynolds equation using the universally applicable mass compensation factor  $K_{meas}$  was studied and a universally applicable, ontologically meaningful dimensionless mass addition similitude parameter was derived. The conclusion is that that this mass addition similitude factor is

proportional to  $Kmeas/c^3$ . When this conclusion is back checked against the  $W/pA$  versus  $h-c$  scans developed for different  $Kmeas$  values the “right shift” of the location coordinate of the maximum achievable bearing efficiency was essentially eliminated. (The “right shift” is where the clearance location of the maximum achievable bearing efficiency increased when  $Kmeas$  was increased.) This means that if the technique used in this thesis to generate the  $W/pA$  versus  $h-c$  scans was modified to create  $W/pA$  versus  $H-Kmeas/c^3$  scans than this single graphic could be used to show the hydrostatic bearing efficiency for a particular mass addition configuration over its entire “design space” independent of clearance and mass addition compensation. *This is indeed a new and powerful tool!*

The mass addition similitude parameter being inversely proportional to the cube of the clearance demonstrates the fatal flaw in the extendibility of results in the hybrid bearing template CFD experiments. The presumption in this template is that results presented in terms of the dimensionless variables  $\Lambda$  (dimensionless speed) and  $\varepsilon$  (the eccentricity ratio) for bearings with mass addition can be extended to geometrically similar bearings with the same  $L/D$  ratio and  $c/R$  ratio without reference to a specific dimensional clearance. This is possible for purely hydrodynamic bearings since  $\Lambda$  is proportional to  $(R/c)^2$ . However for bearings with mass addition these results are not extendable unless it is in the context of an additional mass feeding parameter which is inversely proportional to  $c^3$ .

### 1.3.7. Examination of the Near Surface Effect with the CFD Microscope

Further work is done in section 4.5 to explore the “near surface effect”. In this section the  $W/pA$  versus  $h-c$  scans are used to identify a clearance and mass addition compensation factor combination that amplifies the “near surface effect”. Flight heights were selected that demonstrated the maximum bearing efficiency and the fall off of bearing efficiency with reduction in flight height (rather than the commonly expected increase). Pressure distributions corresponding to these flight heights were placed under the CFD microscope and “cross-sectioned” by integrating various characteristic areas in the pressure distribution to account for cause of the load decrease. It was found that the cause of the near surface effect was a load fall-off when the flight height was very small corresponding to the shape of the pressure plume associated with the feedholes immediately adjacent to the minimum flight height.

All this work was done previous to finding and reading Zhang and Xu’s 2009 paper on *Performance analysis of rotating externally pressurized air bearings* [5]. All other work in the literature follows primarily the template CFD experiment methodology. Zhang and Xu follow a methodology very similar to what is called in this thesis the CFD microscope. In their paper they graphically show the pressure waves for a hybrid bearing using 2 rows of 8 feedholes for the mass addition and a geometrically identical hydrodynamic bearing and show how these waves develop with several “snap shots” of increased speed and increased eccentricity ratios. Pressure profiles are taken in the axial and circumferential directions at various locations in the bearing gap. The results are similar in appearance to those found in section 4.6-4.10 for the feedhole bearing with 2 rows of 6 feedholes.

One interesting factoid emerges from this paper. It has already been noted that when template CFD experiments are run on hybrid bearings that the equivalent hydrostatic bearing was solved as the zero-RPM point on their graphical results.

However none of the papers present the hydrostatic performance of the bearing separately by, for example, showing the load capacity versus radial displacement or the eccentricity relationship for a hydrostatic bearing. Reference [5] is an exception to that. It contains a graph of the load capacity versus eccentricity ratio for the feedhole hybrid bearing with data sets for the various speeds of operation including a zero-RPM curve. Thus here is found the single load versus radial displacement curve for a hydrostatic bearing produced by theory-based numerical analysis in the entire literature search. Interestingly enough it is for a feedhole bearing and it shows a maximum load capacity at an eccentricity ratio of about 0.8 and a light fall-off of load capacity when the eccentricity ratio is increased to 0.9 (the highest eccentricity ratio plotted). In other words, their hydrostatic load versus eccentricity ratio curve is demonstrating the “near surface effect”.

One can speculate that Zhang and Xu also found this result disconcerting as they devote some space to explaining it. They state, “The line with the rectangle(s) shows the load capacity characteristic of the aerostatic bearing. This indicates a phenomenon that does not occur in flat pad configurations of bearings and is termed the static instability region. The static instability region is a ‘load capacity falloff’ that occurs if the bearing is too heavily loaded and the onset of the phenomenon occurs when the operating eccentricity is very high. This phenomenon is also commonly called negative stiffness and should not be confused with pneumatic hammer instability.” The reference used for this information is Stoudt, K. J., *The design of aerostatic bearings*, 1996 p. 119 (Whitestone Business Communications, Nuneaton, UK). So this thesis cannot claim the discovery of the near surface effect which is apparently called the static instability region. The reference for this information could not be found at the time of this writing and thus it is unknown whether the discovery of the “static instability region” is from empirical evidence or numerical work. The suspicion is that it is based on empirical experience. So while this thesis cannot claim new



information on the discovery of the near surface effect, it is still believed that this thesis presents much new causal information for the near surface effect. The  $W/pA$  versus  $h-c$  scans, for example show that porous liner hydrostatic bearings are not subject to this phenomenon and show the regions of  $Kmeas$  and clearance combinations where this phenomenon will occur and predicts the flight height of the maximum load capacity and quantifies the “load capacity fall off”. In section 4.5 the CFD microscope is used to pinpoint the cause of this “instability”.

It might be supposed that this “static instability” is rather obscurely known precisely because previously no theory-based numerical study of hydrostatic bearings appears to have been done. Also “discovery” of the phenomenon by trial and error-type template CFD experiments would not be likely. *One can only suppose the effect of this static load capacity fall off on a rotating bearing with whirl where the minimum flight height location is rotating from feedhole to feedhole. Could it be a cause of some of the chaotic or subperiodic self-excited vibrations reported by the template CFD experiments?*

#### 1.4. Summary, and Scope of the Work Presented

Thus concludes our summary of the scope of the work of this thesis. The cross road has been traversed and this thesis has diverged from the template CFD experimentation that focuses on gravity loaded rotor dynamics back to an examination of the fundamental physics of the gas dynamic phenomena that occurs in the bearing gap of a hybrid gas journal bearing. In particular this thesis appears to be original in studying the much overlooked hydrostatic gas journal bearing phenomena in detail. A practical and useful method of describing mass addition “compensation” from the point of view of the mass addition’s impact on the gas dynamics in the bearing gap as opposed to theoretical predictions based on porous material properties or orifice shapes has been put forward. This compensation factor, derived from gas dynamic theory has been confirmed by experimental results and provides the means for what is thought to be the first “apples-to-apples” comparison of porous-liner type hybrid bearings to feedhole type hybrid bearings. A much needed re-examination of the dimensionless parameters used to provide dynamic similitude to experimental (empirical and numerical) results of gas journal bearings with mass addition is presented and a dimensionless mass addition similitude parameter is found that greatly expands the range of the results. The dimensionless load capacity  $W/pA$  is determined to be *the* static load bearing efficiency. A very practical and efficient methodology is presented that maps the aerostatic load performance of gas journal bearings over their entire design space with ontological similitude ( $W/pA$  versus  $h-c$  scans and  $W/pA$  versus  $H-Kmeas/c^3$  scans). The methodology of placing the pressure waves under the “CFD microscope” in order to “understand” the underlying phenomena behind the hydrodynamic interaction force between the shaft and the bushing, which is the prime mover of rotor dynamics, is re-introduced for what appears to be the first time since the “early explorers” of gas journal bearings used it in the 1960’s to “understand” the underlying phenomenon of purely hydrodynamic bearings. This method is used to identify the development and

movement of the pressure extrema in the pressure waves with increased hydrodynamic activity (rotation speed and eccentricity) for geometrically identical hydrodynamic bearings and hybrid bearings with porous liner-type mass addition and two rows of 6 feedholes-type mass addition over two orders of magnitude of “apples-to-apples” mass addition compensation. Due to the vastly increased computational and graphical power of the modern computer this examination provides much richer detail for the hydrodynamic bearing than was previously possible in earlier work as well providing apparently the first such examination (with the exception of Zhang and Xu [5] who do some similar analysis on feedhole bearings with two rows of 8 feedholes) of hydrostatic gas journal bearings and hybrid gas journal bearings.

These methods when used to examine geometrically identical gas journal bearings with mass addition via porous liners and 2 rows of 6 feedholes resulted in some significant discoveries. It was found that the maximum achievable hydrostatic load efficiency can be quantified and is determined solely by the bearing’s mass addition configuration. It is also demonstrated that the achievement of the maximum hydrostatic bearing efficiency requires the tuning of the bearing clearance to its mass compensation such that increasing the mass compensation requires that the optimum clearance be increased (called the “right shift” of the maximum hydrostatic bearing efficiency on the  $W/pA$  versus  $h-c$  scans). In the studied bearings, the porous liner bearings have a maximum achievable static load efficiency that is 5.42 times that of the bearings with two rows of 6 feedhole bearings. This gives credence to the intuition expressed in some published works that porous liner type bearings have, in general, higher stiffness and load capacity than feedhole bearings.

Also the “static instability region” is re-discovered. It is called the “near surface effect” in this thesis and was originally thought to be a “new” discovery although this effect has been observed previously. Nonetheless this thesis is thought to be the first to determine the cause, range of occurrence, and quantify the “load

capacity fall off” of the phenomenon. Its range of occurrence is determined from the  $W/pA$  versus  $h-c$  when the line delineating the maximum  $W/pA$  versus clearance line (see figure 4-34) leaves the  $h=0$  ordinate. This occurs for the studied feedhole bearings at large clearances above a threshold value that is subject to the already mentioned “right shift”. (The threshold value increases with increased  $Kmeas$  as seen in figure 4-35.) The  $W/pA$  versus  $h-c$  scans also demonstrate that porous liner bearings do not appear to be subject to the “near surface effect” and consequently do not have a “static instability region”. The cause of the of the load capacity fall off was determined by examination of the development of the hydrostatic pressure waves. It is attributable to how the shape of the high pressure plume emanating from the feedholes immediately adjacent to the angular location of the minimum bearing gap develops. (See section 4.5.) In section 4.11 it was determined that using a mass addition factor proportional to  $Kmeas$  and inversely proportional the cube of the bearing clearance (consistent with the dimensionless mass addition similitude parameter) resulted in elimination of the “right shift” in the  $W/pA$  versus  $h-c$  scans. Applying this to the data in figure 4-35 indicates that the threshold clearance for the “onset” of having a “static instability region” for the 2 row by 6 feedholes operating at 100 psig is when  $Kmeas/c^3$  is greater than  $5.4-7.4 \times 10^4 \text{ lb-s}^{-1}\text{-in}^{-3}$ .

In sections 4.5-4.8 the CFD microscope is used to examine the development and characteristics of the pressure waves for hydrostatic and hybrid gas journal bearings with mass addition from porous liners, and with mass addition from two rows of 6 feedholes with the “apples-to-apples” mass-addition compensation factors varying over 2 orders of magnitude as well as for the hydrodynamic pressure wave of the geometrically identical gas journal bearing. The pressure extrema in these waves have been identified as has their development and movement with increased hydrodynamic activity. The build up and movement of these extrema appear to be candidates for the underlying causes of “chaotic” self-excited vibration. In section 5.4 the local Mach (M), Knudsen (Kn), Reynolds

(Re), and Taylor (Ta) numbers are examined within the bearing gap. It was shown in section 4.10 that the pressure extrema for hybrid bearings can be largely seen as the superposition of the pressure waves of the corresponding hydrostatic bearing and hydrodynamic bearing. Their combination creates the interaction force between the bushing and the shaft. For the hybrid bearing the bearing force is nearly identical to the vector addition of the hydrodynamic and hydrostatic bearing forces. It can be hypothesized that the normal to load line component of the hydrodynamic bearing force is the primary driver of periodic bearing whirl. It can also be hypothesized that the subperiodic, aperiodic and chaotic self-excited vibrations found in rotor dynamic studies can be attributed to the break-down of pressure wave extrema along with bearing whirl passing in and out of regions of static instability. If so, understanding these causal relationships requires the kind of “foundational” study of the hydrodynamic activity in the bearing gap presented in this thesis. This writer feels that that this thesis has expanded the fundamental “knowledge” of the gas dynamical phenomena within the hybrid gas journal bearing gap and hopes that these methods will be the basis for further fundamental physical exploration.

### 1.5. Bearing Geometry

In this thesis, all empirically tested prototype bearings and all CFD tested *virtual* bearings had a length of 2" and a nominal bearing diameter of 0.75". Different clearances, operating pressures, speeds, and mass addition modes were tested. The basic mass addition modes tested were Porous Liner (PL) and Feedhole fed (FH) bearings. All the FH bearings had 2 rows of 6 feedholes located 0.350" from each end of the bearing with even angular 60° spacing.

The working space of the gas bearing is the volume of air in the bearing gap. The state of the bearing at any given instant in time is tracked by logging the displacement of the shaft and bushing centers of mass, orientation of the shaft and bushing centerlines (Euler angles of the shaft and bushing centerlines) and velocities of the shaft and bushing centers of mass relative to Cartesian axis defined by the concentric alignment of the bushing and bearing centers of mass and the angular alignment of their centerlines.

Z is chosen as the longitude or *Length* axis, Y is the vertical axis, and X is the orthogonal horizontal axis. Y is called the vertical axis as it is the axis in which fixed loads are applied in the empirical testing and it is the axis in which fixed displacements are imposed in the CFD experiments.

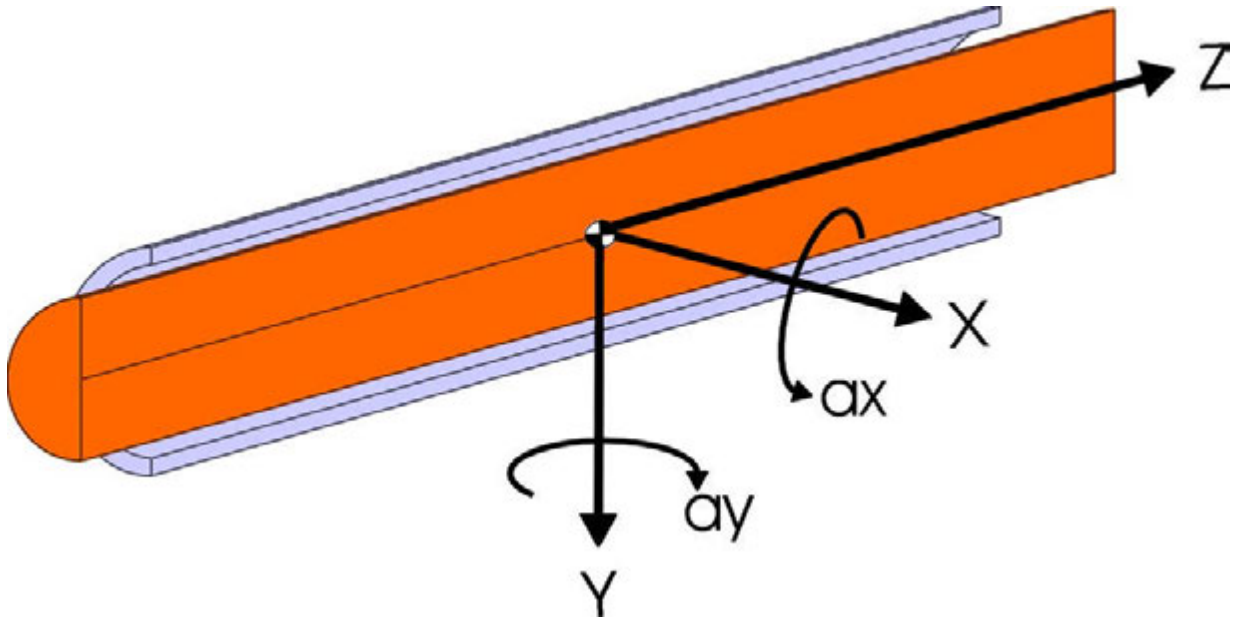


Figure 1-1 Cartesian bearing geometry with axis located at the center of mass of the bushing when the centerlines of the shaft and the bushing are aligned.

The bearing gap height  $h$  is the distance between the surface of the OD of the shaft the ID of the bushing.

Within the bearing gap cylindrical coordinates are used where  $\theta$  is taken from the X axis. By tracking the X and Y translational and angular displacements an eccentricity vector  $\vec{e}$  can be derived for any point along the Z axis that originates on the central axis of the bushing and points towards the central axis of the shaft.

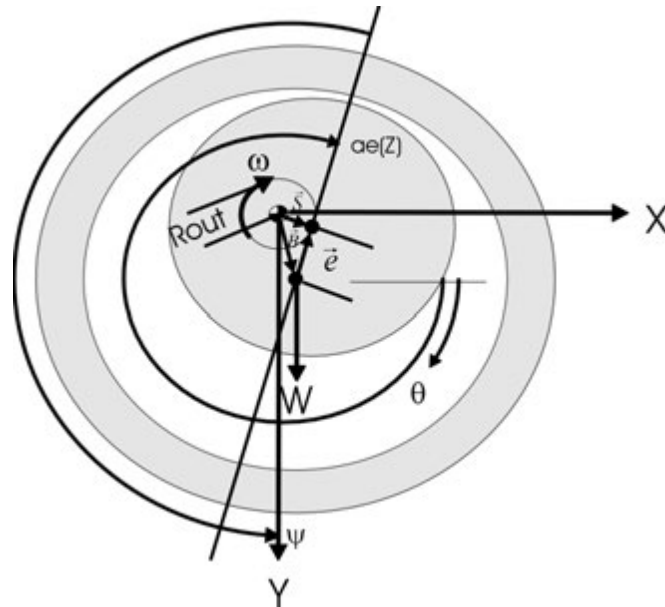


Figure 1-2 Cross sectional view of the shaft and bushing perpendicular to  $Z$  taken at a specified  $Z$  in the bearing.

Figure 1-2 is a fairly standard representation of the bearing gap for a journal bearing with a slight modification that in this representation a provision is made for eccentric shaft rotation with runout of radius  $R_{out}$  which accommodates the possibility of the shaft having an eccentric rotation.

Referring to figure 1-2, if  $\vec{B}$  is the displacement vector of the bushing and  $\vec{S}$  is the displacement vector of the shaft, then the *eccentricity* vector is  $\vec{e} = \vec{S} - \vec{B}$ . A line drawn between the bushing center and the shaft center (at a particular  $Z$ ) will have the magnitude  $e$  which is known as the eccentricity. The clearance of the bearing is a bearing design parameter which is defined as the radius of the bushing minus the radius of the shaft. Thus the bearing gap height at a given  $(Z, \theta)$  location can vary from 0 (grounded bearing) to  $2c$  (bearing grounded  $180^\circ$  from  $\theta$ ). The eccentricity vector as drawn in figure 1-2 (with its tail located on the bushing center) will point to the angular location of the minimum bearing gap.  $\theta$  is the angle around the  $Z$  axis from the  $X$  axis. The angle  $ae(Z)$  is the angle of



the minimum gap indicated by  $\bar{e}$ . It is common terminology to define an *attitude* angle which is the angle of the load from the angle of the eccentricity vector. In the figure 1-2, since it was assumed that  $Y$  would point to the fixed load, the

attitude angle is:  $\psi = ae(Z) - \frac{\pi}{2}$ .

The bearing gap height is  $h = c - e \cos(\theta - ae(Z))$

An eccentricity ratio is commonly defined as:  $\varepsilon = \frac{e}{c}$ .

Thus,  $h = c(1 - \varepsilon \cos(\theta - ae(Z)))$ .

It is also very common to define a dimensionless  $H$  as  $h/c$ .

In this case then:

$$H = 1 - \varepsilon \cos(\theta - ae(Z))$$

## CHAPTER 2. GAS BEARING TESTING

### 2.1. Test Methods

#### 2.1.1. Gas Bearing Test Stand

As noted previously, it was difficult to run the test program parallel to the development of the CFD laboratory as the CFD results were needed to indicate the design of the bearings to be tested. A first test stand was developed on the assumption that a two-bearing system would be tested with loads applied to the shaft. Some brief testing was done trying to rotate shafts between two hydrodynamic bearings. Partly based on these results and partly based on a maturing understanding of the hydrodynamics of gas bearings, it was decided the program would focus on a one bearing system utilizing a hybrid bearing. This bearing would be used in a tethered application, that is, the shaft would have a fixed rotation and the bushing enclosing the shaft would have a fixed load and would have all degrees of freedom of movement except for being constrained against rotation in the Z axis. This led to the abandonment of the first bearing test stand and the design and build of the current test stand.

#### 2.1.1.1. First Bearing Test Stand

The first test stand was built to test a two bearing system of purely hydrodynamic rigidly mounted bearings. The shaft had freedom of movement within the constraints of the bearings and could be loaded with a combination of fixed and dynamic imbalance loads. The eccentric motion of the shaft was measured by using two sets of orthogonal laser vibrometers placed at each end of the bearing.

Hydrodynamic bearings rely on shaft rotation to generate their net hydrodynamic force so that there is no bearing force at zero or low rotating speeds. This causes the start-up problem associated with hydrodynamic bearings.

The shafts used in these tests turned out to have short and dangerous lives as they would freeze up and jam within the initial seconds of operation. Fortunately the test stand was designed to transmit torque to the shaft through a coupling designed to break at low torque providing a “torsional circuit breaker”. A titanium nitride coated shaft was unsuccessfully tried to overcome the start-up problem.

The test stand did successfully demonstrate that the orbit of cylindrical rotating objects could be effectively recorded and measured using the laser vibrometers. Also, the initial tests could be considered successful in that they demonstrated what would *not* work.

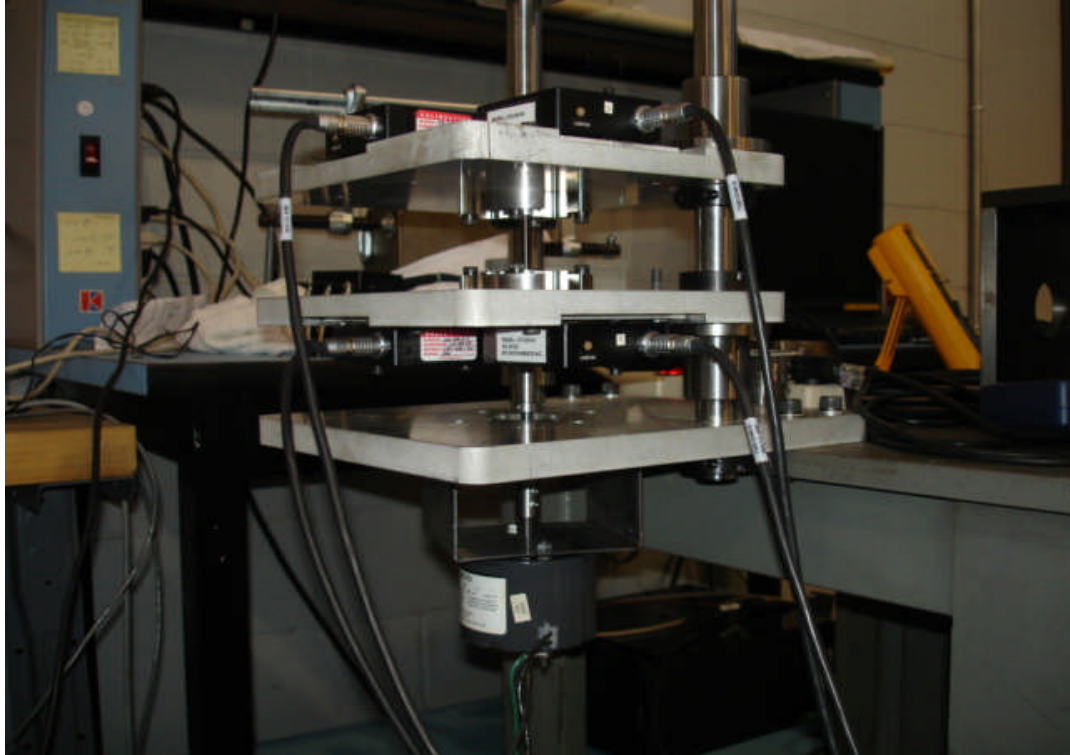


Figure 2-1 The first gas bearing test stand. As shown it is being driven by a slow speed electric motor to calibrate the lasers. In high speed (HS) testing the electric motor is replaced by an air turbine.

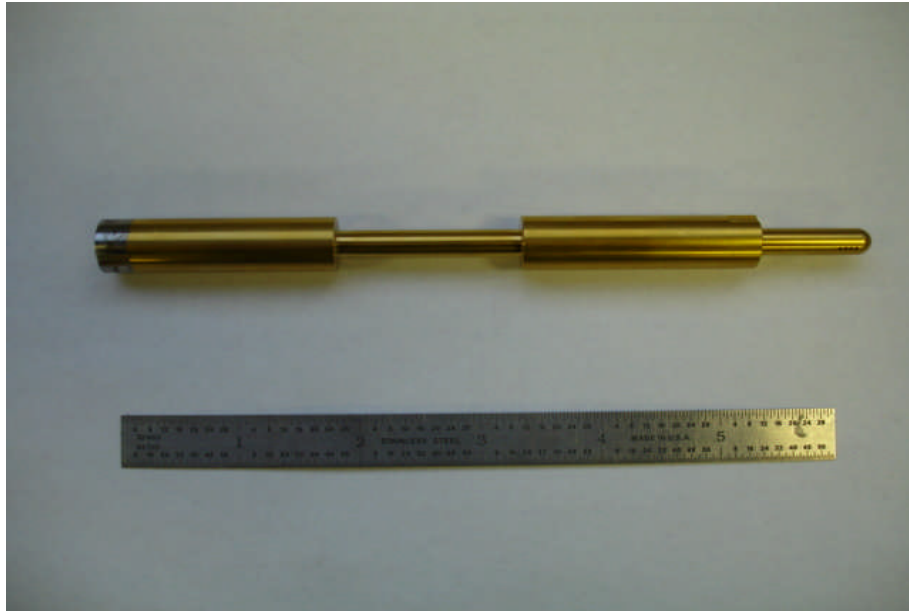


Figure 2-2 Titanium nitride coated test shaft.

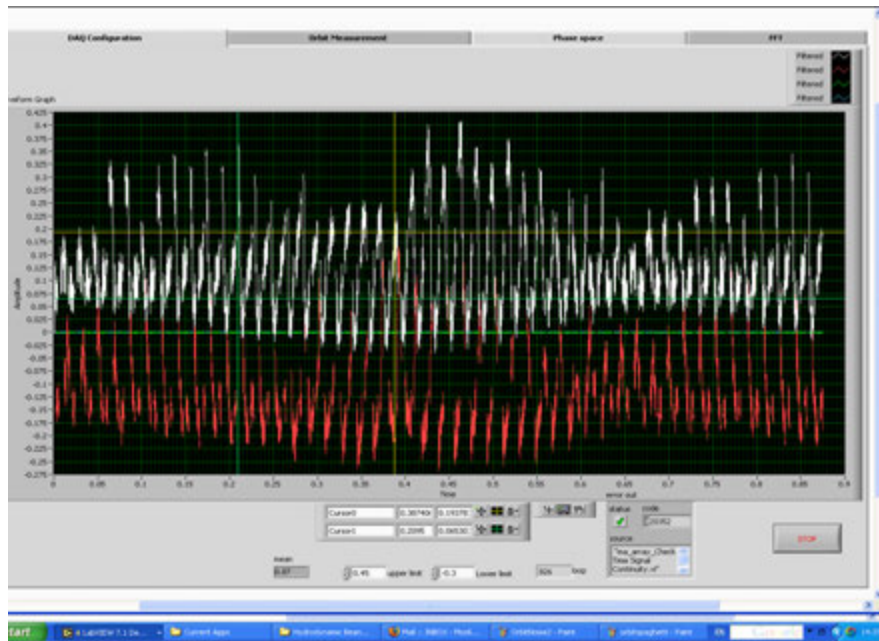


Figure 2-3 X and Y oscillations of shaft as measured by the lasers during HS operation.

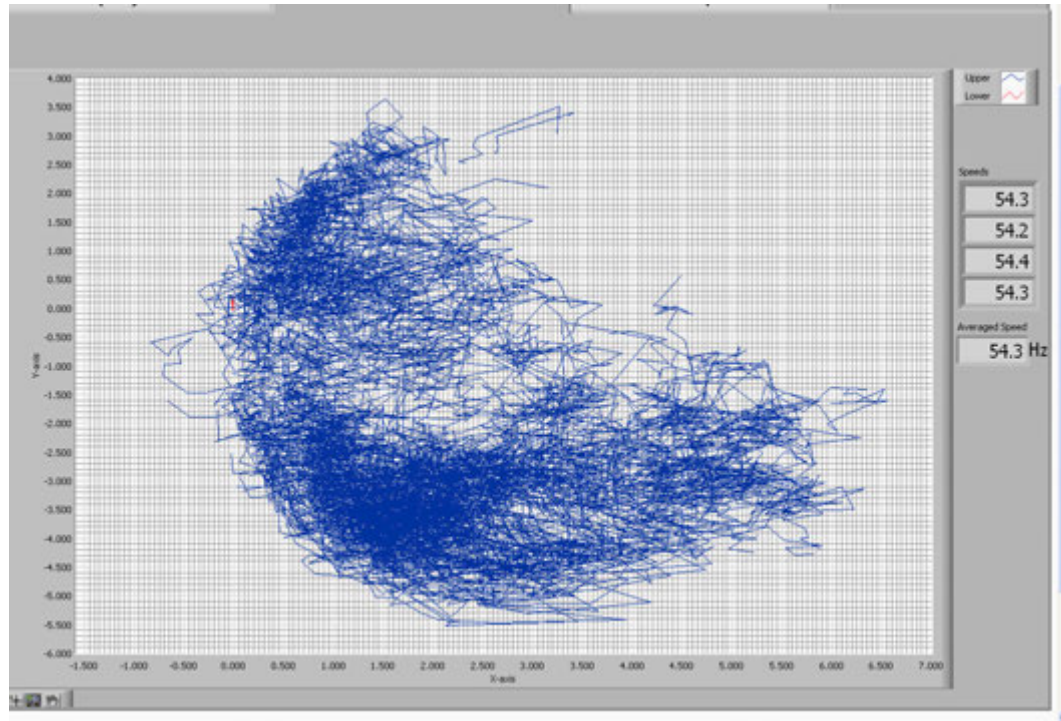


Figure 2-4 Plot of the X-Y oscillations showing very clearly the circular bearing clearance. The pattern suggests that the shaft was bouncing all about the bearing clearance. The unoccupied portion of the bearing clearance circular space is thought to indicate misalignment between the two bearings.

### 2.1.1.2. The Current Gas Bearing Test Stand

The current test stand is designed to test the performance of hybrid gas journal bearing whose bushing is tether mounted to a cantilevered shaft with fixed rotation. The bearing load is a fixed load applied vertically to the bushing. This mimics a bearing in a tethered slip ring application where the device drive shaft supports the slip ring. It should be noted that in this application it is the bushing that is loaded and displaces corresponding to the fixed rotation of the shaft. Thus it is backwards of the traditional bearing problem.

The test stand consists of using standardized stanchions to mount a high speed (HS) intermediate bearing assembly (IBA). The IBA shaft is driven by a HS air turbine on one side and accepts cantilever mounted test shafts on the other side. The IBA shaft thus mimics the drive shaft of a test device. The receiver on the test side of the IBA shaft is made to readily mount test shafts of varying diameters and mount them such that varying degrees of misalignment can be purposely added to create shaft runout.

Below the test shaft are two linear actuators that can be remotely controlled to translate two sets of orthogonal laser vibrometers along the centerline of the shaft. Above the test shaft is a structure that supports a remotely driven motor that adjusts load on the bearing by applying tension on a spring. The bottom of the spring is connected to the top center of the test bushing with a steel cable via a load cell. The test bearing is prevented from rotating on the shaft by a second fixed cable that also has an intervening load cell and attaches to the center side of the bushing. This second load cell measures the torsional drag of the bearing. In addition, a standard Aerodyn gas flow regulation box is used to provide air flow to the hybrid bearing.

All of the controls are designed for remote control and monitoring. In this way the test stand can be run in the spin test bunker where the testing can be monitored by video camera and microphone while the operator is safely located in the control room. For HT operation a small insulated enclosure is fitted over the bearing into which hot air from a regulated heat torch is added.

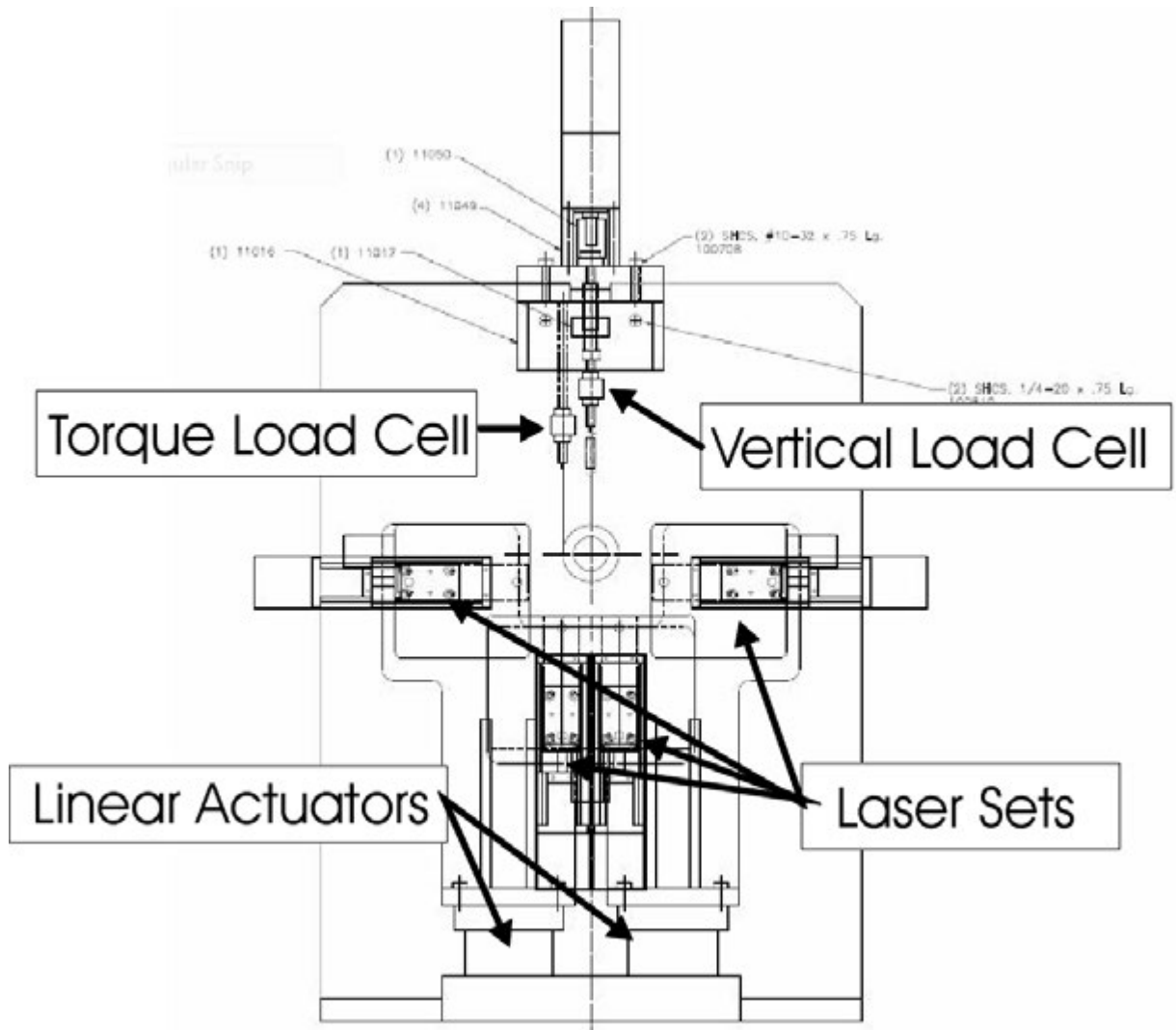


Figure 2-5 Assembly drawing showing a front view of the gas bearing/HSHT slip ring test stand.



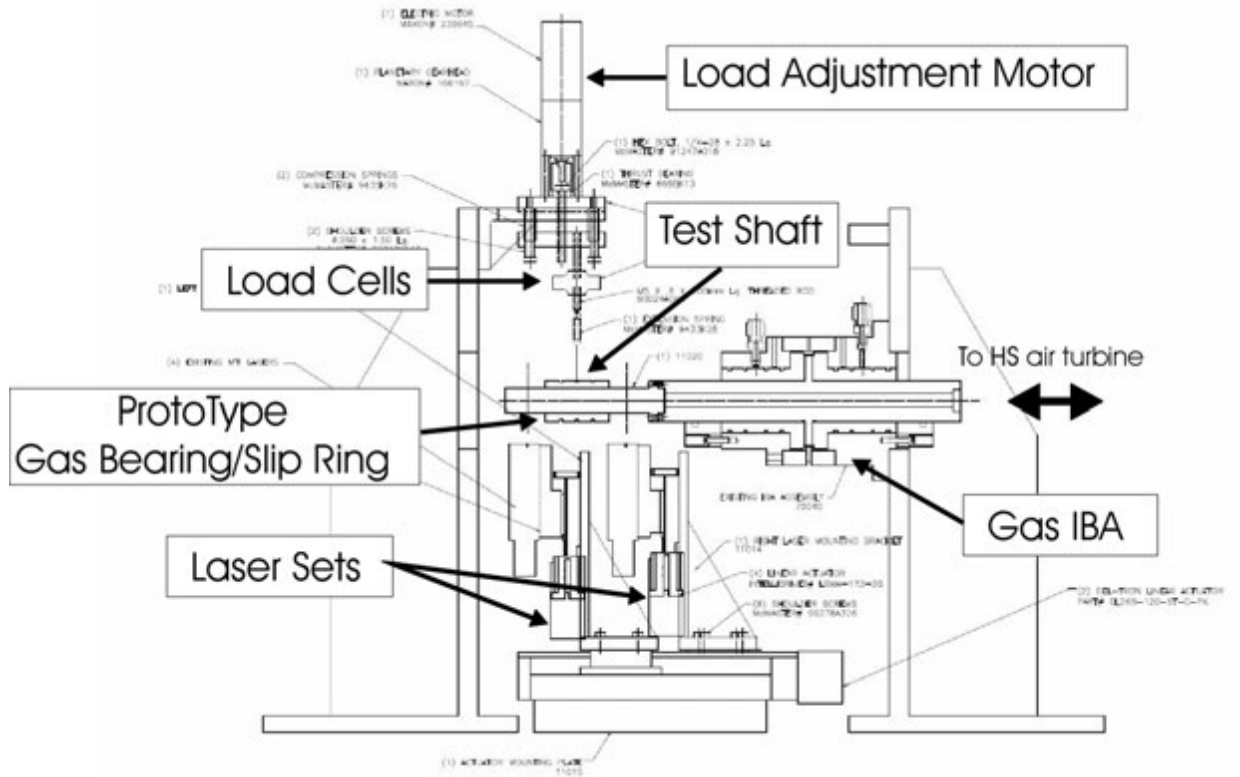


Figure 2-6 Annotated assembly drawing of the side view of the gas bearing test stand.

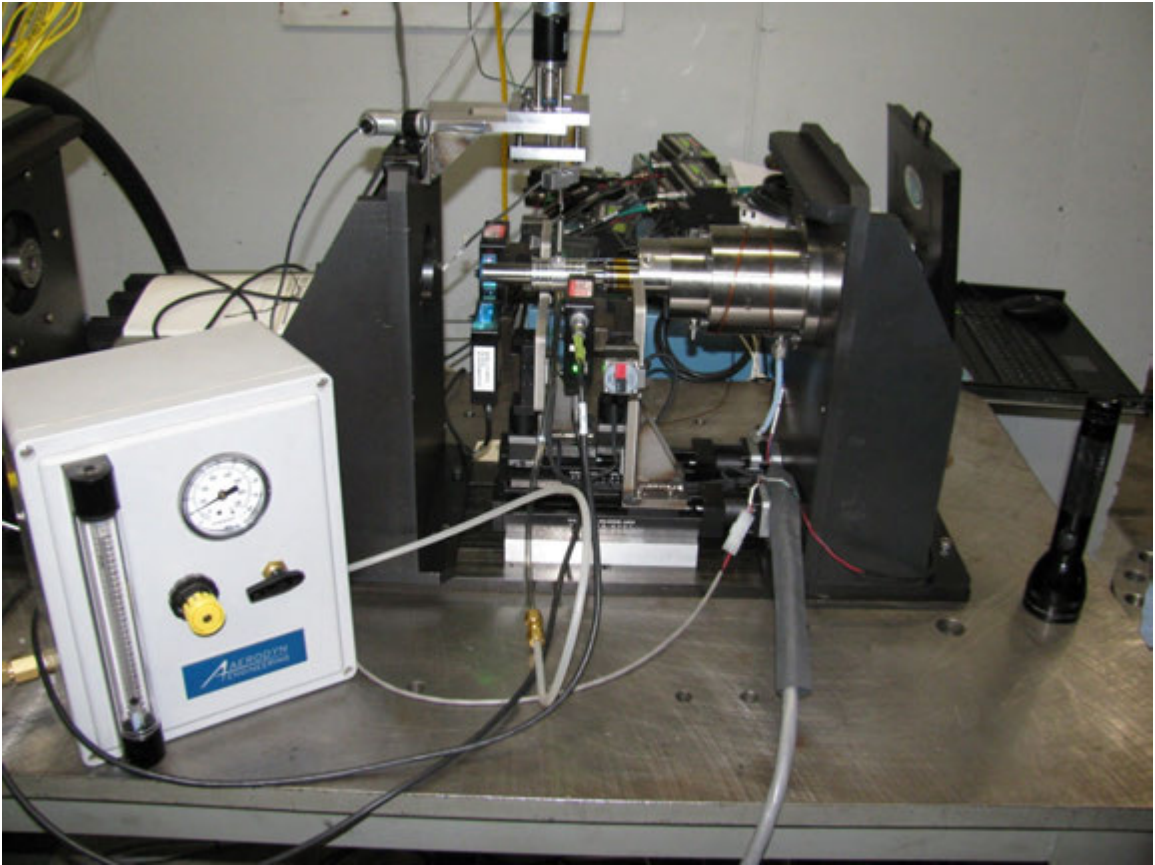


Figure 2-7 The gas bearing test stand.

### 2.1.2. Method for Measurement of Mass Addition, Volumetric Flow, and Permeability

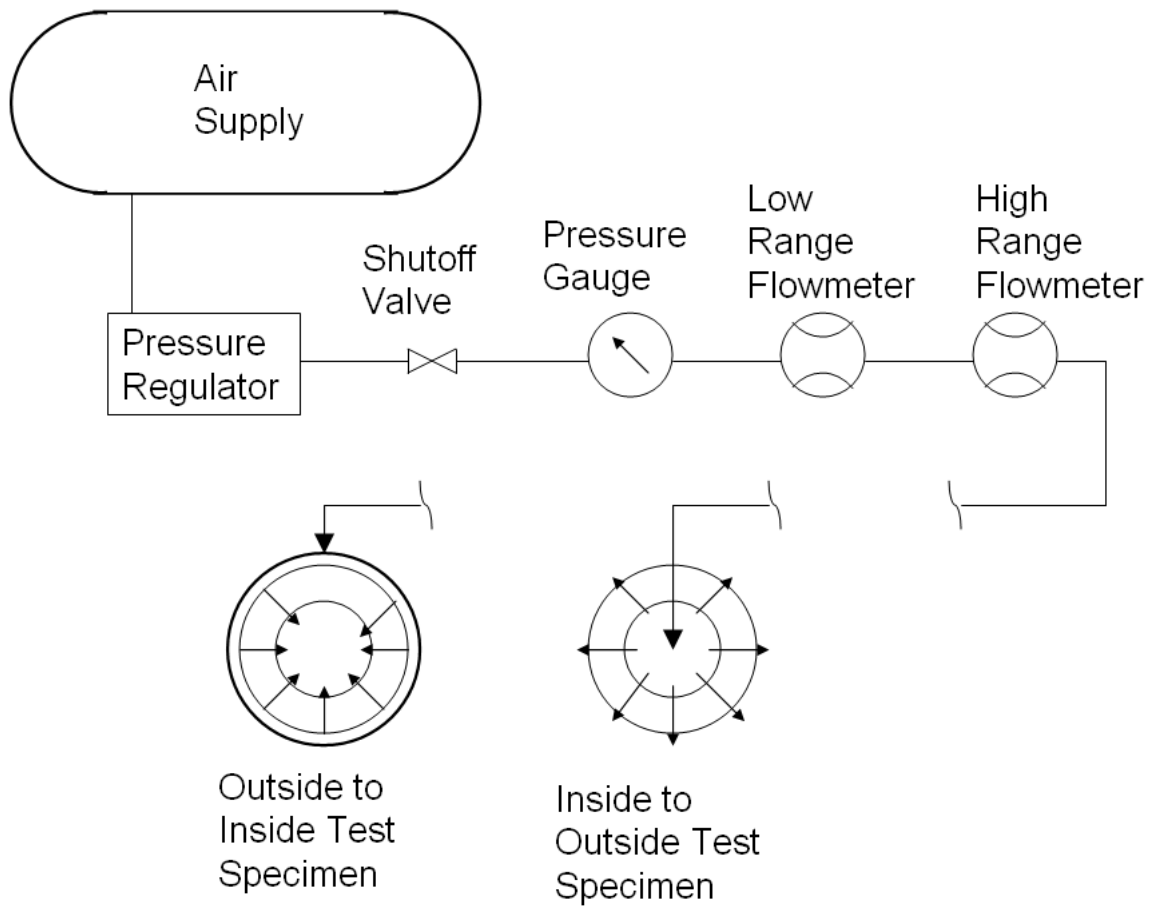


Figure 2-8 Pneumatic schematic of controls and meters used to measure mass addition.

The same method is used to measure and regulate volumetric flow for samples of porous materials, feedhole pressure sleeves, porous material pressure sleeves, and prototype bearings during bearing testing. High pressure (the operating pressure) is applied to one surface of the sample (high pressure side) and then volumetric flow is read as air flows from the high pressure side to the low pressure side. The flow is regulated through a fine tuned flow valve and the pressure and flow rate are recorded on the high pressure side of the sample.

Since the flow is measured on the high pressure side of the sample the mass flow rate is calculated by multiplying the air volumetric flow rate by the density of air at room temperature and the measured operating pressure. This is true even in high temperature applications as the volumetric flow of the air provided to the test specimen is measured by flow meters at room temperature.

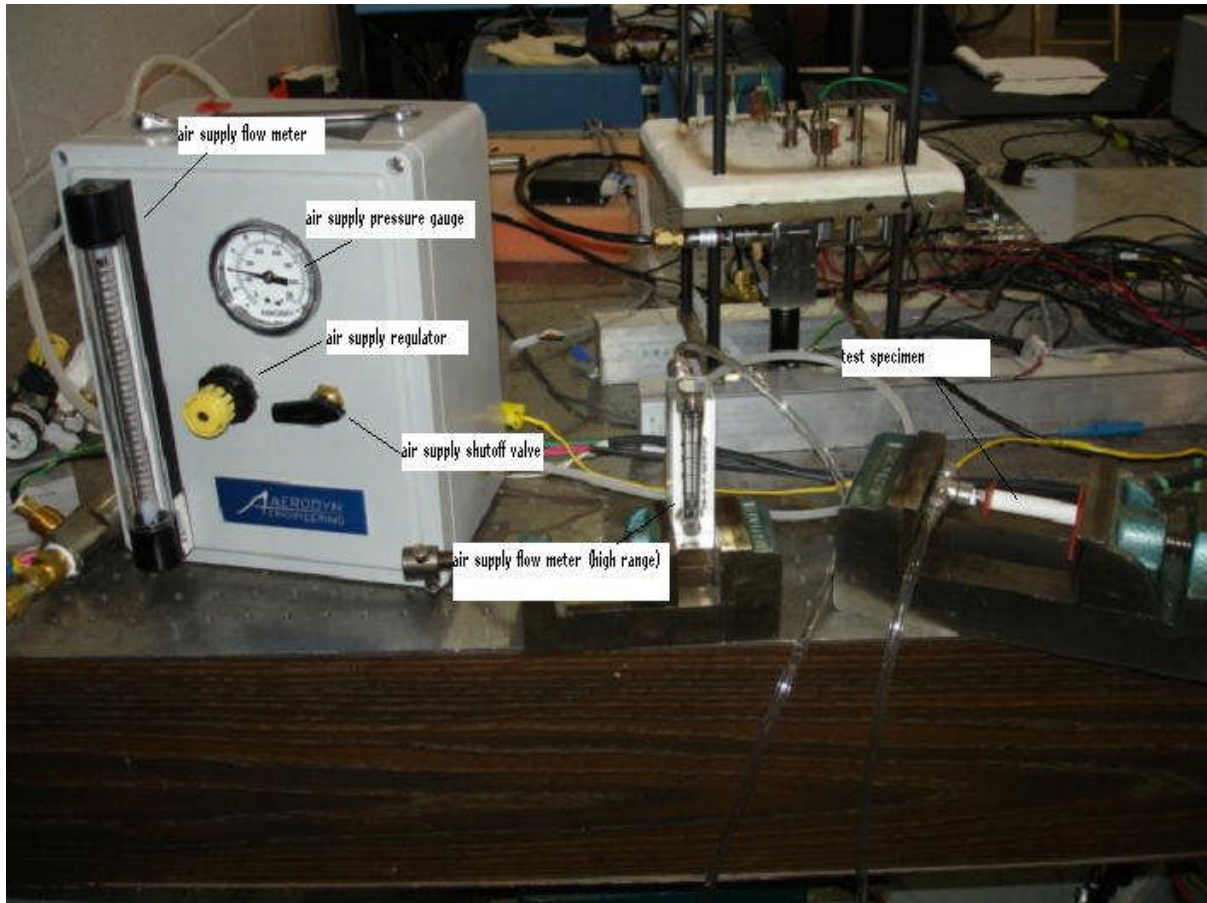


Figure 2-9 Flow rate testing of a porous  $\text{TiB}_2$  cylinder (left) using the inside out method and of a porous graphite New Way air bearing liner (right) using the outside in method.

The flow meter in the flow regulation box is an omega flow meter that claims 3% accuracy. The flow measurements have been among the most reproducible in the test program.

The Omega meter uses a complicated formula for interpretation between millimeter float measurements and flow in LPM. As can be seen from the graph provided the conversion is very nearly linear except for a small kink at very low readings.

## Omega Flowmeter: FL-5571G-NV

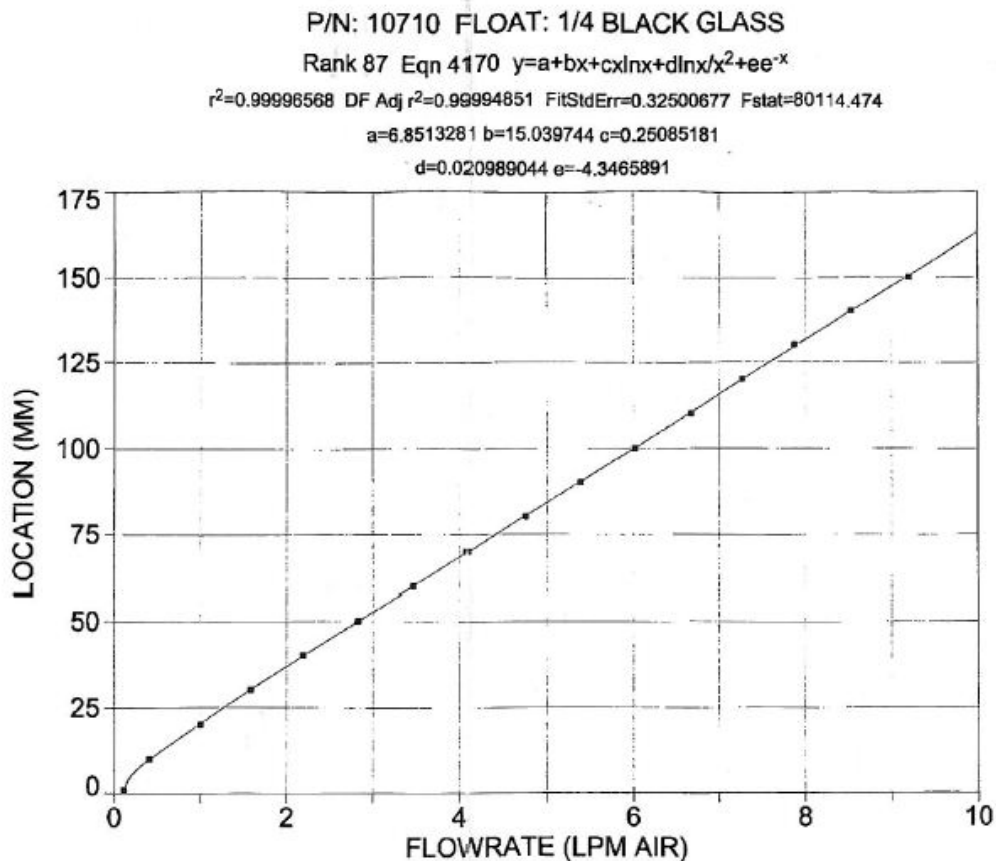


figure 2-10 Calibration curve and formula provided by Omega.

Data reduction and use was greatly streamlined by formulating a kinked-line equation that simulated the Omega calibration equation.

Formula used:

$$Q = \begin{cases} 0.01327 \times (\text{mm reading}) & \text{mm} < 9.8 \\ 0.064752 \times (\text{mm reading}) - 0.5 & \text{mm} \geq 9.8 \end{cases} \rightarrow LPM$$

$$Q = \begin{cases} 0.013496 \times (\text{mm reading}) & \text{mm} < 10 \\ 0.0658568 \times (\text{mm reading}) - 0.5085 & \text{mm} \geq 10 \end{cases} \rightarrow \frac{\text{in}^3}{\text{s}}$$

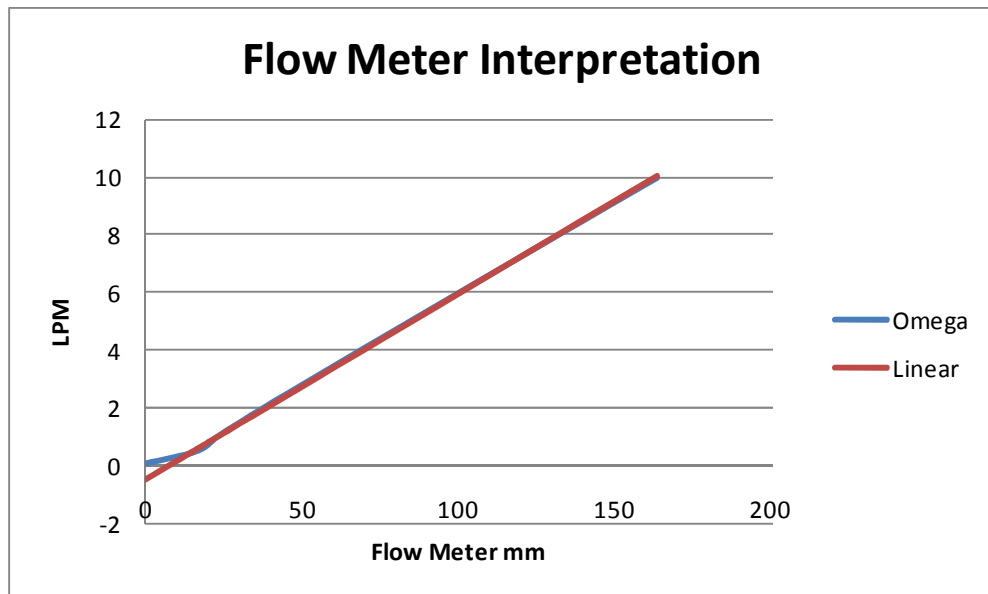


Figure 2-11 Comparison of linear equation for mm readings above 9.8 mm to the Omega equation.

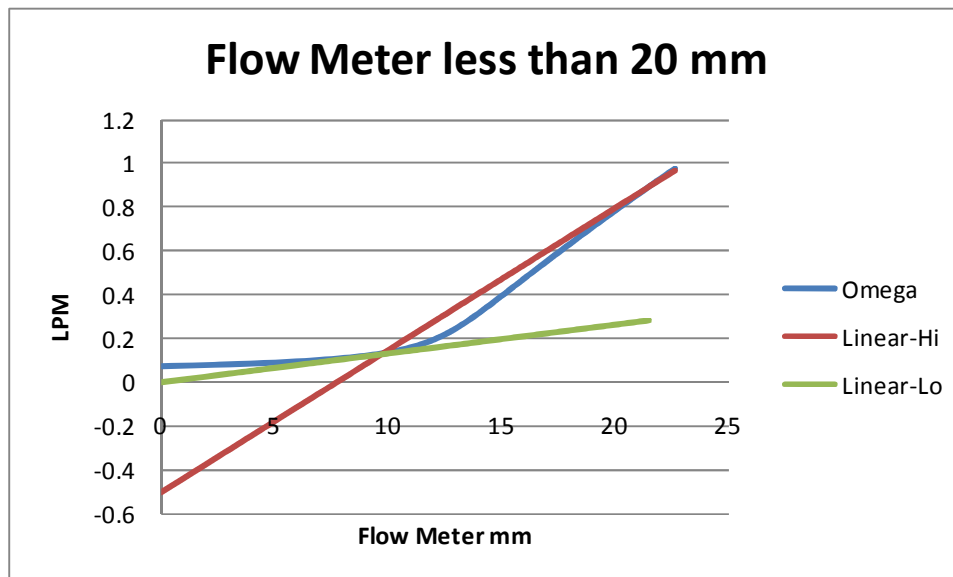


Figure 2-12 Comparison of linear approximation for mm readings below 9.8 mm to the Omega formula.

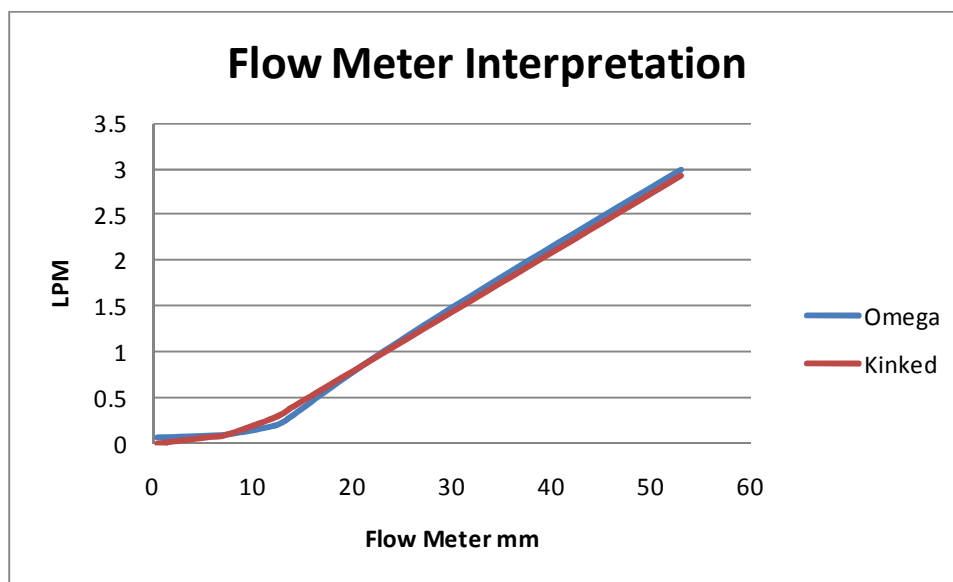


Figure 2-13 Comparison of combined kinked line to the Omega equation.



### 2.1.3. Static Flight Height Versus Load Testing

#### 2.1.3.1. Apparatus

The gas bearing test stand is used for static (non-rotating) testing of the bearings. For static testing the test stand does not need to be in the spin test bunker and does not require an air turbine connection. Only one load cell is used attached to the top center of the test bearing. Both sets of laser vibrometers are used - one set to measure the shaft and the other to measure the bushing. Only the vertical laser of each set is used. Varying loads and pressures are applied using the flow regulation box and the load adjustment motor. When load is applied to the bushing it is in the upward direction, thus it is possible to achieve zero load when the applied load equals the weight of the bearing. As load is applied both the shaft and the bearing move. In order to determine gap height  $h$  both the shaft displacement and the bushing displacement are required. When the test shaft was mounted to the gas IBA there was considerable shaft movement along with bushing movement that had to be accounted for. The movement was far in excess of that expected based on calculating the elastic cantilever beam displacement for the shaft. Also the movement was not always reversible. Considerably better results were achieved when the test shafts were mounted directly to a mounting block attached to the test stand stanchion.



Figure 2-14 gas bearing test stand being used for static flight versus load testing.

### 2.1.3.2. Test Methods

Two methods were used.

**Constant Pressure Method** - In this method bearing pressure is held at a constant pressure and the load is varied from 0 to 4 lbs. When the bearing pressure is zero increasing the load while reading bearing and shaft displacement can: 1) weigh the bearing, and 2) measure the effective bearing gap. When doing flight height versus load measurements for isobars it is difficult to discern what the flight height is as much data correction has to be done as both the bushing and the shaft displace. It must be assumed the absolute position of the laser and bearing be known at 0 load and 0 pressure (bearing top ID grounded on shaft top OD). Then, that the shaft displacement versus load relationship be known so that this can be subtracted from the bearing displacement to determine relative movement. And then lastly, the bearing clearance must be known to subtract from the relative movement to ascertain flight height. All in all this method turned out to be cumbersome and was abandoned in favor of the constant load method.

**Constant Load Method** - In this method the load is set at constant value and the bearing pressure is swept from 0 to 70 psi while the bearing and shaft displacements are noted. The advantage of this method is that the shaft in general does not displace during the pressure sweep since it has already displaced during loading. If the load is greater than the bearing weight than the zero pressure reading can safely be assumed to be the reading with zero flight height as the bearing bottom ID is grounded against the shaft bottom OD. As pressure is increased a flight height is developed as the bushing moves down while the shaft stays stationary. Thus the flight height  $h$  is measured directly. This method proved to be very successful.

## 2.2. Static Bearing Test Results

### 2.2.1. Some Terminology Used in Testing

**Journal Bearing** - A journal bearing is a bushing and shaft combination.

**Clearance,  $c$**  - Journal bearing clearance is defined the difference between the radius of the ID of the bushing and the OD of the shaft.

**Bearing Gap** - the space between the OD of the shaft and the ID of the bushing.

**Flight Height,  $h$**  - For a journal bearing it is the radial distance between the shaft OD surface and the bushing ID surface. When the shaft and bushing are concentric the flight,  $h=c$  all around the bearing gap. When the shaft and bushing are not concentric  $h$  varies throughout the bearing gap. The minimum flight height is 0 when the bearing is grounded (shaft is in contact with bushing). The maximum flight height possible is  $2c$ . This maximum can only be achieved if the bearing is grounded  $180^\circ$  opposite the maximum flight height. The maximum flight height is always  $180^\circ$  opposite the minimum flight height. When flight height is used in conjunction with static testing, it is inferred that the flight height is the minimum flight which ranges from 0 to  $c$  unless negative load is applied to the bearing.

**Stiffness,  $k$**  - Stiffness is spring stiffness defined as  $\frac{\Delta W}{\Delta r}$  in lbf/in where  $W$  is the vertical load on the bushing and  $\Delta r$  is the radial displacement . It is common in contact bearing catalogues to list bearings by stiffness. For gas bearings the stiffness is not a constant but depends on operating parameters and flight height.

**Stiffness factor,  $s(h)$**  - This a factor defined in this study to characterize gas bearing performance. It assumes the stiffness of a hydrostatic gas bearing is

proportional to the projected bearing area ( $D \times L$ ) and the operating pressure applied to the high pressure side of the mass addition pressure sleeve. That is:

$$k(h) = \left( \frac{\Delta W}{\Delta r} \right)_h = s(h) p_{op} A_{bearing} \quad \text{Consequently units of } s(h) \text{ are } in^{-1}.$$

**Dimensionless load  $W/pA$**  - Following the logic that the bearing stiffness is proportional to operating pressure and the projected bearing area, it is assumed that the load carrying capacity of the bearing is also proportional to operation pressure and bearing area. Later analytical work confirmed (see Appendix C) that  $W/pA$  is the hydrostatic bearing efficiency.

**Bearing volumetric flow rate  $Q$**  - This the volumetric flow rate of air being added to the bearing gap through the pressure sleeve. The volumetric flow rate is measured on the high pressure side of the pressure sleeve and therefore the mass addition rate is  $\rho_{pop} Q$  where  $\rho_{pop}$  is the density of air at room temperature and operating pressure.

**Bearing volumetric flow constant,  $Kma$**  - This is another parameter defined by this study to characterize bearings. The volumetric flow of air from the high pressure side of the pressure sleeve (at room temperature) is measured during testing and is a function operating pressure such that it is expected that

$$Q = Kma * p_{op}. \quad \text{Units of } Kma \text{ are } in^5 s^{-1} lbf^{-1}.$$

**Bearing mass flow constant  $Kmeas$**  - At a later date, circa August 2010, after reviewing Poiseuille flow for a compressible fluid it was hypothesized that the mass flow rate for a bearing could be characterized by constant.  $Kmeas$ , to be determined from the experimental data of volumetric flow through the bushing prototypes with no shafts exhausting to ambient air such that

:

$\dot{M} = Kmeas [P_{op}^2 - P^2]$  which when exhausting to ambient air is :

$$\dot{M} = Kmeas [P_{op}^2 - 1].$$

## 2.2.2. Prototype Bearings and Shafts Tested

**Test Matrix**

<b>Mass Addition (sleeve)</b> (low to high)	<b>Bearing Clearance (varied by test shaft diameter)</b>			
	small to large			
	0.07500"	0.7498	0.7494"	0.7486"
<b>Orifices</b>				
0.003" Dia	<b>MA</b>	<b>MA</b>	<b>MA</b>	<b>MA-C-GF-SH</b>
0.006" Dia	<b>MA</b>	<b>MA</b>	<b>MA</b>	<b>MA</b>
0.012" Dia	<b>MA</b>	<b>MA</b>	<b>MA</b>	<b>MA</b>
0.015" Dia	<b>MA</b>	<b>MA</b>	<b>MA</b>	<b>MA</b>
0.018" Dia	<b>MA</b>	<b>MA</b>	<b>MA</b>	<b>MA-C-GF-SH</b>
<b>Porous Sleeve</b>				
Treated Porous Graphite	<b>MA</b>	<b>MA</b>	<b>MA</b>	<b>MA</b>
Porous Alumina	<b>MA</b>	<b>MA</b>	<b>MA</b>	<b>MA</b>

**Test Sequence**

<b>MA</b>	Mass Addition Pressure Curve
<b>C</b>	Effective Clearance
<b>GF</b>	Grounding Force Pop Curve
<b>SH</b>	Static Flight Heights at Pops
<b>LD</b>	Low Temp Dynamic
<b>HD</b>	High Temp Dynamic

Figure 2-15 Table of Test Matrix as reported on 1/18/2010.

A prototype 0.75" diameter x 2" length porous graphite bushing was purchased from New Way bearing company. Other prototype bushings were based on the New Way bushing geometry. In order to test the effect of bearing clearance, shafts were made with OD's varying from 0.75" to 0.7486".

Two porous material liners were tested. One was the porous graphite liner from the purchased New Way bearing. The other was a reverse engineered pressure liner made from porous alumina. It is known that the New Way porous graphite sleeve is treated with a proprietary method that limits its permeability or "hydraulic conductivity". The porous graphite has a porosity of about 10% to 12% (based on density) and the alumina has porosity of about 40% to 45%.

The porous alumina had a no-shaft  $Kma$  of 1.2750 versus 0.047 for the treated porous graphite pressure sleeve. The porous alumina bearing had in all case the highest flow of any of the prototype bearings. It's no-shaft  $Kma$  is 27 times the porous graphite  $Kma$ .



Figure 2-16 Porous pressure liners. New Way treated porous graphite (left), Aerodyn fabricated porous Alumina (right).



The feedhole prototypes were made by making interchangeable aluminum pressure liners each having two rows of 6 equally spaced feedholes placed 0.350" from ends of the liners.



Figure 2-17 Feedhole mass addition pressure sleeve.



Figure. 2-18 Close up two feedholes 0.012" (left) and 0.006" (right).

The feedhole diameters varied from 0.003" to 0.018". As expected the no-shaft  $Kma$  for the larger holes was greater than the smaller holes. The no-shaft  $Kma$

of the 0.18" was too high to measure as it "pegged" the flow meter with < 5 psig operating pressure. The no-shaft *Kma* of the 0.009" liner was .145 compared to .00395 for the 0.003" pressure sleeve.

Thus the combinations of prototype pressure sleeves and shafts makes a test matrix with 28 possible combinations of bearings to test. For testing economy the treated porous graphite and porous alumina sleeves were tested using the 0.7500", 0.7490, and 0.7486", shafts thus giving a test of low and high *Kma* for porous liners with small, medium, and high clearances. For feedhole liners the 0.003", 0.009", 0.015" and 0.018" sleeves were run with the 0.750 shaft and the 0.749" shaft giving results for a range of feedhole diameters with small and large bearing clearance.

### 2.2.3. Test Results

The complete sets of data are graphically presented in Appendix E. which contains graphs of the prototype bearing/shaft combinations for:

- $W/pA$  versus  $h$  by bearing and clearance
- Volumetric Flow vs. Pressure by Load
- Bearing Flow Rates vs. Pressure and Clearance
- Stiffness Factor  $s(h)$  vs.  $h$
- Curve fitting of the Stiffness Factor as a function of pressure

The calculated  $Kma$  factors and stiffness factor  $S(h)$  for the bushing/shaft combinations tested were found to be:

#### Flow rates

Feed Type	Shaft in	Clearance $\mu$ -in	Linked/Kinked	Linear Kma in <sup>4</sup> s/lbf	Low Kma in <sup>4</sup> s/lbf	Medium Kma in <sup>4</sup> s/lbf	High Kma in <sup>4</sup> s/lbf	High Pivot Pressure Psi	Low Pivot Pressure Psi
Porous Graphite	N/A	N/A	Linear	0.0470	N/A	N/A	N/A	N/A	N/A
	0.749	1050	Kinked (Single)	0.0426	0.0095	N/A	0.0517	9.5	N/A
	0.750	322	Kinked (Single)	0.0115	0.0037	N/A	0.0256	32.0	N/A
Porous Alumina	N/A	N/A	Linear	1.2750	N/A	N/A	N/A	N/A	N/A
	0.749	1536	Kinked (Single)	0.6950	0.8812	N/A	0.5516	4.9	N/A
	0.750	282	Linear	0.3120	N/A	N/A	N/A	N/A	N/A
12 x 0.003 Holes	N/A	N/A	Kinked (Single)	0.0040	0.0095	N/A	0.0035	6.0	N/A
	0.749	830	Kinked (Double)	0.0034	0.0039	0.0016	0.0049	40.0	9.0
	0.750	414	Kinked (Double)	0.0014	0.0012	0.0020	0.0006	40.0	30.0
12 x 0.009 Holes	N/A	N/A	Kinked (Single)	0.1450	0.4299	N/A	0.0790	12.1	N/A
	0.749	730	Kinked (Single)	0.0885	0.1829	N/A	0.0362	16.5	N/A
	0.750	85	Linear	0.0141	N/A	N/A	N/A	N/A	N/A
12 x 0.018 Holes	N/A	N/A	N/A	N/A	N/A	N/A	N/A	N/A	N/A
	0.749	971	Kinked (Single)	0.2380	0.3955	N/A	0.1797	7.5	N/A
	0.750	248	Kinked (Single)	0.0225	0.0075	N/A	0.0346	20.0	N/A

Figure 2-19 Table of Kma and S(h) results for prototype bearing/shaft combinations tested.

## Stiffness

Feed Type	Shaft in	Clearance $\mu$ -in	S @ h=50 1/in	S @ h=100 1/in	S @ h=200 1/in	S @ h=300 1/in	S @ h=500 1/in	S @ h=750 1/in	S @ h=1000 1/in
Porous Graphite	0.7490	1050	2341	1703	584	432	251	121	n/a
	0.7494	622	n/a	n/a	892	702	726	n/a	n/a
	0.7500	322	n/a	2109	1246	n/a	n/a	n/a	n/a
Porous Alumina	0.7490	1536	n/a	n/a	n/a	n/a	241	350	93
	0.7494	557	n/a	n/a	604	494	155	n/a	n/a
	0.7500	282	1084	820	293	n/a	n/a	n/a	n/a
12 x 0.003 Holes	0.7490	830	n/a	2077	233	196	89	n/a	n/a
	0.7500	414	n/a	422	320	249	n/a	n/a	n/a
12 x 0.009 Holes	0.7490	730	2253	1113	518	429	276	400	n/a
	0.7500	85	939	n/a	n/a	n/a	n/a	n/a	n/a
12 x 0.015 Holes	0.7490	794	n/a	423	228	294	337	n/a	n/a
	0.7500	97	2573	n/a	n/a	n/a	n/a	n/a	n/a
12 x 0.018 Holes	0.7490	971	n/a	n/a	n/a	n/a	259	284	n/a
	0.7500	248	324	463	n/a	n/a	n/a	n/a	n/a

Figure 2-20 Tabular interpretation of S(h) at selected flight heights. Graphs are in Appendix E.

## Mass Flow *Kmeas*

Bushing No shaft	Kmeas lbs/s
Porous Graphite	2.71E-05
Porous Alumina	5.00E-04
Feed holes 0.003	2.20E-06
Feed holes 0.006	4.73E-05
Feed holes 0.009	8.00E-05
Feed holes 0.012	4.30E-04
Feed holes 0.015	5.20E-04

Figure 2-21 Values of Kmeas for prototype bushings.

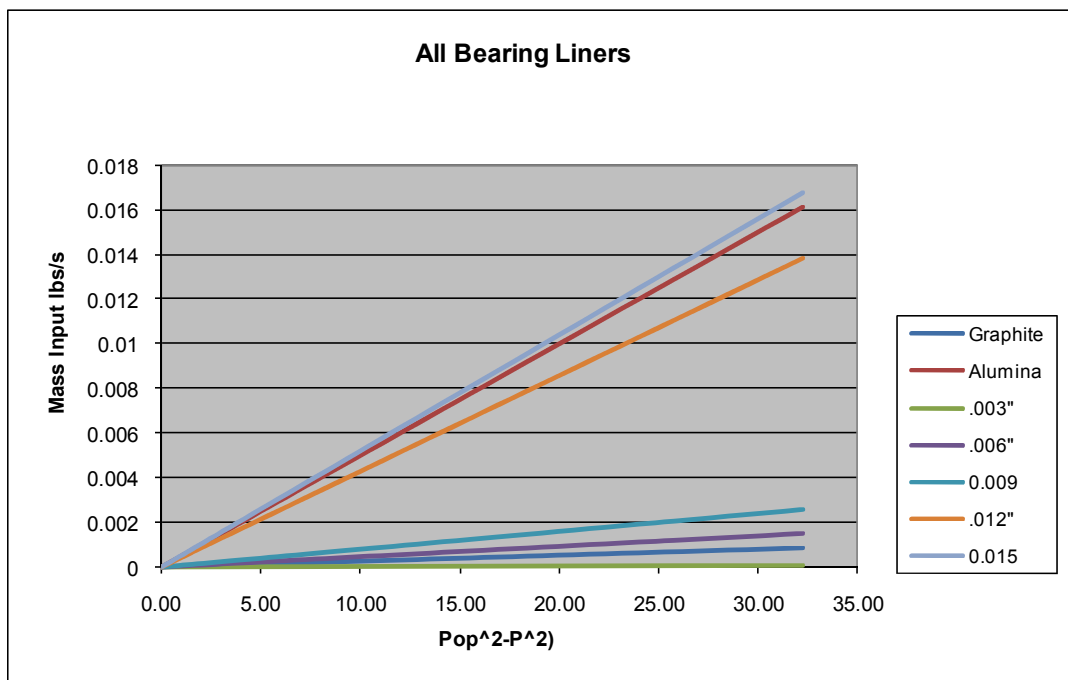


Figure 2-22 Mass flow rates as a function of  $P_{op}^2 - P^2$  using measured values of  $K_{meas}$ .

## 2.2.4. Observations, Conclusions, and Discussion of the Results

**Obs. 1** - When the flight height ( $h$ ) versus load and pressure data taken using the constant load method was reduced to  $W/pA$  versus  $h$  data and plotted, it fell into meaningful series lines based on the bearing clearance.

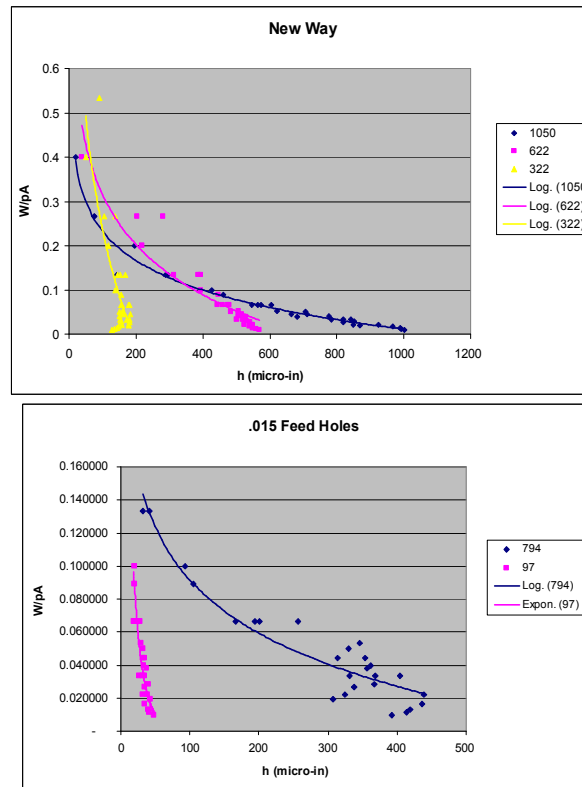


Figure 2-23 Curves of  $W/pA$  as a function of  $h$  for treated porous graphite (left) and 0.015" feedhole liner (right). Each line or series on the graphs represents data for different clearances.

**Obs. 2** - When the flight height ( $h$ ) versus load and pressure data taken using the constant load method was reduced to stiffness factor  $s(h)$  versus  $h$  data it fell into meaningful data series by clearance.

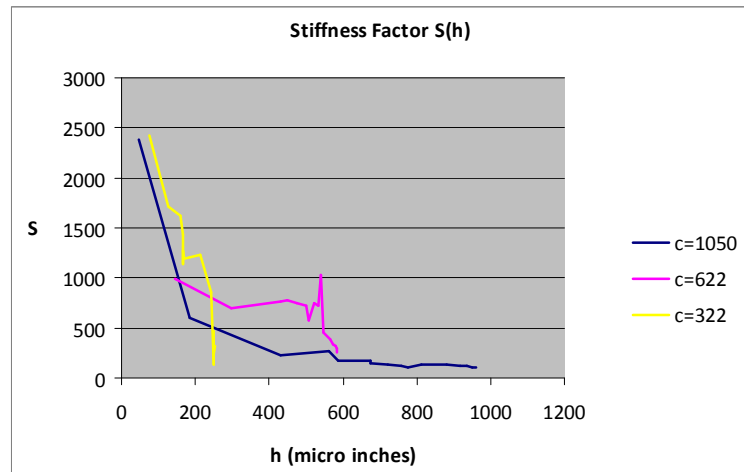


Figure 2-24  $S(h)$  series for New Way porous graphite bearing.

**Obs. 3** - The stiffness Factor  $S(h)$  was originally formulated to try to make sense of the New Way catalog information which listed bearing stiffness  $k$  by bearing size. In this analysis it was noted that the published stiffness  $k$  corresponded to in all cases an operating pressure of 60 psig. The conclusions drawn from the analysis were that 1) that the New Way bearings had a constant stiffness across all sizes of bearings of approximately  $1440 \text{ in}^{-1}$  for bearings larger than 0.75" and 2) that slenderness ratio ( $L/D$ ) to achieve this stiffness factor decreased as the bearing diameter increased. In other words, the slenderness ratio for the 0.25" bearing was 5 and even then it only had an  $S$  of 533 whereas the 3" diameter bearing achieved a stiffness factor of 1,444 with a slenderness of only 1.17.

From Air bushing Product Line Table:											
Dia in	Db-Ds = 2hnom		ave hnom	k lfb/in	L in	L/D in	A in <sup>2</sup>	S in <sup>-1</sup>	mass		
	min	max							oz	lbm	
0.25	0.0007	0.0012	0.000475	10,000	1.25	5.00	0.3125	533	0.3	0.019	
0.5	0.0008	0.0013	0.000525	60,000	2	4.00	1	1,000	1.1	0.069	
0.75	0.0008	0.0013	0.000525	130,000	2	2.67	1.5	1,444	2	0.125	
1	0.0008	0.0013	0.000525	190,000	2.25	2.25	2.25	1,407	3	0.188	
1.5	0.0008	0.0013	0.000525	410,000	3	2.00	4.5	1,519	7.2	0.450	
2	0.0008	0.0013	0.000525	630,000	3.5	1.75	7	1,500	17	1.063	
3	0.0008	0.0013	0.000525	910,000	3.5	1.17	10.5	1,444	22	1.375	

Figure 2-25 Calculation of  $S(h)$  for New Way journal bearings based on New Way's published stiffness data.

**Concl. 1** - From Obs. 1, 2, 3 it appears that reducing the flight height vs. load data into  $W/pA$  and  $S(h)$  vs  $h$  data is very powerful and significant to hydrostatic bearing analysis.

**Concl. 2** - It was assumed that the New Way stiffness data comes from the near linear of their flight height vs, load information at small flight heights  $< 200 \mu\text{in}$ . Using that assumption a stiffness factor of about 1440 was noted for New Way bearings. The stiffness factor for the New Bearing tested and shown in figure 2-24 shows the stiffness factor rapidly increasing from about 1000 to 2300 as the flight height is lowered from 200 to 50  $\mu\text{in}$ . Thus the test and the published New Way information appear to corroborate one another.

**Obs. 4** - The stiffness factor  $S(h)$  is greatest at lowest  $h$ . For higher clearance bearings the maximum  $h$  is larger and falls off much more slowly as  $h$  is increased compared to the lower clearance bearings. As  $h$  increases the difference diminishes. Above  $\sim 150 \mu\text{in}$  the difference is indistinguishable.

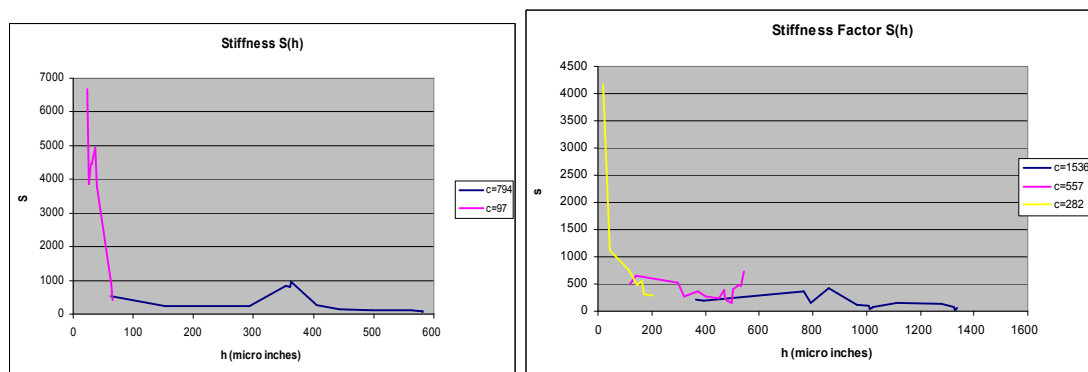


Figure. 2-26  $S(h)$  vs  $h$  appears to be independent of clearance  $c$  when there is little or no overlap in  $h < 100$ . Left - 0.015" feedhole, Right - Alumina.



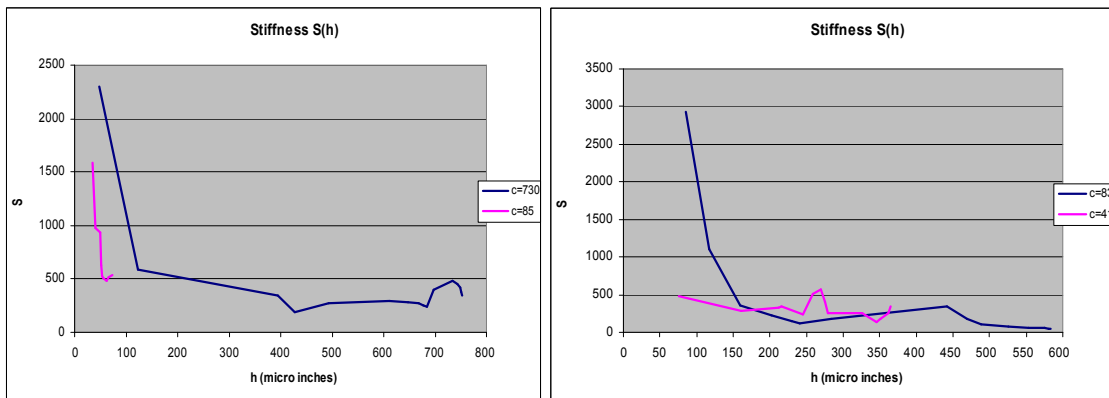


Figure 2-27 When there is overlap for  $h < 100$   $S(h)$  vs  $h$ ,  $S(h)$  appears greater at low  $h$  and falls off more slowly as  $h$  increases for greater clearances. Left - 0.009" feedhole, Right - 0.003 feedhole.

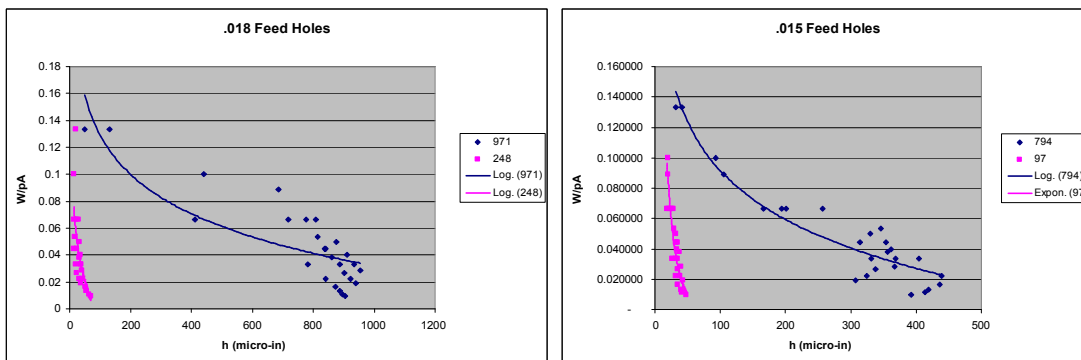


Figure 2-28 For feedhole bearings,  $W/pA$  is highest at lowest  $h$  and falls off with increasing  $h$  very quickly for low clearance bearings vs. high clearance bearings. Left - 0.018" feedholes, Right - 0.015" feedholes.

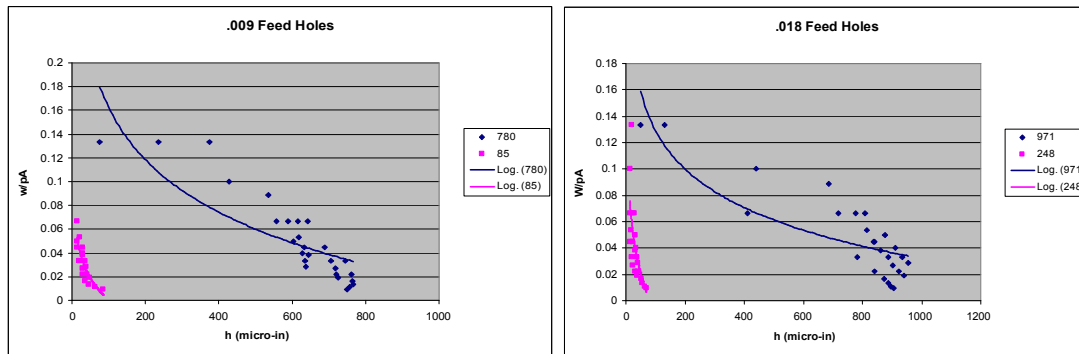


Figure 2-29 For feedhole bearings the difference between the highest  $W/pA$  lessens the greater the feedhole diameter. The difference is 0 at the largest feedhole tested. Left - 0.009", Right - 0.018"

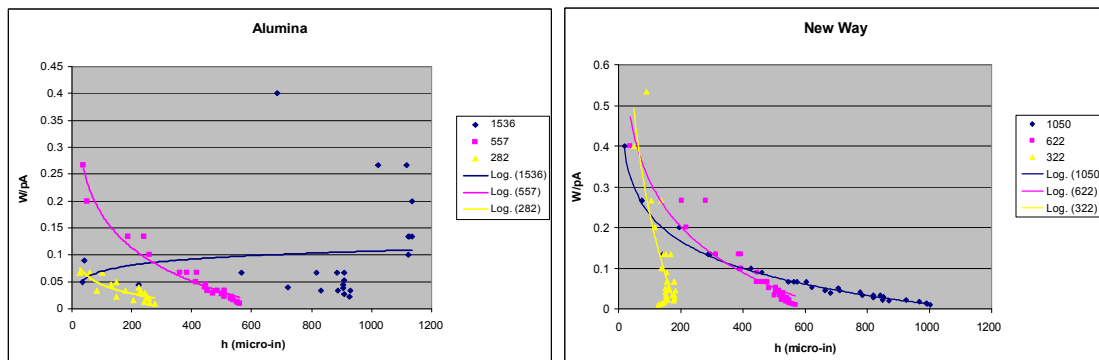


Figure 2-30 For  $W/pA$  vs  $h$  for porous sleeve bearings shows similar trends to large feedhole bearings. The largest clearance series of the Alumina is suspect in that only a few data points were able to be taken as there was large flow and vibrations (humming) occurring. Left - porous alumina, Right - porous graphite.

**Obs. 5** -  $W/pA$  vs  $h$  is highest at lowest  $h$  and decreases exponentially as  $h$  increases. Higher clearance bearings generally have higher maximum  $W/pA$  values. At larger diameter feedholes the maximum  $W/pA$  for the low clearance bearings approaches the maximum  $W/pA$  for the higher clearance bearings. At the largest feedhole 0.018" they are the same. However  $W/pA$  always falls off much more quickly as  $h$  is increased. The New Way porous graphite bearing also shows a similar pattern. Some of the alumina data is suspect especially the high clearance series. This is because data points were limited as flow rates

“maxed out” the flow meter at low operating pressure. At high flow rates the alumina bearings could be heard to hum indicating high frequency vibration.

**Obs. 6** - When the bushing and the shaft are concentric,  $h=c$ . Thus it is expected that  $W/pA = 0$  at  $h=c$ . The  $W/pA$  charts confirm this. This would account for why the  $W/pA$  for lower clearance bearings falls off much more rapidly with increasing  $h$  than higher clearance bearings.

**Premise 1** - From Obs.5 it was noted that for bearings with large mass addition such as the 0.018” bearing or the porous liner bearings, that the maximum  $W/pA$  for low clearance bearings approaches that of high clearance bearings. Since it is also known from Obs.6 that  $W/pA$  goes to 0 at  $h=c$ , could it be that  $W/pA$  is a function of  $H=h/c$  which is independent of  $c$ ?

**Obs. 7** - Graphs were made of  $W/pA$  vs.  $H$ . Of particular interest were the graphs for the New Way bearing and the 0.018” feedhole bearing. In these bearings the maximum  $W/pA$  for the small clearance series was as high as for the high clearance series. The porous alumina was inconsistent and as Obs. 5 pointed out the other smaller feedhole diameters had lower maximum  $W/pA$ . The initial result was that plotting against  $H$  as compared to  $h$  as expected stretched the domain of the plot out but the graph still showed that  $W/pA$  declined faster with increasing  $H$  for the smaller clearance series. However, it was challenged: Why did the lower clearance series for the 0.018” feedhole zero out at about 0.3 and the New Way bearing zero out at 0.6? Shouldn't they, as noted in obs. 6, zero out at  $H=1$ ? The answer to this concerns what the “demonstrated” clearance of the bearing was. The demonstrated clearance was measured by running the bearing through a zero pressure run with increasing load and noting the difference in movement between in the bushing and shaft. When the load is less than the bushing weight the bearing is grounded on the top of the shaft and the shaft and the bushing displace together with increased load. When the load

equals the bushing weight, the shaft stops displacing as it is unloaded while the bushing displaces the distance of 2 times the clearance as it changes from being grounded on the top of the shaft to being grounded at the bottom of the shaft. For loads greater than the bushing weight the shaft and the bushing continue to displace together. The size of the bushing displacement that occurred while there was no shaft displacement was used as the measurement of the demonstrated clearance.

During some static testing performed doing pressure sweeps at constant loads there were cases when the bushing moved somewhat more than the measured demonstrated clearance. For 0.018" feedhole and the New Way bearing when operated with the 0.75" shaft which was their tightest clearance, the opposite happened. In these cases, the measured clearance was used to plot  $W/pA$  vs  $H$ . This indicated that the demonstrated clearance was more than the measured clearance and the demonstrated clearance was increased accordingly to interpret stiffness and flight height data.

In order to test premise 1 the demonstrated clearances were modified to reflect that  $W/pA$  goes to zero when  $h$  goes to  $c$ . Results are shown in figures 2-31 and 2-32.

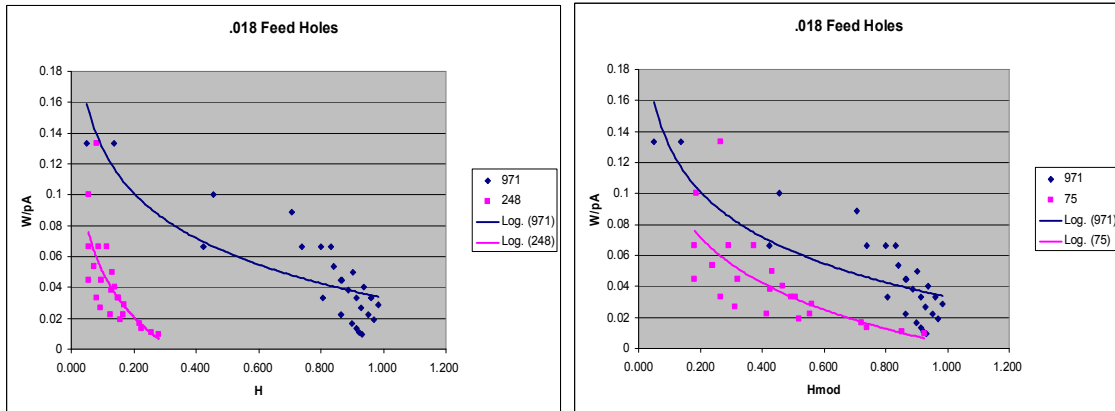


Figure 2-31 Two plots of  $W/pA$  vs  $H$  for different values of the assumed “demonstrated clearance” for the 0.018” feedholes when the 0.750” D shaft was used. Left - as measured. Right - adjusted.

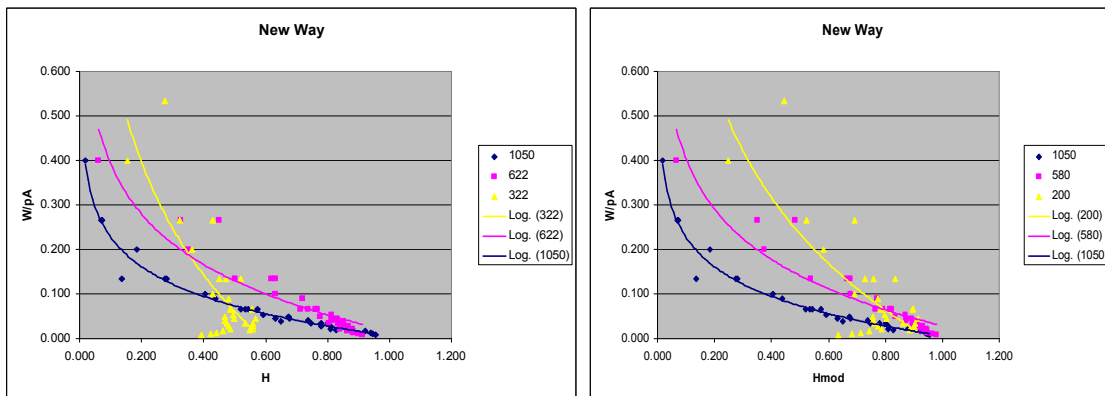


Figure 2-32 Two plots of  $W/pA$  vs  $H$  for different values of the assumed “demonstrated clearance” for the New Way bearing when the 0.750” D shaft was used. Left - as measured. Right - adjusted.

**Obs. 8** - The modified  $W/pA$  vs.  $H$  plot of the New Way bearing moved the lowest clearance series to be generally higher than the high clearance series whereas the unmodified data showed it to start higher and then steeply decline to be generally lower. It is suggested the demonstrated clearance could be adjusted somewhere between the “modified” and “unmodified” demonstrated

clearance to make lowest clearance series fall on top of the higher clearance series. For the 0.018" bearing the low clearance series still falls generally lower than the high clearance series but the highest data points are intermingled. For the most part, the suggested shape of the series continues to exhibit an exponential decay type curve.

**Obs. 9** - The smaller diameter feedhole  $W/pA$  do not definitively confirm or deny premise 1.

**Obs. 10** - Except for 4 data points on the 830  $\mu\text{in}$  series on the 0.003" feedhole bearing, the maximum  $W/pA$  for all the feedhole bearings is slightly below 0.14. For the two porous liner bearings the maximum  $W/pA$  is about 0.4. The no-shaft  $K_{ma}$ 's for the feedhole bearings ranges from 0.004 to 0.238  $\text{in}^5\text{s}^{-1}\text{lb}f^{-1}$ . The no-shaft  $K_{ma}$  for the treated porous graphite liner and porous liner alumina are 0.047 and 1.27  $\text{in}^5\text{s}^{-1}\text{lb}f^{-1}$  respectively.

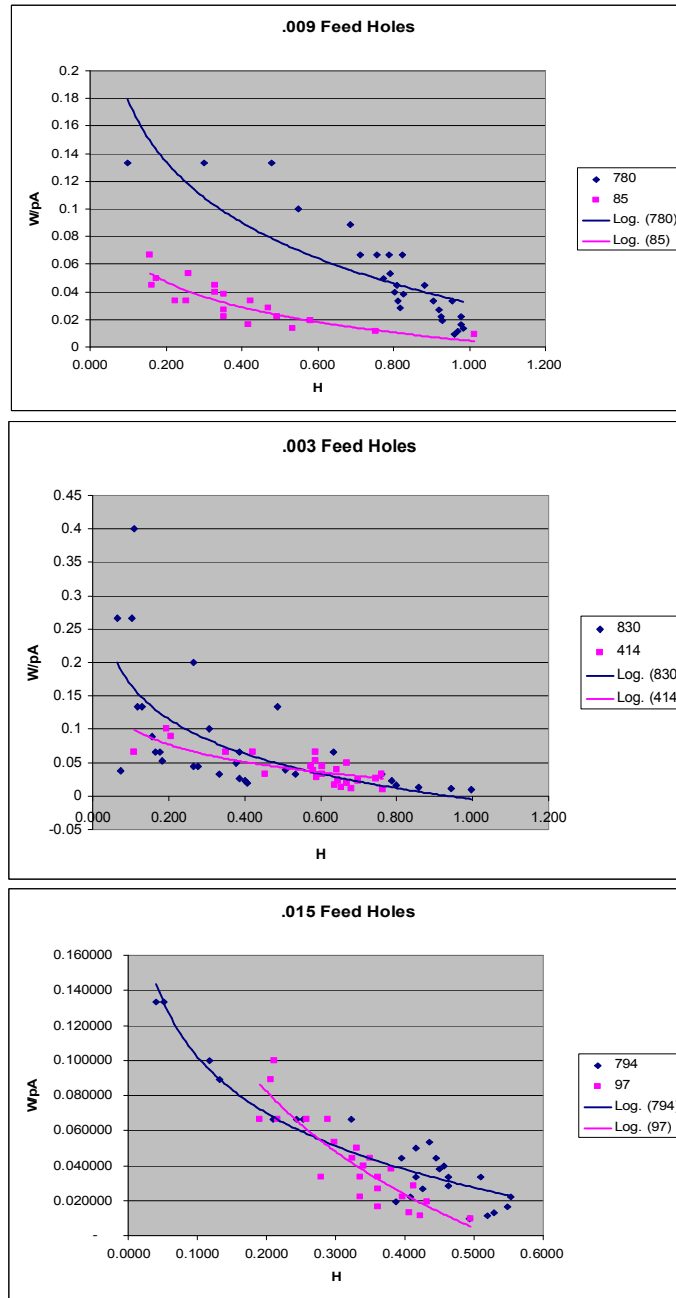


Figure 2-33  $W/pA$  vs.  $H$  for the other feedhole bearings.

**Premise 2** - The  $W/pA$  vs.  $H$  is determined by the mass addition configuration independent of  $K_{ma}$  or clearance. That is, all the bearings with mass addition via 2 rows of 6 feedholes can be generalized by one curve independent of clearance and all bearings with porous liners can be generalized by a different curve independent of clearance.

**Obs. 11** - If premise 2 is accepted so that 3 data points of  $W/pA$  vs.  $H$  were to be picked to represent each bearing independent of clearance, representative points would be as represented in figure 2-34 would look like figure 2-35.

Feed hole bearings		Values of H		
		$W/p^*A$		
hole Dia	$K_{ma}$	0.14	0.08	0.02
0.003	0.004	0.1	0.3	0.7
0.009	0.145	0.1	<0.02-0.6	0.58 - 0.9
0.015	>.92	0.05	0.2	0.55
0.018	>.92	0.1	0.5	0.9
Composite		0.1	0.4	0.8
Porous Liners		$W/p^*A$		
		$K_{ma}$		
Treated graphite	0.047	0.1	0.4	0.8
alumina	1.275	.27 @ .1	0.4	0.7
Composite		0.1	0.4	0.75

Figure 2-34 Order of magnitude values of  $W/pA$  vs.  $H$  based on premise 2.



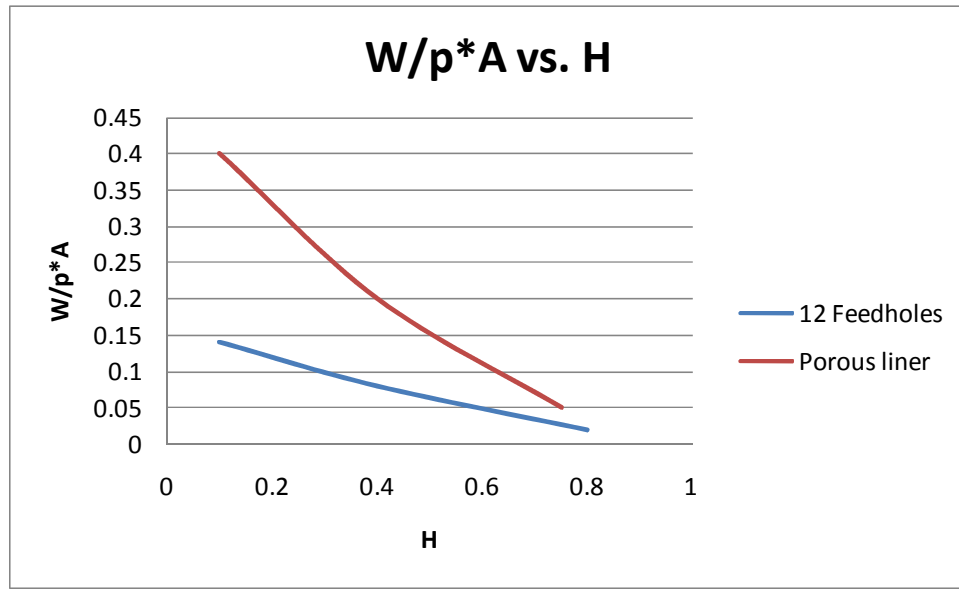


Figure 2-35 Suggested composite curves for  $W/pA$  vs.  $H$  independent of  $Kma$  and  $c$ .

## CHAPTER 3. THE CFD LABORATORY

### 3.1. Overall Computational Scheme

The overall intent of the hybrid bearing CFD (computational fluid dynamics) lab is to develop the capability to perform numerical experiments on a virtual bearing that simulate the real bearing performance under various loads and operating parameters.

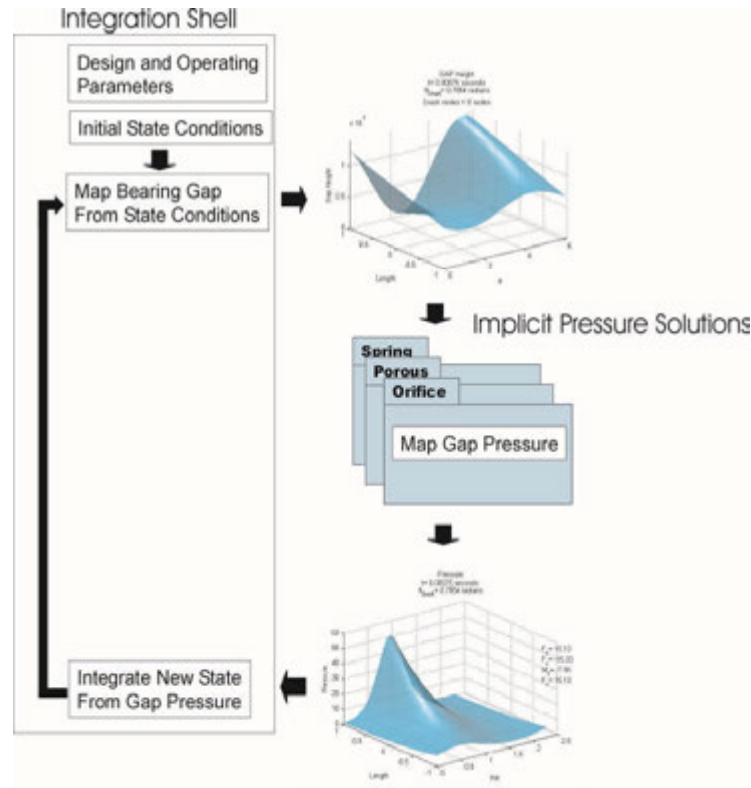


Figure 3-1 Overall Computational Scheme.

The overall computational scheme for the hybrid bearing CFD laboratory is:

1. Define the bearing geometry - length, diameter, clearance etc.
2. Define the bearing dynamic parameters - masses, moments of inertia degrees of freedom, damping and stiffness coefficients etc.
3. Define the mass addition mode -  $Kmeas$ , Feedholes, FH locations, porous liners etc.
4. Set the operating parameters - speed, mass addition operating pressure, ambient pressure and temperature, bearing loads etc.
5. Set initial conditions - bushing/shaft initial displacement, relative velocities etc.
6. Based on 1-5 solve the pressure distribution in the bearing gap.

7. Integrate the pressure distribution and mass fluxes to determine net hydrodynamic force and mass addition.
8. Use the net hydrodynamic force to time integrate bearing/shaft movement and relative velocities.
9. Repeat back to step 6 and solve the pressured distribution for the new shaft/shaft displacement and relative velocities.

Simulating the relative motion between the shaft and the bushing determines the limits of stable bearing performance. This technique is often called the “orbit method” for determining bearing stability.

With the exception of step 6, solving the pressure distribution in the bearing gap, the computational scheme, though complicated, involves straight forward time integration. The solution of the pressure distribution within the bearing gap requires a CFD solution to the appropriate Reynolds equation.

The effort to develop the CFD laboratory started with writing code using MATLAB for steps 1 to 5 and 7 to 8. A simple spring function was inserted in step 6 which modeled the pressure distribution as being inversely proportional to the bearing gap height. This was used to successfully demonstrate the ability of the hybrid bearing CFD lab to time integrate and simulate bearing motion *if* a module for step 6 existed that solved the pressure distribution.

Subsequent analytical work derived the discretized Reynolds equation for hybrid bearings. This was used to find pressure solutions for stationary hydrostatic bearings (bearings with mass addition and no rotation) and stationary rotating bearings. What is meant by stationary bearings are bearings where there is no relative motion between the shaft and bushing except rotation i.e. a quasi-static solution. The solutions for rotating bearings had numerical “speed limits” above which attempts for solutions exhibited numerical instability. These solutions were

used to run a set of CFD experiments exploring the hydrodynamic characteristics of stationary hybrid bearings.

The next step in the development of the hybrid CFD laboratory is to run simulations on “real” bearings. Because such simulations depend very heavily on the specific bearing application this work has been deferred for future effort. Simulations involving movement between the shaft and bushing will require pressure solutions that include the transient terms in the Reynolds equation. Strategies have been developed to solve these pressure distributions but have not been implemented.

### 3.2. Dimensionless, Quasi Linear, Flux Isolated Reynolds Equation

A complete derivation of the Reynolds equation for hybrid gas bearings is given in Appendix A.

The basis for the computational fluid dynamics (CFD) experiments performed in this thesis is the solution of the pressure distribution in the bearing gap (volume of air between the ID of the bushing and OD of the shaft). Integration of the pressure distribution yields the “net hydrodynamic force” which is the interaction force between the shaft and the bushing. The basis for solving the pressure distribution is the Reynolds equation which uses viscous hydrodynamic action to relate mass continuity to pressure.

The Reynolds equation suggests various dimensionless parameters that are widely accepted in works on gas bearings to represent the generalization of the equation into dimensionless terms. The derivation in Appendix A confirms these dimensionless parameters. However, in Appendix A, a non-conventional term for dimensionless time is introduced that is thought to be new and more appropriate than approaches presented in previous writings. Also, as will be discussed later, the results of both the empirical and CFD experiments indicate that the conventional set of dimensionless parameters used to describe the hydrodynamic action is incomplete and the need for further dimensional analysis is identified.

Further, in most presentations of bearing CFD work the Reynolds equation is presented in its most compact form where all the terms deriving from the various contributing hydrodynamic actions are consolidated together so that the equation itself does not easily provide physical insight. The derivation in this thesis deviated from that course and deliberately kept the terms deriving from different

hydrodynamic actions separate. This proved to be very useful in providing physical insight into the hydrodynamic activity in the bearing gap.

A very important part of the Reynolds equation for a hybrid bearing is the term modeling the mass addition to the bearing gap from feedholes or from porous liners. Published works with CFD calculations involving hybrid bearings use differing terms for mass addition usually based solely on theoretical supposition. A novel and simple way of modeling mass addition is used in this thesis. This is based on the observation that the substitution of  $Q$  for  $P^2$  linearizes the Poiseuille flow differential equation and makes an analytical solution possible. This is discussed in Appendix C. Using Poiseuille flow as the model for pressure driven compressible fluid flow through a restriction such as mass addition via feedholes or porous liners, suggested a useful linear characterization constant for mass addition. The empirical flow data confirmed the validity of this model and the CFD experiments in this thesis are based on the actual measured mass characteristics of the prototype bearings.

### 3.2.1. Consolidated Reynolds Equation

The consolidated Reynold's equation with dimensions of  $M/L^2T$

is shown in equation 3-1.

**Equation 3-1** Reynolds equation for gas hybrid bearings

$$-\frac{\partial}{R\partial\theta}\left(\frac{\rho h^3}{\eta}\frac{\partial p}{R\partial\theta}\right)+6\frac{\partial}{\partial\theta}(\omega\rho h)-\frac{\partial}{\partial z}\left(\frac{\rho h^3}{\eta}\frac{\partial p}{\partial z}\right)+12h\frac{d\rho}{dt}+12\rho(V_B-V_S)=12\frac{\dot{M}}{R\delta\theta\delta z}$$

$$\dot{M} = \begin{cases} 0 & \text{for elements with no mass addition} \\ \dot{m}\delta x\delta z & \text{for elements with area scaled mass addition} \\ \dot{M} & \text{for elements with point source mass addition} \end{cases}$$

$\dot{M}$  is the mass addition through the bushing and has dimensions  $M/T$  which in compatible EE units has units of lbs/s.  $\dot{m}$  is the mass addition per unit area such as that of a porous liner and has dimensions  $M/L^2T$  or in EE units is lbs/in<sup>2</sup>s.

Using the following substitutions results in the dimensionless version of the Reynold's equation shown equation 3-2.

**Equation 3-2** Dimensionless Reynolds equations for gas hybrid bearings

$$-\frac{\partial}{\partial\theta}\left(PH^3\frac{\partial P}{\partial\theta}\right)+\Lambda\frac{\partial}{\partial\theta}(PH)-\left(\frac{R}{L}\right)^2\frac{\partial}{\partial Z}\left(PH^3\frac{\partial P}{\partial Z}\right)+\frac{\partial}{\partial t}t_c(PH)=\frac{t_c}{k_{pp}p_a cR\delta\theta\delta z}\dot{M}$$

which is equivalent to:

$$-\frac{\partial}{\partial\theta}\left(PH^3\frac{\partial P}{\partial\theta}\right)+\Lambda\frac{\partial}{\partial\theta}(PH)-\left(\frac{R}{L}\right)^2\frac{\partial}{\partial Z}\left(PH^3\frac{\partial P}{\partial Z}\right)+\frac{\partial}{\partial\tau}(PH)=\frac{t_c}{k_{pp}p_a cR\delta\theta\delta z}\dot{M}$$



Substitutions:

*For density of air as an ideal gas:*

$$\rho = \frac{P}{Rt} = k_{\rho p} p$$

$$k_{\rho p} = \frac{1}{Rt} = \frac{1}{640.2248(^{\circ}F + 459.67)}$$

*Dimensionless pressure P:*

$$P = \frac{P}{P_a}$$

where  $P_a$  is the ambient pressure taken in this thesis to be 14.7psig.

*Dimensionless gap height h:*

$$H = \frac{h}{c}$$

$c$  is the bearing clearance

*Dimensionless length location:*

$$Z = \frac{z}{L}$$

In this thesis  $Z=0$  indicates the center of the bearing.

*Dimensionless time:*

$$\tau = \frac{t}{t_c}$$

where  $t_c$  is named the “characteristic time” and is defined as:

$$t_c = 12 \left( \frac{\eta}{P_a} \right) \left( \frac{R}{c} \right)^2$$

Other results, thus far read, either keep time as a dimensional factor or make time dimensionless by using combinations of the angular velocity of the shaft

rotation (dimensions  $T^{-1}$ ) and the bearing number. It is felt that these approaches are inappropriate as hybrid bearings have considerable hydrodynamic activity even when operated at 0 RPM. The characteristic time introduced above is pleasing in that it relates the viscous properties of the gas to the dimensionless bearing clearance. This expression is meaningful for both rotating and non-rotating hydrodynamic activity.

*Bearing number or compressibility factor:*

$$\Lambda = \frac{6\eta\omega R^2}{c^2 p_a} = \frac{1}{2} t_c \omega$$

### 3.2.2. Flux Isolated Reynold's Equation

The Reynold's equation comes from mass continuity which states that for each differential element of flow:

$$\Phi_{p\theta} + \Phi_{c\theta} + \Phi_{pZ} + \dot{M}_{V\tau} = \dot{M}_R$$

$\Phi_{p\theta}$  is the Poiseuille (pressure driven) mass outflow in the angular direction.

$\Phi_{c\theta}$  is the Couette (rotation driven) mass outflow in the angular direction.

$\Phi_{pZ}$  is the Poiseuille (pressure driven) mass outflow in the length direction.

$\dot{M}_V$  is the mass change rate in the elemental volume.

$\dot{M}_R$  is the mass change rate due to mass addition through the bushing.

In addition, it is common and useful to make the substitution of  $Q=P^2$  to quasi-linearize the equation.

If the hydrodynamic actions are kept separate throughout the derivation and the substitution for Q is made, then the Reynolds equation becomes equation 3-3.

**Equation 3-3** Reynolds equation with separated mass addition terms

$$\begin{aligned} & \left[ -H^3 \frac{\partial^2 Q}{\partial \theta^2} - 3H^2 \frac{\partial Q}{\partial \theta} \frac{\partial H}{\partial \theta} \right]_{p\theta} + \left[ \frac{\Lambda}{P} H \frac{\partial Q}{\partial \theta} + 2\Lambda P \frac{\partial H}{\partial \theta} \right]_{c\theta} \\ & + \left[ -\left(\frac{R}{L}\right)^2 H^3 \frac{\partial^2 Q}{\partial Z^2} - \left(\frac{R}{L}\right)^2 3H^2 \frac{\partial Q}{\partial Z} \frac{\partial H}{\partial Z} \right]_{pZ} + \left[ 2P \frac{\partial H}{\partial \tau} + \frac{H}{P} \frac{\partial Q}{\partial \tau} \right]_{V\tau} = \left[ \frac{2t_c}{k_{\rho\rho} P_a c R \delta \theta \delta z} \dot{M} \right]_R \end{aligned}$$

Equation 3-3 is more cumbersome than 3-2 but it is more useful in that the contribution of each mass addition term can be seen.

### 3.2.3. Discretization and Solution of the Reynolds Equation

Each term can be discretized using 2<sup>nd</sup> order, centered finite difference equation in the spatial axes and first order forward difference equations in the time axis.

Terminology is based on  $Q_{i,j}^n$  where  $i$  and  $j$  indicate the node indexes in the longitudinal  $Z$  and  $\theta$  axes and  $n$  indicates the time step.

#### Poiselle $\theta$ Flux, $\Phi_{P\theta}$

$$\Phi_{P\theta} = \left[ \begin{array}{l} \frac{-(H_{i,j}^n)^3 - \frac{3}{4}(H_{i,j}^n)^2 (H_{i,j+1}^n - H_{i,j-1}^n)}{\Delta\theta^2} Q_{i,j+1}^n \\ + \frac{2(H_{i,j}^n)^3}{\Delta\theta^2} Q_{i,j}^n \\ + \frac{-(H_{i,j}^n)^3 + \frac{3}{4}(H_{i,j}^n)^2 (H_{i,j+1}^n - H_{i,j-1}^n)}{\Delta\theta^2} Q_{i,j-1}^n \end{array} \right]_{P\theta}$$

or

$$\Phi_{P\theta}^{ijn} = (C_{P\theta 1}^{ijn} + C_{P\theta 2}^{ijn}) Q_{i,j+1}^n - 2C_{P\theta 1}^{ijn} Q_{i,j}^n + (C_{P\theta 1}^{ijn} - C_{P\theta 2}^{ijn}) Q_{i,j-1}^n$$

$$C_{P\theta 1}^{ijn} = -\frac{(H_{i,j}^n)^3}{\Delta\theta^2}$$

$$C_{P\theta 2}^{ijn} = -\frac{3(H_{i,j}^n)^2 (H_{i,j+1}^n - H_{i,j-1}^n)}{4\Delta\theta^2}$$

### Couette or Wedge $\theta$ Flux, $\Phi_{P\theta}$

$$\Phi_{C\theta} = \frac{\Lambda}{P_{i,j}^n} H_{i,j}^n \frac{(Q_{i,j+1}^n - Q_{i,j-1}^n)}{2\Delta\theta} + 2\Lambda P_{i,j}^n \frac{(H_{i,j+1}^n - H_{i,j-1}^n)}{2\Delta\theta}$$

or

$$\Phi_{C\theta}^{ijn} = C_{C\theta 1}^{ijn} Q_{i,j+1}^n + C_{C\theta 2}^{ijn} Q_{i,j}^n - C_{C\theta 1}^{ijn} Q_{i,j-1}^n$$

$$C_{C\theta 1}^{ijn} = \frac{\Lambda H_{i,j}^n}{2P_{i,j}^n \Delta\theta}$$

$$C_{C\theta 2}^{ijn} = \frac{\Lambda (H_{i,j+1}^n - H_{i,j-1}^n)}{\Delta\theta P_{i,j}^n}$$

### Poiseuille Z Flux, $\Phi_{P\theta}$

$$\Phi_{PZ} = \left[ \begin{array}{l} -\left(\frac{R}{L}\right)^2 \frac{\left(H_{i,j}^3 + \frac{3}{4}(H_{i,j}^2 - H_{i-1,j}^n)\right)}{\Delta Z^2} Q_{i+1,j}^n \\ -2\left(\frac{R}{L}\right)^2 \frac{H_{i,j}^3}{\Delta Z^2} Q_{i,j}^n \\ +\left(\frac{R}{L}\right)^2 \frac{\left(H_{i,j}^3 + \frac{3}{4}(H_{i,j}^2 - H_{i-1,j}^n)\right)}{\Delta Z^2} Q_{i-1,j}^n \end{array} \right]$$

or

$$\Phi_{PZ}^{ijn} = (C_{PZ1}^{ijn} + C_{PZ2}^{ijn}) Q_{i+1,j}^n - 2C_{PZ1}^{ijn} Q_{i,j}^n + (C_{PZ1}^{ijn} - C_{PZ2}^{ijn}) Q_{i-1,j}^n$$

$$C_{PZ1}^{ijn} = -\left(\frac{R}{L}\right)^2 \frac{H_{i,j}^3}{\Delta Z^2}$$

$$C_{PZ2}^{ijn} = -\left(\frac{R}{L}\right)^2 \frac{3H_{i,j}^2 (H_{i+1,j}^n - H_{i-1,j}^n)}{4\Delta Z^2}$$

### Time Rate of Mass Change in the Element $\dot{M}_{V\tau}$

$$\dot{M}_{V\tau} = 2P_{i,j}^n \frac{(H_{i,j}^{n+1} - H_{i,j}^n)}{\Delta\tau} + \frac{H_{i,j}^n}{P_{i,j}^n} \frac{(Q_{i,j}^{n+1} - Q_{i,j}^n)}{\Delta\tau}$$

or

$$\Phi_{V\tau}^{ijn} = C_{V\tau 1}^{ijn} Q_{i,j}^{n+1} + (C_{V\tau 1}^{ijn} - C_{V\tau 2}^{ijn}) Q_{i,j}^n$$

$$C_{V\tau 1}^{ijn} = \frac{2(H_{i,j}^{n+1} - H_{i,j}^n)}{P_{i,j}^n \Delta\tau}$$

$$C_{V\tau 2}^{ijn} = \frac{H_{i,j}^n}{P_{i,j}^n \Delta\tau}$$

### Mass addition through the bushing

Using the assumption that mass addition would be proportional to the difference of the square of the operating pressure and the square of the bearing gap pressure lead to the characterization of each prototype bearing by an empirically determined  $Kmeas$  with EE units of lbs/s. The bearing  $Kmeas$  was converted to an elemental  $Kmeas$  by either dividing it by the number of feedholes,  $Nfd$ , or the surface area of each elemental bushing face. Thus:

For elements fed by a feedhole:

$$(Kmeas)_{i,j} = \frac{(Kmeas)_{bushing}}{Nfd}$$

For elements fed by a porous liner bushing

$$(Kmeas)_{i,j} = (Kmeas)_{bushing} \frac{A_{element}}{A_{bushingID}} = (Kmeas)_{bushing} \frac{\delta Z R \delta \theta}{L \pi R^2}$$

And for elements with no mass flow:

$$(Kmeas)_{i,j} = 0$$

And thus:

$$\dot{M}_R = \left[ \frac{2t_c (Kmeas)_{i,j}}{k_{\rho\rho} p_a c R \delta \theta \delta z} [P_{op}^2 - Q_{i,j}^n] * \mathbf{Ma} \right]$$

where  $\mathbf{Ma}$  is a logical matrice (0's or 1's) indicating which nodes have mass addition.

or

$$\Phi_M^{ijn} = [C_M^n P_{op}^2 - C_M^n Q_{i,j}^n] * \mathbf{Ma}$$

$$C_M^{ijn} = \frac{2t_c (Kmeas)_{i,j}}{k_{\rho\rho} p_a c R \delta \theta \delta z}$$



### Consolidated discretization of the Reynolds equation

The discretized fluxes when added together are the discretized Reynolds equation:

#### Equation 3-4 Discretized Reynolds equation

$$\Phi_{P\theta}^{ijn} + \Phi_{C\theta}^{ijn} + \Phi_{PZ}^{ijn} + \Phi_{V\tau}^{ijn} = \Phi_M^{ijn}$$

The constants can be rearranged so that the equation takes the form:

$$B_{ijn} Q_{i,j+1}^n + A_{ijn} Q_{i,j-1}^n + C_{ijn} Q_{i,j}^n + R_{ijn} Q_{i+1,j}^n + L_{ijn} Q_{i-1,j}^n + T_{ijn} Q_{i,j}^{n+1} = M_{ijn}$$

where

$$B_{ijn} = C_{P\theta 1}^{ijn} + C_{P\theta 2}^{ijn} + C_{C\theta 1}^{ijn}$$

$$A_{ijn} = C_{P\theta 1}^{ijn} - C_{P\theta 2}^{ijn} - C_{C\theta 1}^{ijn}$$

$$C_{ijn} = -2C_{P\theta 1}^{ijn} + C_{C\theta 2}^{ijn} - 2C_{PZ 1}^{ijn} + C_{V\tau 1}^{ijn} - C_{V\tau 2}^{ijn} + C_M^{ijn}$$

$$R_{ijn} = C_{PZ 1}^{ijn} + C_{PZ 2}^{ijn}$$

$$L_{ijn} = C_{PZ 1}^{ijn} - C_{PZ 2}^{ijn}$$

$$T_{ijn} = C_{V\tau 2}^{ijn}$$

$$M_{ijn} = C_M^{ijn} P_{op}^2$$

### 3.3. CFD Methods for Fixed Displacement Hydrostatic Bearings

#### 3.3.1. CFD Method

Fixed displacement bearings have no time transient terms and hydrostatic bearing have no rotational (Couette) terms. Hence equation 3-4 is reduced to equation 3-5.

**Equation 3-5** Discretized Reynolds equation for a fixed displacement hydrostatic bearing.

$$B_{ijn} Q_{i,j+1}^n + A_{ijn} Q_{i,j-1}^n + C_{ijn} Q_{i,j}^n + R_{ijn} Q_{i+1,j}^n + L_{ijn} Q_{i-1,j}^n = M_{ijn}$$

where

$$B_{ijn} = C_{P\theta 1}^{ijn} + C_{P\theta 2}^{ijn}$$

$$A_{ijn} = C_{P\theta 1}^{ijn} - C_{P\theta 2}^{ijn}$$

$$C_{ijn} = -2C_{P\theta 1}^{ijn} - 2C_{PZ 1}^{ijn} + C_M^{ijn}$$

$$R_{ijn} = C_{PZ 1}^{ijn} + C_{PZ 2}^{ijn}$$

$$L_{ijn} = C_{PZ 1}^{ijn} - C_{PZ 2}^{ijn}$$

$$M_{ijn} = C_M^{ijn} P_{op}^2$$

All the constants are dependent on flight height  $H$  only and thus equation 3-5 is a set of linear equations where the solution for each  $Q_{i,j}$  is dependent on linear contributions from the nearest neighbors equaling a constant.

If a mesh is chosen that has  $NL$  nodes along the bearing length and  $Nazb$  angular ( $R\theta$ ) nodes then the boundary conditions for the gas journal bearings are

that the pressure is ambient pressure at the bearing ends, or

$$Q_{1,j} = Q_{NL,j} = 1$$

and that in  $R\theta$  direction that the nodes wrap so that the nearest  $R\theta$  neighbor

(incrementing  $j$ ) to  $Q_{i,Nazb}$  is  $Q_{i,1}$ .

Equation 3-5 can be seen to be a set of  $(NL-2) \times Nazb$  linear equations. In matrix form they can be written as  $\mathbf{CQ}=\mathbf{M}$  where  $\mathbf{C}$  is a square matrix with dimensions of  $((NL-2) \times Nazb) \times ((NL-2) \times Nazb)$ , and  $\mathbf{Q}$  and  $\mathbf{M}$  have dimensions of  $1 \times ((NL-2) \times Nazb)$ . Put in matrix form the constants form a pattern of clusters so that each equation for  $Q_{i,j}$  has 5  $\mathbf{C}$  constants consisting of a “central” constant  $C_{i,j}$ , and “Left”, “Right”, “Above” and “Below” nearest neighbors ( $C_{i-1,j}$ ,  $C_{i+1,j}$ ,  $C_{i,j+1}$ ,  $C_{i,j-1}$ ) and 1  $\mathbf{M}$  constant. At the boundary conditions where  $Q=1$  there are only 4  $\mathbf{C}$  constants as the  $C_{1,j}$  and  $C_{NL,j}$  constants get subtracted into the  $M_{i,j}$  constant. The “Above” constant for  $j=Nazb$  is  $C_{i,1}$  and the “Below” constant for  $j=1$  is the  $C_{i,Nazb}$  constant. Though the dimensions of  $\mathbf{C}$  are very large scaling to the 4<sup>th</sup> power of the number nodes each row contains only 4 or 5 non-zero constants. This is handled efficiently by using sparse matrices. Because it is a set of linear equations it can be solved in one step using Gaussian elimination.

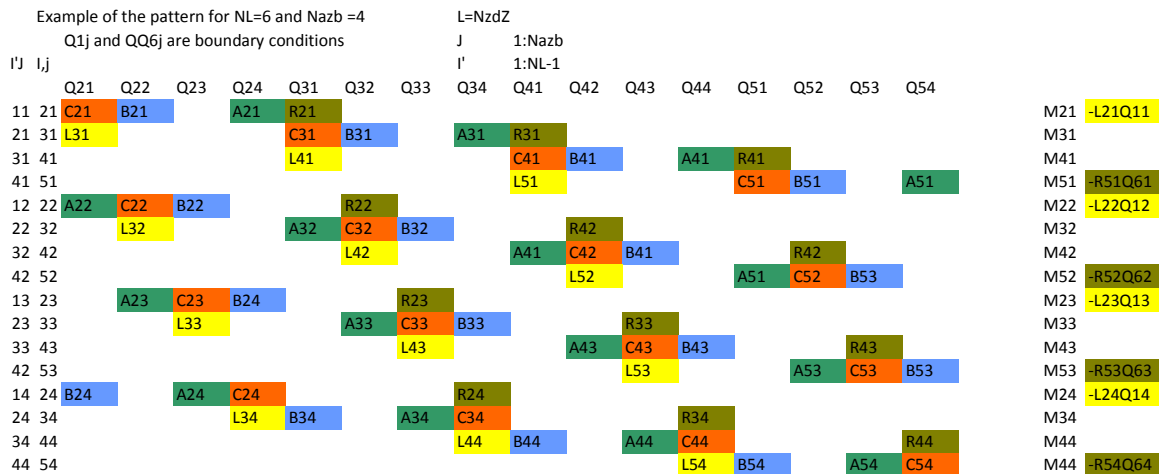


Figure 3-2 Cluster pattern of CQ=M set of equations.

### 3.3.2. Pressure Solution Examples and Integration of Net Hydrodynamic Force

The meshing used for the CFD solutions was a simple 2 dimensional evenly spaced nodes in the  $R\theta$  and  $Length$  ( $Z$ ) directions of the bearing gap. Usually 30 space increments were used (31 nodes) in the  $L$  direction and 96 increments (96 nodes) in the  $R\theta$  direction were used. Thus the key bearing state variables, gap height, pressure, elemental mass addition, elemental mass fluxes, etc. were kept in 2 dimensional matrices.

A good way to view and examine the results is to create a 2D surface plot over the  $R\theta - Length$  plane. These were examined visually by rotating them about in 3 dimensions. Many of the figures in this thesis are taken from “snapshots” of rotating these plots. All of the programs that were written to produce these surface plots were written to label the axes  $R\theta$  and  $Length$ . The programming is independent of units so long as a consistent set of units are used that are consistent with the equations. In this thesis, a consistent set of EE units was used such that:

time -seconds

length - inches

forces - pound force

mass - pound mass

viscosity - reyn or  $\text{lbf}\cdot\text{s}\cdot\text{in}^{-2}$

Temperature - Fahrenheit or Rankine for absolute temperature

The units for  $R\theta$  and  $Length$  are inches. Recalling that all the bearings in this thesis are 2” length by 0.75” bearing diameter explains why the “Length” axis

goes from -1 to +1 (inches) and the  $R\theta$  axes goes from 0 to 2.356 (inches). The most used examples of this are the following programs to display results in rotatable surface maps in the *Length- $R\theta$*  plane.:

Gmesh.m - displays the bearing gap height ( $h$ ) in inches.

Hmesh.m - displays the dimensionless bearing gap height ( $h/c$ ).

Pmesh.m - displays the dimensionless pressure ( $P$ ).

Qmesh.m - displays dimensionless  $Q=P^2$ .

pDmesh - displays the dimensional pressured in psia.

NetMassmesh - displays the sum of the mass flux at each element (lbs/s).

FYMesh - displays the shaft/bushing interaction force in the Y direction in pounds.

FXmesh - displays the shaft/bushing interaction force in the X direction in pounds.

Examples:

Example 1:

Bearing dimensions: 0.75" diameter x 2" length.

Clearance: 0.0005"

Mass Addition: 12 feedholes equally spaced in 2 rows located 0.375" from each end, first feedhole located in direct alignment with the Y axis.

Operating pressure ( $pop$ ) : 60 psig (dimensionless operating pressure  $Pop=5.0816$ )

Operating Temperature: 70° F.

Mass Addition constant ( $Kmeas$ ):  $2.2e-6$  lbs/s per  $Pop^2-Q$

Shaft/Bushing displacement: 0 (shaft and bushing are aligned concentric on the same Z axis).

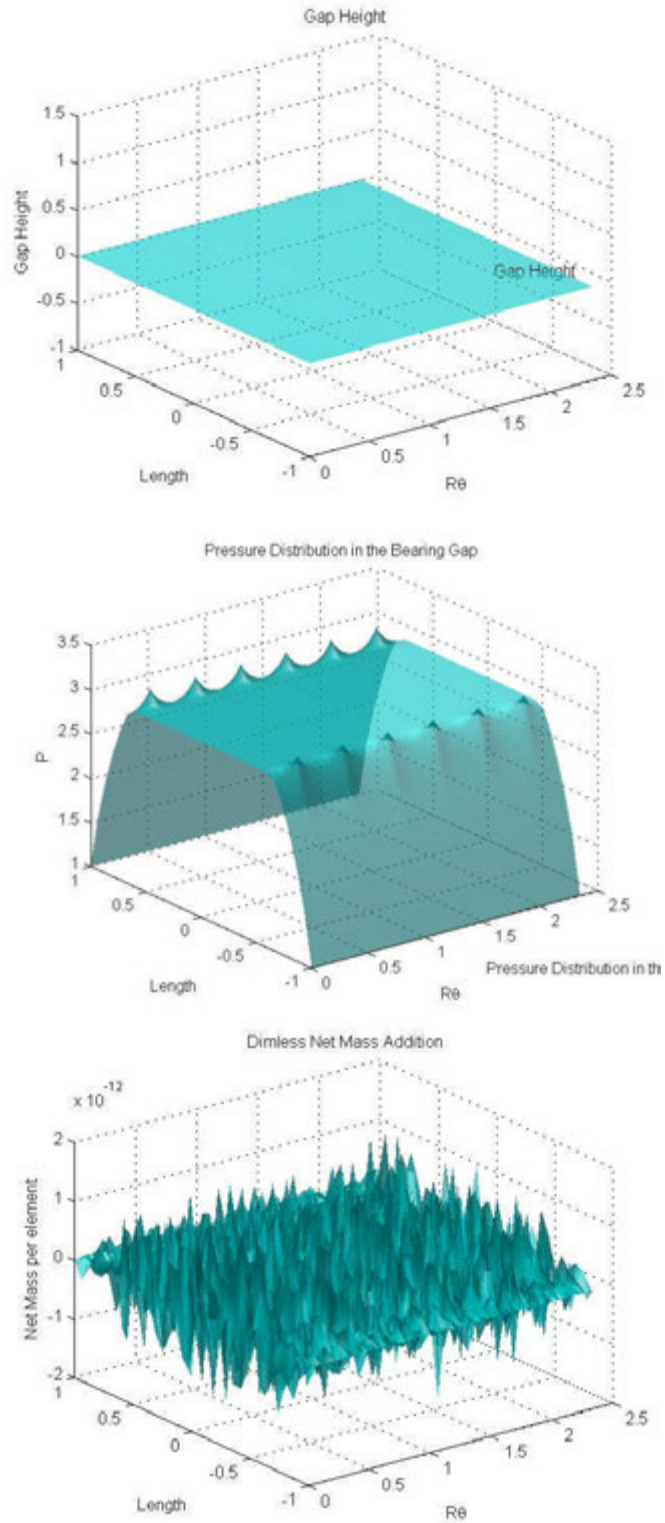


Figure 3-3 Top - Gmesh, Middle - Pmesh, Bottom - NetMassmesh for example 1.



Gmesh shows that the gap height (relative to the neutral axis of the bearing) is 0 all about the bearing gap. Pmesh shows the pressure distribution. The 12 feedholes can easily be seen as point pressure peaks. The pressure distribution is symmetric as expected in the  $R\theta$  direction. As expected the pressure is constant in the  $Z$  area (Length) between the feedholes as symmetry would indicate that the mass flow would be zero in this area. The pressure drops off rapidly in the  $Z$  axis from the feedholes to the edges of the bearing according to the expectation that  $dQ/dZ$  should be constant in that area. At the outside edges of the bearing the dimensionless pressure is 1 (atmospheric). The NetMass distribution shows that the  $P$  solution is good as all the elements meet continuity with net mass flux=0 (order of magnitude of  $10^{-12}$ ). Running Q mesh confirms that  $dQ/dZ$  is in fact constant (linear Q distribution) in the area from the feed holes to the edges.

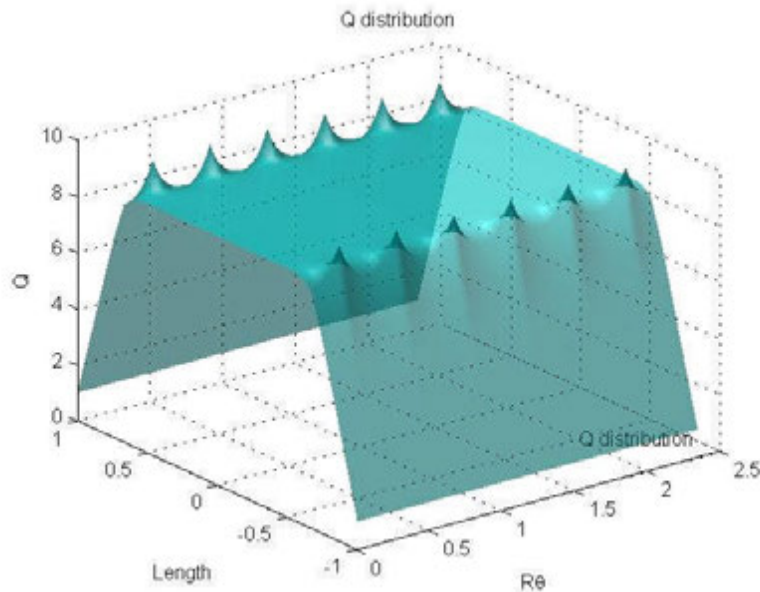


Figure 3-4 Qmesh for example 1.

The net hydrodynamic force vector was found to be zero ( $F_x=-2.98e-14$ lbs and  $F_y=-8.86e-14$ ). The mass addition to the bearing is  $3.53e-5$  lbs/s.

## Example 2:

Example 2 is the same as example 1 except the shaft/bush displacement is set to  $-0.0004$ " in the Y direction (down).

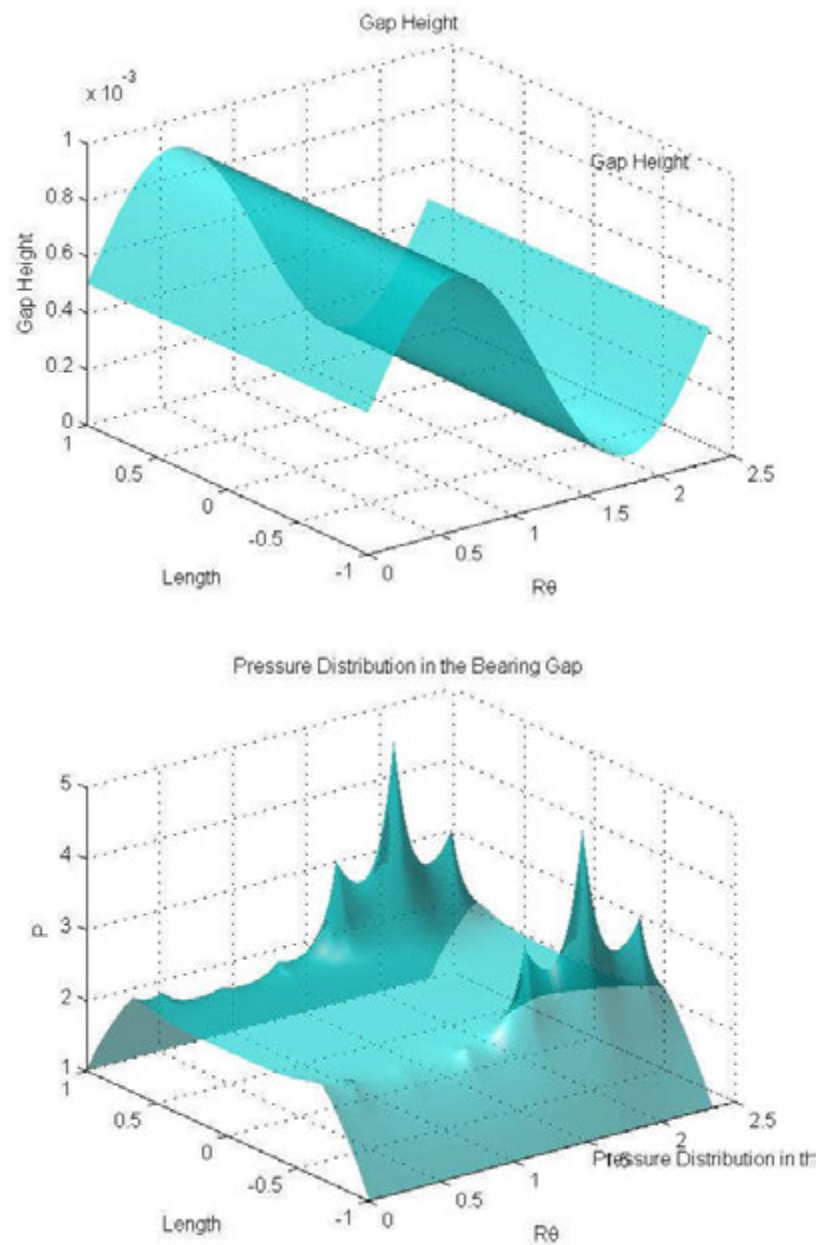


Figure 3-5 Top - Gmesh, Bottom - Pmesh for example 2.

In this case bearing gap height varies from the nominal clearance of 0.0005" to reach a maximum of 0.0009" and a minimum of 0.0001". The pressure distribution is still symmetric in the Z length direction but is not symmetric in the  $R\theta$  direction reaching maximum pressure in the areas of smallest gap height and minimum pressure at maximum height. When integrated the net hydrodynamic force is 5.081lbs in the Y direction ( $F_x=0$ ) centrally located in the bearing gap plane (no net moment). The mass flow rate  $3.33e-5$  lbs/s just slightly lower than what it was when the displacement was zero.

Examples 3 and 4:

Examples 3 and 4 are the same bearing and operating parameters as in examples 1 and 2 except this time the mass addition is through a porous liner of  $K_{meas}=2.7e-4$  lbs/s. This is the equivalent a New Way porous graphite liner is about 10x that of the 0.003" diameter feed hole used in examples 1 and 2. For example 3 the shaft bush displacement is 0 (equivalent to example 1) and for example 4 the displacement is 0.0004", the same as example 1.

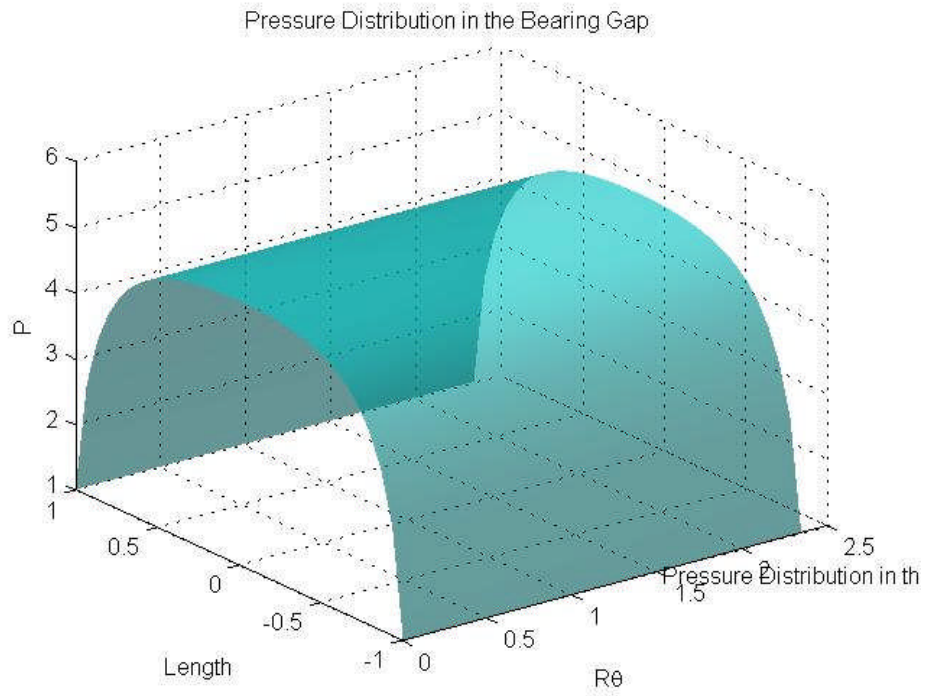


Figure 3-6 Pmesh for example 3.

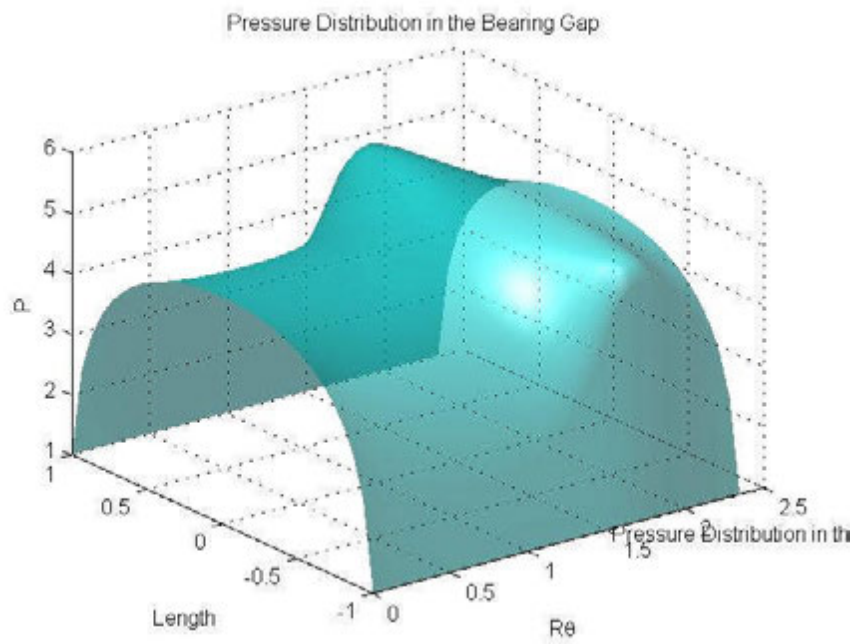


Figure 3-7 Pmesh for example 4.

In example 3 the mass addition through a porous liner causes a smooth “curvy” pressure distribution that is symmetric in both the  $Z$  and  $R\theta$  direction. As expected the net shaft/bearing force is zero. The mass addition is  $1.57\text{e-}5$  lbs/s. In example 4 the pressure distribution continues to be symmetric in the  $Z$  axis but is not symmetric in the  $R\theta$  direction reaching higher pressures where the gap height is smallest. As a result the net hydrodynamic force is 17.22 lbs in the  $Y$  direction. The mass addition is  $1.90\text{e-}5$  lbs/s.

Examples 5 and 6:

Throughout this thesis the shaft/bushing displacement will always be simple translation in the  $Y$  direction parallel to the neutral axis. Nonetheless, the programming is capable of conical displacements. To demonstrate this,  $Kmeas$  is kept at  $2.7\text{e-}5$  lbs/s. The displacement is set to be  $Y$  of  $0.00015$ ”,  $X$  of  $0.0001$ ”, angle about  $Y$  ( $ay$ ) is  $0.0003$  radians and an angle about  $Z$  ( $az$ ) of  $0.0002$  radians (see bearing geometry section 1.3). Example 5 will be this displacement and  $Kmeas$  for a feed hole fed bearing and example 6 will be for a porous liner bearing.

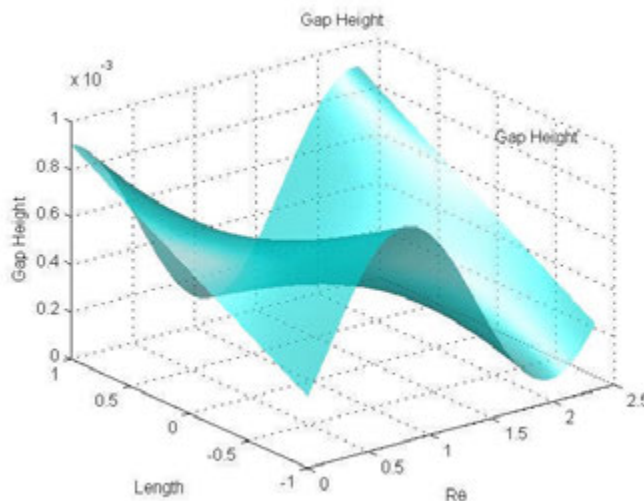


Figure 3-8 Gmesh for examples 5 and 6.

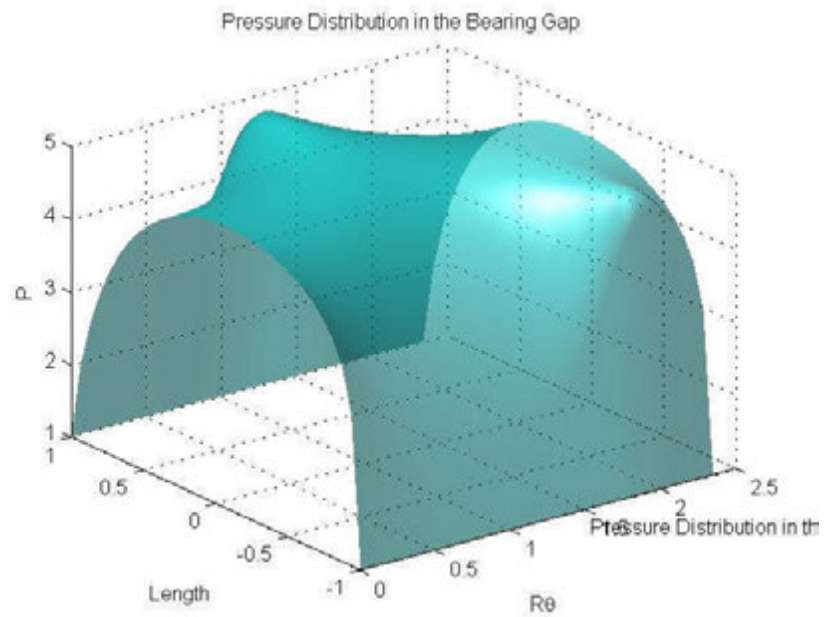
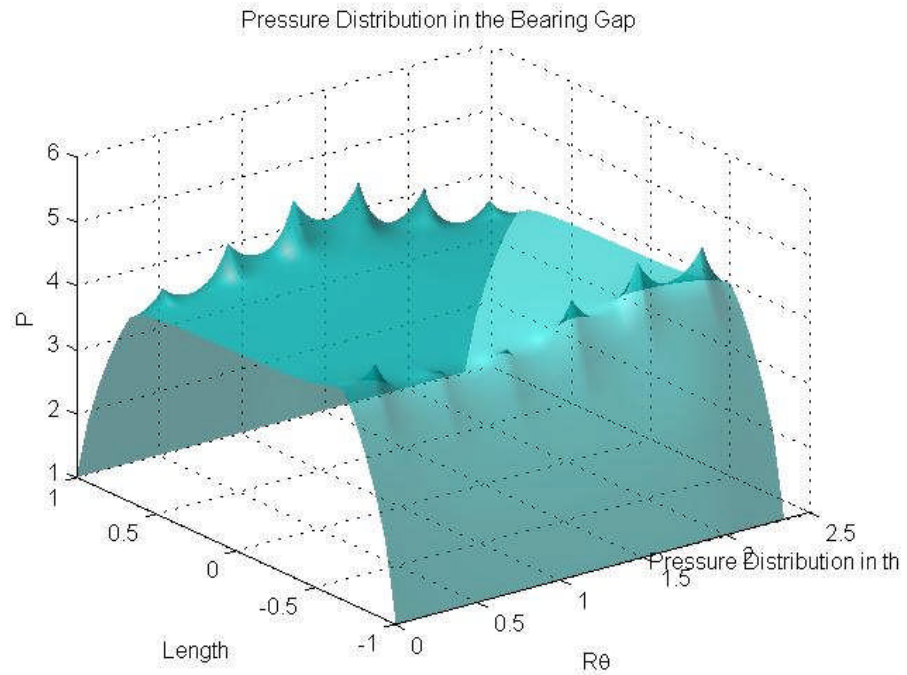


Figure 3-9 Pressure distribution solutions for conical displacements  
Top - feedhole bearing, Bottom - porous liner bearing.

As expected the conical displacements create a bearing gap that is not symmetric in either major bearing axis. For the feedhole fed bearing, example 5, this results in  $F_y=1.64 \text{ lbs}$ ,  $F_x=1.09 \text{ lbs}$  and a moment about the  $Y$  axis of  $2.96 \text{ in-lbs}$  and a moment about the  $X$  axis of  $1.98 \text{ in-lbs}$ . The mass input was  $1.20 \text{ e-4 lbs/s}$ . For the Porous liner bearing, example 6, this results in  $F_y=6.25 \text{ lbs}$ ,  $F_x=4.17 \text{ lbs}$  and a moment about the  $Y$  axis of  $7.61 \text{ in-lbs}$  and a moment about the  $X$  axis of  $5.07 \text{ in-lbs}$ . The mass input was  $1.805 \text{ e-4 lbs/s}$ . Thus it could be noted that considerably more net hydrodynamic force is generated for porous liner bearings than for feedhole bearing with similar mass flow constant  $K_{meas}$ .

### 3.3.3. Sweeping Experiments by Flight Height

For fixed displacement hydrostatic bearings the discretized Reynolds equation form a linear set of equations so that a pressure solution can be found in one iteration using Gaussian elimination. A CFD experiment based on a fixed displacement hydrostatic bearing using a 31x96 grid mesh takes about 5 seconds to execute. This makes it possible to economically perform CFD experiments over a wide range of operating conditions.

A program (MistHSweep.m) was written to execute a number of static bearing experiments and records their results. The bearing and bearing operating conditions are defined in the usual way and then MistHSweep sweeps the  $Y$  shaft/bushing displacement beginning at zero and increasing in increments until the  $Y$  displacement equals the bearing clearance. Thus for a given bearing it runs a series of numerical experiments by first placing the shaft and bearing in their neutral concentric axis and then incrementally moving them together until the bearing is “grounded” (shaft contacting bushing). After each experiment summary results are recorded in a matrix. Thus the stiffness or load force etc. for a given bearing can be plotted as a function “flight height”. In these experiments and all experiments following the effect of a translational displacement of the shaft/bushing are expressed in terms  $h$  and  $H$ . In Gmesh and Hmesh the bearing gap is mapped in terms of  $h$  and  $H$  everywhere in the bearing gap plane. However in this context  $h$  and  $H$  refer to  $h_{min}$  and  $H_{min}$  where  $h_{min}$  is the clearance minus the  $Y$  displacement and  $H_{min}$  is  $h_{min}$  divided by the clearance.

This makes it possible to numerically redo the empirical static bearing tests. For example, figure 3-10 shows a numerical equivalent to the static tests of the New Way bearing (porous liner with  $K_{meas}=2.71 \text{ e-5 lbs/s}$ ) with the three different shafts used which created clearances of 1050, 580, and 200  $\mu\text{in}$ .



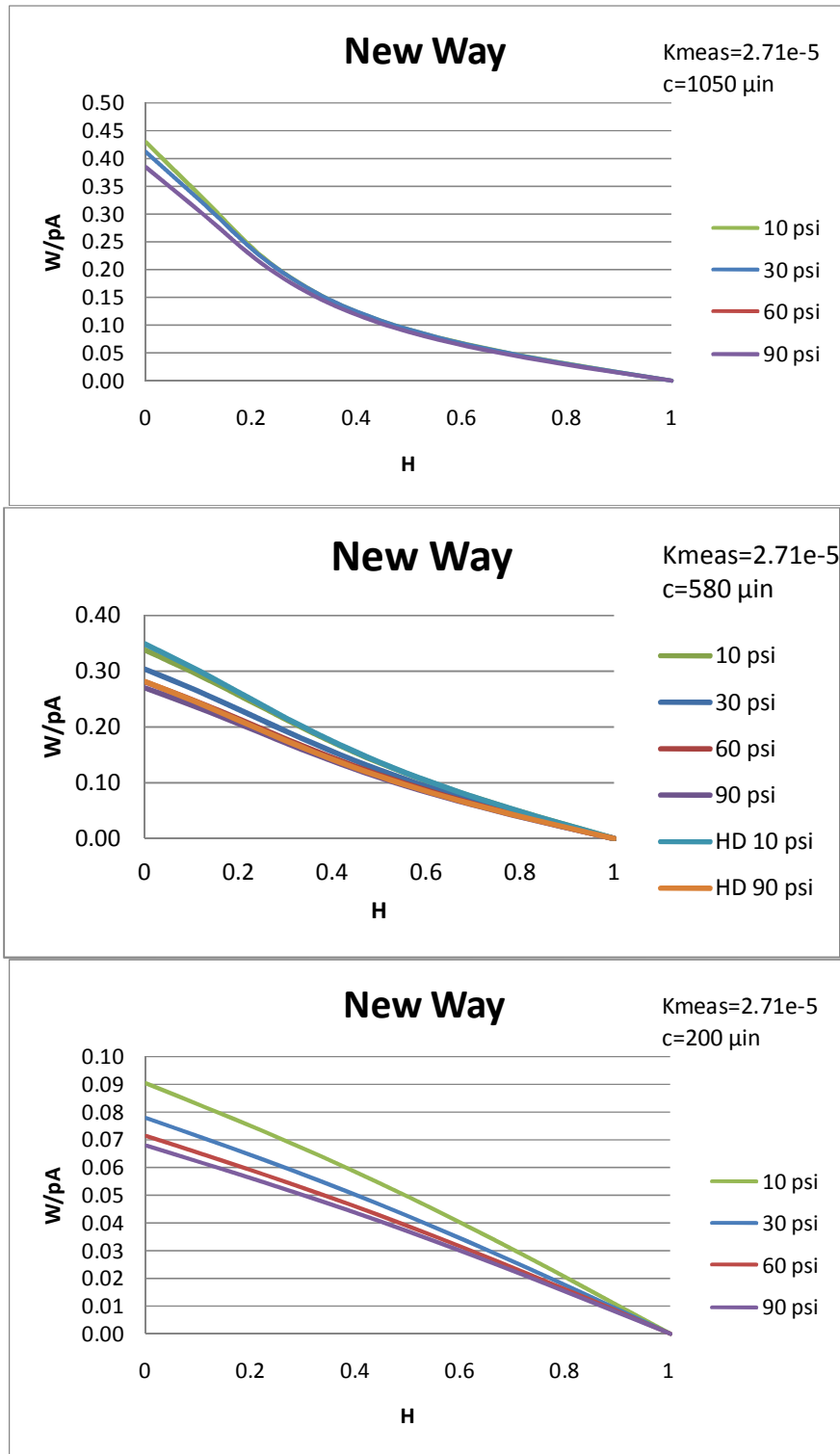


Figure 3-10 Results of performing CFD experiments by sweeping the flight height on a porous liner bearing.

### 3.3.4. Effect of Increasing Grid Resolution

In the sweeping experiments each line on each graph represents 20 pressure solutions taken at even increments of  $H$ . Each set of solutions took about 5 seconds to execute. The results were then pasted into a spreadsheet and graphed. For the 580  $\mu\text{in}$  graph two additional lines, "HD 10psi" and "HD 90psi" are added. The "HD 10 psi" and "HD 90 psi" lines correspond to setting  $NL=120$  and  $Nazb=320$  for a finer 120 x 320 grid (from  $NL=30$  and  $Nazb=96$ ). For  $Nazb$  a choice that is divisible by 6 is preferred as the feedholes bearings have 2 rows of 6 feedholes so that a feedhole locations will exactly correspond to a  $\theta$  increment. Each set of these solutions took about 6 minutes to execute.

Comparison of the 120 x 320 10 psi and 90 psi results to the 31 x 96 results indicates that the added precision in the finer mesh is not, in general, worth the increased execution time.

### 3.3.5. Effect of Increasing the Sweep Increment

When MistHSweep was run to generate sets of solutions for feedhole fed bearings it was found that errors occurred for solutions of  $H=0$ . The error message returned was that precision of the Gaussian elimination solution was lost because the coefficient matrix was too close to being singular. (This does not occur for the porous liner coefficients) To remedy this the  $H$  sweep was set to stop one increment short  $H=0$ .

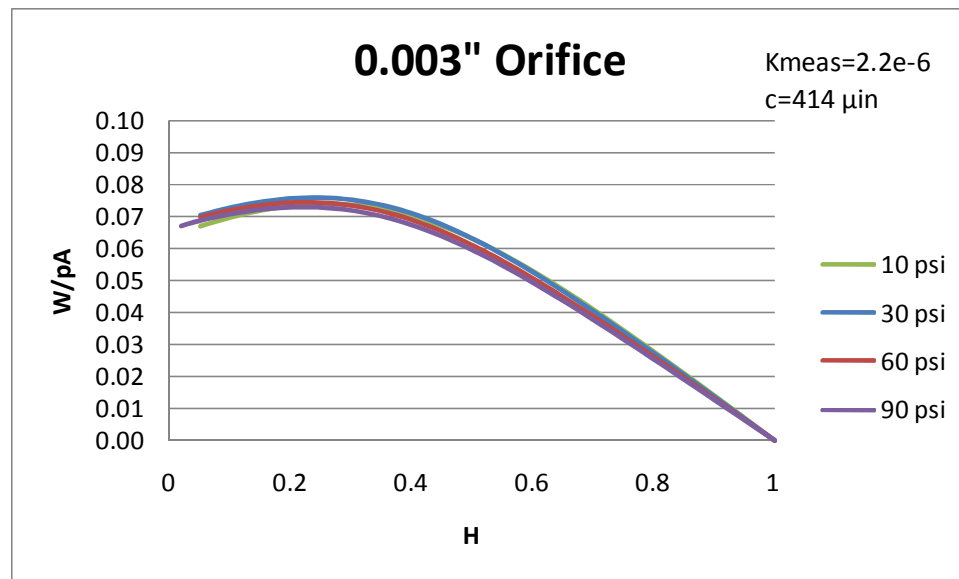


Figure 3-11 Sweeping with 19 and 50  $H$  increments.

Figure 3-11 shows the results for an 0.003" diameter feedhole fed bearing ( $K_{meas}=2.2e-6$ ). In general 19  $H$  increments were used to develop each isobar so that each isobar spans  $H=0.053$  to 1. For the 90 psi line 50  $H$  increments were used so that it spans  $H$  from 0.01 to 1. Inspection of the line indicates that solutions can be found for  $H$  approaching very close to zero and that the  $H=0$  solution is a smooth extension of the curve from  $H$  close to zero.

### 3.3.6. Mapping in the $h$ - $c$ Plane

Examination the results of sweeping  $H$  for selected isobars of the selected bearings indicates some interesting initial observations.

- 1) Measuring bearing performance in terms of dimensionless  $W/pA$  is very powerful. However, the relationship is not as simple as the supposition that small clearances lower  $W/pA$  and that increasing clearance increases  $W/pA$  to with diminishing effect.
- 2)  $W/pA$  vs.  $H$  curves are relatively, but not completely independent of operating pressure. Isobars for a given pressure fan out with low pressure isobars outperforming high isobars. In some cases the spread of the isobars ranges from significant to insignificant. Performance in terms  $W/pA$  drops with increased operating pressure in a diminishing return fashion where increasing operating pressure over 90 psig have little additional effect on  $W/pA$ .
- 3) The shape of the of the  $W/pA$  vs.  $H$  curve changes significantly from the anticipated logarithmic decay where the grounding force at  $H=0$  is expected to be the maximum net hydrodynamic force and hence the maximum  $W/pA$  value for each isobar. Very surprisingly, in some bearing isobars the maximum net hydrodynamic force occurs at  $H>0$  indicating a very interesting “near surface” effect.

These observations lead to the conclusion that it would be very powerful to view bearing performance for a bearing operating pressure and temperature in terms of  $W/pA$  across the practical  $H$ - $c$  plane. To accomplish this `MistHcPlane.m` was written. It sweeps the clearance increments for each clearance then sweeps the  $H$  from 0 to 1. Typically the sweeping is done in 20 height increments for each of 20 clearance increments requiring 400 solutions per planar sweep. At that

sweep density each sweep takes about 3 minutes and produces 400  $W/pA$  data points in the  $h$ - $c$  plane. To visualize the results a matlab function called “TriScatteredInterp” is used to make a data interpolant function. Then a mesh can be chosen and the results presented as a surface above the  $h$ - $c$  plane. The effect is a very powerful tool for examination of bearing performance.

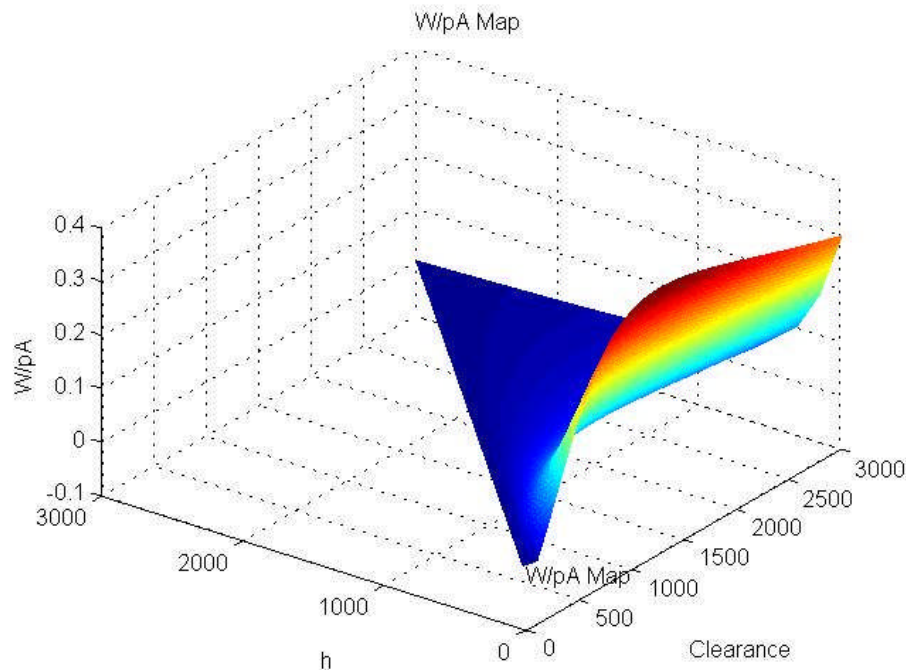


Figure 3-12  $W/pa$  in the  $h$ - $c$  plane for a porous liner bearing.

Figure 3-12 shows the  $W/pa$  performance surface of porous liner bearing with  $K_{meas}=2.5e-5$  (very similar to a New Way bearing) and an operating pressure of 90 psig. The surface can be rotated about any axis and “snapshots” can be taken of different views. The data resulting from the sweeps works in this way. An initial minimum clearance is set for example at 100  $\mu$ in. Then solutions for  $W/pA$  are found in increments of  $h$  ranging  $h=0$  to  $c$  or in the initial sweep this would be  $h$  from 0 to 100  $\mu$ in. Plotted this data would form line at  $c=100$  that would plot  $W/pA$  from  $h=0$  to 100  $\mu$ in. The clearance is incremented to, for example, 150  $\mu$ in. Then solutions would be generated for  $W/pA$  for  $h=0$  to 150

$\mu\text{in}$  which if plotted would be a curve of  $W/pA$  values at clearance=150 ranging from  $h=0$  to 150  $\mu\text{in}$ . This is repeated until the desired maximum clearance is reached. Plotting the results of a 20 x 20 sweep would result in 20 lines each of 20 data points running parallel to each other in the  $c$  dimension indicating the plane of  $W/pA$  performance. The TriScatteredInterp function in matlab is used to interpolate the data between the plots to form a surface.

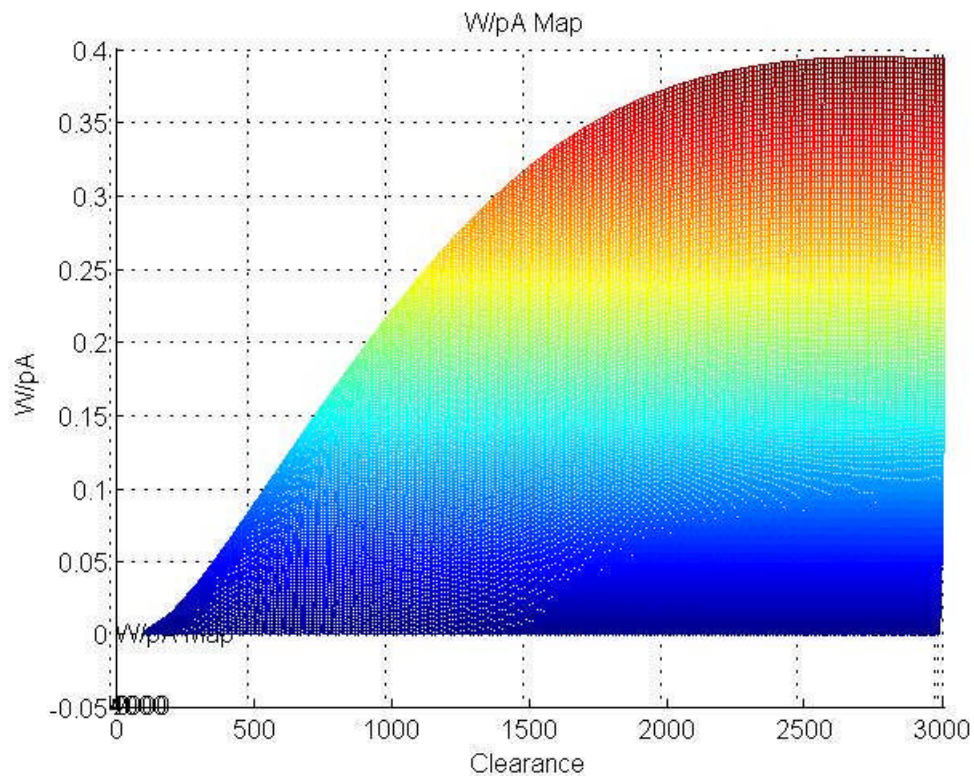


Figure 3-13 The  $W/pA$  in the  $h-c$  plane from the clearance view.

Rotating the surface to the clearance view presents a graph of  $W/pA$  versus clearance. The example in figure 3-13 shows that maximum  $W/pA$  is of just under 0.4 and is achieved at a very large clearance of 3000  $\mu\text{in}$  and appears to be peaking. The clearance range could be set to larger than 3000  $\mu\text{in}$  to see if

$W/pA$  simply peaks or declines with increases clearance (This will be done in the results section).

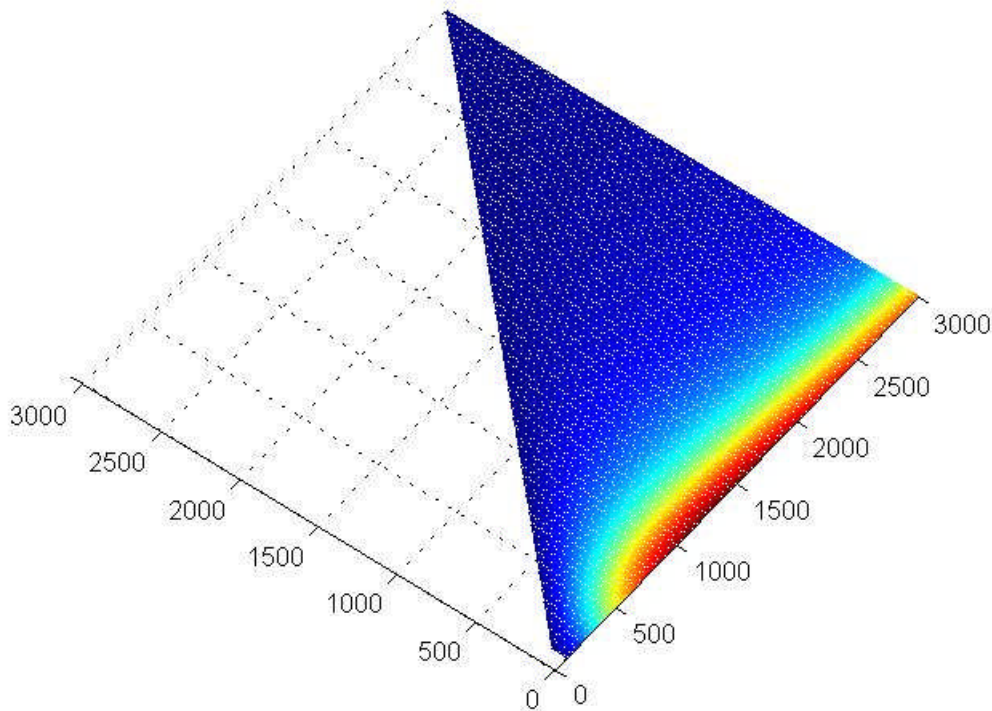
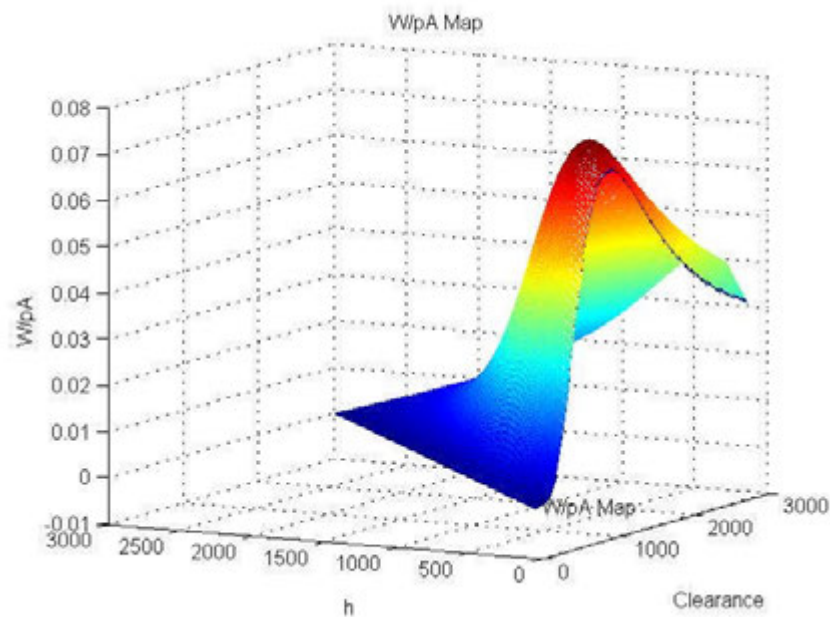


Figure 3-14 Top view looking into the  $h$ - $c$  plane.

Turning the surface so that it viewed looking into the  $h$ - $c$  plane gives color contour of the height at which  $W/pA$  reaches its maximum. In this case, the maximum  $W/pA$  always occurs at  $h=0$  (as was always expected). The fact that  $h$  is swept from 0 to  $c$  explains the diagonal cut of the surface when viewed from above.

Three versions of MistHcPlane have been written. For porous liner bearings solution can be generated for  $h=0$  so that MistHcPlanePorous sweeps from  $h=0$  to  $c$ . As discussed problems occur when solutions are attempted for feedhole bearings at  $h=0$ . Thus MistHcPlaneFH was written that sweeps  $h$  from one

increment above 0 to  $h$ . Since the program sweeps each clearance range with the same number of  $h$  increments, the lowest  $h$  solution becomes increasing larger as the clearance increases and the  $h$  increment increases. A third version, MistHcPlaneProg, works very well for either porous liner or feedhole bearings. It starts each  $h$  sweep at a fixed very small increment above zero (10  $\mu\text{in}$ ). Responding to the observation that  $W/pA$  changes very quickly at small  $h$ , MistHcPlaneProg uses smaller increments at low  $h$  than at high  $h$ .



3-15  $W/pA$  in the  $h$ - $c$  plane for a feedhole fed bearing.

Figure 3-15 shows the  $W/pA$  surface for a feedhole bearing with  $K_{meas}=2.5 \text{ e-}5$ . It can be observed immediately that the surface is very different from the porous liner bearing as the  $W/pA$  shows a definite peak. Also the maximum  $W/pA$  is not located at  $h=0$ .



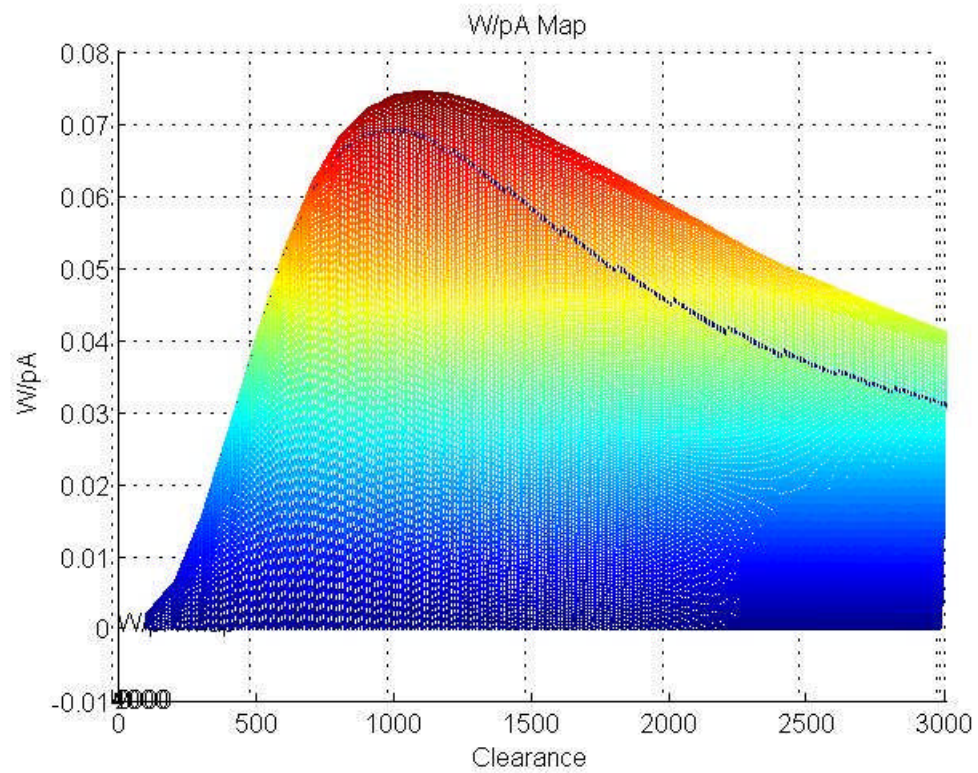


Figure 3-16 Clearance view of  $W/pA$  in the  $h$ - $c$  plane for a feedhole fed bearing.

Looking at the same surface from the clearance side shows the  $W/pA$  peaking at about 0.075 at a clearance of about 1100  $\mu\text{m}$ .

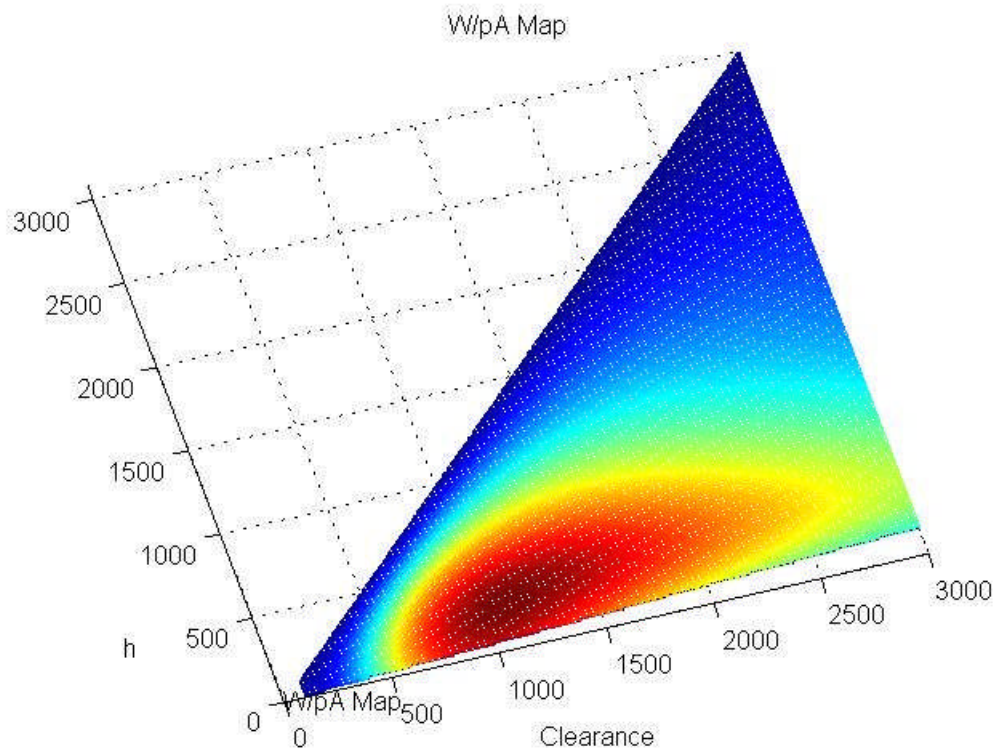


Figure 3-17 Top view of  $W/pA$  in the  $h$ - $c$  plane for a feedhole fed bearing.

Viewing the surface from the top indicates that the peak  $W/pA$  for a given clearance appears to run along a contour that goes from  $h=0$  at  $c=500$  to  $h=250$  at  $c=1250$  then curves back to  $h=3000$  at  $c=2500$ . The increasing increment of the minimum  $h$  for which solutions were found indicates this surface was generated by MistHcPlaneFH which started the  $h$  scans one increment short of 0.

### 3.4. CFD Methods for Fixed Displacement Hydrodynamic and Hybrid Bearings

When there is no rotation and the bushing and shaft are in a fixed location, the discretized Reynold's equation is linear in  $Q$  and the pressure distribution can be solved in a single pass using Gaussian elimination. In the case of an isothermal bearing where the shaft and bushing locations are considered fixed there are no transient terms but nonlinear factors involving  $P$  appear in the Couette terms.

The strategy to solve this nonlinear equation is as follows:

1. Assume a "reasonable" pressure distribution.
2. Calculate the "linear" factors using the current pressure distribution.
3. Solve the quasi-linear equation.
4. Check the mass imbalance as a measure of the accuracy of the new pressure distribution.
5. Replace the current pressure distribution with the new pressure distribution.
6. Repeat steps 2-4 until mass imbalance diminishes to a negligible amount.

**Equation 3-6** Discretized Reynolds equation for fixed displacement rotating bearings

$$\begin{aligned}\Phi_{P\theta}^{ijn} + \Phi_{C\theta}^{ijn} + \Phi_{PZ}^{ijn} + \Phi_{V\tau}^{ijn} &= \Phi_M^{ijn} \\ B_{ijn} Q_{i,j+1}^n + A_{ijn} Q_{i,j-1}^n + C_{ijn} Q_{i,j}^n + R_{ijn} Q_{i+1,j}^n + L_{ijn} Q_{i-1,j}^n &= M_{ijn} \\ B_{ijn} &= C_{P\theta 1}^{ijn} + C_{P\theta 2}^{ijn} + C_{C\theta 1}^{ijn} \\ A_{ijn} &= C_{P\theta 1}^{ijn} - C_{P\theta 2}^{ijn} - C_{C\theta 1}^{ijn} \\ C_{ijn} &= -2C_{P\theta 1}^{ijn} + C_{C\theta 2}^{ijn} - 2C_{PZ 1}^{ijn} + C_M^{ijn} \\ R_{ijn} &= C_{PZ 1}^{ijn} + C_{PZ 2}^{ijn} \\ L_{ijn} &= C_{PZ 1}^{ijn} - C_{PZ 2}^{ijn} \\ M_{ijn} &= C_M^{ijn} P_{op}^2\end{aligned}$$

The Couette terms  $PZ$  are not constants but are inversely proportional to  $P_{ij}$ . Thus equation 3-6 is not a linear equation but can be regarded as a quasi-linear equation. Thus an assumed pressure distribution was used to calculate the Couette terms and used to solve equation 3-6 as a set of linear equations. The resulting pressure distribution was then used to recalculate the Couette constants and process was iterated. The absolute value of the sum of the elemental net mass flux (which would be 0 for the exact pressure distribution) was used as the criteria for determining the pressure solution accuracy. More details are in Appendix C.

Using this procedure accurate pressure solutions were found in a relatively small number of iterations (usually less than 20). However in some cases the iterated solution developed numerical instability and a good solution could not be reached. It was observed that the cases of numeric instability involved high rotation speeds and small  $h_{min}$ . Several methods were attempted to extend this

speed limit of numerical stability. One method was a pressure correction method where the mass elemental mass flux was used to suggest a pressure correction to generate a new more accurate pressure distribution. Combinations of iterations using Gaussian elimination of the quasi-linear equations and pressure corrections were also used. It was found that the numerical speed limit could be extended somewhat by use of numerical viscosity factor  $N_{visc}$  to dampen the iterative numeric corrections. {Heath} has a table of software to solve nonlinear equations (p.244) which lists the Matlab function *fsolve*. Since in most cases solutions could be reached with speeds exceeding 100K RPM which was the speed range of interest in this thesis, CFD experiments were continued and work on broadening the range of numeric stability was deferred.

IterateQProg.m was written and used for these experiments. In this program the user can set 1) the number of iterations for the program to perform, 2) *miniQ* the minimum  $Q$  to filter a solution, and 3) the  $N_{visc}$  so that  $Q_{i+1} = Q_i + N_{visc} * (Q_{i+1} - Q_i)$ . The total error is then recorded per each iteration. IterateQProg is handy to allow the user to set  $N_{visc}$  and then run a number of iterations and see if the pressure solution is converging. In most cases the solution converges at a certain number iterations and then begins to diverge away so that there is an optimum number of iterations to get the best solution at a given  $N_{visc}$ . The user can then look at the iteration log, note the number of iterations achieving the best solution, and then reset IterateQProg to run to that exact number of iterations and reproduce the best pressure solution.

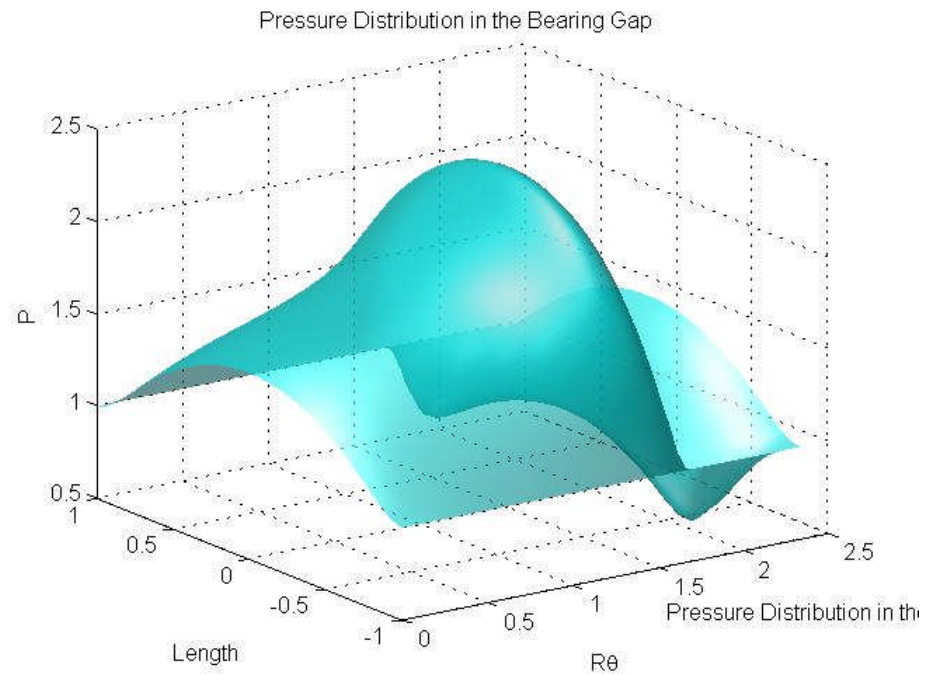


Figure 3-18 Pressure solution for 140K RPM fixed displacement hydrodynamic bearing with the sum of the absolute value of the elemental mass flux error ( $ERR_{Tot}$ )= $3.2307e-4$  after 38 iterations.

## CHAPTER 4. CFD RESULTS

### 4.1. Hydrostatic Bearing Gap Pressure Distributions

The bearing gap pressure distributions for PL and FH bearings operated hydrostatically (no rotation) were studied by CFD experimentation. All CFD experimental displacements were translational so that shaft and bushing centerlines were parallel at all times and the eccentricity was the same along the length of the bearing. Thus the pressure distributions for all bearings in hydrostatic operations (PL and FH) formed a symmetric pressure wave about the location of  $h_{min}$  in the  $R\theta$  direction with the pressure maxima located at  $h_{min}$  and the pressure minima located at  $h_{max}$ ,  $180^\circ$  from  $h_{min}$ . The pressure distributions are also symmetric about  $L=0$  (center of the bearing) in the *Length* view as the porous liners had uniform permeability and the feedholes are symmetrically spaced.

For porous liner (PL) bearings the maximum wave contour (in the  $R\theta$  direction) occurs along the  $L=0$  line so that overall bearing pressure maxima is located at the middle of the bearing (*Lengthwise at  $L=0$* ) and at  $h_{min}$  in the  $R\theta$  direction. The bearing minimum pressure occurs at the two ends of the bearing where the pressure is ambient ( $P=1$ ).

The 12 x feedhole (FH) bearings has a pair of feed holes angularly aligned with  $h_{min}$ . This is the position of the two bearing pressure maxima. Symmetry indicates that no flow can occur in the area between the two rows of feedholes and thus the pressure distribution along the  $L=0$  line is a constant pressure that is higher than ambient and lower than the operating pressure. In this case also the minimum pressure is at the ends of the bearing where it is ambient.

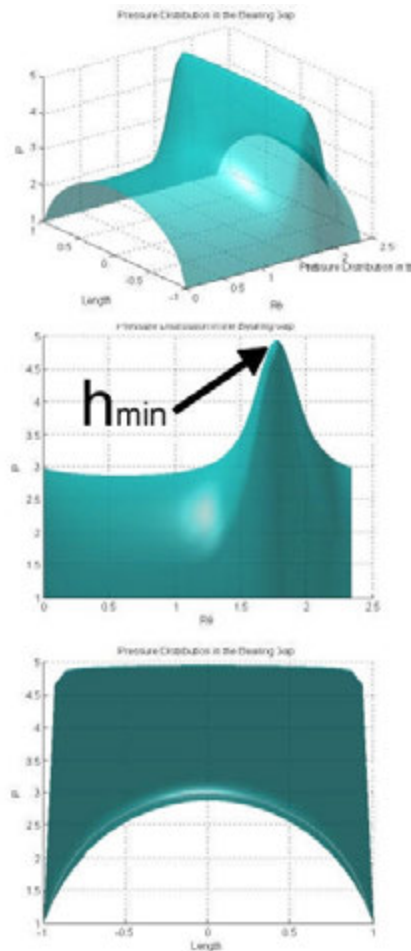


Figure 4-1 Porous liner hydrostatic pressure distribution. Top - angular view, Middle - the  $R\theta$  view, Bottom - the  $Length$  view.



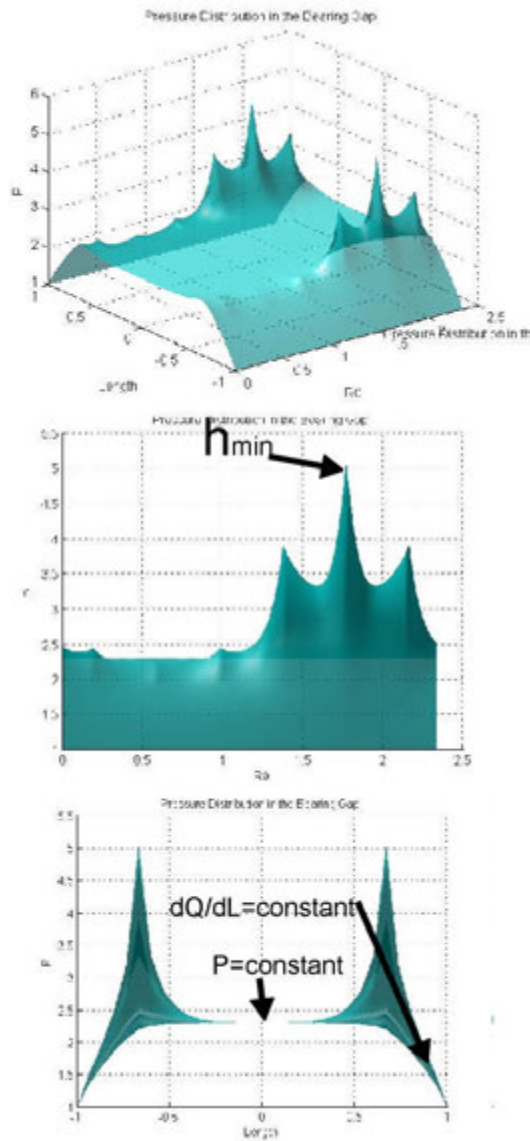


Figure 4-2 Feedhole liner hydrostatic pressure distribution. Top - angular view, Middle - the  $R\theta$  view, Bottom - the  $Length$  view.

#### 4.2. Replication of Prototype Bearing Static Tests

The prototype bushings were all .75" diameter and 2" length. They accommodated mass flow from a high pressure reservoir to bearing gap using either porous liners or 2 rows of 6 feedholes. In each row the feedholes were evenly spaced about the liner circumference. The feedhole rows were located 0.375" from each end of the liner. Two porous liner materials were used. The New Way liner which was made from treated porous graphite and had  $k_{meas}$  of  $2.71 \times 10^{-5}$  lbs/s. A second liner was made from porous alumina and had  $K_{meas}$  of  $5.00 \times 10^{-4}$ . The feedhole liners consisted of feedholes that ranged from 0.003" diameter to 0.015" diameter and consequently had  $K_{meas}$  that ranged from  $2.20 \times 10^{-6}$  lbs/s to  $5.20 \times 10^{-4}$  lbs/s. These were tested using shafts of different diameters to create bearing combinations with different clearances.

One of the conclusions of the bearing testing was that the static load bearing performance was best measured in terms of the dimensionless ratio  $W/pA$  where  $W$  is the bearing load,  $p$  is the mass addition reservoir pressure (operating pressure) and  $A$  is the nominal bearing area which was defined as the product of the bushing length and the bearing diameter.

The static tests put various fixed loads (vertically upwards) on the bushing starting with no mass addition (0 operating pressure). In this condition the bottom of the bushing ID is grounded against the bottom of the shaft OD so that the bearing gap is zero at the bottom of the bearing and is  $2c$  at the top of the bushing. The operating pressure was then varied up to 90 psig and the bushing displacement, shaft displacement and volumetric flow rate of the mass addition were measured at each pressure. See section 2.1.3. From these data  $W/pA$  versus  $H$  curves ( $H=h/c$ ) were generated for each bushing for different clearances.

In order to replicate this test, CFD calculations were performed using the same bearing geometries and clearances as the tested prototypes. For the CFD tests an operating pressure was set and then the shaft and bearing centers were offset (no angular offset) so various bushing displacements were simulated. The pressure distribution solution was attained and integrated to obtain the net shaft/bushing interaction force which corresponds to  $W$ . The total mass input rate was also calculated.

A program was written to step through shaft/bushing offsets from 0 to  $c$  usually in 20 steps. After each step, summary data were logged in a matrix. Then the operating pressure was changed and the process repeated. These results were then plotted as  $W/pA$  vs  $H$  to compare with the test data. Note that  $H=1$  when the bearing and bushing are concentric so that  $h_{min}=c$ , and  $H=0$  corresponds to when the bearing is grounded or  $h_{min}=0$ .

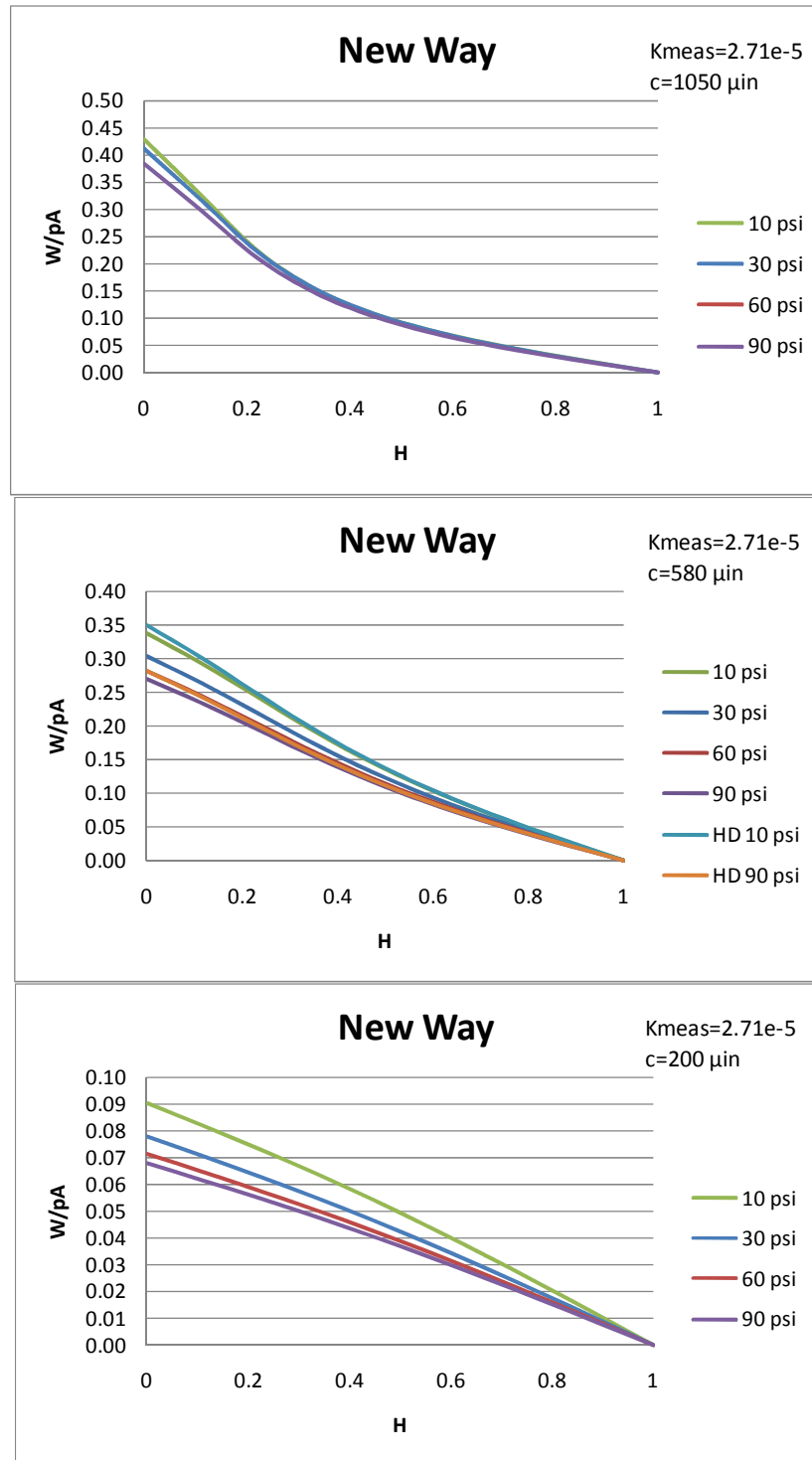


Figure 4-3 CFD results for porous liner with  $K_{meas}$  equivalent to New Way bearing.

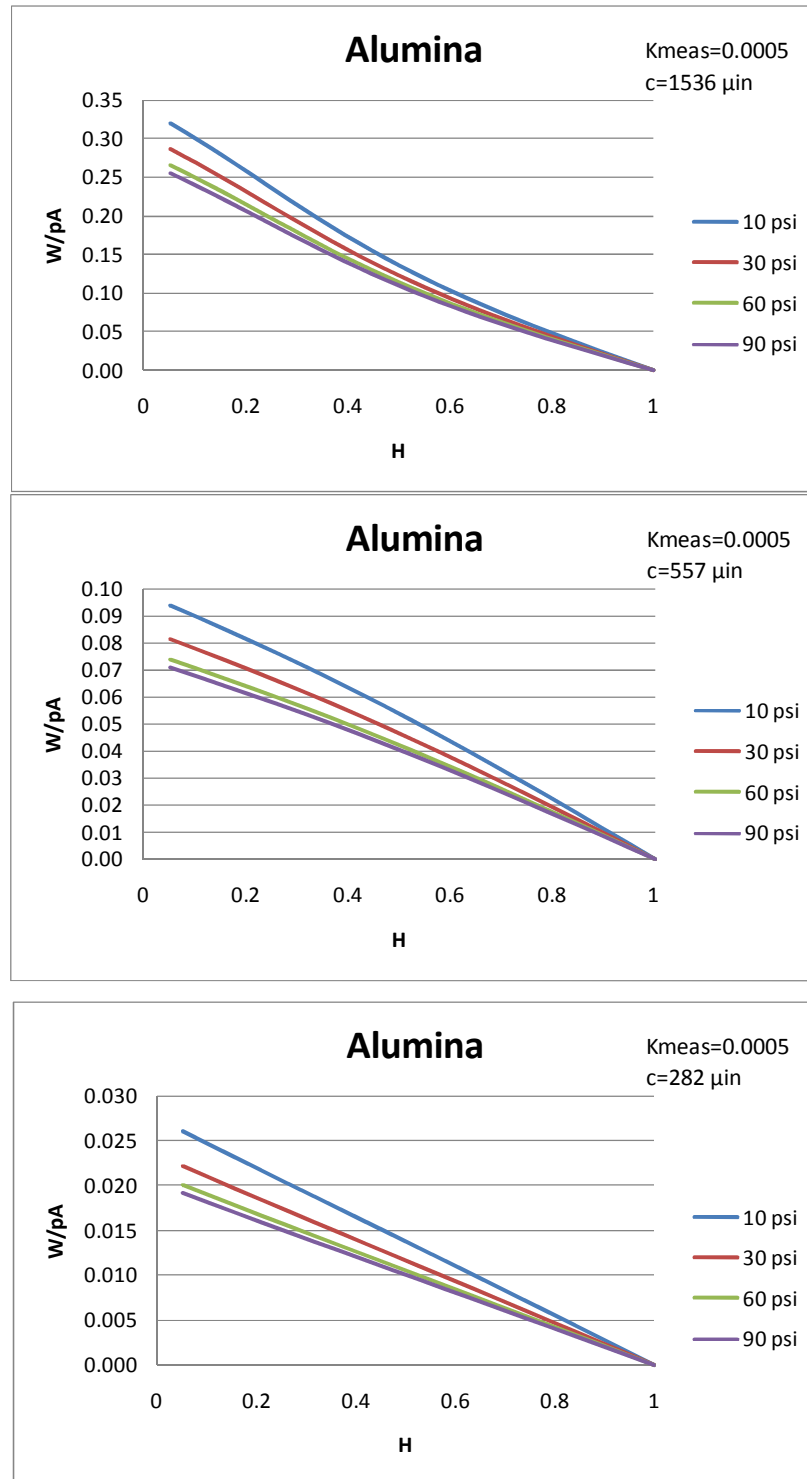


Figure 4-4 CFD results for a porous liner with  $K_{meas}$  equal to that of the alumina liner prototype.

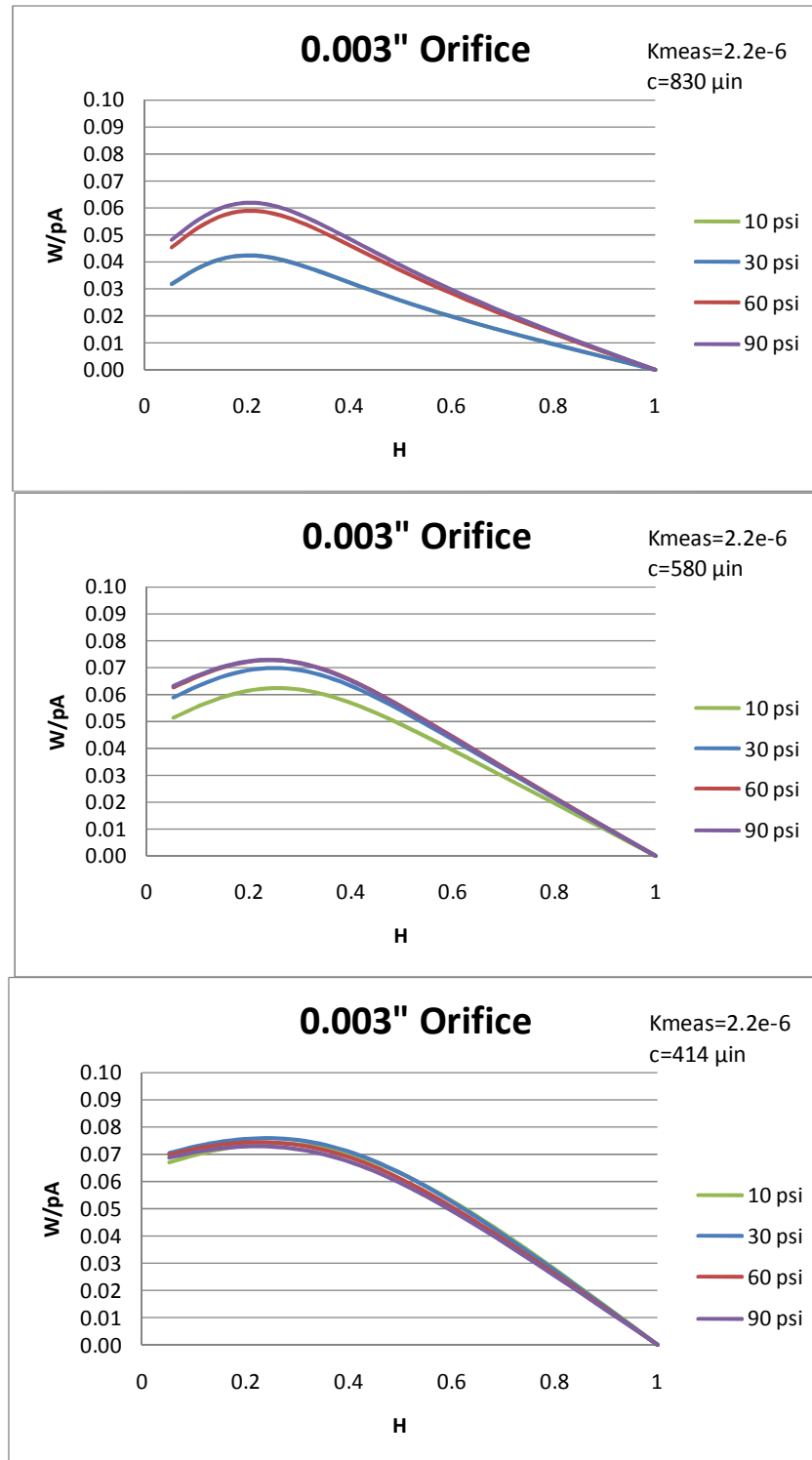


Figure 4-5 CFD results for liner with  $K_{meas}$  appropriate to 0.003"D feedholes.

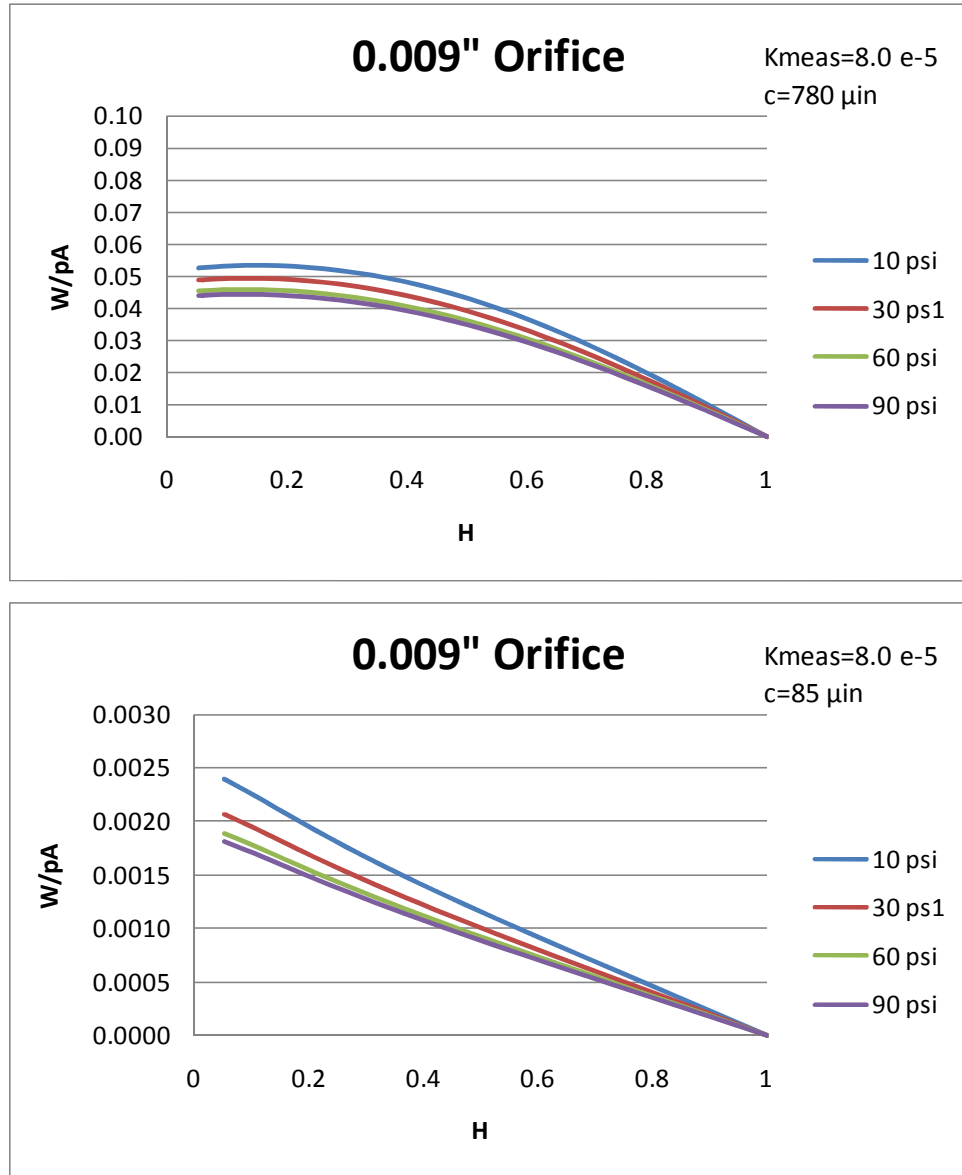


Figure 4-6 CFD results for liner with  $K_{meas}$  appropriate to 0.009'D feedholes.

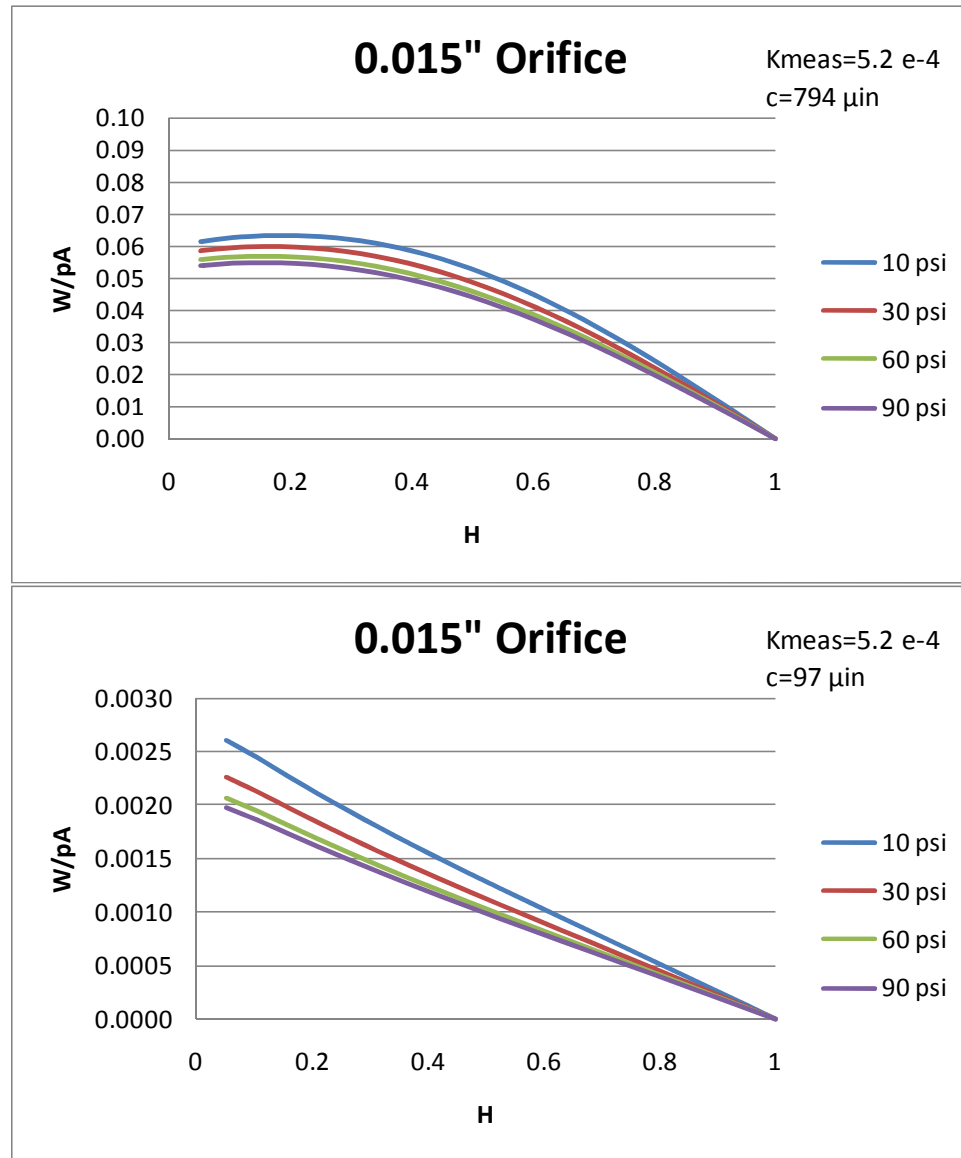


Figure 4-7 CFD results for liner with  $K_{meas}$  appropriate to 0.0015" D feedholes.



### 4.3. Comparison of CFD Calculation to Test Results

To the extent possible all of the static tests were “rerun” numerically and their results compared to actual results to validate the CFD analysis methodology. The results indicate that the CFD analysis is generally confirmed by the empirical test data. Places where large variances occurred were from test results for very small clearances or low operating pressure where the test data is suspect in that the measured displacements were of the same order of magnitude as the laser drift for the laser vibrometer used in the measurements,

There were two unexpected differences between the CFD data and the test data that should be highlighted:

#### *1. Minor dependence of $W/pA$ on operating pressure*

It simply makes common sense that the bearing load capacity  $W$  would be directly proportional to the operating pressure. When the bearing prototypes were tested, no significant differences between  $W/pA$  for different operating pressures was noticed and so all the data for all operating pressures was consolidated on the  $W/pA$  vs.  $H$  plots. The  $W/pA$  vs.  $H$  plots from CFD generated data told a slightly different story. In those plots the different isobars tended to fan apart slightly by varying amounts. The low pressure (10 psig)  $W/pA$  maximum values always were slightly higher than the high pressure (90 psig isobars) although sometimes all the isobar plots fell on top of each other. The 30 and 60 psig isobars fell in between the 10 and 90 psig isobars making a hierarchy of high to low maximum  $W/pA$  with low to high operating pressure. The fanning effect diminished with higher operating pressures with the 60 psig isobar always being very close to the 90 psig isobar.

## *2. Near surface effect of feedhole bearings*

The expectation always has been that decreasing  $h$  results in increasing  $W$  until  $h=0$  and  $W$  reaches its maximum value commonly referred to as the grounding force. The CFD results for some feedhole bearings predicts a small decline in  $W$  (and  $W/pa$ ) as  $h$  nears zero. Refer to the graphical presentation of the empirical data for the 0.003”D FH prototype bearing in Appendix section D.1. Reviewing the test data reveals many discrepant points for  $W/pA$  at small  $h$ . Because this is unexpected, the lower  $W/pA$  points were thought to be anomalies. In some tests it seemed the bushing would not displace with lower operating pressure and then would jump to a larger displacement when the operating pressure was increased. This was attributed to possibly some “stickiness” in the test mechanism or laser drift. However, it might have been a real phenomenon.

#### 4.3.1. Mass Addition

Flow rates tested for bearing liners with no shafts exhausting to atmospheric pressure were used as the basis to determine the  $K_{meas}$  factor for each bearing liner in the CFD analysis. Flow rates were also tested for each bearing liner with 1) a 0.750" D shaft and 2) a 0.749" D shaft, thus representing "small" and "large" bearing gaps. Flow rates were also monitored during loaded static testing as well. In the empirical static tests, a fixed load was applied to the bushing and the mass addition operating pressure was "swept" most often between 0 and 70 psig while the bushing displacement was measured. In the CFD analysis, the program was set to a constant operating pressure and the bushing displacement was swept from  $H$  equals 0 to 1. The resulting bearing load was calculated along with the overall mass input rate. For the CFD calculation fixed pressures of 10, 30, 60, and 90 psig were used to span the operating pressure range. This yields an opportunity to compare the mass input rate predicted by the CFD analysis with the measured values at several points.

**Comparison of measured mass flow rates  
to Predicted mass flow rates.**

From loaded test			Unloaded Shaft Tests	Numerical Results
p	q	lbs/s	lbs/s	lbs/s
New Way with .749 shaft				c=1050
10	0	0	8.48E-06	3.15E-05
30	1.5	2.01E-04	1.41E-04	1.41E-04
60	3	6.71E-04	5.98E-04	4.59E-04
New Way with 0.750 shaft				c=200
10	0	0.00E+00	2.00E-06	2.28E-06
30	0.01	1.34E-06	1.50E-05	1.40E-05
60	1.38	3.09E-04	1.86E-04	4.60E-05
Porous alumina with .749 shaft				c=1536
10	7.9	5.84E-04	5.11E-04	3.23E-04
30	ND	ND	ND	1.35E-03
60	ND	ND	ND	4.00E-03
Porous alumina with .750 shaft				c=282
10	4	2.96E-04	2.65E-05	1.00E-05
30	9.4	1.26E-03	1.19E-03	1.20E-04
60	ND	ND		4.00E-04
0.003 Orifice with 0.749 shaft				c=830
10	0.08	5.91E-06	5.99E-06	3.50E-06
30	0.1	1.34E-05	1.58E-05	1.58E-05
60	0.7	1.57E-04	4.09E-05	4.50E-05
0.003 Orifice with 0.750 shaft				c=414
10	0.02	1.48E-06	1.37E-06	2.08E-06
30	0.035	4.68E-06	4.97E-06	9.38E-06
60	0.09	2.01E-05	1.92E-05	2.80E-05
0.009 Orifice with 0.749 Shaft				c=780
10	2.2	1.63E-04	1.35E-04	2.80E-05
30	4	5.35E-04	4.80E-04	1.30E-04
60	5.1	1.14E-03	1.60E-03	4.00E-04
0.009 Orifice with 0.750 Shaft				c=85
10	0.02	1.48E-06	1.37E-06	5.00E-08
30	0.8	1.07E-04	4.97E-06	2.50E-07
60	1.3	2.91E-04	2.04E-05	8.00E-07

Figure 4-8 Comparison CFD predicted and measured mass input rates.

When volumetric flow rates were measured during constant load/pressure sweeps, the results indicated that the volumetric flow and hence mass input rates were mostly independent of the constant load and hence the displacement  $H$  for a given bearing. The volumetric flow versus pressure lines for a given bearing configuration as plotted for each constant load fell on top of each other within a narrow spread. In some cases, the spread, seemed to fall within a load hierarchy with higher loads having slightly higher flow rates than lower loads (smaller  $H$  having minimally higher flow than high  $H$ ). This was the case for the 0.018 liner with 0.75D shaft. For the 0.003 liner with the 0.749D shaft the hierarchy was reversed with low loads (larger  $H$ ) having larger flow than high loads (small  $H$ ). But for most bearings the difference was indistinguishable. This lead to the hypothesis that the flow rate versus pressure curve was independent of the load (and consequently  $H$ ).

The CFD calculations for the same bearings based on sweeping  $H$  predicted that mass addition for the most part was dependent on the bearing and the operating pressure, however it also varied somewhat with  $H$ .

CFD result for variation in mass flow as  $H$  is varied from 1 to 0

Liner	c- $\mu$ in	Pop-psig			
		10	30	60	90
0.015	794	25%	25%	26%	26%
0.015	97	58%	57%	57%	57%
0.009	180	34%	35%	34%	34%
0.009	85	57%	57%	57%	57%
0.003	830	-17%	-17%	-18%	-18%
Alumina	1538	22%	22%	21%	21%
Alumina	282	40%	20%	17%	16%
New Way	1050	6%	6%	7%	7%
New Way	200	31%	25%	24%	23%

Figure 4-9 CFD variation in mass input between  $H=0$  to 1 for different isobars.

### 4.3.2. Load Capacity $W/pA$ vs. $H$

The results of the CFD replication of the  $W/pA$  versus  $H$  results were pasted as data series and added to the graphs used to present the prototype testing. The results follow.

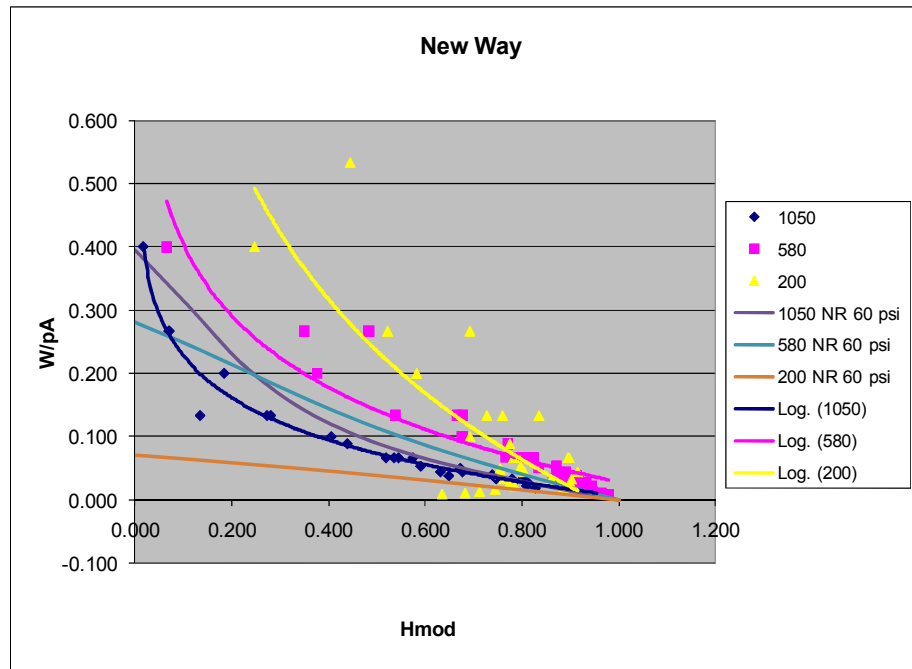


Figure 4-10 Comparison of CFD and test results for porous graphite bearing.

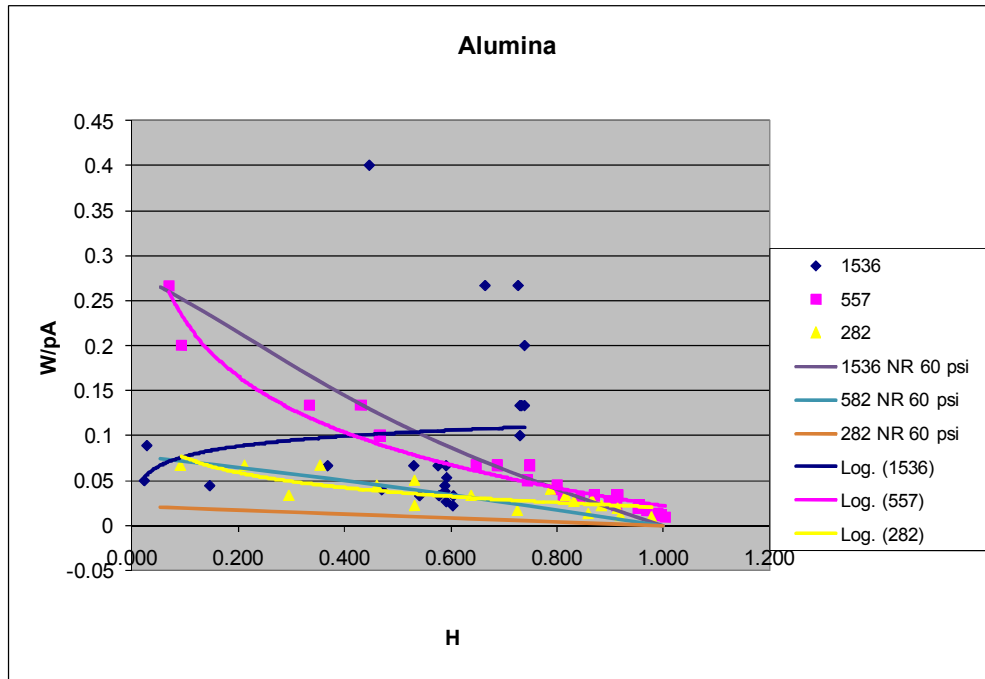


Figure 4-11 Comparison of CFD and test results for porous alumina bearing.

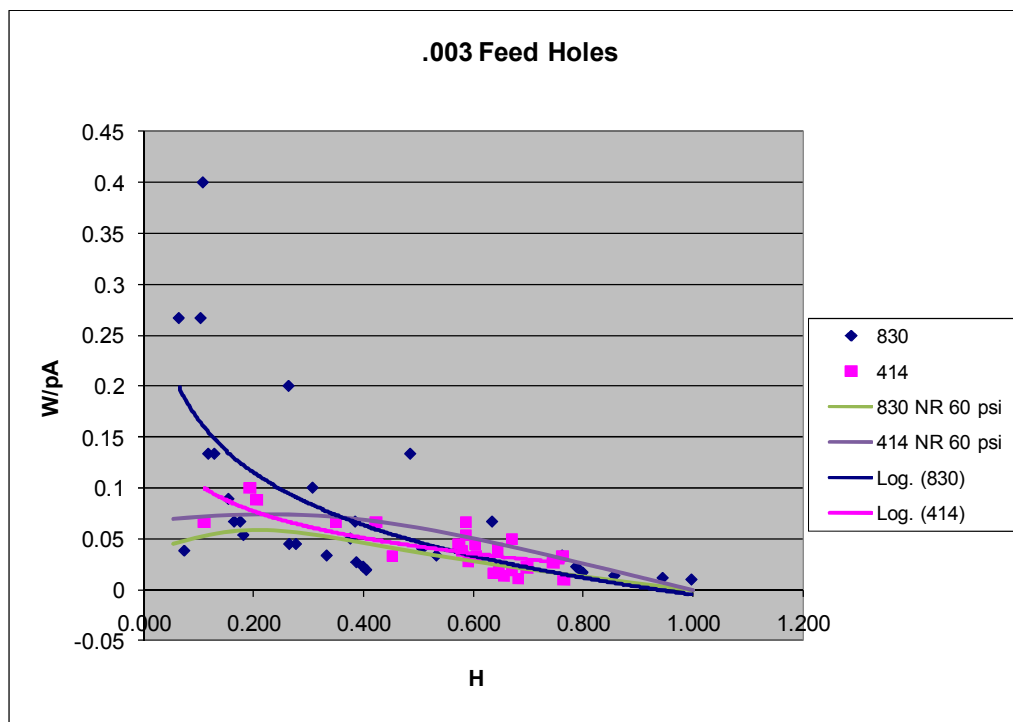


Figure 4-12 Comparison of CFD and test results for .003" D feedhole bearing.

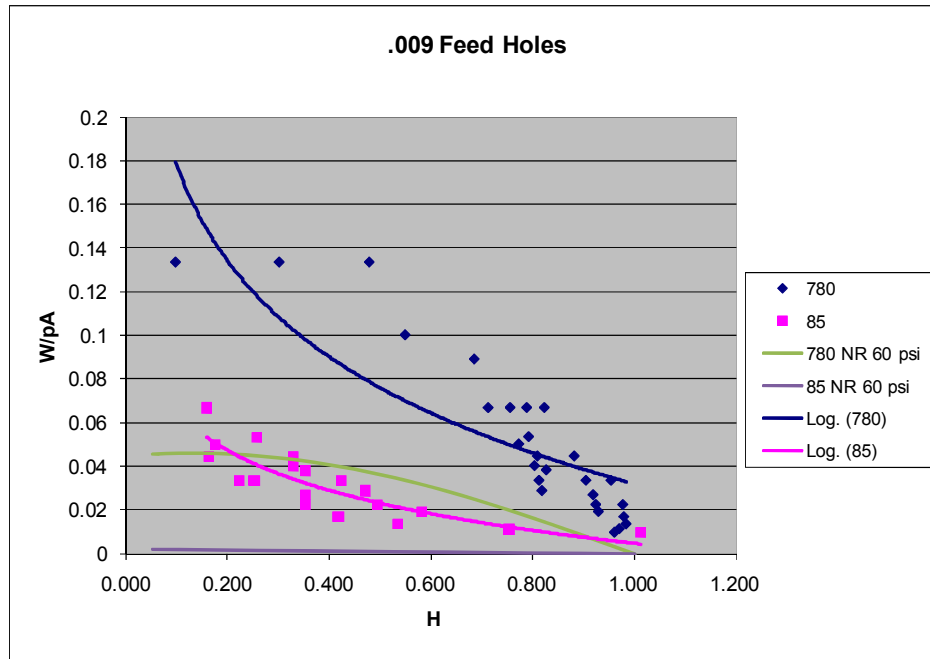


Figure 4-13 Comparison of CFD and test results for .009" D feedhole bearing.

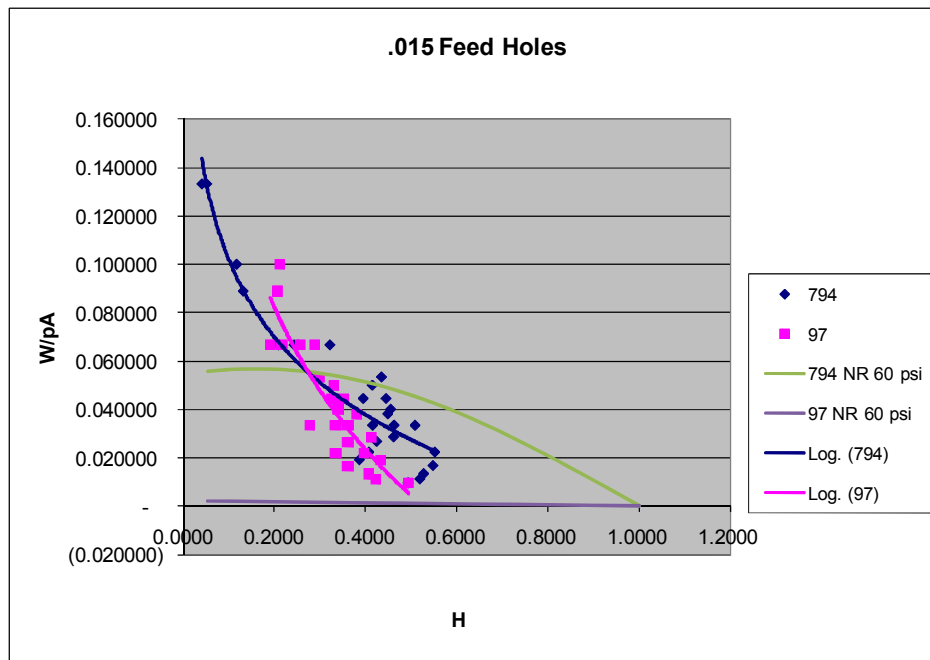


Figure 4-14 Comparison of CFD and test results for .015" D feedhole bearing.



Observations comparing the CFD results (designated NR for Numerical Results in graph legends) with empirical data:

New Way PL Bearing:

- $c=1050 \mu\text{in}$  - Very close match in values and shape of curve.
- $c=580 \mu\text{in}$  - Very close match in values and shape of curve.
- $c=200 \mu\text{in}$  - Numerical results passes through cluster of inconsistent data points and is plausible.

Alumina PL Bearing:

- $c=1536 \mu\text{in}$  - Numerical results passes through cluster of inconsistent data points and is plausible.
- $c=557 \mu\text{in}$  - Very close match in values and shape of curve.
- $c=282 \mu\text{in}$  - Values a little low but match shape of curve.

0.003”D FH Bearing:

- $c=830 \mu\text{in}$  - Very close match in values and shape of curve.
- $c=414 \mu\text{in}$  - Very close match in values and shape of curve.

0.009”D FH Bearing:

- $c=780 \mu\text{in}$  - Values somewhat lower but shape matches data better than assumed logarithmic curve fit.
- $c=85 \mu\text{in}$  - Very low values. Data was higher but also had very low values.

0.015”D FH Bearing:

- $c=794 \mu\text{in}$  - Values agree except for low values of  $H$ .
- $c=97 \mu\text{in}$  - Very low values compared to data.

Thus it is felt that overall the CFD prediction of  $W/pA$  matched the empirical data quite well for broad range of  $K_{meas}$  and clearances for both PL and FH bearings. It is observed that where discrepancies occurred was for very small clearances and small  $H$  where the empirical data would be suspect.

#### 4.4. Comparison of Porous Liner and Feedhole Static Bearings

In this section the tools of the CFD laboratory are applied to test and map the performance a 6 virtual bearings in terms of  $W/pA$  across the  $H-c$  plane. The virtual bearings all have the same 0.75" x 2" diameter to length geometry as the prototype bearings. Three of the bearing are PL bearings and three are FH bearings with the same 2 rows of 6 feedholes configuration as the prototype bearings. Each set of bearings has three different values of  $Kmeas$ . The three values are 2.0e-6 lbs/s which is very low and slightly less than the 0.003" feedhole prototype bearing (2.2e-6 lbs/s), 2.0 e-5 lbs/s which is moderate and the same order of magnitude as a New Way treated porous graphite bearing (2.71e-5 lbs/s) and the 0.009" feedhole prototype (8.00 e-5), and 2e-4 lbs/s which is very high and of the order magnitude as the porous alumina (5.0 e-5 lbs/s) and the 0.015" D feedhole prototype (5.2 e-4 lbs/s).

In the replications of the prototype bearing tests, it was noticed that the maximum  $W/pA$  versus  $H$  depended somewhat on the operating pressure. Thus two  $H-c$  scans were made for each virtual bearing. One with the operating pressure set at 10 psig and one with the operating pressure set at 90 psig. Then the  $W/pA$  data from the 10 psig scan was subtracted from the  $W/pA$  data taken from the 100 psig operating pressure scan and this difference was examined of the  $H-c$  plane to determine where the differences lie.

##### 4.4.1. Resultant $h-c$ Plane Scans

In the following pages are shown the resultant  $H-c$  scans. In general each scan used 30 intervals to span the clearance dimension and 20 intervals to span the  $h$  dimension. Thus the study is the result of more than 3,600 pressure solutions.

The resulting arrays of  $W/pA$  data can be queried for details such as the maximum value of  $W/pA$  and its location on the plane in addition to displaying the overall trends.

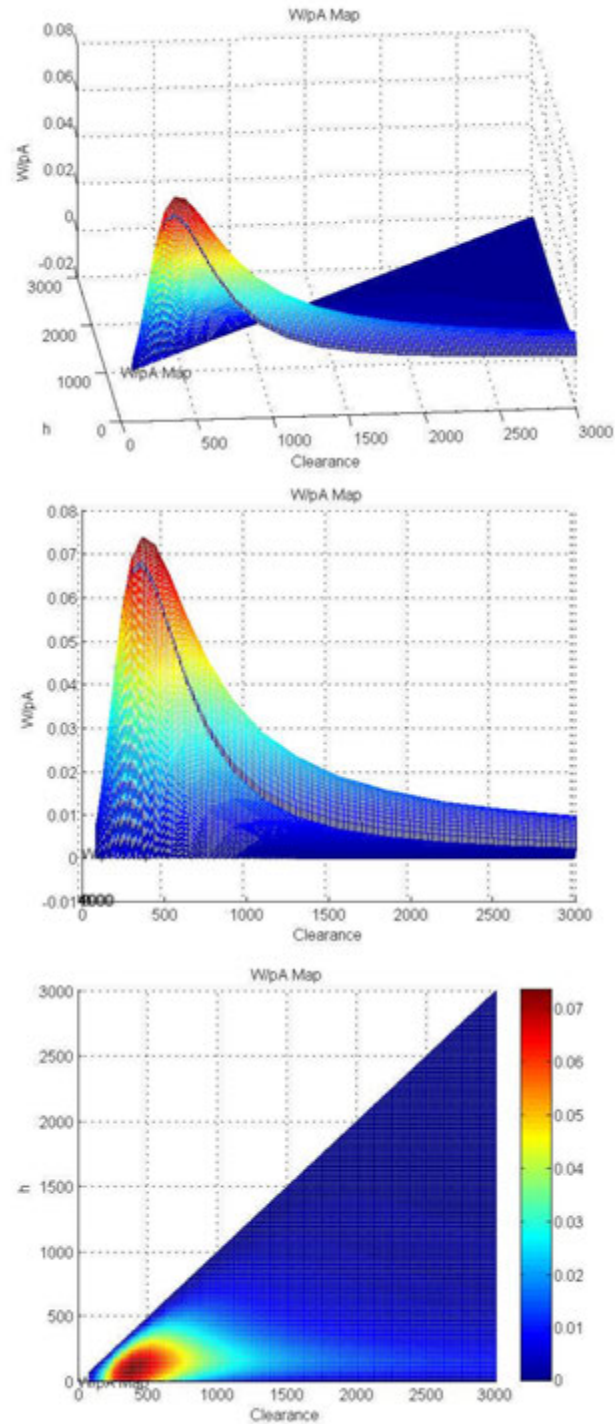


Figure 4-15 Views of  $W/pA$  in the  $h$ - $c$  plane for a feedhole bearing with  $K_{meas}=2 \text{ e-6 lb/s}$  and operating pressure=10 psig.  
 Top - isometric, Center - clearance axis, Bottom - planar view.

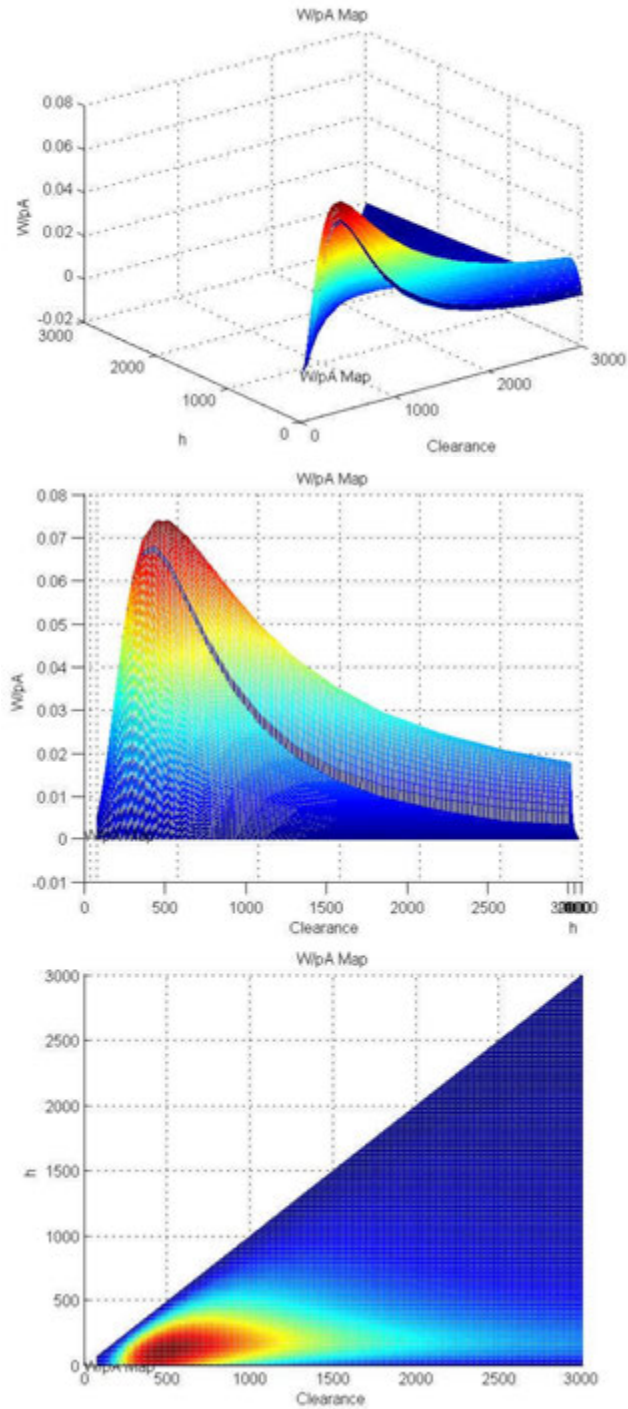


Figure 4-16 Views of  $W/pA$  in the  $h$ - $c$  plane for a feedhole bearing with  $K_{meas}=2$  e-6 lb/s and operating pressure=100 psig.  
 Top - isometric, Center - clearance axis, Bottom - planar view.

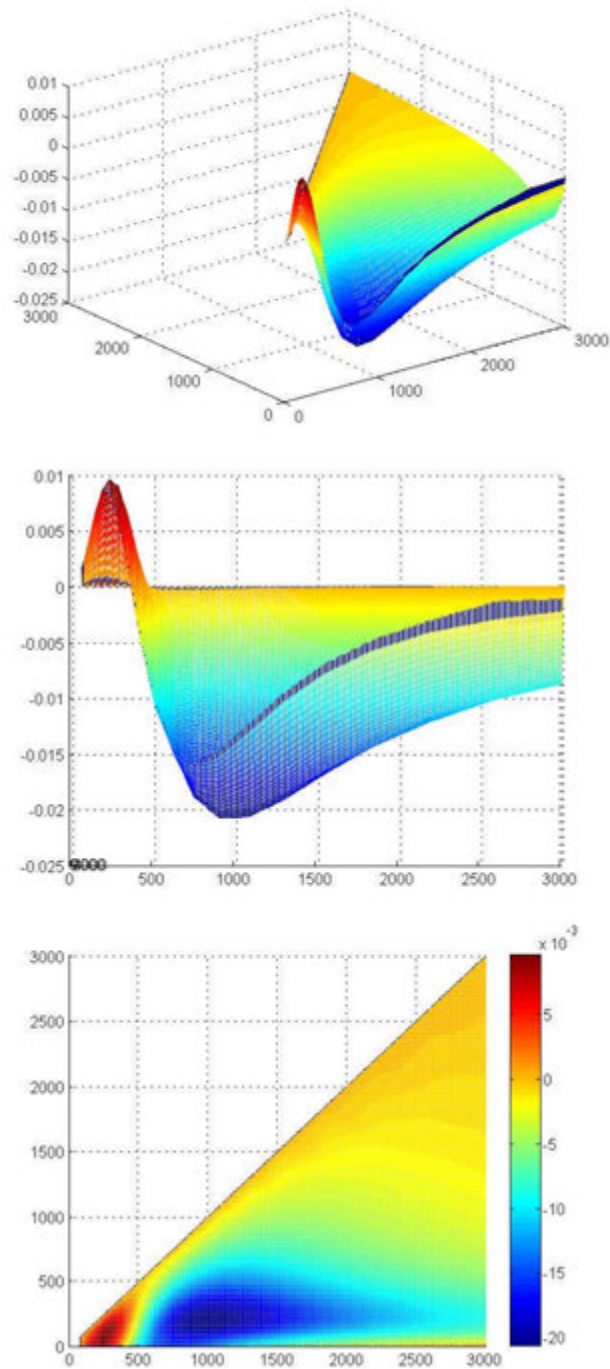


Figure 4-17 Views of  $(W/pA$  at 10psig)- $(W/pA$  at 100psig) in the  $h-c$  plane for feedhole bearing with  $K_{meas} = 2 \times 10^{-6}$  lbs/s.  
 Top - isometric, Center, - clearance axis, Bottom - planar view.

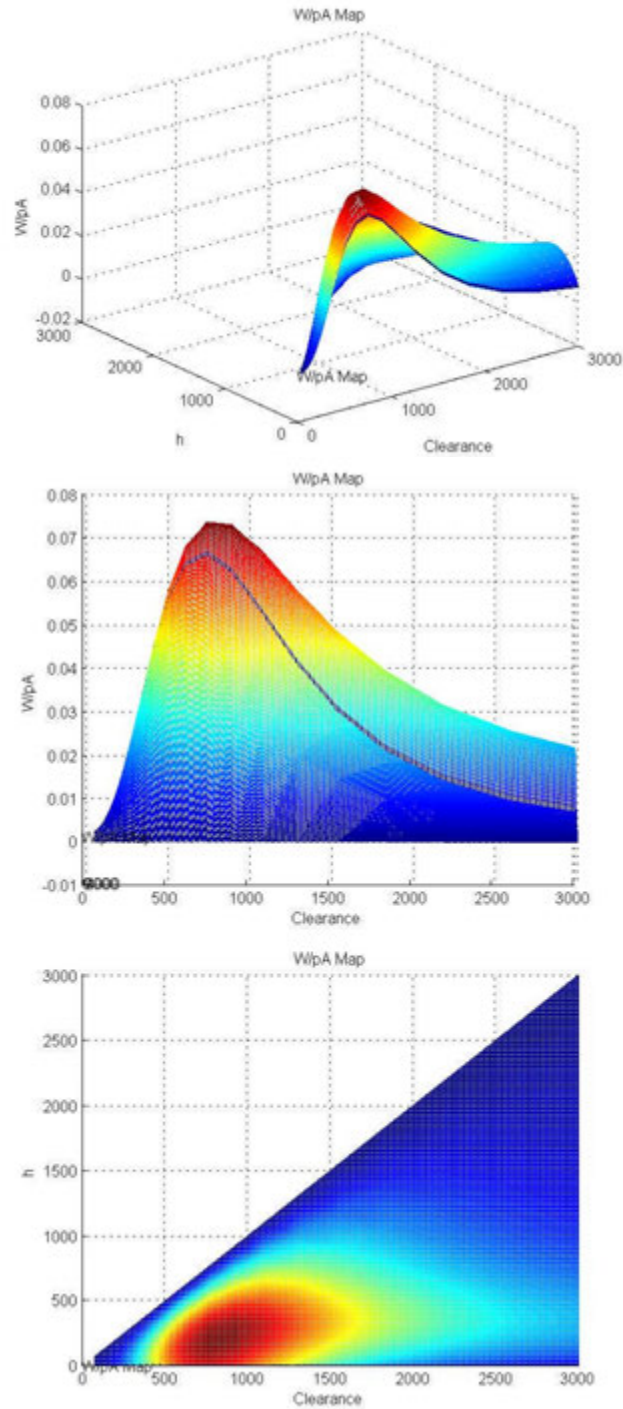


Figure 4-18 Views of  $W/pA$  in the  $h$ - $c$  plane for a feedhole bearing with  $K_{meas} = 2 \times 10^{-5}$  lb/s and operating pressure = 10 psig.  
 Top - isometric, Center - clearance axis, Bottom - planar view.

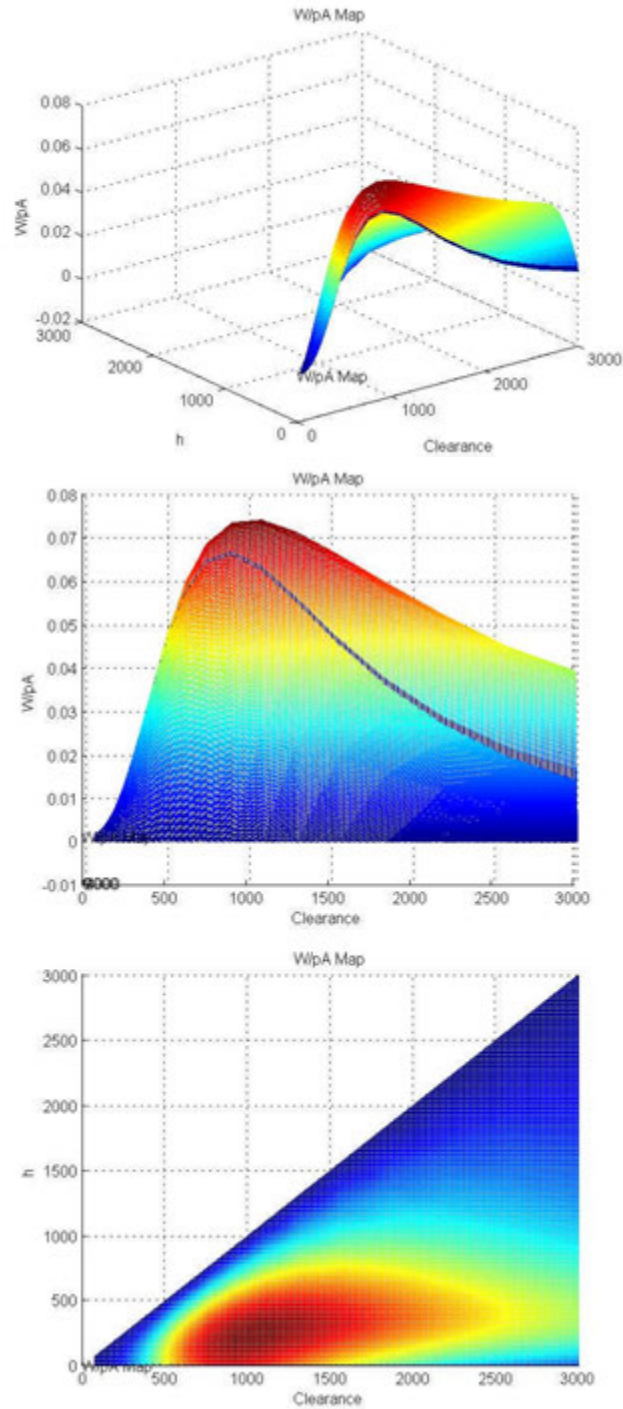


Figure 4-19 Views of  $W/pA$  in the  $h$ - $c$  plane for a feedhole bearing with  $K_{meas} = 2 \times 10^{-5}$  lb/s and operating pressure = 100 psig.  
 Top - isometric, Center - clearance axis, Bottom - planar view.



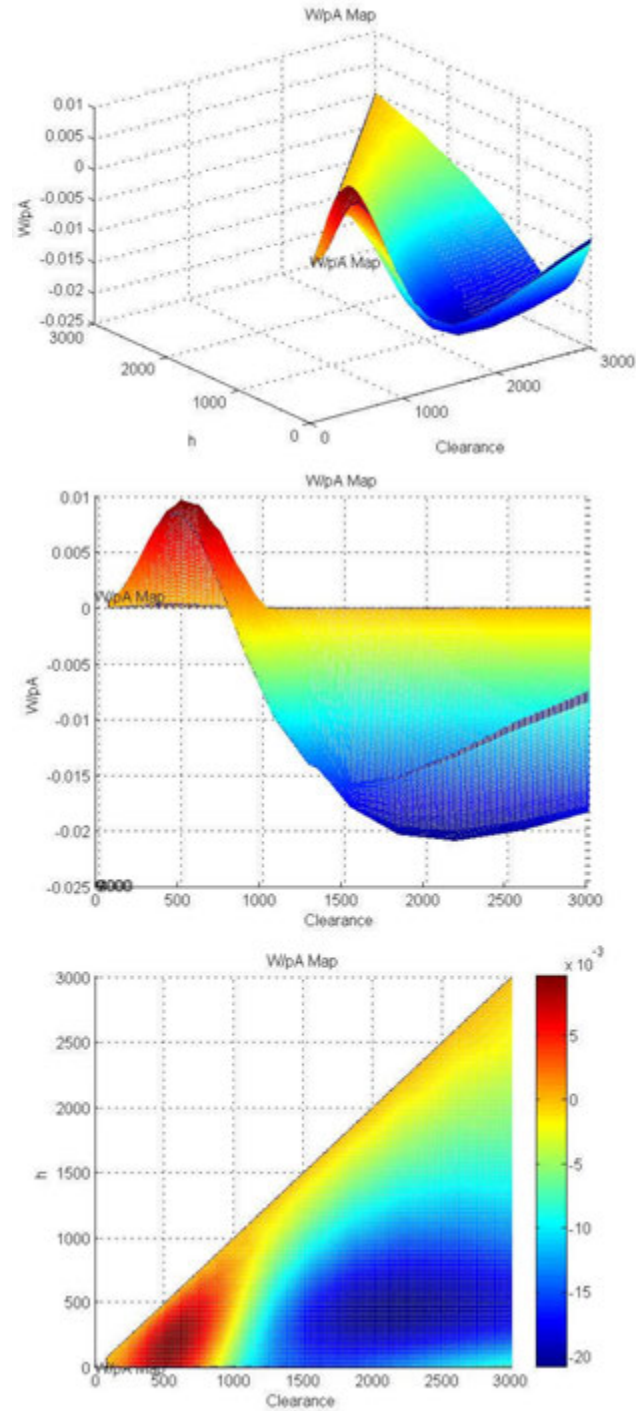


Figure 4-20 Views of  $(W/pA$  at 10psig)- $(W/pA$  at 100psig) in the  $h$ - $c$  plane for feedhole bearing with  $K_{meas} = 2 \times 10^{-5}$  lbs/s.  
 Top - isometric, Center, - clearance axis, Bottom - planar view.

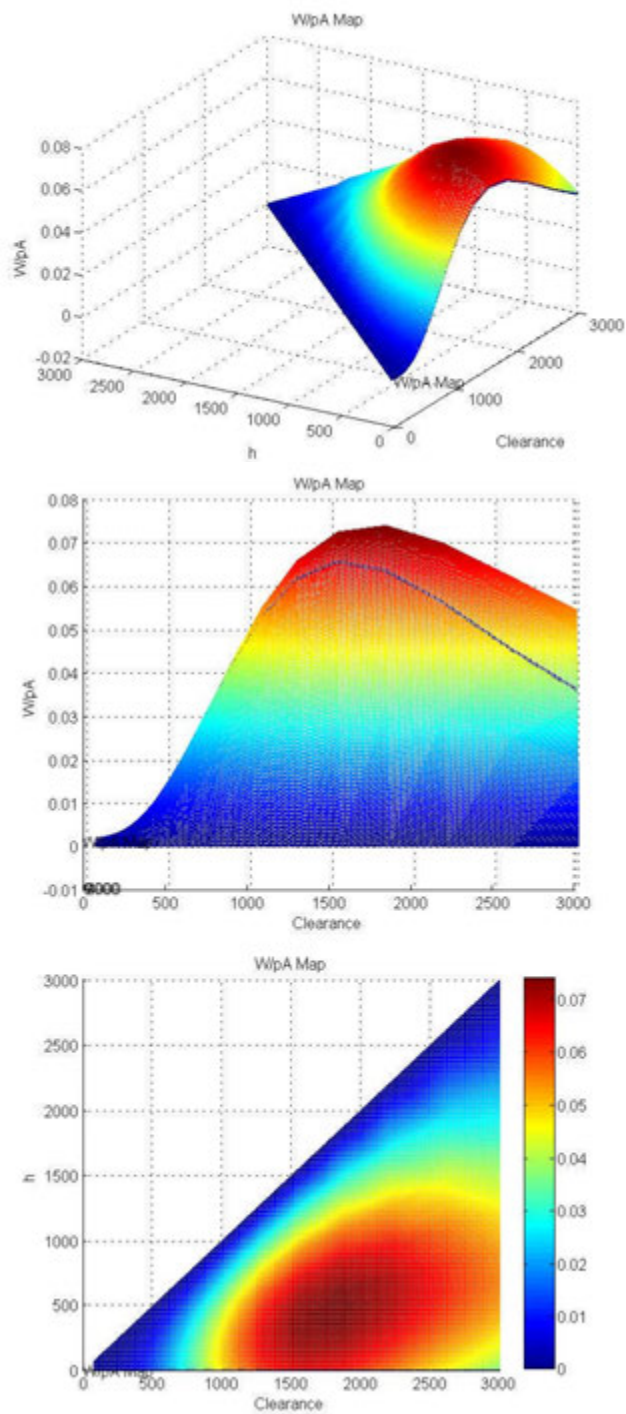


Figure 4-21 Views of  $W/pA$  in the  $h$ - $c$  plane for a feedhole bearing with  $K_{meas}=2 \text{ e-4 lb/s}$  and operating pressure=10 psig.  
 Top - isometric, Center - clearance axis, Bottom - planar view.

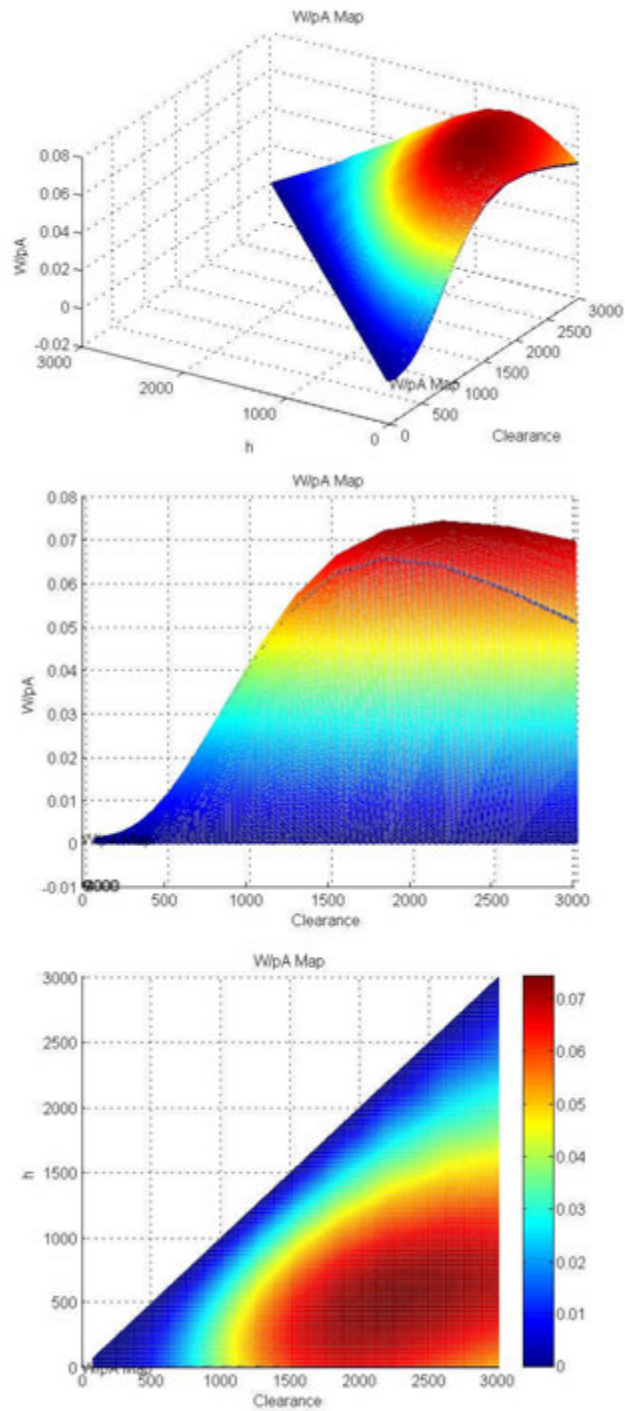


Figure 4-22 Views of  $W/pA$  in the  $h$ - $c$  plane for a feedhole bearing with  $K_{meas} = 2 \times 10^{-4}$  lb/s and operating pressure = 100 psig.  
Top - isometric, Center - clearance axis, Bottom - planar view.

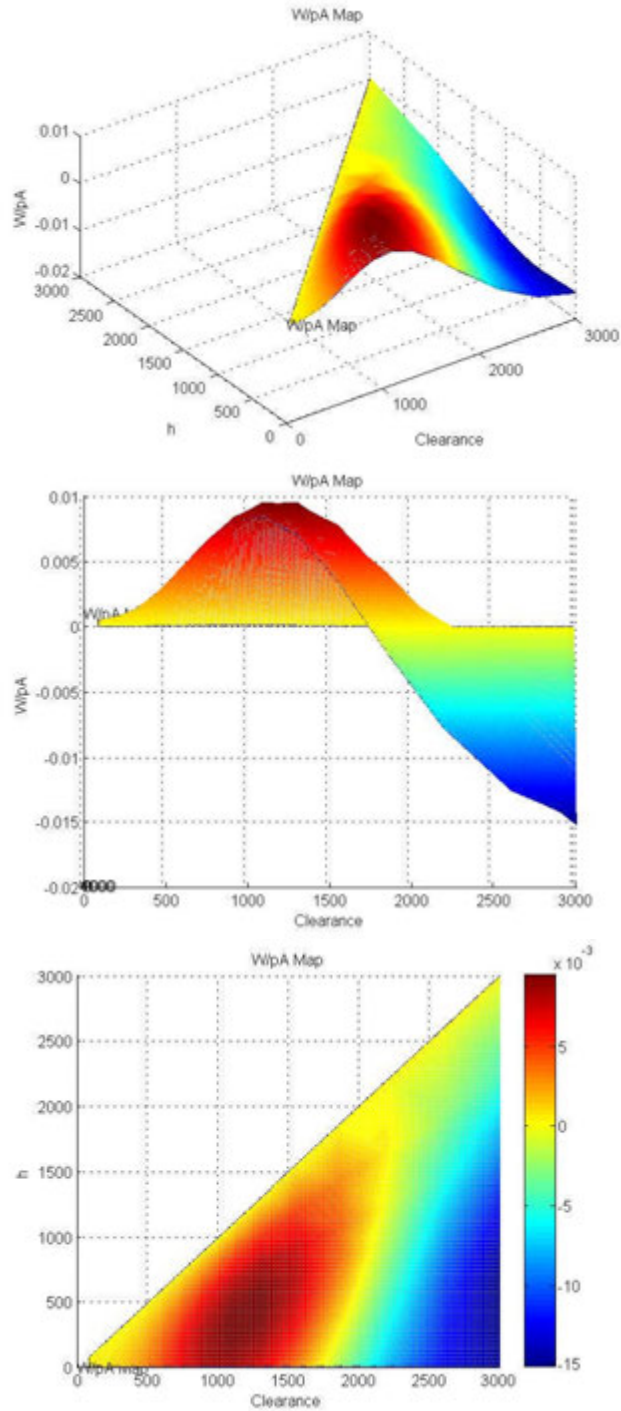


Figure 4-23 Views of ( $W/pA$  at 10psig)-( $W/pA$  at 100psig) in the  $h$ - $c$  plane for feedhole bearing with  $K_{meas} = 2 \times 10^{-4}$  lbs/s.  
Top - isometric, Center, - clearance axis, Bottom - planar view.

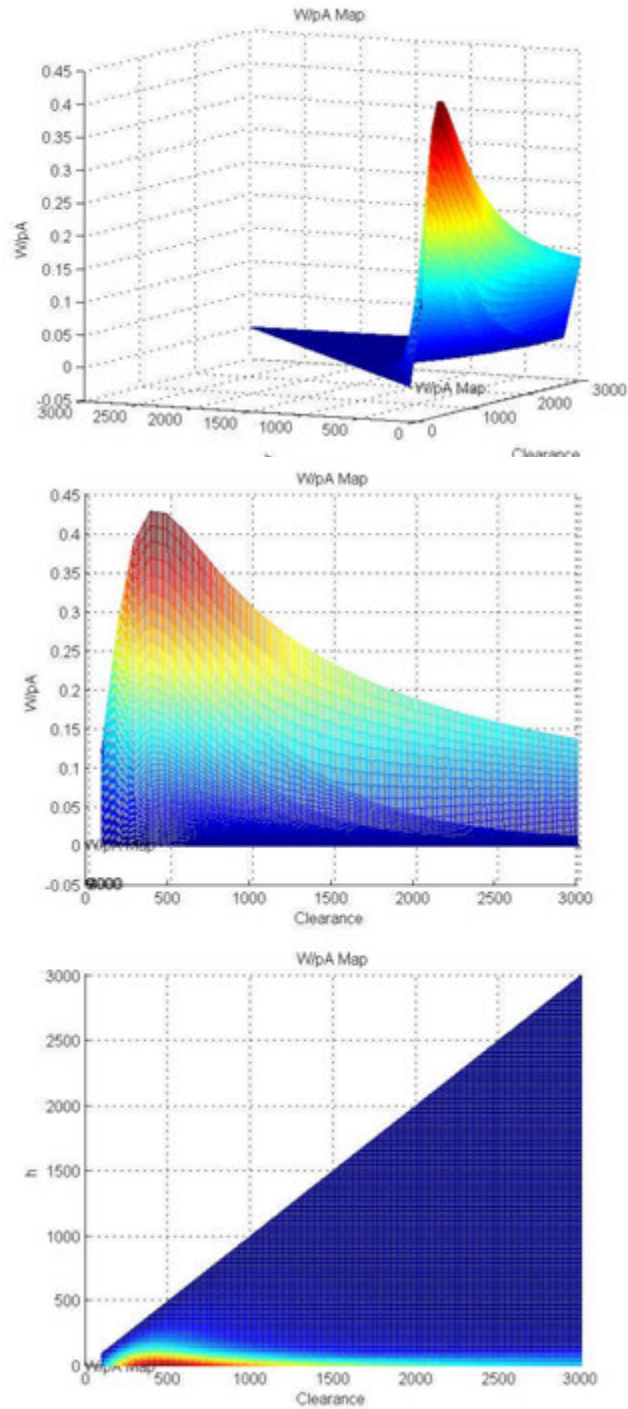


Figure 4-24 Views of  $W/pA$  in the  $h$ - $c$  plane for a porous liner bearing with  $K_{meas} = 2 \times 10^{-6}$  lb/s and operating pressure = 10 psig.  
 Top - isometric, Center - clearance axis, Bottom - planar view.

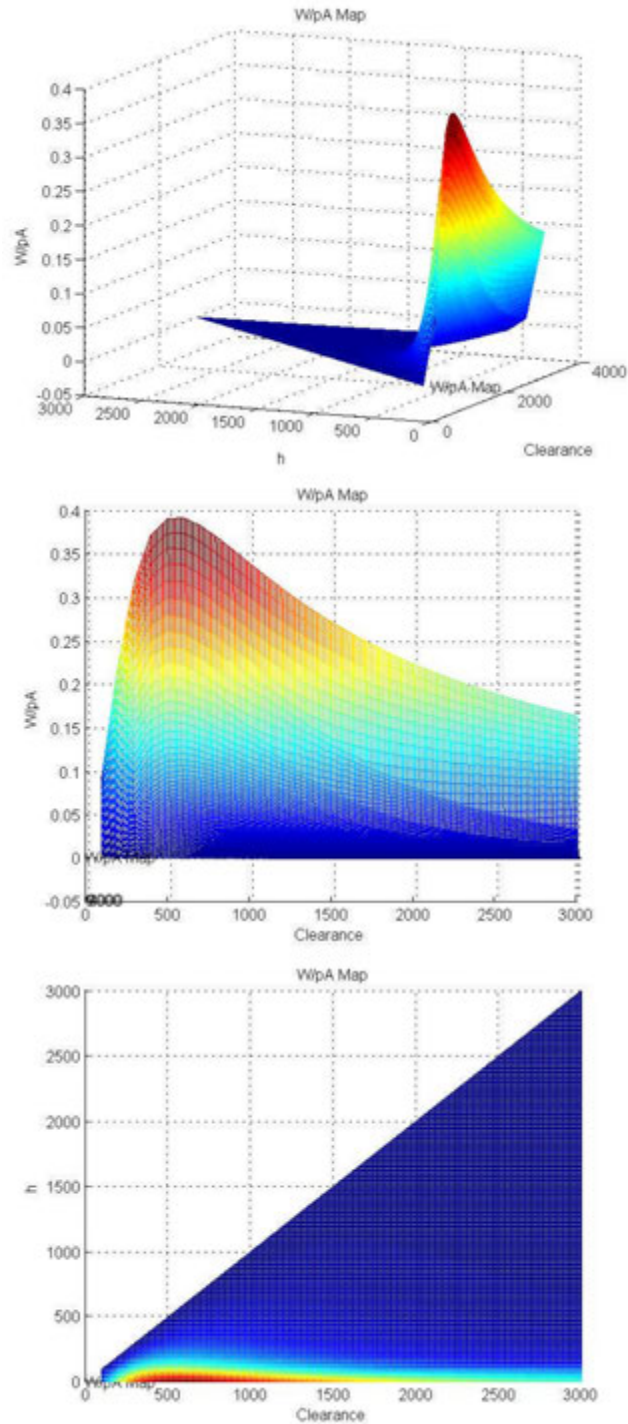


Figure 4-25 Views of  $W/pA$  in the  $h$ - $c$  plane for a porous liner bearing with  $K_{meas}=2 \text{ e-6 lb/s}$  and operating pressure=100 psig.  
 Top - isometric, Center - clearance axis, Bottom - planar view.

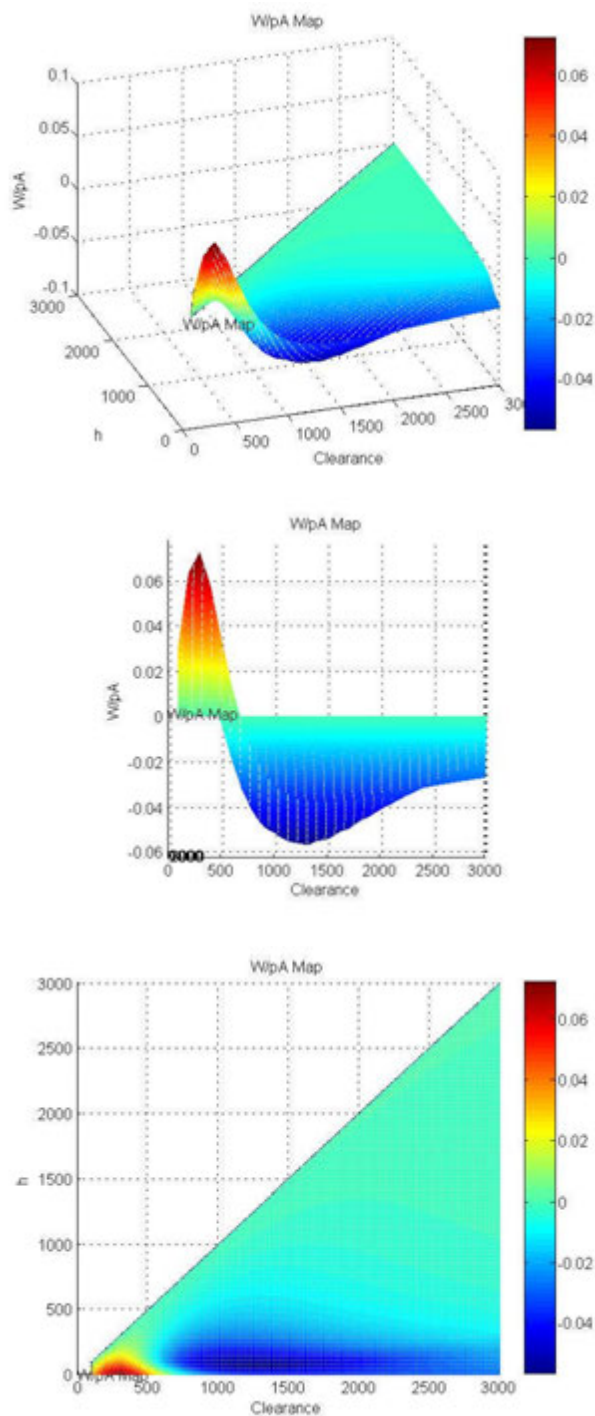


Figure 4-26 Views of ( $W/pA$  at 10psig)-( $W/pA$  at 100psig) in the  $h-c$  plane for porous liner bearing with  $K_{meas} = 2 \times 10^{-6}$  lbs/s.  
Top - isometric, Center, - clearance axis, Bottom - planar view.

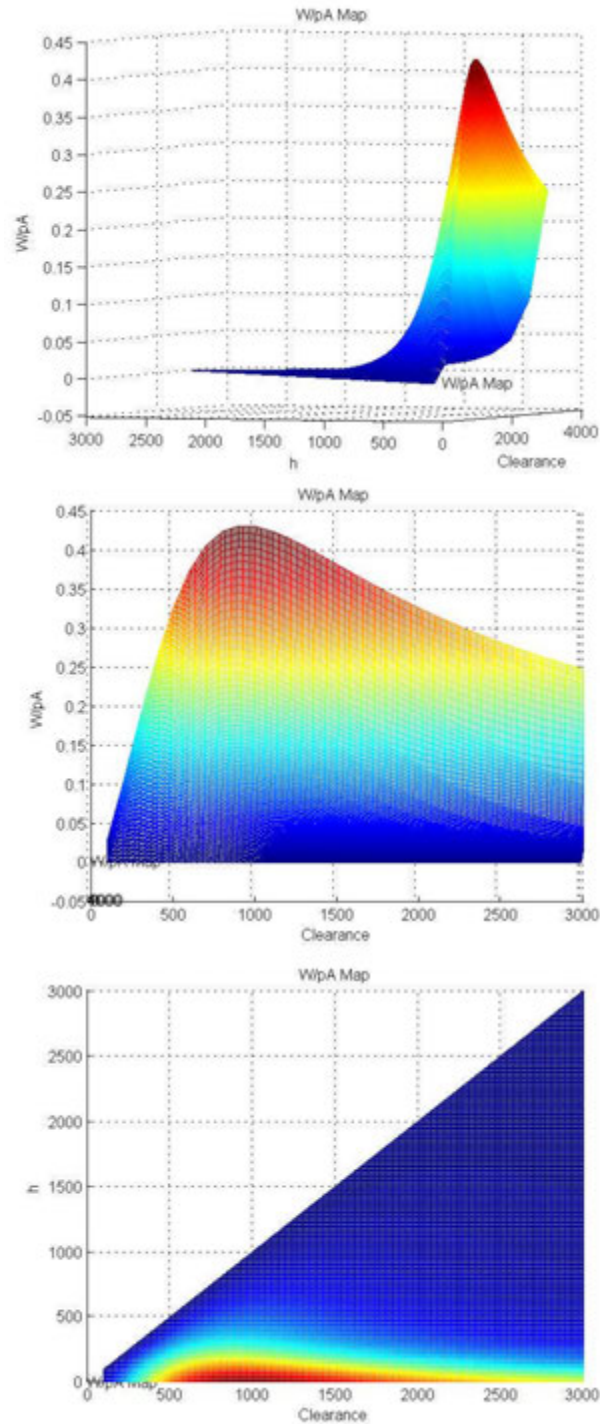


Figure 4-27 Views of  $W/pA$  in the  $h$ - $c$  plane for a porous liner bearing with  $K_{meas}=2 \text{ e-}5 \text{ lb/s}$  and operating pressure=10 psig.  
 Top - isometric, Center - clearance axis, Bottom - planar view.



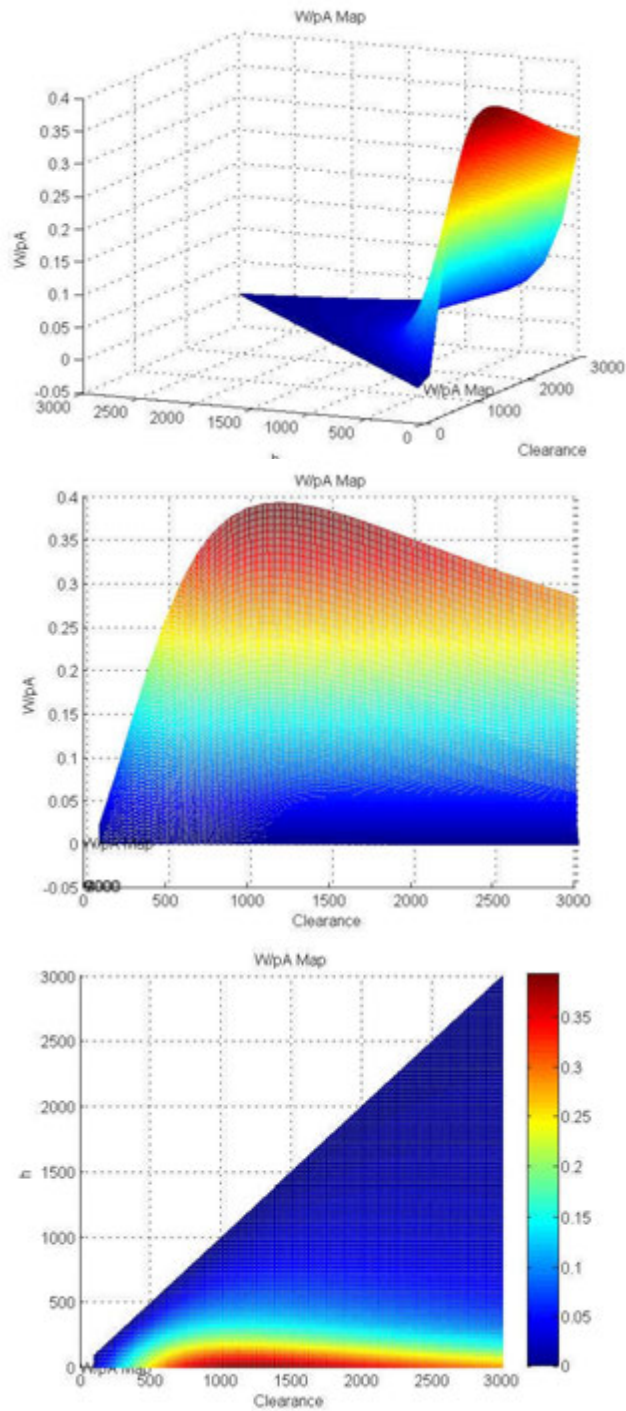


Figure 4-28 Views of  $W/pA$  in the  $h$ - $c$  plane for a porous liner bearing with  $K_{meas}=2 \text{ e-5 lb/s}$  and operating pressure=100 psig.  
 Top - isometric, Center - clearance axis, Bottom - planar view.

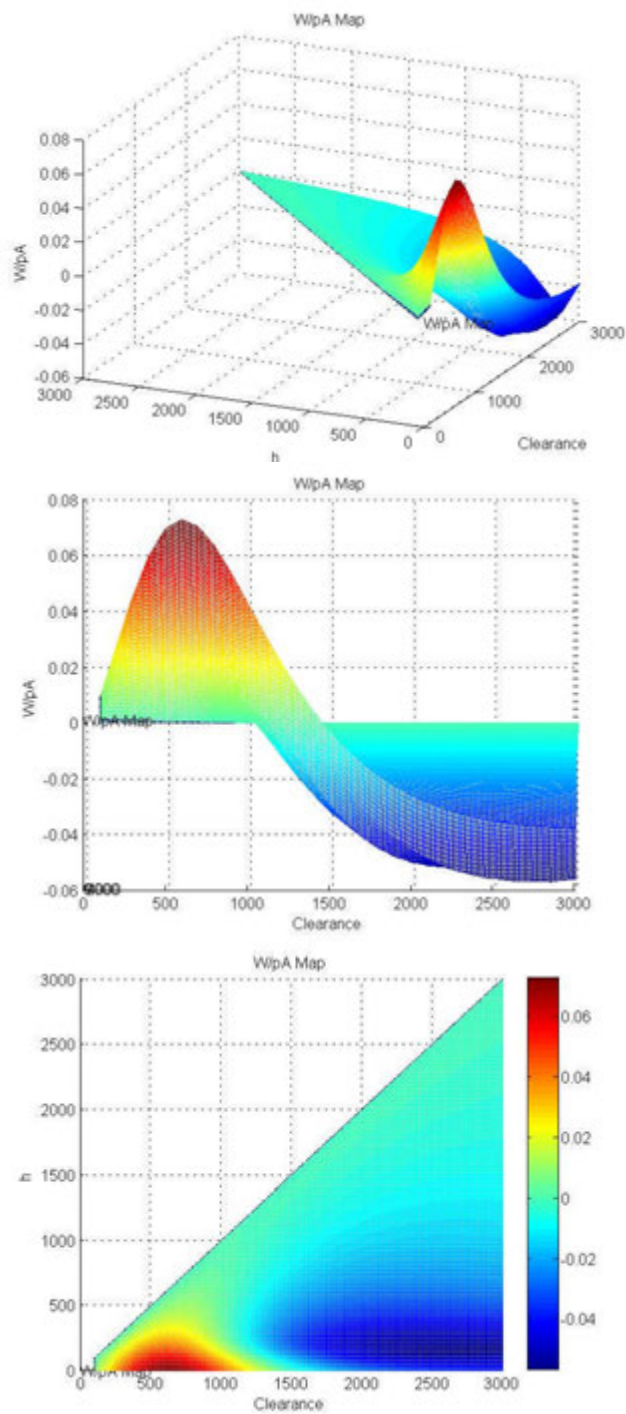


Figure 4-29 Views of ( $W/pA$  at 10psig)-( $W/pA$  at 100psig) in the  $h$ - $c$  plane for porous liner bearing with  $K_{meas} = 2 \times 10^{-5}$  lbs/s.  
 Top - isometric, Center, - clearance axis, Bottom - planar view.

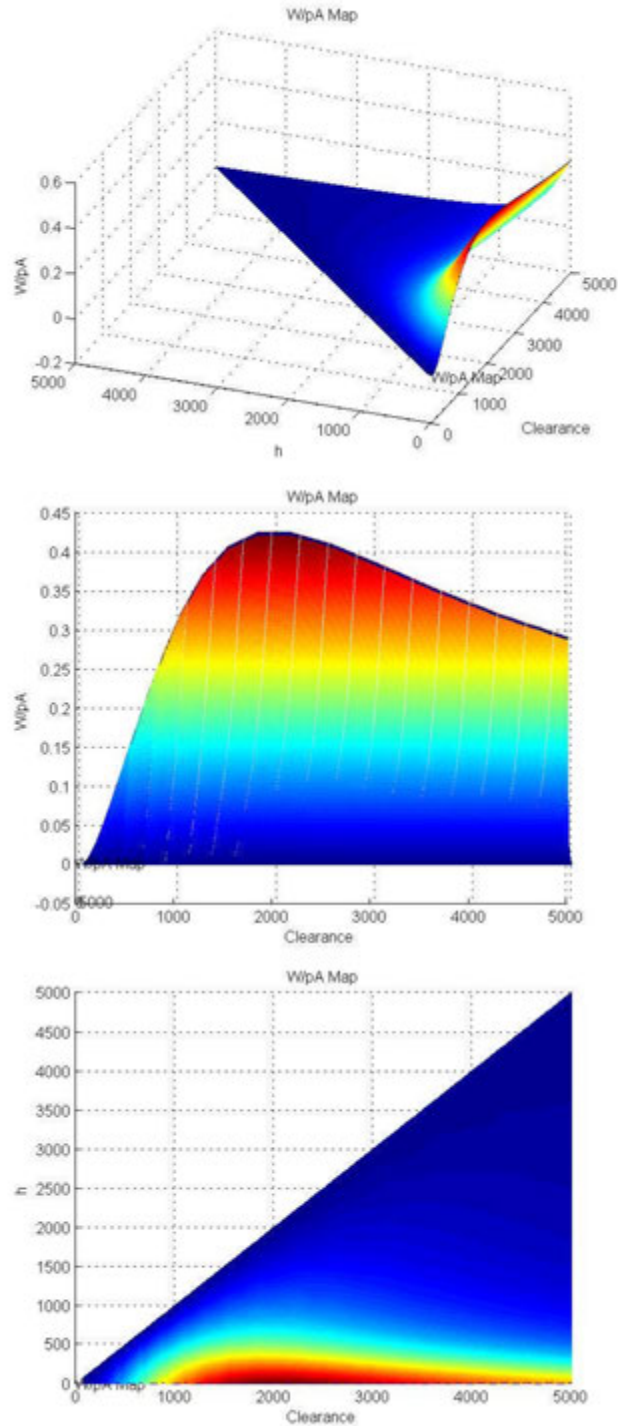


Figure 4-30 Views of  $W/pA$  in the  $h$ - $c$  plane for a porous liner bearing with  $K_{meas}=2 \text{ e-}4$  and operating pressure=10 psig.  
 Top - isometric, Center - clearance axis, Bottom - planar view.

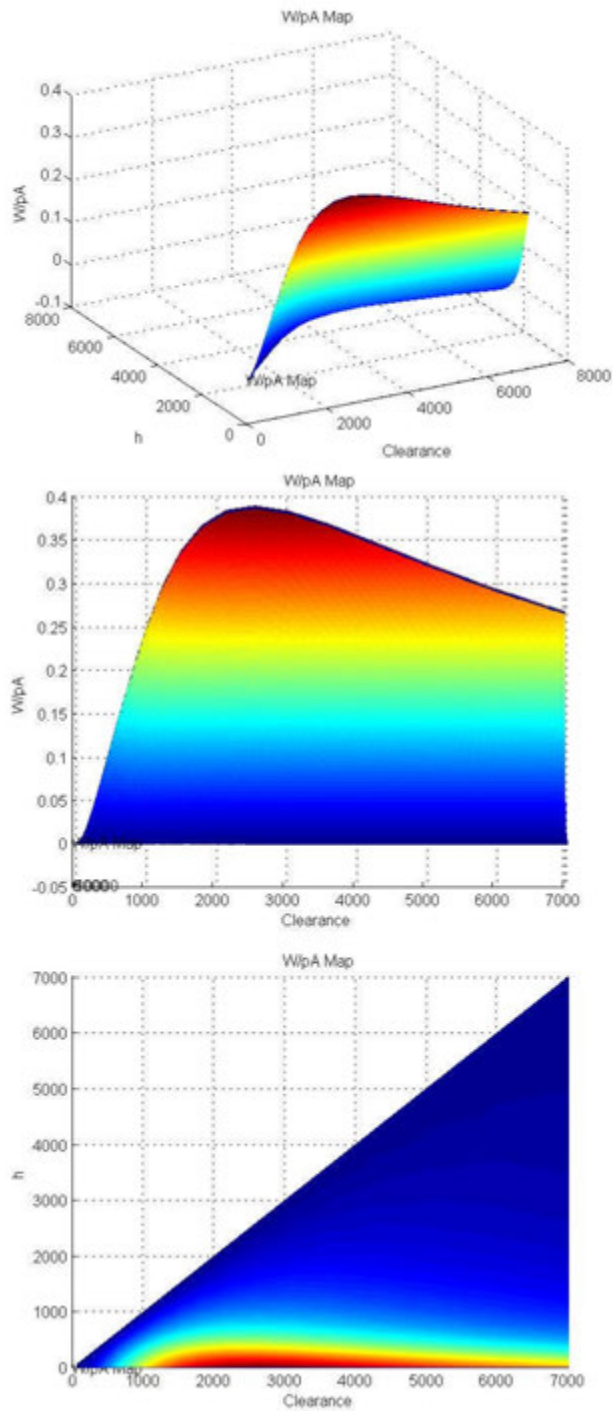


Figure 4-31 Views of  $W/pA$  in the  $h$ - $c$  plane for a porous liner bearing with  $K_{meas}=2 \text{ e-}4 \text{ lb/s}$  and operating pressure=100 psig.  
 Top - isometric, Center - clearance axis, Bottom - planar view.

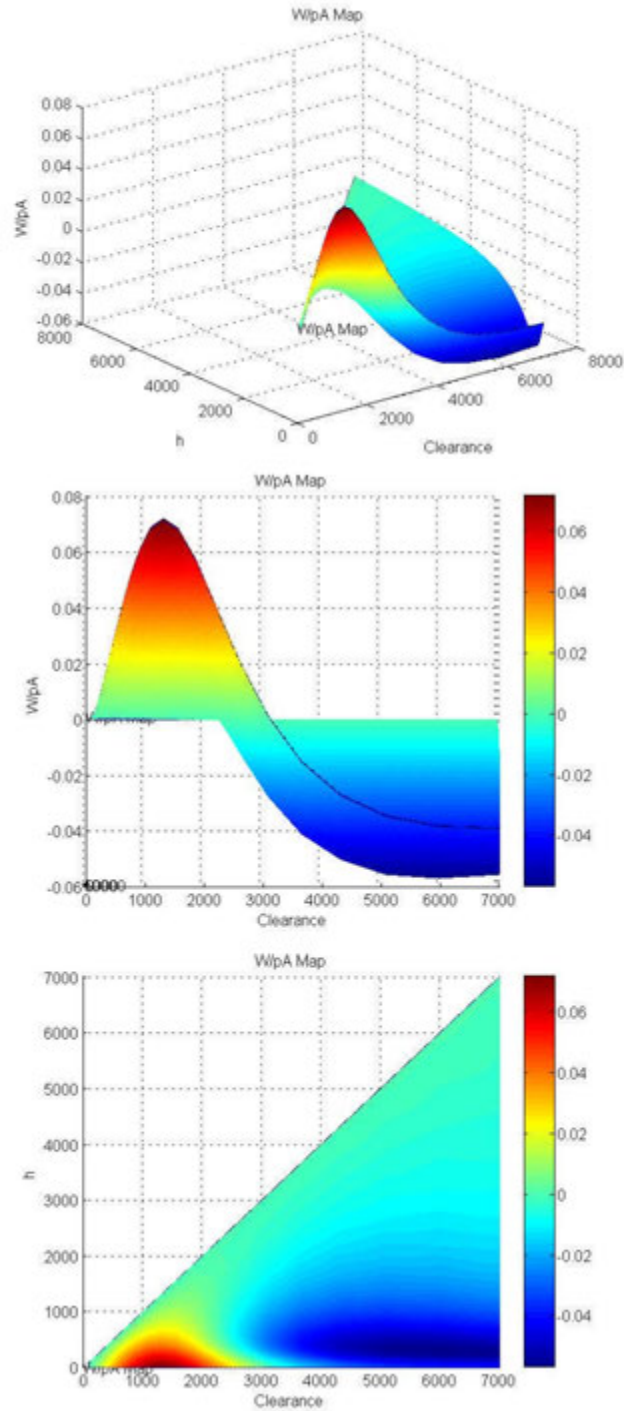


Figure 4-32 Views of  $(W/pA \text{ at } 10\text{psig})-(W/pA \text{ at } 100\text{psig})$  in the  $h$ - $c$  plane for porous liner bearing with  $K_{meas}=2 \text{ e-4 lbs/s}$ .  
 Top - isometric, Center, - clearance axis, Bottom - planar view.

#### 4.4.2. Introduction and Definition of Bearing Load Efficiency

It is appropriate at this point to introduce and define a new concept: bearing load efficiency. The bearing load force is the shaft/bushing interaction force which is generated by integrating the force in the bearing gap caused by the pressure acting normal to the shaft/bearing surface. Using the bearing geometry of section 1.3 this is:

$$F_x = \int_0^L \int_0^{2\pi} p \cos \theta R d\theta dz$$

$$F_y = \int_0^L \int_0^{2\pi} p \sin \theta R d\theta dz$$

For the special but common static case (and the one used in this thesis) where the shaft/bearing centers are displaced from each other parallel to the bearing neutral axis and the displacement is chosen to be in the  $Y$  (vertical) direction only, it can be seen that the pressure distribution is symmetric about  $Y$  so that there is no net shaft/bearing interaction force in the  $X$  axis. Also, intuitively, the bearing load  $W$  can be written as the difference between the integral of the pressure on the bottom side of the bearing and the top side of the bearing or:

$$W = \int_0^L \int_0^{\pi} p \sin \theta R d\theta dz + \int_0^L \int_0^{\pi} p \sin \theta R d\theta dz$$

The "difference" is actually a sum because the sign change in the sine function will subtract the pressure force of the top of the bearing from the bottom. The equation for  $W$  is, of course, simply the equation for  $F_y$  where the integral is broken into two parts. But it is done to introduce the concept of separating the side of the bearing where  $h_{min}$  occurs from the side where  $h_{max}$  occurs. Higher  $W$  is obtained by making the pressure on the bottom of the bearing ( $h_{min}$  side) as high as possible and the pressure on the top side of the bearing ( $h_{max}$  side) as low as possible. In the static case the highest pressure possible is the operating pressure and the lowest pressure possible is atmospheric pressure. Thus if the

top of the bearing is assumed to have a uniform pressure distribution  $p_a$  and the bottom side of the bearing is assumed to have an operating pressure of  $p_{op}$  then the maximum possible  $W$  is seen to be simply:

$$W_{\max} = LD(p_{op} - p_a)$$

Or if the operating pressure is measured (as it always is in this thesis) in gage pressure (psig) then the maximum possible force is simply:

$$W_{\max} = LDp_{op}$$

Example:

The integration of the pressure about the bearing gap for the pressure distribution solution of a .75" x 2" bearing with a clearance of 3000  $\mu\text{in}$  operating at 100 psig and a  $h_{min}$  of 1263  $\mu\text{in}$  ( $Y$  displacement of 1737  $\mu\text{in}$ ) is found to have a net hydrodynamic force of 8.6882 lbs. Integrating the pressure induced interaction force separately about the top of the bearing gap versus the bottom of the bearing gap yields that the total  $F_y$  on the bottom surface of the bearing is 62.9317 lbs and on the top -54.2435. This indicates that pressure difference is small compared to the total forces involved. Applying the just introduced concept of maximum possible static bearing force yields a maximum force of 150 lbs. Thus this bearing can be said to have a bearing load efficiency of 8.6882/150 or 5.79%.

The dimensionless load  $W/pA$  is used predominantly in this study where  $W$  is the bearing load and  $p$  is the gage operating pressure and  $A$  is the nominal bearing area  $LD$ . Hence, the bearing load efficiency  $W/W_{\max}$  turns out to be  $W/pA$ .

For dynamic bearings the situation is not quite so straight forward since the bearing can develop pressures less than gage pressure and higher than the operating pressure. Nonetheless it is the writer's opinion that it is still a useful concept with the proviso that an efficiency of over 100% is theoretically possible.



#### 4.4.3. Summary of $W/pA$ vs $h$ - $c$ Scan Results

Queries were run to ascertain the magnitude and locations of the maximum  $W/pA$  and the maximum and minimum  $W/pA$  difference between operation at 10 psig and 100 psig. Usually a maximum clearance of 3000  $\mu\text{in}$  was used. In some cases it appeared that minimum  $W/pA$  difference occurred at a clearance greater than the maximum clearance used. So additional scans were run at 5000 and 7000  $\mu\text{in}$  until the minimum  $W/pA$  difference became obvious. The data matrices represent interpolations at discreet points in the  $h$ - $c$  plane.

Therefore it should be remembered that queries asking for maximum and minimum values and locations return the discreet point that matches the query.

A tabular summary of these queries is presented below:

Bearing	$Kmeas$	pop 100			pop 10			100-10			WpA min	c	h	clmax
		WpA max	c	h	WpA max	c	h	WpA max	c	h				
Porous	2.00E-06	0.3906	600	0	0.4276	400	0	0.072	300	0	-0.0567	1300	68.4	3000
Porous	2.00E-05	0.3917	1200	0	0.4291	900	0	0.0725	600	0	-0.0567	2800	147.4	3000
Porous	2.00E-04	0.3917	2600	0	0.4296	2000	0	0.0725	1300	0	-0.249	3000	473	3000
Porous	2.00E-04	0.3882	2600	0	0.4237	2190	0	0.0719	1300	0	-0.0548	5000	370	5000
Porous	2.00E-04	0.3882	2600	0	0.4237	2190	0	0.0719	1300	0	-0.0566	5970	290	7000
12 x FH	2.00E-06	0.0737	450	110	0.0736	370	100	0.0096	250	80	-0.0206	920	180	3000
12 x FH	2.00E-05	0.074	1090	250	0.0735	760	190	0.0096	530	160	-0.0208	2190	400	3000
12 x FH	2.00E-04	0.0742	2190	530	0.0738	1840	470	0.0095	1090	320	-0.0151	3000	490	3000
12 x FH	2.00E-04	0.0742	2190	530	0.0738	1840	470	0.0095	1090	320	-0.0208	4310	870	5000

#### 4-33 Results of queries determining maximum and minimum locations.

Observations:

1. The maximum  $W/pA$  for PL bearings is about 0.429 and about 0.0738 for the FH bearings. This is independent of altering  $Kmeas$  by 2 orders of magnitude.
2. The maximum  $W/pA$  for porous liners operating at 100 psig is 0.087 lower (8.6%) than for bearings operated at 10 psig. The maximum  $W/pA$  for feedhole bearings operated at 100 psig was 0.0004 higher (0.5%) than for bearings operated at 10psig. Again, this is independent of  $Kmeas$ .

3. In order to obtain the maximum  $W/pA$ , the clearance must be increased for increasing  $K_{meas}$ . When  $K_{meas}$  is increased by a factor of 10 the clearance must be increased by about 2. This result applies to both porous liner and feedhole bearings.
4. For a given bearing of a specific clearance, the maximum  $W/pA$  will always occur at  $h=0$  (as expected) for porous liner bearings.
5. For feedhole bearings the “near surface effect” was seen at all levels of  $K_{meas}$ . This is to say that if a contour line of the maximum  $W/pA$  versus  $h$  is drawn across the  $c$  axis, it will intersect with  $h=0$  at some point and then move ‘inboard’ of  $h=0$  in a logarithmic manner. For clearances to the left of the  $h=0$  intercept the maximum  $W/pA$  for the bearing will be found, as usual, at  $h=0$ . For clearances to the right of the intercept maximum  $W/pA$  will be found at some  $h>0$ . This is what is being described in this thesis as the “near surface effect”. This is because the bearing will perform contrary to common expectations for small  $h$ . As  $h$  is decreased it is expected that  $W$  will increase whereas for a bearing subject to the near surface effect,  $W$  will actually *decrease* as  $h$  is decreased for a range of small  $h$ .

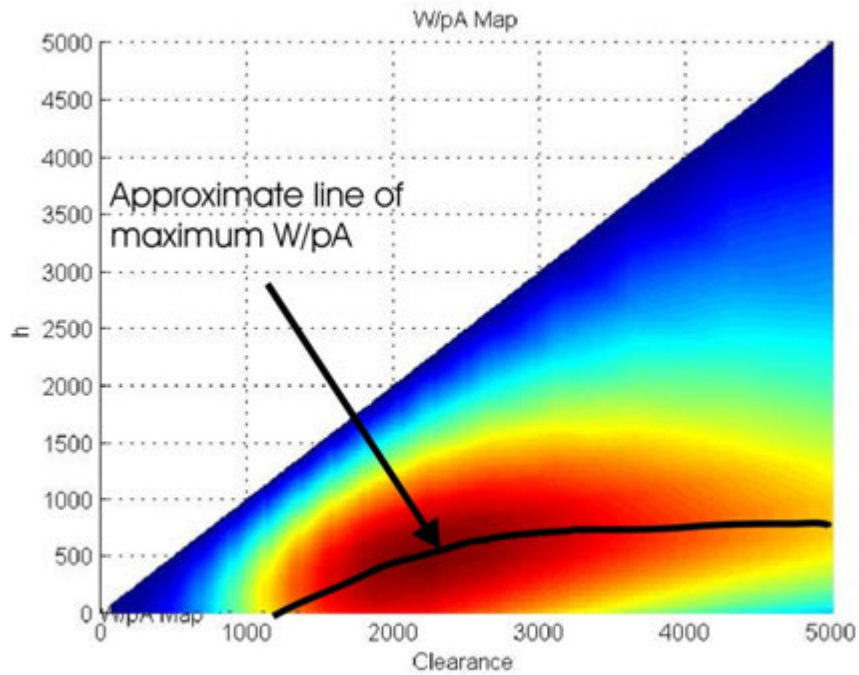


Figure 4-34 Sketch of the line delineating maximum  $W/pA$  for a feedhole bearing with  $K_{meas}$  or  $2 \times 10^{-4}$ .

If the top view of the  $W/pA$  in the  $h-c$  plane plots is observed for the feedhole bearings, it appears that the line of maximum  $W/pA$  intercepts  $h=0$  at approximately these locations:

$K_{meas}$	Pop psig	intercept $\mu\text{in}$
e-6	10	250
e-6	100	300
e-5	10	600
e-5	100	700
e-4	10	1440
e-4	100	1550

Figure 4-35 Visual estimate of  $W/pA$  maximum- $h=0$  intercept.

Once again, the same interesting pattern of almost a 2:1 increased clearance for each 10x increase in  $Kmeas$  is noted. Also the approximately 25 to 30% increase in significant clearances between 10 psig operation and 100 psig operation is noted.

6. 10 psig operation does not always outperform 100 psig operation in terms of  $W/pA$ . At many points of operation the 10 psig and 100 psig performances are the same or the 100 psig operation exceeds the 10 psig operation. However the range where 10 psig operation exceeds 100 psig overlaps the location of maximum  $W/pA$  on the  $h-c$  plane. Thus it is always true that 10 psig operation results in the highest  $W/pA$  for the bearing. The ranges where 100 psig exceeds 10 psig operation are in the area of low performance in  $W/pA$  on the  $h-c$  plane. The location of maximum  $W/pA$  difference is at a clearance shifted about 25 to 30% less than the clearance of maximum 10 psig operation in  $W/pA$ . The location of the minimum difference is about 2 times the clearance of the maximum 100 psig operation  $W/pA$ . The location in  $h$  of the maximum  $W/pA$  difference always occurs at  $h=0$  for porous liners and inboard for the feedhole bearings. All the minimum difference  $W/pA$  values occur inboard of  $h=0$ . How much they are inboard is predictable by again applying the 2:1 increase rule for every 10:1  $Kmeas$  increase.

7. It is the opinion of this researcher that a characteristic height that is a function of  $Kmeas$  is missing that would be very useful in creating a dimensionless  $c$  that would universalize the  $W/pA$  bearing performance map independently of  $Kmeas$ .

#### 4.5. Using The CFD Microscope for Further Study of the Near Surface Effect

The unexpected “near surface effect” for feedhole bearings has already been discussed in some detail. It is the phenomenon where  $W/pA$  decreases with decreasing  $h$  in some areas of the  $h$ - $c$  plane.

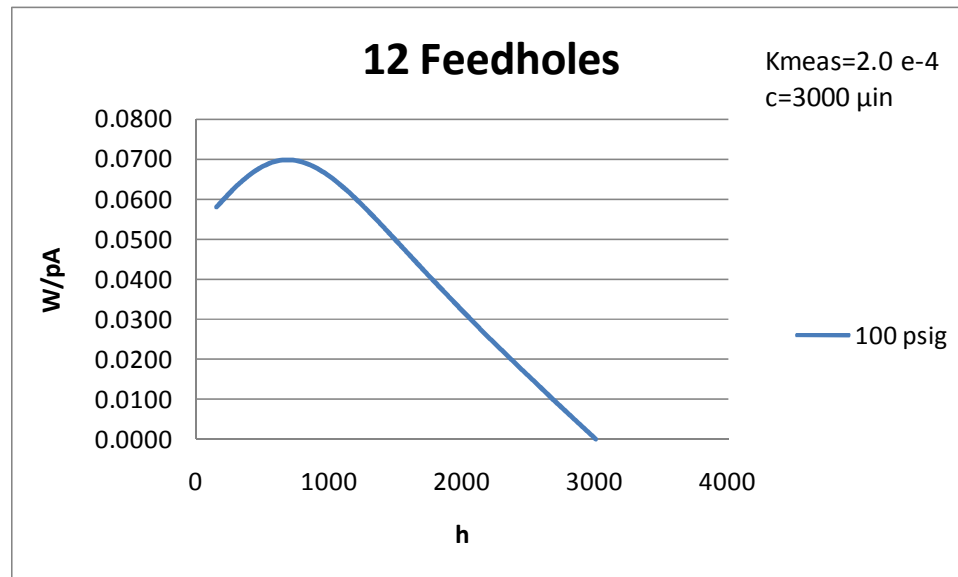


Figure 4-36 Profile for a feedhole bearing showing near surface phenomena.

Why does this occur? The feedhole bearings have 2 rows of 6 feedholes. Each feedhole is separated circumferentially from its nearest neighbor by  $60^\circ$ . The angular orientation of the feedholes is such that one feedhole is directly “below” the line of minimum  $h$  and one feedhole is directly “above” that of maximum  $h$ .

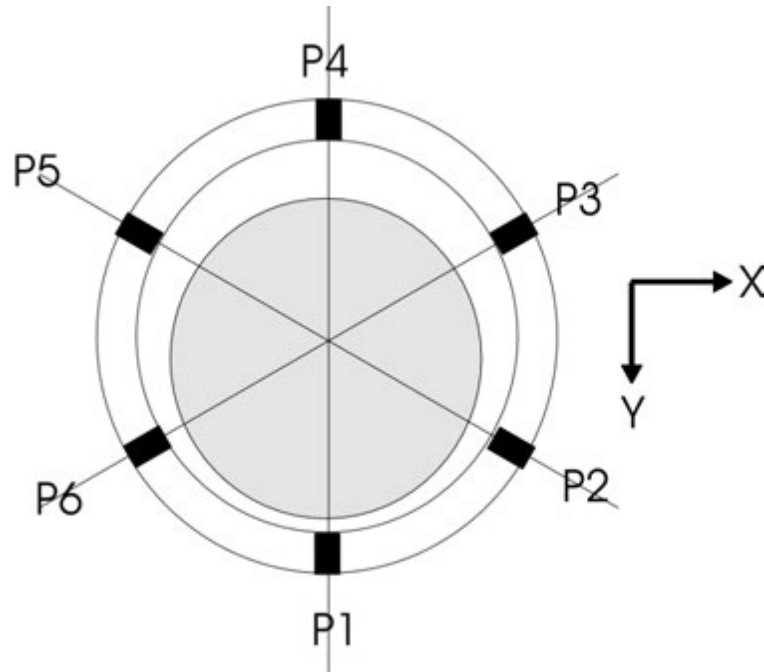


Figure 4-37 Feedhole geometry.

Feedhole geometry and bearing gap geometry can be used to examine the gap height  $h$  as function of the  $Y$  shaft/bushing displacement. It is also known that pressure is a nonlinear function of gap height. However when  $Y$  displacement is increased ( $h_{min}$  decreased), the gap height at each feedhole location on the “lower” half of the bearing gap decreases while the gap height on the “upper” half of the gap height increases. Correspondingly it would be assumed that the pressure values in the lower half of the bearing gap would increase and the pressure values in the upper half would decrease. Thus no rule of thumb type calculation seems to explain the near surface phenomenon.

In order to examine further this result  $W/pA$  vs.  $h-c$  plane scan for a feedhole bearing was reviewed. What was sought was a bearing that would demonstrate most clearly the phenomenon so that the pressure distribution could be calculated at points of varying  $h$  in order to examine them and ascertain the root

causes of the phenomenon. The intent is use the CFD “microscope” of the pressure distribution solution to examine the details.

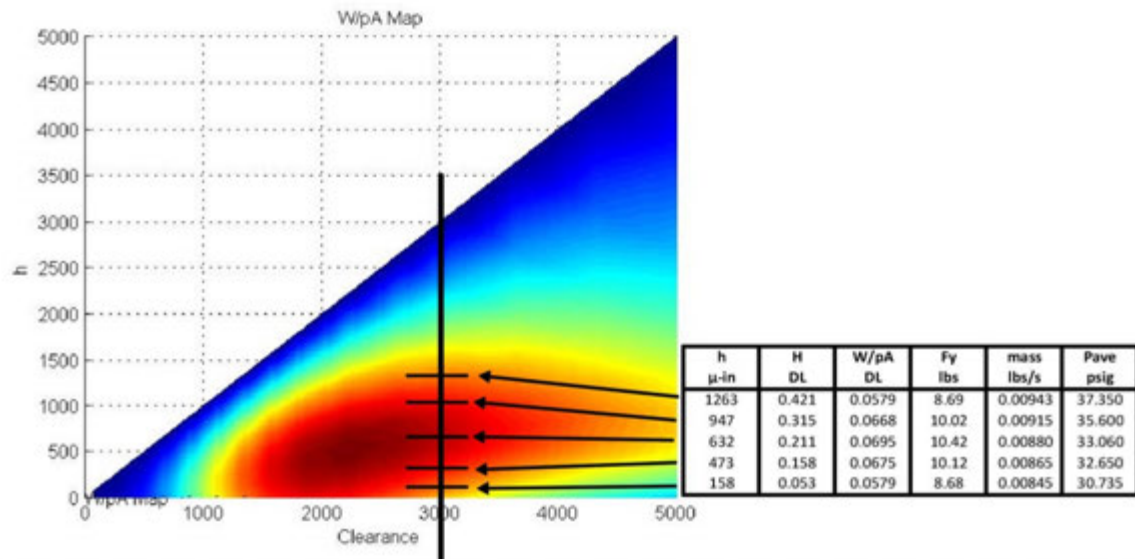


Figure 4-38 Choice of different points on a 3000  $\mu$ in c bearing.

A bearing with 3000  $\mu$ in clearance operating at 100 psig was chosen because it had a wide span of  $h$  demonstrating the near surface effect. For this bearing  $W/pA$  maximum of 0.0695 is reached at  $h=632$   $\mu$ in. This generates a maximum  $W$  of 10.42 lbs. Two pairs of interesting points were chosen where one of the pair had  $h$  greater than 632  $\mu$ in and one had  $h$  less than 632  $\mu$ in but each had nearly identical values of  $W$  less than 10.42 lbs. The pairs were  $h=947$  and 473  $\mu$ in with  $W (F_y)$  of 10.02 and 10.12 lbs and  $h=1263$  and 158  $\mu$ in with  $W (F_y)$  of 8.69 and 8.68 lbs.

Pressure distributions were run comparing the 1263, 632, and 158  $\mu$ in data points and snap shots were taken of different views of each distribution. Close up snap shots were taken of the feedhole sections and the land sections as well. The land section is the center of the bearing between the rows of feedholes. The

feedhole section is from the inside of the bearing just beyond the feedholes to the outer edge of the bearing.

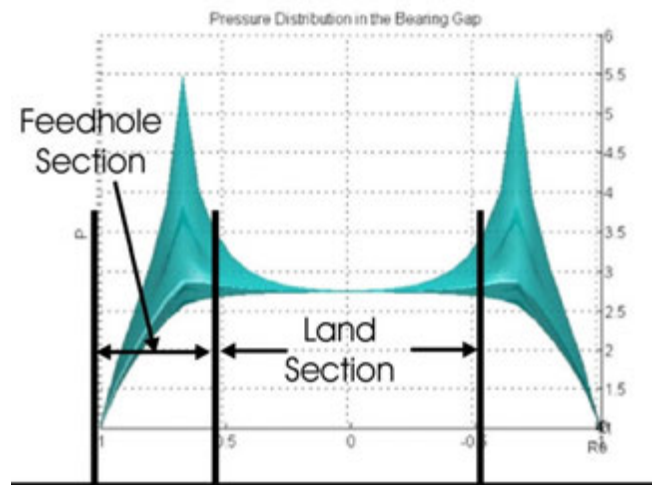


Figure 4-39 Separation of the feedhole and land sections by looking at the pressure distribution snap shot in the z (Length) direction.

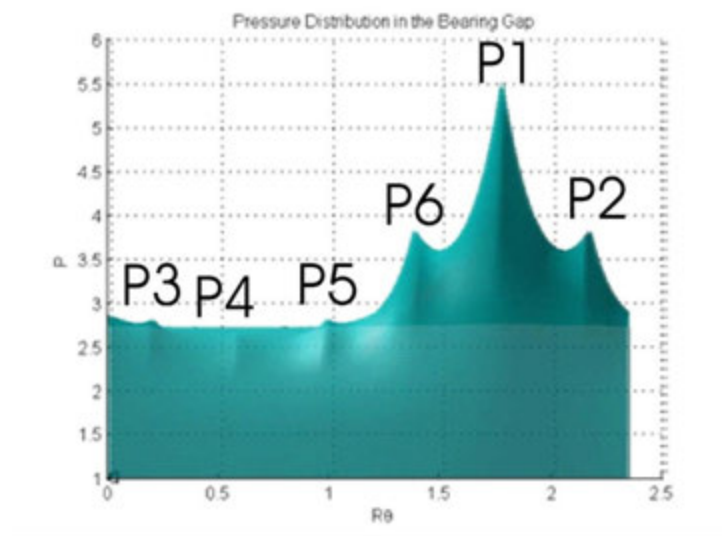


Figure 4-40 View of the feedholes looking the  $R\theta$  direction labeled according to figure 4-38.

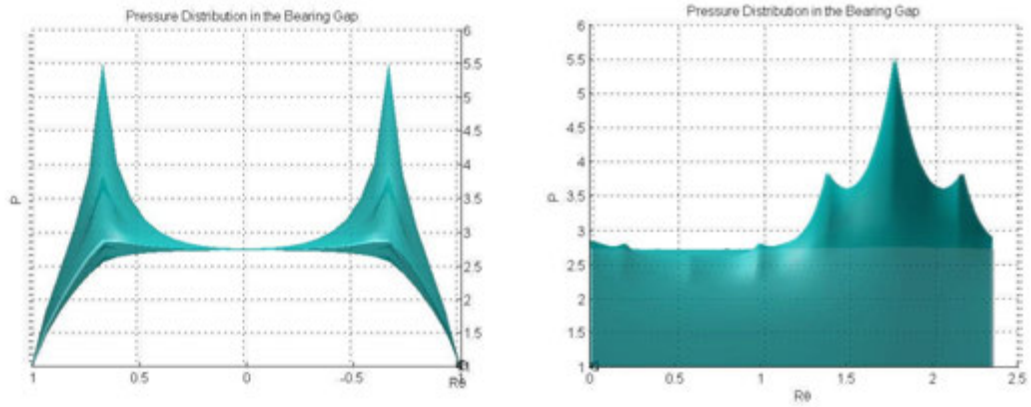


The total shaft/bearing interaction force  $W$  is calculated by summing the elemental  $F_Y$  distribution where:

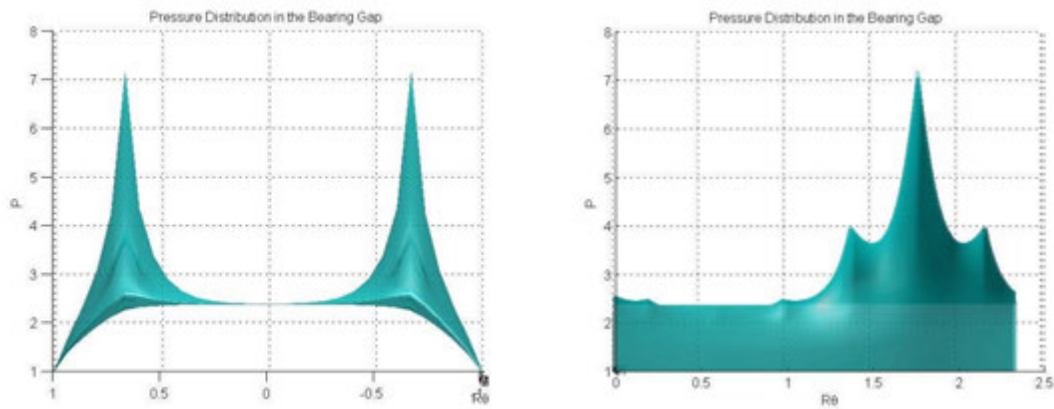
$$F_{Yi,j} = P_{i,j} \sin\theta d\theta$$

Results of equation were used to make make  $F_Y$  distribution snap shots presented in figures 4-43 and 4-44.

$h=1263$



$h=632$



$h=158$

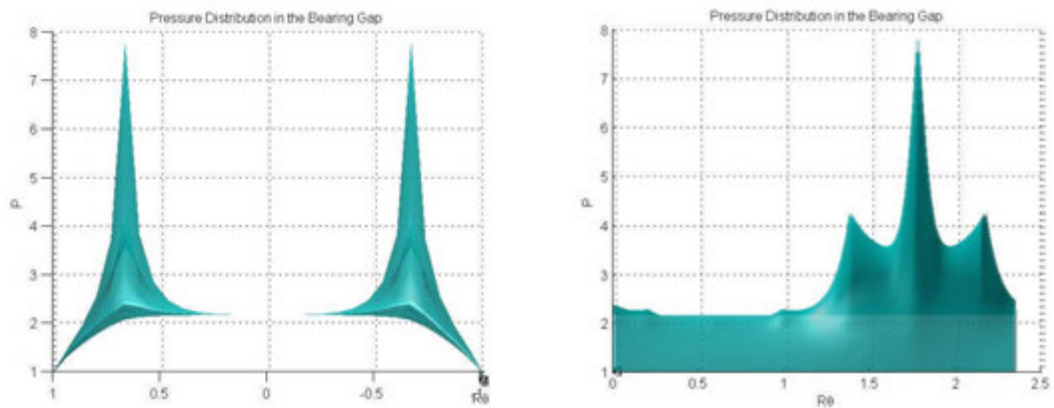
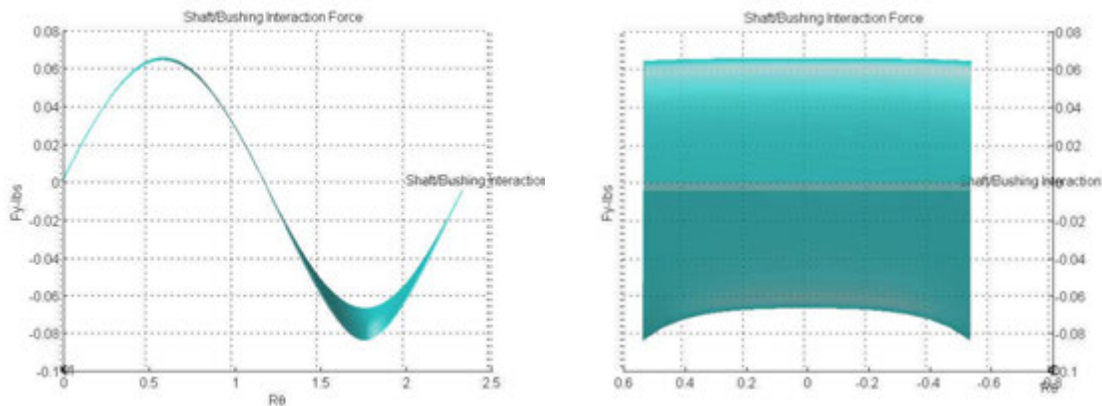
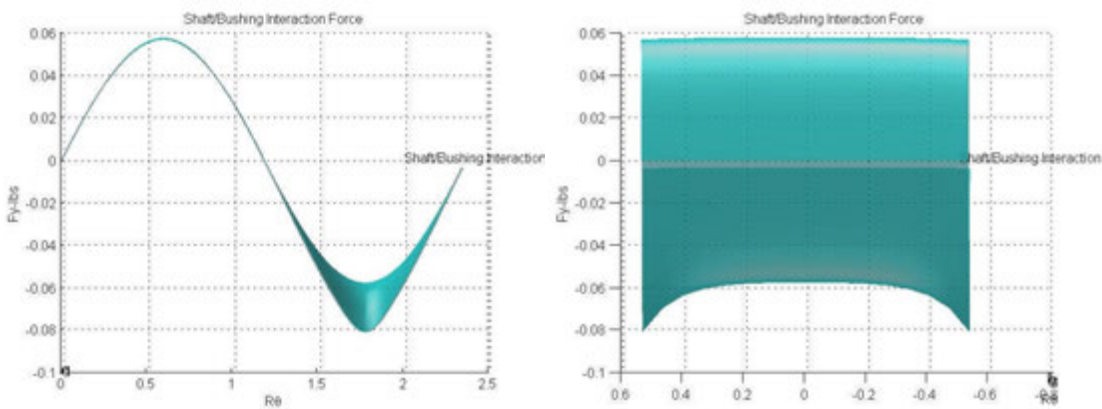


Figure 4-41 Pressure distribution snapshots left: variation in  $L$ , right: variation by  $R\theta$ .

$h=1263$



$h=632$



$h=158$

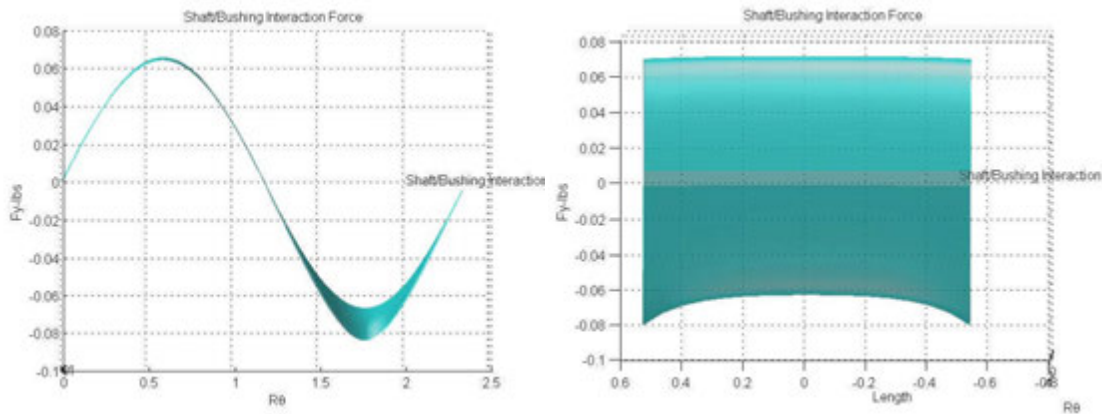
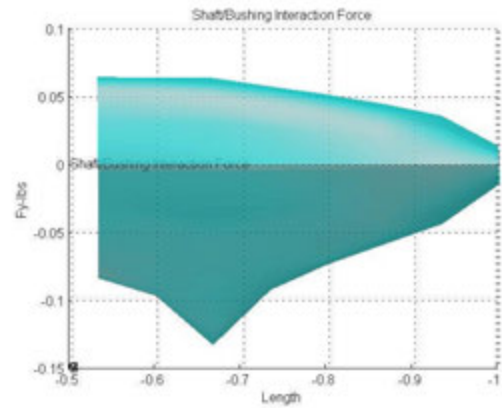
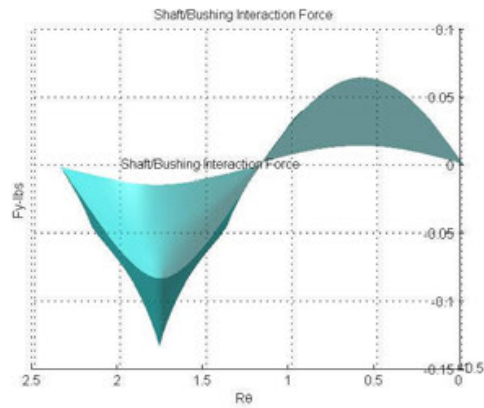
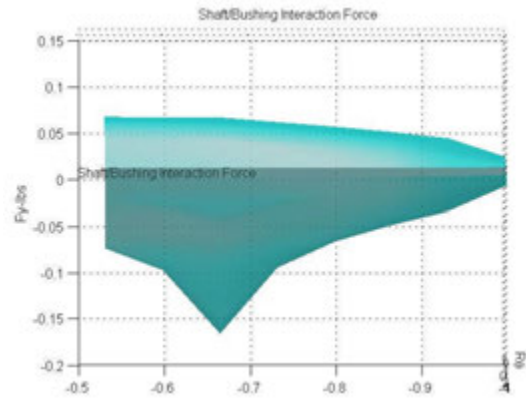
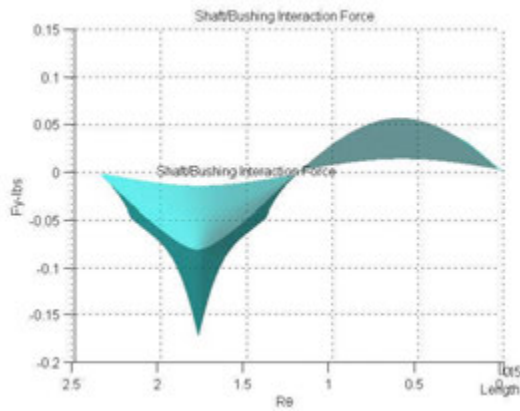


Figure 4-42 Elemental  $F_y$  distribution close-ups of the land section of the bearing gap. left: variation in  $R\theta$ , right: variation by  $L$ .

$h=1263$



$h=632$



$h=158$

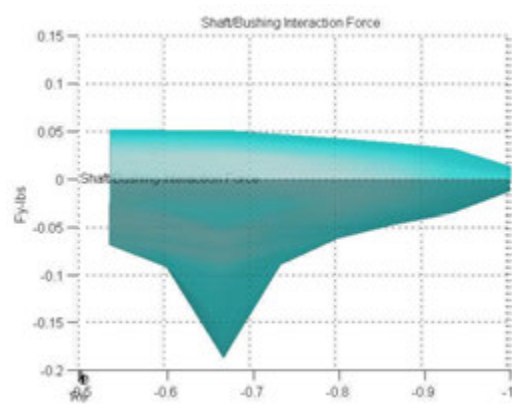
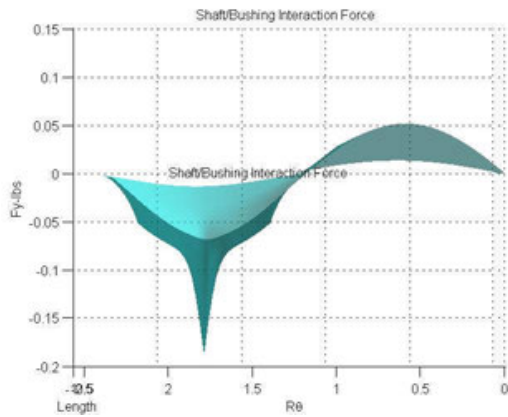


Figure 4-43 Elemental  $F_Y$  close-ups of the feedhole section of the bearing gap. left: variation in  $R\theta$ , right: variation by  $L$ .

Viewing the overall pressure variation it can be observed that as  $h$  decreases the pressure at hole locations P1, P2, and P6 increase while P3, P4, and P5 decrease. Also as expected from symmetry  $P2=P6$ ,  $P3=P5$  while P1 is the maximum pressure and P4 is the minimum pressure. The average pressure along the centerline in the middle of the land was also calculated. It is interesting to note that P4 is slightly less than this value.

hmin	holes						
	P1 P(6&26,73)	P2 P(6&26,89)	P3 P(6&26,9)	P4 P(6&26,25)	P5 P(6&26,41)	P6 P(6&26,57)	Center Pave
1263	5.5089	3.8261	2.8097	2.635	2.8097	3.8261	2.73947
632	7.1821	3.994	2.4952	2.3176	2.4952	3.994	2.386715
158	7.7855	4.25	2.2931	2.1197	2.2931	4.25	2.170804

Figure 4-44 Query results for pressure at feedhole locations.

Bearing gap geometry yields that contribution to  $W$  at any element in the bearing gap is:

$$\delta W_{i,j} = P_{i,j} \sin \theta dA$$

With this it can be supposed that the contribution to  $W$  caused by the pressure peaks corresponding to the feedholes would be proportional (by  $dA$ ) to:

$$P1-P4+(P2+P6-P3-P5)\sin(30)=P1-P4+.5*(P2+P6-P3-P5)$$

If this is called the geometric sum of the pressure peaks it is found that this sum increases as  $h$  decreases. So that the pressure peaks can be eliminated as the source of the near surface phenomenon.

	Geometric
hmin	sum
1263	3.8903
632	6.3633
158	7.6227

Integration of the pressure distribution in the land section of the bearing resulted in negligible contribution to the load force  $W$ . Examination of the close-ups in figure 4-33 gives ample explanation. The pressure variations throughout the area are small going from about  $-0.07$  to  $+0.07$ . Further they are mostly asymmetric such that integration leads to near zero net force.

The explanation for the near surface phenomenon must lie, therefore, in the feedhole section of the bearing gap around but excluding the feedhole pressure peaks themselves.

Examination of the  $F_Y$  distribution around the feedhole sections for  $h=1263 \mu\text{in}$  compared with  $h=158 \mu\text{in}$  as well as integration of the forces in about select bearing areas confirms the above hypothesis. The peak in  $F_Y$  and  $P$  corresponding to feedhole P1 is greater for the  $158 \mu\text{in}$  case than for the  $1263 \mu\text{in}$  case. Pressure in the land section is also greater for  $158 \mu\text{in}$  case than for the  $1263 \mu\text{in}$  case but the resulting  $F_Y$  integrates to near zero. In fact, the average pressure for the  $158 \mu\text{in}$  case is greater than for the  $1263 \mu\text{in}$  case but integrates to approximately the same  $F_Y$  as the  $1263 \mu\text{in}$  case primarily because the peak pressure at P1 falls off more rapidly for the  $158 \mu\text{in}$  case than for the  $1263 \mu\text{in}$  case leaving a wider distribution of higher pressure in the bottom half of the bearing gap around the feedholes P1, P2, and P6.

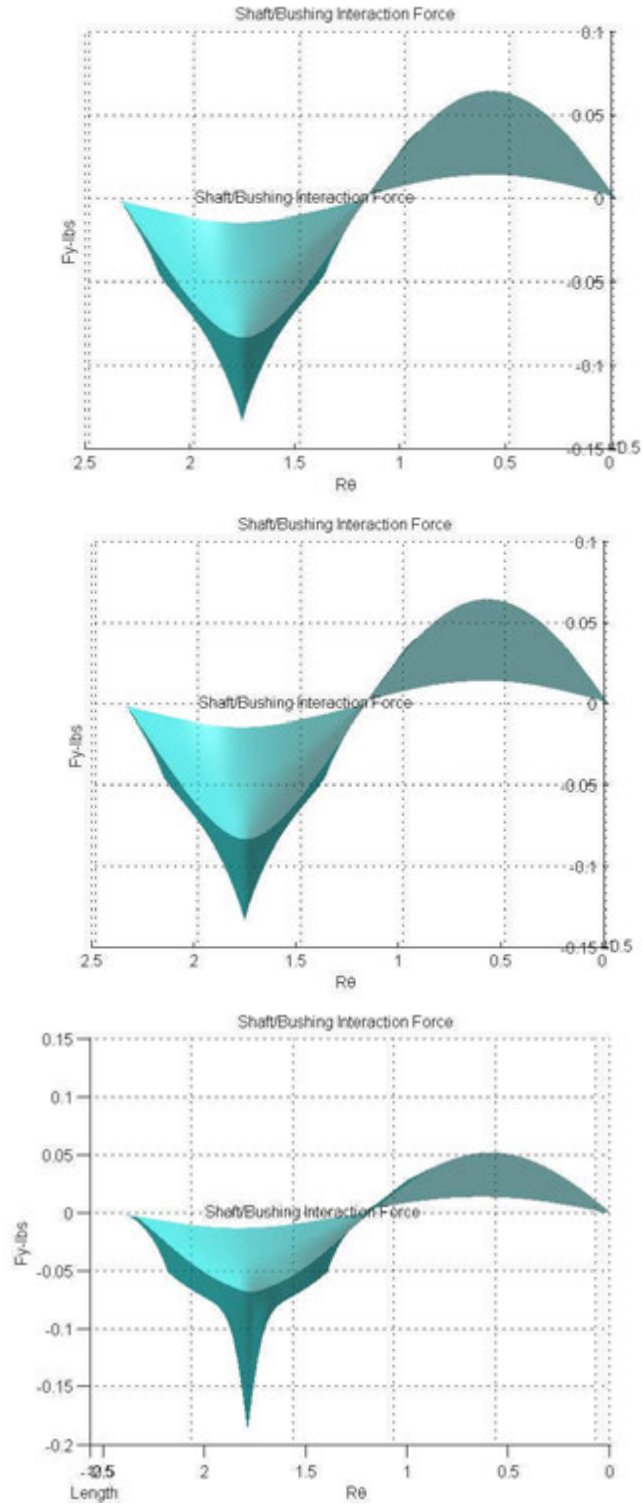


Figure 4-45 A closer look at the pressure distribution about the feedhole  
 top:  $h=1263 \mu\text{in}$ , center:  $h=632 \mu\text{in}$ , bottom:  $h=158 \mu\text{in}$ .

This raised a question about the mesh size. The grid size in all the CFD experiments consisted of length elements ( $NL$ ) of 30 and (31 length nodes) and circumferential elements ( $Nazb$ ) of 96 (96 nodes) for a total of 2880 elements. The slope of the pressure distribution around the feedholes are steep and change rapidly. Could the surface phenomenon be an anomaly of integration of a rapidly changing distribution with too coarse a grid pattern?

To test this, pressure solutions were rerun using first a grid size of 90 x 192 or 17,280 elements. When this finer mesh was used the overall results changed somewhat but the near surface phenomenon still remained and for the same reasons. Finally, another run was made with a grid of 180x386 nodes (69,480 elements) and the near surface phenomenon remained intact.

NL	Nazb	elements	h	Yd	Fy-total	Fy-web	Fy-edge	Fy-FH
30	96	2,880	1263	1737	8.6882	1.288	7.4002	0.1871
30	96	2,880	632	2368	10.4242	1.0397	9.3846	0.3061
30	96	2,880	158	2842	8.6855	0.5933	8.0902	0.3667
90	192	17,280	1263	1737	7.904	0.8375	7.0664	0.0349
90	192	17,280	632	2368	8.8808	0.5831	8.2976	0.0542
90	192	17,280	158	2842	7.4601	0.3166	7.1435	0.0638
180	386	69,480	1263	1737	7.5409	0.7712	6.7697	0.0091
180	386	69,480	632	2368	8.2583	0.4945	7.7638	0.0139
180	386	69,480	158	2842	6.9859	0.2664	6.7195	0.0162

Figure 4-46 Tabular results of increasing the number of elements.

Viewing figure 4-47, it can be seen that increasing the number of elements had the overall effect of reducing  $F_Y$  indicating that a courser mesh created more apparent net force by failing to capture the steepness of the pressure gradient as well as the finer mesh did. With the finer mesh  $F_y$  for  $h=158 \mu\text{in}$  is no longer the same as for  $1263 \mu\text{in}$  which was the reason for pairing those two points. Also, it is not known if  $632 \mu\text{in}$  is still the precise  $h$  corresponding to the maximum  $F_y$  which was the reason for including it as a data point. What is known, however, is that even with the 180x386 mesh that when  $h$  was lowered from  $632 \mu\text{in}$  to  $158$



$\mu\text{in}$  that  $F_y$  dropped 1.2724 lbs from 8.2583 lbs to 6.9859 lbs for a 15.4% reduction. This drop is comparable to results with the 30x96 mesh where  $F_y$  dropped 1.7387 lbs from 10.4242 lbs to 8.6855 lbs, for a 16.7% reduction.

So what is the physical cause of the near surface phenomenon? We speculate that as  $h$  goes to zero, the pressure at P1 goes to operating pressure. However, the bearing gap height profile between P6, P1, and P2 is such that flow is essentially stopped causing large pressure reduction in the areas very close to P1.

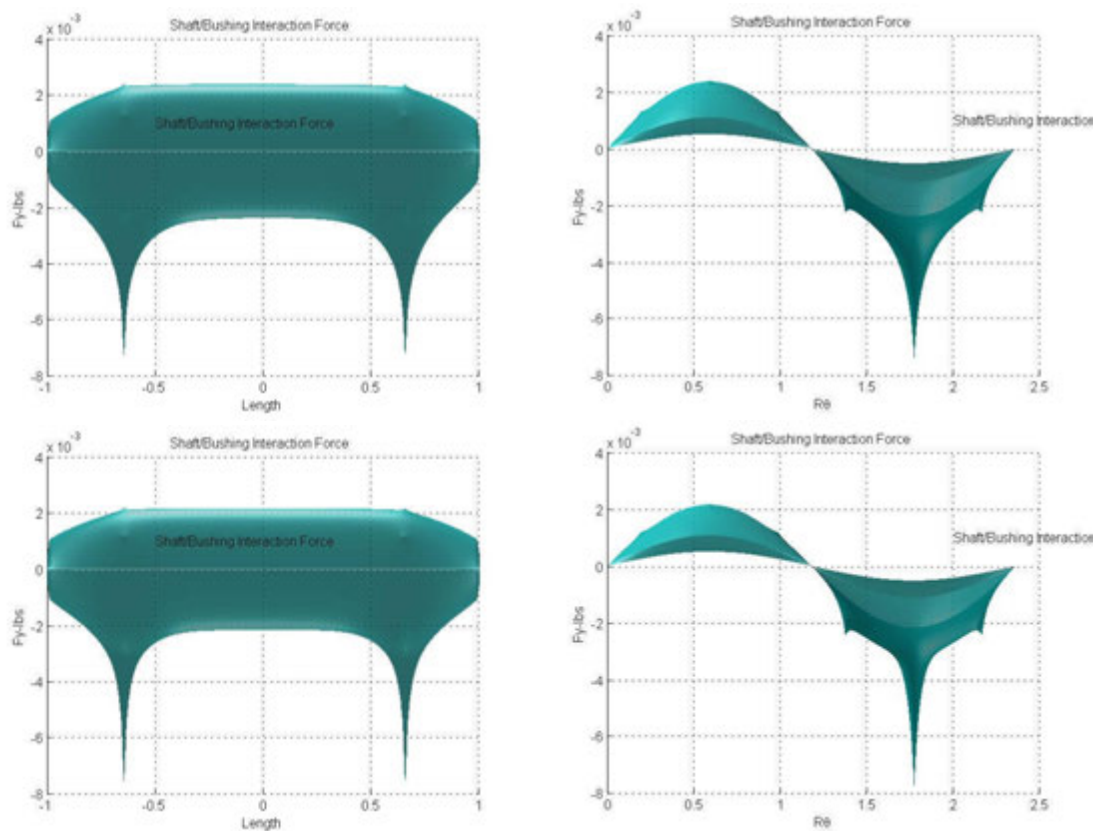


Figure 4-47  $F_y$  profiles with 180x386 mesh, top  $h=632 \mu\text{in}$ , bottom  $h=158 \mu\text{in}$ .

## 4.6. Hydrodynamic Bearing Results

### 4.6.1. Theoretical Expectations - Sommerfeld Long Bearing Solution

Following is a synopsis of the Sommerfeld “long bearing as it is presented in Williams *Engineering Tribology* (Williams pp 308-311 [19])

A gas bearing is well modeled by the Sommerfeld boundary conditions (in the circumferential direction), that is that the pressure is allowed to go below the ambient pressure where the bearing gap diverges. A solution can be found (one method is to use the Sommerfeld substitution (p269):

$$\cos \gamma = \frac{\varepsilon + \cos \theta}{1 + \cos \theta}$$

This results in a dimensionless load capacity:

$$\frac{W}{2RLp_a} = \Lambda \frac{\pi \varepsilon}{(1 - \varepsilon^2)^{1/2} (2 + \varepsilon^2)}$$

$$\text{where } \varepsilon = \frac{e}{c} \text{ and } \Lambda = \frac{6\eta\omega R^2}{c^2 p_a}$$

This solution is good for only for small  $\varepsilon$  and small  $\Lambda$ .  $\Lambda$ , the bearing number is also called the compressibility factor. Given that the ambient pressure, the bearing radius, and the clearance are all fixed, the bearing number is proportional to the viscosity and the rotational speed only. Further the viscosity for air is a function of temperature only and hence in isothermal operation it is fixed as well.

The dimensionless load can be rewritten as :

$$W = g(\varepsilon) K_{op} \left( \frac{R^3 L}{c^2} \right)$$

where  $g(\varepsilon)$  is a function of the eccentricity ratio only and is:

$$g(\varepsilon) = \frac{\varepsilon}{(1 + \varepsilon^2)^{1/2} (2 + \varepsilon^2)}$$

and  $K_{op}$  is function operating parameters only and is:

$$K_{op} = 12\pi\eta\omega$$

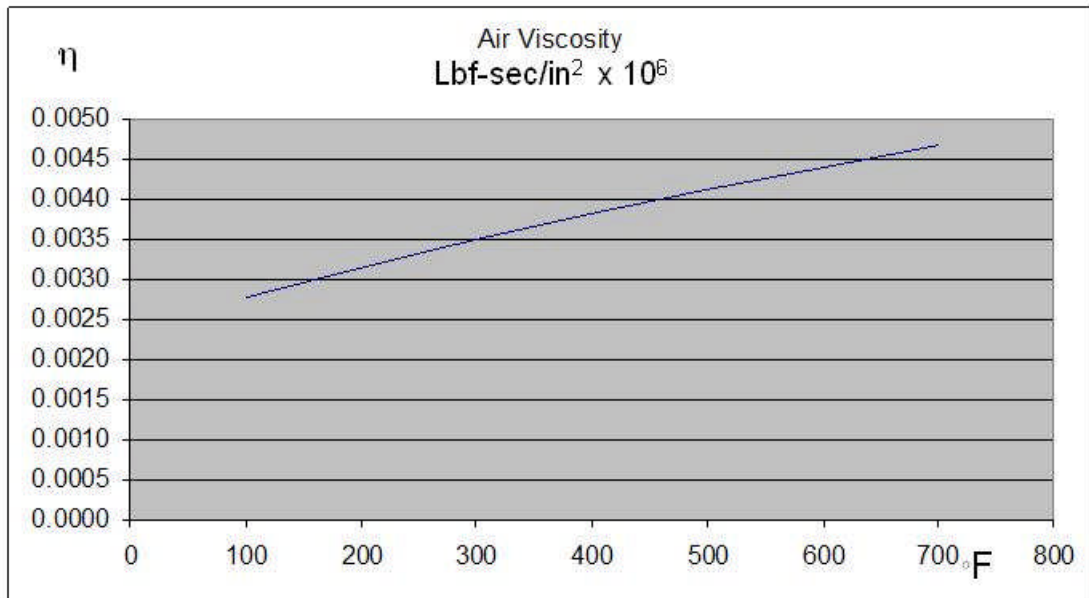


Figure 4-48 Air viscosity as function of temperature using the empirically based

relationship,  $\eta = \frac{\sqrt{t}}{A_0 + \frac{A_1}{t} + \frac{A_2}{t^2} + \frac{A_3}{t^3} + \frac{A_4}{t^4}}$  from Zucrow [20].

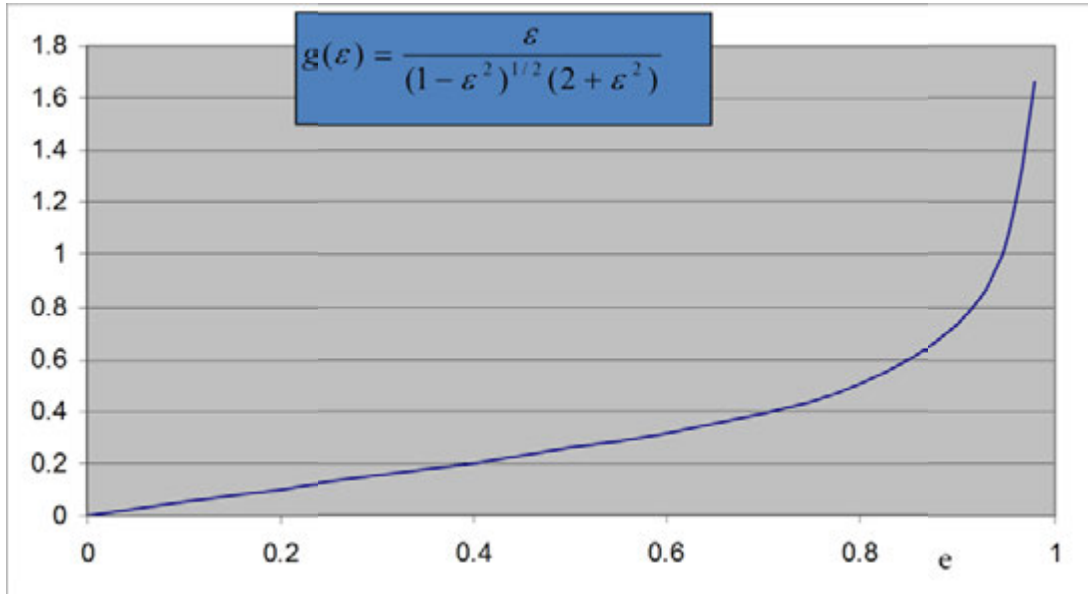


Figure 4-49  $g(\varepsilon)$  as a function of the eccentricity ratio.

Within the bearing gap an asymmetric pressure distribution is expected for very low bearing numbers which results in an attitude angle (angle between the load line and the line of connecting the bushing and shaft centers) of  $90^\circ$ .

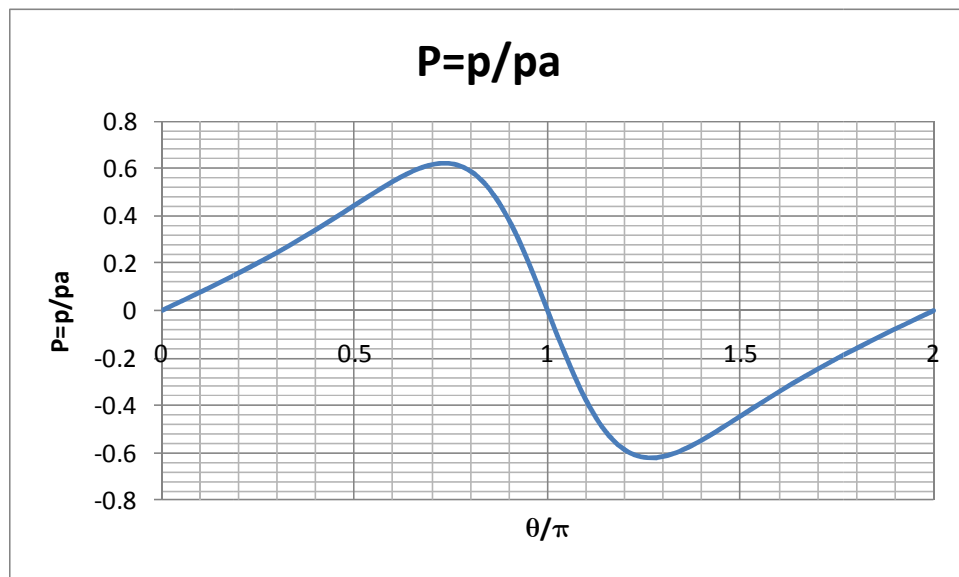


Figure 4-50 Circumferential pressure distribution for a long bearing with small bearing number. (asymmetric “full Sommerfeld condition”).

#### 4.6.2. CFD Hydrodynamic Bearing Results

In this thesis, for basis of comparison basis, a 0.75" diameter by 2" long journal bearing operating at room temperature and atmospheric ambient pressure has been chosen. The experimental hyperspace for the hydrodynamic bearing includes the clearance, the eccentricity ratio, and the rotation speed. Running CFD at selected locations within the experimental range is somewhat time consuming as the method described in section 3.9 takes a minimum of 6 to 7 minutes per CFD experiment and even longer when the numerical viscosity has to be altered by trial and error to find a pressure solution.

Nonetheless, a series of experiments were run sampling the range using a bearing with a clearance of 0.002" (rather large) and running at eccentricity ratios of 0.5, 0.75 and 0.9 through a range of speeds. In general the higher the eccentricity ratio the more difficult it was to find high speed solutions thus narrowing the speed range sampled. For the eccentricity ratio of 0.5, it was possible to get results up to 200,000 RPM. For eccentricity ratios of 0.75 and 0.9 it was only possible to get solutions to up to 140,000 RPM and 60,000 RPM respectively. This imposed an apparent numerical "speed limit" on the CFD range of experiments

As expected, the higher the speed and greater the eccentricity ratio the higher the net hydrodynamic force that was generated in the bearing gap. For example, at 60,000 RPM the net force generated was 3.13 lbs, 5.47 lbs, and 8.02 lbs for eccentricity ratios of 0.5, 0.75, and 0.9.

The numerical speed limits encountered along with some major bearing performance factors are shown in figure 4-53. The generated Y component of the net hydrodynamic force (component in the direction of the eccentricity vector

or line of centers) might have something to do with the apparent speed limit as these were oddly similar.

$\varepsilon$	Speed RPM	Fy lbs	Fx lbs	Ftotal lbs	Pmax atm	Pmax atm
0.5	200,000	3.35	-9.11	9.71	2.09	0.92
0.75	140,000	3.71	-11.24	11.84	2.35	0.67
0.9	60,000	3.36	-7.29	8.02	1.89	0.38

Figure 4-51 Comparison of pressure distribution characteristics of the highest speed solutions found for the tested eccentricity ratios.

As expected the net hydrodynamic force was fairly linear with respect to speed with higher slopes for higher eccentricity ratios.

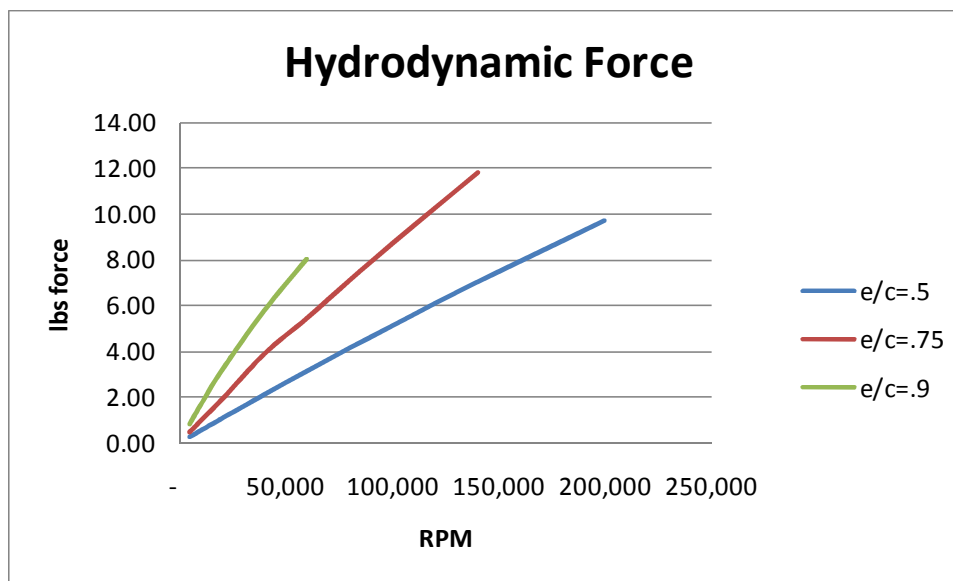


Figure 4-52 Net hydrodynamic forces generated.

At low bearing numbers (low speed) the attitude angle was very close to  $90^\circ$ . With increased speed the attitude angle increased.

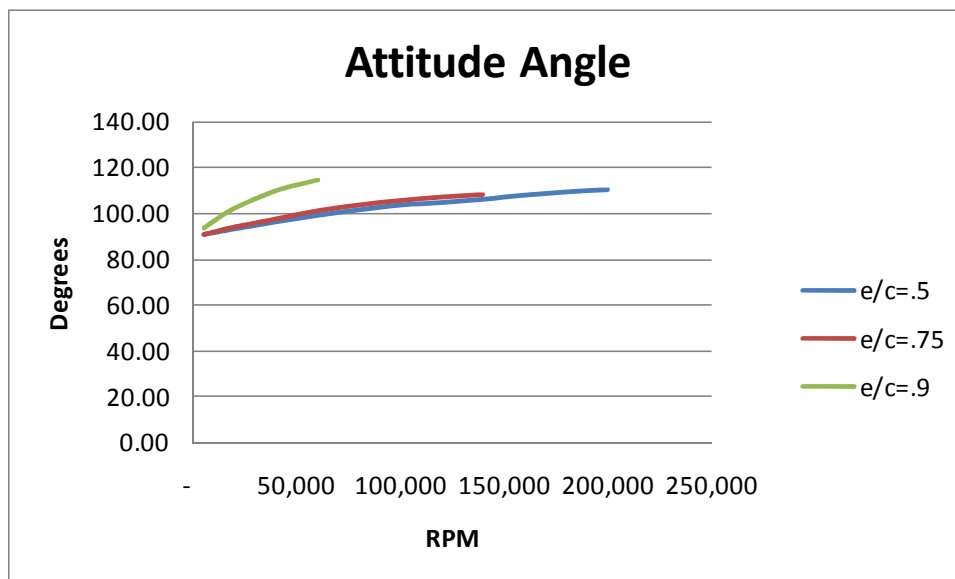


Figure 4-53 Attitude angles as function of speed and eccentricity ratio.

The net hydrodynamic force generated by the pressure distribution is directly related to the difference in pressure between the converging and the diverging halves of the bearing gap. Figure 4-56 shows the maximum and minimum pressures as a function of speed and the eccentricity ratio. At any given speed the difference between the maximum and minimum pressures is greater for smaller eccentricity ratios. The locations of the maximum and minimum pressures will be discussed in the next section, however the maximum pressure is always on the converging side of the bearing gap and the minimum pressure is on the diverging side.

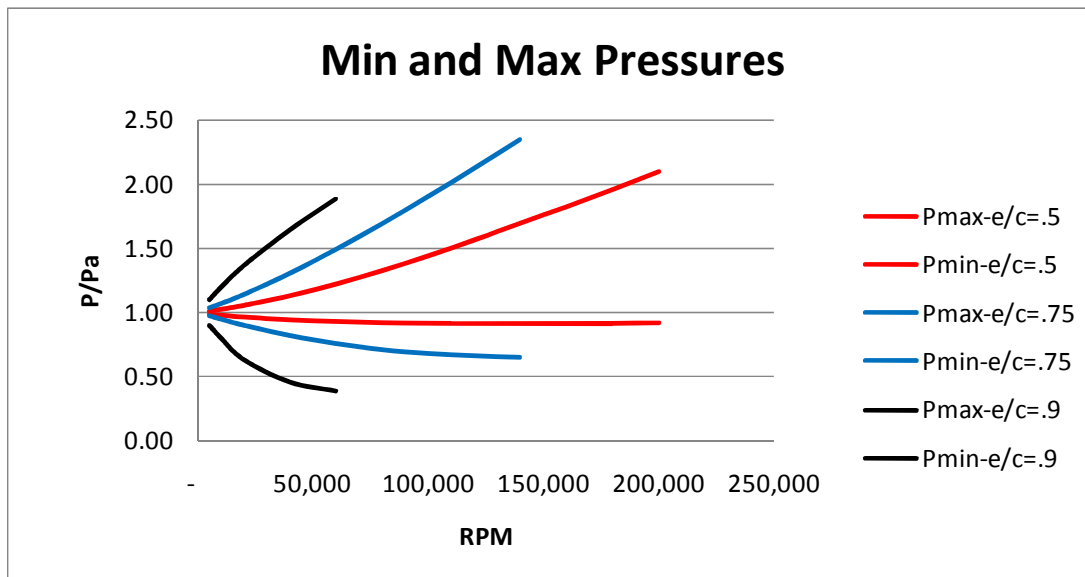


Figure 4-54 Minimum and maximum pressures in the bearing gap as function of eccentricity ratio and speed.

Although the eccentricity ratio is a classic dimensionless number used to describe journal bearings, it does not tell the whole story. This is because there is much more hydrodynamic action at small minimum flight heights, ( $h_{min}=c-e$ , where  $e$  is the eccentricity), regardless of the eccentricity ratio. As has been discussed in previous sections, there seems to be a characteristic length to describe this that is missing from the analysis. Since the clearance in these experiments is 0.002" the minimum flight heights are 0.001", 0.0005", and 0.0002" corresponding to eccentricity ratios of 0.5, 0.75, and 0.9 respectively. When the minimum gap height is as large as 0.001", there are few places where the pressure is less than ambient ( $<1$ ). It is expected, for example, that if this sequence of experiments were run for eccentricity ratios versus speed for a larger clearance or a smaller clearance, that significantly different results would occur. Also it should be noted that when the pressure gets close to zero the "no slip" condition of the solutions has to be challenged as there would be an onset of a slip regime.



#### 4.6.3. Hydrodynamic Bearings Under the CFD Microscope

In section 4.5.2 the following observations were made of the overall bearing performance based on the results of integrating the pressure distribution about the bearing gap. These observations were:

- 1) As RPM increases and eccentricity ratio increases the net total hydrodynamic force increases. And,
- 2) As RPM increases and eccentricity ratio increases the attitude angle increases from  $90^\circ$ .

Beyond that, the “CFD microscope” can be used to examine the characteristic shape of the pressure distribution and how it changes with increased RPM and eccentricity ratio. This yields considerable insight into the causes of the increasing attitude angle and the increased hydrodynamic force with increased RPM.

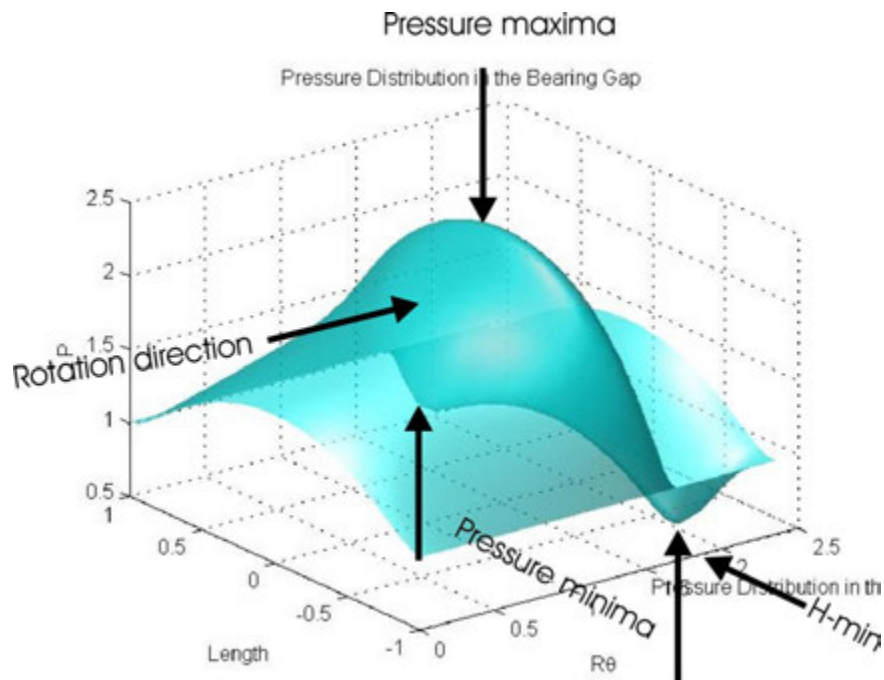


Figure 4-55 Pressure distribution in the bearing gap for a hydrodynamic bearing with  $c=0.002''$ ,  $h_{min}=.001''$  (eccentricity ratio=0.5) at 140K RPM.

A typical pressure distribution for the hydrodynamic bearing is shown in figure 4-57 which shows a bearing with an eccentricity ratio of 0.5 rotating at 140K RPM. The direction of rotation is positive, that is, moving from left to right in the  $R\theta$  axis. The location of the  $h_{min}$  is at  $R\theta=1.7671$  and  $h_{max}=0.5890$ . Along the the rotation direction, the bearing gap is converging from  $R\theta=0.5890$  to  $1.7671$  and diverging from  $R\theta=1.7671$  to  $0.5890$ . Going from left to right in  $R\theta$ , the pressure in the center of the bearing gap ( $Length=0$ ) increases until it meets its maximum value at some angular offset before  $h_{min}$  after which it quickly decreases going to  $P=1$  in the neighborhood of  $h_{min}$  and continuing to its minimum at an angular offset just beyond  $h_{min}$  where the pressure is less than the ambient pressure. Then the pressure increases again. Moving away from the center of the bearing, the

pressure curves to  $P=1$  at  $Length=\pm 1.0$ " (these are the boundary conditions for the 2" bearing).

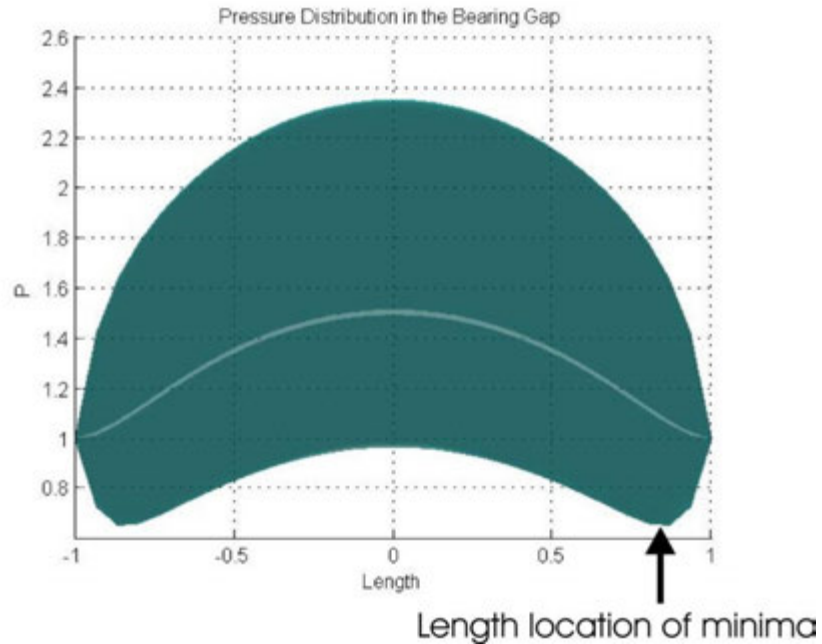


Figure 4-56 Pressure distribution rotated to look normal to the length axis demonstrating that the distribution is symmetric.

Because the bushing/shaft displacement is a pure translation in the  $Y$  axis, the bearing gap is symmetric in the length axis resulting in a symmetric pressure distribution. The pressure maximum is always located in the center of the bearing at  $Length=0$ . The pressure minima are located at two lobes displaced an equal length from the center.

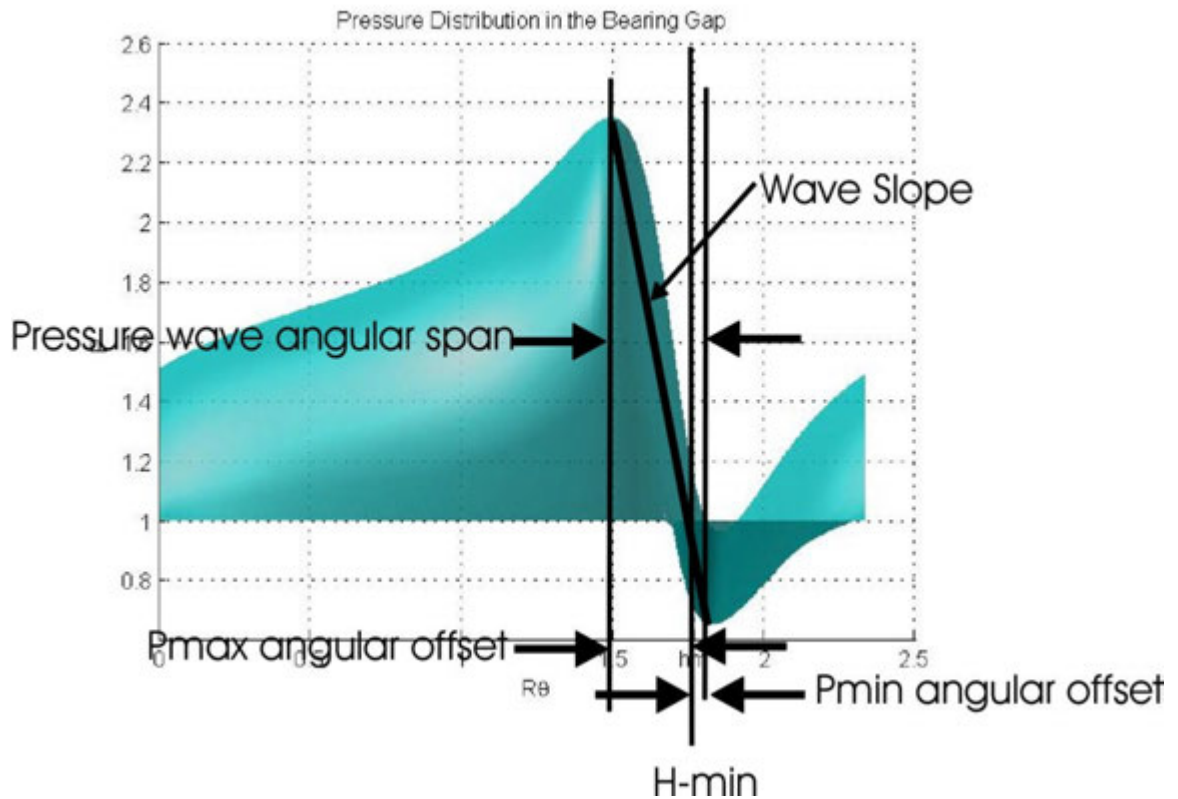


Figure 4-57 Pressure distribution rotated to view it normal to the  $R\theta$  direction.

Viewing the pressure distribution normal to  $R\theta$  direction the shape and size of what has been dubbed in this thesis as “the wave” where, within just a small angular displacement around  $h_{min}$ , the pressure drops from its maximum to its minimum .

To characterize each bearing solution, the pressure distribution was queried to determine:

- Angular offsets from  $h_{min}$  of  $P_{max}$  and  $P_{min}$
- Slope of the wave= $(P_{max}-P_{min})/(\theta_{max}-\theta_{min})$
- The span of the wave  $\theta_{max}-\theta_{min}$
- The angular offset from  $h_{min}$  of the center of the wave.
- The *length* offset from center of the pressure minima's.
- The span of the End Wave (described later)
- The slope of the End Wave

In reviewing the tabulated characteristic data, it must be remembered that all numerical experiments were run with a 30 x 96 grid size which equates to a lengthwise resolution of 0.067" and an angular resolution 0.06545 radians or 3.75° the latter translating to an  $R\theta$  resolution of 0.020". The graphs were plotted to make the limited resolution of the calculation apparent in the jaggedness of the curves.

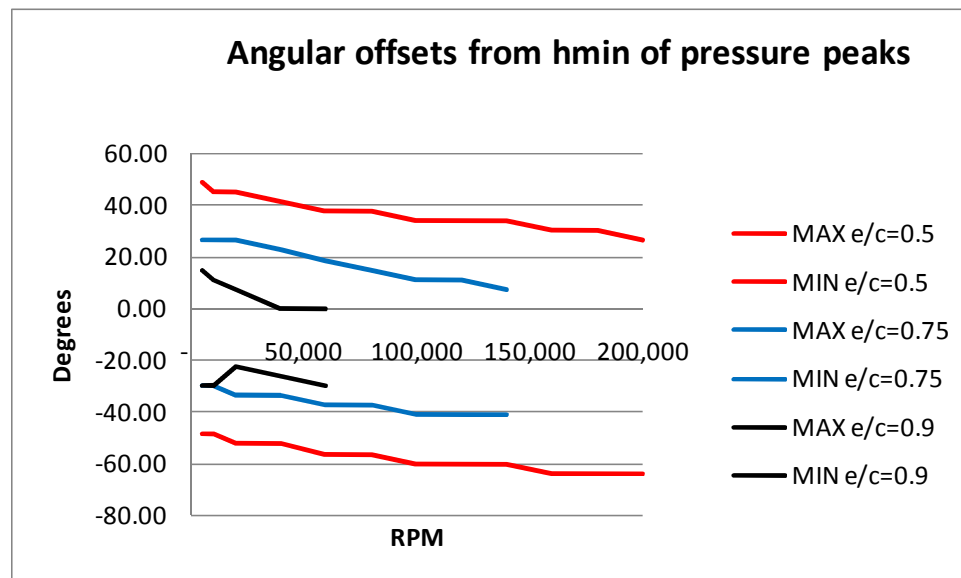


Figure 4-58 Angular offsets from  $h_{min}$ . The  $P_{max}$  offsets are negative since they come before  $h_{min}$  and the  $P_{min}$  are positive since they lag  $h_{min}$ .

The angular offsets for  $P_{max}$  and  $P_{min}$  are much larger for smaller eccentricity ratios. As the rotation is increased, they both shift to the left, that is,  $P_{max}$  shifts away from  $h_{min}$  while  $P_{min}$  shifts closer to  $h_{min}$ .

The  $P_{min}$  angular offset shift is very interesting given that it approaches zero for an eccentricity ratio of 0.5 at 60K RPM and an eccentricity ratio of 0.75 at 140K RPM, the maximum speeds for which a numerical solution was obtainable for those eccentricities. The angular offset for an eccentricity ratio of 0.5 was still  $26.25^\circ$  at 200K RPM. But it is not known that this was the absolute maximum speed for which a solution could be obtained for eccentricity ratio of 0.5. Solutions were found for increasing speed in increments of 20K RPM up to 200K RPM. Subsequently a 300K RPM attempt failed. A large effort to determine the speed limit to the solutions was not made, however, the numerical viscosity had to be decreased from 1 for all solutions over 120K RPM and a numerical viscosity of 0.6 was used for the 200K solution. Our experience indicates that 200K was very near the limit. Also the  $P_{min}$  angular offset decreased with increased speed in a nearly linear manner from 5K to 200K RPM, dropping off  $22.5^\circ$  over the range. Extrapolation indicates that a speed of 427K RPM would be required to shift the  $P_{min}$  angular offset to zero.

Nonetheless this is interesting because it does not seem physically reasonable to think that the  $P_{min}$  angular offset could occur on the convergent side of the bearing gap ( $P_{min}$  angular offset  $<0$ ). This suggests some hydrodynamic limit or discontinuity reminiscent of sonic velocity in a diverging/converging nozzle although the surface speeds involved are much below sonic. It does seem to indicate again a missing characteristic height parameter based on hydrodynamic variables.

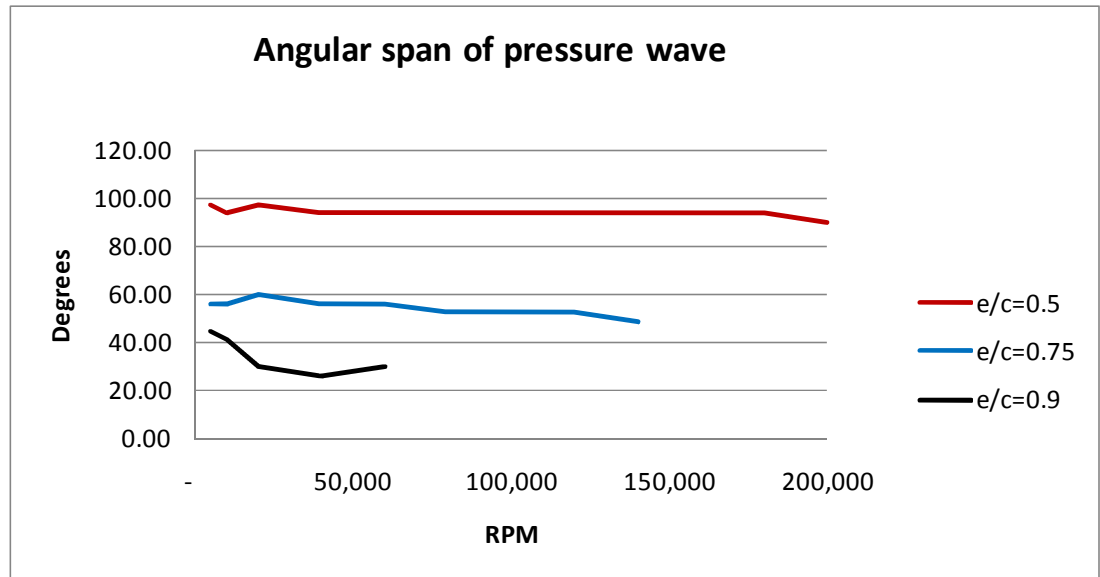


Figure 4-59 Angular span of the pressure wave (difference of the angular offsets).

Because both angular offsets shift to the left, the angular span of the wave remains relatively constant with a tendency to decrease slightly with increased RPM. The span of the wave decreases significantly with increased eccentricity ratio. The spans ranged from 97.5° to 90°, 56.26° to 48.75°, and 45.00° to 30.00° for eccentricity ratios of 0.5, 0.75, and 0.9 respectively.

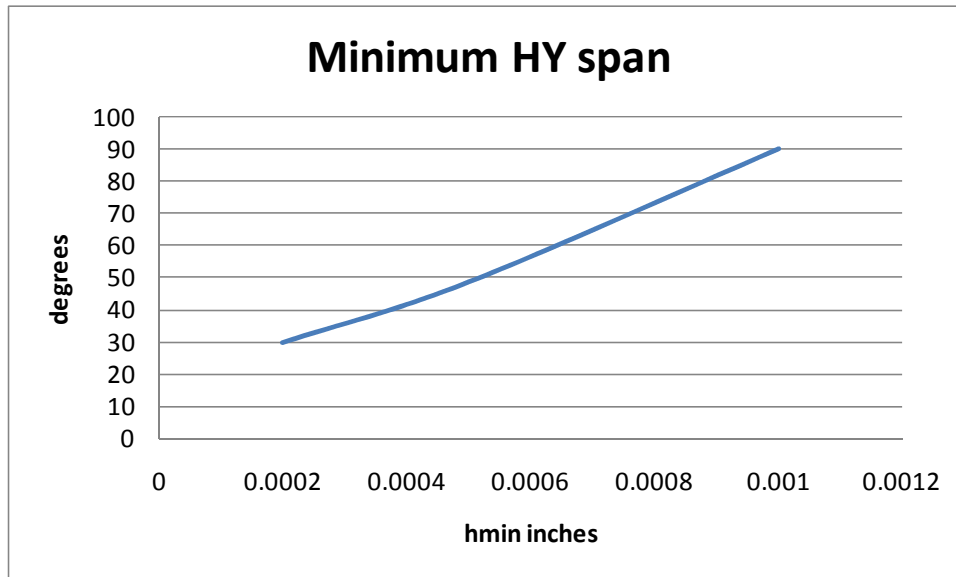


Figure 4-60 Minimum hydrodynamic (HY) bearing span as function of  $h_{min}$ .

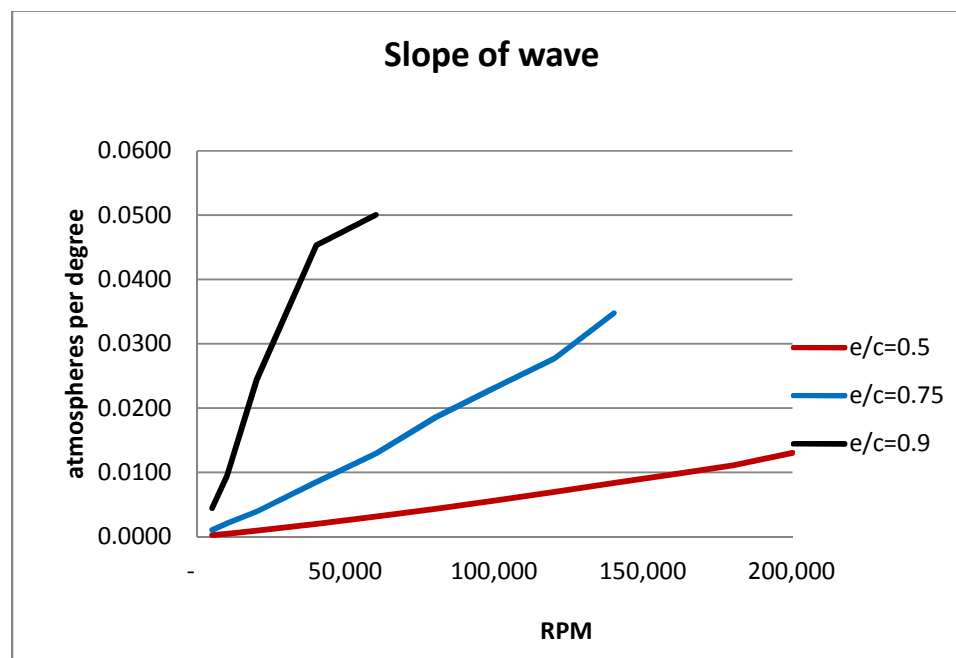


Figure 4-61 Slope of the wave span.

Since the difference between the pressure maximum and minima increases with increased RPM and increased eccentricity ratio, while the angular span of the



wave decreases with increased eccentricity ratio and speed, there is a dramatic increase in the slope of the wave with increased eccentricity ratio and increased speed.

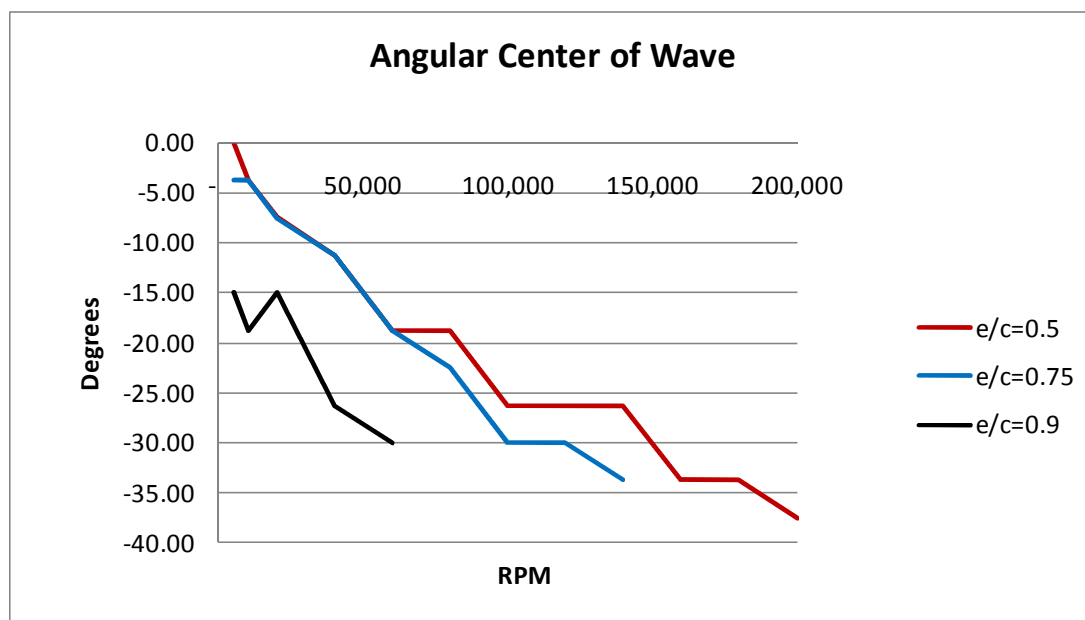


Figure 4-62 The angular center of the waves (sum of three angular offsets).

The net effect of the wave span shift to the left (opposite the rotation) means that the center of the wave shifts left, or more forward, of  $h_{min}$  with increased speed. This leftward shift also accounts for the increased attitude angle with increased speed and increased eccentricity. It should be noted that both shift of the wave with speed and the attitude angle with speed are very similar for eccentricity ratios of 0.5 and 0.75, but more dramatic at an eccentricity ratio of 0.9.

The single pressure maxima is always at the center of the bearing along its length. The pressure minima, however, are located at two lobes symmetrically displaced in length away from the center of the bearing. As speed is increased, the lobes are pushed outward toward the ends of the bearing. This shift with increased speed is slightly greater for higher eccentricity ratios. Once again the

eccentricity ratios of 0.5 and 0.75 are very similar. The outwards shift of the lobes is very dramatic. They start at the center of the bearing and move out to approximately .9" near the end of the bearing.

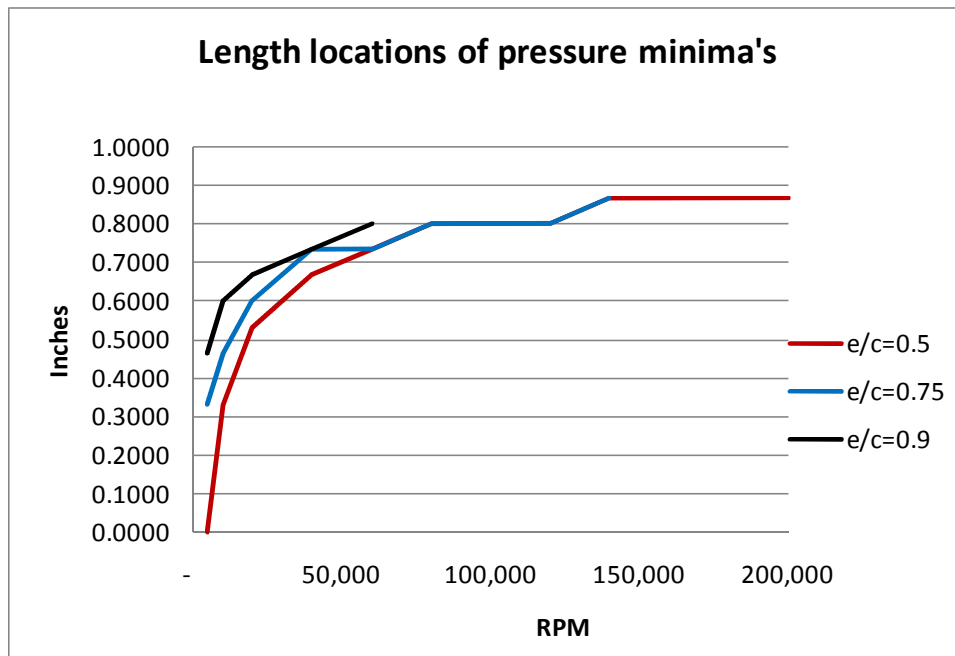


Figure 4-63 Length locations of the pressure minima's from bearing center.

The described behavior produces an extreme situation as the pressure minima become smaller and move closer to the bearing ends with increased rotation speed, as a result the pressure must slope upward very quickly to meet the ambient pressure boundary conditions at the bearing ends. The characteristic distribution data tabulated from the numerical analysis is sufficient to calculate an "End Wave" span and slope.

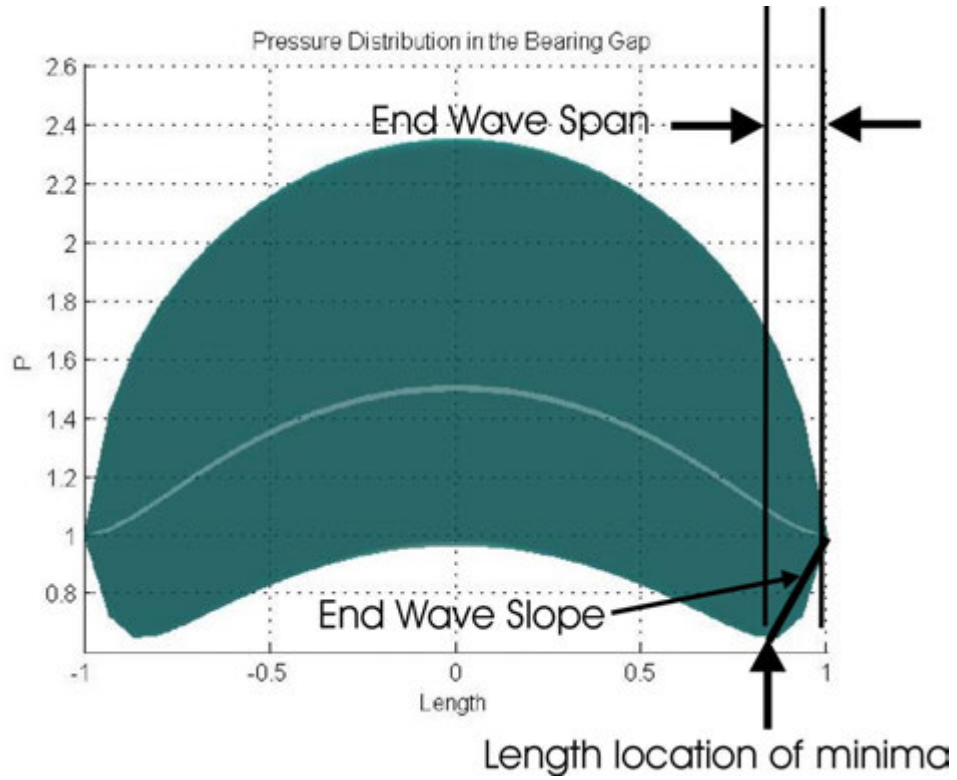


Figure 4-64 End Wave location, span and slope.

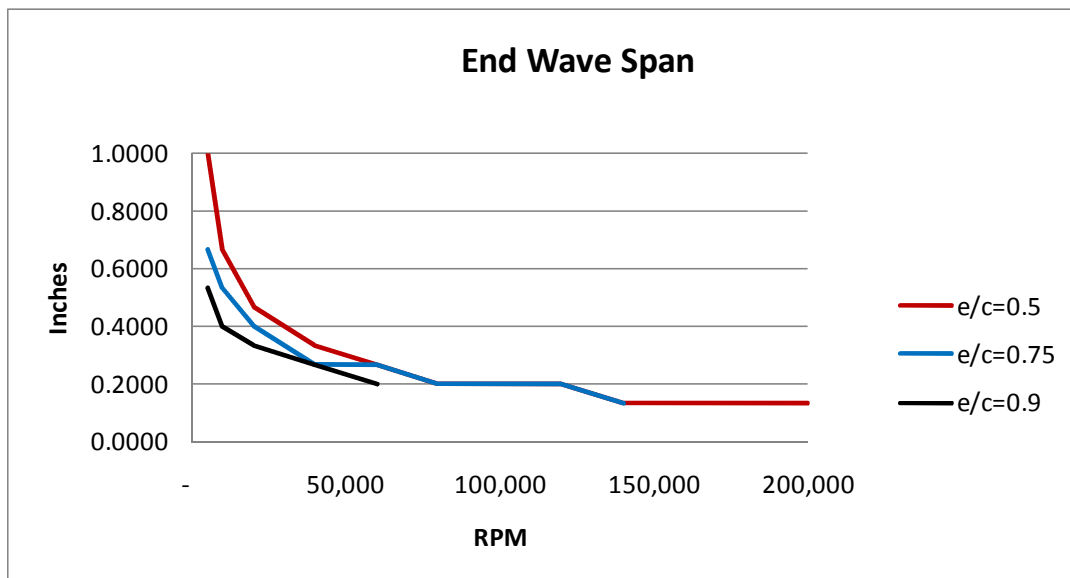


Figure 4-65 End Wave Span.

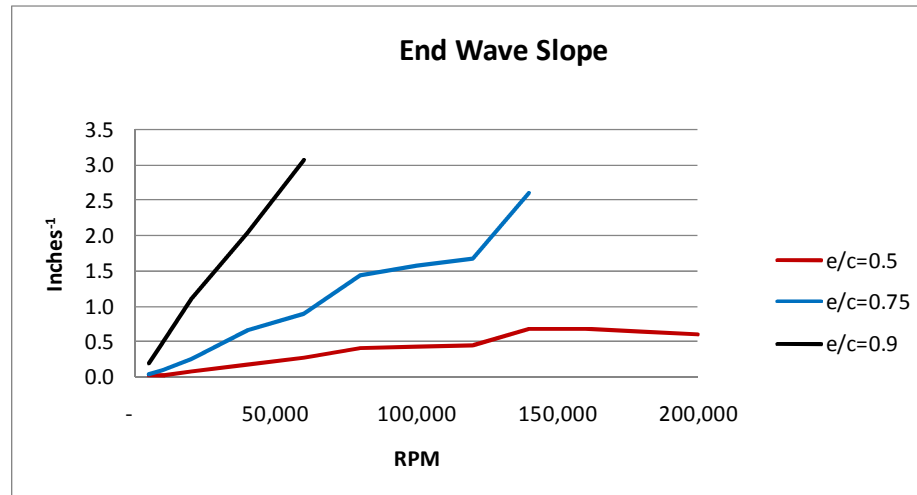


Figure 4-66 End Wave Slope.

The end wave span goes from 1.0" to .1333", 0.667" to 0.1333", and .5333" to 0.200" with increased speed for eccentricity ratios of 0.5, 0.75, and 0.9 respectively. The end-wave slopes rise very dramatically with increased speed. They go from .0104 to .6122 inches<sup>-1</sup>, .0415 to 2.5994 inches<sup>-1</sup>, and .1873 to 3.0765 inches<sup>-1</sup> for the eccentricity ratios of 0.5, 0.75, and 0.9. As listed the largest end wave slope tabulated was 3.0765 inches<sup>-1</sup> for eccentricity ratio of 0.9 operating at 60K RPM. These operating conditions generated a wave with an angular slope of .0501 degrees<sup>-1</sup>. For a 0.75" diameter bearing, each degree translates to 0.0654 inches on the circumference. Thus for comparison, the maximum end slope of 0.501 degrees<sup>-1</sup> translates to a slope of 7.65 inches<sup>-1</sup> compared with the maximum end wave slope of 3.0765 inches<sup>-1</sup>. It is also important to note that the shortest end wave span of 0.1333" translates to being just two finite elements away from the bearing ends. This might be the origin of the numerical analysis "speed limits" since increased speed could push the pressure minima too close to the bearing ends. Thus we are led to the conclusion that the numerical analysis would be greatly assisted by a much finer mesh size in the bearing gap area around  $h_{min}$ .

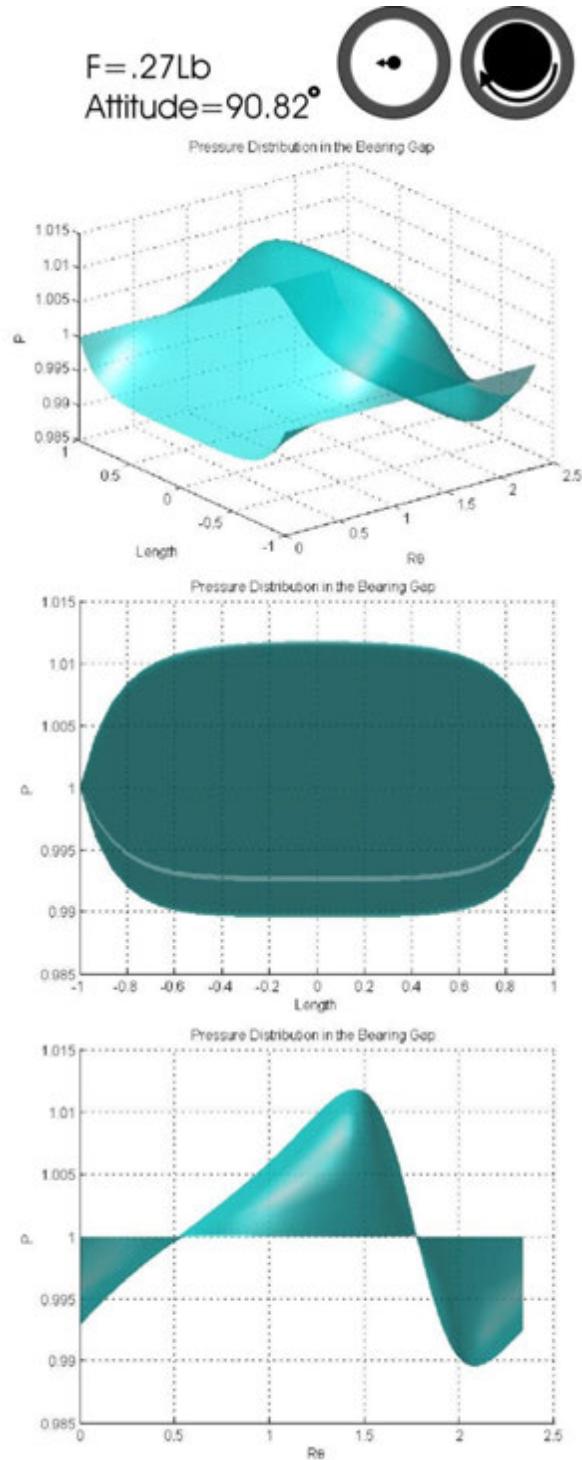


Figure 4-67 Pressure distribution pictures of hydrodynamic bearing with an eccentricity ratio of 0.5 operating at 5K RPM. The bearing force is .27lbs and the attitude angle is  $90.8^\circ$ . Top - angular view, Middle - *length* view, Bottom -  $R\theta$  view.

Figure 4-67 shows the pressure distribution of a bearing with an eccentricity ratio of 0.5 operating at 5K RPM. The hydrodynamic force acting on the bushing (opposite to the force acting on the shaft) is very small 0.27 lbs and its attitude angle is close to perpendicular the line of centers ( $90.8^\circ$ ). This pressure distribution has the greatest span and least slope or any of the bearing data points analyzed. It is the only pressure distribution where there is a single minimum lies at the center of the bearing along the length rather than two minima in two lobes symmetrically located a distance from the bearing center.

The low pressure lobes begin to form as early as 10K RPM for an eccentricity ratio of 0.5. They can be seen to form about 0.3333" from the center of the bearing along the length as with the low pressure area inverting slightly upwards at the bearing center. For higher eccentricity ratios operation at 5K RPM has well established lobes.

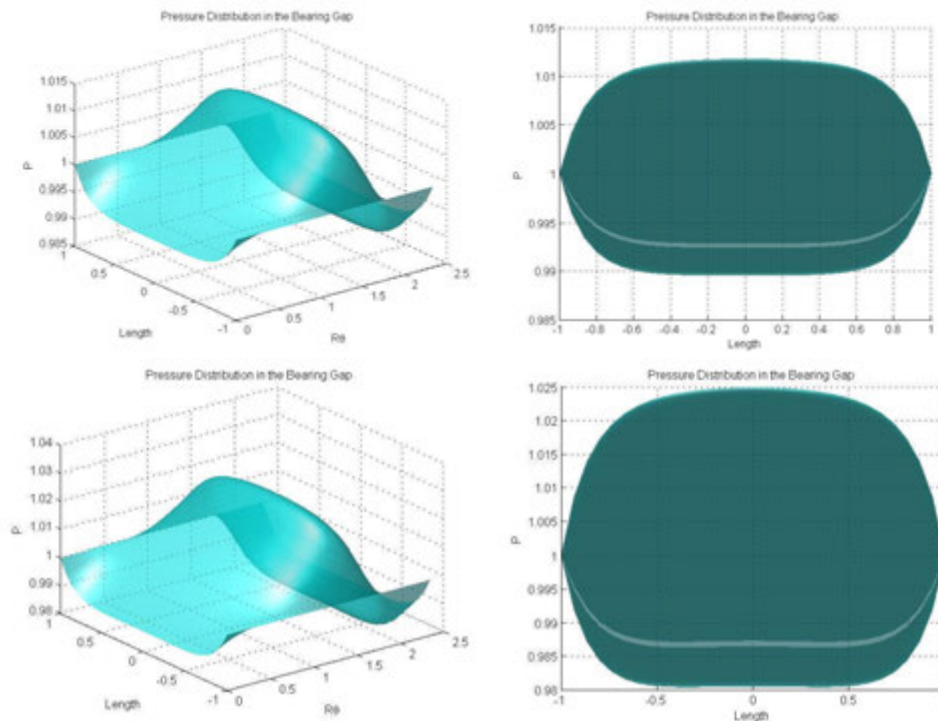


Figure 4-68 Comparison of pressured distributions showing formation of minimum pressure lobes between operation at 5K RPM (top) and 10K RPM (bottom) with eccentricity ratio of 0.5.

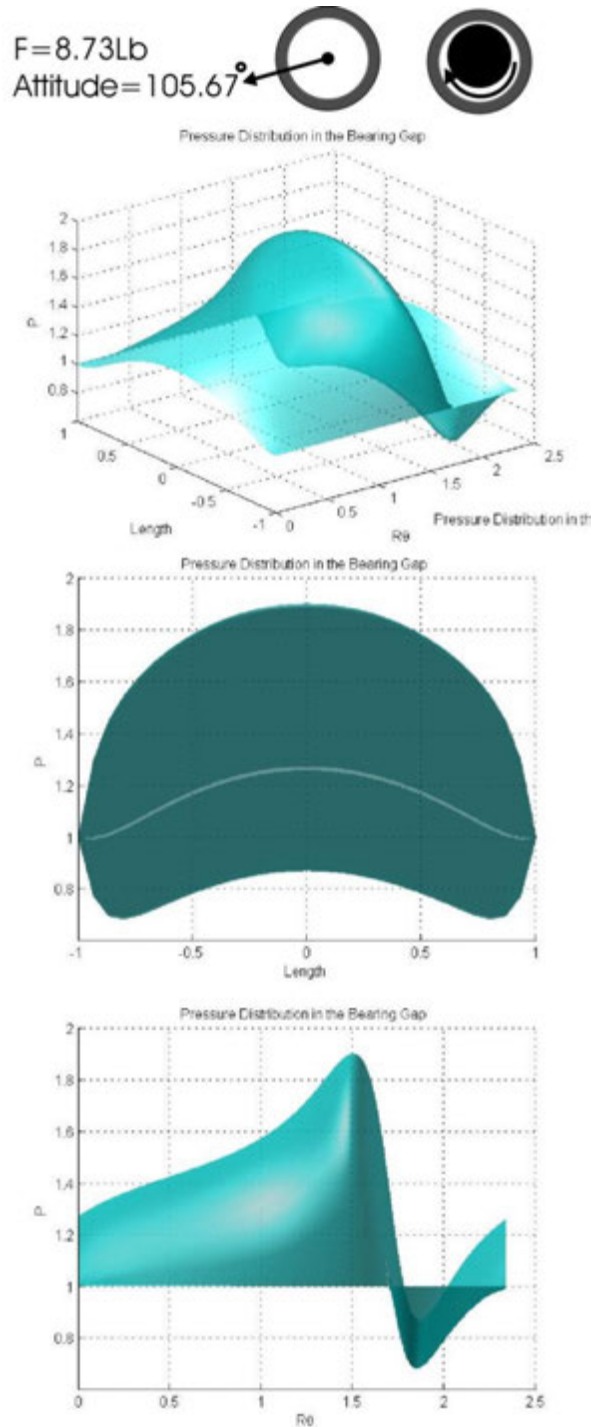


Figure 4-69 Pressure distribution pictures of a hydrodynamic bearing with an eccentricity ratio of 0.75 operating at 100K RPM, The bearing force is 8.73 lbs; attitude angle is  $105.67^\circ$ ,

Top - angular view, Middle - length view, Bottom -  $R\theta$  view.

When the eccentricity ratio or RPM is increased, pressure maximum increases and the pressure minima decrease, the spans of the angular pressure wave shifts left (into the flow), the hydrodynamic force increases, and the attitude angle increases. Comparing the eccentricity ratio of 0.5 operating at 5K RPM to the 0.75 eccentricity ratio operating at 100K RPM, we see the maximum pressure going from 1.01 to 1.90 while the minimum pressure goes from 0.99 to 0.68. The hydrodynamic force goes from 0.27 lbs with an attitude angle of  $90.82^\circ$  to 8.73 lbs at  $105.67^\circ$ . The span of the angular pressure wave goes from  $97.5^\circ$  to  $52.5^\circ$  and the minimum pressure has switched from occurring at the center of the bearing in length to two symmetric lobes each located 0.800" from the center.



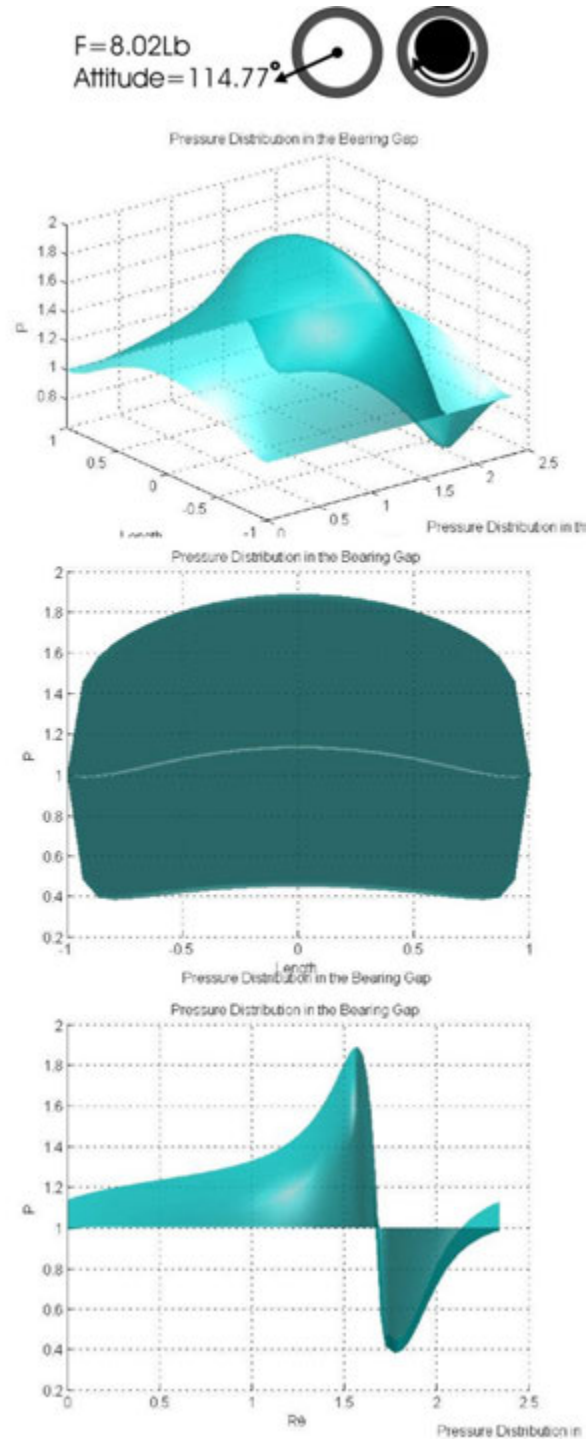


Figure 4-70 Pressure distribution pictures of hydrodynamic bearing with an eccentricity ratio of 0.90 operating at 60K RPM. The bearing force is 8.02 lbs; attitude angle is  $114.77^\circ$ ,

Top - angular view, Middle - length view, Bottom- $R\theta$  view.

Figure 4-70 shows the pressure distribution profiles for a bearing with the eccentricity ratio increased to 0.90 but the speed decreased to 60K RPM. As a result, it has a similar hydrodynamic force compared with the 0.75 eccentricity ratio bearing operating at 100K RPM (8.02 lbs versus 8.73 lbs). They also have similar maximum and minimum pressures (1.89 versus 1.90 and 0.63 versus 0.68). However the angular pressure wave has a very steep slope at higher eccentricity ratio and its span is shortened from  $52.50^\circ$  to  $30.00^\circ$ . As a result the attitude angle is increased from  $105.67^\circ$  to  $114.77^\circ$ . The low minimum pressure lobes are located again at 0.800" from the center in length, however it worth noting that the lobes are not nearly as distinct as they are for the 0.75 eccentricity ratio bearing operating at 100K. The negative pressure inflection at the center of the bearing is very slight for the higher eccentricity, lower speed bearing.

Examination of the pressure wave in the center of the bearing gap along the length shows the effects of increasing speed and eccentricity ratio on the hydrodynamic pressure. Looking at the plot for  $\epsilon=0.5$ , it can be observed that for small eccentricity ratios, higher speeds are required to generate the same peak pressure. The waves can be described as long and languid as there is a considerable separation in  $R\theta$  between the pressure maximum and minimum spanning the  $h_{min}$  location. Also little or no sub-atmospheric pressure is generated by the wave and the minimum pressures are higher for waves with higher RPM. As the eccentricity ratio is increased to 0.75, the waves become short with steeper slopes and less speed is required to generate higher pressure maxima. Sub-atmospheric pressures are generated at all speeds. The higher speeds still have higher minimum pressures but the differences in those pressure minima is very small so that the minimum troughs are bunching together close to the location of  $h_{min}$ . When the eccentricity ratio is increased to 0.90 the waves are very short. A much smaller speed generates greater maximum pressures. The minimum pressures become inverted from  $\epsilon=0.5$  in that the higher speeds

generate the lower minimum pressures. The pressure minima crowd very near the  $h_{min}$  location. The highest speed solution is only 60K RPM. Its pressure minimum is right at  $h_{min}$  and shows some discontinuity. Similar phenomena were observed in centerline waves for FH hybrid bearings and PL hybrid bearings leading to the hypothesis that it is not possible to shift the pressure minimum forward of the position of  $h_{min}$ .

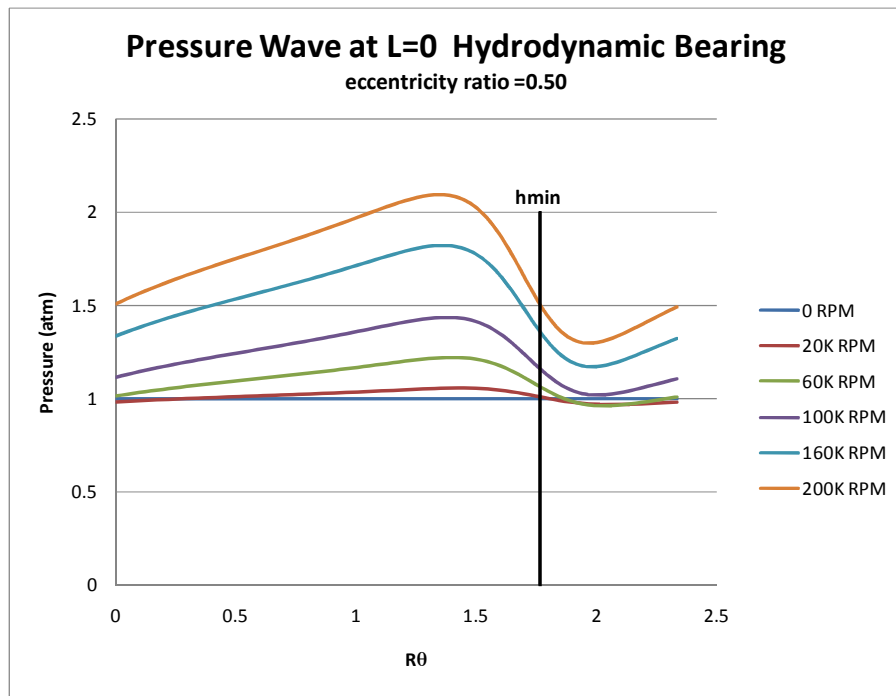


Figure 4-71 Middle bearing along the length axis pressure wave profile for eccentricity ratio of 0.5.

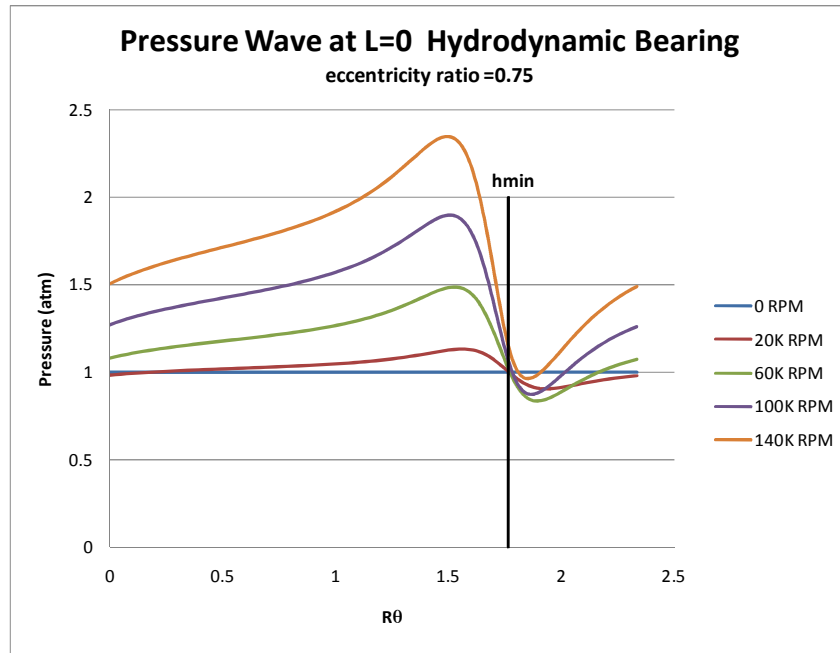


Figure 4-72 Middle bearing along the length axis pressure wave profile for eccentricity ratio of 0.75.

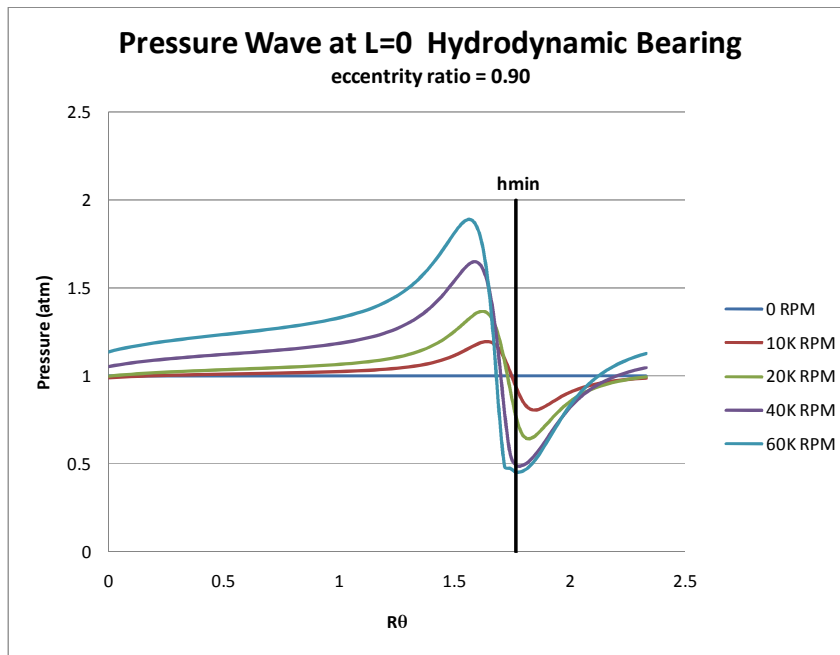


Figure 4-73 Middle bearing along the length axis pressure wave profile for eccentricity ratio of 0.9.

Tabulated Characteristic Data for : $\epsilon=0.5$														
RPM	Fy	Fx	Pmax	Pmin	Ftotal	Attitude	Max peak	Min Peak	Span	Wave Ctr	Slope	Min Z	End Span	End Slope
-	lbs	lbs	atm	atm	lbs	degrees	degrees	degrees	degrees	degrees	degrees <sup>-1</sup>	inches	inches	inches <sup>-1</sup>
5,000	0.00	-0.27	1.01	0.99	0.27	90.82	-48.75	48.75	97.50	0.00	0.0002	0.0000	1.0000	0.0104
10,000	0.02	-0.53	1.02	0.98	0.53	91.63	-48.75	45.00	93.75	-3.75	0.0005	0.3333	0.6667	0.0292
20,000	0.06	-1.06	1.06	0.97	1.06	93.24	-52.50	45.00	97.50	-7.50	0.0009	0.5333	0.4667	0.0748
40,000	0.23	-2.10	1.13	0.94	2.11	96.31	-52.50	41.25	93.75	-11.25	0.0020	0.6667	0.3333	0.1713
60,000	0.49	-3.10	1.22	0.93	3.13	99.08	-56.25	37.50	93.75	-18.75	0.0031	0.7333	0.2667	0.2681
80,000	0.82	-4.05	1.33	0.92	4.13	101.49	-56.25	37.50	93.75	-18.75	0.0043	0.8000	0.2000	0.4015
100,000	1.20	-4.96	1.44	0.91	5.10	103.55	-60.00	33.75	93.75	-26.25	0.0056	0.8000	0.2000	0.4320
120,000	1.53	-5.88	1.56	0.91	6.07	104.63	-60.00	33.75	93.75	-26.25	0.0069	0.8000	0.2000	0.4430
140,000	1.94	-6.74	1.69	0.91	7.02	106.03	-60.00	33.75	93.75	-26.25	0.0084	0.8667	0.1333	0.6737
160,000	2.42	-7.54	1.82	0.91	7.92	107.80	-63.75	30.00	93.75	-33.75	0.0097	0.8667	0.1333	0.6714
180,000	2.90	-8.32	1.95	0.91	8.81	109.19	-63.75	30.00	93.75	-33.75	0.0111	0.8667	0.1333	0.6489
200,000	3.35	-9.11	2.09	0.92	9.71	110.19	-63.75	26.25	90.00	-37.50	0.0130	0.8667	0.1333	0.6122

Tabulated Characteristic Data for $\epsilon=0.75$														
RPM	Fy	Fx	Pmax	Pmin	Ftotal	Attitude	Max peak	Min Peak	Span	Wave Ctr	Slope	Min Z	End Span	End Slope
-	lbs	lbs	atm	atm	lbs	degrees	degrees	degrees	degrees	degrees	degrees <sup>-1</sup>	inches	inches	inches <sup>-1</sup>
5,000	0.01	-0.48	1.03	0.97	0.48	91.08	-30.00	26.25	56.25	-3.75	0.0010	0.3333	0.6667	0.0415
10,000	0.04	-0.95	1.06	0.95	0.95	92.18	-30.00	26.25	56.25	-3.75	0.0021	0.4667	0.5333	0.1003
20,000	0.14	-1.89	1.13	0.90	1.89	94.31	-33.75	26.25	60.00	-7.50	0.0039	0.6000	0.4000	0.2505
40,000	0.53	-3.87	1.30	0.82	3.90	97.77	-33.75	22.50	56.25	-11.25	0.0085	0.7333	0.2667	0.6700
60,000	1.07	-5.36	1.49	0.76	5.47	101.26	-37.50	18.75	56.25	-18.75	0.0129	0.7333	0.2667	0.8999
80,000	1.69	-6.93	1.69	0.71	7.13	103.70	-37.50	15.00	52.50	-22.50	0.0186	0.8000	0.2000	1.4330
100,000	2.36	-8.41	1.90	0.68	8.73	105.67	-41.25	11.25	52.50	-30.00	0.0232	0.8000	0.2000	1.5845
120,000	3.04	-9.84	2.12	0.67	10.30	107.15	-41.25	11.25	52.50	-30.00	0.0277	0.8000	0.2000	1.6695
140,000	3.71	-11.24	2.35	0.65	11.84	108.28	-41.25	7.50	48.75	-33.75	0.0348	0.8667	0.1333	2.5994

Tabulated Characteristic Data for : $\epsilon=0.9$														
RPM	Fy	Fx	Pmax	Pmin	Ftotal	Attitude	Max peak	Min Peak	Span	Wave Ctr	Slope	Min Z	End Span	End Slope
-	lbs	lbs	atm	atm	lbs	degrees	degrees	degrees	degrees	degrees	degrees <sup>-1</sup>	inches	inches	inches <sup>-1</sup>
5,000	0.05	-0.82	1.10	0.90	0.82	93.33	-30.00	15.00	45.00	-15.00	0.0044	0.4667	0.5333	0.1873
10,000	0.19	-1.61	1.19	0.80	1.62	96.58	-30.00	11.25	41.25	-18.75	0.0095	0.6000	0.4000	0.4940
20,000	0.67	-3.07	1.37	0.63	3.14	102.26	-22.50	7.50	30.00	-15.00	0.0245	0.6667	0.3333	1.1077
40,000	1.98	-5.41	1.64	0.45	5.76	110.06	-26.25	0.00	26.25	-26.25	0.0453	0.7333	0.2667	2.0454
60,000	3.36	-7.29	1.89	0.38	8.02	114.77	-30.00	0.00	30.00	-30.00	0.0501	0.8000	0.2000	3.0765

Figure 4-74 Tabulated characteristic data for hydrodynamic bearing CFD experiments, Top -  $\epsilon=0.5$ , Center -  $\epsilon=0.75$ , Bottom -  $\epsilon=0.9$

#### 4.7. Feedhole Hybrid Bearings Results

In order to sample the hyperspace of feedhole hybrid bearing parameters, we performed a sweep of experiments with an operating pressure (reservoir pressure driving mass addition) of 60 psig and a large mass addition factor  $K_{meas}=2e-4 \text{ lbs}\cdot\text{s}^{-1}$ . In order to make a comparison with the hydrodynamic results, the bearing clearance of 0.002" was used. The smaller the  $h_{min}$  (the larger the eccentricity ratio), the more hydrodynamic action occurs. An eccentricity ratio of 0.9 was used since this was the largest eccentricity ratio used in the hydrodynamic bearing tests. In the hydrodynamic tests an eccentricity ratio of 0.9 had the lowest numerical solution speed limit of 60K RPM. Solutions were obtainable from 0 to 140K RPM for the FH hybrid bearing. Mass addition clearly increased the numerical speed limit.

The hydrostatic 0 RPM solution has a bearing force of 6.42 lbs acting with an attitude angle of 0. So  $F_y=-6.42 \text{ lbs}$  and  $F_x=0$ . As the rotation is increased, the hydrodynamic effect of the rotation is to generate an ever increasing component of force perpendicular to the displacement ( $F_x<0$ ) and an  $F_y$  contribution opposing the hydrostatic force. As a result the magnitude of  $F_y$  decreases until it changes sign to be in the opposite direction of the hydrostatic force. The net result is that the magnitude of the net hydrodynamic bearing force increases from 6.42 lbs to 17.52 lbs and the attitude angle runs from  $0^\circ$  to  $94.8^\circ$  as the speed is varied from 0 to 140K RPM.

The pressure distributions for two rotation speeds are shown in figure 4-75.

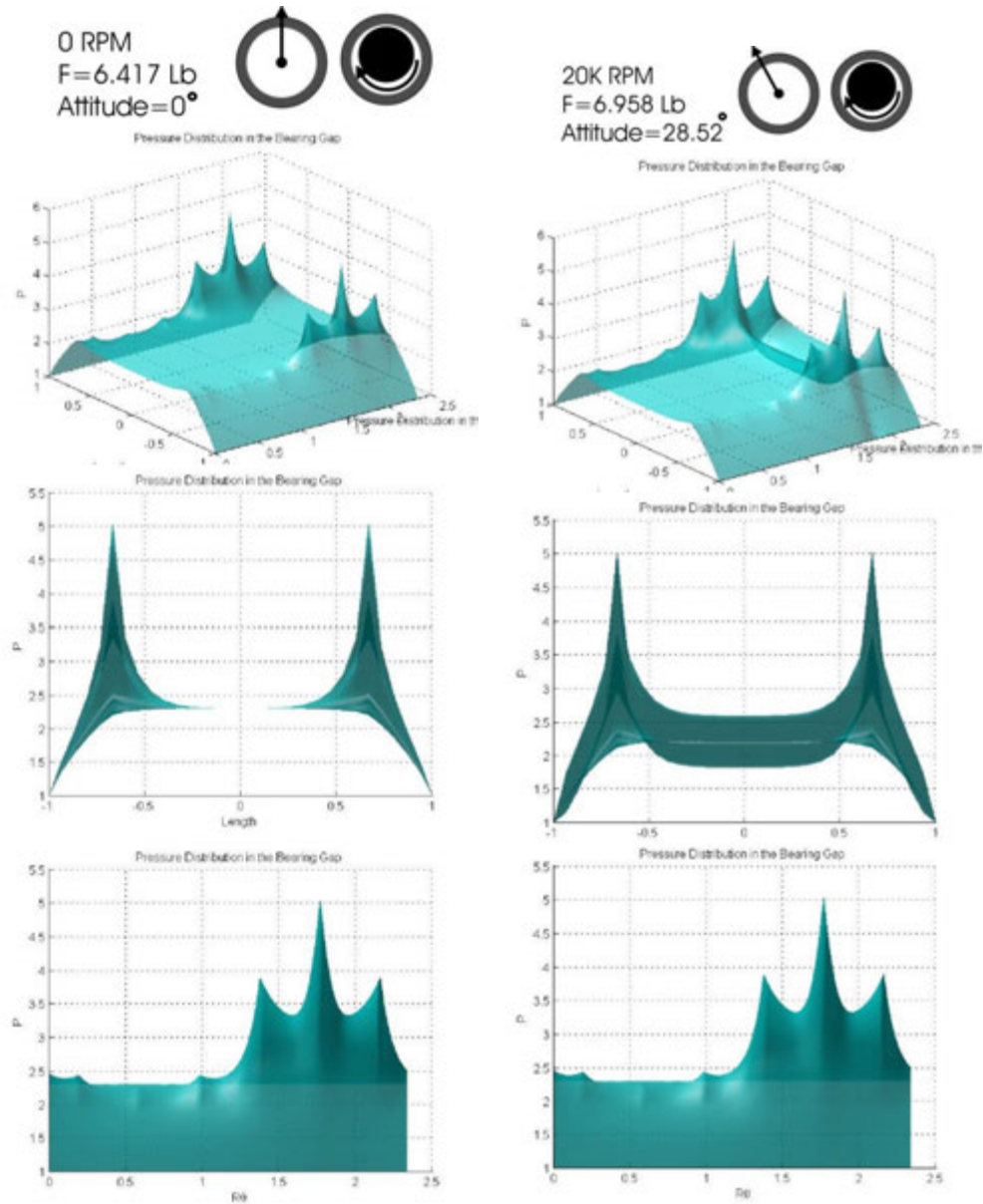


Figure 4-75 Views of the pressure distribution for a hybrid, feedhole fed bearing with  $k_{meas}=2e-4$  lbs/s, reservoir pressure of 60 psig, clearance=0.002" and eccentricity ratio of 0.9. Left - 0 RPM. Right - 20K RPM.

The static bearing with eccentricity ratio of 0.9 and clearance of 0.002" has  $h_{min}=0.0002$ " and generates significant hydrodynamic force. Its attitude angle, as with all hydrostatic bearings, is 0°. As discussed in previous sections, the hydrostatic bearing has high pressure peaks corresponding to the 12 feedholes with the highest pressure resulting from the feedhole that aligns with  $h_{min}$ . The pressure drops from these peaks to a constant pressure in the center of the bearing along its length. Away from the holes, the pressure drops to  $P=1$  at the bearing ends, the standard boundary conditions. The maximum pressure is 5.06 corresponding to 59.7 psig which is very near the operating pressure of 60 psig. The minimum pressure of 1 is at the ends of the bearings. The center or previously dubbed "land" area of the bearing gap (between the feedholes along the length) has by graphical inspection a constant pressure of about 2.3 or about 34 psig.

As the speed of the feedhole bearing is increased to 20K RPM, the hydrodynamic wave begins to impose itself on the hydrostatic pattern. The peak pressure and minimum pressures remain 5.06 and 1 respectively but the blurring of the land area in the length view is indicative of the hydrodynamic pressure wave developing. The pressure of the wave in the land area varies from about 1.8 to 2.6 (by graphical inspection) compared with the constant 2.3 for the 0 RPM hydrostatic solution noted above.



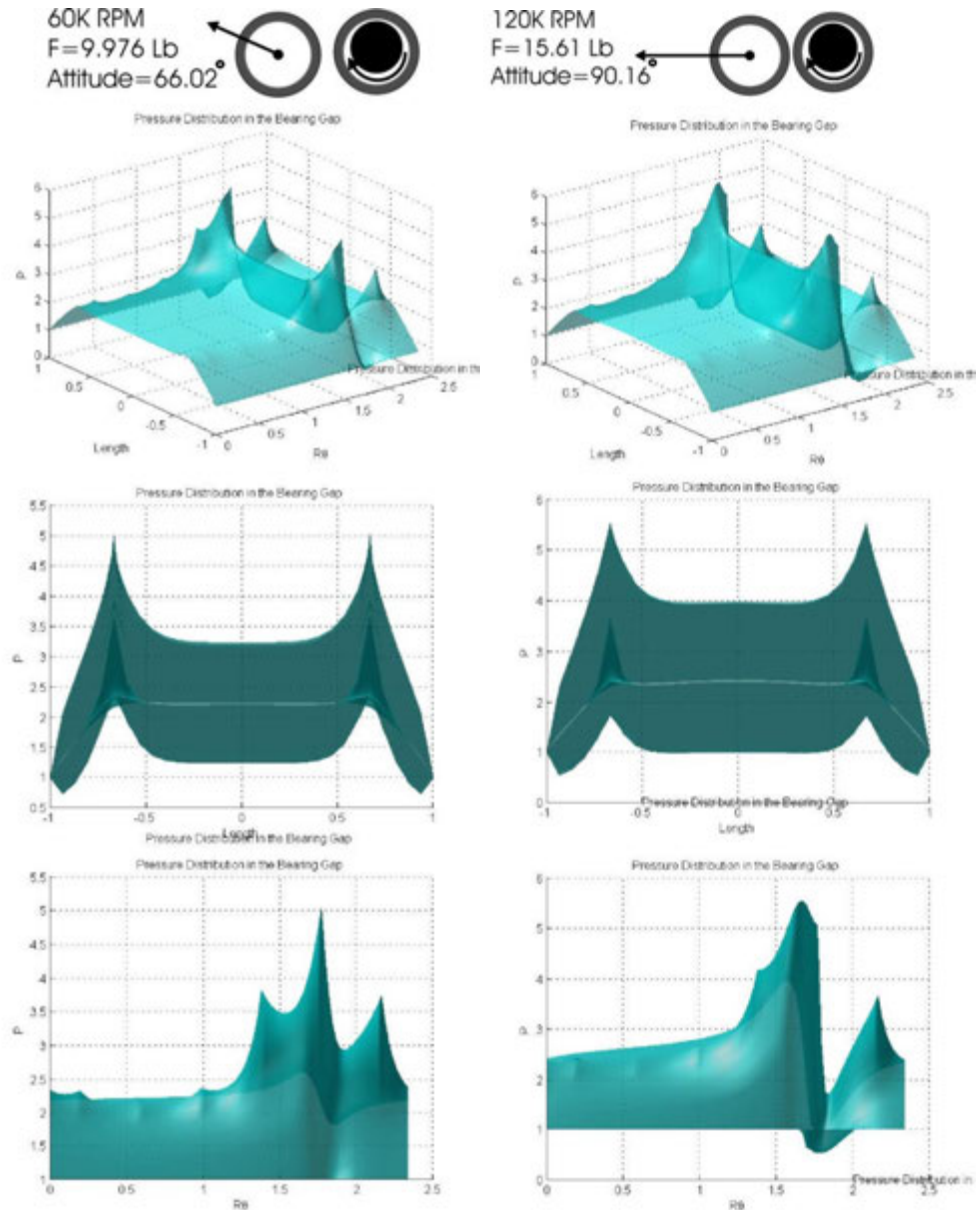


Figure 4-76 Pressure distributions in the FH bearing.  
Left - 60 RPM Right 120K RPM.

As the speed is increased further, the minimum pressure between feedholes 1 and 2 (1 is directly aligned with  $h_{min}$  and 2 is the nearest downstream hole) falls below atmospheric pressure 0.067" in from either end of the bearing. The feedholes are 0.375" away from the bearing ends and the lengthwise grid

spacing is .0667". Thus this minima is located at the first node in from the ends. The separation between the minimum and maximum pressures in the land area continues to increase as the speed increases. The minimum pressure in bearing gap is located just in from the ends between feedholes 1 and 2. The maximum pressure is located at feedhole 1 and remains at 5.06 from 0 to 80K RPM. After 80K RPM, the maximum pressure increases reaching 5.30 at 100K RPM and 5.76 at 140K RPM. The reservoir pressure is 5.082 so that the maximum pressure exceeds the reservoir pressure. However, flow reversal does not occur at P1 as the maximum pressure is no longer located at P1 but is located just forward of P1 at the angular position of  $h_{min}$ . This observation is consistent with the hydrodynamic results where the pressure maxima always occurred forward of  $h_{min}$  in the convergent area of the bearing gap and quickly decreased to atmospheric at about  $h_{min}$  and decreased to less than atmospheric just beyond  $h_{min}$  in the divergent area of the bearing gap. For the hybrid feedhole bearing, the pressure maximum occurs just forward of  $h_{min}$  and then the pressure falls to about 5.05 at P1 and plunges very rapidly toward it's minimum just beyond  $h_{min}$  and P1, and before P2. Thus at P1 there is still a small amount of mass input.

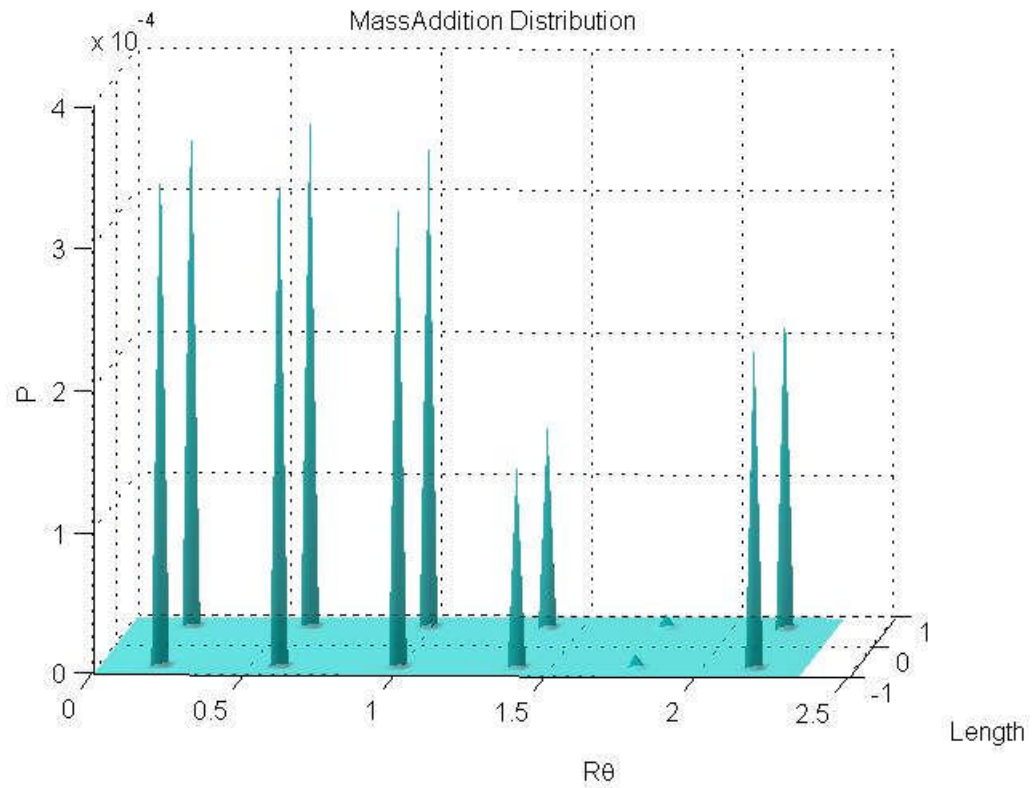


Figure 4-77 Mass addition in the bearing gap corresponding to the feedholes at 120K RPM. At P1 there is still small positive mass addition.

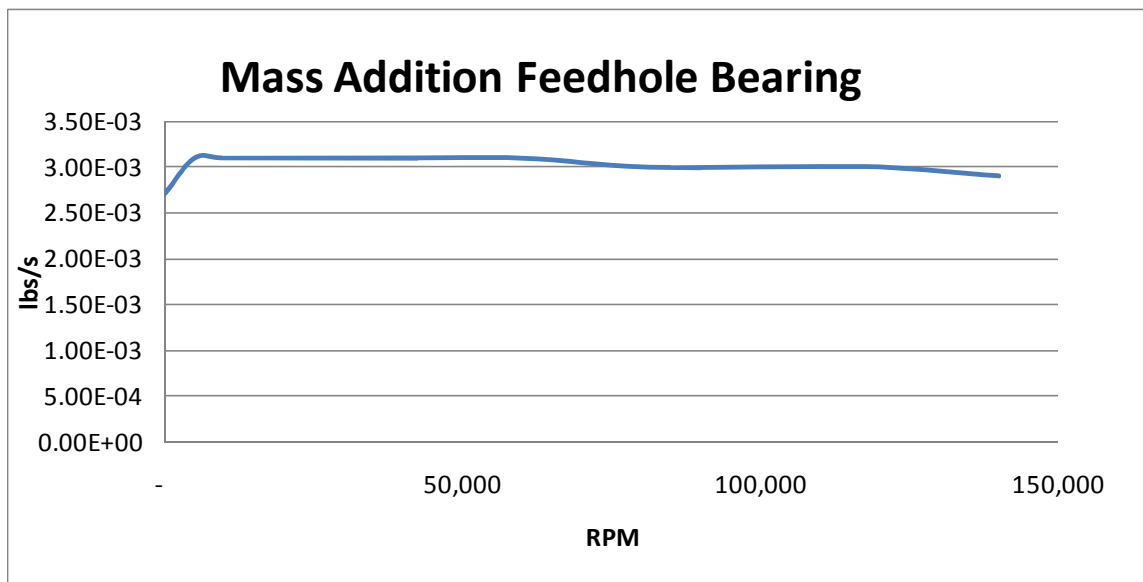


Figure 4-78 Mass Addition of feedhole fed bearing operated at 60 psig.

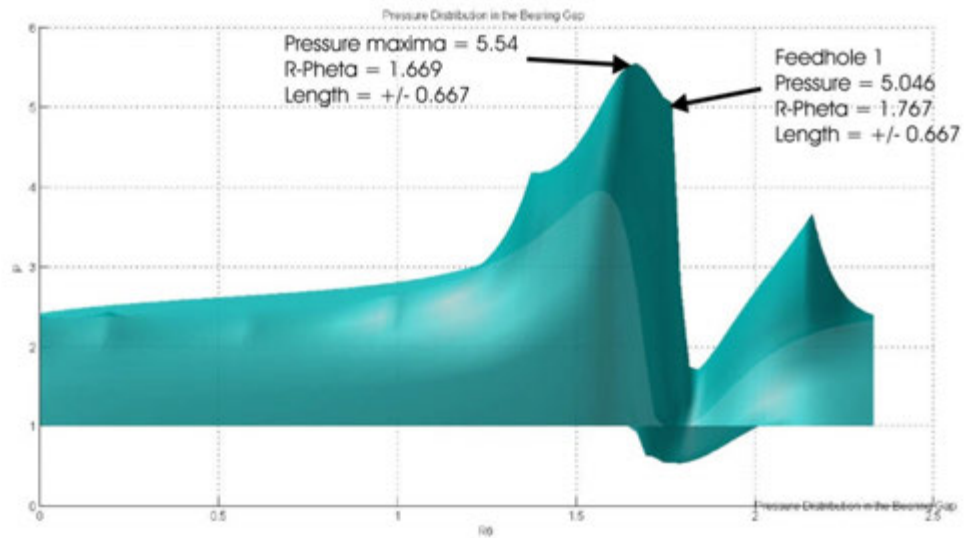


Figure 4-79 R $\theta$  view of feedhole hybrid bearing at 120K RPM showing locations of the pressure maxima and feedhole P1.

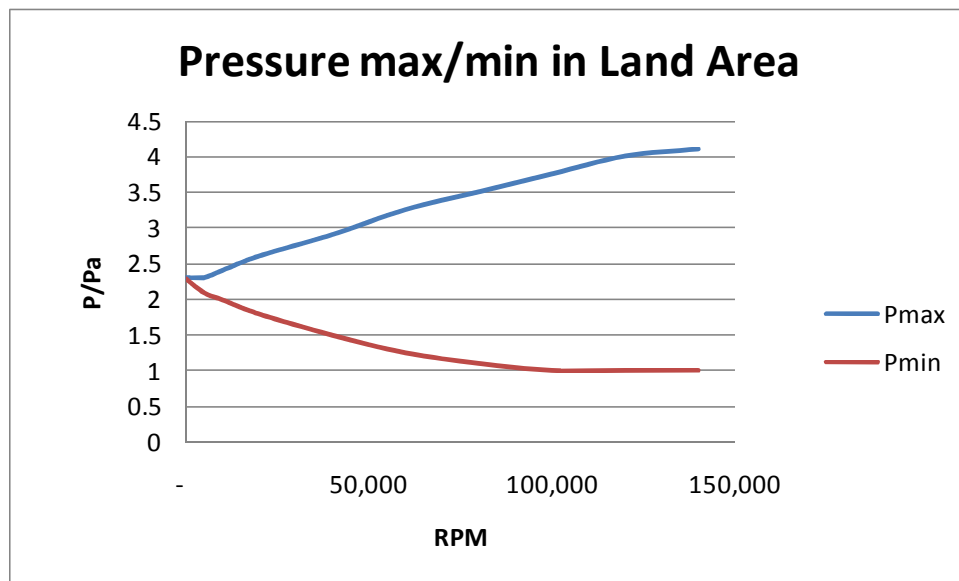


Figure 4-80 Pressure maxima and minima in the land area between the feedholes.

At 140K RPM the pressure solution manifests some numerical instability with an oscillating false pressure maxima/minima at  $R\theta=1.792$  and  $L=\pm 0.667$ , the next node downstream from P1. This behavior indicates that the numerical speed limit might increase with a higher resolution mesh around P1 extending to the edge of the bearing where the bearing gap pressure minimum is also located one node in from the end of the bearing.

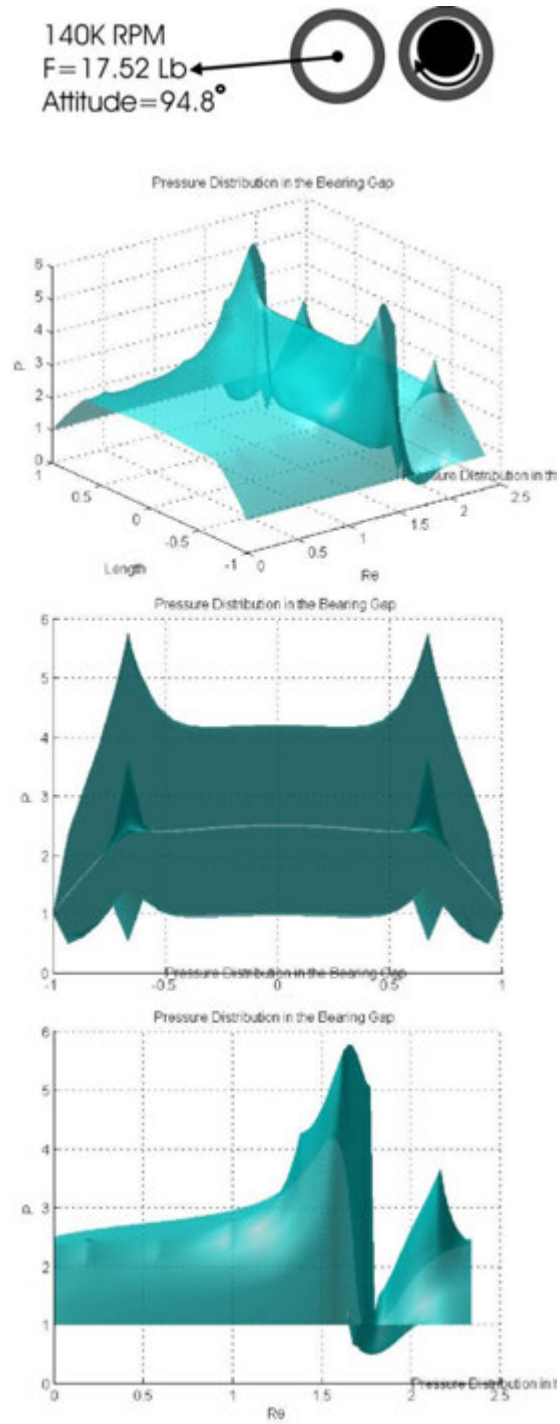


Figure 4-81 Pressure views for 140K RPM. A false oscillating minimum is appearing at  $R\theta=1.792$ .

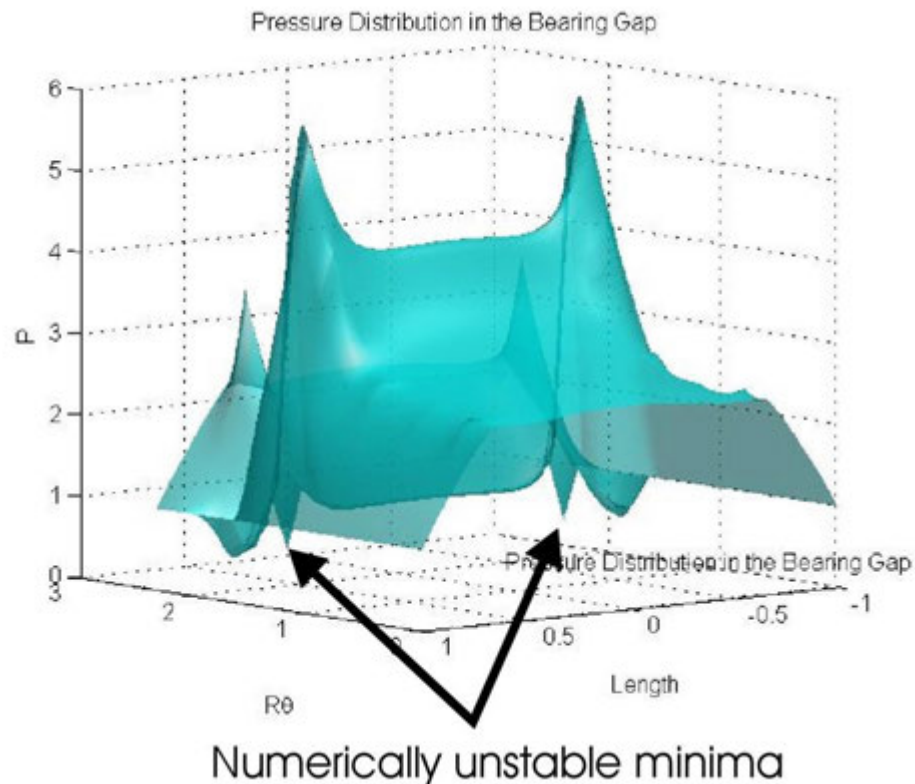


Figure 4-82 A rotated view of the 140K RPM pressure distribution showing the unstable pressure minima development one node from P1.

The plot of the centerline for 0 RPM shows a constant pressure of about 2.298 which could be considered the gage pressure in the land area of the bearing gap and is elevated due to the mass addition. As the speed is increased, the maximum pressure increases to 4.10, about 2 atm higher than the gage pressure. The minimum pressure decreases with increased speed. At 100K RPM the minimum pressure drops to atmospheric pressure. At 100K RPM the leftward shift of the wave drives the pressure minimum into the location of  $h_{min}$  and the minimum pressure becomes atmospheric. When the speed is increased to 120K the pressure minimum remains at  $h_{min}$  and stays atmospheric. As speed is increased to 140K RPM pressure baubles about the pressure minimum indicating numerical instability.

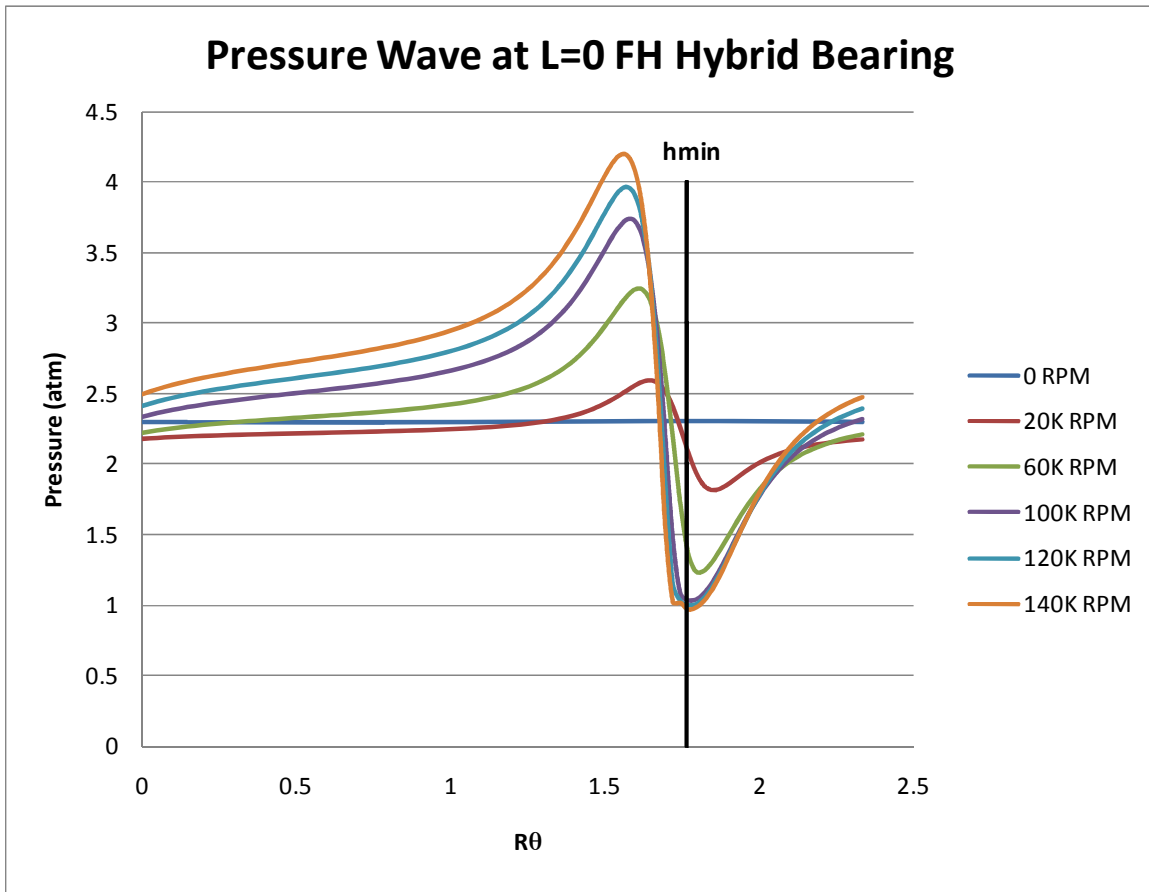


Figure 4-83 Pressure wave of an FH hybrid bearing operating 60 psig.

Feedhole Liner		Operating pressure = 60 psig				Kmeas = 2e-4 and e=0.9			
Speed RPM	Fy lbs	Fx lbs	Fbush lbs	Attitude degrees	Pmax atm	Pmin atm	P land min atm	P-land max atm	Mass Add lbs/s
-	-6.42	0.00	6.42	0.00	5.07	1.00	2.30	2.30	2.70E-03
5,000	-6.43	-0.84	6.48	7.43	5.06	1.00	2.10	2.30	3.10E-03
10,000	-6.36	-1.68	6.58	14.76	5.06	1.00	2.00	2.40	3.10E-03
20,000	-6.11	-3.32	6.96	28.52	5.06	1.00	1.80	2.60	3.10E-03
40,000	-5.24	-6.40	8.27	50.71	5.06	0.88	1.50	2.90	3.10E-03
60,000	-4.05	-9.12	9.98	66.02	5.06	0.73	1.25	3.25	3.10E-03
80,000	-2.74	-11.51	11.83	76.60	5.06	0.64	1.10	3.50	3.00E-03
100,000	-1.37	-13.67	13.74	84.27	5.30	0.58	1.00	3.75	3.00E-03
120,000	0.05	-15.61	15.61	90.17	5.54	0.54	1.00	4.00	3.00E-03
140,000	1.48	-17.45	17.52	94.84	5.76	0.50	1.00	4.10	2.90E-03

Figure 4-84 Tabulated characteristic data for a hybrid feedhole bearing.



Some additional observations can be made from the characteristic data:

- The pressure minimum goes sub-atmospheric between 20 to 40K RPM;
- The pressure maximum exceeds the operating pressure at 100K RPM;
- The attitude angle reaches  $90^\circ$  at 120K RPM as  $F_y$  goes to zero;
- The minimum land pressure goes to atmospheric for speeds  $\geq 100$ K RPM.

## 4.8. Porous Liner Hybrid Bearing Results

### 4.8.1. Overall Results

Pressure solutions were found for a range of speeds for a porous-liner fed hybrid bearing with a clearance of 0.002", eccentricity ratio of 0.9, and mass addition factor of  $2e-4$  lbs/s matching conditions for the feedhole hybrid bearing.

Numerically stable solutions were found for speeds up to 300K RPM. A solution was tried at 400K RPM but a stable solution was not found.

The hydrostatic porous liner bearing had approximately 4.4x the hydrostatic force of the feedhole bearing (28.45 lbs versus 6.417 lbs). As the speed is increased, the hydrodynamic contribution to  $F_y$  (in the axis of the bearing displacement) increases in the opposite direction to the hydrostatic force. The magnitude of  $F_y$  decreases throughout the speed range that was analyzed. However, even at 300K RPM the hydrodynamic contribution only lowered  $F_y$  to 13.56 lbs. The component of force perpendicular to the displacement is 0 for the hydrostatic case and increases to 38.04 lbs at 300K RPM. As a result the net hydrodynamic bearing force is at 28.45 lbs for 0 RPM and increases slowly to 40.38 lbs at 300K RPM. The attitude angle ranges from 0 with no rotation to 70.38° at 300K RPM.

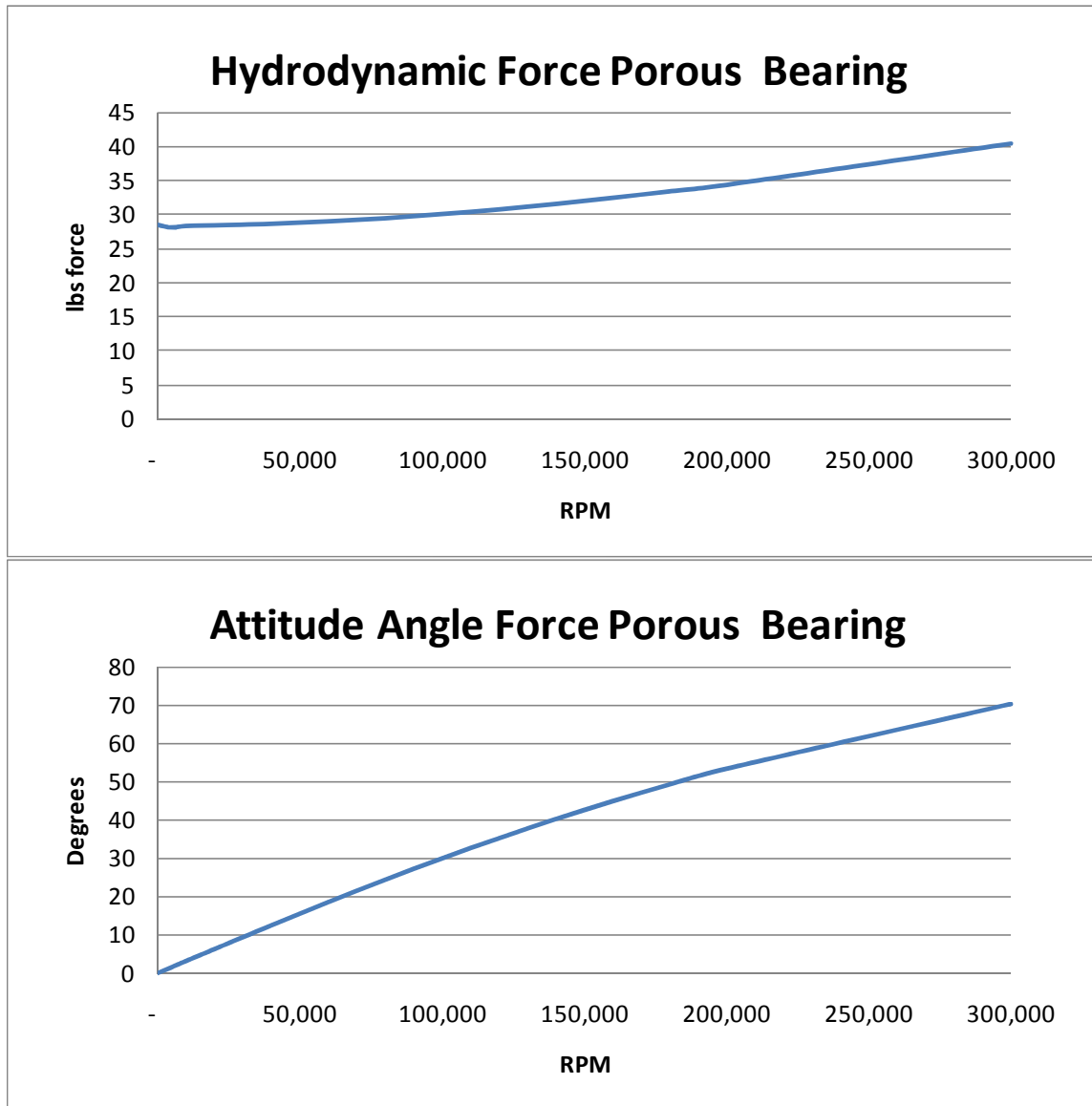


Figure 4-85 Hydrodynamic bearing force and attitude angle for hybrid porous liner bearing with clearance=0.002" and eccentricity ratio of 0.90.

#### 4.8.2. Examination Under the CFD Microscope and Characterization

The results of PL hybrid bearing CFD experiments are shown schematically and graphically in figures 4-86 to 4-89.

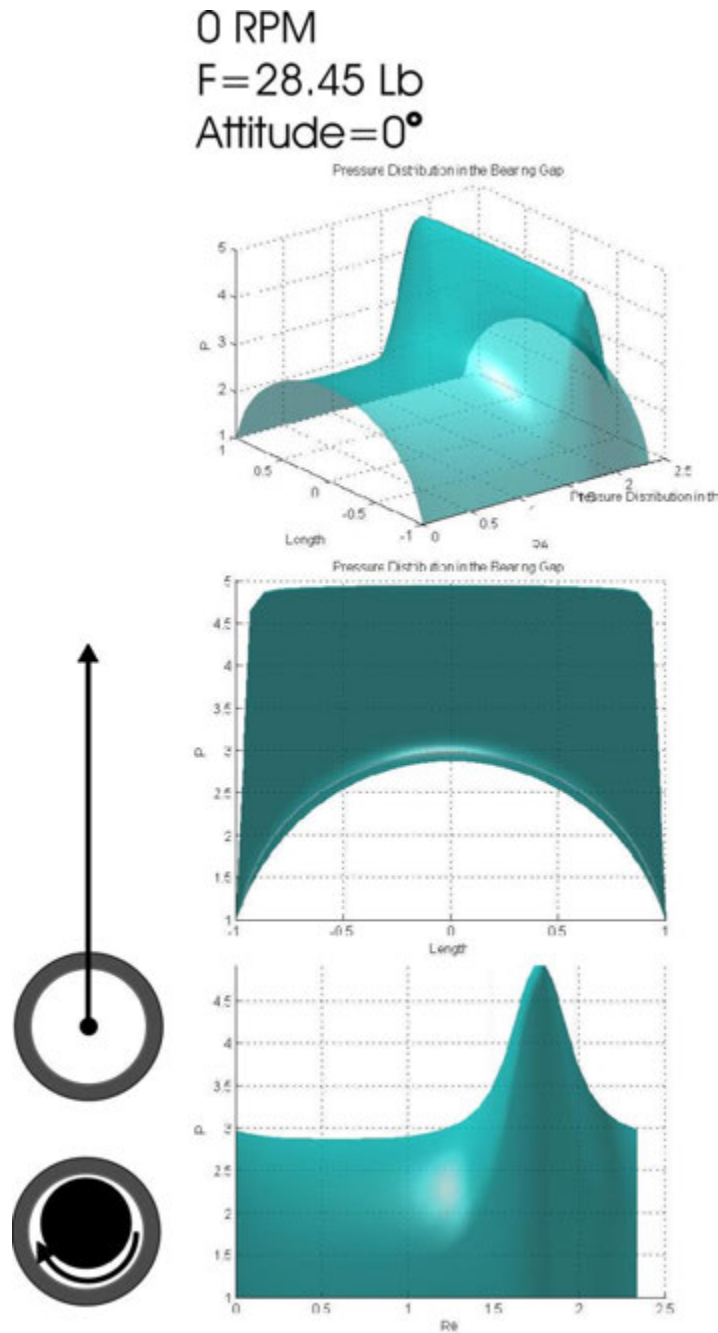


Figure 4-86 Hydrostatic force of the porous liner fed bearing (0 RPM).

20K RPM  
 F=28.35 Lb  
 Attitude=6.29°

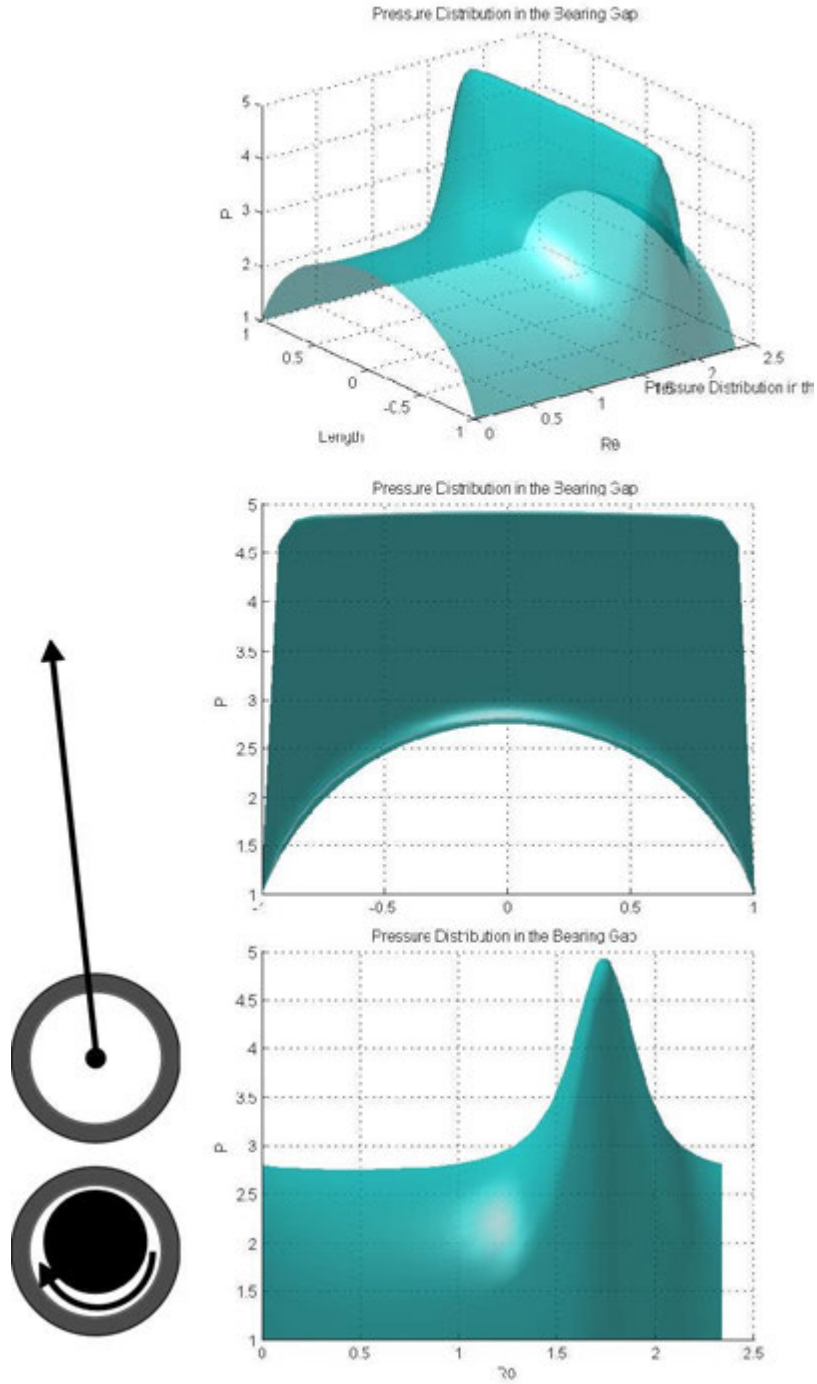


Figure 4-87 Pressure distribution and net bearing force at 20K RPM.

100K RPM  
 F=30.02 Lb  
 Attitude=30.00°

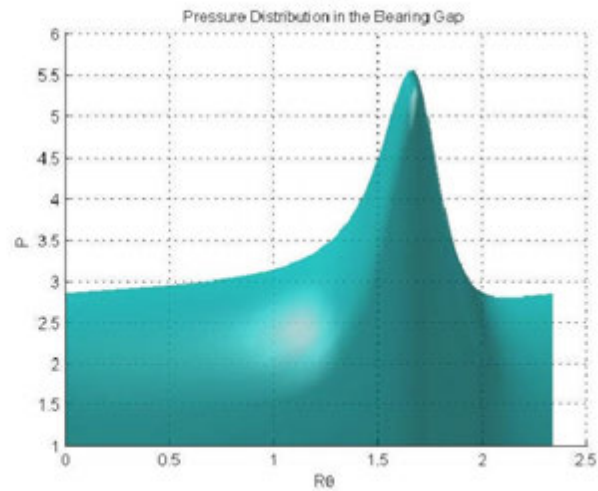
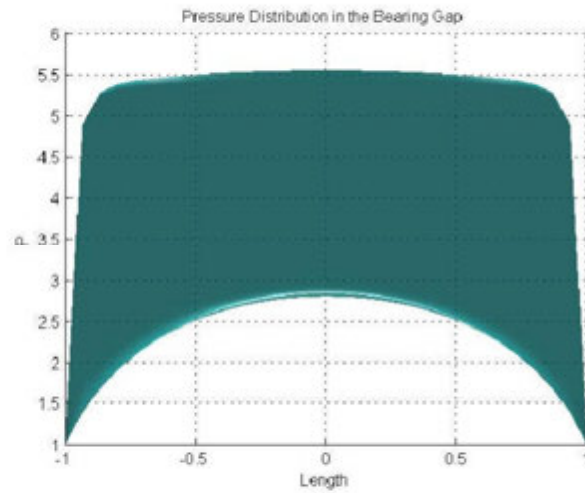
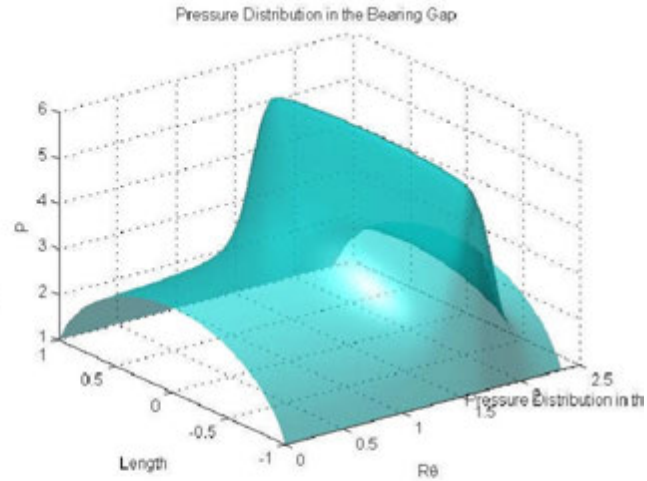


Figure 4-88 Pressure distribution and net bearing force at 100K RPM.

300K RPM  
 F=40.39 Lb  
 Attitude=70.38°

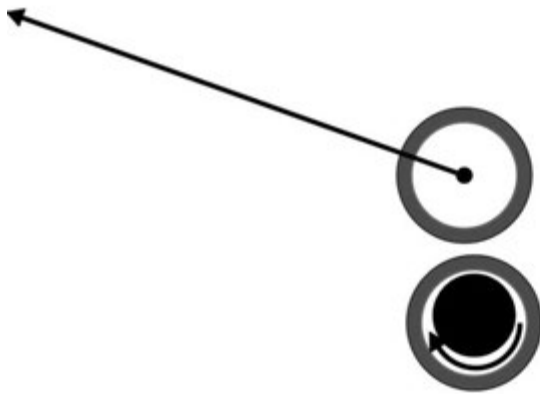
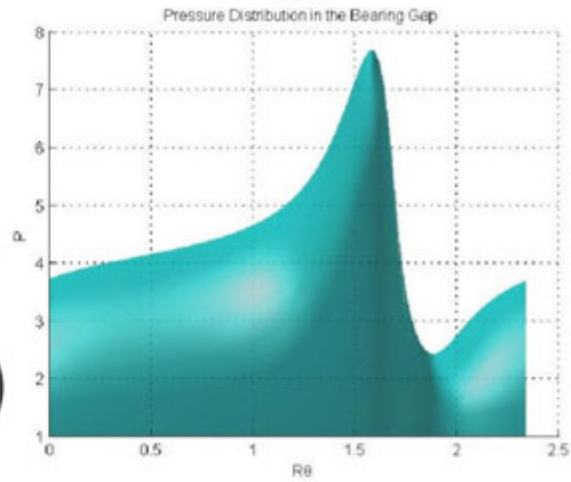
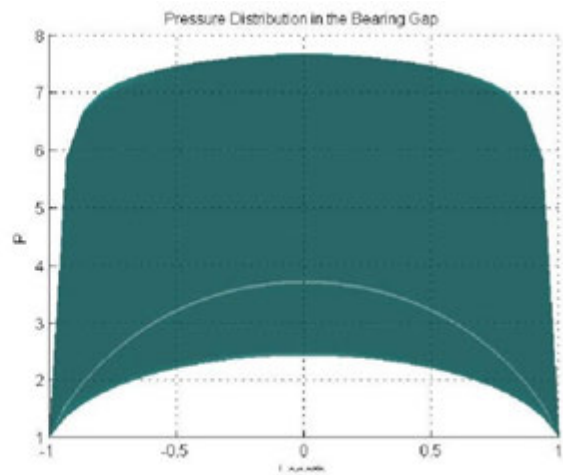
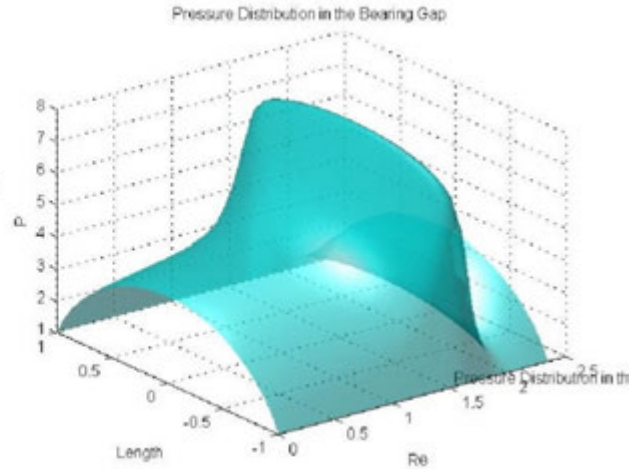


Figure 4-89 Pressure distribution and net bearing force at 300K RPM.

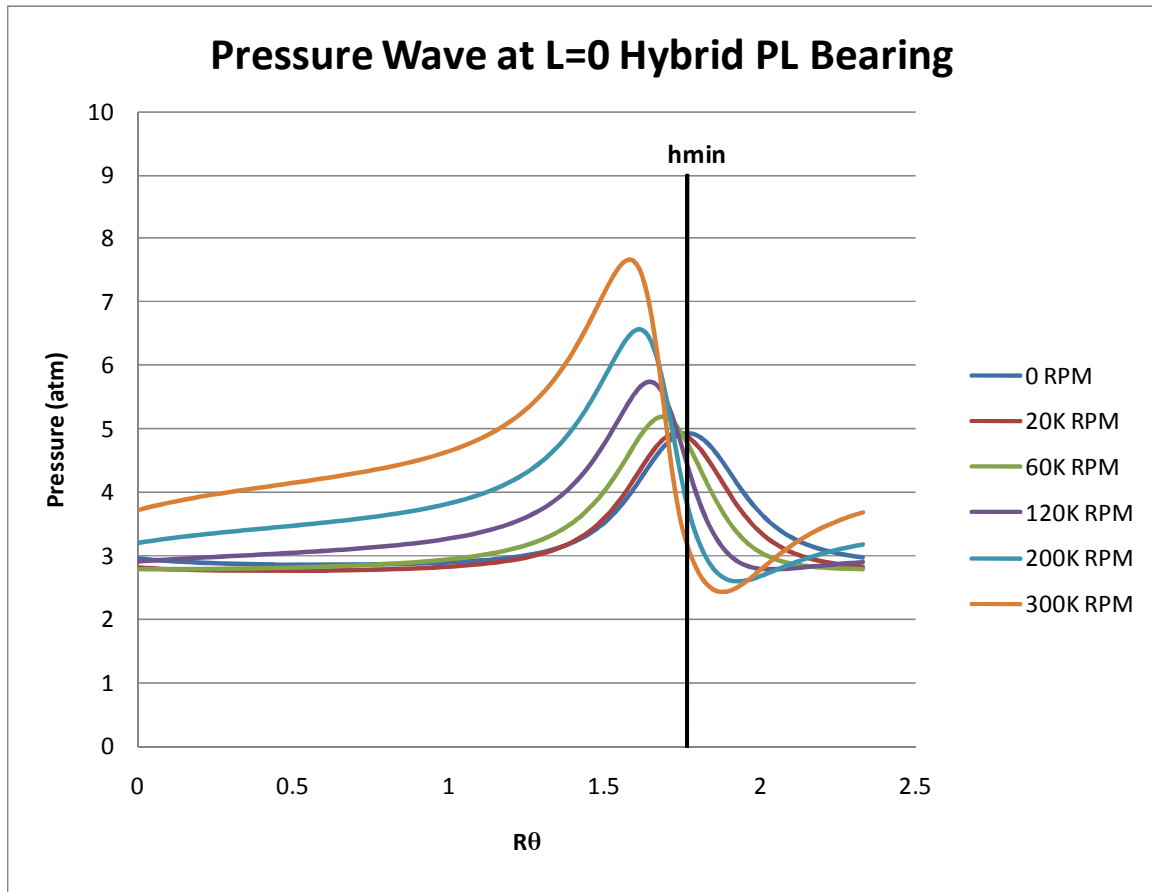


Figure 4-90 Pressure wave at the center of the PL hybrid bearing operating at 60 psig.

As with the hydrodynamic bearing and the FH hybrid bearing, both the difference between the pressure wave maximum and minimum increases with increased speed. Also as the speed increases both the pressure wave maximum and minimum moves forward (into the flow). It is speculated that the cause of the numerical instability at 400K RPM might be due to the resistance of the wave minimum occur forward of  $h_{min}$ . For the 300K RPM solution the pressure maximum is 7.6628 and occurs at node 65, 7 nodes forward of  $h_{min}$  located at node 78 where the pressure is 3.1619. The pressure minimum is 2.434 at node 78, 5 nodes aft of  $h_{min}$ .



As a result the pressure must change 5.23 atm in 13 nodes. The exact onset of numerical stability is not known since 400K RPM was tried and did not yield a stable solution. So the speed limit for numerical instability must lie between 300K RPM and 400K RPM.

It should also be noted that a section of the hydrodynamic wave has  $P > 5.08$  at 300K RPM which is the 60 psig operating pressure. As a result there are regions where the mass addition flow is reversed.

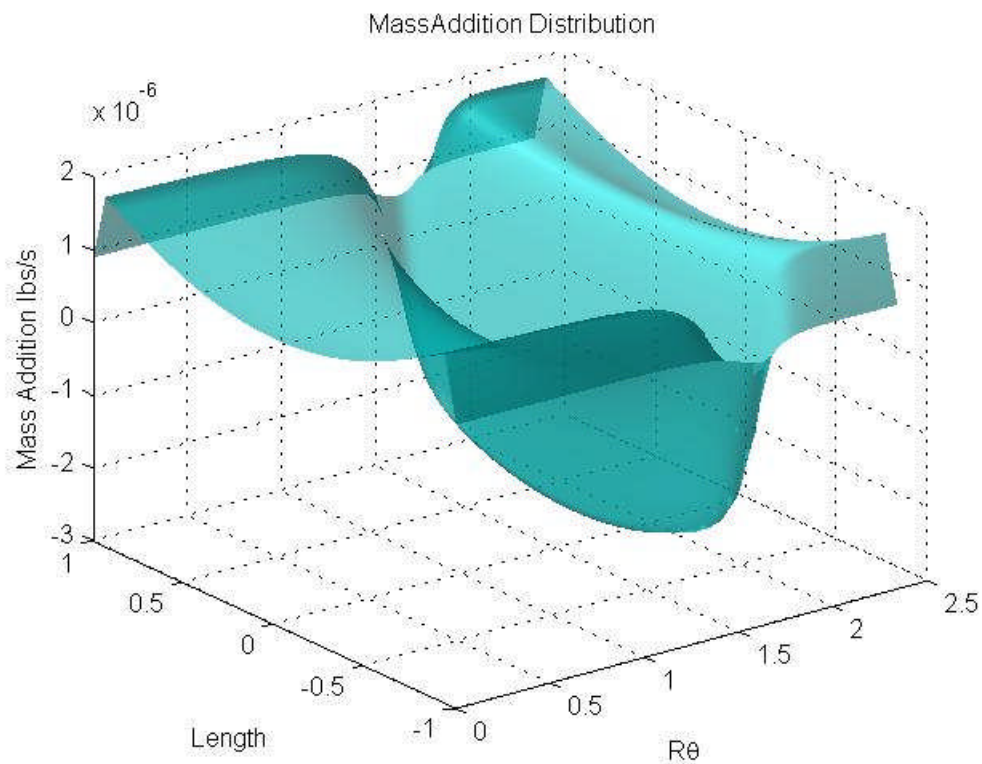


Figure 4-91 Mass addition in the bearing gap for the porous liner bearing at 300K RPM.

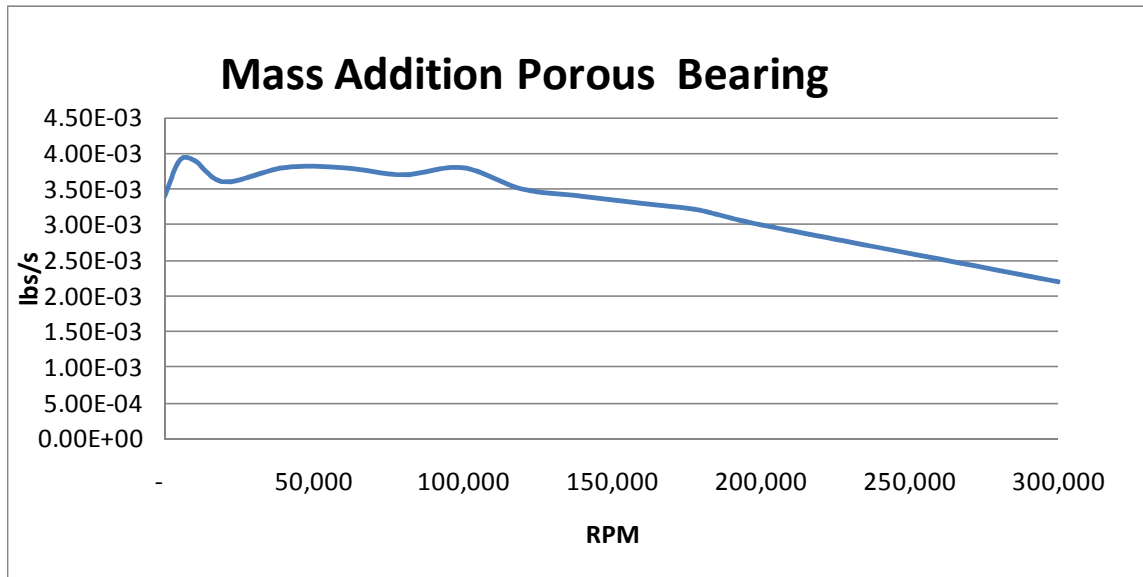


Figure 4-92 Mass Addition for the porous liner bearing.

As a result of the flow reversal, the mass addition stays fairly constant until about 100K RPM after which it declines about 40% at 300K RPM. The peak pressure begins to exceed the reservoir pressure at about 60K RPM.

Hybrid Bearing Operating pressure = 60 psig Porous liner with $K_{meas}=2e-4$ and $\epsilon=.9$								
Speed RPM	Fy lbs	Fx lbs	Fbush lbs	Attitude degrees	Pmax atm	Pmin stm	Max R $\theta$ degrees	Mass Add lbs/s
-	-28.45	0.00	28.45	0.00	4.94	1.00	1.77	3.40E-03
5,000	-28.03	-0.77	28.04	1.57	4.87	1.00	1.77	3.90E-03
10,000	-28.23	-1.55	28.27	3.15	4.89	1.00	1.74	3.90E-03
20,000	-28.18	-3.11	28.35	6.29	4.92	1.00	1.74	3.60E-03
40,000	-27.91	-6.19	28.59	12.51	5.03	1.00	1.72	3.80E-03
60,000	-27.44	-9.22	28.95	18.57	5.18	1.00	1.69	3.80E-03
80,000	-26.79	-12.16	29.42	24.42	5.36	1.00	1.67	3.70E-03
100,000	-26.00	-15.01	30.02	30.00	5.54	1.00	1.67	3.80E-03
120,000	-25.08	-17.75	30.73	35.29	5.75	1.00	1.64	3.50E-03
140,000	-24.06	-20.39	31.54	40.28	5.94	1.00	1.64	3.40E-03
160,000	-22.94	-22.91	32.42	44.96	6.16	1.00	1.62	3.30E-03
180,000	-21.74	-25.31	33.36	49.34	6.38	1.00	1.62	3.20E-03
200,000	-20.44	-27.56	34.32	53.44	6.57	1.00	1.62	3.00E-03
300,000	-13.56	-38.04	40.39	70.38	7.66	1.00	1.57	2.20E-03

Figure 4-93 Tabulated characteristic data for the porous liner bearing.

#### 4.9. Comparison of Hydrodynamic, Hybrid Feedhole, and Hybrid Porous Liner Bearings

##### 4.9.1. Hydrodynamic Force and Attitude Angle

It is shown in section 4.1 that the hydrostatic results (0 RPM) for both the feedhole and porous liner bearings result in an attitude angle of 0. That is, all the hydrodynamic force is in the  $-Y$  direction (reaction force against the bushing) which is aligned with the bushing/shaft displacement and is in the restorative direction (opposing further  $Y$  displacement). The magnitude of the force increases non-linearly with increased eccentricity ratio (excepting the “near surface” effect for the feedhole bearing) with the largest increases (greater stiffness) occurring as the eccentricity ratio goes to 1. The hydrodynamic force was primarily linearly proportional to the operating pressure for a fixed eccentricity ratio. The porous liner bearings have a  $W/pA$  efficiency that is much higher than that of the feedhole bearings. In the comparison tests, the eccentricity ratio was 0.9 and operating pressure was 60 psig. The 0 RPM bearing force for the PL hybrid bearing is 28.45 lbs compared with 6.42 lbs for the FH hybrid bearing while the bearing force for hydrodynamic bearing is, of course, 0.

As the rotation is increased, the hydrodynamic force increases mostly in the  $-X$  direction (perpendicular to the the displacement) but also increases to a lesser extent in the  $Y$  direction (anti-restorative and opposite to the hydrostatic force). As a result, for the hybrid bearings the magnitude of the restorative  $-F_y$  force diminishes with increased speed and eventually changes direction and continues to increase as  $+F_y$  (antirestorative). Thus the attitude angle increases from 0 and becomes  $90^\circ$  when the  $F_y$  component of the hydrodynamic force goes to 0 and becomes greater than  $90^\circ$  as the  $F_y$  component becomes positive. For the

feedhole bearing this occurred at about 120K RPM. For the porous liner bearing the  $F_y$  component of the hydrostatic force was still negative at the highest pressure solution of 300K RPM therefore the attitude angle was always  $< 90^\circ$ .

For the hydrodynamic bearing (no mass addition) the hydrodynamic force is 0 with 0 RPM. Increasing speed results in an increasing  $-F_x$  and  $+F_y$ . At low speeds and/or low eccentricity ratios the  $-F_y$  component is very small so that the attitude angle starts out close to  $90^\circ$ . As the speed is increased (or eccentricity ratio is increased), the  $-F_x$  component becomes more substantial and the attitude angle exceeds  $90^\circ$ .

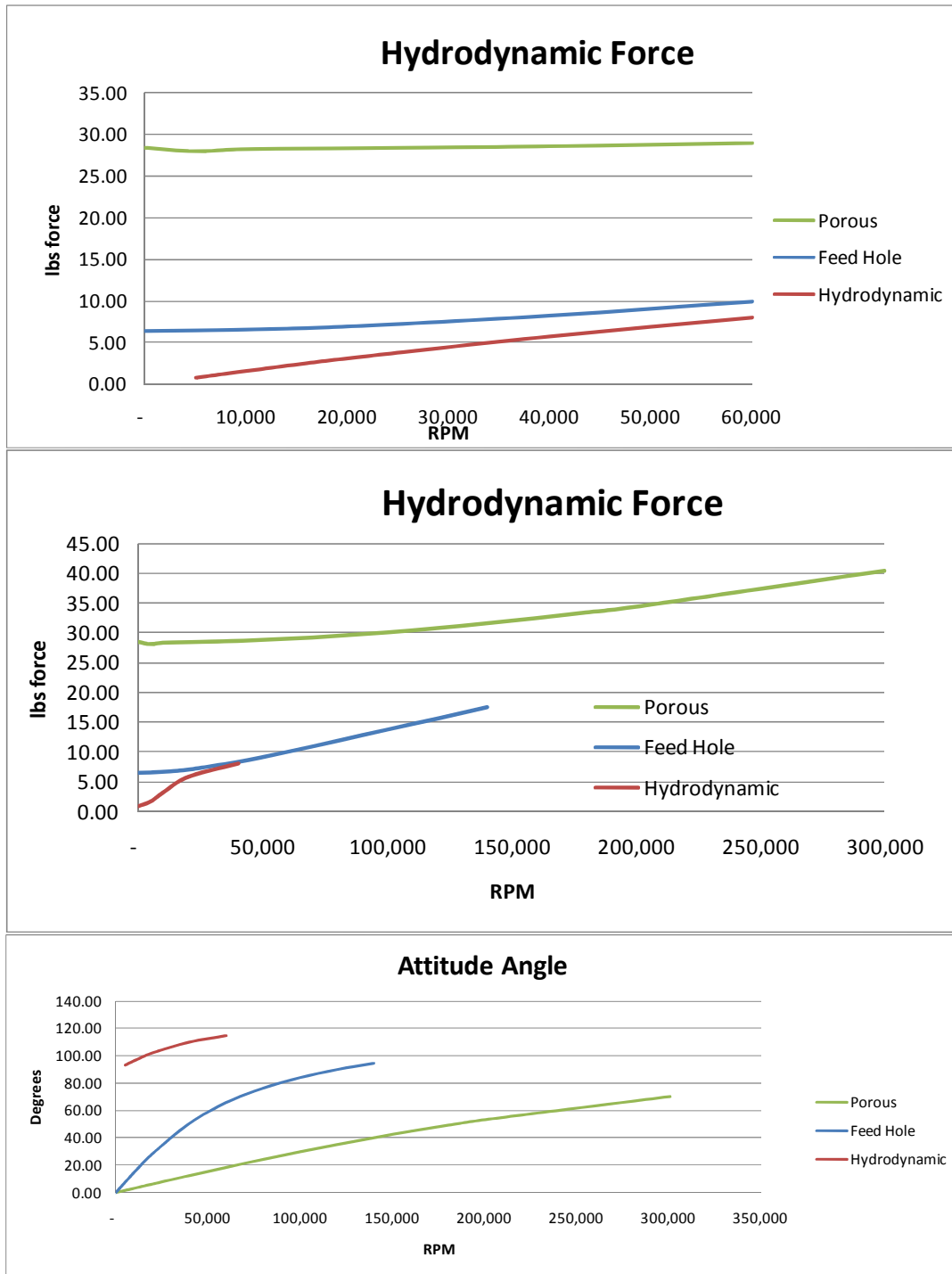


Figure 4-94 Graphs comparing the hydrodynamic force and attitude angle for eccentricity ratio of 0.9 for a hydrodynamic bearing and feedhole and porous liner hybrid bearings operated at 60 psig.

In terms of pressure distributions, the net hydrodynamic force is dependent on creating pressure differences in the bearing gap with the greater differences generating the greater hydrodynamic force. For the hydrodynamic bearing at 0 RPM the pressure distribution is simply atmospheric throughout the bearing gap. As the speed is increased, the maximum pressure quickly increases and the minimum pressure quickly decreases until at 60K RPM they are 1.89 and 0.38 respectively. The hybrid bearings, on the other hand, start at 0 RPM with a large pressure difference. The maximum pressure is the operating pressure  $P=5.08$  and the minimum pressure is the ambient pressure  $P=1$ . Because of the mass addition of the hybrid bearings the maximum and minimum pressures show a reluctance to both go above the operating pressure or below ambient pressure respectively. The increased hydrodynamic force is due primarily to the changes in the pressure wave distribution in the bearing gap. At high speed the maximum pressure can exceed the operating pressure. This occurs between 40K to 60K RPM for the porous bearing and between 80K to 100K RPM for the feedhole bearing. The feedhole bearing does generate some slightly sub-atmospheric pressure outboard of the feedholes along the bearing length. However, the pressure in the land area of the feedhole bearing (between the feedholes along the length) develops somewhat similar to that in a pressurized hydrodynamic bearing where at 0 RPM the minimum and maximum pressures are both 2.30 (compared with 1 for the hydrodynamic bearing) and separate with increased speed to 3.75 for the maximum pressure and 1.00 for the minimum pressure at 100K RPM. With further speed increase the land pressure wave acts more like a porous liner pressure wave in that the maximum pressure continues to increase with speed but the minimum pressure is held at 1.00. At 140K RPM the maximum and minimum pressures are 4.10 and 1.00 respectively.

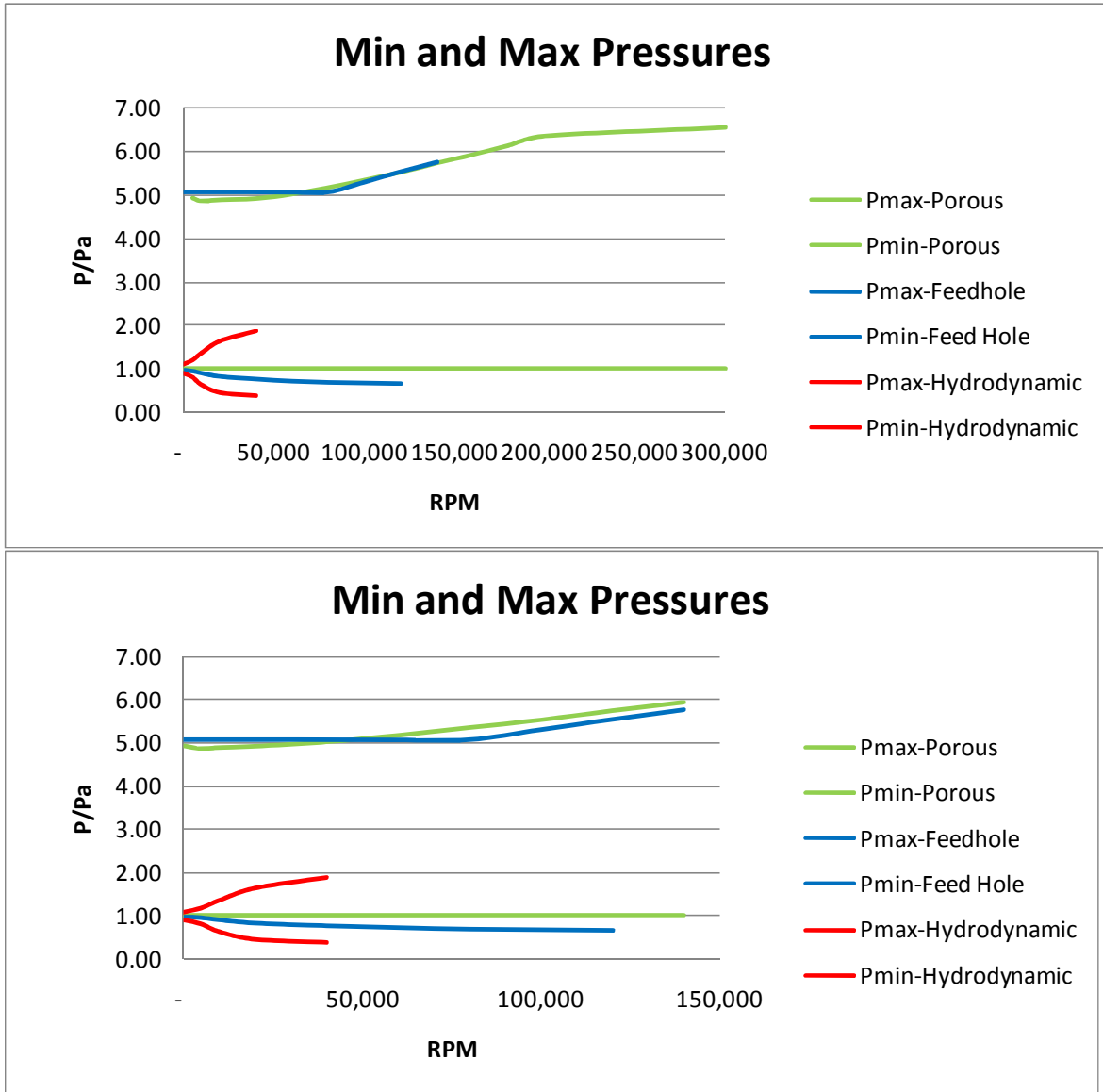


Figure 4-95 Minimum and Maximum Bearing Pressures.

#### 4.9.2. Comments on Stability

Although stability analysis was not done in this thesis, it can be intuited that for a bearing with a static load (load always in the same direction caused for example by gravity compared to a dynamic load caused for example from imbalance) that the porous liner hybrid bearing would be the most stable. The reasoning behind this is shown in figure 4-96 which shows the time displacement progression of two hypothetical bearings. The top series of displacements (left to right) represents a purely hydrodynamic bearing moving from an initial position where the eccentricity ratio is 0 (position 1) to a situation of a force equilibrium (position 5). The bottom series shows the same progression for a “strong” hybrid bearing. What is meant by a strong hybrid bearing is a bearing such as a porous liner bearing whose static characteristics provide a strong restorative hydrodynamic force against displacement. Figure 4-96 is drawn from the standpoint that the shaft is rotating in a clockwise direction and its center (white dot) is kept in a fixed location. The load is applied to the bushing which is allowed to translate but not rotate. The load is a constant magnitude and is always in the Y direction (downwards). The hydrodynamic bearing gap interaction forces are drawn relative to the bushing.

In position (1) where the shaft and bushing are concentric there is no hydrodynamic force for either the hydrodynamic bearing (top) or the strong hybrid bearing (bottom). Thus the only force on the bushing is the downward static load  $W$ . Thus the initial displacement position (1) for both bearings is that bushing center (blue dot) displaces downwards compared to shaft center (white dot). This displacement generates a hydrodynamic force  $F_H$ . For the hydrodynamic bearing the magnitude of the force is small compared with that of the strong hybrid bearing and the bearing has an attitude angle just slightly larger than  $90^\circ$ . Vector addition of the load force and the hydrodynamic force indicates that the net force on the bushing is of greater magnitude than  $W$  and points downwards



and slightly to the left. Thus the next displacement, position (3) shows an additional bushing displacement larger than the initial displacement pulling the bushing center further away from the shaft center in the downward and to the left in the direction of the net force. This means that  $h_{min}$  is diminished and is located slightly to the right of the top of the shaft. The diminished  $h_{min}$  means an increase in the eccentricity ratio which in turn generates a larger hydrodynamic reaction force with a somewhat larger attitude angle also shown in position (3). This creates an even larger displacement shown in position (4) that moves the bushing center further downward and more to the left. Position (4) shows that, depending on the magnitude of these displacements, the bearing has nearly crashed (or has crashed) with a very small  $h_{min}$  located to the right of the top of the shaft. The very small  $h_{min}$  generates a comparatively large hydrodynamic force (shown in position (4)). As shown in position (4) the resulting net interaction force still has a direction that would certainly crash the bearing. The force equilibrium position is shown in position (5). In this position the eccentricity vector has a magnitude such that the magnitude of the hydrodynamic force is equal to the magnitude of the load force. The direction of the eccentricity vector places the center of the bushing slightly *above* (even the load force is downward) and to the left of the shaft center. Whether the bearing crashes or not depends on the relative speed of the radial increase in the eccentricity vector versus the angular speed of the bushing whirl. It can also be seen readily that if the hydrodynamic force generated at eccentricity ratios approaching 1 are not larger than the load force  $W$  surely the bearing will crash. Equilibrium position (5) is not a stable equilibrium position. To go from the neutral position (1) to the equilibrium position (5) requires that bushing be *drawn into the whirl*. As a result upon reaching position (5), it would be expected that the bushing would continue past it and at best establish a stable orbit with an orbit radius less than the bearing clearance.

The strong hybrid bearing starting at the concentric position (1) also has no hydrodynamic force and its initial displacement, position (2), is such that the bushing center drops slightly below the shaft center. In this position, however, the strong hybrid bearing generates a hydrodynamic force that is quite different from that of the hydrodynamic bearing. Its major component is restorative in that its direction is mostly upwards with just a very small component to the left (position (2) lower row). Thus the resultant net bearing force is much smaller than the load force  $W$  as the hydrodynamic force mostly subtracts from the load force. Thus the next displacement shown in position (3) is very close to its equilibrium position also shown in position (3). The equilibrium position will be where the bushing center will be *below* and slightly to the left of the shaft center. Like the hydrodynamic bearing, the strong hybrid bearing can be expected to pass through its equilibrium position and establish an orbit. But it can be anticipated based on the relative sizes and attitude angles of the hydrodynamic bearing versus the strong hybrid bearing that the orbit radius would be much smaller for the strong hybrid bearing.

It could be supposed that by tabulating the hydrodynamic force and attitude of a particular bearing as a function of speed and eccentricity ratio that an actual time integration of the motion of the bearing could be accomplished providing that the mass and moments of inertia of the moving parts are known. Such a solution is called the "orbit method". As noted in section 3.1 the time integration features for such an analysis have been written into the CFD programs produced in this thesis. They have also been demonstrated to work for known "spring functions". However, it should also be noted that the solutions thus far presented have been quasi-static for a bushing and shaft in a fixed position. As such the two transient terms in the Reynolds equation corresponding to the elemental volume change with respect to time and the elemental pressure change with respect to time have been ignored. Once relative motion between the shaft and the bushing is

allowed, these terms must be included. Solution schemes for this have been devised but their implementation is left for further work.

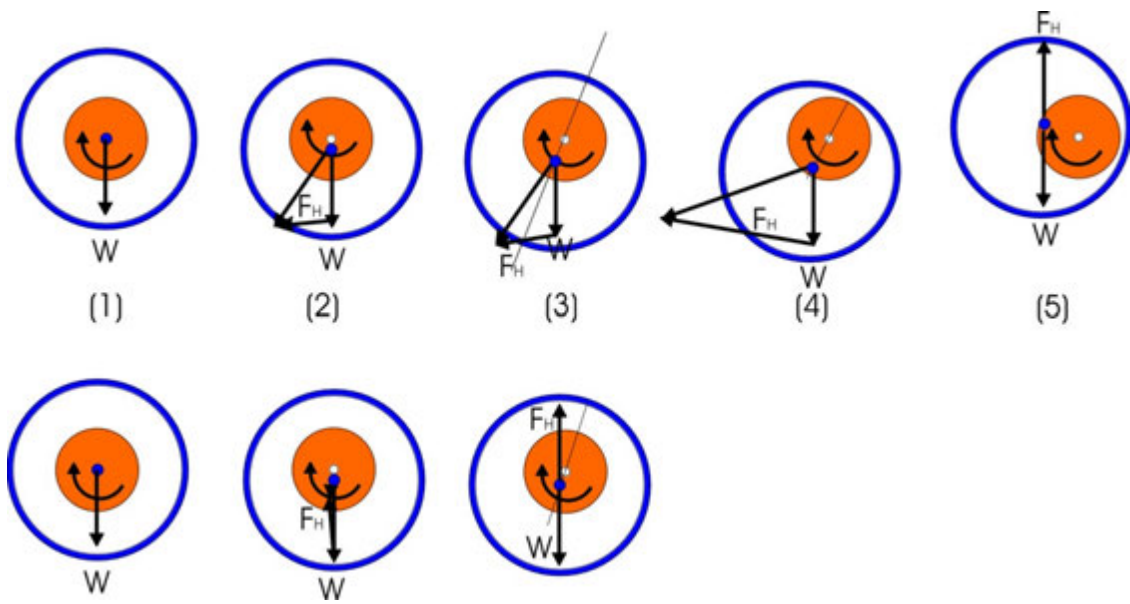


Figure 4-96 Progression from concentric position to equilibrium position for a hydrodynamic bearing (top) and a "strong" hybrid bearing such as the porous liner bearing.

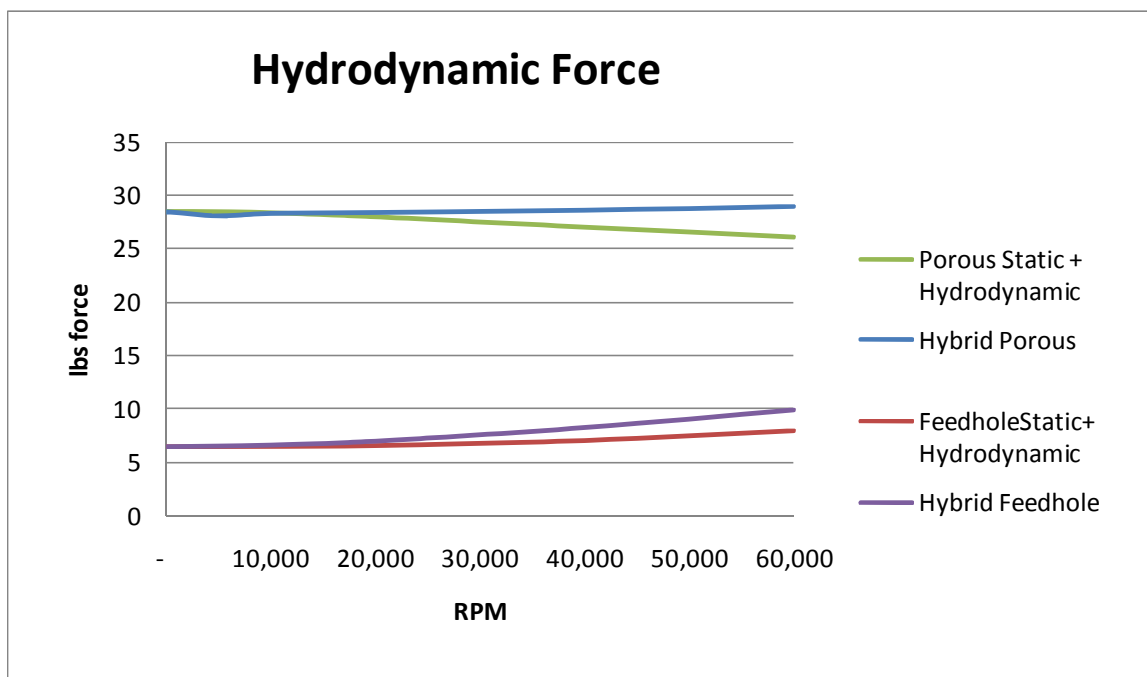
#### 4.10. Comparison of Hybrid Bearings to Hydrostatic Bearing Superimposed on a Dynamic Bearing

The analysis done so far enables a comparison of the relative performance of hybrid bearings compared with simply superimposing a hydrodynamic bearing solution onto the hydrostatic bearing solution. Pressure solutions have been obtained over the broadest range of speeds possible for hydrodynamic, porous hybrid, and feedhole hybrid bearings. Thus it is possible to add the hydrostatic solution (0 RPM) for the porous liner bearing to the hydrodynamic solution at the same speed. Likewise it is possible to add the hydrostatic feedhole liner solution to the matching speed hydrodynamic solution. What is meant here by adding is adding the force components  $F_x$  and  $F_y$ . Unfortunately the solutions for the hydrodynamic bearing were only found up to 60K RPM so that the speed range of comparison is not very large.

On a cursory level the net hydrodynamic force and the attitude angle do not differ greatly. In each case, the 0 RPM values are the same since they simply are the hydrostatic solutions as the hydrodynamic contribution is 0 at 0 RPM. Also at speeds up to 60K, the hydrodynamic force goes from 0 lbs to 8.02 lbs with attitude angle going from 90° (hypothetical as the force is 0) to 114.8° (93.3° to 114.8° for 5K to 60K RPM). As a result the hydrodynamic  $F_y$  contribution goes from 0 to 3.36 lbs in the opposite direction of the hydrostatic force and the  $F_x$  contribution goes from 0 lbs to 7.82 lbs.

The resultant forces of the hybrid bearings are always slightly higher than the sum of the forces from the hydrodynamic and hydrostatic results. Comparing over the range 0 to 60K RPM, the porous hybrid bearing force increased from 28.45 to 28.95 lbs while the hydrostatic plus hydrodynamic solution fell from 28.45 to 26.12 lbs. For the feedhole bearing the force increased from 6.42 to 9.98 lbs while for the hydrostatic plus hydrodynamic result it only increased from 6.42

to 7.90 lbs. As a result, the attitude angles changed slightly less for the hybrid bearings than they do for the respective hydrostatic plus hydrodynamic result. As a result the attitude angles were also slightly different. The attitude angle for the porous static plus hydrodynamic solution increased slightly less than the porous hybrid bearing solution with increased speed, while the feedhole static plus hydrodynamic solution increased slightly less than the feedhole hybrid solution with increased speed.



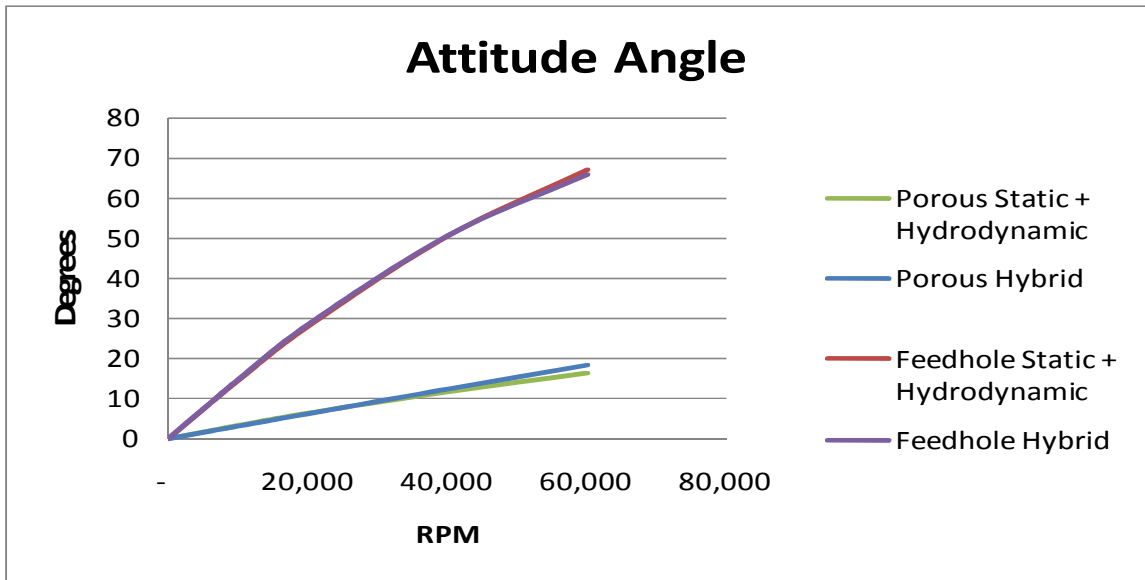


Figure 4-97 Net Hydrodynamic Force and Attitude Angles comparing PL and FH hybrid bearings to adding PL and FH hydrostatic results to Hydrodynamic results.

#### 4.11. The Metaphysics of Gas Bearings (Dimensionless Analysis)

When dimensionless numbers are properly formulated they have great ontological significance. A quick example would be the writer's experience in gold plating for the Parker Pen Company. A particular type of gold plating bath was constantly subject to plating out "cloudy", an unacceptable condition in a piece of jewelry. When this occurred analysis of the offending bath's chemical composition would be made with the intention of making chemical additions to bring the bath back into the supplier's (a large well-known chemical company) recommended parameters. It was well known that excursions of either Au or CN were the primary causes of cloudy deposition. The problem was that when the bath was depositing cloudy, that the analysis often showed the Au and CN to be within specification. Other times either the Au or CN or both could be well out of specification and the bath would plate well. In those times there was a reluctance to make any adjustments so long as the bath was plating well as a bath with Au and CN in specification might or might not plate properly. Despite technical assistance from the supplier and tireless examination of bath compositions during good and bad conditions no correlations could be found. Then, at some great expense, a plating technician from Parker France was brought over to see if he could help. Parker France operated the same bath without any cloudy issues. The first question he asked solved the whole problem. It was, "What Au to CN *ratio* do you operate your bath at?" As it turned out Au or CN could be high or low or in specification so long as the other concentration was proportionally high or low. So Au and CN by themselves had little significance, it was their *ratio* that was all important.

This brings up the subject of *dimensional analysis* and similitude. Dimensionless numbers can of course be easily made by dividing the parameter involved by another parameter of the same dimension. The question is whether the dimensionless number formed has ontological significance. Two basic methods

of dimensional analysis are 1) The Buckingham pi method (a good discussion is found in *Physical Fluid Dynamics* [21]), and 2) analysis of the governing equations (a good discussion is found in *Fluid Flow* [22]). Both methods require insight into the physical system of interest - either the governing equations themselves or the exclusive set of dependent and independent variables. Such analysis has been invaluable to identifying the many well-known fundamental dimensionless numbers that provide the foundation of similitude in gas dynamics and all physics.

Equally important to meaningful similitude is that the physical system be described by a *complete set* of ontologically significant dimensionless parameters. Only then can solutions expressed in these terms be extended to a whole class of similar parameters.

The procedure for non-dimensionalization (the writer knows this is not a word but it should be and is used in [23]) is essentially a two step process. The first step is to select a reference quantity for each of the variables. According to *Fluid Flow* [22] "The reference quantities may be selected arbitrarily, but they must be well-defined quantities of the problem." The reference quantities are then used to create dimensionless variables from which the governing equations are recast.



#### 4.11.1. “Standard” Dimensionless Variables in the Reynolds Equation

As has been remarked repeatedly, the history of progress in gas journal bearings starts back in the 1950’s with the study of purely “self-acting” or hydrodynamic gas journal bearings while purely “aerostatic” or hydrostatic bearings were ignored. The governing equation for the hydrodynamic gas journal bearing is the Reynolds equation (derived in Appendix A) without the mass addition term. In viewing the dimensionless Reynolds equation  $H$ ,  $P$ ,  $Z$ , and  $\theta$  are the typical dimensionless variables of the equation.

#### 4.11.2. Dimensionless Time and the Hydrodynamic Bearing Equation

As was discussed in Appendix A.1.3.4, many researchers also include a dimensionless time,  $\tau$ . The question is what reference quantity to use to create the dimensionless time? As was discussed in A.1.3.4 many different reference quantities are used. However, the most common is to use the rotational speed of the bearing,  $\omega$ , so that  $\tau = \omega t$ . This seems logical and very appropriate for a *purely hydrodynamic* bearing. When the Reynolds equation without mass addition is recast using this form of dimensionless time the result is:

$$\Lambda \frac{\partial}{\partial \theta} (PH) + \sigma \frac{\partial}{\partial \tau} (PH) = \frac{\partial}{\partial \theta} \left( PH^3 \frac{\partial P}{\partial \theta} \right) + \left( \frac{R}{L} \right)^2 \frac{\partial}{\partial Z} \left( PH^3 \frac{\partial P}{\partial Z} \right)$$

Which results in a complete set of similitude parameters of  $\Lambda$ , the bearing number often called the dimensionless speed, the slenderness ratio ( $L/D$  - which appears as  $R/L$  in the equation) and a new term (not used in Appendix A),  $\sigma$ , which is often called the squeeze film term where:

$$\Lambda = \frac{6\eta\omega}{p_a} \left( \frac{R}{c} \right)^2$$

$$\sigma = \frac{12\eta\omega}{p_a} \left( \frac{R}{c} \right)^2$$

Other names for  $\sigma$  are simply another bearing number [23] or *bearing number for transient analysis* [5]. Thus the results of the study of purely hydrodynamic gas journal bearings are expressed in terms of the eccentricity ratio,  $\varepsilon$ ,  $\Lambda$ , and L/D and are extendable as the clearance,  $c$ , is implicit or scaled into both the bearing number and the squeeze term such that they are both inversely proportional to the square of the clearance.

#### 4.11.3. Dimensionless Time and the Hydrostatic and Hybrid Bearing Equations

Obviously, as discussed in Appendix A.1.3.4, the use of  $\omega$  for the reference time quantity is not appropriate for the study of bearings with an “aerostatic” component such as purely hydrostatic bearings (which have been almost completely ignored) or hybrid bearings. This is obvious from the simple observation that  $\Lambda$  and  $\sigma$  are both scaled by  $\omega$  and time does not stop nor does the aerostatic phenomena cease just because rotation stops.

In other words, as has often been mentioned in earlier portions of this thesis, results expressed in terms of  $\varepsilon$  are not extendable to bearings of similar  $L/D$  and  $R/c$  ratios since both the hydrodynamic and hydrostatic activities within the bearing gap are related to the actual dimensional gap height  $h$ .  $\varepsilon$  by itself does not describe  $h$ . So results for either hydrostatic or hybrid bearings can lead only to the very weakest conclusions; that is, they are only valid for bearings with the same length, diameter, and clearance so that results presented in terms  $\varepsilon$  must be made with reference to the specific clearance used.

In fact, although it was unknown to this writer at the undertaking of this study of gas journal bearings, it seems to be an unstated but understood (by the gas bearing community both commercial and academic) underlying principal of gas bearing hydrodynamic activity that most hydrodynamic activity takes place only when the bearing gap height is less than 500  $\mu\text{in}$  and hence all bearing clearances tend to fall within the range of approximately 300-1000  $\mu\text{in}$  regardless of the diameter, length, or speed of the bearing.

### *Examples*

1) Powell writes in his 1970 review of the "progress in gas lubrication" [1] when discussing hydrodynamic journal bearings that "Most early experimental bearings were 2" in diameter and employed radial clearances of around  $10^{-3}$  in (0.25mm)...."

2) The New Way air application design guide [24] shows load capacity versus flight height curves for various sizes of flat bearings. While the larger bearings have higher load capacity forces each shows a rapid increase in load capacity as the flight height is decreased below 500  $\mu\text{in}$  and each has its load capacity diminish to nearly 0 as the flight height is increased above 800 to 1000  $\mu\text{in}$ .

New Way hydrostatic gas journal bearings use the same radial clearance of about 400  $\mu\text{in}$  for their complete line of bearings which range in diameter from 0.25 in to 3.00 in. They also know that small diameter bearings need to be longer than large diameter bearings so that they decrease the slenderness ratio for large diameter bearings so that as the diameters vary from 0.25 to 5 in, the slenderness ratio varies from 5 to 1.16.

3) The hydrostatic bearing CFD results presented in this thesis clearly show that using  $\varepsilon$  as a variable of the problem is clearly meaningless unless it is given in the context of the bearing clearance (simply review the  $W/pA$  versus  $h-c$  scans in section 4.4.1).

If one reads the academic literature, one would be deluded into thinking that it was the eccentricity ratio that was important so that the expectation would be that the hydrodynamic activity for a bearings with eccentricity ratios for example of 0.5 would be the same for a bearing with a clearance of 0.002" (which would have a minimum flight height of 0.001") as for a bearing with a clearance of 0.0008" (which would have a minimum flight height of 0.0004"). But this is simply not

true. Nonetheless in virtually every paper in the body of work reviewed in the literature search ranging from the 1950's to present, the results are reported in terms of  $\varepsilon$ . Some give in addition particular details of the subject bearings diameter, length and clearance, but many do not. Is this appropriate? The answer is - it depends.

The use of  $\varepsilon$  independent of the clearance is justified for purely hydrodynamic bearings as long as the bearing speed is also reported in terms of  $\Lambda$  (which it almost always is). That is because  $\Lambda$ , the similitude parameter for hydrodynamic action due to rotation, invokes the ratio of  $c/R$  and is inversely proportional to the square of the clearance. Thus it can be seen that for a given bearing (fixed radius) that the relationship between hydrodynamic action which has been described in this thesis as being increased by either reducing the minimum bearing gap height (increasing the eccentricity) or increasing the speed is taken in account with  $\Lambda$  such that a four-fold increase in speed, for example, can be seen as an increase in the hydrodynamic action equivalent to reducing the minimum flight height by half.

*The problem for hybrid and hydrostatic bearings is determining an equivalent similitude factor appropriate for describing aerostatic action.* For this reason, it is interesting to review the work done on hybrid and hydrostatic bearings in the literature. This is done in Appendix C.3 so the results can be briefly summarized here. Overall 5 references are reviewed that present results for feedhole bearings and 7 references for porous liner bearings. These numbers include only one reference (J. Su and K. Lie [18]) which compares porous liner hybrid bearings to feedhole hybrid bearings. Only one Z-S Liu et al. [5], describes the pressure wave within the bearing gap. All others present most or all of their results in terms of rotor dynamic stability factors.

#### 4.11.4. Metaphysics of Mass Addition used in this Thesis

##### 4.11.4.1. Dimensionless Time

In Appendix A.1.3.4 it was recommended that the best choice for a dimensionless time is  $\tau=t/t_c$  where  $t_c$  is called the characteristic time which derives naturally from the Reynolds equation and has units of seconds and dimension of  $T$  and is defined as:

$$t_c = 12 \left( \frac{\eta}{p_a} \right) \left( \frac{R}{c} \right)^2$$

The mass addition term from the Reynolds equation is (see Appendix A):

$$\frac{t_c}{k_{\rho\rho} p_a c R \delta \theta \delta z} \dot{M}$$

where the mass, length, time ( $M, L, T$ ) dimensions are :

$$\frac{t_c}{k_{\rho\rho} p_a c R \delta \theta \delta z} \rightarrow \frac{T}{M}$$

$$\dot{M} \rightarrow \frac{M}{T}$$

There has been some concern about the use of  $\delta$ 's in a differential equation although this is how the equation is stated in most literature. To help reconcile this it should be understood that  $cR\delta\theta\delta z$  is the elemental nominal volume of the bearing gap such that the mass flow rate is per unit bearing gap volume. For cosmetic purposes the mass addition term could be rewritten as:

$$\frac{t_c}{k_{\rho\rho} p_a V_{gap}} \dot{M}$$

substituting back in for the characteristic time yields:

$$\frac{12\eta R}{k_{\rho\rho} p_a^2 c^3 \delta \theta \delta z} \dot{M}$$

It should also be noted that the first term contains no variables and is a constant based on “quantities of the problem”. When the bearing has radial displacement

a local bearing gap height and consequently differential gap volume distribution is generated in the bearing gap. The bearing gap volume used in the mass addition term is the nominal volume based on the clearance. However, it is dimensional having dimensions  $T/M$ .

#### 4.11.4.2. Mass Addition Compensation- $Kma$

The problem that each researcher shares is what to use for the mass addition variable,  $\dot{M}$ , which is a function of the operating pressure and the bearing gap pressure (the fundamental variable of the problem) and must have dimensions of  $M/T$ . As was discussed other workers use a mass addition variable based on Darcy flow for porous liners and a different mass addition variable based on orifice theory for feedhole liners. For Darcy flow the “constant of the problem” is expressed in terms proportional to the permeability of the porous liner. The feedhole mass addition variable expression is far more varied and far more complex usually using various discharge coefficients. More problematic is the fact that the feedhole mass addition is considered a point source and is applied only to the differential elements where feedholes are located.

*The theory based numerical CFD work done in this thesis is based on empirically measured mass addition characteristics found for the prototype bushings. The volumetric flow rate for each bushing was measured as the operating pressure was varied from 0 to 60 psig for the bushing exhausting to atmospheric pressure (no shaft present representing infinite clearance).*

For porous liner bushings the expectation was that they would exhibit Darcy flow based on the liner’s permeability. Thus their *volumetric* flow  $Q$  would be expected to be:

$$Q = \frac{KA_{bearing}}{\eta T_{Liner}} (p_{op} - p_a)$$

Since all the measurements were done at ambient pressure  $K$ ,  $A_{bearing}$ ,  $\eta$  and  $T_{Liner}$ , are constant so that a dimensional mass addition constant named in this thesis to be  $Kma$  could be directly measured is:

$$Kma = \frac{KA_{bearing}}{\eta_a T_{Liner}}$$

$Kma$  has EE units of in<sup>5</sup>/s-lbf. The porous liner permeability can easily be calculated from  $Kma$  but this was deemed superfluous and circular since the permeability's use in the Darcy flow model of the mass addition would require the use of the same constants to again recalculate a mass addition factor equal to the empirically determined  $Kma$ . ( $Kma$  is adjusted for temperature in the CFD code based on the viscosity- temperature relationship for air.)

Since the volumetric flow was measured on the pressurized inlet to the bushing it would be expected that the mass flow would be:

$$\dot{M} = \rho Q = Kma \left( k_{\rho p} P_{op} \right) (P_{op} - P_a)$$

The same method was used to determine the equivalent  $Kma$  for feedhole liner bearings.

These results were then used to derive a mass addition constant for each prototype bushing based on the dimensionless pressure variable  $(PP_{op}-P^2)$  where  $P$ , the dimensionless bearing gap pressure was 1 during the testing as bushings were discharging to ambient pressure (see sections 2.1.2 and 2.2.3). One advantage to actually measuring the flow rate constant,  $Kma$ , is that it made an apples-to-apples comparison possible between porous liners and the equivalent feedhole liners that would discharge equivalent total volume of flow at equivalent pressure differences. For the CFD model of porous liner-hybrid bearings  $Kma$  for the bushing was converted to an elemental  $Kma$  by dividing it by the bearing area to derive an equivalent mass flow factor per unit area to be multiplied by the element surface area and applied to all the bearing gap elements (effectively dividing it by the number elements for which mass addition is applied). For feedhole liners  $Kma$  was divided by the number of feedholes and applied directly



as a point source to the elements corresponding to the locations of the feedholes.

Unfortunately, the empirical data indicated that the  $Kma$  factors were not always well represented by a single linear constant and were sometimes better represented by a kinked line with a low pressure differential  $Kma$  and a high pressure differential  $Kma$  and a pivot pressure difference. (see sections 2.2.3 and Appendix D.5).

#### 4.11.5. *Kmeas*

Then the thesis took a different route based on observations of the equations of Poiseuille flow which govern laminar, compressible, viscous flow through a channel. These observations discussed thoroughly in Appendix C, led to the conclusion that both porous mass flow and feedhole mass flow could be expected to be proportional to  $(P_{op}^2 - P^2)$ . The volumetric air flow measurement data was then re-interpreted to determine a different mass flow constant, called *Kmeas*, which was based on this assumption. This mass addition factor, *Kmeas*, did result in a single linear constant for each porous liner and feedhole bushing that modeled the mass flow (see Appendix D.6).

#### 4.11.6. An Ontologically Meaningful Dimensionless Mass Compensation Number

The ramifications of this are important and two-fold. First, the mass addition factor in the equation becomes linearized when the common substitution of  $Q=P^2$  is made. This means that for quasi-static hydrostatic bearings that the Reynolds equation becomes a totally linear equation. This was used to great advantage to generate the  $W/pA$  versus  $h-c$  scans as each scan depended on generating over 400 pressure solutions.

But the second ramification is even more important. When  $Kmeas$  is used in the Reynolds equation the mass addition term becomes (see Appendix C.3.2) for an element is:

$$\left[ \frac{t_c (Kmeas)_{i,j}}{k_{\rho p} p_a c R \delta \theta \delta z} [P_{op}^2 - Q_{i,j}] * \mathbf{Ma} \right]_{MR}$$

where  $\mathbf{Ma}$  is a logical matrix indicating which elements have mass flow. The elemental mass flow constant,  $(Kmeas)_{i,j}$  is simply the total  $Kmeas$  as measured for the bushing divided by the number of elements with mass flow. Thus we can see that mass flow component for the bearing can be written as:

$$\frac{t_c}{k_{\rho p} p_a V_{gap}} Kmeas [P_{op}^2 - Q]$$

$Kmeas$  has units of lb/s or dimensions of  $M/T$ . Thus the term  $\frac{t_c}{k_{\rho p} p_a V_{gap}} Kmeas$

is dimensionless and is completely comprised of “constants of the problem” and is therefore an ontologically meaningful similitude parameter. Substituting for  $t_c$  this term can be seen to formulate an ontologically correct, dimensionless “mass flow bearing number” that incorporates all critical quantities of the bearing dimensions, lubricating fluid properties, and mass addition configuration.

$$\Lambda_m = \frac{6\eta R}{\pi k_{\rho p} p_a^2 L c^3} Kmeas$$

Since this term is inversely proportional to the cube of the clearance it can be seen that for a bearing of fixed  $R$  and  $L$  dimensions that increasing  $K_{meas}$  by a factor of 10 would have the same effect on the mass flow bearing number as increasing the clearance by  $10^{1/3}$  or 2.154. It may be recalled that one of the conclusions brought out in section 5.3.2 (written months previous to this analysis) based on observations of the CFD results presented in section 4.4.3 was that “Changing the  $K_{meas}$  value by a factor of 10 increased the clearance location of the  $W/pA$  maxima by 2-2.7 times with the most common increase being approximately 2.2 times.”

Thus if the  $W/pA$  versus  $h-c$  scans were re-run as  $W/pA$  versus  $H-\Lambda_m$  scans the observed “right shift” would be removed.

Recalling the summary of  $h-c$  locations for the maximum  $W/pA$  value found for porous liner and feedhole bearings when  $K_{meas}$  was varied from  $2 \times 10^{-6}$  to  $2 \times 10^{-4}$  for operating pressures of 100 psig and 10 psig it was previously reported in section 4.4.3 and a summary is repeated here that:

Bearing	$K_{meas}$	pop 100			pop 10		
		WpA max	c	h	WpA max	c	h
Porous	2.00E-06	0.3906	600	0	0.4276	400	0
Porous	2.00E-05	0.3917	1200	0	0.4291	900	0
Porous	2.00E-04	0.3882	2600	0	0.4237	2190	0
12 x FH	2.00E-06	0.0737	450	110	0.0736	370	100
12 x FH	2.00E-05	0.074	1090	250	0.0735	760	190
12 x FH	2.00E-04	0.0742	2190	530	0.0738	1840	470

Repeat of figure 4-33 showing the location of the maximum  $W/pA$  in the  $h-c$  plane.

Reporting these locations in terms of  $Kmeas/c^3$  and  $H$  results in this restatement:

Bearing	$Kmeas$	pop 100			pop 10		
		WpA max	$Kmeas/c^3$	H	WpA max	$Kmeas/c^3$	H
Porous	2.00E-06	0.3906	9,259	0	0.4276	31,250	0
Porous	2.00E-05	0.3917	11,574	0	0.4291	27,435	0
Porous	2.00E-04	0.3882	11,379	0	0.4237	19,041	0
12 x FH	2.00E-06	0.0737	21,948	0.244	0.0736	39,484	0.270
12 x FH	2.00E-05	0.074	15,444	0.229	0.0735	45,561	0.250
12 x FH	2.00E-04	0.0742	19,041	0.242	0.0738	32,105	0.255

Figure 4-98 Results of replacing  $c$  and  $h$  with  $Kmeas/c^3$  and  $H$ .

Although use of  $Kmeas/c^3$  does not precisely fix the clearance location (independent of  $Kmeas$ ) it is interesting to note that  $H>0$  location of the maximum  $W/pA$  for the feedhole bearings which demonstrates their “near surface effect” or in the terminology Liu and Xu [5] could be called the onset of static instability, is found at a very narrow band of  $H=0.24-0.27$  which corresponds to  $\varepsilon=0.73-0.76$ .

If it is assumed that the  $Kmeas/c^3$  is independent of  $Kmeas$  and that the average value found for each grouping is the closest expression of the “true” value, then it is possible to back-calculate what the clearance would have to be for  $Kmeas/c^3$  to reach the average value.

Bearing	$Kmeas$	pop 100					pop 10				
		WpA max	c μin	c for ave $Kmeas/c^3$	diff	% diff	WpA max	c μin	c for ave $Kmeas/c^3$	diff	% diff
Porous	2.00E-06	0.391	600	571	-29	-4.8%	0.428	400	426	26	6.4%
Porous	2.00E-05	0.392	1200	1230	30	2.5%	0.429	900	917	17	1.9%
Porous	2.00E-04	0.388	2600	2651	51	2.0%	0.424	2190	1976	-214	-9.8%
12 x FH	2.00E-06	0.074	450	474	24	5.3%	0.074	370	371	1	0.4%
12 x FH	2.00E-05	0.074	1090	1021	-69	-6.4%	0.074	760	800	40	5.3%
12 x FH	2.00E-04	0.074	2190	2199	9	0.4%	0.074	1840	1724	-116	-6.3%

Figure 4-99 Comparison of calculated clearance using average value of  $Kmeas/c^3$  to clearance value used in  $W/pA$  versus  $h-c$  scan.

When this is done it can be seen that clearance differences are relatively small. It has to be remembered that the  $W/pA$  surface generated in the  $W/pA-hc$  scans is an interpolant from 400 data points taken in a  $20 \times 20$  mesh of clearances in the  $h-c$  plane. The clearance increments run from  $100 \mu\text{in}$  to  $3000 \mu\text{in}$ . Thus the clearance increment is  $142 \mu\text{in}$ . The  $h$  increment depends on the clearance. For a clearance of  $100 \mu\text{in}$  it is as small as  $5 \mu\text{in}$  whereas for a clearance of  $3000 \mu\text{in}$  it is as large as  $150 \mu\text{in}$ . Thus when the apparent clearance error is viewed in terms of the size of the interpolant mesh it can be seen that it is smaller than the interpolant grid size.

Appendix A.1.3.4 concluded that the most appropriate way to create a dimensionless time was to scale it against a “critical time”,  $t_c$ , which is suggested from the governing Reynolds equation and is purely comprised of constants of the problem. Its value can now be seen. If the Reynolds equation is non-dimensionalized using  $t_c$  to scale dimensionless time such that  $\tau = t/t_c$  it becomes (equation A-2):

**Equation A-2** Dimensionless Reynolds Equation:

$$-\frac{\partial}{\partial \theta} \left( PH^3 \frac{\partial P}{\partial \theta} \right) + \Lambda \frac{\partial}{\partial \theta} (PH) - \left( \frac{R}{L} \right)^2 \frac{\partial}{\partial Z} \left( PH^3 \frac{\partial P}{\partial Z} \right) + \frac{\partial}{\partial \tau} (PH) = \frac{t_c}{k_{pp} p_a c R \delta \theta \delta z} \dot{M}$$

which can now be seen to be rewritten as simply:

$$-\frac{\partial}{\partial \theta} \left( PH^3 \frac{\partial P}{\partial \theta} \right) + \Lambda \frac{\partial}{\partial \theta} (PH) - \left( \frac{R}{L} \right)^2 \frac{\partial}{\partial Z} \left( PH^3 \frac{\partial P}{\partial Z} \right) + \frac{\partial}{\partial \tau} (PH) = \Lambda_M (P_{op}^2 - P^2)$$

where  $\Lambda$ ,  $\Lambda_m$ , and  $L/D$  ( $L/D$  appears as  $R/L$  in the equation but the slenderness ratio of  $L/D$  is traditional) form a complete set of ontologically correct similitude parameters that allow the extension of results to all hybrid bearings that share the same similitude factors and mass addition configurations. It should be noticed that the squeeze parameter or transient bearing number,  $\sigma$ , disappears from this form of the equation. This is highly appropriate. And the reason is straightforward and clear. In equation A-2 the characteristic time  $t_c$  is used to

non-dimensionalize time. The characteristic time is a function of the bearing geometry and the gas properties only which is appropriate when there are multiple, independent, dynamic actions taking place.

#### 4.11.7. A Re-Examination of Non-Dimensionalizing the Reynolds Equation

The examination so far calls into question the accepted methodology of non-dimensionalizing the Reynolds equation. It can clearly be seen that the equation can easily be made dimensionless by multiplying through each term of the equation by a set of “constants of the problem” with the inverse dimensions of the dimensional equation. When this is done some constants of the system disappear from the terms of the equation where they naturally occurred, and re-appear in terms of the equation unrelated to the constant of the system. This is particularly problematic when there are multiple, independent, hydrodynamic activities occurring, such as the hybrid bearing with rotation and external pressurization. Another example is the “squeeze-film” bearings [69] [75] where piezoelectric excitation is applied to the bushing to create a “self generated” squeeze film pressure. This has been used as substitute for aerostatics to provide support at low rotational speeds and boost stability at high rotation speeds.

As has been discussed, the primary culprit in inappropriate non-dimensionalization has been the reference constants used to non-dimensionalize time. References have been cited that have used rotation speed, the orifice air flow velocity, the whirl frequency etc. to accomplish this with the result that “time stands still” for all hydrodynamic activities when the “chosen” hydrodynamic activity is stopped. Early on this was recognized in this thesis so that a “characteristic time” was defined that naturally occurred in the Reynolds equation and was only a function of geometric constants and gas properties. This characteristic time is based on the observation that the ratio of viscosity and pressure has a pure time dimension so that it makes sense to apply it across the board to all terms of the equation. However, the characteristic time used in Appendix A was taken from the cluster of constants arising naturally in the prefactor of the circumferential Poiseuille term. As such it carries with it not only



the viscosity to pressure ratio that contributes the time dimension but also uses the square of the dimensionless  $R/c$  ratio. In fact,  $t_c$  is very similar to  $\Lambda$  in this regard so that  $t_c = 2\Lambda/\omega$ . Interestingly, this is what Czolczynski [25] used to create his dimensionless time. But is this the best method?

Let us return to equation A-10 derived in Appendix A as the “pure” form of the Reynolds equation for the bearing gap in cylindrical coordinates before any dimensionless substitutions were made and “start over”.

**Equation A-10** Dimensional Reynolds equation in cylindrical coordinates

$$-\frac{\partial}{R\partial\theta}\left(\frac{\rho h^3}{\eta}\frac{\partial p}{R\partial\theta}\right) + 6\frac{\partial}{\partial\theta}(\omega\rho h) - \frac{\partial}{\partial z}\left(\frac{\rho h^3}{\eta}\frac{\partial p}{\partial z}\right) + 12h\frac{d\rho}{dt} + 12\rho(V_B - V_S) = 12\frac{\dot{M}}{R\delta\theta\delta z}$$

We see that equation A-10 actually has 6 terms each relating to different hydrodynamic activities. From left to right they are:

- 1) Pressure gradient driven circumferential flow (Poiseuille flow).
- 2) Circumferential flow caused by the parallel relative velocity of the surfaces (rotation driven Couette flow)
- 3) Pressure gradient driven axial flow (Poiseuille flow).
- 4) Transient term for time gradient of density change in the bearing gap volume.
- 5) Flow caused by the relative normal velocity of the surfaces (squeeze term).
- 6) Mass addition to the bearing gap by external pressurization.

A-10 could be rewritten as:

$$-\frac{\partial}{R\partial\theta}\left(\frac{\rho h^3}{\eta}\frac{\partial p}{R\partial\theta}\right) + 6\frac{\partial}{\partial\theta}(\omega\rho h) - \frac{\partial}{\partial z}\left(\frac{\rho h^3}{\eta}\frac{\partial p}{\partial z}\right) + 12h\frac{d\rho}{dt} + 12\rho(V_B - V_S) = \frac{12}{R\delta\theta\delta z}\frac{dM_{ext}}{dt}$$

where  $M_{ext}$  is the mass flowing through the bushing surface due to external pressurization.

Let us proceed to replace density with pressure using the ideal gas law so that:

$$\rho = \frac{P}{Rt} = k_{\rho p} P$$

and make the usual dimensionless substitutions.

$$H = \frac{h}{c} \text{ and } Z = \frac{z}{L}$$

However, in this analysis let us challenge the common method of using the ambient pressure as the reference pressure. It should be recalled from section 4.4.2 that it was shown that  $W/pA$  was the hydrostatic bearing efficiency where the reference pressure,  $p$ , was the *operating* pressure. This suggests that for an externally pressurized bearing that the operating pressure might be the more appropriate reference pressure as the operating pressure is generally 4 to 5 times the ambient pressure. For the moment let us simply make the dimensionless pressure substitution based on an unspecified reference pressure,  $p_{ref}$ . As a result we get:

$$\begin{aligned} & -\frac{c^3 p_{ref}^2 k_{\rho p}}{\eta R^2} \frac{\partial}{\partial \theta} \left( PH^3 \frac{\partial P}{\partial \theta} \right) + 6c\omega k_{\rho p} p_{ref} \frac{\partial}{\partial \theta} (PH) \\ & -\frac{c^3 p_{ref}^2 k_{\rho p}}{L^2 \eta} \frac{\partial}{\partial Z} \left( PH^3 \frac{\partial P}{\partial Z} \right) + 12cp_{ref} k_{\rho p} H\dot{P} + 12cp_{ref} k_{\rho p} P\dot{H} = 12 \frac{\dot{M}}{R\delta\theta\delta z} \end{aligned}$$

While this equation is expressed in terms of purely dimensionless variables  $(P, H, Z, \theta)$  each term has the dimensions of  $M/TL^2$  corresponding to mass flux.

The most typical approach to non-dimesionalizing the equation would be to multiply each term by the inverse of the first cluster of constants:

$$\frac{\eta R^2}{c^3 p_{ref}^2 k_{\rho p}}$$

Doing this would result in the familiar dimensionless form of the Reynolds equation. But let us pause a moment and express some concern about this procedure. While it algebraically simplifies the equation and makes it dimensionless, it also applies “constants of the problem” to terms in which they do not naturally occur and removes them from terms from which they do occur.

For the sake of argument let us try a different tack. In order to non-dimensionalize each term we must multiply the equation by something with dimensions of  $TL^2/M$ . Are there any combinations of constants of the system that might be more universally applicable to each term?

Two candidates come immediately to mind they are:  $c/\eta$  and  $\eta/ck_{\rho\rho}p_{ref}^2$  both of which have dimensions of  $TL^2/M$ . Of the two, the second looks the more interesting as the product of  $k_{\rho\rho}$  and  $p_{ref}$  would be the reference density of the gas so that the second suggestion contains all the relevant gas properties along with the clearance that is the critical reference length for every hydrodynamic activity in the bearing gap. Applying this result in:

$$-\left(\frac{c}{R}\right)^2 \frac{\partial}{\partial \theta} \left( PH^3 \frac{\partial P}{\partial \theta} \right) + \frac{6\omega\eta}{p_{ref}} \frac{\partial}{\partial \theta} (PH)$$

$$-\left(\frac{c}{L}\right)^2 \frac{\partial}{\partial Z} \left( PH^3 \frac{\partial P}{\partial Z} \right) + \frac{12\eta}{p_{ref}} (H\dot{P} + P\dot{H}) = \frac{12\eta}{k_{\rho\rho} p_{ref}^2 \delta V_{gap}} \dot{M}$$

where

$$\delta V_{gap} = cR\delta\theta\delta z$$

Applying the observations from Appendix C.2 that,

$$\dot{M} = K_{meas} [P_{op}^2 - P^2]$$

results in equation 4-1.

**Equation 4-1** Restatement of the dimensionless Reynolds equation:

$$-\left(\frac{c}{R}\right)^2 \frac{\partial}{\partial \theta} \left( PH^3 \frac{\partial P}{\partial \theta} \right) + \frac{6\omega\eta}{p_{ref}} \frac{\partial}{\partial \theta} (PH)$$

$$-\left(\frac{c}{L}\right)^2 \frac{\partial}{\partial Z} \left( PH^3 \frac{\partial P}{\partial Z} \right) + \frac{12\eta}{p_{ref}} (H\dot{P} + P\dot{H}) = \frac{12\eta}{k_{\rho p} p_{ref}^2 \delta V_{gap}} K_{meas} [P_{op}^2 - P^2]$$

where

$$\delta V_{gap} = cR\delta\theta\delta z$$

This appears to be a very likeable equation and appears to more properly define dimensionless bearing numbers that are more ontologically correct for similitude comparisons. In terms of geometric similitude the traditional parameters are the slenderness ratio,  $L/D$ , and  $c/R$ . Equation 4-1 uses instead  $c/R$  and  $c/L$  which is pleasing in that it emphasizes the importance of the clearance in determining all the hydrodynamic action. Obviously, however, bearings that are geometrically similar in  $L/D$  and  $c/R$  will also be geometrically similar in  $c/R$  and  $c/L$ . The advantage of equation 4-1 lies in the bearing numbers related to transient terms (the squeeze terms) and the time rate driven mass addition term. Other strategies to non-dimensionalize these terms results in either the rotation speed appearing in the squeeze and mass addition terms or an orifice velocity appearing in the squeeze term.

While equation 4-1 is dimensionless the time variable,  $t$ , is dimensional. The pitfalls of selecting the wrong time dimensioned reference constant has already been discussed. The recommendation was made that the ratio of the reference

viscosity and pressure be used as these are constants of the system shared by all sources of hydrodynamic activity in the bearing gap. Doing so eliminates the squeeze term and equation 4-1 becomes equation 4-2.

**Equation 4-2** The restated dimensionless Reynolds equation

$$-\left(\frac{c}{R}\right)^2 \frac{\partial}{\partial \theta} \left( PH^3 \frac{\partial P}{\partial \theta} \right) + \frac{6\omega\eta}{p_{ref}} \frac{\partial}{\partial \theta} (PH)$$

$$-\left(\frac{c}{L}\right)^2 \frac{\partial}{\partial Z} \left( PH^3 \frac{\partial P}{\partial Z} \right) + 12H \frac{\partial P}{\partial \tau} + 12P \frac{\partial H}{\partial \tau} = \frac{12\eta}{k_{\rho p} p_{ref}^2 \delta V_{gap}} K_{meas} [P_{op}^2 - P^2]$$

where

$$\delta V_{gap} = cR\delta\theta\delta z$$

The changes to these terms are shown in figure 4-98.

Bearing numbers	Common	Equation 4-1
Rotational	$\Lambda = \frac{6\eta\omega}{p_a} \left(\frac{R}{c}\right)^2$	$\Lambda = \frac{6\eta\omega}{p_{ref}}$
Squeeze term	$\sigma = \frac{12\eta\omega}{p_a} \left(\frac{R}{c}\right)^2$	$\sigma = 12$
Mass addition	No common agreement	$\Lambda_m = \frac{12\eta}{k_{\rho\rho} p_a^2 \delta V_{gap}} K_{meas}$
Time	Common approaches use $\omega$ , or an orifice velocity, or the whirl frequency across the board.	$t_c = 12 \left(\frac{\eta}{p_a}\right) \left(\frac{R}{c}\right)^2$ Was used in Appendix A. Equation 4-1 uses $\eta/p_{ref}$
Universal non-dimensionalization constant	$\frac{\eta R^2}{c^3 p_a^2 k_{\rho\rho}} = \frac{\eta}{p_a \rho_a c} \left(\frac{R}{c}\right)^2$	$\frac{\eta}{c k_{\rho\rho} p_{ref}^2} = \frac{\eta}{c \rho_{ref} p_{ref}}$

Figure 4-100 Different approaches to non-dimensionalizing the Reynolds equation for a hybrid gas journal bearing.

At first glance it appears that the mass addition bearing number derived in equation 4-1 “shoots in the foot” the previous argument that for a given bearing with a fixed length and diameter (or radius) that increasing  $K_{meas}$  was equivalent to increasing the inverse of the cube of the clearance. But if one looks at the hydrostatic form of equation 4-1 which is,

$$-\left(\frac{c}{R}\right)^2 \frac{\partial}{\partial \theta} \left( PH^3 \frac{\partial P}{\partial \theta} \right) - \left(\frac{c}{L}\right)^2 \frac{\partial}{\partial Z} \left( PH^3 \frac{\partial P}{\partial Z} \right) = \frac{12\eta}{k_{\rho\rho} p_{ref}^2 c R \delta \theta \delta z_{gap}} Kmeas [P_{op}^2 - P^2]$$

versus the hydrostatic form of equation A-1 which is,

$$-\frac{\partial}{\partial \theta} \left( PH^3 \frac{\partial P}{\partial \theta} \right) - \left(\frac{R}{L}\right)^2 \frac{\partial}{\partial Z} \left( PH^3 \frac{\partial P}{\partial Z} \right) = \frac{12Kmeas}{k_{\rho\rho} p_a c R \delta \theta \delta z} \left(\frac{\eta}{p_a}\right) \left(\frac{R}{c}\right)^2 (P_{op}^2 - P^2)$$

one can see that both equations support that conclusion. With the assumption that the only “constants of the system” being varied are  $c$  and  $Kmeas$ , either equation can be manipulated into the form

$$-\frac{\partial}{\partial \theta} \left( PH^3 \frac{\partial P}{\partial \theta} \right) - \left(\frac{R}{L}\right)^2 \frac{\partial}{\partial Z} \left( PH^3 \frac{\partial P}{\partial Z} \right) = (Kmeas/c^3) x [P_{op}^2 - P^2].$$

In section 6.1 *Future Analytical Work* (written months before this section) the need was identified to “Search for the speculated dimensionless clearance factor that relates static  $W/pA$  maxima locations on the h-c plane to  $Kmeas$ .” It is felt that this section has successfully completed that task.

## CHAPTER 5. CONCLUSIONS, HYPOTHESIS, AND DISCUSSION

### 5.1. Conclusions and Hypothesis from Analytical Work

#### ***Value of maintaining separate terms***

Maintaining separate terms for Couette  $\theta$ , Poiseuille  $\theta$ , Poiseuille Z, “air hammering” (change in element volume with respect to time), pressure time transient, and mass addition fluxes in the Reynolds equation and subsequent discretization, proved to be a valuable asset in subsequent examination and characterization of CFD results.

The dynamics of a hybrid bearing are the result of the interaction of these very different hydrodynamic phenomena. It is of utmost importance to the designer of a bearing that is required to meet certain application demands, to have an intuitive insight into the interplay among these hydrodynamic “actions”.

#### ***Use of $t_c$ as a basis for dimensionless time***

Using a characteristic time based on the ratio of viscosity and pressure as a means to form a dimensionless time is meaningful. Pressure, with dimensions of  $M/LT^2$  is the driving force of viscous flow. Viscosity, which has dimensions of  $M/LT$  is the resistance factor that proportions how viscous flow is accelerated by a pressure gradient. The ratio of viscosity to pressure yields units of time. How quick will the flow change? It depends on the on the magnitude of the pressure gradient in relation to how viscous the fluid is.



In the derivation of the dimensionless Reynolds equation the following characteristic time presented itself:

$$t_c = 12 \left( \frac{R}{c} \right)^2 \left( \frac{\eta}{p_a} \right)$$

Thus a dimensionless time was defined by:

$$\tau = \frac{t}{t_c}$$

The CFD solutions in this thesis deal only with steady state bearings so this factor is not used but it will be useful in future time-dependent work.

***W/pA where p is the gage operating pressure is the static journal bearing efficiency.***

The ratio of the bearing load capacity  $W$  to the product of a significant pressure  $p$  times the nominal bearing area  $A$  ( $LxD$ ) is commonly used as the dimensionless load capacity. *For a purely hydrodynamic journal bearing* (rotating shaft without mass addition) the ambient pressure is typically used for  $p$ . For example,

Williams pg 308 uses  $\frac{W}{2RLp_a}$  for the dimensionless load.  $W$ , the bearing load

force is what in this thesis we have been calling the net hydrodynamic force. For a purely hydrodynamic bearing it is worth noting that this force is mostly perpendicular to the bearing displacement and is thus not a restorative force but generates bearing whirl.

*For a hydrostatic journal bearing* (mass addition but no shaft rotation) with mass addition supplied by a high pressure gas reservoir at an “operating pressure”,  $p_{op}$ , we presented analytical arguments that indicate that if the gage operating pressure is used as the scaling pressure in  $W/pA$  then  $W/pA$  is in fact the static journal bearing efficiency in that it represents the ratio of the bearing load capacity to its maximum possible bearing load capacity. For a hydrostatic

bearing the attitude angle is 0 and the net hydrodynamic load is completely restorative and hence it is a true representation of the bearing's load capacity.

What scaling pressure should be used in  $W/pA$  for a *hybrid journal bearing* (shaft rotation and mass addition)? The two obvious choices are either the ambient pressure or the operating pressure. A third option would be to use the average of the ambient and operating pressures.

A suggestion would be to use the gage operating pressure (operating pressure minus the ambient pressure) as this would represent the amount of "pressurization" of the bearing gap.

***The substitution of  $Q$  for  $P^2$  linearizes Poiseuille flow and makes an analytical solution possible. Using Poiseuille flow as the model for pressure driven compressible fluid flow through a restriction such as mass addition via feedholes or porous liners, suggested a useful linear characterization constant for mass addition.***

This mass addition factor, which was labeled  $K_{meas}$  in this thesis is the compressible fluid analogy to the Darcy which is used in hydraulics to quantify the permeability of porous media in relation to an incompressible fluid. The Darcy represents a resistive factor that scales volumetric flow as proportional to the pressure gradient, and area perpendicular to the pressure gradient, and inversely proportional to the viscosity. The Darcy has dimensions of  $L^2$ . For incompressible flow, the volumetric flow and the mass flux are the same thing. However, if the gradient of the square of the pressures is used a similar factor,  $K_{meas}$ , can be used to scale mass flux of a compressible fluid.  $K_{meas}$  has dimensions of  $M/T$  and in this thesis it has EE units of lbs/s.

## 5.2. Conclusions from Testing

***Use of a single, mass addition constant,  $K_{meas}$ , (lbs/s) proportioning mass addition to the square of the operating pressure was an effective and simple way to characterize mass addition of both porous liners and feedhole liners.***

The analytical work of solving Poiseuille flow by substituting  $Q=P^2$  and relating it to pressure driven mass addition of a compressible fluid through a restriction brought the conclusion that mass addition could be expected to follow the linear relationship:

$$\dot{M} = K_{meas} (P_{op}^2 - P^2)$$

A re-examination of the flow data found this to be in good agreement with the flow measurements taken so that the mass addition of feedhole bearings and porous liner bearings was well modeled and characterized by the linear scaling factor,  $K_{meas}$ . This greatly simplified the CFD calculations.

### 5.3. Conclusions from CFD Experiments

#### 5.3.1. Overall CFD Conclusions

***Use of the CFD microscope to characterize gap pressure distributions is very useful to a conceptual understanding of the hydrodynamic phenomena.***

#### 5.3.2. Static (Hydrostatic) Testing Conclusions

***CFD experiments duplicating the empirical static tests of prototype bearings confirmed the credibility of the CFD calculations.***

***Mapping static journal bearing  $W/pA$  on either the  $h-c$  or  $H-c$  plane is a very powerful method of characterizing and visualizing bearing performance.***

***For purely hydrostatic bearings (bearings with mass addition but no rotation):***

- ***The attitude angle is always  $0^\circ$  so that the hydrodynamic force is always restorative (opposite direction to the bearing displacement).***
- ***The hydrodynamic force is 0 when  $H=1$  (eccentricity ratio=0) and generally increases as the eccentricity ratio increases ( $H$  goes to 0) to a maximum “grounding force” at  $H=0$  (eccentricity ratio=1). However the rate of increase is non-linear and under some circumstances, a “near surface effect” occurs where the maximum force is generated at  $H>0$  so that bearing has negative stiffness for small  $H$ .***

***The  $W/pA$  versus  $H$  plots can have very different shapes than is commonly supposed. Some circumstances create a “near surface effect” where the maximum  $W/pA$  does not occur at  $H=0$ .***

It is common belief that the dimensionless load,  $W/pA$  as a function of dimensionless minimum flight height,  $H$  for air journal bearings follows curves similar to those found from testing flat static bearings. The expected characteristic curve was that  $W/pA$  would have its maximum when  $H=0$  corresponding to the “grounding force” which is generated when the minimum gap height goes to 0. As  $H$  increases  $W/pA$  is expected to decrease, quickly at first, and then more gradually so that it is 0 when the shaft and bushing are concentric at  $H=1$ .

In all cases examined here  $W/pA=0$  when  $H=1$ , and in most cases  $W/pA$  reaches its maximum value as  $H$  goes to 0 (numerical solutions for  $H=0$  are not possible using the CFD methods developed in this thesis for FH bearings). What differs from expectation is the shape of the curve. The slope of the curve indicates the bearing stiffness. The expectation was that the stiffness would be greatest at small  $H$  and decrease to 0 as  $H$  increased to 1. Such was the response for porous liners with large clearances, but as the clearance was decreased, the curve became nearly linear (constant stiffness) and then inverted so that the stiffness was decreasing with increasing  $H$ .

Thus porous liner bearings lived up to the common expectation in that the largest  $W/pA$  (which would be the grounding force) occurs as  $H$  goes to 0. But the porous liner bearings did not always follow the common expectation that the greatest stiffness would correspond to smallest  $H$ . At times the stiffness was nearly constant and at times the greatest stiffness was found at larger values of  $H$ .

Feedhole bearing results differed by an even greater extent. Bearings with larger feedholes (higher  $K_{meas}$ ) and low clearances gave the expected response. However, as clearance was increased and  $K_{meas}$  was decreased, not only did the stiffness first become constant and then decrease so that the highest stiffness was at  $H>0$ , the stiffness became *negative* in cases of large clearances with low  $K_{meas}$  at small  $H$  and the maximum  $W/pA$  was not at  $H=0$  but at  $H>0$ . Thus the feedhole bearings defied common expectations in every way. In some cases they did show highest  $W/pA$  and highest stiffness at smallest  $H$  but in other cases they did not. Under some conditions the highest  $W/pA$  did not occur at  $H=0$  leading to negative stiffness at small  $H$ . This latter phenomena is what has been called in this thesis the “Near Surface Effect”.

***Mapping  $W/pA$  on either the  $h-c$  or  $H-c$  plane explains the variation in the shape of  $W/pA$  versus  $H$  plots.***

For porous liner bearings the  $W/pA$  maximum is always at a clearance on the  $H=0$  line. A plot of  $W/pA$  vs.  $H$  at a specific clearance is a contour line that represents the cross-section of the  $W/pA$  surface at the specified clearance. Because the  $W/pA$  maxima is always on the  $H=0$  line, the porous liner bearings always meet the common expectation of having the highest  $W/pA$  at  $H=0$ . The shape of the  $W/pA$  vs  $H$  curve depends on the clearance at which the cross-section is taken.

For the Feedhole bearings, the maximum of the  $W/pA$  surface in the  $H-c$  plane always occurs at an  $H>0$  but, depending on the clearance for which a contour plot is taken, the contour plot maximum of  $W/pA$  may or may not occur at  $H=0$ . A line may be drawn on the  $W/pA$  versus  $H-c$  plane that joins the maximum  $W/pA$  for each clearance. This line intersects the  $H=0$  axis at a characteristic clearance and then sweeps upwards with increasing  $H$  as the clearance increases.  $W/pA$  versus  $H$  plots taken at clearances less than this characteristic intersecting clearance will have maximum  $W/pA$  at  $H=0$ .  $W/pA$  versus  $H$  plots taken at

clearances greater than this characteristic intersecting clearance will indicate the near surface effect and have maximum  $W/pA$  at  $H>0$ . The maximum  $W/pA$  will occur at greater  $H$  locations as the clearance of the  $W/pA$  versus  $H$  plot increases.

Detailed discussion is in section 4.3.

***Use of the CFD microscope indicates that the near surface effect is due to the pressure distribution about the feedholes located at the angular position of  $h_{min}$ .***

Discussion of this is in section 4.5.3.

***The  $W/pA$  vs  $H$ -c maps indicated that the  $W/pA$  maximum value is primarily determined by the mode of the of mass addition. Porous liner bearings have much higher maximum  $W/pA$  of 0.388 to 0.429 than the 12xfeedhole fed bearings which have maximum  $W/pA$  of 0.0735 to 0.0742.***

The CFD results indicated that the maximum  $W/pA$  for porous liners was about 0.429. This occurs at an optimum clearance that depends mostly on the mass addition factor  $Kmeas$  and to a far lesser degree on the operating pressure. For example for operation at 100psig, the maximum  $W/pA$  of 0.39 occurred at clearances of 600  $\mu$ in, 1200  $\mu$ in, and 2600  $\mu$ in for  $Kmeas$  values of  $2 \times 10^{-6}$  lbs/s,  $2 \times 10^{-5}$  lbs/s, and  $2 \times 10^{-4}$  lbs/s. Slightly higher values of about 0.429 were found with an operating pressure of 10 psig. These occurred at clearances of 400  $\mu$ in, 900  $\mu$ in, 2000  $\mu$ in for the same values of  $Kmeas$ .

We hypothesized from the empirical tests that  $W/pA$  for porous liner bearings would have a maximum of about 0.40 and decrease with increasing  $H$ . This result confirms the CFD  $W/pA$  maximum values. The amendment that needs to be made to the empirical hypothesis is that in order to achieve maximum  $W/pA$ , the clearance must be tuned to  $Kmeas$ . In the empirical testing two porous liners were used (porous graphite and porous alumina) with very different  $Kmeas$  of  $2.71 \times 10^{-5}$  lbs/s and  $5.0010^{-4}$  lbs/s. The maxima occurred for clearances of 1050

$\mu\text{in}$ , 622  $\mu\text{in}$ , and 322  $\mu\text{in}$  for the porous graphite and 1536  $\mu\text{in}$ , 557  $\mu\text{in}$ , and 282  $\mu\text{in}$  for the porous alumina.

For feedhole bearings the CFD results indicated maximum  $W/pA$  of 0.0737 to 0.0742 for 100 psig operation and 0.0735 to 0.0742 for 10 psig operation. The hypothesis was made from the experimental test results that the maximum  $W/pA$  was about 0.14 and dropped with  $H$  to  $<0.1$  at  $H=0.2$ . Re-examination of the test data indicates that there are many data points with a maximum  $W/pA$  of around 0.06 to 0.07 with some “outliers” of higher values. The maximum  $W/pA$  occurs around  $H=0$ , and, for such small values of  $W/pA$ , in the empirical testing it was difficult to ascertain when the bearing was grounded versus when the bearing still had a small  $H$ . This could lead to mistakenly high  $W/pA$  readings near  $H=0$ . Regardless the empirical testing confirms that the maximum  $W/pA$  for feedhole bearings was small compared the porous liner bearings and was in the order of magnitude of 0.1, the same as the CFD results.

***The  $W/pA$  versus  $H$ - $c$  maps for greatly varying  $K_{meas}$  had essentially the same maximum values of  $W/pA$  but the location of the maximum  $W/pA$  in the  $H$ - $c$  plane shifted fairly predictively to increased clearances with increased  $K_{meas}$ .***

Changing the  $K_{meas}$  value by a factor of 10 increased the clearance location of the  $W/pA$  maxima by 2 to 2.7 times with the most common increase being approximately 2.2 times. Each mapping was the result of interpolating results of the integration of 600 pressure distributions with a relatively coarse 31x96 numerical grid. This could account for the variation of the  $K_{meas}$  to clearance scaling factor which is here hypothesized to be a constant value of about 2.2.

These results lead us to further speculation that there is a missing length characteristic parameter that is related strongly to  $K_{meas}$  and might also involve operating pressure and viscosity. Such a characteristic length, if it exists, could be used to create a dimensionless clearance so that a single  $W/pA$  versus  $H$ -



*dimensionless clearance* could be found to represent a bearing under all operating conditions.

### 5.3.3. Rotating Bearings

***With the CFD methodology developed in this thesis, numerical speed limits were encountered above which pressure distributions could not be found. Factors that expanded the numerical speed limit were the hydrostatic strength of the bearing and small eccentricity ratios.***

The highest speed for which a pressure distribution solution was obtainable depended on the type of bearing and the eccentricity ratio. The most restrictive were hydrodynamic bearings. Mass addition eased the restriction with the highest speeds obtained for PL hybrid bearings which were the “stronger” of the two hybrid bearings in that they have a much higher hydrostatic force contribution. The “hydrostatic strength” of the bearing follows which is the magnitude of the hydrostatic force contribution to the net hydrodynamic force. Thus hydrostatic strength would be the static  $W/pA$  of the bearing multiplied by the operating pressure.

Bearing	$\epsilon$	Max speed RPM
HY	0.50	200K
HY	0.75	140K
HY	0.90	60K
PL	0.90	300K
FH	0.90	140K

Figure 5-1 Numeric speed limits found for obtaining pressure solutions for rotating bearings with a clearance of 0.002” operating pressure of 60 psig.

***For purely hydrodynamic bearings (bearings with rotation and no mass addition):***

- ***Hydrodynamic force increases relatively linearly with speed with higher slopes for higher eccentricity ratios.***
- ***The attitude angle approaches 90° when the speed approaches 0 and increases with increased speed. The speed effects the attitude angle more for bearings with higher eccentricity ratios.***

***For hybrid bearings***

- ***The attitude angle is 0 at 0 RPM (static bearing solution) and increases with increased RPM. The increase in attitude angle with speed is smaller for hybrid bearings with greater “hydrostatic strength”.***
- ***The net hydrodynamic force increases non-linearly with speed with larger rates of increase for higher speeds as the rotating hydrodynamic strength becomes larger compared to the hydrostatic strength.***
- ***Hybrid bearings are hypothesized to be more stable than purely hydrodynamic bearings relative to their hydrostatic strength.***

The concept of hydrostatic and hydrodynamic strength comes from the observation that for both hydrostatic and purely hydrodynamic bearing the strength of the hydrodynamic force depends mostly on  $h_{min}$  rather than the dimensionless  $H$  or the eccentricity ratio. In this regard, the PL hybrid bearings have much higher hydrodynamic strength in that they generate net hydrodynamic forces 4-6 times greater than FH hybrid bearings at 0 RPM for equivalent  $h_{min}$ ,

clearance and  $K_{meas}$ . The net hydrodynamic force of a hybrid bearing operating at 0 RPM is, of course, its static bearing force ( $W$ ). This force is always at 0 attitude angle and is restorative in that it resists further displacement of the bearing and tries to return the bearing to its neutral concentric position. The net hydrodynamic force generated by a purely hydrodynamic bearing (rotation and no mass addition) is very different. This force has an attitude angle that approaches  $90^\circ$  at small RPM then increases to greater than  $90^\circ$  as speed is increased. Its force components compared with the bearing displacement behave in the following manner. As speed is increased from 0, a significant perpendicular component is generated while the anti-restorative component is near 0. As speed is increased further the perpendicular component increases quickly compared with the anti-restorative component but the rate of change of the anti-restorative component increases so that at high RPM it is more influential.

For the most part, for hybrid bearings, the net hydrodynamic forces can be understood as the sum of the hydrodynamic force and the hydrostatic force. At 0 RPM the net hydrodynamic force is simply the hydrostatic force and is completely restorative with a 0 attitude angle. As speed is increased, the growing anti-restorative component of the hydrodynamic force contribution subtracts from the restorative hydrostatic force while it adds a perpendicular force so that the net hydrodynamic force increases only slightly in magnitude while the attitude angle increases. As speed increases further, the restorative force component continues to decline and then reverses to become anti-restorative while the perpendicular force component continues to increase. When the restorative component is 0 the attitude angle is  $90^\circ$ . The speed at which this occurs depends on the hydrodynamic strength of the bearing. For example the weak FH hybrid bearing with  $h_{min}=0.0002''$ , a clearance of  $0.002''$ , and  $K_{meas}=2 \times 10^{-4}$  lbs/s, operated at 60psig will have an attitude angle of  $90^\circ$  at about 120K RPM

whereas an equivalent PL hybrid bearing under the same conditions has an attitude angle of  $70.38^\circ$  at 300K RPM.

The effects of these observations on bearing stability are discussed in section 4.8.2.

#### 5.3.4. Pressure Wave Development

***Examination of the  $R\theta$  contour of the pressure distribution in the bearing gap on the line  $L=0$  (center of the bearing) gives a good conceptual understanding of the pressure wave development that is responsible for the net hydrodynamic force.***

***When there is no rotation:***

- ***The contour is always symmetric about  $h_{min}$ .***
- 
- ***Mass addition causes a general increase in contour pressure to a value between the ambient pressure and the operating pressure. The size of the pressure increase depends on the mode of mass addition.***
- ***The contour pressure maximum always occurs at the angular location of  $h_{min}$ .***
- ***The contour pressure minima always occurs at the angular location of  $h_{max}$   $180^\circ$  from  $h_{min}$ .***
- ***For porous liner bearings there is one pressure maxima which is located lengthwise at the center of the bearing.***
- ***For the 12xfeedhole bearings (where two of the feedholes are angularly aligned with  $h_{min}$ ) there are 2 maxima located along the length of the bearing at the locations of the rows of feedholes.***
- ***The bearing pressure minima are always located at the ends of the bearings where the pressure is ambient.***
- ***When the eccentricity ratio is 0, the contour pressure distribution is constant along any given  $R\theta$  contour.***
- ***As eccentricity is increased, pressure maxima develop and increase in value at the angular position of  $h_{min}$ .***

When the mode of mass addition is symmetric along the length axis and the shaft/bushing displacements are such that axes remain parallel, symmetry dictates that the pressure distribution in the bearing gap will also be symmetric along the length axis there will be no mass flow across the bearing centerline.

For the case of a purely hydrodynamic bearing operating at 0 RPM the symmetric contour is a flat line constant ambient pressure.

In the case of the 12xfeedhole bearings studied in this thesis, the symmetry dictates that the centerline pressure distribution is a flat line at an elevated pressure greater than ambient pressure but less than the operating pressure. For example, in the case of the 12xfeedhole bearing operated at 60psig which equates to 5.08atm the centerline contour pressure is a constant 2.297atm. Because the angular orientation of the feedholes has 2 feedholes (one for each row) that are aligned with  $h_{min}$  there are 2 pressure maxima located angularly at  $h_{min}$  and lengthwise at the locations of the feedhole rows. However this would be expected to change depending on the angular orientation of the feedholes to  $h_{min}$ .

When the mode of mass addition is through a porous liner with homogenous permeability, the centerline pressure contour is a symmetric wave.

***When there is rotation:***

- ***Rotational hydrodynamic activity (RHA) in the  $R\theta$  direction increases with increased speed, and decreased  $h_{min}$ .***
- ***Along the  $R\theta$  pressure contour taken at the center of the bearing (c/l contour) a pressure maximum develops a short distance forward***

**(upstream against the rotation velocity in the  $R\theta$  direction) of  $h_{min}$  and a pressure minima develops a distance aft (downstream with the rotation velocity) of  $h_{min}$  so that an asymmetric pressure gradient develops about  $h_{min}$ .**

- **Increased RHA increases the pressure difference between the centerline pressure maximum and minimum.**
- **As RHA increases, the c/l contour pressure maximum and minimum both “left shift” with the maximum moving further forward of  $h_{min}$  and the minimum moving closer to  $h_{min}$ .**
- **When RHA is initiated, the c/l contour maximum makes small leftward shifts while the minima moves more quickly towards  $h_{min}$  which causes the span of the pressure wave between the maximum and the minimum to decrease.**
- **Since both the span of the c/l contour pressure wave decreases and the pressure difference increases with increased RHA, the slope of the pressure wave increases.**
- **As the leftward shift of the c/l contour pressure minima approaches  $h_{min}$  the size of the shift diminishes. When the location of the pressure minima reaches  $h_{min}$ , both the minimum and the maximum stop shifting leftward. The minimum wave span and maximum wave slope are reached and increases in RHA lead to numerical instability.**
- **For bearings with low RHA, the bearing minimum pressure occurs at the bearing ends where the boundary conditions ensure that the pressure is atmospheric.**
- **At high RHA, sub-atmospheric pressure minima develop at an angular position slightly aft of  $h_{min}$  and shift from the middle of the bearing (along the length) with increased RHA until they near the**



**ends of the bearing. When they shift to within 2 nodes of the ends of the bearing (at which  $P=1$ ) it appears that another numerical instability speed limit is reached.**

- ***PL hybrid bearings increase the pressure throughout the bearing gap so that these sub-atmospheric minima never developed at the speeds for which solutions were found.***

For a hydrodynamic bearings, the span of the pressure wave across  $h_{min}$  is greatly affected by the eccentricity ratio and is largest for small eccentricity ratios and smallest for large eccentricity ratios. It is suspected that that this shortening of the span is related more to the size of  $h_{min}$  than to the eccentricity ratio itself. The span for a hydrodynamic bearing with  $h_{min}=0.0002$ " (eccentricity ratio of 0.9) was about 1/3 that of hydrodynamic bearing with  $h_{min}=0.001$ " (eccentricity ratio of 0.5). The spans of the hydrodynamic bearings also compacted about 8 to 50% with increased speed with higher percentage compacting occurring with smaller  $h_{min}$  (larger eccentricity ratio). As speed is increased the wave shifts forward (upstream). The compacting of the span with speed is speculated to be caused by the pressure minimum apparently not being able to go upstream of  $h_{min}$ .

The hybrid bearing CFD experiments were all performed with an eccentricity ratio of 0.9 with a bearing with clearance of 0.002" which corresponds to an  $h_{min}$  of 0.0002" so observations of the affect of eccentricity ratio increase on span length are not available. However in comparing centerline contour plots the hybrid bearings behaved in a similar manner to hydrodynamic bearing in that the spans compacted slightly with increased speed And it is speculated that it is for the same reason (that pressure minimum cannot go forward of  $h_{min}$ ).

Centerline contour plots were made from CFD pressure distributions found for a hydrodynamic (HY) bearing, a hybrid porous liner (PL) bearing, and a hybrid

feedhole bearing (FH) each with a clearance of 0.002" and an eccentricity ratio of 0.9 ( $h_{min}=0.0002$ "). Both hybrid bearings are operated at 60psig. The static centerline contour for a PL bearing is a symmetric wave spanning from  $h_{min}$  to  $h_{max}$  which for the 0.75" diameter bearings is an  $R\theta$  distance of 1.178". The static centerline contours of the HY and FH bearings are both flat constant pressure lines of  $P=1$  for the HY bearing and  $P=2.297$  for the FH bearing. It can be argued that the span of a flat line is half the circumference of the bearing or 1.178" as it is for the static PL bearing. In any case that was the value used for plotting the span length at 0 RPM for the HY and FH bearings.

The results are very interesting. In the speed range of 20 to 120K RPM the FH bearing had a span 0.1963" (140K RPM was the highest speed solved for the FH bearing but its pressure minimum was suspect since the solution was becoming unstable). For the HY bearing, the 10K RPM span was 0.2209" and was 0.1963" for speeds of 20 to 60K RPM (60K RPM was the highest HY speed solved). It is very interesting that this the span for the HY is exactly the same as that for the FH bearing. However equality is not quite as amazing as it appears in that the  $R\theta$  mesh size is 0.0245" and that both the FH and HY bearings had spans of 8 increments. The centerline contour pressure minimum for the FH bearing was located at  $h_{min}$  for the 100K RPM, 120K RPM and the slightly unstable 140K RPM solutions. The centerline contour pressure minimum for the HY bearing was located at  $h_{min}$  for only the 60K RPM solution.

For the PL bearing at 0 RPM, the centerline contour had a strong symmetric wave with pressure maximum located at  $h_{min}$  with  $P=4.938$ . Its pressure minimum located at  $h_{max}$  was  $P=2.864$ . The effect of rotation was to move the pressure maximum just slightly forward of  $H_{min}$  and to create a pressure minima aft of  $h_{min}$ . As usual the pressure wave "left shifted" with increased speed so that the maximum moved somewhat further ahead of  $h_{min}$  while the pressure minimum

moved much more quickly closer to  $h_{min}$  quickly decreasing the wave span. However, as the minimum approaches  $h_{min}$ , it's rate of shifting lessens so that the decline in the span decreases. At 300K RPM, the highest speed pressure solution for the PL bearing, the pressure minimum was still located 0.122" aft of  $h_{min}$  and the span was 0.319". It would be supposed that with further increases in speed the minima would left shift to  $h_{min}$  and then stop shifting while the span would continue to gradually decline. At very high speed would the minimum span length for the PL decline to 0.1963? Figure 5-2 indicates that it would be close to that value.

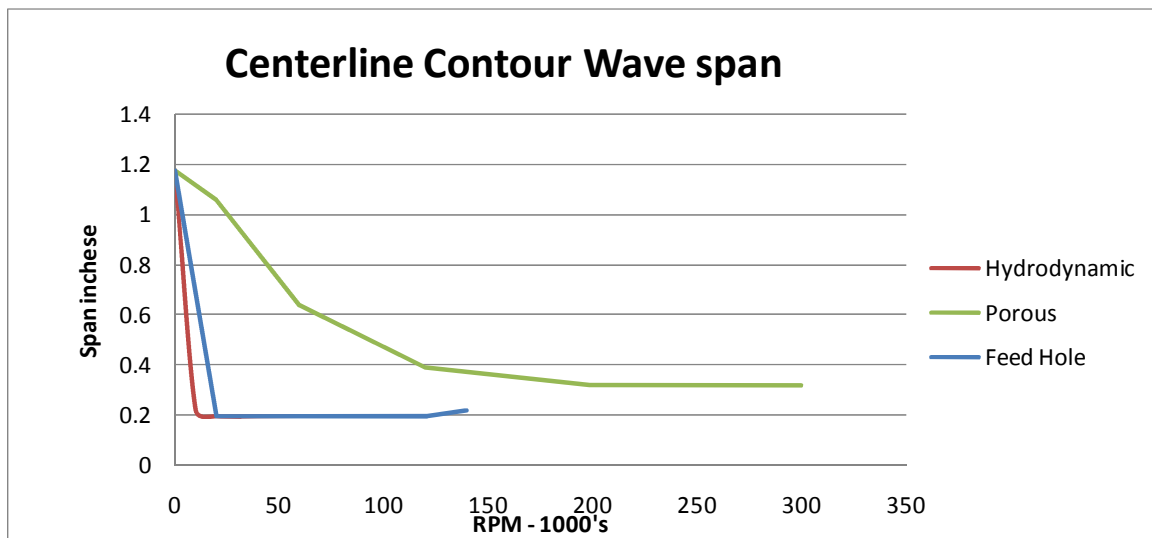


Figure 5-2 Centerline contour wave span as a function of speed.

An examination of the HY bearing results for different eccentricity ratios yields the following:

$\epsilon$	$h_{min}$ in	Bearing	speed 1000 RPM	Span Length in	span/ $h_{min}$	$\epsilon \times$ Span in
0.5	0.001	HY	200	0.614	614	0.307
0.75	0.0005	HY	140	0.344	688	0.258
0.9	0.0002	HY	60	0.1963	982	0.17667
0.9	0.0002	FH	140	0.1963	982	0.17667
0.9	0.0002	PL	400?	0.1963?	982	0.176

Figure 5-3 Comparison of minimum spans found in CFD experiments.

***RHA causes a pressure wave that spans the angular location of  $h_{min}$ . As RHA is increased, the characteristics of the pressure wave are compacted. It appears that numerical instability occurs when the grid is too coarse to resolve the extrema of the pressure wave especially as the extrema approach apparent singularity limits.***

- ***Pressure minimum shifting leftward to the  $h_{min}$  angular location***
- ***Sub-atmospheric pressure minima being out shifted to the ends of the bearing***
- ***A large wave slope (exceeding  $0.10 \text{ degrees}^{-1}$ )***

### **HY Bearings**

The hydrodynamic bearing speed limit appears to be determined by either the centerline contour pressure minimum reaching the  $h_{min}$  angular location or the sub-atmospheric bearing pressure minimum reaching the ends of the bearing.

For eccentricity ratios of 0.5 and 0.75 ( $h_{min}$  of 0.001" or 0.0005"), there was much less hydrodynamic action as reflected in compacting the span of the centerline pressure wave. When the numerical speed limits of 200K RPM and 140K RPM were reached, the centerline contour pressure minima were located a good angular distance from  $h_{min}$  ( $30^\circ$  or  $R\theta$  of 0.5236" for  $\epsilon=0.5$  and  $11.25^\circ$  or  $R\theta$  of

0.07361" for  $\varepsilon=0.75$ ). But the bearing sub-atmospheric pressure minima ( $P=0.91$  and  $P=0.65$ ) were moved to within 0.1333" of the bearing ends. They were only two nodes away from the bearing end node where the boundary condition dictated that  $P=1$ .

For an eccentricity ratio of 0.9, corresponding to  $h_{min}$  of 0.0002," the centerline contour hydrodynamic wave was much more compact with a span of only  $30^\circ$ . When the numerical speed limit was reached, the centerline contour pressure minimum was pushed to  $h_{min}$  while the bearing sub-atmospheric pressure minima ( $P=0.38$ ) were located three nodes or 0.200" from the bearing ends.

#### **PL hybrid bearings:**

CFD experiments were run only at an eccentricity ratio of 0.9 and a clearance of 0.002" corresponding to  $h_{min}$  of 0.0002". The highest speed pressure solution found was for 300K RPM. Unsuccessful attempts were made to find a solution at 400K RPM. The wave form of the PL bearing does not have any sub-atmospheric pressure minima away from the bearing centerline (the bearing pressure minima are the bearing end locations with  $P=1$ ). At 300K RPM the centerline contour pressure minimum was  $18.75^\circ$  or ( $R\theta=0.1227$ ") aft of  $h_{min}$ .

Another candidate for the cause of the numerical speed limit might be the magnitude of the slope of the pressure wave. The slope of the pressure wave for the 300K solution was  $0.107\text{degrees}^{-1}$  which was the largest found for any of the CFD experiments run.

### **FH hybrid bearings:**

The highest speed pressure solution was found at 120K RPM where the centerline contour minimum was located at  $h_{min}$ . The 100K RPM solution also had the pressure minimum located at  $h_{min}$  and a reasonably good solution was found at 140K RPM that also had the pressure minimum located at  $h_{min}$ . As the speed is increased, the pressure difference between the centerline contour pressure maximum and minimum increases and the span decreases so that slope of the wave increases. The progression of the slope for the 100K RPM, 120K RPM and 140K RPM solutions was  $0.0901\text{degrees}^{-1}$ ,  $0.0991\text{degrees}^{-1}$ , and  $0.0905\text{degrees}^{-1}$ . The location of the pressure minimum for all 3 solutions was at  $h_{min}$  while the maximum occurred  $30^\circ$  forward of  $h_{min}$  for the 100K RPM and 120K RPM solutions. The unstable 140K RPM solution placed the maximum at  $33.75^\circ$  (one additional node) forward of  $h_{min}$ . Thus between the 100K RPM and 120K RPM solutions, the pressure wave span and location was fixed so that additional hydrodynamic activity was reflected entirely in increased pressure difference between the maxima and minima and increased wave slope. The 120K RPM solution reached a slope of  $0.0991\text{degrees}^{-1}$  which is very close to the  $0.107\text{degrees}^{-1}$  slope of the maximum speed (300K RPM) solution of the PL hybrid bearing. The unstable 140K RPM solution tried to increase the span of the wave and lower the slope. Increasing the span of the wave with increased speed is counter to all of the CFD observations made in this thesis.

FH hybrid bearings can develop sub-atmospheric pressure minimum toward the ends of the bearing beyond the rows of feedholes. For the 120K RPM solution, these minima were at  $R\theta=1.792$  which is one node aft of  $h_{min}$ , and  $Z=\pm 0.9333$  which is one node from the ends of the bearing.

The 140K RPM solution showed an oscillating false minimum at  $R\theta=1.792$  which is one node aft of  $h_{min}$ . It was in line with the rows of feedholes. The bearing

pressure minimum was located one node inside the ends of the bearing, the minimum also “wobbled”. The solution placed two minima around each  $h_{min}$  angular location (total of 4 minima). One minimum was one node ahead of  $h_{min}$  and the other was one node aft of  $h_{min}$ . At  $h_{min}$ , the pressure increased slightly.

#### 5.4. Examination Of Local Dimensionless Dynamic Similitude Numbers

Numerical “speed limits” were encountered in generating results for rotating bearings that depended on the bearing type and the amount of hydrodynamic action (either increased speed or increased eccentricity). These were presented in Table 5-1 which for the reader’s convenience is repeated here. The hierarchy of these speed limits is obviously dependent on their hydrostatic (or aerostatic strength), that is, porous liner bearings (PL) which have a much highest aerostatic strength component have the highest speed limit followed by feedhole bearings (FH) followed by purely hydrodynamic bearings (HY) which have no aerostatic strength component.

Bearing	$\varepsilon$	Max speed RPM
HY	0.50	200K
HY	0.75	140K
HY	0.90	60K
PL	0.90	300K
FH	0.90	140K

Figure 5-1 (repeated) Numeric speed limits found for obtaining pressure solutions for rotating bearings with a clearance of 0.002” operating pressure of 60 psig.

In section 4.9.2 a gedanken experiment is presented that suggests that bearings with high aerostatic strength can be expected to have higher stability than bearings with low hydrostatic strength. It also appears that this applies to numerical stability as well. Thus both cases indicated a “just cause” to examine the standing pressure waves in the bearing gap under the CFD microscope (as is done in sections 4.6.3 for HY bearings, section 4.7 for FH bearings and section 4.8.2 for PL bearings and section 4.9 which compares hybrid FH and PL bearings to the superposition of FH and PL hydrostatic bearings and the HY



bearing. What phenomenon is occurring that creates the numerical instability?

This subject was discussed thoroughly in sections 5.3.3 and 5.3.4.

In this section we apply our new “knowledge” of the standing pressure wave development to examine the local dimensionless characteristics in terms of some of the “classical” dimensionless parameters used in gas dynamics to differentiate “regimes of flow” in order to determine how much the standing wave characteristics challenge the underlying assumptions implicit in the Reynolds equation used for continuous, laminar, no-slip flow.

#### 5.4.1. Mach Number of the Shaft Surface

The nominal bearing diameter was 0.75". This equates to a surface speed of 13,744 in/s at 350,000 RPM. Based on the speed of sound in air at 70°F being approximately 1129 ft/s, this equates to a Mach number of 1.01. The highest speed for which valid pressure solutions were found was 300,000 RPM. Unsuccessful attempts were made at 400,000 RPM and 350,000 RPM. When sonic velocity is reached a pressure discontinuity or shock wave develops that results in downstream vorticity and greatly increased drag. What happens in the bearing gap?

### 5.4.2. Knudsen Number

Lee et al. [26] in 2004 make predictions about the effect of slip flow on small hydrodynamic bearings for micro-rotating machines. Lee et al. report that the nominal clearance of micro-rotating machinery is about 2 to 3  $\mu\text{m}$  (about 80 to 120  $\mu\text{in}$ ). Micro gas turbines also operate at high temperatures which increases the mean free path of gasses. Lee et al. state that if the Knudsen number,  $Kn$ , for a bearing is between 0.01 to 10 then the fluid should be treated as a rarefied gas and the Reynolds number should be modified with rarefaction coefficients.

Would any of the bearings in this thesis be subject to slip flow?  $Kn = \lambda / h$  where  $\lambda$  is the mean free path and for the bearing  $h$  would be the bearing gap height.

From the kinetic theory of gases it is known that  $\lambda$  is proportional to temperature and inversely proportional to pressure. So the highest  $Kn$  would occur in areas in the bearing gap at locations of low pressure coinciding with a small gap height. From our knowledge of pressure waves of hydrostatic, hydrodynamic and hybrid bearings that is presented in sections 4.6.4 to 4.6.10 an immediate candidate comes to mind. We know that sub-atmospheric pressures occur near the minimum bearing gap height for hydrodynamic bearings. (External pressurization raises the overall pressure in the bearing gap). Also this pressure is lower with increased hydrodynamic activity especially increasing with the eccentricity ratio which in turn decreases the minimum flight height.

The pressure wave of the hydrodynamic bearing operating at 60,000RPM with an eccentricity ratio of 0.9 (60K RPM HY bearing) immediately comes to mind. It had a minimum pressure of 0.45 atm located exactly at the position of the minimum flight height which for this bearing has a value of 200  $\mu\text{in}$ . Plugging in the numbers based on the mean free path of air being about 68 nm at

atmospheric pressure and ambient temperatures, the local Knudsen number at his point would be about 0.030 which falls into the area of a rarefied gas.

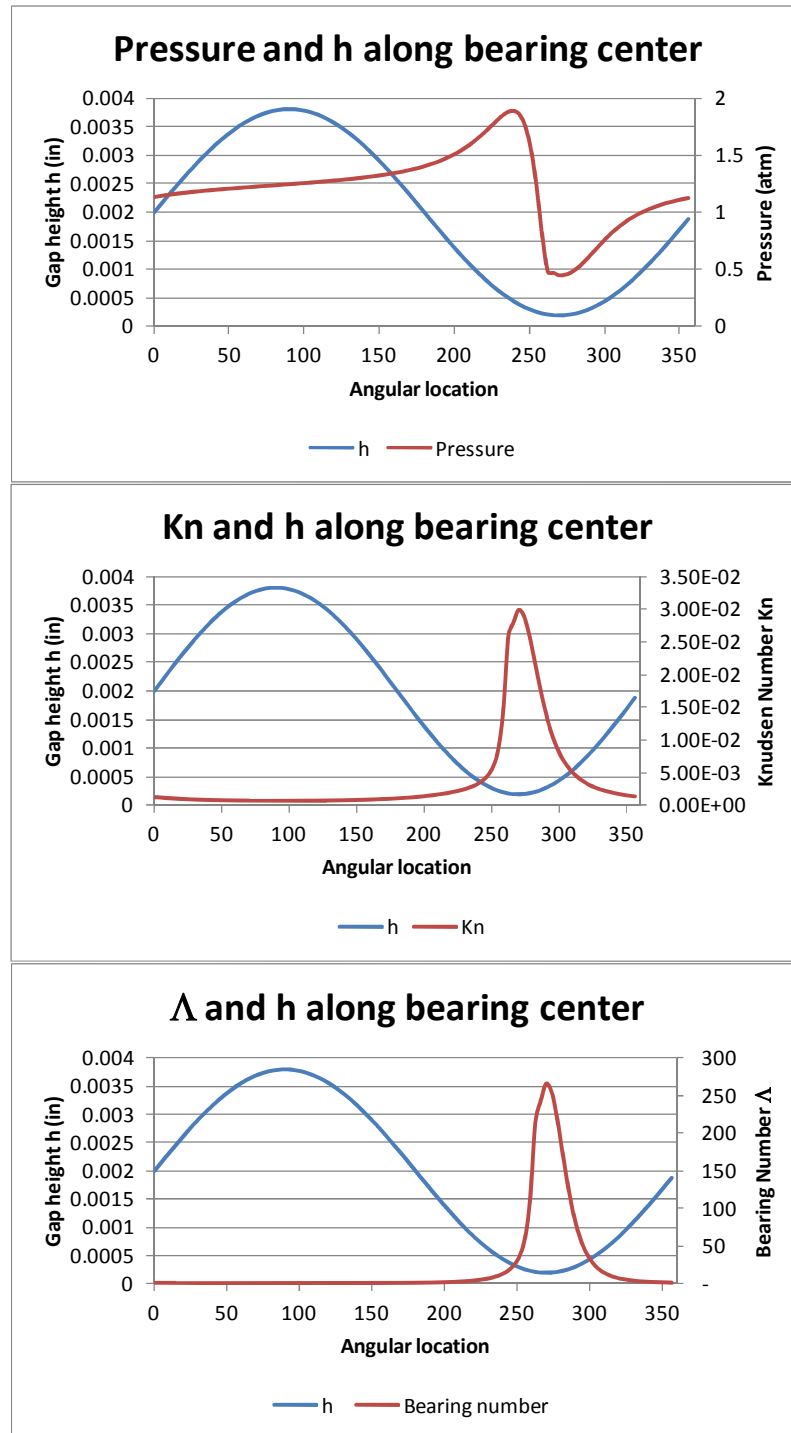


Figure 5-4 Local property profiles along the center of a hydrodynamic bearing with a clearance of 0.002", an eccentricity ratio of 0.9 and a speed of 60K RPM. Top - standing pressure wave, Middle - local Knudsen number, Bottom - local bearing number.

Recalling the definition of the bearing number results in the definition of a local bearing as:

$$\Lambda = \frac{6\eta\omega R^2}{c^2 p_a} = 6\omega \left( \frac{\eta}{p_a} \right) \left( \frac{R}{c} \right)^2$$

$$\Lambda_{local} = 6\omega \left( \frac{\eta}{p} \right) \left( \frac{R}{h} \right)^2$$

As a result the local bearing number “blows up” at the location of the minimum bearing gap as it represents the location of peak pressure as well as the minimum flight height so that both the Knudsen number and the bearing number are inversely proportional to the product of the pressure and the flight height. The bearing number is also proportional to the bearing rotational speed and the bearing radius (the shaft surface speed). Increasing either or both of those parameters would increase the hydrodynamic action in the bearing gap and have the effect of further lowering the pressure minimum which in turn would increase the Knudsen number as well. So the local bearing number could be interpreted as a possible slip indicator. It must be remembered, however, that the local bearing number is significantly different than the general bearing number. In this example the bearing number is only 0.239 while the local bearing number peaks at 265.

### 5.4.3. Reynolds Number, Taylor Number, Bearing Speed and Laminar Flow

The Reynolds number,  $Re$ , is the ratio between inertial and viscous hydrodynamic forces. It is typically used to predict the onset of turbulent versus laminar flow. For example the onset of turbulent flow is generally known to occur for flow over a flat plate at  $Re \sim 5 \times 10^5$ . For flow in a pipe the transition range occurs for a Reynolds number between 2300 and 4000. The Reynolds number for a bearing is generally taken to be [25]:

$$Re = \frac{c\omega R\rho_a}{\eta}$$

The nominal channel width is very important to the Reynolds number along with the flow velocity as they scale the amount of shear. For Couette flow in a rotating journal the shear is scaled by the bearing clearance  $c$  and the shaft surface speed  $R\omega$ .

The Taylor number,  $Ta$  is the ratio between the centrifugal forces to the viscous forces. For a journal bearing it is defined as [3]:

$$Ta = Re \left( \frac{c}{R} \right)^{1/2} = \omega c^{3/2} R^{1/2} \left( \frac{\rho_a}{\eta} \right)$$

According to Czolczynski [25] the assumptions of neglecting inertial forces and assuming the flow to be laminar are justified for  $Ta < 40$ .

As a result the local Taylor number and Reynolds number are:

$$Re_{local} = \frac{h\omega R\rho}{\eta}$$

$$Ta_{local} = Re \left( \frac{h}{R} \right)^{1/2} = \omega h^{3/2} R^{1/2} \left( \frac{\rho}{\eta} \right)$$

Thus the bearing number, the Reynolds number and the Taylor number are both proportional to speed. However both the Reynolds number and the Taylor number increase with increased pressure (density) or increased gap height

whereas the bearing number decreases. Thus for our virtual bearing which had a diameter of 0.75" and a clearance of 0.002", as the speed would go from 0 RPM to 300,000 RPM,  $Re$  goes from 0 to 1,015,  $Ta$  goes from 0 to 74.6, and breaks the limit of 40 at about 160,000 RPM while the dimensionless speed (bearing number  $\Lambda$ ) goes from 0 to 1.19.

Thus according to Czolczynski [25] our choice of an extra large bearing clearance makes the laminar flow assumptions suspect above 160,000 RPM. If a more typical clearance of 0.0008" had been chosen then at 300,000 RPM,  $Re$  and  $Ta$  would only be 406 and 18.9 respectively which would make them laminar, while  $\Lambda$  would increase to 7.46.

If the "microscopic" view is taken then the local gap height would be used as the channel width parameter rather than the clearance. Also, the local pressure (and density) of the pressure wave would be used rather than the ambient pressure. Some discussion has already been presented (section 4.11) about whether the ambient pressure or the operating pressure (or something in between) is the more appropriate reference pressure for a hybrid bearing. For a given speed, both the local Reynolds number and the local Taylor number are greatest where the product of the gap height and the pressure (density) are greatest.

Once again, our knowledge of the pressure waves comes in handy in selecting the candidate localities for turbulence. The virtual porous liner bearing operating at an eccentricity ratio of 0.9 (clearance 0.002") that represents has the numerical speed limit of 300K RPM (300K RPM PL bearing) immediately comes to mind. We know (now) that the hybrid bearing waves are of the form of the hydrodynamic wave superimposed on the hydrostatic wave. The angular hydrostatic pressure wave contour at the axial center of the bearing has its pressure maximum at the location of the minimum gap height and forms a symmetric wave that has its minimum (which will be higher than atmospheric



pressure) at the location of the maximum bearing gap located  $180^\circ$  away. When rotation occurs the hydrodynamic wave “pushes” the peak pressure just “forwards” (into the flow or the opposite direction of the rotation) of the minimum gap height and creates a pressure minimum just “aft” of the minimum gap height while the pressure at the maximum gap height increases. Our candidate bearing has the highest overall axial centerline pressure contour. For this bearing the centerline pressure contour has its maximum pressure of 7.66 atm located  $30^\circ$  forwards of the minimum gap height where the gap height is  $441\ \mu\text{in}$ , the minimum pressure is 2.43 atm and is located  $18.75^\circ$  aft of the minimum gap height where the gap height is  $296\ \mu\text{in}$ , and at the maximum gap height of  $3,800\ \mu\text{in}$  the pressure is still 4.22 atm. Thus the pressure drops off approximately 45% from the maximum pressure location to the location of the maximum gap height, but the gap height increases 8.6 times so that this location would be the expected location of the maximum local Reynolds number and the maximum local Taylor number. Figure 5-5 confirms this.

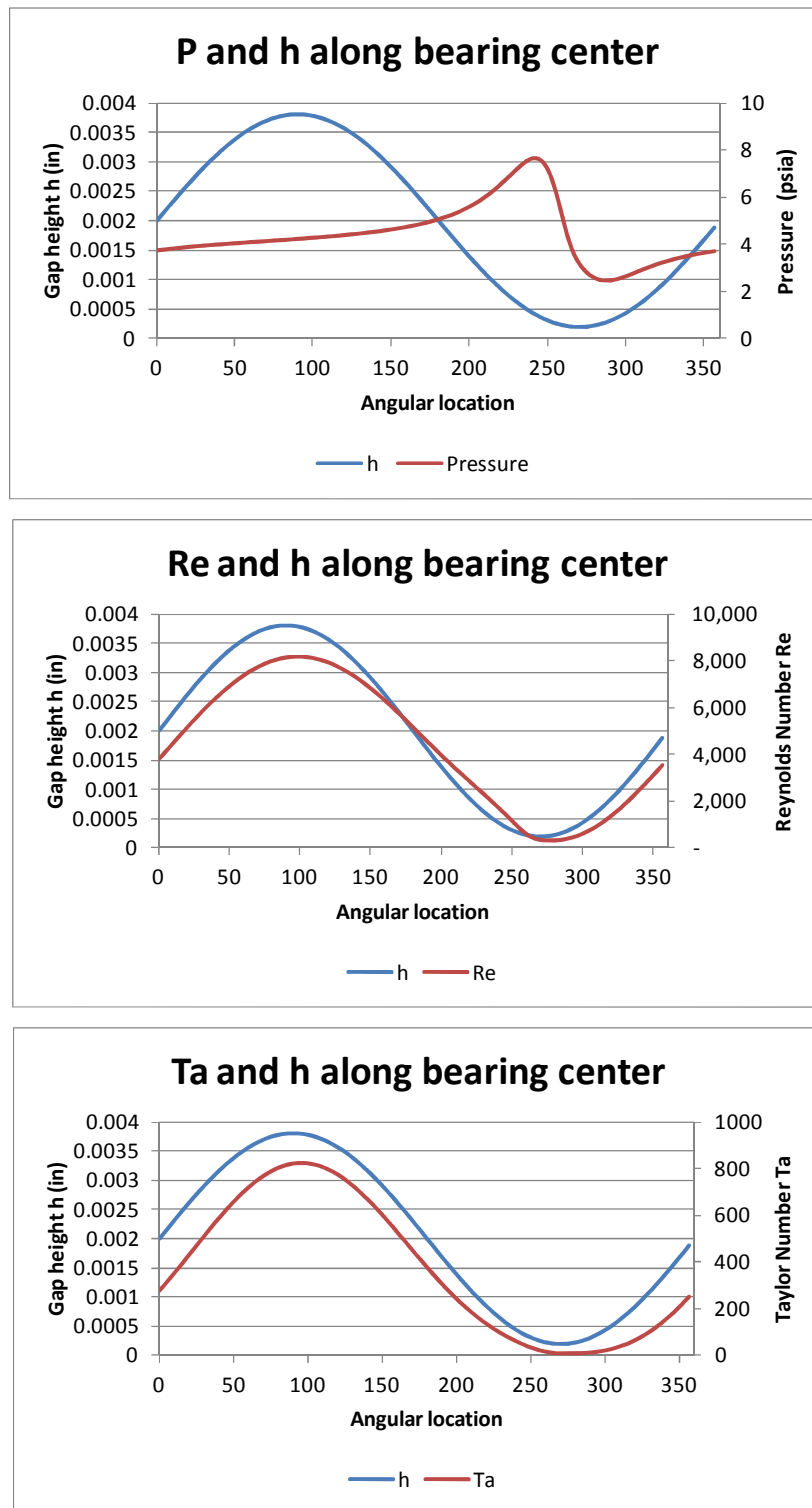


Figure 5-5 Pressure, Re number, and Ta number angular profiles at the axial middle of the porous liner hybrid bearing with a clearance of 0.002", speed of 300K RPM,  $K_{meas}=2 \times 10^{-4}$  lbs/s and eccentricity ratio of 0.9.

The results indicate that a maximum local Reynolds number of 8,162 is reached  $3.75^\circ$  aft of the maximum gap height (the Reynolds number at the maximum gap height is 8,135) and that the maximum local Taylor number of 821 is also reached at this location (the Taylor number is 819 at the location of the maximum gap height). The transition range from laminar flow to turbulent flow in an infinitely long narrow gap (the bearing gap) is unknown to this writer. However, local Reynolds numbers in the 8,000's are pushing laminar limits. For the local Taylor number which is even more sensitive to bearing gap height, Taylor numbers in the 800's are certainly way beyond Czolczynski's [25] criteria of 40 and remain greater than 40 throughout almost all of the bearing gap except the small area located  $22.5^\circ$  forwards of the minimum gap height to  $41.25^\circ$  aft of the minimum gap height .

In general we can therefore observe that from the microscopic viewpoint that at 300K RPM the laminar flow assumption is justified only in the relatively small angular location close to and just aft of the minimum bearing gap while turbulence (due especially to centrifugal forces) is likely in the much larger angular area centered about the location of the maximum bearing gap. As speed would be decreased, the laminar area would increase and the turbulent area would decrease.

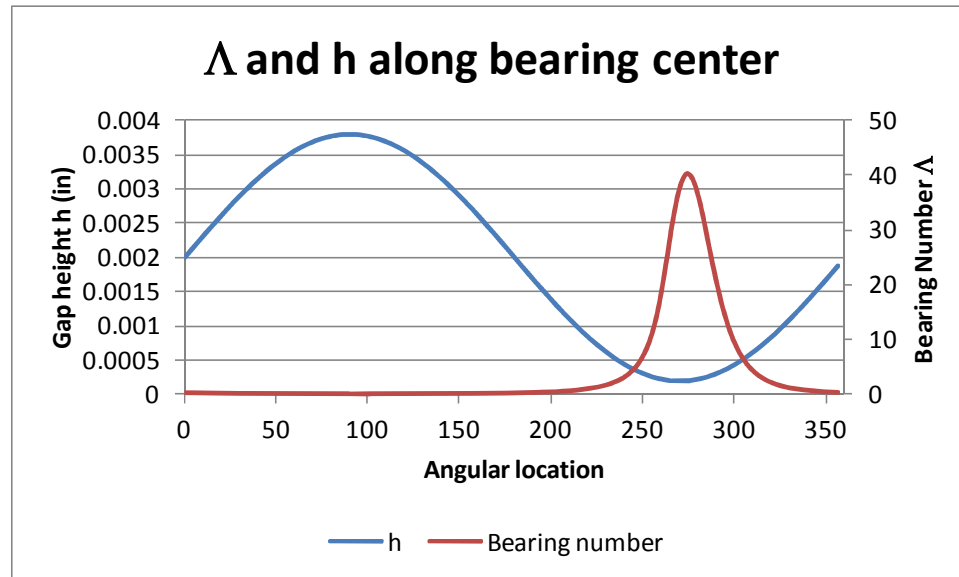


Figure 5-6 Angular centerline profile of the local bearing number for the porous liner bearing at 300K RPM and eccentricity ratio of 0.9.

We also see that the local bearing number is useless as an indicator of turbulence since it gives “mixed signals” increasing with speed as do both the Reynolds numbers and Taylor number, but decreasing with increased pressure or gap height which is opposite the local Reynolds and Taylor numbers. We have just observed that the local bearing number might be useful in indicating slip. The overall high pressure of the 300K PL bearing would give the expectation that it is immune to slip. If it were to have slip we know from our pressure wave knowledge that it would be most likely to occur just aft of the location of the minimum gap height where the pressure is minimum and the gap height is small. This is also the location where the local bearing number “blows up”. For the 300K RPM PL bearing the maximum local bearing number is located 3.75° aft of the minimum gap height and is only 40 (compared to 265 for the 60K RPM HY bearing) even though its overall bearing number is 1.19 (compared to .239 for the 60K RPM HY bearing). Thus as a slip indicator the local bearing number confirms our knowledge-based intuition that the no-slip

assumption is good for the porous liner hybrid bearing even at relatively high speeds.

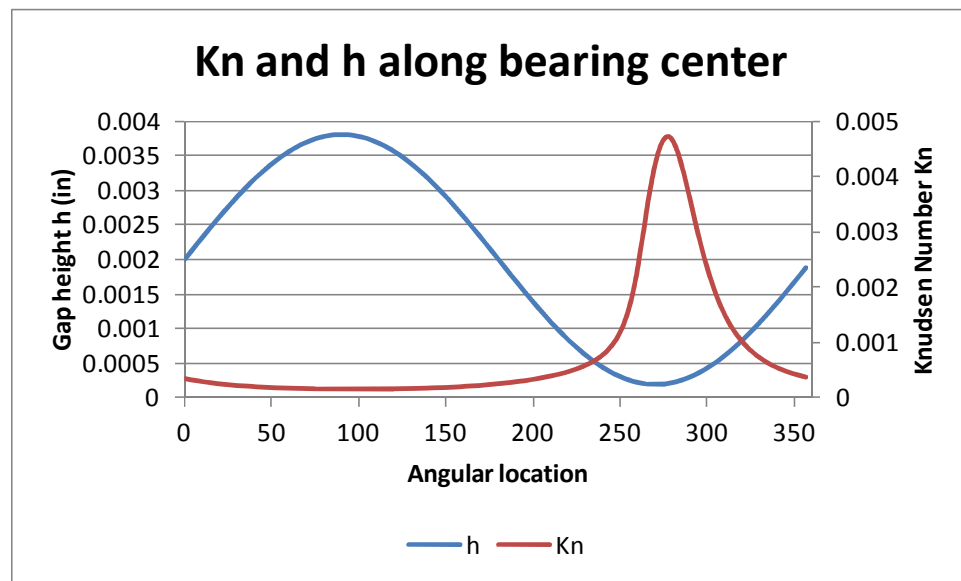


figure 5-7 Angular centerline profile of the local Knudsen number for the porous liner bearing at 300K RPM and eccentricity ratio of 0.9.

The centerline profile of the Knudsen number for the 300K PL bearing confirms this. The Knudsen number maximum is located  $7.75^\circ$  aft of the minimum gap height location and is 0.004715 which is below Lee et al.'s stated lower threshold of 0.01 for rarified gas conditions. Thus the Knudsen number for the 60K RPM HY bearing (which is 0.298) is 6.6 times that of the 300K RPM porous liner bearing. It is interesting to note that even though the 60K RPM HY bearing has a rotation speed that is 1/5 that of the 300K RPM porous liner hybrid bearing that its maximum local "dimensionless speed" (bearing number) is 6.32 times that of the porous liner bearing (very similar to the Kn increase). And while this would seem counterintuitive to the "lay" reader, our "advanced" knowledge of the development of the pressure extrema in the bearing gap anticipated this.

#### 5.4.4. Overall

*Thus it can be seen that the bearing gap of a gas bearing can be viewed as a MEMs scale wind tunnel for which the CFD microscope method can be used to predict flow patterns in the various regions of the bearing gap. When there is no rotation, the overlooked hydrostatic case, it is a micro-fluidic pressure driven wind tunnel. When rotation occurs, it presents the novel case of a wind tunnel with one wall translating at high-speed introducing a strong Couette flow element.*

Experimental confirmation of the pressure wave characteristics and transitions to different regimes of flow using a rotating gas journal bearing as a micro-wind tunnel are not practicable with current off-the-shelf pressure gages. However, the writer was approached for a letter of support for a research group attempting to use a small diameter optic fiber for a probe head for a high speed, high temperature dynamic pressure gage. It is envisioned that as MEMs and nanotechnologically based instrumentation comes of age, that a micro-gas dynamic research program will be feasible.

#### 5.4.5. Final Comments on Speed Limits

Numerical instability is generally seen as a subject independent of system stability. And thus it seemed quite strange to this writer to use one to study the other. However, if one were to write numerical code to determine the quotients of a particular number over a range of divisors, that code would obviously fail to resolve a quotient whenever the divisor went to zero. Of course it is obvious to the reader that dividing by zero is a singularity of the system and thus any attempt at a numerical result will be fruitless. However, in a more complicated system where the singularities are complex and unknown to the analyst, quite a lot of fruitless effort could be expended in trying to improve numerical techniques to perform the impossible.

That was this writer's point of reference in engaging in the study of the standing pressure waves in the bearing gap. Although good and accurate pressure solutions were achieved within the range of interest of the original program it was a frustration that pressure solutions could not be found over any range of input variables, particularly speed and minimum flight height (eccentricity). In all the literature read at the time of developing the CFD numerical methodology, no mention was made of any authors encountering any numerical speed limits as were encountered by this writer. Indeed, many papers presented results with dimensionless speeds that were orders of magnitude greater than the speed limits encountered by this writer.

The only comment encountered in the literature as to any "difficulty" was C-C Wang's and C-K Chen's comment in their 2003 paper [7] that, "Due to the non-linearity of the gas-film pressure, it is very difficult to determine the modified Reynolds equation solutions." They then devote an additional line as to their method, "In this study they are obtained by applying finite difference methods and the SOR (successive overrelaxation) method." Nonetheless, one is left with

the impression that they could find solutions over any range of input variables. The results of the paper are presented exclusively in rotordynamic terms for a rigid rotor with a static load of 710N while the rotor mass is varied in kilograms. They use bifurcation for their rotor dynamics but it is well known that their calculations firstly depend on finding a quasi-static wave solution. For example, they make the comment, “The procedure begins with the initial static equilibrium state. The initial conditions are selected from the static model.” Thus it would be expected that their method would be subject to the same speed limits found in this thesis. As is typical their paper does not present what the actual clearance, or range of static eccentricities, mass addition (it is a porous liner bearing), or operating pressure etc. are used for their virtual bearing. And thus it is impossible to determine from reading their paper whether it falls within our encountered speed limits.

As has already been discussed it became apparent that the encountered numerical speed limits fit a predictable pattern namely that 1) the higher the eccentricity the lower the speed range available, and 2) the more aerostatic strength applied to the bearing, the higher the speed range available. That seemed to this writer to be trying to “say something”. And thus the numerical efforts to “break the speed limits” were put aside and an effort was taken up to put the pressure waves under the CFD microscope to determine the “where and what” that was causing the problem. Chapter 4 reports the findings that the speed limits seem to be related to developing pressure extrema in the standing wave. Conclusions based on these observations are thoroughly discussed in section 5.3.4. The discussion in this section has demonstrated that the numerical speed limits appear to correspond to violations of the laminar, no-slip, continuous pressure distribution assumptions.

As was mentioned in the introduction some recent papers, mostly from micro-turbine programs have reported the need for modifications in certain cases to the



Reynolds equation for slip conditions. The implications, however, is not that they could not achieve pressure solutions with the unmodified Reynolds equation but that the results from previous work with the unmodified Reynolds equation did not match experimental results.

Only one fairly recent (2009) reference was found mentioning numerical solution difficulties due to flow discontinuities. It is Z-S Liu's and H-J Xu's [5] *Performance analysis of rotating externally pressurized air bearings* which has already been cited as one of only two papers found that presents and examines the pressure wave development of hybrid bearings (a 2 row of 8 feedhole bearing in both cases). In it they state in discussing their numerical methods "Among various numerical approaches, finite-difference methods (FDM) and finite-element methods (FEM) are commonly used for the lubrication analysis. The main advantage of the FEM is that it has flexibility in dealing with irregular domains. And also the flow discontinuities (shock waves) of gas bearings can be solved by the CE/SE method in (their) reference [13]." However their paper does not appear to use this method and their results which give "snap shots" of pressure wave development and centerline pressure profiles (similar to section 4.7) do not have any shock waves and the highest speed result presented is for 100,000 RPM with an eccentricity ratio of 0.9. Although the clearance and mass addition parameters are not stated these results appear to fall within our encountered speed limits (140,000 RPM for feedhole bearing with 2 rows of 6 feedholes with an eccentricity ratio of 0.9).

All of the above strongly reinforces the opinion held by this writer, that if any significant progress is to be made in externally pressurized gas journal bearings (or any other bearing type for that matter) that "a back to basics" approach, similar to that taken in this thesis, including complete similitude analysis defining the complete set of proper variables and the study of pressure wave

development and the causes and ranges of their discontinuities will have to be taken.

## 5.5. Summary Conclusions

In the introduction, we began with the “at the cross roads” dilemma caused by trying to “understand” the gas dynamical phenomena of the hybrid gas journal bearing by trial and error using empirical and CFD experimentation. It was stated that this thesis would take a different tack from the template CFD experiment method by going back to basics and beginning a journey of exploration into the hybrid gas journal bearing much as the early explorers of gas journal bearings did in the 1960’s as they sought to “understand” the mysterious purely hydrodynamic gas journal bearing. The results of this (probably never compete) exploration has been voluminous, rich, and fruitful. Its specific conclusions have been discussed in detail in sections 5.1 to 5.4. In this section we (at last!) attempt a concise and brief answer to the question “What does it all mean?” At least so far...

### ***18 Fundamental theses of the thesis***

1) A strong aerostatic load bearing capacity = higher stability.

This is explored in the gedanken experiment presented section 4.9.2 which seems to confirm a conclusion made by V. Kamala [27] in an early 1979 work with feedhole hybrid bearings where the number of feedholes was increased from 2 rows of 8 feedholes to 5 rows of 8 feedholes with the result that the bearings with the increased number of feedholes had high stability. To this Kamala comments: “The attitude angle  $\phi$  is very low  $\sim 0$  ( $1^\circ$ ) due to the fact that 70 percent of the load is borne by the aerostatic action. The low attitude angle indicates that the bearing is stable.”

2) That  $W/pA$  (where  $W$  is the load capacity,  $p$  is the operating pressure, and  $A$  is the nominal bearing area  $LxD$ ) is the definitive hydrostatic bearing efficiency

(HBE) which indicates the aerostatic bearing “strength”. This is derived in section 4.4.2.

3) That the maximum attainable hydrostatic bearing efficiency (MAHBE) is determined solely by the mass addition configuration independent of mass-addition compensation and clearance such that the clearance and mass addition compensation must be tuned to each other to obtain the MAHBE.

This would explain V. Kamala’s [27] findings in working with feedhole hybrid bearings with varying clearances while keeping the mass addition compensation factor constant that “For a given orifice size and number of orifices per row there is an optimum value of the radial clearance for which the load capacity is a maximum.”.

4) That mass addition is well modeled by the relationship of  $\dot{M} = K_{meas}(P_{op}^2 - P^2)$  which works well for both porous-liner and feedhole mass-addition configurations to provide a previously lacking means of making apples-to-apples comparisons between different mass addition configurations.

That this assumption is reasonable based on the equations of viscous, laminar, compressible, Poiseuille flow, is demonstrated in Appendix C. That experimental results based on testing prototype bearings exhibited this relationship is shown in section 2.2.3 and Appendix D.6.

5) Conclusion 4 can be applied to the Reynolds equation for a hydrostatic gas journal bearing with the result that it can be linearized using the substitution  $Q=P^2$ .

6) Using conclusions 4 and 5 enables a definitive apples-to-apples mapping of the MAHBE over the entire range of radial flight height and clearance possibilities for a hydrostatic gas bearing mass addition configuration.

The method for this is the  $W/pA$  versus  $h-c$  scans and is described in section 3.3.6. Apples-to-apples results for porous liner bearings and feedhole bearings with 2 rows of 6 feedholes over 2 orders of magnitude of mass-addition compensation,  $Kmeas$ , are given in sections 4.4.1 to 3.

7) That there is a dearth of theory-based numerical studies of hydrostatic bearings and that all discovered previous work for gas journal bearings with an aerostatic component (hydrostatic or hybrid) lack an ontologically meaningful similitude parameter representing the mass addition component so that their results lack extendibility (This is the subject of section 4.11 and Appendix C.3).

8) Based on conclusion 4 (see section 4.11) an ontologically meaningful dimensionless mass addition parameter can be derived from the Reynolds equation such that:

$$\Lambda_m = \frac{6\eta R}{\pi k_{\rho\rho} p_a^2 L c^3} Kmeas$$

which is applied against the dimensionless variable  $(P_{op}^2 - P^2)$ . When the similitude factor  $Kmeas/c^3$  is applied to the  $W/pA$  versus  $h-c$  scan results, it seems to stop the “right shifting” of results based on increased  $Kmeas$  so that the MAHBE location becomes “fixed” and is based entirely on the mass addition configuration (section 4.11).

As an example, reiterating results presented in section 4.4.3 and section 4.11 that summarized the  $W/pA$  scan results, the MAHBE for a 2 row of 6 feedhole type bearing (L/D =2.666) with an operating pressure of 100 psig was found to be 0.074 regardless of the mass-addition compensation factor,  $Kmeas$ . However,

when  $K_{meas}$  was increased, the location of the MAHBE in the  $h$ - $c$  plane “right shifted” so that its location was  $h=110 \mu\text{in}$  and  $c=450 \mu\text{in}$  when  $K_{meas}=2.00 \times 10^{-6} \text{ lbs/s}$ ,  $h=250 \mu\text{in}$  and  $c=1090 \mu\text{in}$  when  $K_{meas}=2.00 \times 10^{-5} \text{ lbs/s}$ , and  $h=530 \mu\text{in}$  and  $c=2190 \mu\text{in}$  when  $K_{meas}=2.00 \times 10^{-4} \text{ lbs/s}$ . What section 4.11 demonstrated was that if the  $W/pA$  or HBE had been mapped onto the  $H$ - $K_{meas}/c^3$  plane rather than the  $h$ - $c$  plane, the location of the MAHBE would be fixed at the single location of  $H=.238$ ,  $K_{meas}/c^3=10,737 \text{ lb/s-in}^3$  location.

- 9) Porous-liner mass-addition configuration bearings have a much higher MAHBE than bearings with a 2 row of 6 feedhole configuration (section 4.4).
- 10) Conclusion 9 suggests that a porous liner bearing probably represents the optimum MAHBE (for externally pressurized “round” journal bearings) as it can be perceived as a bearing with infinite feedholes. This could be demonstrated running  $W/pA$  versus  $h$ - $c$  scans and  $W/pA$  versus  $H$ - $K_{meas}/c^3$  scans on feedhole mass-addition bearings with increasing feedhole density configurations (Good topic for a paper!).
- 11) Feedhole bearings are subject to the “near surface effect” where they demonstrate a region of “static instability” whereas porous liner bearings are not (Section 4.4).
- 12) The region of static instability and the extent of the resulting “stiffness falloff” are well quantified by the  $W/pA$  versus  $h$ - $c$  scan method (Section 4.4.3).

At the first presentation of the “near surface effect” some doubt was expressed as to the accuracy of the counterintuitive result of the stiffness falloff at small values of  $h_{min}$  which is the signature of the “near surface effect” and does not occur with porous-liner bearings. At the time of that presentation no other work

had been found that presented the pressure distribution in the bearing gap for feedhole hydrostatic bearings (see conclusion 7). Also no work had been found that demonstrated the complex non-linear load capacity versus radial deflection relationships of hydrostatic gas journal bearings.

Our knowledge of the near surface effect indicates that it is most evident (or amplified) for feedhole bearings with both high  $K_{meas}$  and high clearance. None of the experimental prototype bearings matched this criteria so the anticipated near surface effect for the prototypes occurs at very low flight heights that fall within the drift error of the lasers used to experimentally determine flight height. Confirming experimental study would require building a new set of prototypes to amplify the effect (another interesting paper).

The method for evaluating pressure distribution solution accuracy, however, is presented in section 3.3.1. In the CFD calculation the net mass flux of each finite volume element is evaluated. According to mass continuity a correct pressure solution must result in the mass flux of each element being zero. The absolute value of the elemental mass fluxes is added to evaluate a total mass error. A nice picture of the elemental mass flux is shown in figure 3-3.

As was stated numerous times and most recently in conclusion 5, the mass-addition compensation factor,  $K_{meas}$ , linearizes the hydrostatic Reynolds equation so that a pressure solution can be found without iteration. The total error of the hydrostatic solutions was in the order of  $10^{-12}$  and are thus felt to be proven very accurate. Solutions for rotating bearings are also considered to be proven accurate by their total mass flux error but, by contrast, the rotating bearing Reynolds equation is non-linear and solutions which had to be iterated were accepted as accurate when the total error was in the  $10^{-4}$  to  $10^{-5}$  range.

This is exploited to create the  $W/pA$  versus  $h-c$  surfaces that were used to study the “near surface effect” domain. Each  $W/pA$  surface is an interpolant of 400 hydrostatic pressure solutions. The near surface effect (and lack thereof in the porous-liner bearings) is the result of the shape of the smooth and continuous curvature of the surface which is caused by the results of numerous pressure solutions (not just one anomalous point for example). Hence, the results are deemed accurate.

In any event, additional literature searching has uncovered 2 recent papers [5][6] that present the pressure waves in the bearing gap of gas journal bearings externally pressurized by 2 rows of 8 feedholes. These distributions are very similar in appearance to those in this thesis for 2 rows of 6 feedholes. Additionally Z-S Liu et al.’s 2009 paper [5] *Performance analysis of rotating externally pressurized air bearings* shows a load capacity versus radial deflection curve for the bearing at 0 RPM. This curve has a peak load capacity at an eccentricity ratio of 0.8 and falls off in load capacity as the eccentricity is increased to 0.9 (the highest eccentricity ratio on the curve). Thus their curve is displaying the near surface effect. It seems that this surprises Liu et al. as well as they feel the need to explain it which they do in the following comment:

“The line with the rectangle(s) shows the load capacity characteristic of the aerostatic bearing. This indicates a phenomenon that does not occur in flat pad configurations of bearings and is termed the static instability region. The static instability region is a ‘load capacity falloff’ that occurs if the bearing is too heavily loaded and the onset of the phenomenon occurs when the operating eccentricity is very high. This phenomenon is also commonly called negative stiffness and should not be confused with pneumatic hammer instability.” The reference cited by Z-S Liu et al. is a 1996 little known British source that could not be found. However, it appears that Z-S Liu et al. had to search hard for the reference and



that the “static instability region” is an obscure phenomenon observed from empirical testing for bearing design.

So regrettably, this thesis cannot claim to be the first to discover the counterintuitive “near surface effect”. However, the reader can take some comfort in that the phenomenon has been confirmed and was previously named the “static instability region”. The use of the  $W/pA$  versus  $h-c$  scan method unique to this thesis appears to be the most detailed examination and quantization of the range and stiffness falloff of the “static instability region” (Zhang et al. do not pursue it and do not have the  $W/pA$  versus  $h-c$  scan method). And the unique use of the CFD microscope method in this thesis appears to be the first study to identify the “cause” of the phenomenon (as will be discussed in conclusion 15).

13) Studying the characteristics of the standing pressure wave in the bearing gap using the CFD microscope methodology is very useful in determining the “causes” of the complex phenomena exhibited by hybrid gas journal bearings.

14) The standing pressure wave of a hybrid gas journal bearing can be seen as the superposition of a hydrostatic pressure wave and the hydrodynamic pressure wave and the resulting load force (interaction force between the shaft and the bushing) is very nearly the vector sum of the hydrostatic and hydrodynamic load force. (section 4.10).

15) The near surface effect or the region of static instability is caused by the shape of the pressure plume “exhausting” from the feedholes immediately adjacent to the location of the minimum bearing gap height which is restricted from widening due to the limited area at that location (section 4.5).

16) The development of the standing pressure wave in the bearing gap with increased hydrodynamic action (increased rotation speed or increased eccentricity) causes the development of conflicting local extrema which challenge the underlying numerical assumptions of continuous, laminar, no-slip flow in the bearing gap. These appear, along with the near surface effect for feedhole bearings, to be good candidates for further study of the underlying causes of aperiodic, self-excited, vibration (section 5.4).

17) The dimensionless analysis presented in section 4.11 found that equation 4-2 (repeated here for convenience) provides a complete set of ontologically meaningful dimensionless similitude parameters that do not inappropriately “muddle” the 6 independent (or perhaps co-dependent) hydrodynamic phenomena taking place in the bearing gap of an externally pressurized, rotating gas journal bearing. The effect of using equation 4-2 is a slight redefinition of the classic dimensionless speed,  $\Lambda$  and the effective elimination of a “squeeze” number. The effective changes to the bearing numbers are listed in figure 4-98.

Repeat of equation 4-2 derived in section 4.11.

$$-\left(\frac{c}{R}\right)^2 \frac{\partial}{\partial \theta} \left( PH^3 \frac{\partial P}{\partial \theta} \right) + \frac{6\omega\eta}{p_{ref}} \frac{\partial}{\partial \theta} (PH)$$

$$-\left(\frac{c}{L}\right)^2 \frac{\partial}{\partial Z} \left( PH^3 \frac{\partial P}{\partial Z} \right) + 12H \frac{\partial P}{\partial \tau} + 12P \frac{\partial H}{\partial \tau} = \frac{12\eta}{k_{\rho p} p_{ref}^2 V_{gap}} K_{meas} [P_{op}^2 - P^2]$$

where

$$\tau = t \frac{p_{ref}}{\eta}$$

$$V_{gap} = cR\delta\theta\delta z$$

All other presentations of the Reynolds equation found in the literature appear to start with the Reynolds equation for the purely hydrodynamic gas bearing, tack on a mass addition term and then non-dimensionlize it by substitution of the conventional dimensionless variables  $P, H$ , and  $\theta$  and a variety of different

dimensionless times,  $\tau$ , without regard to similitude. Inevitably similitude is lost and mixed terms appear. These mixed terms imply, for example, when the dimensionless time is scaled by the rotation speed ( $\omega t$ ) that independent phenomena such as mass addition become inappropriately scaled to rotation (See section 4.11 for a more complete discussion.).

18) All of the above strongly reinforces the opinion held by this writer, that if any significant progress is to be made in “understanding” externally pressurized gas journal bearings (or any other bearing type for that matter) that “a back to basics” approach, similar to that taken in this thesis, including complete similitude analysis defining the complete set of proper variables and the study of pressure wave development and the causes and ranges of their discontinuities will have to be taken.

Many of the fundamental relationships explored in this endeavor seem to be implicitly known by some, but not all, of the “gas bearing community” as is evidenced by the commentary in their papers (some of which has been quoted above). Namely, it is generally understood or hypothesized by some writers that a stronger aerostatic stiffness equates to higher stability, that the bearing clearance does not scale (at least linearly) to the bearing radius and length, that there is some (unknown to the community) relationship that optimizes bearing performance by clearance, that, in general, porous-liner bearings have higher stiffness and load capability than feedhole bearings (we know now that we must add, “if the clearance is properly tuned”), that lightly loaded bearings are subject to periodic whirl instabilities while heavily loaded high eccentricity bearings are subject to “random” aperiodic vibration, and so forth. However, the CFD experiment method and the lack of extendibility of the Reynolds equations used based on poor similitude analysis fail to provide a means to examine and definitively explore these complex relationships. The “back to basics” methods,

used in this thesis, enable this exploration. And that is probably the largest contribution of this work."

## CHAPTER 6. FUTURE AND CONTINUING WORK

### 6.1. Future Analytical Work

***Search for the speculated dimensionless clearance factor that relates static  $W/pA$  maxima locations on the  $h$ - $c$  plane to  $K_{meas}$ .***

It was observed that as  $K_{meas}$  was increased by a factor of 10 that the clearance location of the  $W/pA$  maximum increased by 2 to 2.7. It was speculated that, within the precision of the CFD experiments, there might be a constant factor characterized by a dimensionless clearance relating the behavior of  $W/pA$  with  $K_{meas}$ .

***Search for the speculated dimensionless minimum flight height factor that relates  $h_{min}$  to hydrodynamic behavior.***

Rotational hydrodynamic behavior is related to the size of  $h_{min}$  independent of the clearance. That is, for a bearing with a large clearance hydrodynamic effects will be minimal at large eccentricity ratios compared to hydrodynamic effects of a bearing with smaller clearance smaller eccentricity ratio if that bearing has smaller  $h_{min}$ .

Again this observation might relate to the same “missing characteristic length” factor observed when examining static  $W/pA$  versus minimum flight height.

**Based on the concept of “the hydrostatic strength” of a bearing, formulate an equivalent “hydrodynamic bearing strength” and use the two to determine a dimensionless bearing number for hybrid bearings.**

The numerical instability speed limits in the CFD testing were attributed to the extrema of the characteristic hydrodynamic wave approaching singularities, especially the pressure minima located aft of  $h_{min}$  shifting forwards to approach  $h_{min}$ . The physical limit that the pressure minimum cannot occur forwards of  $h_{min}$  along with the steep slopes of the dynamic pressure waves is strongly reminiscent of sonic phenomena. For flow in the  $R\theta$  direction  $h_{min}$  is the point of convergence so that the bearing gap in the  $R\theta$  direction forms a convergent/divergent nozzle at  $h_{min}$ .

**Search for a limiting maximum attitude angle for rotating bearings based on their hydrostatic and hydrodynamic strengths.**

We observed the development of a hydrodynamic wave based on RHA with the property that with small RHA, the pressure wave has a long span which is usually asymmetric at the angular location of  $h_{min}$ . As the speed is increased, the pressure maximum and minimum both shift forward into the flow and the span of the wave shortens. The pressure minimum and maximum appear to reach the limit of their shift when the pressure minimum reaches the angular location of  $h_{min}$ . The minimum span of the pressure wave appears to be determined by  $h_{min}$ . Is this true and does this imply a maximum attitude angle?

## 6.2. Future Testing

### 6.2.1. Further Static Tests

***Static tests of prototype bearings to confirm unusual  $W/pA$  versus  $H$  curve shapes (especially the near surface effect) indicated by CFD results.***

Prototype bearings should be tested that according to the CFD results should exhibit very measurable unexpected curve shapes. For example, the “near surface effect” would be most noticeable with a large clearance bearing with high flow feedholes where the alignment of the first feedhole is at the location of minimum flight height.

Experiments could then easily be done to rotate the alignment of the feedholes so that 2 feedholes straddle the  $h_{min}$  an equal angular distance apart. Would this eliminate the the surface effect?

### 6.2.2. Dynamic Testing

No dynamic testing was done for this thesis. Dynamic testing was deferred until CFD calculations could determine bearings most likely to succeed and then use empirical testing to confirm the predicted bearing performance. Since this is very complicated and the predicted performance, especially stability performance, depends on many physical characteristics of the bearing such as masses, moments of inertia etc., and operating parameters relating to degrees of motion and modes of loading the total bearing system, this will be deferred to be used in an actual bearing program where the need for a gas bearing to perform a specific task is specified.



### 6.3. Future CFD Work

#### 6.3.1. Static Bearing Studies

***CFD experiments should be run with other feedhole configurations and possibly models of porous liners as a matrix of feedhole elements and nonporous elements to test the range of the near surface effect.***

***Perform CFD mapping of the  $W/pA$  versus  $H-c$  plane for a variety of different mass addition configurations.***

This thesis has demonstrated that the  $W/pA$  maximum on the  $H-c$  plane is fundamentally determined by the mass addition configuration. If a dimensionless clearance can be found to stop the  $H-c$  shifting of the maxima with increased  $K_{meas}$ , then a single mapping could characterize the hydrodynamic strength of a given mass addition configuration. Such a cataloging would be useful and interesting.

### 6.3.2. Rotating Bearings

***Develop techniques to expand the range of pressure distribution solutions.***

It was hypothesized that numerical instability occurs when the grid is too coarse to resolve the extrema of the pressure wave especially as the extrema approach apparent singularity limits such as:

- Pressure minimum left shifting to  $h_{\min}$  angular location
- Sub-atmospheric pressure minimum being shifted to the ends of the bearing
- Too large of a wave slope (exceeding  $0.10 \text{ degrees}^{-1}$ )

Some experiments that could be performed:

Test and explore further the hypothesis that “stronger” hybrid bearings have higher numerical speed limits. This could be easily (though time consuming) done by repeating the hybrid bearing experiments using higher and lower operating pressures.

Test the hypothesis that a finer mesh especially in the bearing gap near the minimum flight height location might expand the range of possible pressure solutions. This could be easily (though time consuming) done by increasing the mesh size and redoing the hybrid bearing experiments.

***Do CFD experiments that include stability using the “orbit method” and take in account the time transient terms in the Reynolds equation.***

This effort would be best suited to a specific bearing program.

**Determine whether and how Ansys or other commercial CFD applications can be used for bearing CFD calculations.**

All the CFD results in this thesis were the result of programming using the discretized Reynolds equation found in Appendix A. The custom written programming is fairly flexible in being able to perform CFD experiments on any variety of mass addition configurations for cylindrical bearings of any given dimensions with variations in temperature and ambient pressure. However using an irregular grid pattern or alternate shapes would require tedious reprogramming. It would be very useful if 3D CAD drawings could be used to define the bearing and flexible meshing could be done.

## LIST OF SYMBOLS

## LIST OF SYMBOLS

Basic dimensions are length (L), time (T) and temperature ( $\theta$ ). In addition either mass (M) or force (F) is required. In this work the L, T, M,  $\theta$  will be used.

Dimensional associated with ammeters used are accumulated here.

Symbols			
Symbol	Description	EE units	Dimensions
$\tau$	Shear Stress	$\frac{lbf}{in^2}$ or psi	$\frac{F}{L^2} = \frac{M}{LT^2}$
$\dot{\gamma}$	Shear Rate	$s^{-1}$	$\frac{L}{TL} = \frac{1}{T}$
Q	Volumetric flow rate (in Appendix A)	$\frac{in^3}{s}$	$\frac{L^3}{T}$
$q_x, q_y, q_z$	Volumetric outflow per unit width	$\frac{in^2}{s}$	$\frac{L^3}{T}$
$\eta = \frac{\tau}{\dot{\gamma}}$	Dynamic or absolute viscosity	$\frac{lbf \cdot s}{in^2}$ or reyn	$\frac{M}{LT^2} T = \frac{M}{LT}$
$p$	Pressure	$\frac{lbf}{in^2}$ or psia	$\frac{F}{L^2} = \frac{M}{LT^2}$
$p_a$	Ambient pressure	$\frac{lbf}{in^2}$ or psia	$\frac{F}{L^2} = \frac{M}{LT^2}$
$p_p$	Pivot pressure	$\frac{lbf}{in^2}$ or psig	$\frac{F}{L^2} = \frac{M}{LT^2}$
$p_{op}$	Operating pressure Gage pressure of pressure reservoir	$\frac{lbf}{in^2}$ or psig	$\frac{F}{L^2} = \frac{M}{LT^2}$

Symbols - Continued			
Symbol	Description	EE units	Dimensions
$\rho$	Density	$\frac{lb}{in^3}$	$\frac{M}{L^3}$
$h$	Bearing gap height Or flight height	in	$L$
$u, v, w$	flow velocity in x, y, z	$\frac{in}{s}$	$\frac{L}{T}$
$U, V, W$	Surface velocity in x, y, z	$\frac{in}{s}$	$\frac{L}{T}$
$\bar{U}, \bar{V}, \bar{W}$	Entrainment velocity in x, y, z	$\frac{in}{s}$	$\frac{L}{T}$
$\omega$	Angular velocity	$s^{-1}$	$T^{-1}$
$\dot{m}$	Mass flow through face	$\frac{lb}{s \cdot in^2}$	$\frac{M}{TL^2}$
$\dot{M}$	Mass flow from point source	$\frac{lb}{s}$	$\frac{M}{T}$
$k_{\rho p}$	Density-pressure constant (1/Rt)	$\frac{lb}{lb_f \cdot in}$	$\frac{T^2}{L^2}$
$k_{ma}$	Flow addition constant $\frac{\Delta Q}{\Delta p}$	$\frac{in^3}{s \cdot psi}$	$\frac{L^4 T}{M}$
$k_{hc}$	Mass addition permeability	$in^2$	$L^2$
$k_{fh}$	Point source feed hole constant	in	$L$
$t$	Time	s	$T$
$W$	Load	lb <sub>f</sub>	$\frac{ML}{T^2}$

Bearing Design Parameters		
$R$	Bearing Radius	in
$L$	Bearing Length	in
$D_{fh}$	Feedhole Diameter	in
$c$	Clearance	in

Ratios and Dimensionless Parameters Symbol			
Symbol	Description	Formula	Dimensions
$P$	Dimensionless pressure	$\frac{p}{p_a}$	None
$P_{op}$	Dimensionless operating pressure	$\frac{p_{op} + p_a}{p_a}$	None
$P_p$	Dimensionless pivot pressure	$\frac{p_p + p_a}{p_a}$	None
$H$	Dimensionless gap height or flight height	$\frac{h}{c}$	None
$\Lambda$	Compressibility or bearing number	$\frac{6\eta\omega R^2}{c^2 p_a}$	None
$t_c$	Characteristic time	$12 \left( \frac{\eta}{p_a} \right) \left( \frac{R}{c} \right)^2$	$s$
$\tau$	Dimensionless time	$\frac{t}{t_c}$	None
$Q$	Square of $P$	$P^2$	None
$W/pA$	Static Bearing efficiency	$\frac{W}{p_{op} 2RL}$	None

## REFERENCES



## REFERENCES

- [1] J. Powell, *A review of progress in gas lubrication*, review of Physics in Technology, Vol. 1, pp. 96-129, 1970.
- [2] A. Raimondi, *A numerical solution for the gas lubricated full journal bearing of finite length*, ASLE Transactions Vol. 4, pp. 131-155, 1961.
- [3] J. Ausman, *Theory and design of self-acting gas-lubricated journal bearings including misalignment effects*, Proceedings of the 1<sup>st</sup> International Symposium of Gas Lubricated Bearings, ACR-49, ONR, Washington D.C., pp. 161-192, 1959.
- [4] H. Marsh, *The Stability of aerodynamic gas bearings*, Institution of Mechanical Engineers, Westminster, SW, 1965.
- [5] Z-S Liu et al., *Performance analysis of rotating externally pressurized air bearings*, IMechE Vol. 223 Part J:, pp. 653-663, 2009.
- [6] Y. Chen et al. *Influences of operational conditions and geometric parameters on the stiffness of aerostatic journal bearings*, Precision Engineering 24, pp. 722-734, 2010.
- [7] C-C Wang C-K Chen, *Bifurcation analysis of externally pressurized porous gas journal bearings*, Proc. Instn Mech. Engrs Vol. 217 Part C, pp.1325-1338, 2003.

- [8] B. Ertas, *Compliant hybrid journal bearings using integral wire mesh dampers*, Journal of Engineering for Gas Turbines and Power, Vol. 131, 022503, March 2009.
- [9] C-C Wang et al., *Bifurcation and nonlinear dynamic analysis of a flexible rotor supported by relative short gas journal bearings*, Chaos Solutions and Fractals 32, pp. 566-582, October 2005.
- [10] C-C Wang, *Analysis of an aerodynamic grooved journal bearing with plain sleeve*, Proc. IMechE Vol. 220 Part C, 2006
- [11] C-C Wang, *Nonlinear dynamic behavior and bifurcation analysis of a rigid rotor supported by relatively short externally pressurized porous gas journal bearing system*, Acta Mechanica 183, pp. 41-60, 2006.
- [12] C-C Wang, *Theoretical and nonlinear behavior analysis of a flexible rotor supported by a relatively short herring-grooved gas journal-bearing system*, Physica D 23, pp. 2282-2295, 2008.
- [13] P. Yang et al., *On the non-linear stability of self-acting gas journal bearings*, Tribology International 42, pp. 71-76, 2009.
- [14] J-B Zhou et al., *Bifurcation analysis of ultrashort self-acting gas journal bearings for MEMS*, IEEE Transactions on Industrial Electronics, Vol. 56, No. 8, pp. 3188-3194, August 2009.
- [15] Y. Lee et al., *Numerical prediction of slip flow effect on gas-lubricated journal bearings for MEMS/MST-based micro-rotating machinery*, Tribology International 38 pp. 89-96, 2005.

- [16] W-M Zhang, J-B Zhou, G. Meng, *Performance and stability analysis of gas-lubricated journal bearings in MEMs*, Tribology International 44, pp. 887-897, 2011.
- [17] C. Teo et al., *Unsteady flow and dynamic behavior of ultrashort Lomakin gas bearings*, Journal of Tribology Vol. 130, 011001, January 2008.
- [18] J. Su, K. Lie, *Rotor dynamic instability analysis on hybrid journal bearings*, Tribology International 29 pp. 238-248, 2006.
- [19] J. Williams, *Engineering Tribology*, Cambridge University Press, New York, NY, 2005, pp. 301-326
- [20] M. Zucrow, J. Hoffman, *Gas Dynamics*, John Wiley and Sons, Hoboken, NJ, 1976.
- [21] P. McCormack, L. Crane, *Physical fluid dynamics*, Academic Press, New York 1973, pp. 95-111.
- [22] R. Sabersky et al. *Fluid Flow*, The Macmillan Company, New York, 1971.
- [23] C-C Wang et al., *Non-linear dynamic analysis of a flexible rotor supported by self-acting gas journal bearings*, Proc Instn Mech. Engrs. Vol. 218 Part C, pp. 1527-1538, 2004.
- [24] *Air bearing application and design guide*, New Way Air Bearings, revision E, January 2006.
- [25] K. Czolczynski, *Rotordynamics of gas-lubricated journal bearing systems*, Springer-Verlag, New York, NY, 1999.

- [26] Y.B. Lee et al. *Numerical prediction of slip flow effect on gas-lubricated journal bearings for MEMS/MST-based micro-rotating machinery*, Tribology International 38 pp. 89-96, 2005.
- [27] V. Kamala, *The hybrid isothermal Air lubricated Journal Bearing*, Transactions of the ASME Vol. 101, pp. 444-450, October 1979.
- [28] N. Ene, F. Dimofte, T. Keith, *A Dynamic analysis of hydrodynamic wave journal bearings*, Tribology Transactions, 51 pp. 82-91, 2008
- [29] M. Barnett, A. Silver, *Application of air bearings to high-speed turbomachinery*, SAE Technical Paper series, 700720, September 1970.
- [30] D. Ruscitto, J. Mc Cormic, S. Gray, *Hydrodynamic air lubricated compliant surface bearing for an automotive gas turbine engine I -journal bearing performance*, NASA Report no. CR-135368, April 1978.
- [31] S. Gray, *Foil type bearings for the Chrysler automotive gas turbine engine program-development and operational experiences*, SAE Technical Paper Series, 790109, 1979.
- [32] G. Agrawal, *Foil air/gas bearing technology - an overview*, ASME Pub. 97-GT-347, pp. 2-11, March 1979.
- [33] R. Trippet, *Air bearing development for a GM automotive gas turbine*, SAE Technical Paper Series, 790107, 1979.
- [34] H. Heshmat et al., *Analysis of gas-lubricated foil journal bearings*, Journal of Lubrication Technology, Vol. 105 pp. 647-655, October 1983.

- [35] R. Murry, *An air bearing fan for EVA suit ventilation*, SAE technical paper series, 901432, 1990.
- [36] P. Fukumoto, N. Allen, G. Stonesifer, *Development of an air-bearing fan for space extravehicular activity (EVA) suit ventilation*, SAE Technical Paper Series, 921297, 1992
- [37] C. Dellacorte, *A new foil air bearing test rig for use to 700° C and 70,000 rpm*, NASA Technical Memorandum, 107405, Tribology Conference, London, England, September 1997.
- [38] C. DellaCorte, M. Valco, *Load capacity estimation of foil air journal bearings for oil-free turbomachinery applications*, NASA/TM -2000-209782, October 2000.
- [39] H. Salehei, H. Heshmat, et al., *Operation of a mesoscopic gas turbine simulator at speeds in excess of 700,000 rpm on foil bearings*, Transactions of the ASME, Vol. 129, pp. 170-176, January 2007.
- [40] S. Howard, *Misalignment in gas foil journal bearings: An experimental study*, Journal of Engineering for Gas Turbines and Power, Vol. 130, 02250, March 2009.
- [41] S. Whitley, D. Phil, C. Betts, *Study of gas-lubricated, hydrodynamic, full journal bearings*, British Journal of Applied Physics, Vol. 10, October 1959.
- [42] H. Mori, H. Yabe, *Theoretical investigation of externally pressurized gas-lubricated porous journal bearing with surface-loading effect*, Journal of Lubrication Technology, pp. 195-202, April 1973.
- [43] M. Cohen, *On the dynamic stability of self-aligning journal gas bearings*, Transactions of the ASME, pp. 434-440, October 1977.

- [44] E. Gargiulo, *Porous gas lubricated journal bearings: experimental investigation*, Transactions of the ASME Vol. 101, pp. 466-473, October 1979.
- [45] S. Wadhwa, R. Sinhasan, D. Singh, *Analysis of orifice compensated externally pressurized gas bearings*, Tribology International Vol. 16, No. 4, pp. 203-211, 1983.
- [46] F. Dimofte, *Wave Journal Bearing With Compressible Lubricant-Part I: The Wave Bearing Concept and a Comparison to the Plain Circular Bearing*. STLE Tribol. Trans. 1995:38:1, pp. 153-160, 1995.
- [47] F. Dimofte, *Wave Journal Bearing With Compressible Lubricant-Part II: A Comparison of the Wave Bearing With a Wave Groove Bearing and Lobe Bearing*, STLE Tribol. Trans. 1995:38:2, pp.364-372, 1995.
- [48] E. Piekos, K. Breuer, *Pseudospectral orbit simulation of non-ideal gas-lubricated journal bearings for microfabricated turbomachines*, Journal of Tribology 121, pp. 604-609, July 1999.
- [49] N. Saha, B. C. Mujumdar, *Study of externally-pressurized gas-lubricated two-layered porous journal bearings: a steady state analysis*, Proc Instn Mech Engrs Vol. 216 Part J, 2002.
- [50] V. Grabovskii, *Optimum gas journal bearing with open bearing ends and feeder slot*, Fluid Dynamics, Vol. 39, No. 4, pp. 540-550, 2004.
- [51] A. Senatore, N. Popescu, *Influence of wear conditions on non-cylindrical gas bearings pressure and rotor stability*, The Annals of University "Dunarea de Jos" of Galati Fascicle VIII, ISSN 1221-4590 Tribology, 2004.

- [52] J. Peirs et al. *Development of high-speed bearings for micro gas turbines*, MicroMechanics Europe Workshop, Leuven Belgium, 5-7 September 2004.
- [53] I. Liu, Z. Spakovszky, *Effects of bearing stiffness anisotropy on hydrostatic micro gas journal bearing dynamic behavior*, Journal of Engineering for Gas Turbines and Power, Vol. 129, pp. 177-184, January 2007.
- [54] R. Ruiz, et al., *Asynchronous dynamic coefficients of a three-lobe air bearing*, Journal of Engineering for Gas Turbines and Power, Vol. 130, 052502, September 2008.
- [55] N. Savoulides et al., *Fabrication and testing of a high-speed microscale turbocharger*, Journal of Micromechanical Systems, Vol. 17, No 5, October 2008.
- [56] V. Grabovskii, *Numerical investigation of the load capacity of a gas journal bearing of finite length with end seals* Fluid Dynamics, 2009, Vol. 44, No. 6, pp. 836-841, 2009.
- [57] B. Ertas et al., *A general purpose test facility for evaluating gas lubricated journal bearings*, Journal of Engineering for Gas Turbines and Power, Vol. 131, 022502, March 2009.
- [58] T. Stolarski, *Running characteristics of aerodynamic bearing with self-lifting capacity at low rotational speed*, Advances in Tribology, Volume 20111, Article Article ID 973740, 2011.
- [59] J. Su, *Approximate solution for a hydrostatic porous journal bearing with low eccentricity and permeability*, Lubrication Engineering, pp. 22-28, December 2002.

- [60] J. Reddy, *An introduction to the finite element method*, McGraw-Hill Higher Education, New York, NY, 2006.
- [61] M. Heath, *Scientific Computing*, McGraw-Hill Higher Education, New York, NY, 2002.
- [62] D. Tannehill, D. Anderson, R. Pletcher, *Computational fluid mechanics and heat Transfer*, Taylor and Francis, Philadelphia, PA. 1997.
- [63] F. Sahlin et al., *Two-dimensional CFD-analysis of micro-patterned surfaces in hydrodynamic lubrication*, Transactions of the ASME, Vol. 127, pp. 96-102, January, 2005.
- [64] M. Zengeya M. Gadala, *Optimization of journal bearings using a hybrid scheme*, Proc. I, MechE Vol. 221, Part J, 2007.
- [65] S. Biloe, S. Mauran, *Gas flow through highly porous graphite matrices*, Carbon 41, pp. 525-537, 2003.
- [66] N. Wang et al., *Comparison of iterative methods for solutions of compressible-fluid Reynolds equation*, Journal of Tribology, Vol. 133, 021702, April 2011.
- [67] A. Almqvist, *Homogenization of the Reynolds equation governing hydrodynamic flow in a rotating device*, Journal of Tribology, Vol. 133 021701, April 2011.
- [68] J. Powell, *Gas lubricated bearings*, Butterworths, London, pp. 92-108, 1964.



- [69] J. Miner, J. Dell, A. Galbato, *F117-PW-100 hybrid ball bearing ceramic technology insertion*, Transactions of the ASME 95-GT-390, September 1995.
- [70] L. Burgmeier, M. Poursaba, *Ceramic hybrid bearings in air-cycle machines*, Transactions of the ASME 94-GT-393, September 1994.
- [71] M. Dezzani, P. Pearson, *Hybrid ceramic bearings for difficult applications*, Transactions of the ASME 95-GT-391, June 1995.
- [72] J. Lauer, L. Davis, *Wear reduction in ceramic bearings by surface generated pyrolytic carbon continuously replenished by ethylene gas*, NASA report No. CR-189214, December 1993.
- [73] T. Lawrence, D. Lawrence, *SBIR Phase I final report for advanced high-speed high-temperature slip ring for turboshaft engines*, U.S. Army Research Development and Engineering Command, AATD, Fort Eustis VA, June 2005.
- [74] NASA, *Oil-free turbomachinery program - advanced foil bearings*, [HTTP://WWW.GRC.NASA.GOV/WWW/OILFREE/BEARINGS.HTM](http://www.grc.nasa.gov/www/oilfree/bearings.htm), last accessed 1/13/2010.
- [75] B. Dykas, S. Howard, *Journal design considerations for turbomachine shafts supported on foil air bearing*, Society of Tribologists and Lubrication Engineers, Oct-Dec 2004.
- [76] *Creating a turbomachinery revolution fact sheet: research at Glenn enables an oil-free turbine engine*, NASA Fact Sheet, FS-2001-07-014-GRC, last accessed 6/18/2011.

[77] H. Hashimoto, K. Matsumoto, *Improvement of operating characteristics of high-speed hydrodynamic bearings journal bearings by optimum design: part I - formulation of methodology and its application to elliptical bearing design*, Journal of Tribology, Vol. 23, pp. 305- 312, April 2001.

[78] J. Farron, R. Teitelbaum, *Squeeze film bearings*, US patent # 3,471,205, Oct. 1969.

## APPENDICES

Appendix A Derivation And Discretization Of Reynolds Equation For Hybrid Gas Journal Bearing

A.1. Summary

Equation A-1 is the Reynolds equation in cylindrical coordinates for a gas journal bearing with rotation and mass addition.

**Equation A-1** Reynolds equation for hybrid journal bearing

$$-\frac{\partial}{R\partial\theta}\left(\frac{\rho h^3}{\eta}\frac{\partial p}{R\partial\theta}\right)+6\frac{\partial}{\partial\theta}(\omega\rho h)-\frac{\partial}{\partial z}\left(\frac{\rho h^3}{\eta}\frac{\partial p}{\partial z}\right)+12h\frac{d\rho}{dt}+12\rho(V_B-V_S)=12\frac{\dot{M}}{R\delta\theta\delta z}$$

$$\dot{M} = \left\{ \begin{array}{l} 0 \text{ for elements with no mass addition} \\ \dot{m}R\delta\theta\delta z \text{ for elements with area scaled mass addition} \\ \dot{M} \text{ for elements with point source mass addition} \end{array} \right\}$$

Dimensions of A-1 are  $M/L^2T$ .

**Equation A-2** Dimensionless Reynolds Equation

$$-\frac{\partial}{\partial\theta}\left(PH^3\frac{\partial P}{\partial\theta}\right)+\Lambda\frac{\partial}{\partial\theta}(PH)-\left(\frac{R}{L}\right)^2\frac{\partial}{\partial Z}\left(PH^3\frac{\partial P}{\partial Z}\right)+\frac{\partial}{\partial\tau}(PH)=\frac{t_c}{k_{\rho p}p_a cR\delta\theta\delta z}\dot{M}$$

or

$$-\frac{\partial}{\partial\theta}\left(PH^3\frac{\partial P}{\partial\theta}\right)+\Lambda\frac{\partial}{\partial\theta}(PH)-\left(\frac{R}{L}\right)^2\frac{\partial}{\partial Z}\left(PH^3\frac{\partial P}{\partial Z}\right)+\frac{\partial}{\partial t}t_c(PH)=\frac{t_c}{k_{\rho p}p_a cR\delta\theta\delta z}\dot{M}$$

Where :

$$\rho = \frac{p}{Rt} = k_{\rho p} p$$

$$k_{\rho p} = \frac{1}{Rt} = \frac{1}{640.2248(^{\circ}F + 459.67)}$$

$$P = \frac{p}{p_a}$$

$$H = \frac{h}{c}$$

$$Z = \frac{z}{L}$$

$$\Lambda = \frac{6\eta\omega R^2}{c^2 p_a} = \frac{1}{2} t_c \omega$$

$$t_c = 12 \left( \frac{\eta}{p_a} \right) \left( \frac{R}{c} \right)^2$$

$$\tau = \frac{t}{t_c}$$

Physical Meaning of terms of the equations:

1. Mass *outflow* in the  $\theta$  direction due to the pressure driven Poiseuille flow.

$$-\frac{\partial}{R\partial\theta} \left( \frac{\rho h^3}{\eta} \frac{\partial p}{R\partial\theta} \right) \text{ and } -\frac{\partial}{\partial\theta} \left( PH^3 \frac{\partial P}{\partial\theta} \right)$$

The negative sign signifies that the outflow will be greater than the inflow only if the pressure gradient is in the opposite direction of the  $\theta$  axis. (see figure A-1).

2. Shear driven Couette mass outflow in the  $\theta$  direction due to rotation and convergence of the bearing gap.

$$6 \frac{\partial}{\partial\theta} (\omega \rho h) \text{ and } \Lambda \frac{\partial}{\partial\theta} (PH)$$

In the dimensionless form where the density has been replaced by pressure, it is seen that positive pressure gradient in the  $\theta$  direction (as would be expected if the flow gap is converging) *increases* the mass outflow. This is because the

volumetric flow rate is determined by the rotation of the shaft in the  $\theta$  direction and the mass flux is determined by multiplying the volumetric flow rate by the density which is increasing with a positive pressure gradient. This is sometimes called the convergent wedge term or just wedge term as it represents  $\rho \bar{U} \frac{\partial h}{\partial x}$

where  $\bar{U}$  is the entraining velocity.

3. Mass out flow in z or Z direction due to the pressure driven Poiseuille flow.

$$-\frac{\partial}{\partial z} \left( \frac{\rho h^3}{\eta} \frac{\partial p}{\partial z} \right) \text{ and } -\left( \frac{R}{L} \right)^2 \frac{\partial}{\partial Z} \left( PH^3 \frac{\partial P}{\partial Z} \right)$$

4. The squeeze film terms representing rate of mass increase within the fluid element.

$$+12h \frac{d\rho}{dt} + 12\rho (V_B - V_S) \text{ and } \frac{\partial}{\partial \tau} (PH)$$

5. Mass input to the fluid element through the bushing ID surface.

$$12 \frac{\dot{M}}{R\delta\theta\delta z} \text{ and } \frac{t_c}{k_{\rho p} p_a c R \delta\theta\delta z} \dot{M}$$

## A.2. Continuity of a Fluid Element in the Bearing Gap

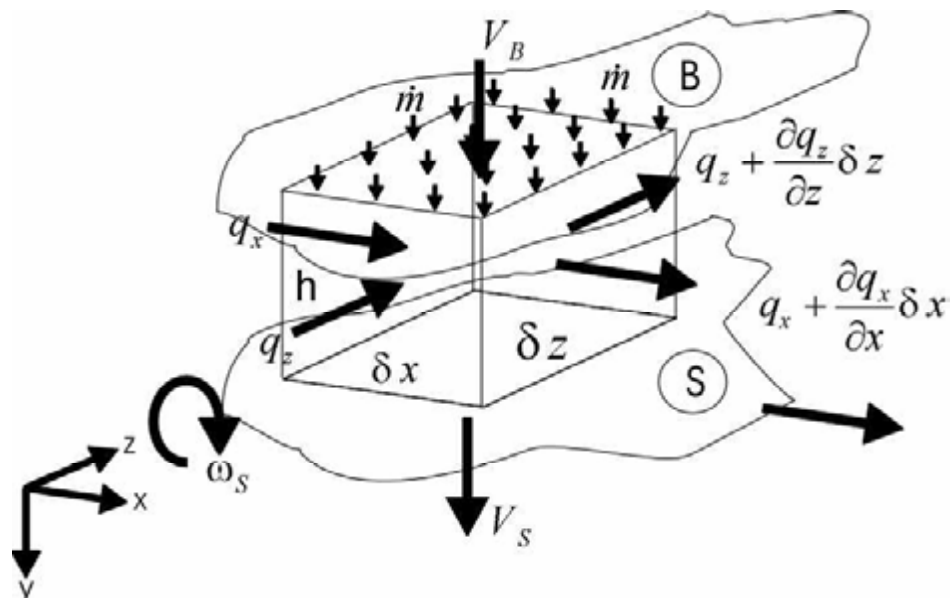


Figure A-1 Fluid element in the bearing gap

Figure A-1 depicts a Fluid element in a bearing gap between the OD surface of the shaft, S, and the ID bushing surface B. The “y” axis in A-1 represents the radial axis pointing towards the center of the bearing. The shaft rotates about the “z” axis. Mass addition is possible through the bushing surface. Both surfaces can have radial motion  $V_S$  and  $V_B$ . The dimensions of the element are  $\delta x$  by  $\delta y$  by  $h$ . Where  $h$  is the height of the bearing gap.

In plain terms mass continuity states that:

**(the net mass outflow in x) + (the net mass outflow in z) =  
(the mass input in y) - (change in mass in the finite element)**

In the chosen EE units, these terms are in *lbs/s*.

#### A.2.1. Net Mass Outflow in the “x” Rotation Axis

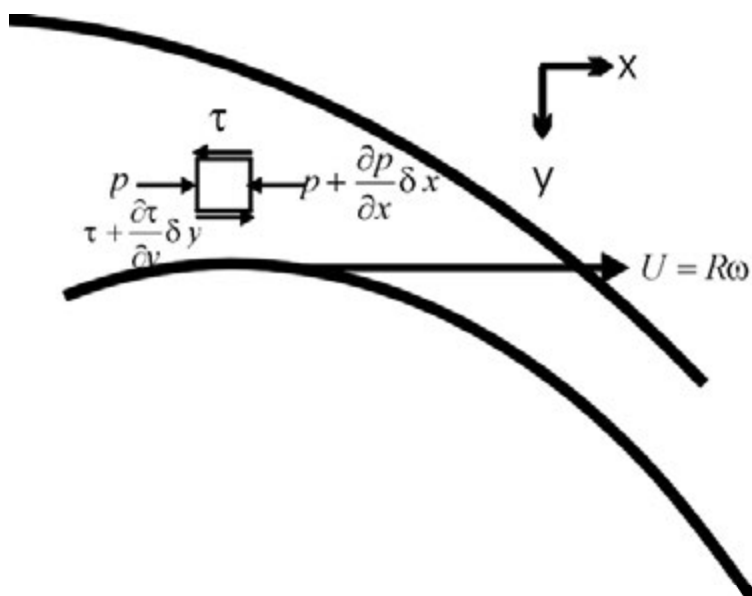


Figure A-2 A smaller fluid element

In order to determine the net mass outflow in the “x” direction, a smaller fluid element can be considered in the bearing gap that does not span the distance between the shaft OD and the bushing ID. The shaft ID surface has a velocity  $U$



in the x direction where  $U = R\omega$  and  $R$  is the nominal bearing radius ( $R \gg h$ ) and  $\omega$  is the shaft rotation speed.

From balancing forces in x direction on the fluid element:

$$\sum F_x = p\delta y\delta z - \left( p + \frac{\partial p}{\partial x} \delta x \right) \delta y\delta z + \left( \tau + \frac{\partial \tau}{\partial y} \delta y \right) \delta x\delta z - \tau\delta x\delta z$$

$$\sum F_x = -\frac{\partial p}{\partial x} \delta x\delta y\delta z + \frac{\partial \tau}{\partial y} \delta y\delta x\delta z$$

So that :

$$\frac{\partial p}{\partial x} = \frac{\partial \tau}{\partial y}$$

Shear  $\tau$  for a Newtonian fluid is:

$$\tau = \eta \dot{\gamma} = \eta \frac{\partial u}{\partial y}$$

Where  $\dot{\gamma}$  is the local shear strain rate or  $\frac{\partial u}{\partial y}$  and  $\eta$  is the dynamic or absolute viscosity which is shear stress/velocity gradient.  $\eta$  therefore has dimensions  $FT/L^2$  or  $M/TL$ .

Therefore:

$$\frac{\partial p}{\partial x} = \eta \frac{\partial^2 u}{\partial y^2}$$

Since  $p$  in this one dimensional case is a function only of  $x$  it can be integrated twice with respect to  $y$ .

$$\frac{\partial p}{\partial x} = \eta \frac{\partial^2 u}{\partial y^2}$$

$$\frac{\partial^2 u}{\partial y^2} = \frac{1}{\eta} \frac{\partial p}{\partial x}$$

$$\frac{\partial u}{\partial y} = \frac{1}{\eta} \frac{\partial p}{\partial x} \int dy = \frac{1}{\eta} \frac{\partial p}{\partial x} y + C_1$$

$$u = \int \left( \frac{1}{\eta} \frac{\partial p}{\partial x} y + C_1 \right) dy = \frac{1}{2\eta} \frac{\partial p}{\partial x} y^2 + C_1 y + C_2$$

$C_1$  and  $C_2$  are constants of integration which we can evaluate by the no-slip boundary conditions that  $u=U$  at  $y=h$ , and  $u=0$  at  $y=0$ . Thus:

$$C_2 = 0$$

$$C_1 = \frac{U}{h} - \frac{1}{2\eta} \frac{\partial p}{\partial x} h$$

So that:

$$u = \frac{1}{2\eta} \frac{\partial p}{\partial x} y(y-h) + U \frac{y}{h}$$

The term  $\frac{1}{2\eta} \frac{\partial p}{\partial x} y(y-h)$  is pressure driven Poiseuille flow contribution and the term  $U \frac{y}{h}$  is the Couette shear distribution.

The volumetric flow rate per unit depth  $z$ , in the  $x$  direction,  $q_x$ , across a radial surface spanning the bearing gap  $h$  can be determined by:

$$q_x = \int_0^h u dy$$

or

$$q_x = \frac{1}{2\eta} \frac{\partial p}{\partial x} \left( \int_0^h y^2 dy - h \int_0^h y dy \right) + \frac{U}{h} \int_0^h y dy$$

$$q_x = \frac{1}{2\eta} \frac{\partial p}{\partial x} \left( \frac{h^3}{3} - \frac{1}{2} h^3 \right) + \frac{U}{2h} h^2$$

$$q_x = -\frac{1}{12\eta} \frac{\partial p}{\partial x} h^3 + \frac{U}{2} h$$

Dimensions of  $q$  are volume per time per unit depth or :  $q \rightarrow \frac{L^3}{T} \frac{1}{L} = \frac{L^2}{T}$ .

This is obvious for the second term, to see that it also applies for the first term units of mass times acceleration are substituted for force in pressure so that:

$$\frac{h^3}{12\eta} \frac{dp}{dx} \rightarrow L^3 \left( \frac{LT}{m} \right) \frac{mL}{T^2 L^2 L} = \frac{L^2}{T}$$

Since  $U = R\omega$ ,

**Equation A-3** Volumetric flow in x

$$q_x = -\frac{1}{12\eta} \frac{dp}{dx} h^3 + \frac{R\omega}{2} h$$

Looking at figure A-1 it can be seen that the mass flux through the surface  $h$  by  $\delta z$  is  $\rho q_x \delta z$ .

$$\text{(the net mass outflow in x)} = \left( \frac{\partial}{\partial x} (\rho q_x) \delta x \right) \delta z$$

Substituting in equation A-1 leads to:

**Equation A-4** Net mass outflow in x

$$\text{(the net mass outflow in x)} = -\frac{\partial}{\partial x} \left( \frac{\rho h^3}{12\eta} \frac{dp}{dx} \right) \delta x \delta z + \frac{\partial}{\partial x} \left( \frac{\rho h R \omega}{2} \right) \delta x \delta z$$

EE units of equation A-4 are *lbs/s*.

$$\frac{\partial}{\partial x} \left( \frac{\rho h^3}{12\eta} \frac{\partial p}{\partial x} \right) \delta x \delta y \rightarrow \frac{1}{L} \frac{ML^3LT}{L^3M} \frac{ML}{T^2L^2L} LL \rightarrow \frac{L^7M^2T}{L^7MT^2} \rightarrow \frac{M}{T}$$

$$\frac{\partial}{\partial x} \left( \frac{R\omega\rho h}{2} \right) \delta x \delta y \rightarrow \frac{1}{L} \frac{LML}{TL^3} LL \rightarrow \frac{L^4M}{L^4T} \rightarrow \frac{M}{T}$$

### A.2.2. Mass Outflow in the “z” Longitudinal Axis

An analogous analysis in the “z” direction yields:

$$\frac{\partial p}{\partial z} = \eta \frac{\partial^2 w}{\partial y^2}$$

$$\frac{\partial^2 w}{\partial y^2} = \frac{1}{\eta} \frac{\partial p}{\partial z}$$

$$\frac{\partial w}{\partial y} = \frac{1}{\eta} \frac{\partial p}{\partial z} \int dy = \frac{1}{\eta} \frac{\partial p}{\partial z} y + C_1$$

$$w = \int \left( \frac{1}{\eta} \frac{\partial p}{\partial z} y + C_1 \right) dy = \frac{1}{2\eta} \frac{\partial p}{\partial z} y^2 + C_1 y + C_2$$

In the z direction there is no relative tangential velocity between the surfaces and thus the boundary conditions due to no slip assumption are:  $w=0$  at  $y = 0$ , and  $w= 0$  at  $y=h$ .

So it is seen immediately from  $w=0$  at  $y =0$  that  $C_2=0$ .

From  $w=0$  at  $y = h$

$$\frac{1}{2\eta} \frac{\partial p}{\partial z} h^2 + C_1 h = 0$$

$$C_1 = -\frac{1}{2\eta} \frac{\partial p}{\partial z} h$$

so:

$$w = \frac{1}{2\eta} \frac{\partial p}{\partial z} y^2 - \frac{1}{2\eta} \frac{\partial p}{\partial z} hy$$

$$w = \frac{1}{2\eta} \frac{\partial p}{\partial z} (y^2 - hy) = \frac{1}{2\eta} \frac{\partial p}{\partial z} y(y - h)$$

$w$  has only the pressure driven Poiseuille flow (as expected). So that:

$$q_z = \int_0^h w dy = \frac{1}{2\eta} \frac{\partial p}{\partial z} \left( \frac{y^3}{3} - \frac{hy^2}{2} \right)_0^h = -\frac{1}{12\eta} \frac{\partial p}{\partial z} h^3$$

and:

**Equation A-5** Net mass outflow in z

$$\text{(the net mass outflow in z)} = -\frac{\partial}{\partial z} \left( \frac{\rho h^3}{12\eta} \frac{\partial p}{\partial z} \right) \delta z \delta x$$

### A.2.3. Mass Input in y

In areas where there is mass input either orifice fed or porous liner fed, there is a mass input  $\dot{m}$  where  $\dot{m}$  is the mass input per unit time unit area. Thus the mass input is:

**Equation A-6** Net mass input in y

$$\text{(the mass input in y)} = \dot{m} \delta x \delta z$$

The mass input has dimensions of M/T or EE units of lbs/s but  $\dot{m}$  as defined here for the mass addition has dimensions of M/TL<sup>2</sup> or EE units of  $lbs \cdot s^{-1} \cdot in^{-2}$ . Also it should be noticed that the positive direction of mass *input* is in the y direction.

That is *into* the bearing gap.

#### A.2.4. Change in Mass in the Finite Element

The mass in the finite element is  $\rho V$  where  $V$  is the volume of the element and is  $h\delta x\delta z$ .

Therefore the change in mass in the element is:

$$\frac{d}{dt}(\rho V) = \frac{d}{dt}(\rho h\delta x\delta z) = h\delta x\delta z \frac{d\rho}{dt} + \rho\delta x\delta z \frac{dh}{dt} = \left( h \frac{d\rho}{dt} + \rho \frac{dh}{dt} \right) \delta x\delta z$$

It is easily seen from figure A-1 that  $\frac{dh}{dt} = V_s - V_B$  and therefore:

**Equation A-7** Mass change within the element volume

$$\left( h \frac{d\rho}{dt} + \rho (V_s - V_B) \right) \delta x\delta z$$

$\rho (V_s - V_B) \delta x\delta z$  is the “air hammering” term and is positive when the shaft velocity is greater than the bearing velocity which corresponds to the element volume expanding.

$h \frac{d\rho}{dt} \delta x\delta z = \frac{d\rho}{dt} h\delta x\delta z$  is the mass change in the element volume due to overall density change in time.

## A.2.5. Putting It Together

**(the net mass outflow in x) + (the net mass outflow in z) =  
(the mass input in y) - (change in mass in the finite element)**

Therefore:

**Equation A-8** Mass continuity of a bearing gap element

$$-\frac{\partial}{\partial x} \left( \frac{\rho h^3}{12\eta} \frac{\partial p}{\partial x} \right) \delta x \delta z + \frac{\partial}{\partial x} \left( \frac{R\omega\rho h}{2} \right) \delta x \delta z - \frac{\partial}{\partial z} \left( \frac{\rho h^3}{12\eta} \frac{\partial p}{\partial z} \right) \delta z \delta x$$

$$= \dot{m} \delta x \delta z - \left( h \frac{d\rho}{dt} + \rho (V_S - V_B) \right) \delta x \delta z$$

This assumes that the mass addition  $\dot{m}$  is in terms of mass per unit time per unit area and that it scales with the elemental surface area of the bearing face. This is valid for mass addition done via a porous liner. However when the mass addition is done using a feed hole the mass addition will be considered to be coming from a point source. For a point source a term  $\dot{M}$ , mass flow per unit time, will be used in place of  $\dot{m} \delta x \delta z$ . Henceforth the term  $\dot{M}$  will be used in the development with the understanding that:

$$\dot{M} = \left\{ \begin{array}{l} 0 \text{ for elements with no mass addition} \\ \dot{m} \delta x \delta z \text{ for elements with area scaled mass addition} \\ \dot{M} \text{ for elements with pointsource mass addition} \end{array} \right\}$$

Each term in the equation is of the form  $[ ] \delta x \delta z$  where  $[ ]$  has units  $M/L^2T$  and the overall expression is in units of  $M/T$ . This can be simplified by dividing through by  $\delta x \delta z$  so that:

**Equation A-9** Reynolds Equation for a hybrid bearing

$$-\frac{\partial}{\partial x} \left( \frac{\rho h^3}{12\eta} \frac{\partial p}{\partial x} \right) + \frac{\partial}{\partial x} \left( \frac{R\omega\rho h}{2} \right) - \frac{\partial}{\partial z} \left( \frac{\rho h^3}{12\eta} \frac{\partial p}{\partial z} \right) = \frac{\dot{M}}{\delta x \delta z} - h \frac{d\rho}{dt} - \rho (V_S - V_B)$$

Equation A-9 therefore has units of  $M/L^2T$ .

In order to maintain a common sense feel for equation A-10 it is convenient to note the source of each term.

1. Mass flow out of the element due to the pressure gradient in the x direction:

$$-\frac{\partial}{\partial x} \left( \frac{\rho h^3}{12\eta} \frac{\partial p}{\partial x} \right)$$

2. Mass flow out of the element due to shear force caused by shaft rotation. This is sometimes called the convergent wedge term or just wedge term as it represents  $\bar{U} \frac{\partial h}{\partial x}$  where  $\bar{U}$  is the entraining velocity:

$$\frac{\partial}{\partial x} \left( \frac{R\omega\rho h}{2} \right)$$

3. Mass flow out of the element due pressure gradient in the z direction:

$$-\frac{\partial}{\partial z} \left( \frac{\rho h^3}{12\eta} \frac{\partial p}{\partial z} \right)$$

4. Mass flow into the element due to mass addition through the bushing:

$$\frac{\dot{M}}{\delta x \delta z}$$

5. Decrease (minus increase in mass) in mass in the element due time change in density:

$$-h \frac{d\rho}{dt}$$

6. Decrease (minus increase in mass) in mass in the element due change in element volume from change in gap height. This is sometimes called the squeeze film term.

$$-\rho(V_S - V_B)$$



### A.2.6. Comparison with Other Results

Williams [19] uses a similar analysis to determine the Reynolds Equation in 2 dimensions for an incompressible fluid element in a gap between two surfaces with entraining velocities between the surfaces of  $\bar{U}$  and  $\bar{V}$  in the orthogonal parallel  $x$  and  $y$  axis of the surfaces. The result which is 7.57 on page 254 is:

$$\frac{\partial}{\partial x} \left\{ h^3 \frac{\partial p}{\partial x} \right\} + \frac{\partial}{\partial y} \left\{ h^3 \frac{\partial p}{\partial y} \right\} + = 12\eta \left\{ \bar{U} \frac{\partial h}{\partial x} + \bar{V} \frac{\partial h}{\partial x} + (W_2 - W_1) \right\}$$

This can be shown to be identical equation A-9 when the following considerations are made:

- $(W_2 - W_1)$  are the normal velocity of the surfaces or “air hammering” also known as the *squeeze film* term such that  $\frac{dh}{dt} > 0$  when  $W_2 > W_1$ . Thus it is equivalent to  $(V_S - V_B)$  in figure A-1.
- The  $y$  axis in equation 7.57 is the  $z$  axis in figure A-1.
- Equation 7.57 assumes an incompressible fluid so that the density is divided out of the equation.
- Equation 7.57 assumes the viscosity is constant and multiplies all terms through by  $-12\eta$ .
- Equation 7.57 does not contain terms for mass addition or change in density with time.
- Equation A-7 based on figure A-1 has an entraining velocity in the  $x$  direction of  $\bar{U} = \frac{R\omega}{2}$  and  $\bar{V} = 0$ .

### A.2.7. Cylindrical Coordinates

Figure A.1 represented that  $z$  corresponded to the longitudinal axis of the bearing,  $x$  corresponded to  $R\theta$  axis and  $y$  to the  $R$  axis. Thus:

$$\begin{aligned} z &\rightarrow z \\ \frac{\partial}{\partial z} &\rightarrow \frac{\partial}{\partial z} \\ x &\rightarrow R\theta \\ \frac{\partial}{\partial x} &\rightarrow \frac{\partial}{R\partial\theta} \\ \delta x &\rightarrow R\delta\theta \end{aligned}$$

Also the  $y$  axis was the bearing gap height axis, but as drawn in figure A-1,  $y$  points towards the bearing center so that  $y$  corresponds to  $r$  axis. That is:

$$y \rightarrow -r$$

The effect of this is that if the normal surface velocities of the bushing ID and the shaft OD are redefined as being positive when they are moving away from the bearing center then  $(V_B - V_S) = \frac{dh}{dt}$  rather than  $(V_S - V_B)$ .  $\dot{M}$  still corresponds to mass addition to the element through the bushing ID even though that implies a flow in the  $-r$  direction.

Making these substitutions into A-9 and doing some algebra (multiplying through by 12) yields:

**Equation A-10** Reynolds equation in cylindrical coordinates

$$-\frac{\partial}{R\partial\theta} \left( \frac{\rho h^3}{\eta} \frac{\partial p}{R\partial\theta} \right) + 6 \frac{\partial}{\partial\theta} (\omega \rho h) - \frac{\partial}{\partial z} \left( \frac{\rho h^3}{\eta} \frac{\partial p}{\partial z} \right) + 12h \frac{d\rho}{dt} + 12\rho(V_B - V_S) = 12 \frac{\dot{M}}{R\delta\theta\delta z}$$

Equation A-10 still has dimensions of  $M/L^2T$ .

Comparison with other results:

Equation A-10 matches Czolczynski [25] equation 1.3, page 13 except that equation 1.3 appears to have neglected multiplying the mass addition term by 12.

Equation 1.3 has the term  $12 \frac{\partial}{\partial t}(\rho h)$  whereas equation A-10 has

$12h \frac{d\rho}{dt} + 12\rho(V_B - V_S)$  which is equivalent.

### A.3. Dimensionless Version

#### Equation A-11 Dimensionless Reynolds equation

$$-\frac{\partial}{\partial \theta} \left( PH^3 \frac{\partial P}{\partial \theta} \right) + \Lambda \frac{\partial}{\partial \theta} (PH) - \left( \frac{R}{L} \right)^2 \frac{\partial}{\partial Z} \left( PH^3 \frac{\partial P}{\partial Z} \right) + \frac{\partial}{\partial \tau} (PH) = \frac{t_c}{k_{\rho p} p_a c R \delta \theta \delta z} \dot{M}$$

#### A.3.1. Replacement of Density with Pressure

Applying the ideal gas law the density of dry air is:

$$p = \rho R t$$

$$\rho = \frac{p}{R t} = k_{\rho p} p$$

$$k_{\rho p} = \frac{1}{R t} = \frac{1}{640.2248(^{\circ}F + 459.67)}$$

$k_{\rho p}$  has units of  $T^2/L^2$ .

Equation A-9 becomes:

$$-\frac{\partial}{R \partial \theta} \left( \frac{k_{\rho p} p h^3}{\eta} \frac{\partial p}{R \partial \theta} \right) + 6 \frac{\partial}{\partial \theta} (\omega k_{\rho p} p h) - \frac{\partial}{\partial z} \left( \frac{k_{\rho p} p h^3}{\eta} \frac{\partial p}{\partial z} \right) + 12 h k_{\rho p} \frac{dp}{dt} + 12 k_{\rho p} p (V_B - V_S) = 12 \frac{\dot{M}}{R \delta \theta \delta z}$$

### A.3.2. Dimensionless Pressure

A dimensionless pressure can be defined as:

$$P = \frac{p}{p_a}$$

Where  $p_a$  is atmospheric pressure. So that:

$$p = p_a P \quad \text{and} \quad \frac{\partial p}{\partial []} = p_a \frac{\partial P}{\partial []}$$

Thus:

$$-\frac{\partial}{R\partial\theta} \left( \frac{p_a^2 k_{\rho p} P h^3}{\eta} \frac{\partial P}{R\partial\theta} \right) + 6 \frac{\partial}{\partial\theta} (\omega k_{\rho p} p_a P h) - \frac{\partial}{\partial z} \left( \frac{p_a^2 k_{\rho p} P h^3}{\eta} \frac{\partial P}{\partial z} \right) + 12 h p_a k_{\rho p} \frac{dP}{dt} + 12 p_a k_{\rho p} P (V_B - V_S) = 12 \frac{\dot{M}}{R\delta\theta\delta z}$$

### A.3.3. Dimensionless Gap Height

Dimensionless bearing gap height is commonly defined as:

$$H = \frac{h}{c}$$

Where  $c$  is the bearing clearance  $c = R_B - R_S$ . As a consequence the range of  $H$  is  $0 \leq H \leq 2$ .

Thus:  $h = cH$  and  $\partial h = c\partial H$

Some care is required with the term  $(V_B - V_S)$  as this represents  $\frac{dh}{dt}$  or  $\dot{h}$ . Thus:

$$-\frac{\partial}{R\partial\theta} \left( \frac{c^3 p_a^2 k_{\rho\rho} P H^3}{\eta} \frac{\partial P}{R\partial\theta} \right) + 6 \frac{\partial}{\partial\theta} (c\omega k_{\rho\rho} p_a P H)$$

$$-\frac{\partial}{\partial z} \left( \frac{c^3 p_a^2 k_{\rho\rho} P H^3}{\eta} \frac{\partial P}{\partial z} \right) + 12 c p_a k_{\rho\rho} H \dot{P} + 12 c p_a k_{\rho\rho} P \dot{H} = 12 \frac{\dot{M}}{R\delta\theta\delta z}$$

where  $\dot{H} = \frac{(V_B - V_S)}{c}$

### A.3.4. Dimensionless Time

$$-\frac{\partial}{R\partial\theta}\left(\frac{c^3 p_a^2 k_{\rho\rho} PH^3}{\eta} \frac{\partial P}{R\partial\theta}\right) + 6 \frac{\partial}{\partial\theta}(c\omega k_{\rho\rho} p_a PH) - \frac{\partial}{\partial z}\left(\frac{c^3 p_a^2 k_{\rho\rho} PH^3}{\eta} \frac{\partial P}{\partial z}\right) + 12c p_a k_{\rho\rho} H \dot{P} + 12c p_a k_{\rho\rho} P \dot{H} = 12 \frac{\dot{M}}{R\delta\theta\delta z}$$

Some reference use a dimensionless time. To create a dimensionless time it is necessary to divide time by a characteristic time. To be meaningful the characteristic time should be a meaningful characteristic of the system.

Some approaches found in references:

Do not use a dimensionless time: Williams [19], Marsh [4]

Use the shaft rotation frequency: Marsh [4],

Use the air velocity through the orifice:

Some examples are:

Marsh: divides by  $\omega_s$ .

Ene, Dimofte, and Keith [28]: divide by  $\omega_s$ .

Su and Lie [18]: use the whirl frequency of the journal which is related to  $\omega_s$ .

Czolczynski [25]: uses  $\tau = \frac{\omega t}{2\Lambda}$ .

Zhang and Xu [16]: use the velocity of air through the orifice.

One problem caused by using a dimensionless time based on shaft angular velocity is that it tends to interject the angular velocity into terms of the equation that are not related the angular velocity.

For example, one characteristic time could be the period of the shaft rotation

$$\frac{2\pi}{\omega_s} \text{ so}$$

that:

$$\tau = \frac{t}{\text{Period}} = \frac{\omega_s}{2\pi} t$$

$$\partial t = \frac{2\pi}{\omega_s} \partial \tau$$

substituting yields:

$$-\frac{\partial}{\partial \theta} \left( PH^3 \frac{\partial P}{\partial \theta} \right) + \Lambda \frac{\partial}{\partial \theta} (PH) - \left( \frac{R}{L} \right)^2 \frac{\partial}{\partial Z} \left( PH^3 \frac{\partial P}{\partial Z} \right) + 6 \frac{\omega_s}{\pi} \left( \frac{\eta}{p_a} \right) \left( \frac{R}{c} \right)^2 \frac{\partial}{\partial \tau} (PH) = \frac{12\eta R}{k_{\rho\rho} p_a^2 c^3 \delta \theta \delta z} \dot{M}$$

This has good appearance in that it looks like it will give the opportunity to substitute the bearing number into the fourth term which is related to the change of mass in the element volume. The  $\pi$  is messy so it is more elegant to define:

$$\tau = \omega_s t$$

Then after substitution the result will be:

$$-\frac{\partial}{\partial \theta} \left( PH^3 \frac{\partial p}{\partial \theta} \right) + \Lambda \frac{\partial}{\partial \theta} (PH) - \left( \frac{R}{L} \right)^2 \frac{\partial}{\partial Z} \left( PH^3 \frac{\partial P}{\partial Z} \right) + 2\Lambda \frac{\partial}{\partial \tau} (PH) = \frac{12\eta R}{k_{\rho\rho} p_a^2 c^3 \delta \theta \delta z} \dot{M}$$

Which indeed looks very elegant.

One of the great advantages of a hybrid bearing is that it can have considerable bearing stiffness when the shaft is not rotating. When the shaft is not rotating dimensionless times chosen to proportion to  $\omega_s$  become zero. Also the bearing number goes to zero. It is appropriate that the second term of the equation go to zero as it is related to the mass flux caused by the rotation. But it is not appropriate for the fourth term to go to zero.



Thus, if a nondimensionalized time parameter is to be used it should be based on a characteristic time that is both meaningful and not based exclusively on the shaft angular velocity.

$$\text{Czolczynski [25] used } \tau = \frac{\omega t}{2\Lambda}.$$

By recalling the definition of the dimensionless bearing number this dimensionless time can be seen to be independent of the angular velocity.

$$\tau = \frac{t}{12 \left( \frac{\eta}{p_a} \right) \left( \frac{R}{c} \right)^2}$$

And since:

$$\tau = \frac{t}{\text{characteristic } t}$$

It is evident that:

$$\text{characteristic } t = t_c = 12 \left( \frac{\eta}{p_a} \right) \left( \frac{R}{c} \right)^2$$

This characteristic time is very pleasing in that it is based on the gas characteristics  $\eta/p_a$  and the dimensionless bearing clearance  $c/R$ , both of which are fundamentally related to viscous flow in the bearing gap.

Using this then yields equation A-11.

$$-\frac{\partial}{\partial \theta} \left( PH^3 \frac{\partial P}{\partial \theta} \right) + \Lambda \frac{\partial}{\partial \theta} (PH) - \left( \frac{R}{L} \right)^2 \frac{\partial}{\partial Z} \left( PH^3 \frac{\partial P}{\partial Z} \right) + \frac{\partial}{\partial \tau} (PH) = \frac{t_c}{k_{\rho p} p_a c R \delta \theta \delta z} \dot{M}$$

Which is as good as it gets.

## Appendix B Discretizations of the Reynolds Equation

### B.1. Substitution of Q for P<sup>2</sup>

$$-\frac{\partial}{\partial \theta} \left( PH^3 \frac{\partial P}{\partial \theta} \right) + \Lambda \frac{\partial}{\partial \theta} (PH) - \left( \frac{R}{L} \right)^2 \frac{\partial}{\partial Z} \left( PH^3 \frac{\partial P}{\partial Z} \right) + \frac{\partial}{\partial \tau} (PH) = \frac{t_c}{k_{\rho p} p_a c R \delta \theta \delta z} \dot{M}$$

A common substitution is to note that  $P \frac{\partial P}{\partial \theta} = \frac{1}{2} \frac{\partial P^2}{\partial \theta}$  and  $P \frac{\partial P}{\partial Z} = \frac{1}{2} \frac{\partial P^2}{\partial Z}$ .

Czolczynski[25] substitutes  $Q=P^2$ . If this is done it is noted that:

$$P = \frac{Q}{P}$$

$$\frac{\partial Q}{\partial [ ]} = 2P \frac{\partial P}{\partial [ ]} \text{ or,}$$

$$P \frac{\partial P}{\partial [ ]} = \frac{1}{2} \frac{\partial Q}{\partial [ ]} \text{ and,}$$

$$\frac{\partial P}{\partial [ ]} = \frac{1}{2P} \frac{\partial Q}{\partial [ ]}$$

#### Poiseuille $\theta$ Flux

$$-\frac{\partial}{\partial \theta} \left( PH^3 \frac{\partial P}{\partial \theta} \right) = -H^3 \frac{\partial}{\partial \theta} \left( P \frac{\partial P}{\partial \theta} \right) - \left( P \frac{\partial P}{\partial \theta} \right) \frac{\partial}{\partial \theta} H^3 = -\frac{H^3}{2} \frac{\partial^2 Q}{\partial \theta^2} - \frac{3}{2} H^2 \frac{\partial Q}{\partial \theta} \frac{\partial H}{\partial \theta}$$

### Couette or wedge $\theta$ Flux

$$\Lambda \frac{\partial}{\partial \theta} (PH) = \frac{\Lambda}{2P} H \frac{\partial Q}{\partial \theta} + \Lambda P \frac{\partial H}{\partial \theta}$$

$$-\left(\frac{R}{L}\right)^2 \frac{\partial}{\partial Z} \left( PH^3 \frac{\partial P}{\partial Z} \right) = -\left(\frac{R}{L}\right)^2 \frac{H^3}{2} \frac{\partial^2 Q}{\partial Z^2} - \left(\frac{R}{L}\right)^2 \frac{3}{2} H^2 \frac{\partial Q}{\partial Z} \frac{\partial H}{\partial Z}$$

### Time Rate of Mass Change in the Element

$$\frac{\partial}{\partial \tau} (PH) = P \frac{\partial H}{\partial \tau} + \frac{H}{2P} \frac{\partial Q}{\partial \tau}$$

### Reynolds Equation

When these elements are re-assembled and multiplied by 2 equation A-11 becomes:

$$\left[ -H^3 \frac{\partial^2 Q}{\partial \theta^2} - 3H^2 \frac{\partial Q}{\partial \theta} \frac{\partial H}{\partial \theta} \right]_{P\theta} + \left[ \frac{\Lambda}{P} H \frac{\partial Q}{\partial \theta} + 2\Lambda P \frac{\partial H}{\partial \theta} \right]_{C\theta} \\ + \left[ -\left(\frac{R}{L}\right)^2 H^3 \frac{\partial^2 Q}{\partial Z^2} - \left(\frac{R}{L}\right)^2 3H^2 \frac{\partial Q}{\partial Z} \frac{\partial H}{\partial Z} \right]_{PZ} + \left[ 2P \frac{\partial H}{\partial \tau} + \frac{H}{P} \frac{\partial Q}{\partial \tau} \right]_{V\tau} = \left[ \frac{2t_c}{k_{\rho\rho} p_a c R \delta \theta \delta z} \dot{M} \right]_{MA}$$

## B.2. Discretization by Term

Each term can be discretized using 2<sup>nd</sup> order, centered FDE in the spatial axis and first order forward difference equations in the time axis. Terminology is based on  $Q_{i,j}^n$  where  $i$  and  $j$  indicate the node indexes in the longitudinal and  $\theta$  axis and  $n$  indicates the time step.

### Poiselle $\theta$ Flux, $\Phi_{P\theta}$

$$\left[ -H^3 \frac{\partial^2 Q}{\partial \theta^2} - 3H^2 \frac{\partial Q}{\partial \theta} \frac{\partial H}{\partial \theta} \right]_{P\theta} \rightarrow \left[ \begin{array}{l} -(H_{i,j}^n)^3 \frac{(Q_{i,j+1}^n - 2Q_{i,j}^n + Q_{i,j-1}^n)}{\Delta \theta^2} \\ -3(H_{i,j}^n)^2 \frac{(H_{i,j+1}^n - H_{i,j-1}^n)(Q_{i,j+1}^n - Q_{i,j-1}^n)}{4\Delta \theta^2} \end{array} \right]_{P\theta}$$

or:

$$\Phi_{P\theta} \rightarrow \left[ \begin{array}{l} \frac{-(H_{i,j}^n)^3 - \frac{3}{4}(H_{i,j}^n)^2 (H_{i,j+1}^n - H_{i,j-1}^n)}{\Delta \theta^2} Q_{i,j+1}^n \\ + \frac{2(H_{i,j}^n)^3}{\Delta \theta^2} Q_{i,j}^n \\ + \frac{-(H_{i,j}^n)^3 + \frac{3}{4}(H_{i,j}^n)^2 (H_{i,j+1}^n - H_{i,j-1}^n)}{\Delta \theta^2} Q_{i,j-1}^n \end{array} \right]_{P\theta}$$

### Couette or Wedge $\theta$ Flux, $\Phi_{P\theta}$

$$\left[ \frac{\Lambda}{P} H \frac{\partial Q}{\partial \theta} + 2\Lambda P \frac{\partial H}{\partial \theta} \right]_{C\theta} \rightarrow \left[ \frac{\Lambda}{P_{i,j}^n} H_{i,j}^n \frac{(Q_{i,j+1}^n - Q_{i,j-1}^n)}{2\Delta\theta} + 2\Lambda P_{i,j}^n \frac{(H_{i,j+1}^n - H_{i,j-1}^n)}{2\Delta\theta} \right]_{C\theta}$$

or:

$$\Phi_{C\theta} = \frac{\Lambda}{P_{i,j}^n} H_{i,j}^n \frac{(Q_{i,j+1}^n - Q_{i,j-1}^n)}{2\Delta\theta} + 2\Lambda P_{i,j}^n \frac{(H_{i,j+1}^n - H_{i,j-1}^n)}{2\Delta\theta}$$

### Poiseuille Z Flux, $\Phi_{Pz}$

$$\left[ -\left(\frac{R}{L}\right)^2 H^3 \frac{\partial^2 Q}{\partial Z^2} - \left(\frac{R}{L}\right)^2 3H^2 \frac{\partial Q}{\partial Z} \frac{\partial H}{\partial Z} \right]_{PZ} \rightarrow \left[ -\left(\frac{R}{L}\right)^2 H_{i,j}^3 \frac{(Q_{i+1,j}^n - 2Q_{i,j}^n + Q_{i-1,j}^n)}{\Delta Z^2} - \left(\frac{R}{L}\right)^2 3H_{i,j}^2 \frac{(Q_{i+1,j}^n - Q_{i-1,j}^n)(H_{i+1,j}^n - H_{i-1,j}^n)}{4\Delta Z^2} \right]_{PZ}$$

or

$$\Phi_{PZ} = -\left(\frac{R}{L}\right)^2 \frac{(H_{i,j}^3 + \frac{3}{4}(H_{i,j}^2 - H_{i-1,j}^n))}{\Delta Z^2} Q_{i+1,j}^n - 2\left(\frac{R}{L}\right)^2 \frac{H_{i,j}^3}{\Delta Z^2} Q_{i,j}^n + \left(\frac{R}{L}\right)^2 \frac{(H_{i,j}^3 + \frac{3}{4}(H_{i,j}^2 - H_{i-1,j}^n))}{\Delta Z^2} Q_{i-1,j}^n$$

### Time Rate of Mass Change in the Element $\dot{M}_V$

$$\left[ 2P \frac{\partial H}{\partial \tau} + \frac{H}{P} \frac{\partial Q}{\partial \tau} \right]_{V\tau} \rightarrow \left[ 2P_{i,j}^n \frac{(H_{i,j}^{n+1} - H_{i,j}^n)}{\Delta \tau} + \frac{H_{i,j}^n (Q_{i,j}^{n+1} - Q_{i,j}^n)}{P_{i,j}^n \Delta \tau} \right]_{V\tau}$$

$$\dot{M}_V = 2P_{i,j}^n \frac{(H_{i,j}^{n+1} - H_{i,j}^n)}{\Delta \tau} + \frac{H_{i,j}^n (Q_{i,j}^{n+1} - Q_{i,j}^n)}{P_{i,j}^n \Delta \tau}$$

### B.3. Reynolds Equation

$$\Phi_{P\theta} + \Phi_{C\theta} + \Phi_{PZ} + \dot{M}_V = \dot{M}_R$$

Where  $\Phi_{P\theta}$ ,  $\Phi_{PC\theta}$ , and  $\Phi_{PZ}$  are the mass *outflows* such that the element is losing mass when the outflows are positive and  $\dot{M}_V$  and  $\dot{M}_R$  are the mass change rates of the element and are positive when the element is gaining mass.

or:

$$\begin{aligned} & \left[ -(H_{i,j}^n)^3 \frac{(Q_{i,j+1}^n - 2Q_{i,j}^n + Q_{i,j-1}^n)}{\Delta\theta^2} - 3(H_{i,j}^n)^2 \frac{(H_{i,j+1}^n - H_{i,j-1}^n)(Q_{i,j+1}^n - Q_{i,j-1}^n)}{4\Delta\theta^2} \right]_{P\theta} + \\ & \left[ \frac{\Lambda}{P_{i,j}^n} H_{i,j}^n \frac{(Q_{i,j+1}^n - Q_{i,j-1}^n)}{2\Delta\theta} + 2\Lambda P_{i,j}^n \frac{(H_{i,j+1}^n - H_{i,j-1}^n)}{2\Delta\theta} \right]_{C\theta} + \\ & \left[ -\left(\frac{R}{L}\right)^2 H_{i,j}^3 \frac{(Q_{i+1,j}^n - 2Q_{i,j}^n + Q_{i-1,j}^n)}{\Delta Z^2} - \left(\frac{R}{L}\right)^2 3H_{i,j}^2 \frac{(Q_{i+1,j}^n - Q_{i-1,j}^n)(H_{i+1,j}^n - H_{i-1,j}^n)}{4\Delta Z^2} \right]_{PZ} + \\ & \left[ 2P_{i,j}^n \frac{(H_{i,j}^{n+1} - H_{i,j}^n)}{\Delta\tau} + \frac{H_{i,j}^n (Q_{i,j}^{n+1} - Q_{i,j}^n)}{P_{i,j}^n \Delta\tau} \right]_{MV} = \left[ \frac{2t_c}{k_{\rho\rho} p_a c R \delta\theta \delta z} \dot{M} \right]_{MR} \end{aligned}$$

## B.4. Residual Error Tests

### B.4.1. Complete Equation

$$\Phi_{P\theta} + \Phi_{C\theta} + \Phi_{PZ} + \Phi_{V\tau} = \Phi_M$$

$$\Phi_{P\theta} = (C_{P\theta 1}^n + C_{P\theta 2}^n) Q_{i,j+1}^n - 2C_{P\theta 1}^n Q_{i,j}^n + (C_{P\theta 1}^n - C_{P\theta 2}^n) Q_{i,j-1}^n$$

$$C_{P\theta 1}^n = -\frac{(H_{i,j}^n)^3}{\Delta\theta^2}$$

$$C_{P\theta 2}^n = -\frac{3(H_{i,j}^n)^2 (H_{i,j+1}^n - H_{i,j-1}^n)}{4\Delta\theta^2}$$

$$\Phi_{C\theta} = C_{C\theta 1}^n Q_{i,j+1}^n + C_{C\theta 2}^n Q_{i,j}^n - C_{C\theta 1}^n Q_{i,j-1}^n$$

$$C_{C\theta 1}^n = \frac{\Lambda H_{i,j}^n}{2P_{i,j}^n \Delta\theta}$$

$$C_{C\theta 2}^n = \frac{\Lambda (H_{i,j+1}^n - H_{i,j-1}^n)}{\Delta\theta P_{i,j}^n}$$

$$\Phi_{PZ} = (C_{PZ 1}^n + C_{PZ 2}^n) Q_{i+1,j}^n - 2C_{PZ 1}^n Q_{i,j}^n + (C_{PZ 1}^n - C_{PZ 2}^n) Q_{i-1,j}^n$$

$$C_{PZ 1}^n = -\left(\frac{R}{L}\right) \frac{H_{i,j}^3}{\Delta Z^2}$$

$$C_{PZ 2}^n = -\left(\frac{R}{L}\right)^2 \frac{3H_{i,j}^2 (H_{i+1,j}^n - H_{i-1,j}^n)}{4\Delta Z^2}$$

$$\Phi_{V\tau} = C_{V\tau 1}^n Q_{i,j}^{n+1} + (C_{V\tau 1}^n - C_{V\tau 2}^n) Q_{i,j}^n$$

$$C_{V\tau 1}^n = \frac{2(H_{i,j}^{n+1} - H_{i,j}^n)}{P_{i,j}^n \Delta\tau}$$

$$C_{V\tau 2}^n = \frac{H_{i,j}^n}{P_{i,j}^n \Delta\tau}$$

### B.4.2. Residual Error for fixed Displacement Bearings

The elemental error formulas are as follows:

$$ERR_{i,j} = \Phi_{P\theta} + \Phi_{PZ} - \Phi_M \rightarrow \text{for fixed displacement hydrostatic bearing}$$

$$ERR_{i,j} = \Phi_{P\theta} + \Phi_{PZ} + \Phi_{C\theta} \rightarrow \text{for fixed displacement hydrodynamic bearing}$$

$$ERR_{i,j} = \Phi_{P\theta} + \Phi_{PZ} + \Phi_{C\theta} - \Phi_M \rightarrow \text{for fixed displacement hybrid bearing}$$

$$\Phi_{P\theta} = (C_{P\theta 1}^n + C_{P\theta 2}^n) Q_{i,j+1}^n - 2C_{P\theta 1}^n Q_{i,j}^n + (C_{P\theta 1}^n - C_{P\theta 2}^n) Q_{i,j-1}^n$$

$$C_{P\theta 1}^n = -\frac{(H_{i,j}^n)^3}{\Delta\theta^2}$$

$$C_{P\theta 2}^n = -\frac{3(H_{i,j}^n)^2 (H_{i,j+1}^n - H_{i,j-1}^n)}{4\Delta\theta^2}$$

$$\Phi_{C\theta} = \frac{1}{P_{i,j}^n} D_{C\theta 1}^n Q_{i,j+1}^n + \frac{1}{P_{i,j}^n} D_{C\theta 2}^n Q_{i,j}^n - \frac{1}{P_{i,j}^n} D_{C\theta 1}^n Q_{i,j-1}^n$$

$$C_{C\theta 1}^n = \frac{\Lambda H_{i,j}^n}{2P_{i,j}^n \Delta\theta} = \frac{1}{P_{i,j}^n} D_{C\theta 1}^n$$

$$D_{C\theta 1}^n = \frac{\Lambda H_{i,j}^n}{2\Delta\theta}$$

$$C_{C\theta 2}^n = \frac{\Lambda (H_{i,j+1}^n - H_{i,j-1}^n)}{\Delta\theta P_{i,j}^n} = \frac{1}{P_{i,j}^n} D_{C\theta 2}^n$$

$$D_{C\theta 2}^n = \frac{\Lambda (H_{i,j+1}^n - H_{i,j-1}^n)}{\Delta\theta}$$

$$\Phi_{PZ} = (C_{PZ 1}^n + C_{PZ 2}^n) Q_{i+1,j}^n - 2C_{PZ 1}^n Q_{i,j}^n + (C_{PZ 1}^n - C_{PZ 2}^n) Q_{i-1,j}^n$$

$$C_{PZ 1}^n = -\left(\frac{R}{L}\right) \frac{H_{i,j}^3}{\Delta Z^2}$$

$$C_{PZ 2}^n = -\left(\frac{R}{L}\right)^2 \frac{3H_{i,j}^2 (H_{i+1,j}^n - H_{i-1,j}^n)}{4\Delta Z^2}$$



### B.4.3. Quasi-static Pressure Correction Method

For the pressure correction method, each  $P_{i,j}$  is examined such that a correction pressure,  $P^c_{i,j}$ , can be determined so that the  $ERR_{i,j}$  will be 0 if:

$$P^{n+1}_{i,j} = P^n_{i,j} + P^c_{i,j}$$

If the error is to be 0, then the discretized Reynolds equation can be used to

determine  $\frac{\partial ERR_{i,j}}{\partial P_{i,j}}$ . Since it is desired that:

$$ERR_{i,j} \rightarrow 0$$

then:

$$\Delta ERR_{i,j} = - ERR_{i,j}$$

$$\Delta ERR_{i,j} = \frac{\partial ERR_{i,j}}{\partial P_{i,j}} \Delta P_{i,j}$$

$$P_{i,j} = \Delta P_{i,j} = - \frac{ERR_{i,j}}{\left( \frac{\partial ERR_{i,j}}{\partial P_{i,j}} \right)}$$

$$ERR_{i,j} = \Phi_{P\theta} + \Phi_{C\theta} + \Phi_{PZ}$$

$$ERR_{i,j} = (C_{P\theta 1}^n + C_{P\theta 2}^n) Q_{i,j+1}^n - 2C_{P\theta 1}^n Q_{i,j}^n + (C_{P\theta 1}^n - C_{P\theta 2}^n) Q_{i,j-1}^n$$

$$+ \frac{1}{P_{i,j}^n} D_{C\theta 1}^n Q_{i,j+1}^n + \frac{1}{P_{i,j}^n} D_{C\theta 2}^n Q_{i,j}^n - \frac{1}{P_{i,j}^n} D_{C\theta 1}^n Q_{i,j-1}^n$$

$$+ (C_{PZ 1}^n + C_{PZ 2}^n) Q_{i+1,j}^n - 2C_{PZ 1}^n Q_{i,j}^n + (C_{PZ 1}^n - C_{PZ 2}^n) Q_{i-1,j}^n$$

$$ERR_{i,j} = -(2C_{P\theta 1}^n + 2C_{PZ 1}^n) P_{i,j}^2 + D_{C\theta 2}^n P_{i,j} + (D_{C\theta 1}^n Q_{i,j+1}^n - D_{C\theta 1}^n Q_{i,j-1}^n) P_{i,j}^{-1} + (C_{P\theta 1}^n + C_{P\theta 2}^n) Q_{i,j+1}^n$$

$$+ (C_{P\theta 1}^n - C_{P\theta 2}^n) Q_{i,j-1}^n + (C_{PZ 1}^n + C_{PZ 2}^n) Q_{i+1,j}^n + (C_{PZ 1}^n - C_{PZ 2}^n) Q_{i-1,j}^n$$

$$\frac{\partial ERR_{i,j}}{\partial P_{i,j}} = -4(C_{P\theta 1}^n + C_{PZ 1}^n) P_{i,j} + D_{C\theta 1}^n (Q_{i,j-1}^n - Q_{i,j+1}^n) P_{i,j}^{-2} + D_{C\theta 2}^n$$

$$C_{P\theta 1}^n = -\frac{(H_{i,j}^n)^3}{\Delta\theta^2}$$

$$D_{C\theta 1}^n = \frac{\Lambda H_{i,j}^n}{2\Delta\theta}$$

$$D_{C\theta 2}^n = \frac{\Lambda (H_{i,j+1}^n - H_{i,j-1}^n)}{\Delta\theta}$$

$$C_{PZ 1}^n = -\left(\frac{R}{L}\right) \frac{H_{i,j}^3}{\Delta Z^2}$$

### Appendix C Observations On Poiseuille Flow

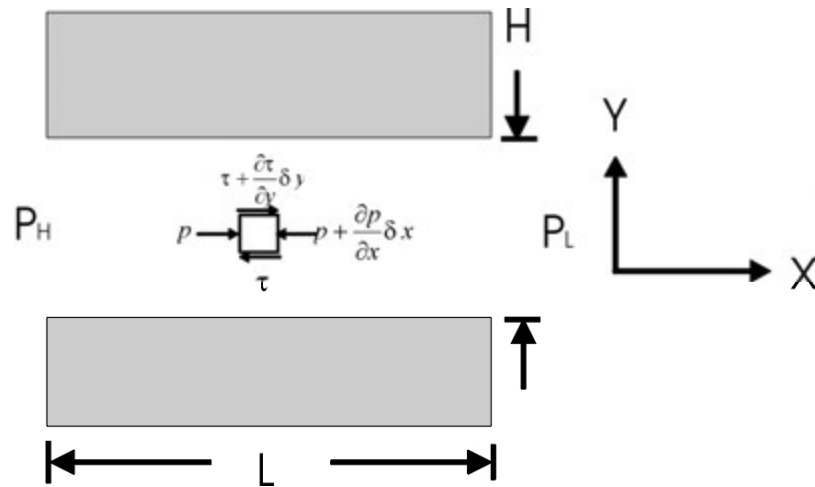


Figure C-1 2 Flow through a channel

#### C.1. Flow through a Channel

It is useful to examine the laminar, viscous flow of a compressible fluid from a high pressure reservoir with pressure  $P_H$  to a low pressure reservoir with pressure  $P_L$  through a channel of infinite depth, length  $L$ , and height  $H$ . This will result in Poiseuille flow in the  $X$  direction,  $q_x$  such that the volumetric flow per unit depth across any cross section in the channel will be (see Appendix A.2.2):

$$q_x = \int_0^H u dy = \frac{1}{2\eta} \frac{\partial p}{\partial x} \left( \frac{y^3}{3} - \frac{Hy^2}{2} \right)_0^H = -\frac{1}{12\eta} \frac{\partial p}{\partial x} H^3$$

$q_x$  has dimensions of  $L^3/TL$  ( $L^2/T$ ).

Multiplying  $q_x$  by the density  $\rho$  yields the mass flux across any cross section of the channel so that:

$$\dot{M} = \rho q_x = k_{\rho p} p q_x = -\frac{H^3 k_{\rho p}}{12\eta} p \frac{\partial p}{\partial x}$$

If the substitution of  $Q=p^2$  is made then:

$$\dot{M} = -\frac{H^3 k_{\rho p}}{24\eta} \frac{\partial Q}{\partial x}$$

Since continuity dictates that the mass flux across any section of the channel be constant the Q gradient in X must also be constant such that:

$$\frac{\partial Q}{\partial x} = -\frac{P_H^2 - P_L^2}{L}$$

so that:

$$\dot{M} = \frac{H^3 k_{\rho p}}{24L\eta} (P_H^2 - P_L^2)$$

Where  $\dot{M}$  has units of  $M/TL$ . To get the total mass flux this needs to yet be multiplied by the depth of the channel (which had been assumed infinite) such that:

$$\dot{M} \approx \frac{H^3 D k_{\rho p}}{24L\eta} (P_H^2 - P_L^2)$$

A similar analysis can be done for Poiseuille flow in a tube resulting in the volumetric flow rate across any section being:

$$q_r = -\frac{\pi R^4}{8\eta} \frac{\partial p}{\partial z}$$

Using the ideal gas law at a constant temperature and using  $p \frac{\partial p}{\partial z} = \frac{1}{2} \frac{\partial Q}{\partial z}$  results

in:

$$\dot{M} = -\frac{\pi k_{\rho p} R^4}{16\eta} \frac{\partial Q}{\partial z}$$

with units  $M/T$ . Since the mass flow must be constant across any section must be constant this leads to the conclusion once again that Q gradient in the longitudinal direction must be a constant so that:

$$\dot{M} = \frac{\pi k_{\rho p} R^4 p_a^2}{16\eta L} (P_{op}^2 - P^2)$$

Both results support the conclusion that for a channel with longitudinal characteristic length  $L$  and characteristic transverse dimension  $D$  that

$$\dot{M} = K_{SHAPE} p_a^2 \left( \frac{k_{\rho p}}{\eta} \right) \left( \frac{D^4}{L} \right) (P_{op}^2 - P^2)$$

where  $K_{SHAPE}$  is a dimensionless shape factor:

## C.2. Application to Mass Addition

Generalizing, it can be concluded that for a bushing that provides mass addition to the bearing gap via a liner with a pressure reservoir with pressure  $P_{op}$  on the liner OD to the bearing gap with pressure  $P$  that the mass addition can be characterized (so long as it is laminar and isothermal by:

$$\dot{M} = K_{meas} (P_{op}^2 - P^2)$$

where :

$$K_{meas} = K_{SHAPE} P_a^2 \left( \frac{k_{\rho P}}{\eta} \right) \left( \frac{D^4}{L} \right)$$

For each liner data was taken for the volumetric flow rate at various high pressure reservoir operating gage pressures when there was no shaft so that the liner was exhausting to ambient pressure. The volumetric flow rate was measured on the high pressure side of the liner. Thus the expectation is that the experimental volumetric flow rate data can be translated to mass flow rate by multiplying the volumetric rate by the density of the high pressure air. And that for each liner, the flow rate versus operating pressure data points can be used to determine  $K_{meas}$  for the liner using:

$$(K_{meas})_{Bushing} = \frac{\dot{M}}{P_{op}^2 - 1}$$

Units of  $K_{meas}$  are  $M/T$ . In the EE units in this study  $K_{meas}$  was determined in lbs/s.

For CFD analysis a  $Kmeas$  is required for each fluid element. Thus for a feedhole fed bushing of 12 feedholes where the individual feedhole area is generally smaller than the element area adjacent to the bushing ID, each feedhole acts as a point source such that:

$$(Kmeas)_{i,j} = \frac{(Kmeas)_{bushing}}{Nfd} \quad \text{elements with mass addition}$$

$$(Kmeas)_{i,j} = 0 \quad \text{elements without mass addition}$$

For a porous liner where each element has mass addition proportional to its element area adjacent to the liner ID:

$$(Kmeas)_{i,j} = (Kmeas)_{bushing} \frac{A_{element}}{A_{bushingID}} = (Kmeas)_{bushing} \frac{\delta Z R \delta \theta}{L \pi R^2}$$

where  $R$  and  $L$  are the bushing ID/2 and the length.

It is expected that  $Kmeas$  is proportional to the  $k_{\rho\rho}$ /viscosity ratio so that a temperature adjustment can be made to  $Kmeas$  for operating temperatures at  $T$ . Since the tests were run at 70°F  $Kmeas$  should be temperature adjusted when operated at an isothermal temperature other than 70°F ( $T$ ) to:

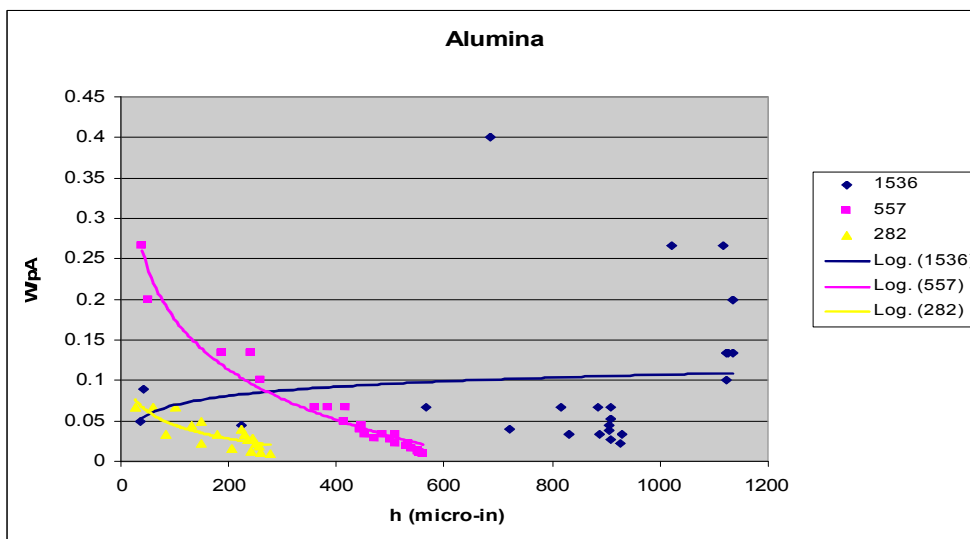
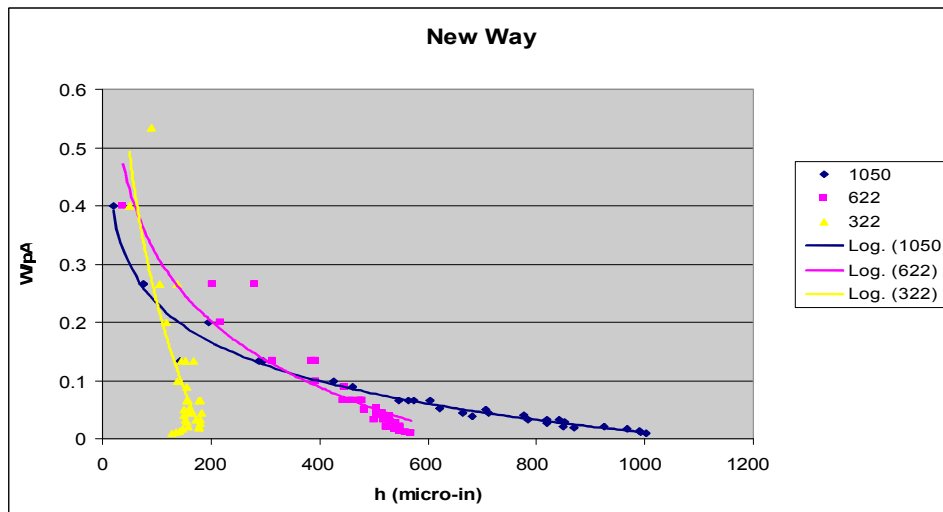
$$(Kmeas)^T = (Kmeas)^{70} \left( \frac{\eta^{70}}{\eta^T} \right) \left( \frac{k_{\rho\rho}^T}{k_{\rho\rho}^{70}} \right)$$

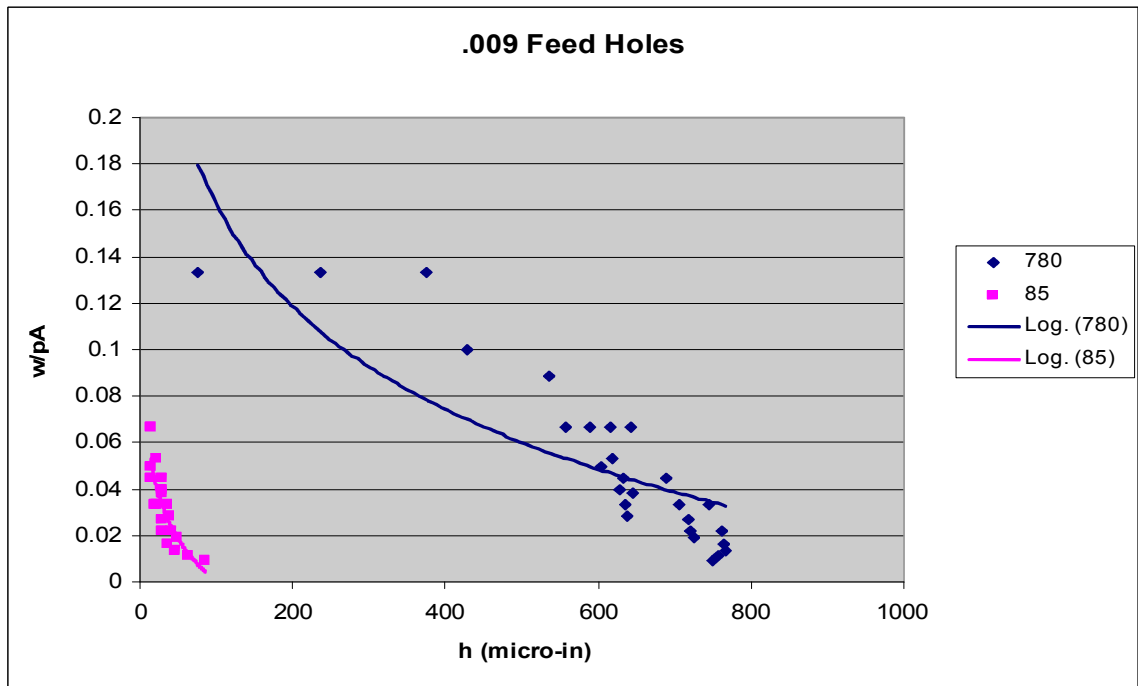
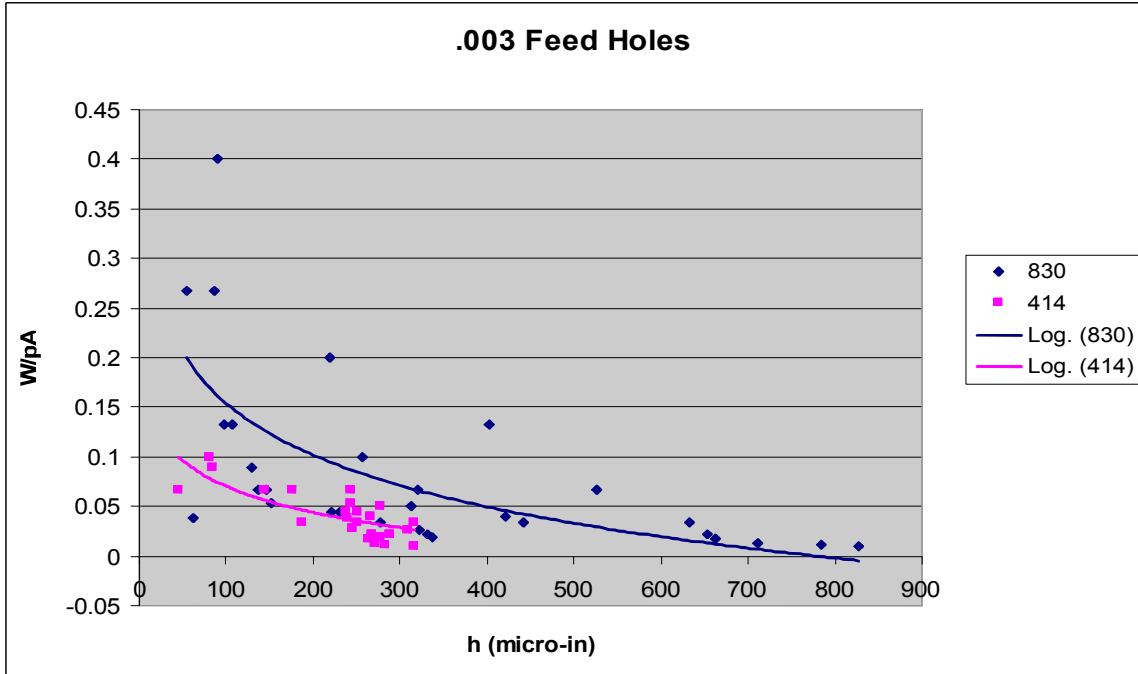
For use in the discretization of the dimensionless Reynold's number this means that the mass addition term becomes:

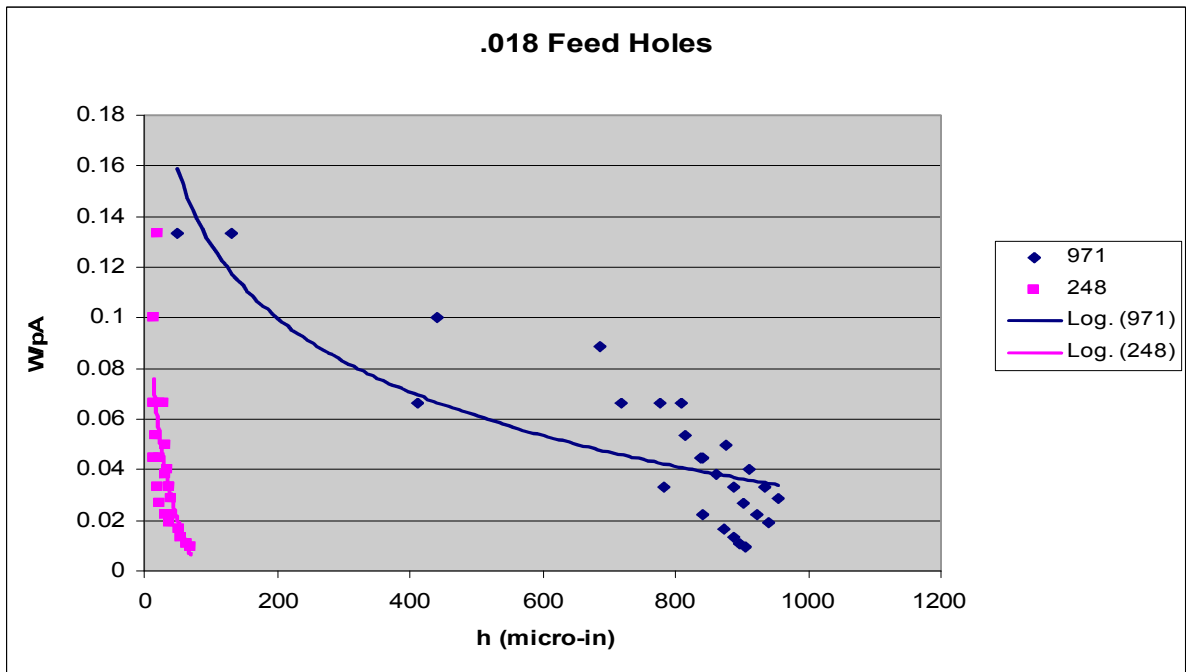
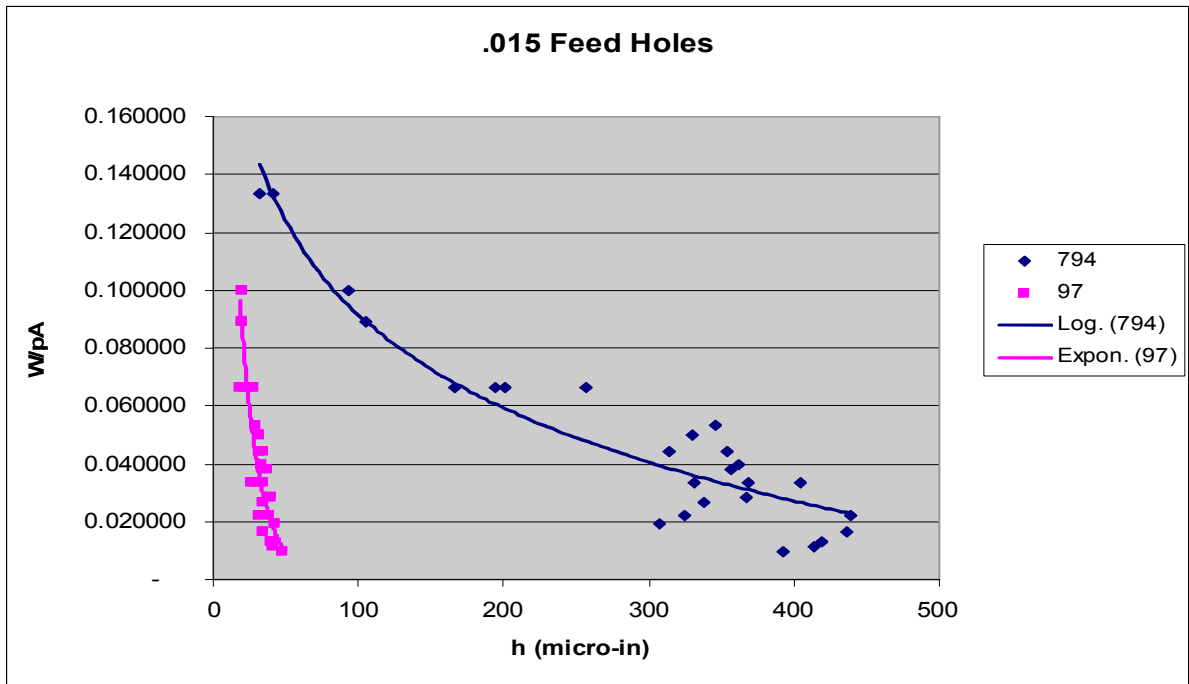
$$\left[ \frac{2t_c (Kmeas)_{i,j}}{k_{\rho\rho} P_a c R \delta \theta \delta z} [P_{op}^2 - Q_{i,j}^n] * \mathbf{Ma} \right]_{MR}$$

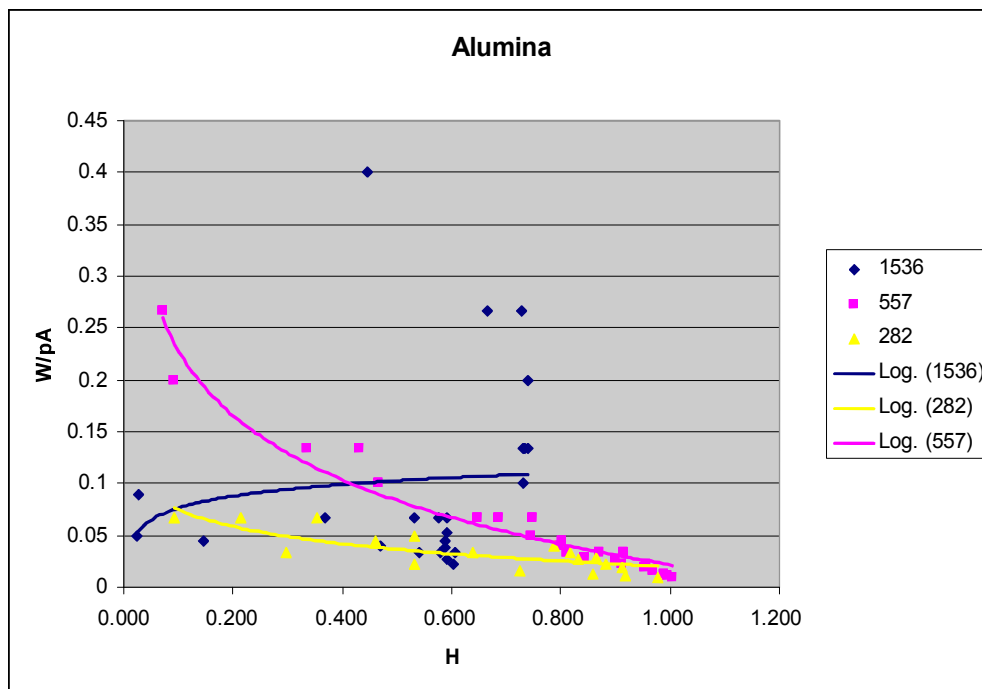
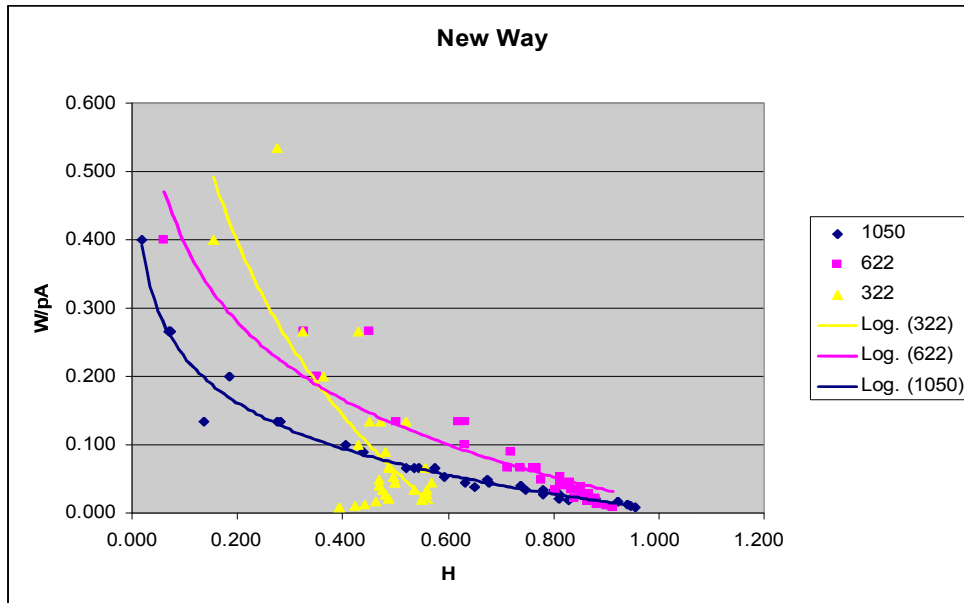
where **Ma** is a logical matrix indicating (0 or 1) which nodes have mass addition and “\*” represents the elemental product of the two arrays (versus them matrix product).

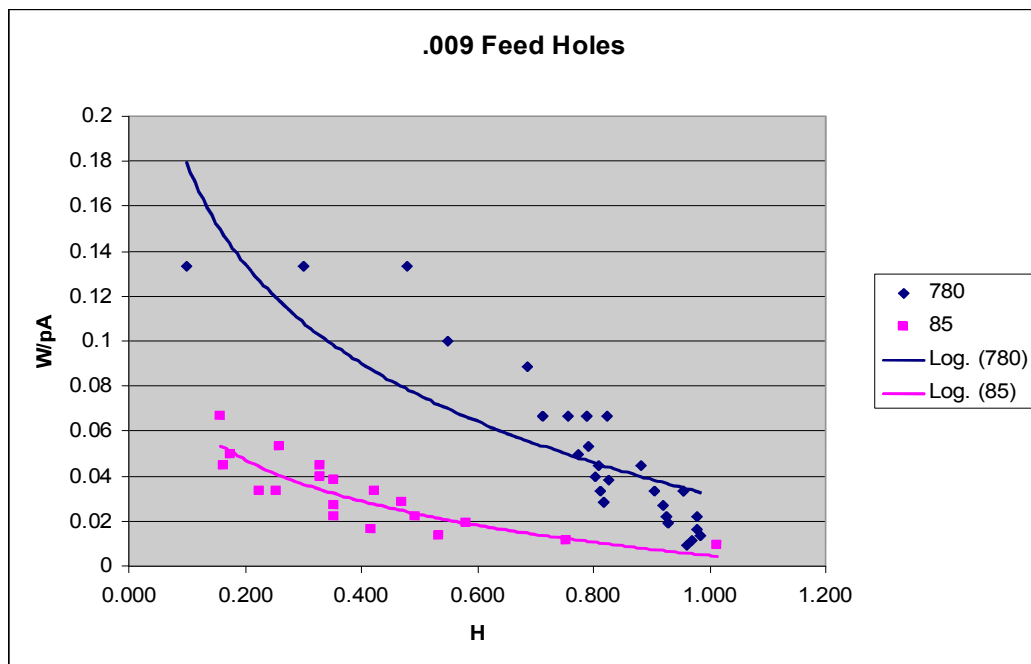
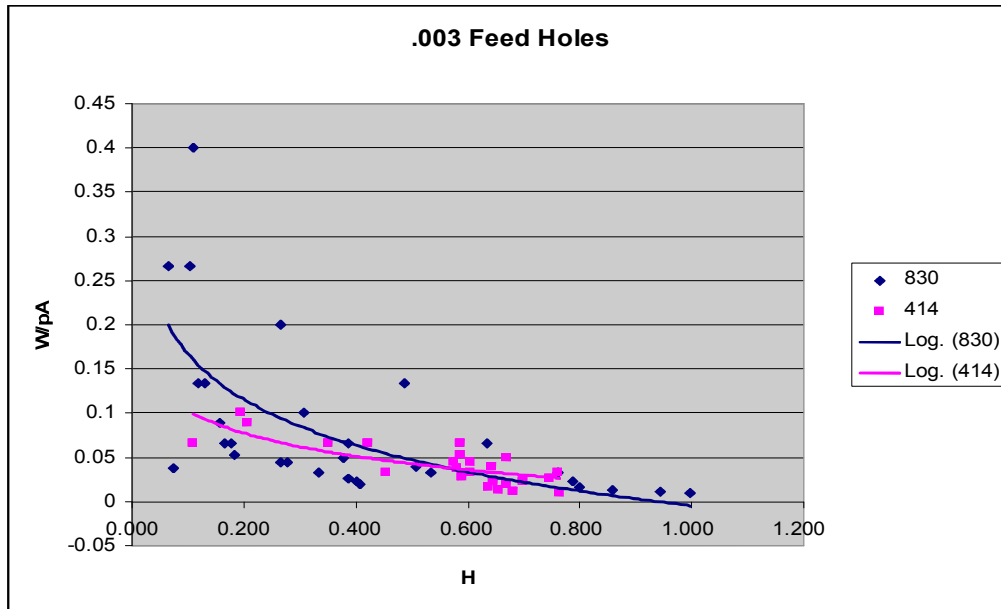


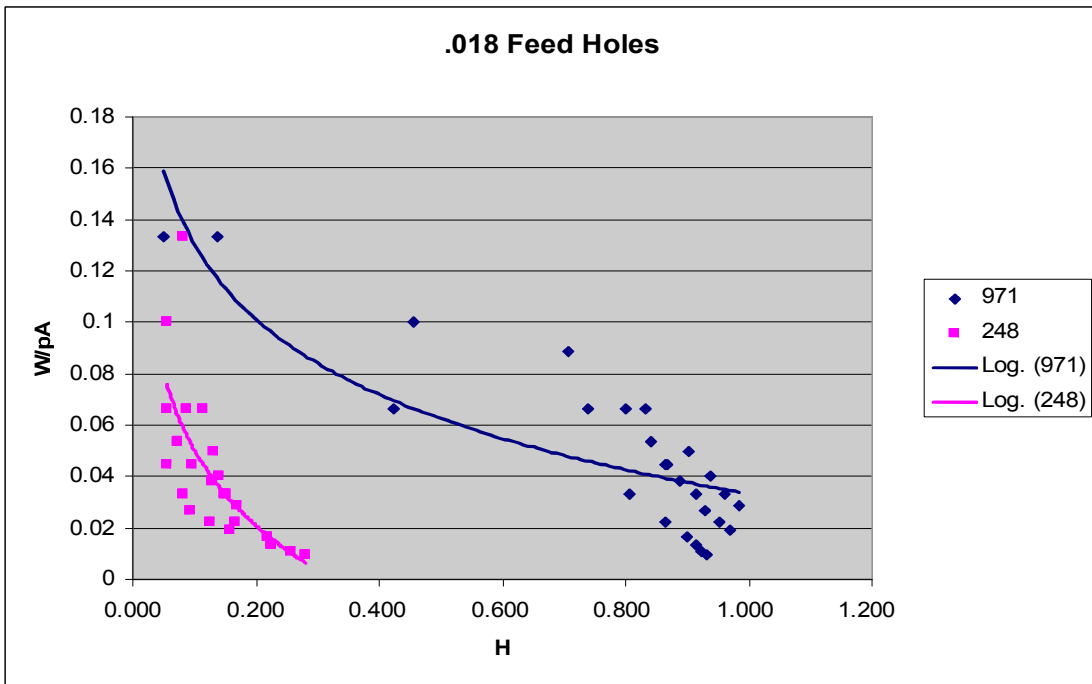
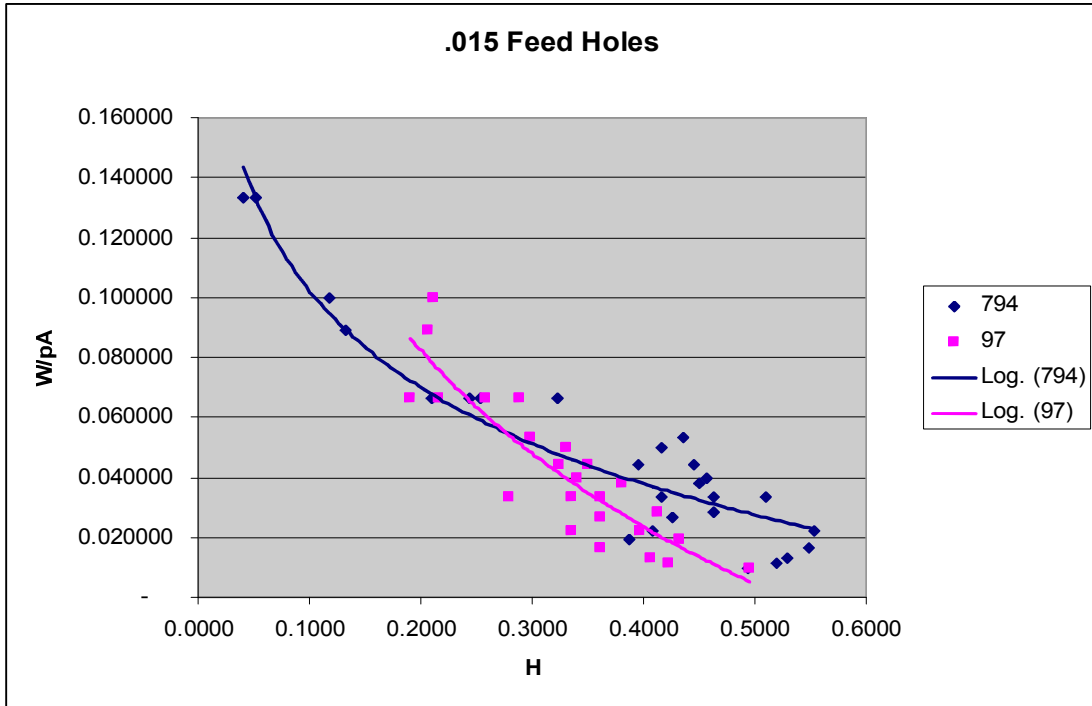
Appendix D Graphical Presentation of Experimental DataD.1.  $W/pA$  vs  $h$ 



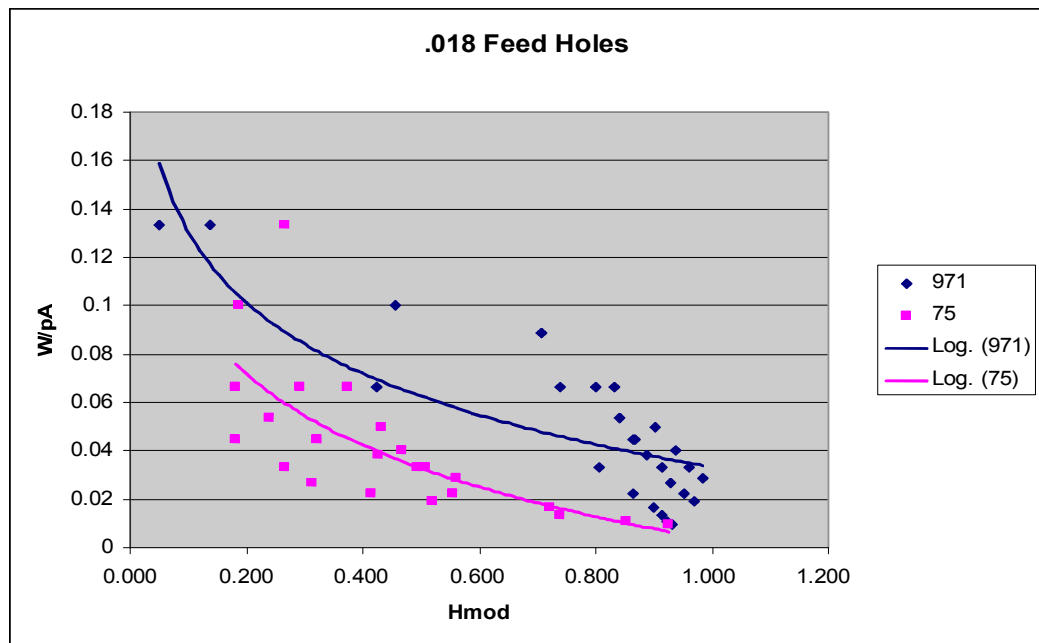
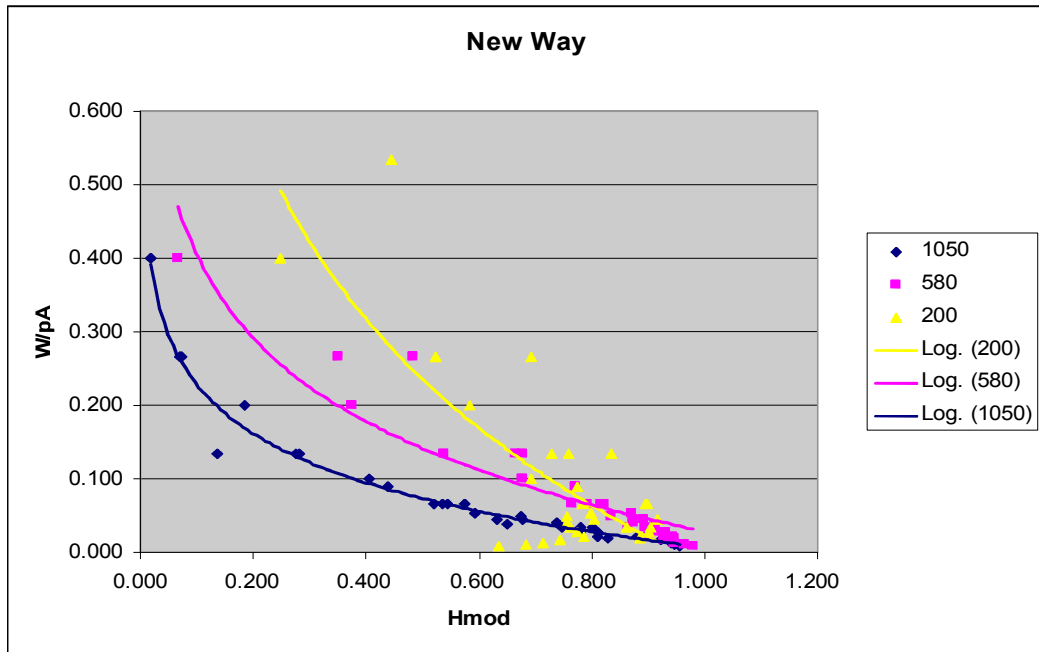


D.2.  $W/pA$  vs  $H$ 



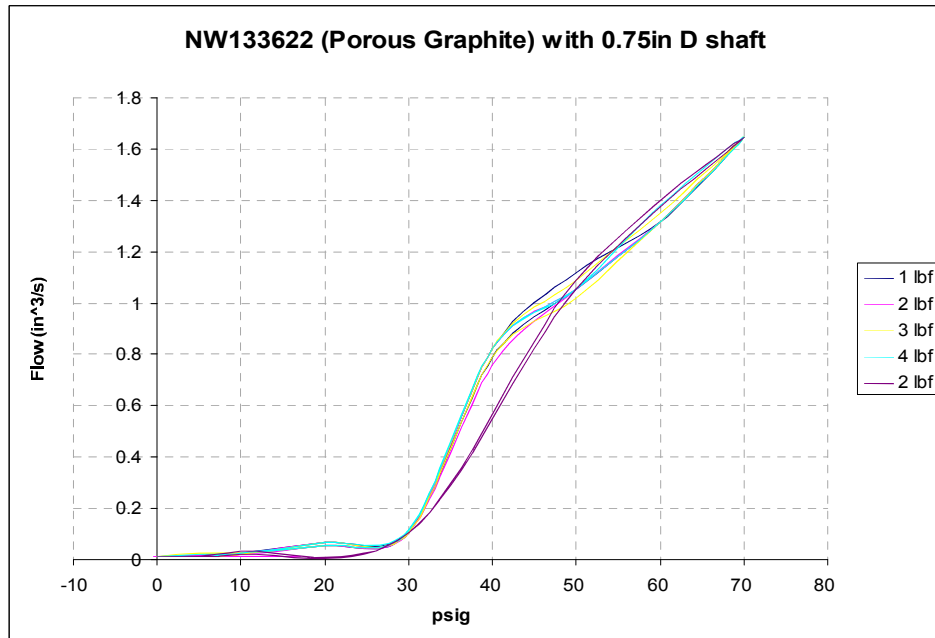
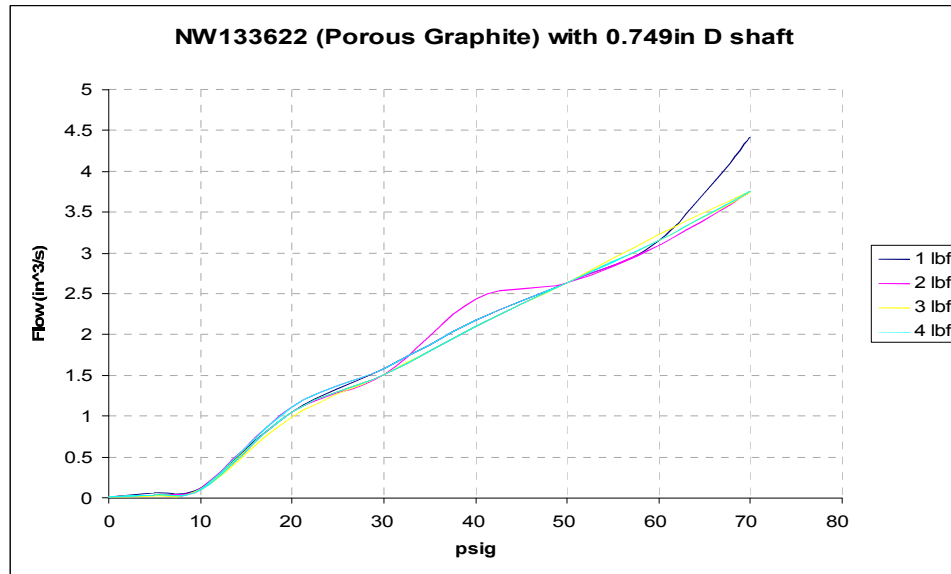


D.3.  $W/pA$  vs modified  $H$



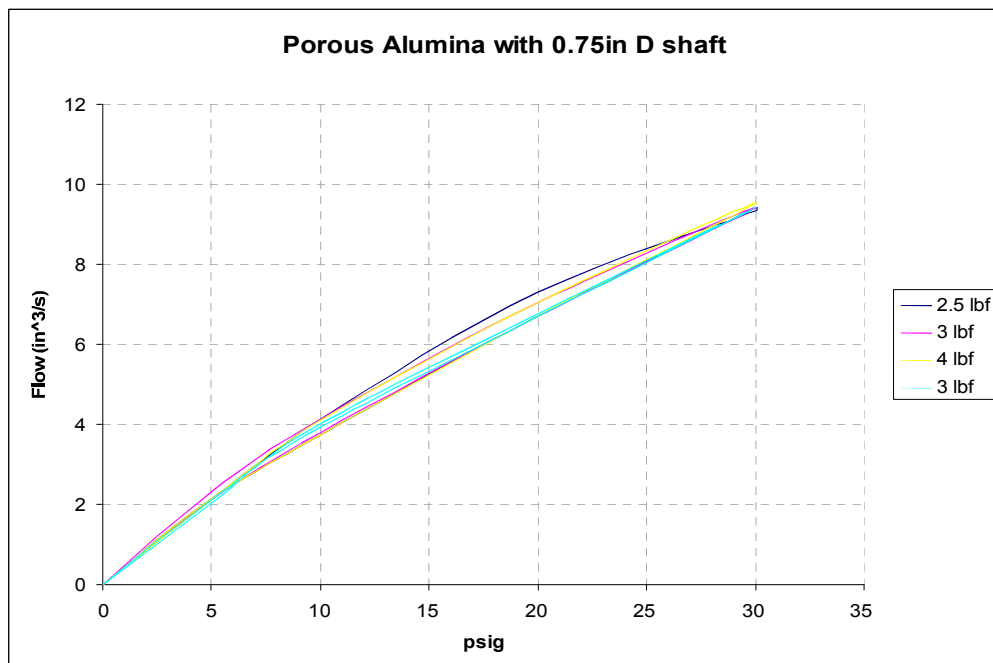
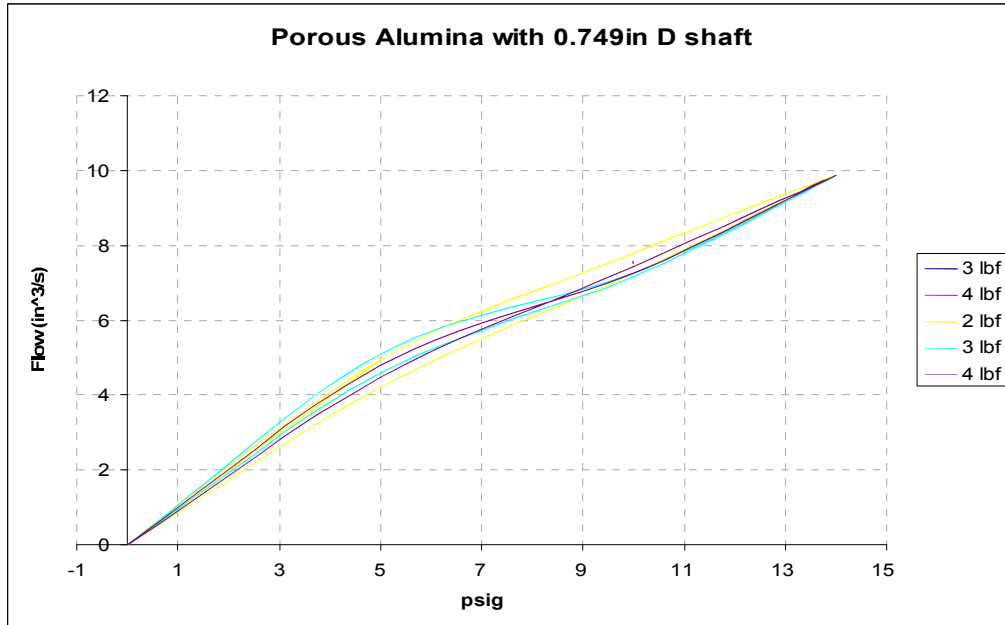
D.4. Volumetric Flow vs Pressure by Load

New Way

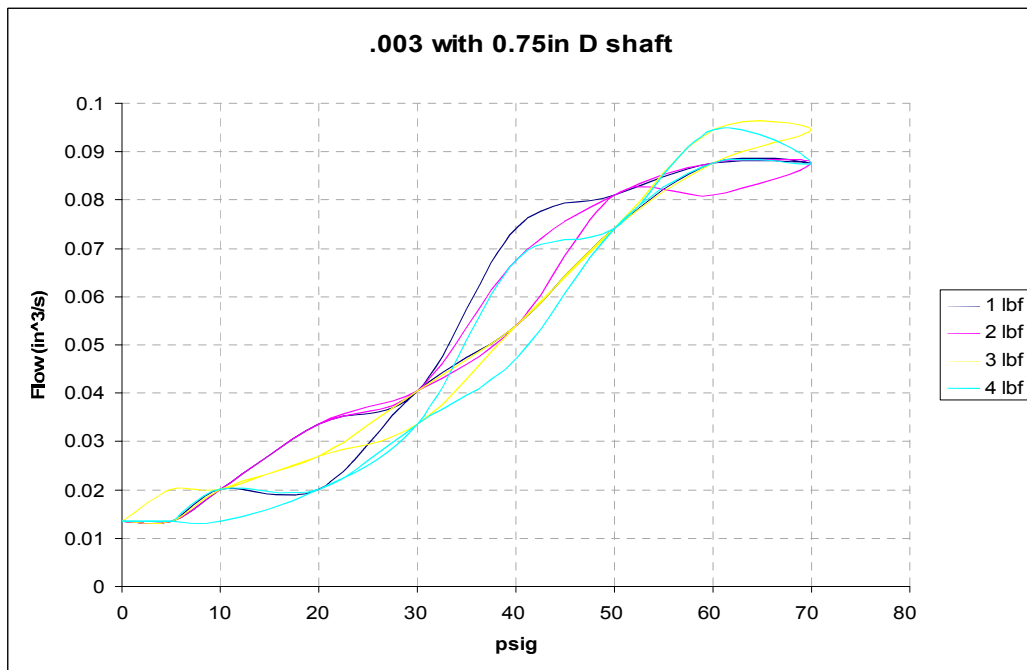
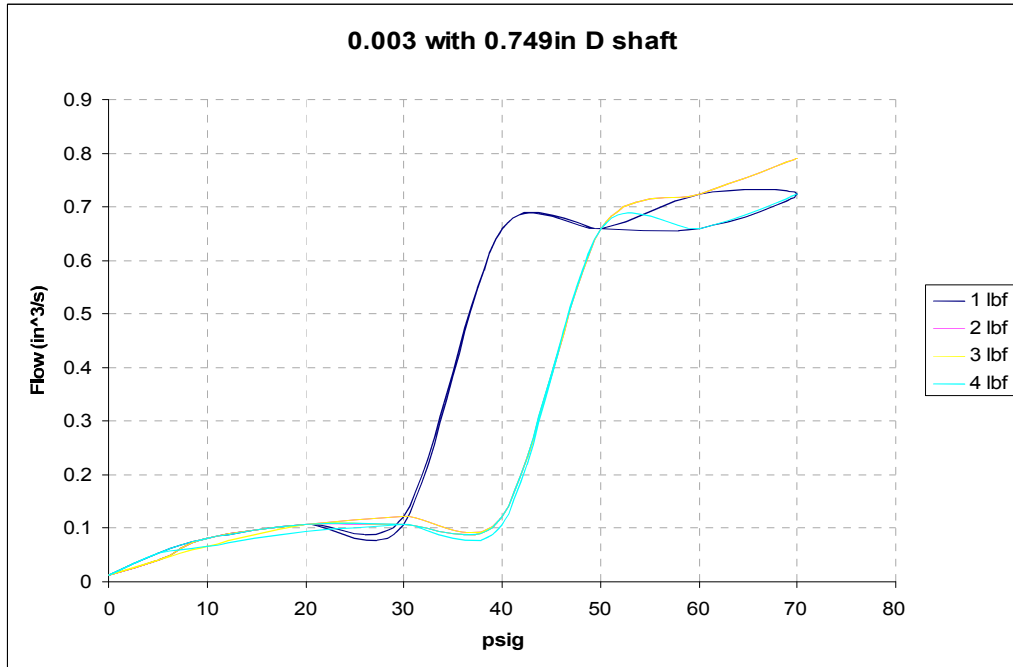




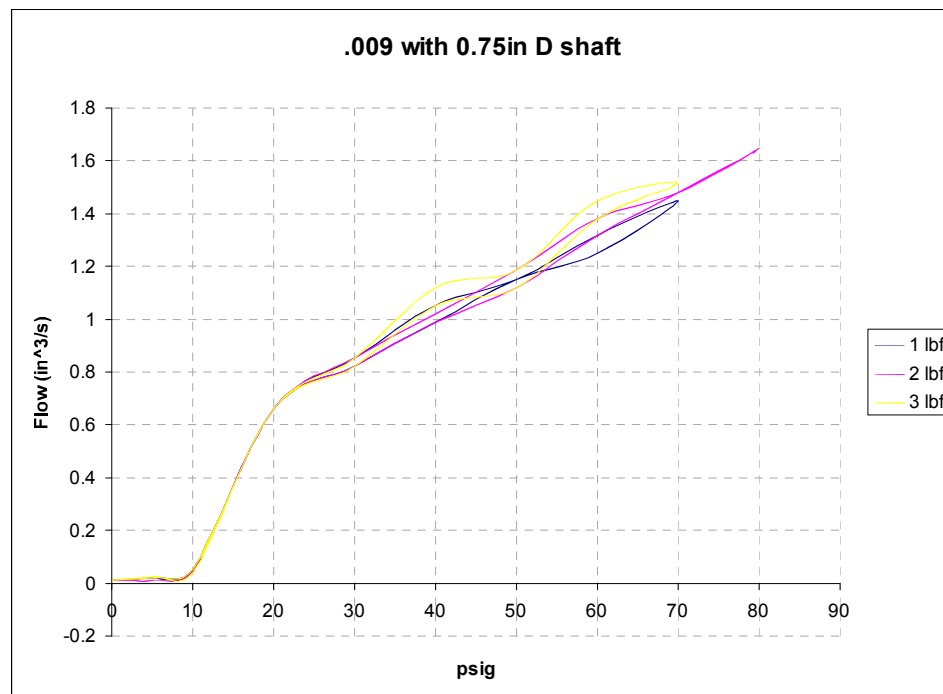
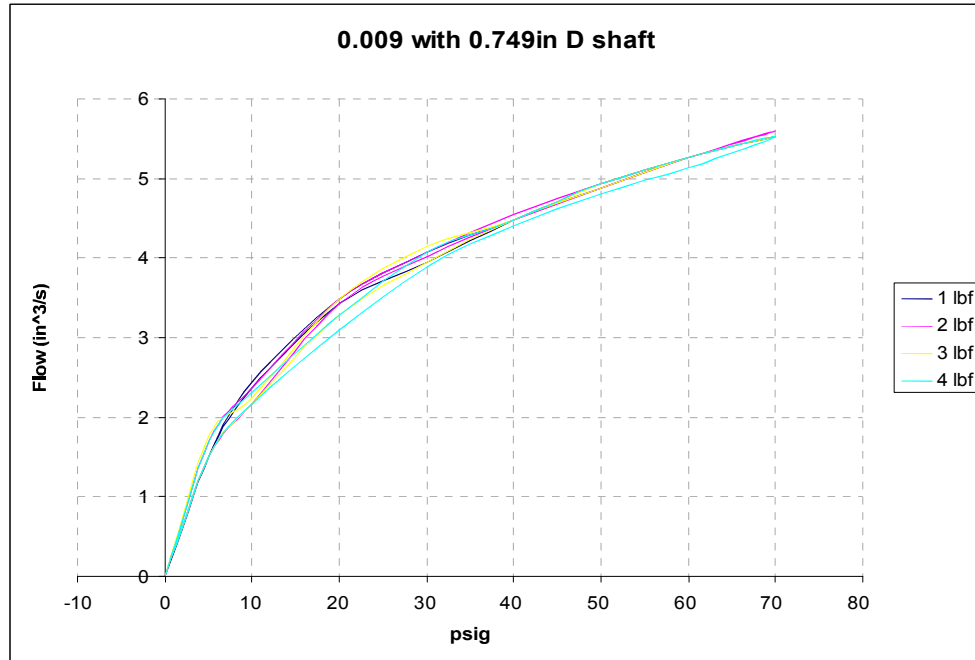
## Alumina



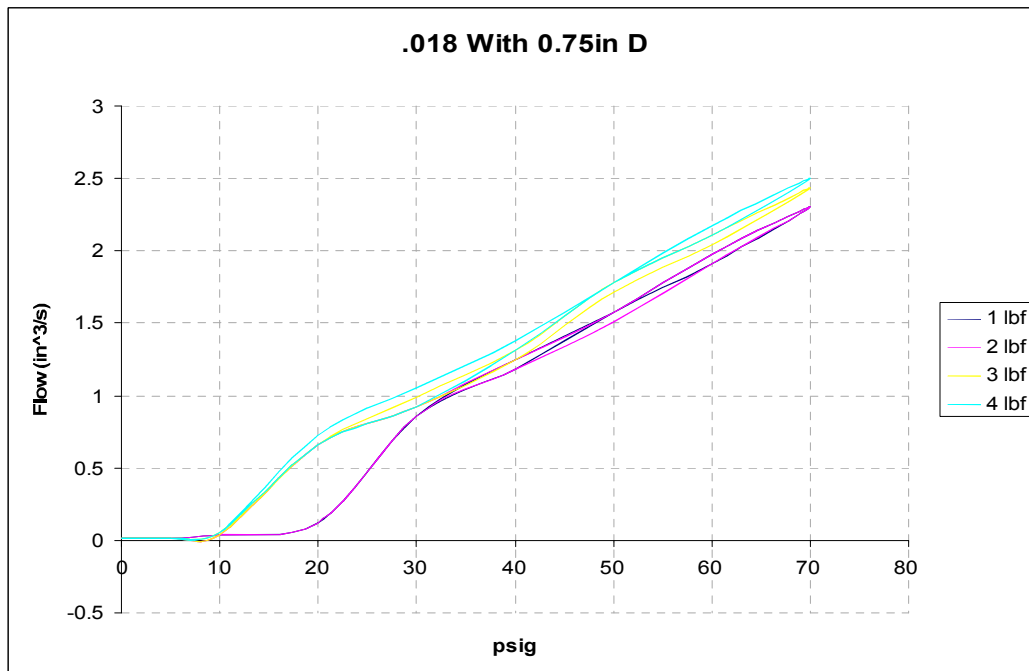
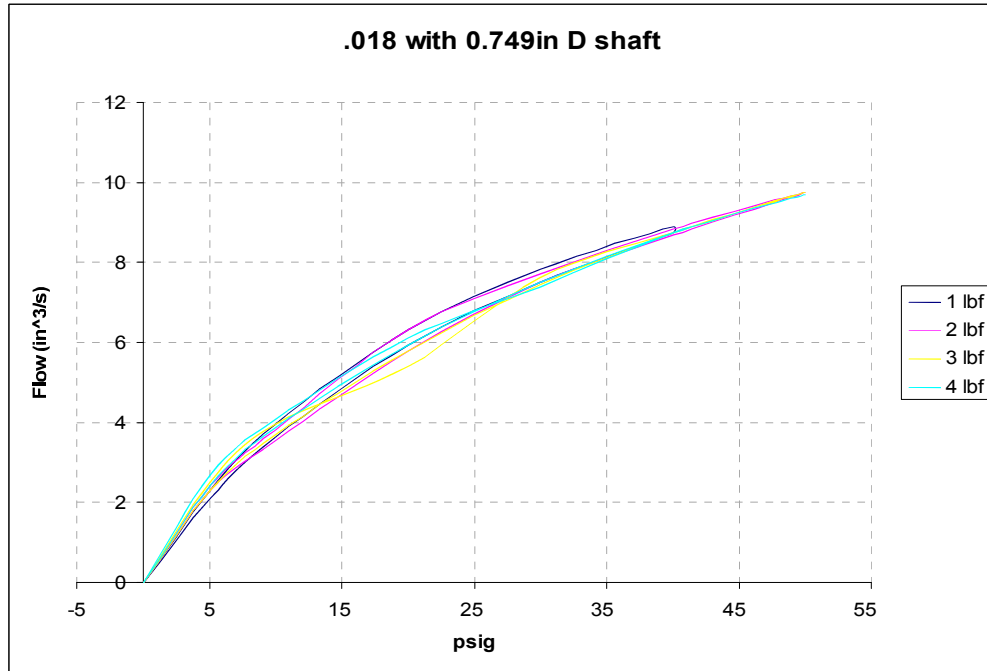
.003 Feed Holes



### .009 Feed Holes



.018 Feed Holes

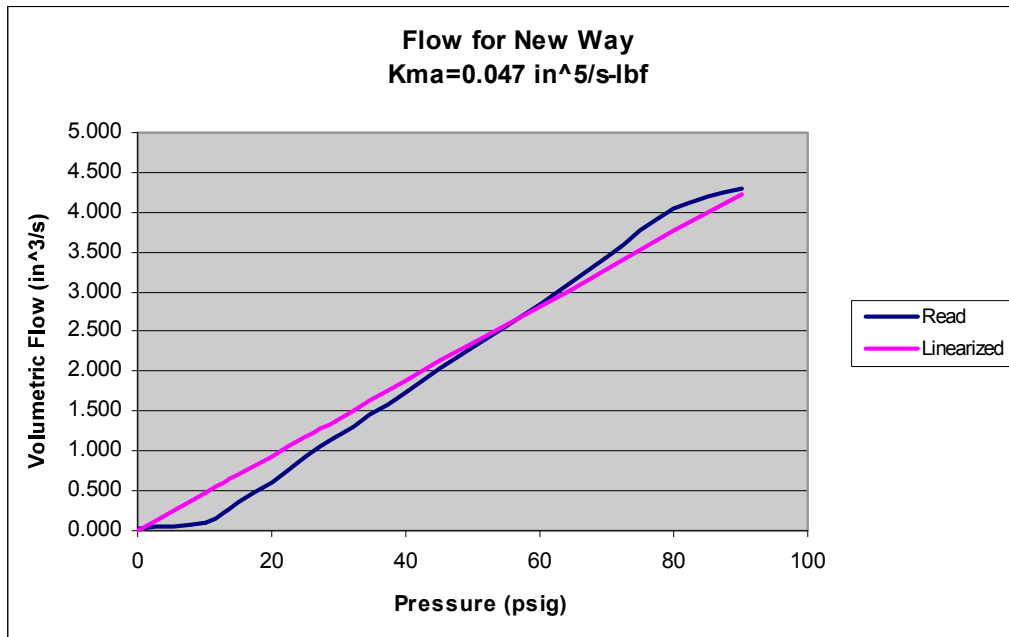


D.5. Bearing Flow Rates vs Pressure and Clearance

New Way S/N 133622 / no shaft

Slope or Kma in <sup>5</sup> /s-lbf
0.04700

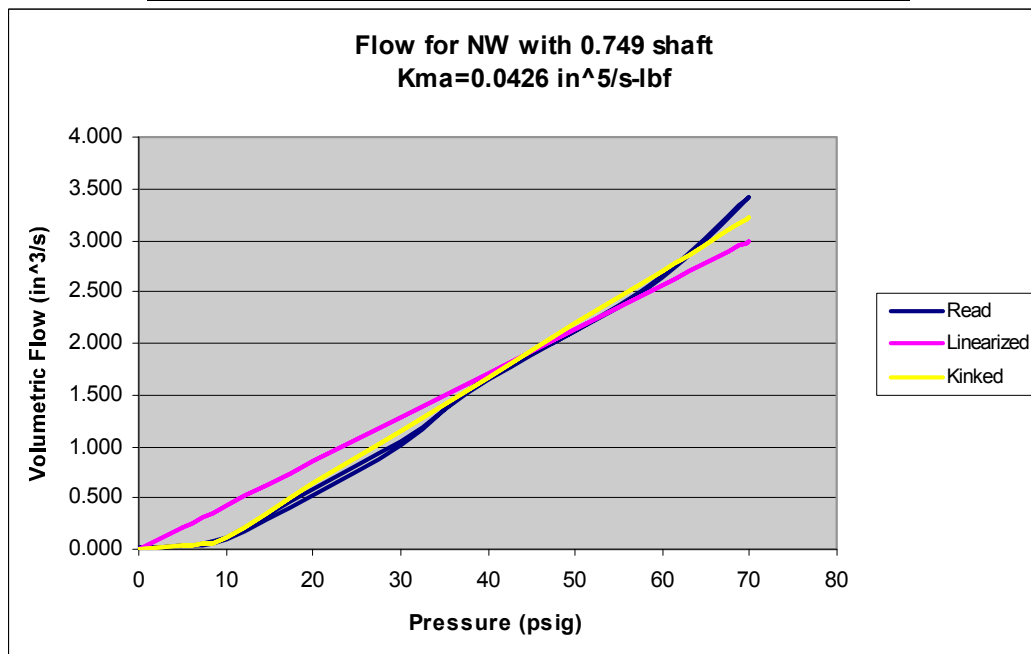
Flow Rate Readings				
Pressure psig	Read mm	Read LPM	Read in <sup>3</sup> /s	Linear in <sup>3</sup> /s
0	1	0.013	0.013	0.000
10	7	0.093	0.094	0.470
15	13	0.342	0.348	0.705
20	17	0.601	0.611	0.940
25	22	0.925	0.940	1.175
30	26	1.184	1.204	1.410
40	34	1.702	1.731	1.880
50	43	2.284	2.323	2.350
60	51	2.802	2.850	2.820
70	60	3.385	3.443	3.290
80	69	3.968	4.036	3.760
90	73	4.227	4.299	4.230



**New Way S/N 133622 / .749" shaft**

Low pressure Kma:	0.00945	Slope or Kma
High Pressure Kma:	0.05173	
Pivot Pressure:	9.500	in <sup>5</sup> /s-lbf
Pivot Flow:	0.090	0.04260

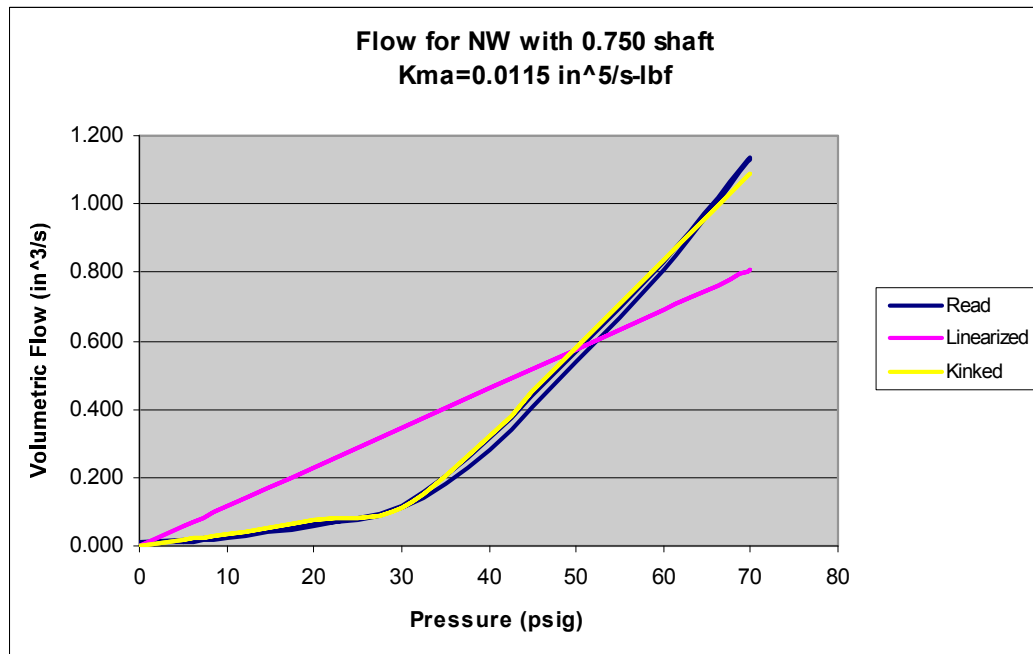
Flow Rate Readings						
Pressure psig	Read mm	Read LPM	Read in <sup>3</sup> /s	Linear in <sup>3</sup> /s	Kinked in <sup>3</sup> /s	
0	1.0	0.013	0.013	0.000	0.000	
5	3.5	0.046	0.047	0.213	0.047	
10	8.5	0.113	0.115	0.426	0.116	
20	16.5	0.568	0.578	0.852	0.633	
30	23.8	1.038	1.056	1.278	1.150	
40	32.8	1.621	1.648	1.704	1.668	
50	40.0	2.090	2.126	2.130	2.185	
60	48.0	2.608	2.653	2.556	2.702	
70	59.5	3.353	3.410	2.982	3.220	
60	47.8	2.592	2.636	2.556	2.702	
50	40.0	2.090	2.126	2.130	2.185	
40	33.3	1.653	1.681	1.704	1.668	
30	23.0	0.989	1.006	1.278	1.150	
20	15.8	0.520	0.529	0.852	0.633	
10	7.5	0.100	0.101	0.426	0.116	
5	2.8	0.036	0.037	0.213	0.047	
0	1.0	0.013	0.013	0.000	0.000	



**New Way S/N 133622 / .750" shaft**

Low pressure Kma:	0.00371	Slope or Kma in <sup>5</sup> /s-lbf
High Pressure Kma:	0.02558	
Pivot Pressure:	32.000	
Pivot Flow:	0.119	

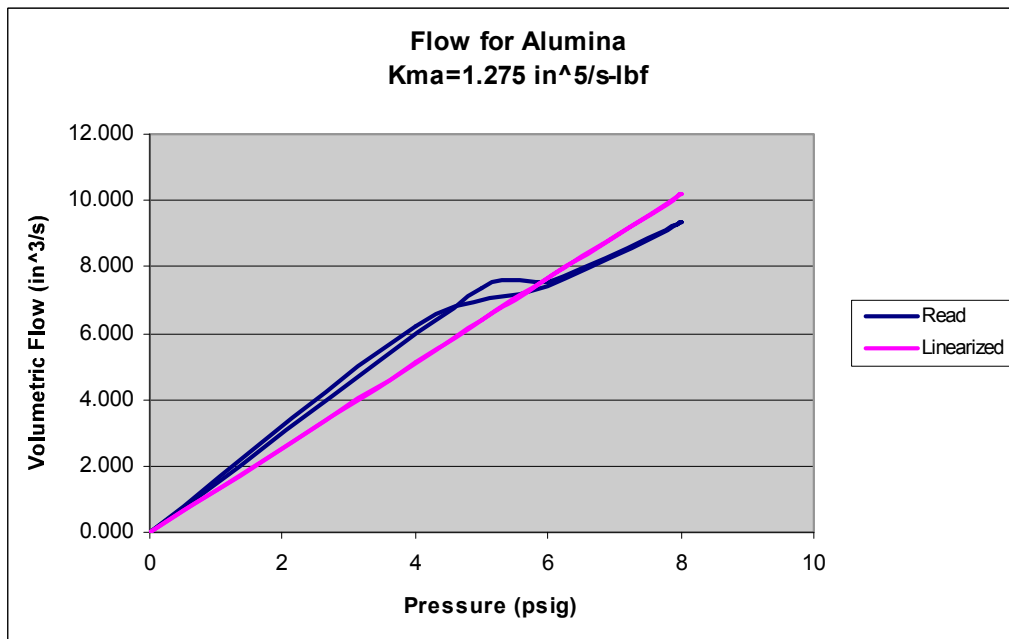
Flow Rate Readings					
Pressure psig	Read mm	Read LPM	Read in <sup>3</sup> /s	Linear in <sup>3</sup> /s	Kinked in <sup>3</sup> /s
0	1.0	0.013	0.013	0.000	0.000
5	1.4	0.018	0.019	0.058	0.019
10	2.0	0.027	0.027	0.115	0.037
20	4.8	0.063	0.064	0.230	0.074
30	8.5	0.113	0.115	0.345	0.111
40	12.5	0.309	0.315	0.460	0.323
50	16.4	0.560	0.570	0.575	0.579
60	20.4	0.819	0.833	0.690	0.835
70	25.0	1.119	1.138	0.805	1.091
60	20.0	0.795	0.809	0.690	0.835
50	15.9	0.528	0.537	0.575	0.579
40	12.0	0.277	0.282	0.460	0.323
30	8.1	0.108	0.110	0.345	0.111
20	4.3	0.056	0.057	0.230	0.074
10	1.8	0.023	0.024	0.115	0.037
5	1.0	0.013	0.013	0.058	0.019
0	1.0	0.013	0.013	0.000	0.000



Alumina / no shaft

Slope or Kma in <sup>5</sup> /s-lbf
1.27500

Flow Rate Readings					
Pressure psig	Read mm	Read LPM	Read in <sup>3</sup> /s	Linear in <sup>3</sup> /s	
0	1	0.013	0.013	0.000	
5	119	7.205	7.328	6.375	
6	122	7.400	7.526	7.650	
8	150	9.213	9.370	10.200	
6	120	7.270	7.394	7.650	
4	102	6.105	6.209	5.100	
0	1	0.013	0.013	0.000	

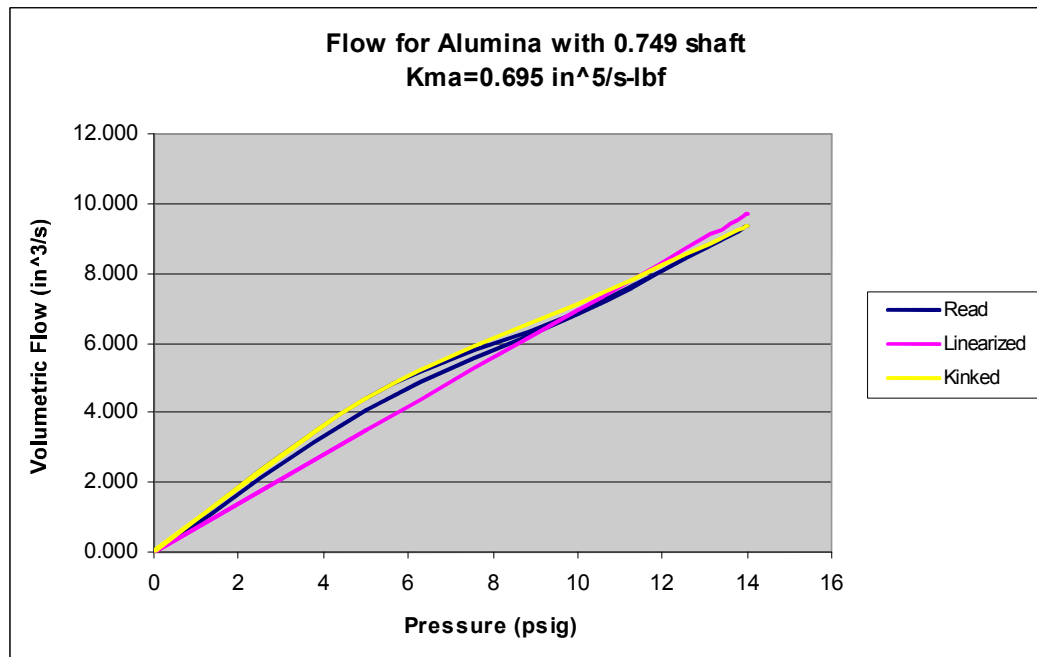




**Alumina / .749" shaft**

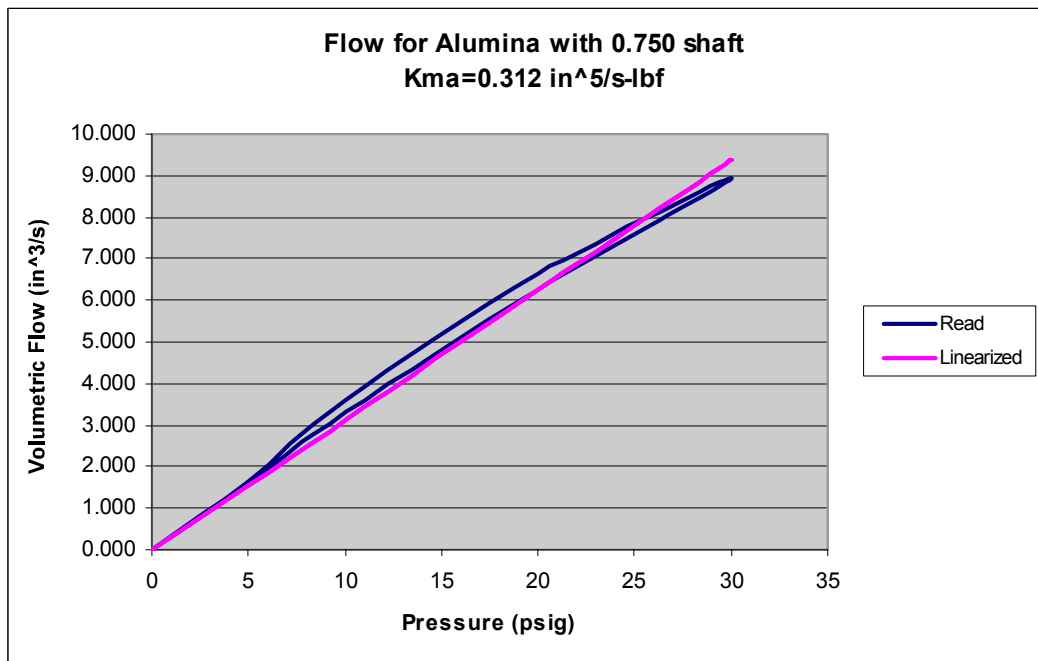
Low pressure Kma:	0.88121	Slope or Kma
High Pressure Kma:	0.55155	
Pivot Pressure:	4.900	in <sup>5</sup> /s-lbf
Pivot Flow:	4.318	0.69500

Flow Rate Readings					
Pressure psig	Read mm	Read LPM	Read in <sup>3</sup> /s	Linear in <sup>3</sup> /s	Kinked in <sup>3</sup> /s
0	1.0	0.013	0.013	0.000	0.000
5	74.6	4.332	4.406	3.475	4.406
10	112.8	6.801	6.917	6.950	7.131
14	150.0	9.213	9.370	9.730	9.337
10	111.5	6.720	6.835	6.950	7.131
5	69.5	4.000	4.069	3.475	4.406
0	1.0	0.013	0.013	0.000	0.039



**Alumina / .750" shaft**

				Slope or Kma in <sup>5</sup> /s-lbf
				0.31200
Flow Rate Readings				
Pressure psig	Read mm	Read LPM	Read in <sup>3</sup> /s	Linear in <sup>3</sup> /s
0	1.0	0.013	0.013	0.000
5	32.8	1.621	1.648	1.560
10	62.1	3.523	3.583	3.120
20	108.3	6.509	6.620	6.240
30	143.3	8.776	8.925	9.360
20	102.8	6.153	6.258	6.240
10	58.1	3.264	3.319	3.120
5	32.0	1.572	1.599	1.560
0	1.0	0.013	0.013	0.000

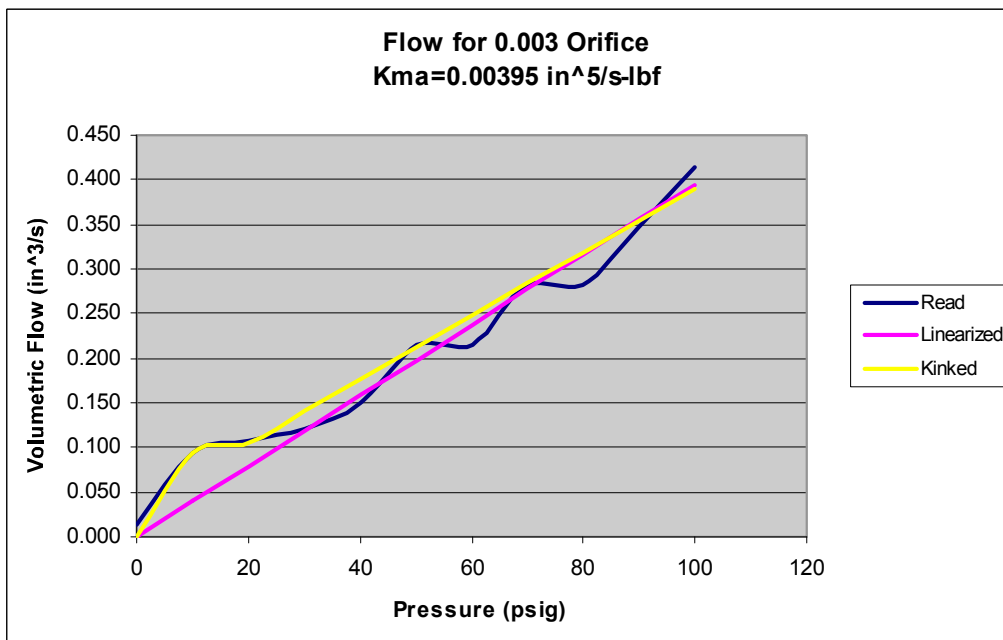


**0.003" Orifice Bearing**

**Al Housing / .003" dia Al Sleeve / no shaft**

Low pressure Kma:	0.00945	Slope or Kma
High Pressure Kma:	0.00354	
Pivot Pressure:	6	in <sup>5</sup> /s-lbf
Pivot Flow:	0.057	0.00395

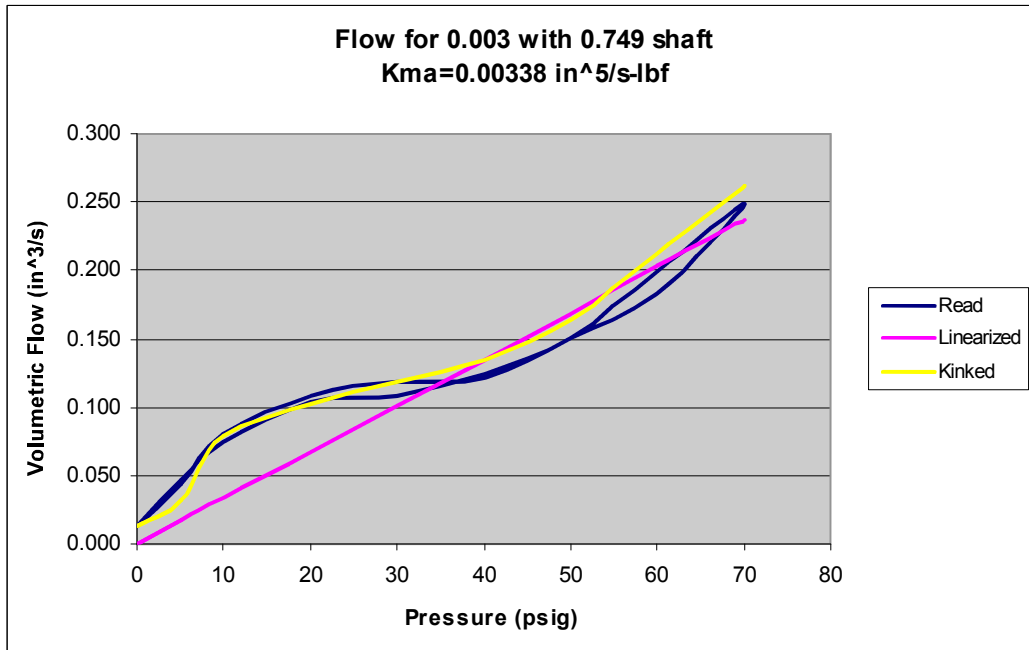
Flow Rate Readings					
Pressure psig	Read mm	Read LPM	Read in <sup>3</sup> /s	Linear in <sup>3</sup> /s	Kinked in <sup>3</sup> /s
0		1	0.013	0.013	0.000
10		7	0.093	0.094	0.094
20		8	0.106	0.108	0.106
30		9	0.119	0.121	0.142
40		10	0.148	0.150	0.177
50		11	0.212	0.216	0.213
60		11	0.212	0.216	0.248
70		12	0.277	0.282	0.284
80		12	0.277	0.282	0.319
90		13	0.342	0.348	0.354
100		14	0.407	0.413	0.390



**Al Housing / .003" dia Al Sleeve / .749" shaft**

Low pressure Kma:	0.00394	
Med pressure Kma:	0.00160	
High Pressure Kma:	0.00494	
Low Pivot Pressure:	9.000	Slope or
LowPivot Flow:	0.035	Kma
High Pivot Pressure:	40.000	in <sup>5</sup> /s-lbf
High Pivot Flow:	0.0640	0.00338

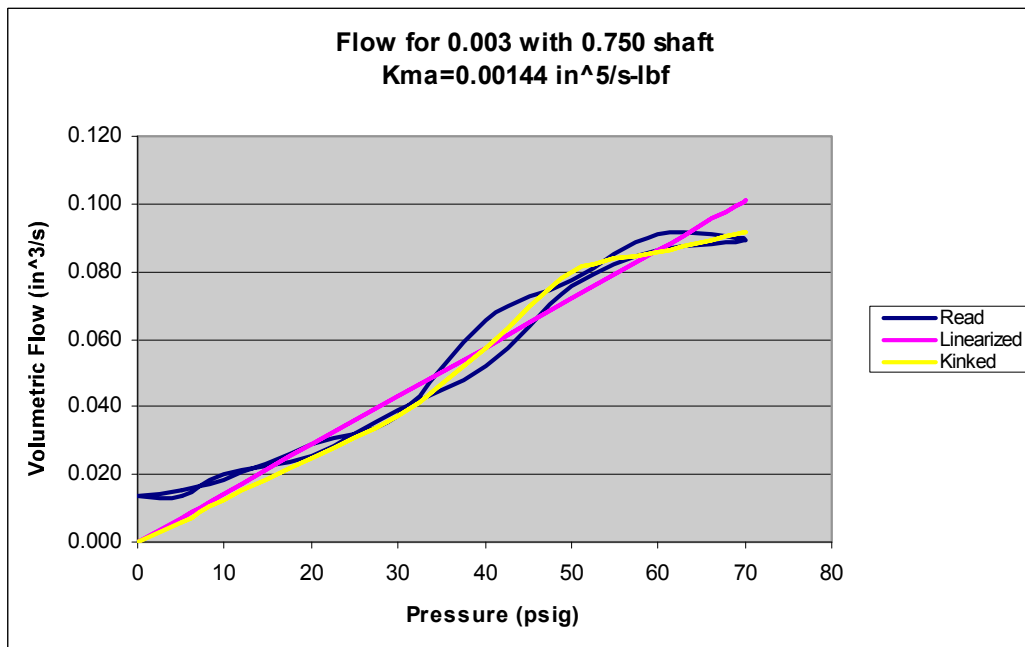
Flow Rate Readings					
Pressure psig	Read mm	Read LPM	Read in <sup>3</sup> /s	Calc in <sup>3</sup> /s	Kinked in <sup>3</sup> /s
0	1.0	0.013	0.013	0.000	0.013
5	3.3	0.043	0.044	0.017	0.033
10	6.0	0.080	0.081	0.034	0.079
20	8.0	0.106	0.108	0.068	0.103
30	8.8	0.116	0.118	0.101	0.119
40	9.0	0.119	0.121	0.135	0.135
50	10.0	0.148	0.150	0.169	0.163
60	10.5	0.180	0.183	0.203	0.213
70	11.5	0.245	0.249	0.237	0.262
60	10.8	0.196	0.199	0.203	0.213
50	10.0	0.148	0.150	0.169	0.163
40	9.3	0.123	0.125	0.135	0.135
30	8.0	0.106	0.108	0.101	0.119
20	7.8	0.103	0.105	0.068	0.103
10	5.5	0.073	0.074	0.034	0.079
5	3.5	0.046	0.047	0.017	0.033
0	1.0	0.013	0.013	0.000	0.013



**Al Housing / .003" dia Al Sleeve / .750" shaft**

Low pressure Kma:	0.00124	
Med pressure Kma:	0.00202	
High Pressure Kma:	0.00059	
Low Pivot Pressure:	30.000	Slope or Kma
LowPivot Flow:	0.037	
High Pivot Pressure:	35.000	in <sup>5</sup> /s-lbf
High Pivot Flow:	0.070854	

Flow Rate Readings						
Pressure psig	Read mm	Read LPM	Read in <sup>3</sup> /s	Calc in <sup>3</sup> /s	Kinked in <sup>3</sup> /s	
0	1.0	0.013	0.013	0.000	0.000	
5	1.1	0.015	0.015	0.007	0.006	
10	1.4	0.018	0.019	0.014	0.012	
20	2.1	0.028	0.029	0.029	0.025	
30	2.8	0.036	0.037	0.043	0.037	
40	4.9	0.065	0.066	0.058	0.057	
50	5.8	0.076	0.078	0.072	0.080	
60	6.8	0.090	0.091	0.086	0.086	
70	6.6	0.088	0.089	0.101	0.092	
60	6.4	0.085	0.086	0.086	0.086	
50	5.6	0.075	0.076	0.072	0.080	
40	3.9	0.051	0.052	0.058	0.057	
30	2.9	0.038	0.039	0.043	0.037	
20	1.9	0.025	0.025	0.029	0.025	
10	1.5	0.020	0.020	0.014	0.012	
5	1.0	0.013	0.013	0.007	0.006	
0	1.0	0.013	0.013	0.000	0.000	

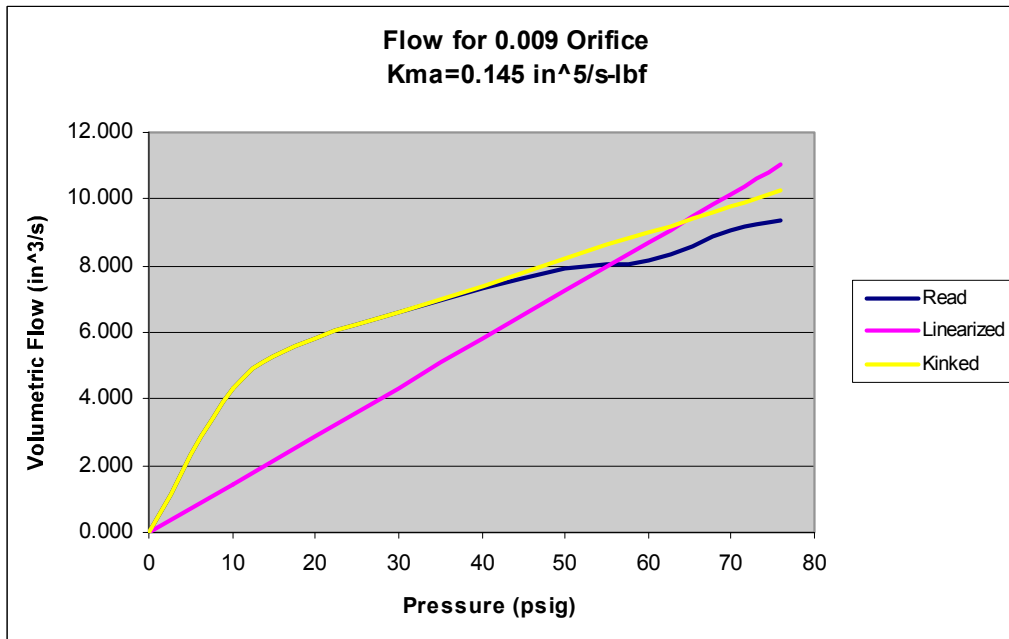


**0.009" Orifice Bearing**

**Al Housing / .009" dia Al Sleeve / no shaft**

Low pressure Kma:	0.42990	Slope or Kma
High Pressure Kma:	0.07903	
Pivot Pressure:	12.100	in <sup>5</sup> /s-lbf
Pivot Flow:	5.202	
		0.14500

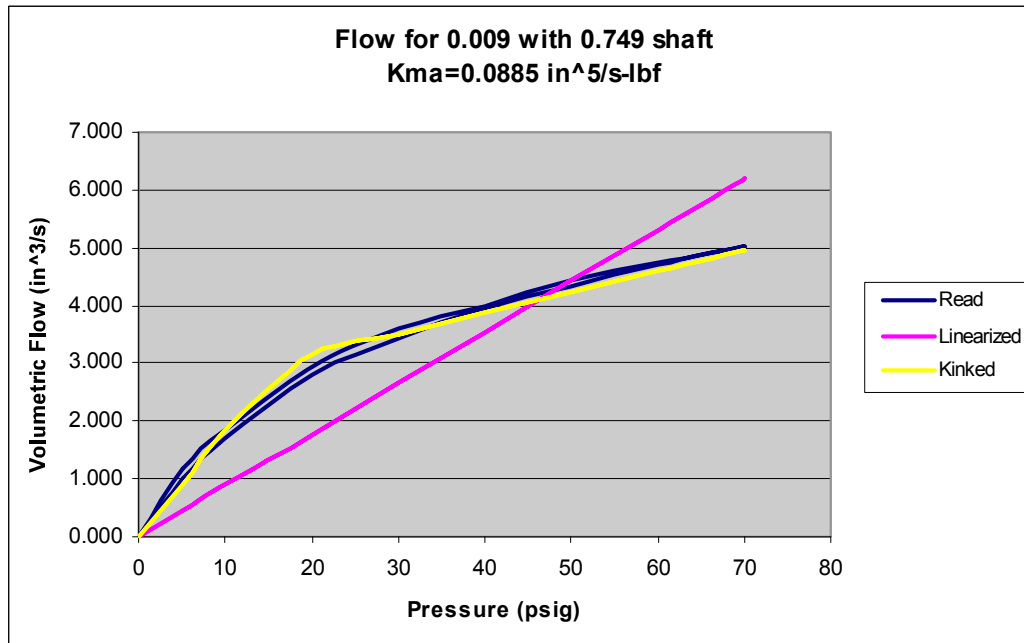
Flow Rate Readings					
Pressure psig	Read mm	Read LPM	Read in <sup>3</sup> /s	Linear in <sup>3</sup> /s	Kinked in <sup>3</sup> /s
0	1	0.013	0.013	0.000	0
10	73	4.227	4.299	1.450	4.299
20	96	5.716	5.814	2.900	5.826
30	108	6.493	6.604	4.350	6.616
40	119	7.205	7.328	5.800	7.407
50	128	7.788	7.921	7.250	8.197
60	132	8.047	8.185	8.700	8.987
70	145	8.889	9.041	10.150	9.778
76	150	9.213	9.370	11.020	10.252



**Al Housing / .009" dia Al Sleeve / .749" shaft**

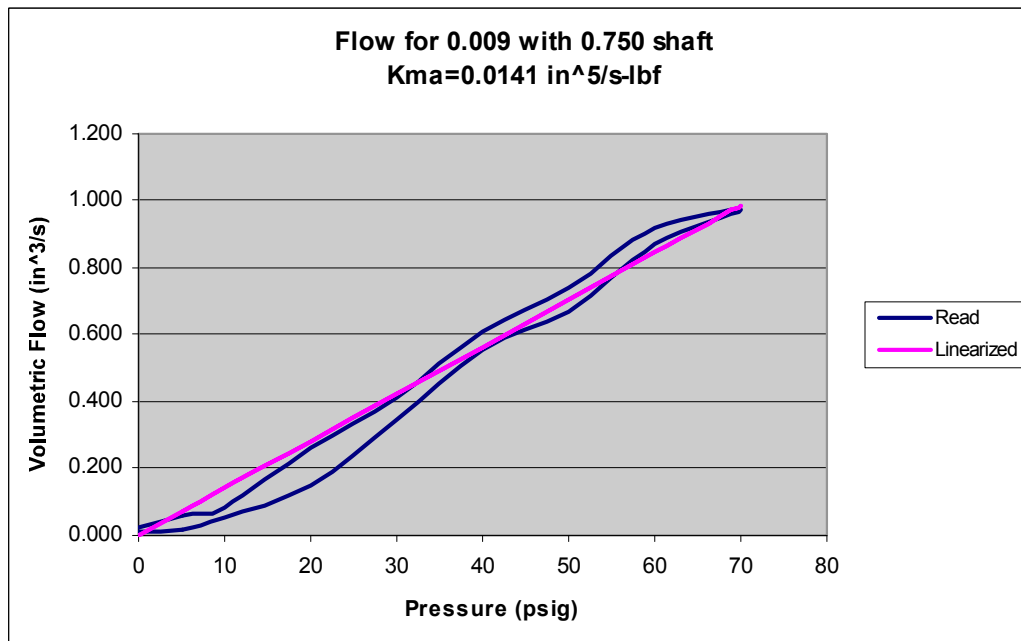
Low pressure Kma:	0.18294	Slope or Kma in <sup>5</sup> /s-lbf
High Pressure Kma:	0.03622	
Pivot Pressure:	16.500	
Pivot Flow:	3.019	
		0.08850

Flow Rate Readings						
Pressure psig	Read mm	Read LPM	Read in <sup>3</sup> /s	Calc in <sup>3</sup> /s	Kinked in <sup>3</sup> /s	
0	1.0	0.013	0.013	0.000	0.000	
5	25.5	1.151	1.171	0.443	0.915	
10	35.5	1.799	1.829	0.885	1.829	
20	52.3	2.883	2.933	1.770	3.145	
30	62.3	3.531	3.591	2.655	3.508	
40	68.3	3.919	3.986	3.540	3.870	
50	75.0	4.356	4.431	4.425	4.232	
60	80.0	4.680	4.760	5.310	4.594	
70	84.3	4.955	5.040	6.195	4.956	
60	79.5	4.648	4.727	5.310	4.594	
50	73.8	4.275	4.348	4.425	4.232	
40	67.8	3.887	3.953	3.540	3.870	
30	60.0	3.385	3.443	2.655	3.508	
20	50.3	2.754	2.801	1.770	3.145	
10	33.8	1.685	1.714	0.885	1.829	
5	23.0	0.989	1.006	0.443	0.915	
0	1.0	0.013	0.013	0.000	0.000	



Al Housing / .009" dia Al Sleeve / .750" shaft

				Slope or Kma in <sup>5</sup> /s-lbf
				0.01410
Flow Rate Readings				
Pressure psig	Read mm	Read LPM	Read in <sup>3</sup> /s	Calc in <sup>3</sup> /s
0	1.0	0.013	0.013	0.000
5	1.3	0.018	0.018	0.071
10	3.8	0.051	0.052	0.141
20	10.0	0.148	0.150	0.282
30	13.0	0.342	0.348	0.423
40	16.2	0.547	0.556	0.564
50	17.8	0.655	0.666	0.705
60	21.0	0.860	0.874	0.846
70	22.5	0.957	0.973	0.987
60	21.7	0.903	0.918	0.846
50	19.0	0.730	0.743	0.705
40	17.0	0.601	0.611	0.564
30	14.0	0.407	0.413	0.423
20	11.7	0.255	0.260	0.282
10	6.3	0.084	0.085	0.141
5	4.5	0.060	0.061	0.071
0	1.8	0.024	0.025	0.000





**0.018" Orifice Bearing**

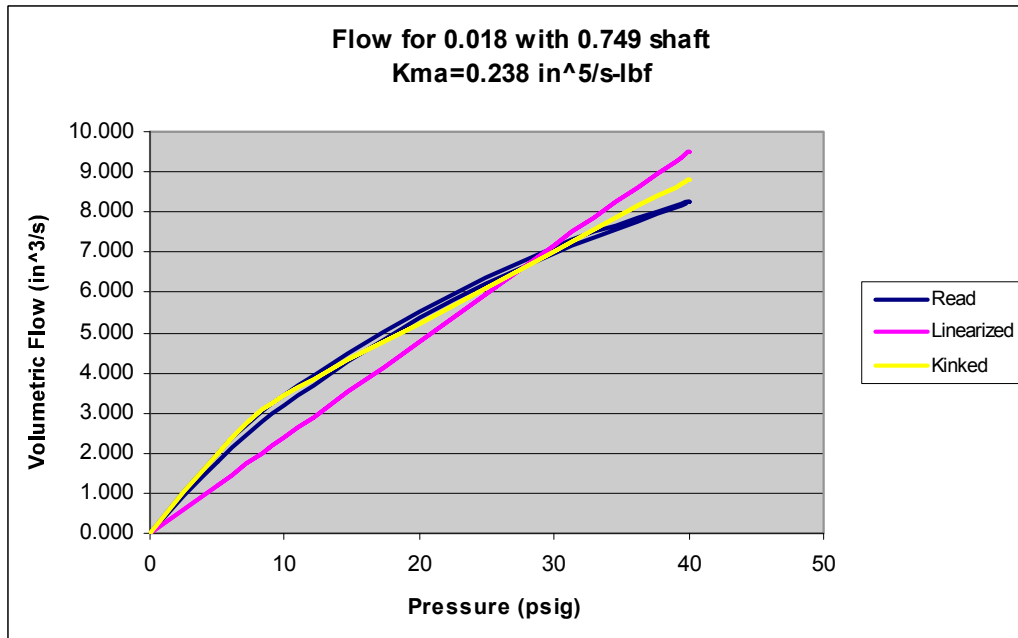
0.018 / No Shaft

No readings available due to very high flow rates at very low pressures.

**Al Housing / .018" dia Al Sleeve / .749" shaft**

Low pressure Kma:	0.39552	Slope or Kma
High Pressure Kma:	0.17969	
Pivot Pressure:	7.500	in <sup>5</sup> /s-lbf
Pivot Flow:	2.966	0.23800

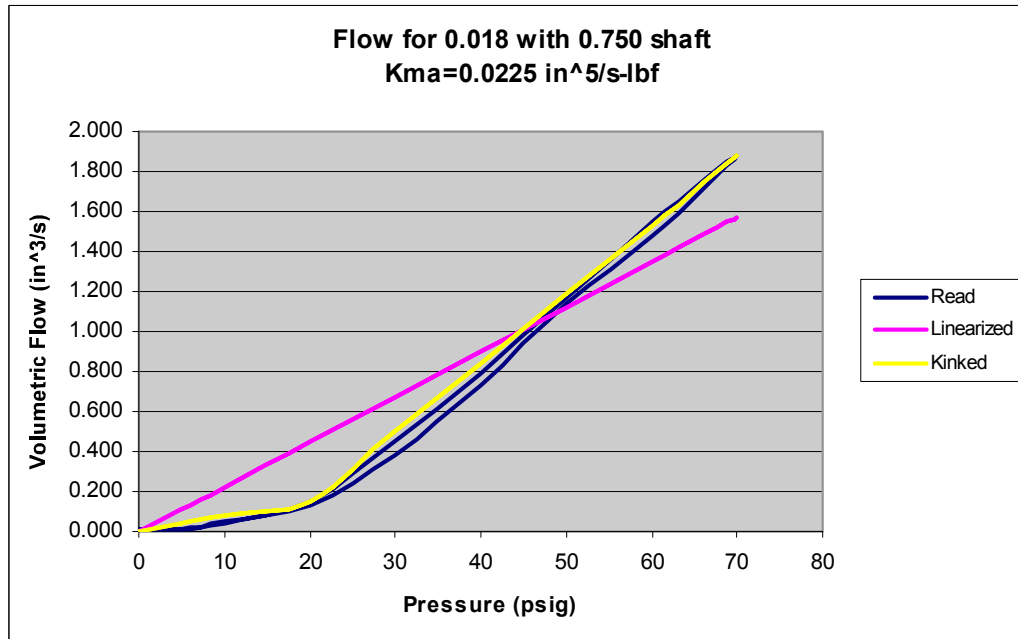
Flow Rate Readings						
Pressure psig	Read mm	Read LPM	Read in <sup>3</sup> /s	Calc in <sup>3</sup> /s	Kinked in <sup>3</sup> /s	
0	1.0	0.013	0.013	0.000	0.000	
5	37.8	1.944	1.978	1.190	1.978	
10	60.0	3.385	3.443	2.380	3.416	
20	91.8	5.441	5.534	4.760	5.213	
30	116.0	7.011	7.131	7.140	7.010	
40	133.3	8.128	8.267	9.520	8.806	
30	113.8	6.866	6.983	7.140	7.010	
20	89.0	5.263	5.353	4.760	5.213	
10	56.0	3.126	3.179	2.380	3.416	
5	34.8	1.750	1.780	1.190	1.978	
0	1.0	0.013	0.013	0.000	0.000	



**Al Housing / .018" dia Al Sleeve / .750" shaft**

Low pressure Kma:	0.00750	Slope or Kma in <sup>5</sup> /s-lbf 0.02250
High Pressure Kma:	0.03457	
Pivot Pressure:	20.000	
Pivot Flow:	0.150	

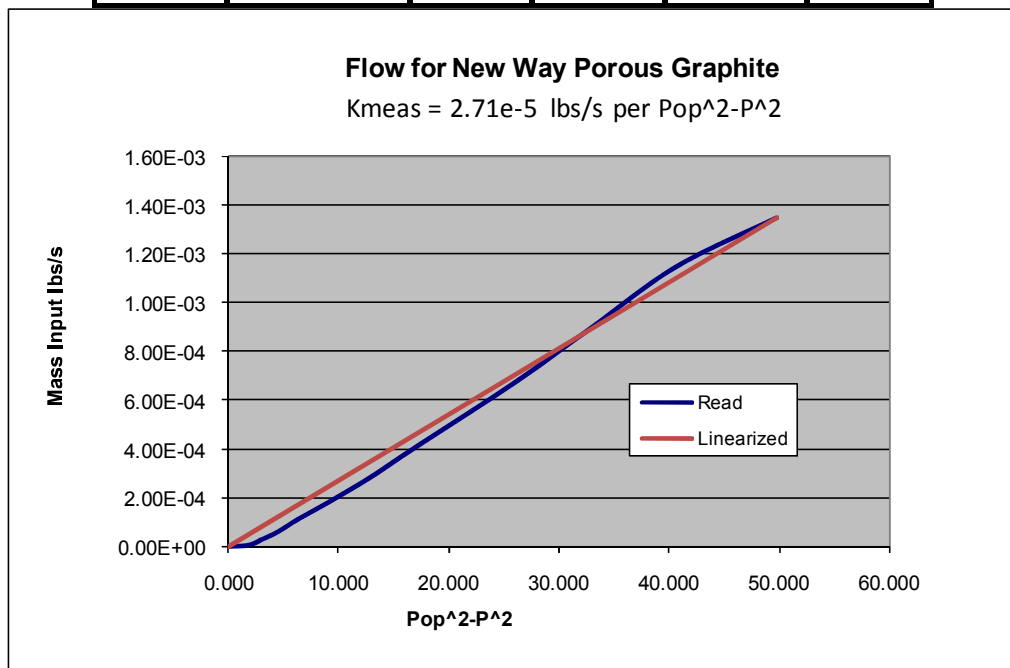
Flow Rate Readings						
Pressure psig	Read mm	Read LPM	Read in <sup>3</sup> /s	Calc in <sup>3</sup> /s	Kinked in <sup>3</sup> /s	
0	1.0	0.013	0.013	0.000	0	
5	1.0	0.013	0.013	0.113	0.038	
10	3.3	0.043	0.044	0.225	0.075	
20	10.0	0.148	0.150	0.450	0.150	
30	14.5	0.439	0.446	0.675	0.496	
40	19.8	0.779	0.792	0.900	0.842	
50	25.5	1.151	1.171	1.125	1.187	
60	31.3	1.524	1.550	1.350	1.533	
70	36.3	1.847	1.879	1.575	1.879	
60	30.3	1.459	1.484	1.350	1.533	
50	25.0	1.119	1.138	1.125	1.187	
40	18.8	0.714	0.726	0.900	0.842	
30	13.5	0.374	0.381	0.675	0.496	
20	9.5	0.126	0.128	0.450	0.150	
10	3.5	0.046	0.047	0.225	0.075	
5	1.0	0.013	0.013	0.113	0.038	
0	1.0	0.013	0.013	0.000	0.000	



D.6. Mass Flow Rate vs (Pop)2

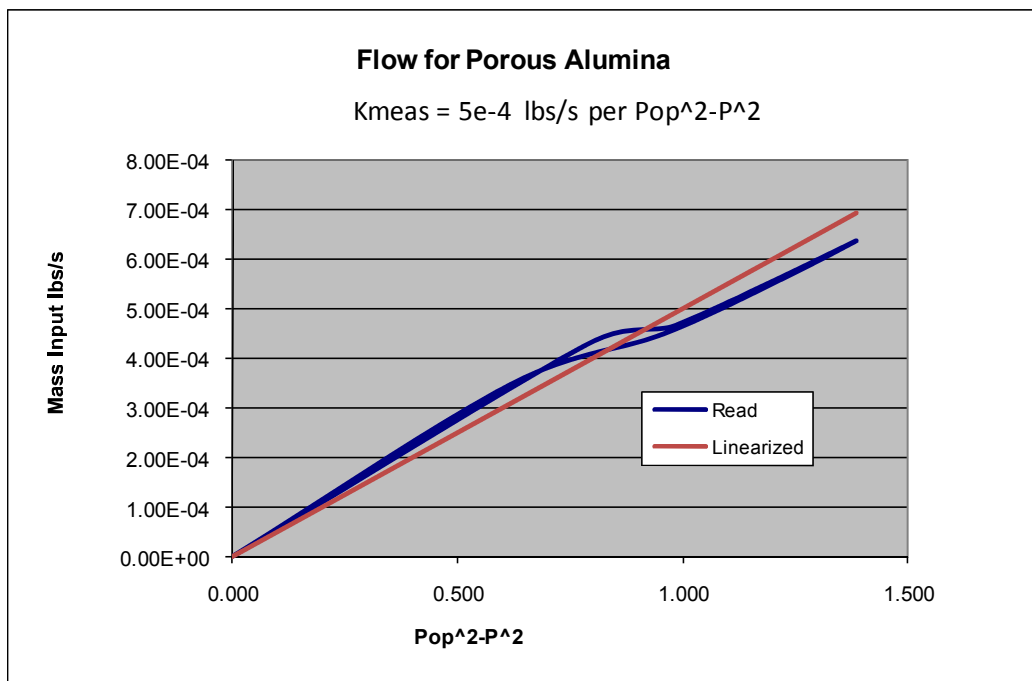
D.6.1. New Way Porous Graphite Liner

Pressure psig	Read flow in <sup>3</sup> /s	density lbs/in <sup>3</sup>	Mass in lbs/s	Kmeas 2.7E-05	
				Pop <sup>2</sup> -P <sup>2</sup> 1	lbs/s
0	0.013	4.40E-05	5.94E-07	0.000	0
10	0.094	7.39E-05	6.98E-06	1.823	4.94E-05
15	0.348	8.89E-05	3.09E-05	3.082	8.35E-05
20	0.611	1.04E-04	6.35E-05	4.572	1.24E-04
25	0.940	1.19E-04	1.12E-04	6.294	1.70E-04
30	1.204	1.34E-04	1.61E-04	8.247	2.23E-04
40	1.731	1.64E-04	2.83E-04	12.846	3.48E-04
50	2.323	1.94E-04	4.50E-04	18.372	4.98E-04
60	2.850	2.24E-04	6.37E-04	24.823	6.72E-04
70	3.443	2.54E-04	8.73E-04	32.200	8.72E-04
80	4.036	2.83E-04	1.14E-03	40.502	1.10E-03
90	4.299	3.13E-04	1.35E-03	49.729	1.35E-03



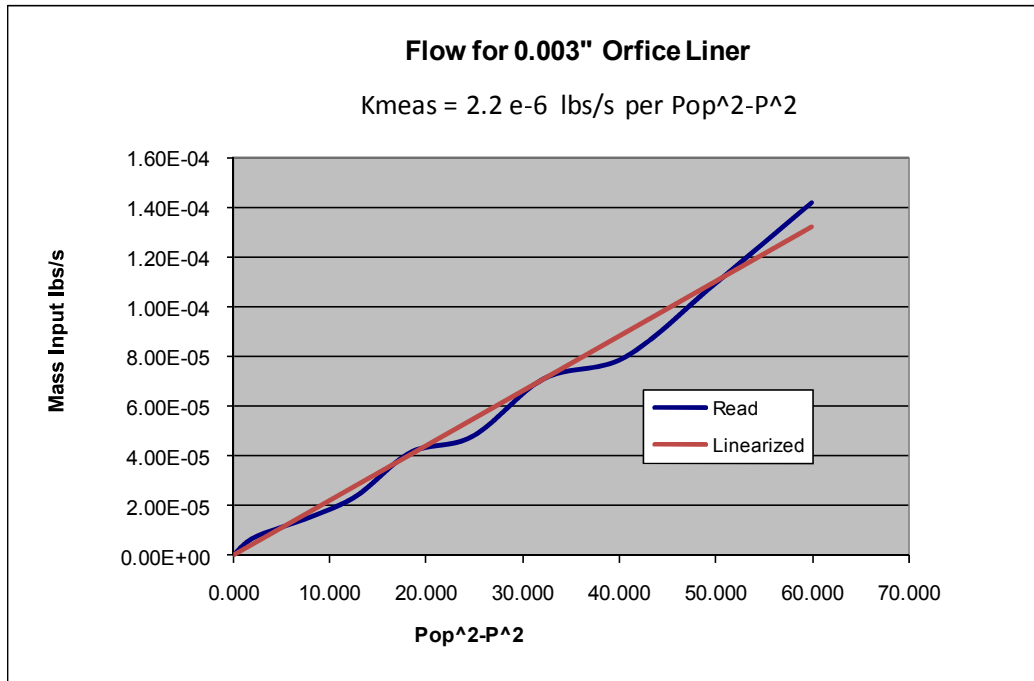
D.6.2. Porous Alumina Liner

				Kmeas 0.0005	
Pressure psig	Read flow in <sup>3</sup> /s	density lbs/in <sup>3</sup>	Mass in lbs/s	Pop <sup>2</sup> -P <sup>1</sup>	lbs/s
0	0.013	4.40E-05	5.94E-07	0.000	0
5	7.328	5.90E-05	4.32E-04	0.796	0.0004
6	7.526	6.20E-05	4.66E-04	0.983	0.00049
8	9.370	6.79E-05	6.37E-04	1.385	0.00069
6	7.394	6.20E-05	4.58E-04	0.983	0.00049
4	6.209	5.60E-05	3.48E-04	0.618	0.00031
0	0.013	4.40E-05	5.94E-07	0.000	0



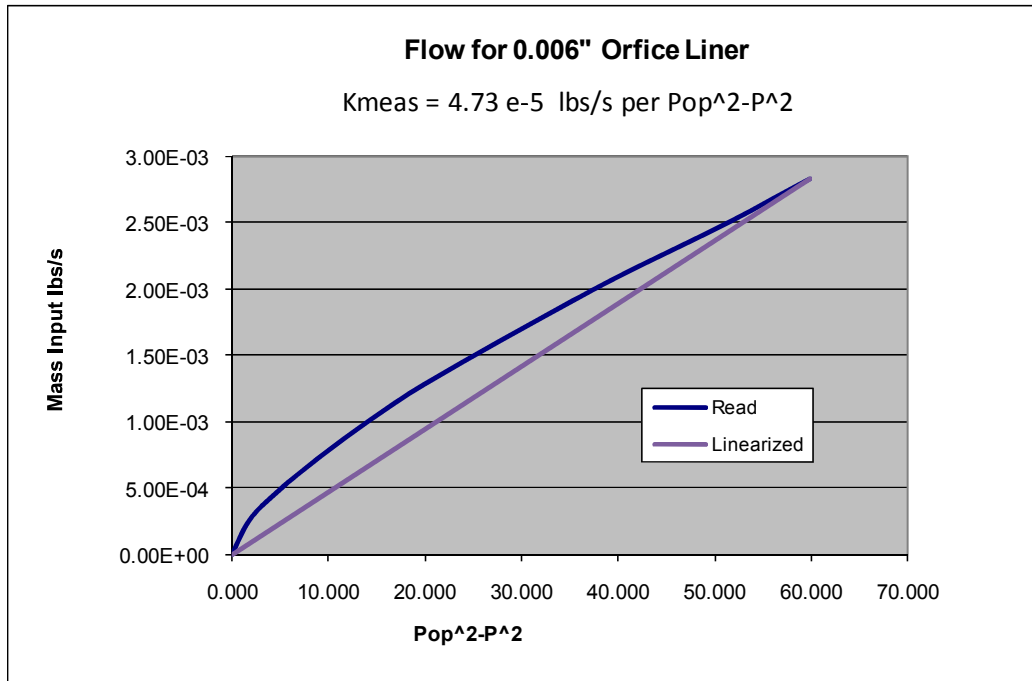
D.6.3. 12 x 0.003" Feedhole Liner

Pressure psig	Read flow in <sup>3</sup> /s	density lbs/in <sup>3</sup>	Mass in lbs/s	Kmeas 2.20E-06	
				Pop <sup>2</sup> -P <sup>1</sup>	lbs/s
0	0.013	4.40E-05	5.94E-07	0.000	0
10	0.094	7.39E-05	6.98E-06	1.823	4E-06
20	0.108	1.04E-04	1.12E-05	4.572	1E-05
30	0.121	1.34E-04	1.63E-05	8.247	1.8E-05
40	0.150	1.64E-04	2.46E-05	12.846	2.8E-05
50	0.216	1.94E-04	4.18E-05	18.372	4E-05
60	0.216	2.24E-04	4.83E-05	24.823	5.5E-05
70	0.282	2.54E-04	7.14E-05	32.200	7.1E-05
80	0.282	2.83E-04	7.99E-05	40.502	8.9E-05
90	0.348	3.13E-04	1.09E-04	49.729	0.00011
100	0.413	3.43E-04	1.42E-04	59.882	0.00013



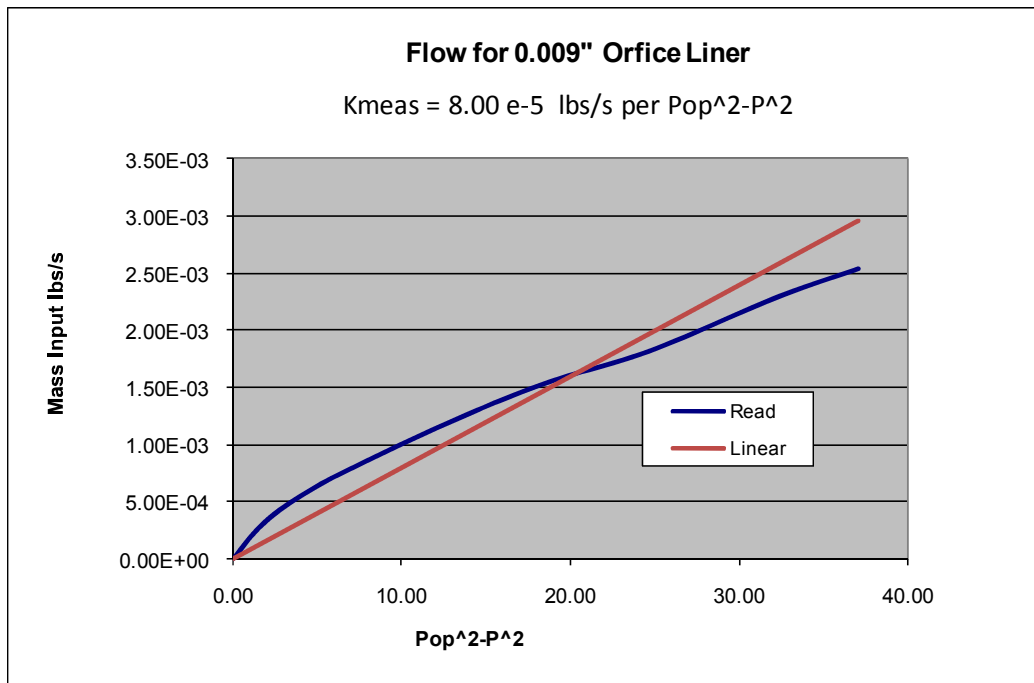
D.6.4. 12 x 0.006" Feedhole Liner

Pressure psig	Read flow in <sup>3</sup> /s	density lbs/in <sup>3</sup>	Mass in lbs/s	Kmeas 4.73E-05	
				Pop <sup>2</sup> -P <sup>1</sup>	lbs/s
0	0.013	4.40E-05	5.94E-07	0.000	0
10	3.575	7.39E-05	2.64E-04	1.823	8.62E-05
20	4.497	1.04E-04	4.67E-04	4.572	2.16E-04
30	5.155	1.34E-04	6.90E-04	8.247	3.90E-04
40	5.748	1.64E-04	9.41E-04	12.846	6.08E-04
50	6.275	1.94E-04	1.22E-03	18.372	8.69E-04
60	6.670	2.24E-04	1.49E-03	24.823	1.17E-03
70	7.065	2.54E-04	1.79E-03	32.200	1.52E-03
80	7.460	2.83E-04	2.11E-03	40.502	1.92E-03
90	7.789	3.13E-04	2.44E-03	49.729	2.35E-03
100	8.250	3.43E-04	2.83E-03	59.882	2.83E-03



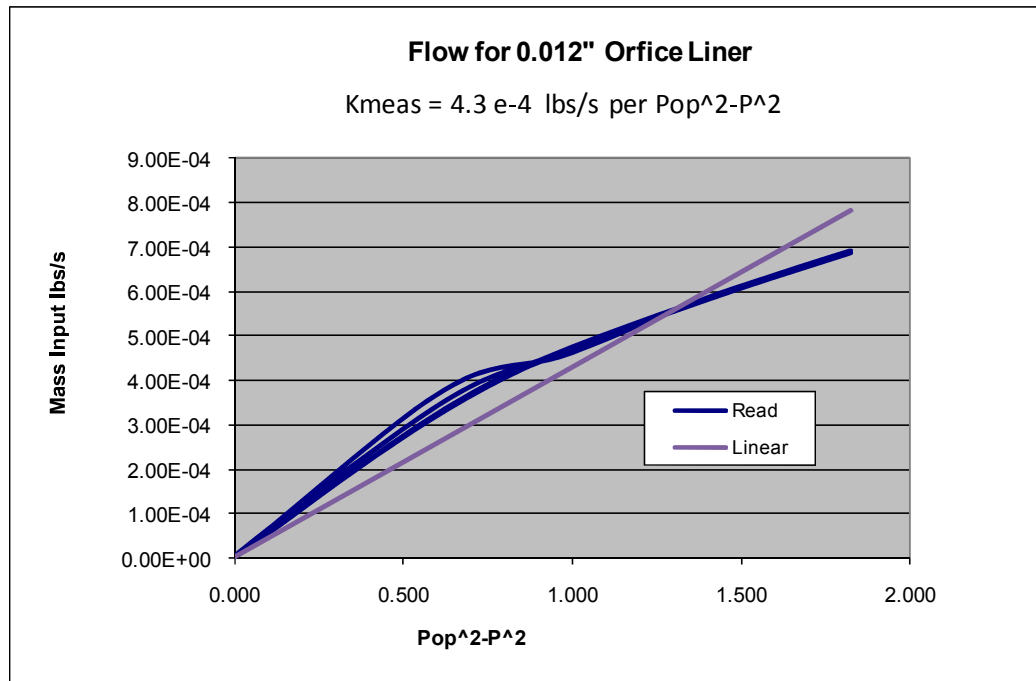
D.6.5. 12 x 0.009" Feedhole Liner

Pressure psig	Read flow in <sup>3</sup> /s	density lbs/in <sup>3</sup>	Mass in lbs/s	Kmeas 8.00E-05	
				Pop <sup>2</sup> -P <sup>1</sup>	lbs/s Linear
0	0.013	4.40E-05	5.94E-07	0.00	0
10	4.299	7.39E-05	3.18E-04	1.82	1.46E-04
20	5.814	1.04E-04	6.04E-04	4.57	3.66E-04
30	6.604	1.34E-04	8.84E-04	8.25	6.60E-04
40	7.328	1.64E-04	1.20E-03	12.85	1.03E-03
50	7.921	1.94E-04	1.53E-03	18.37	1.47E-03
60	8.185	2.24E-04	1.83E-03	24.82	1.99E-03
70	9.041	2.54E-04	2.29E-03	32.20	2.58E-03
76	9.370	2.71E-04	2.54E-03	37.07	2.97E-03



D.6.6. 12 x 0.012" Feedhole Liner

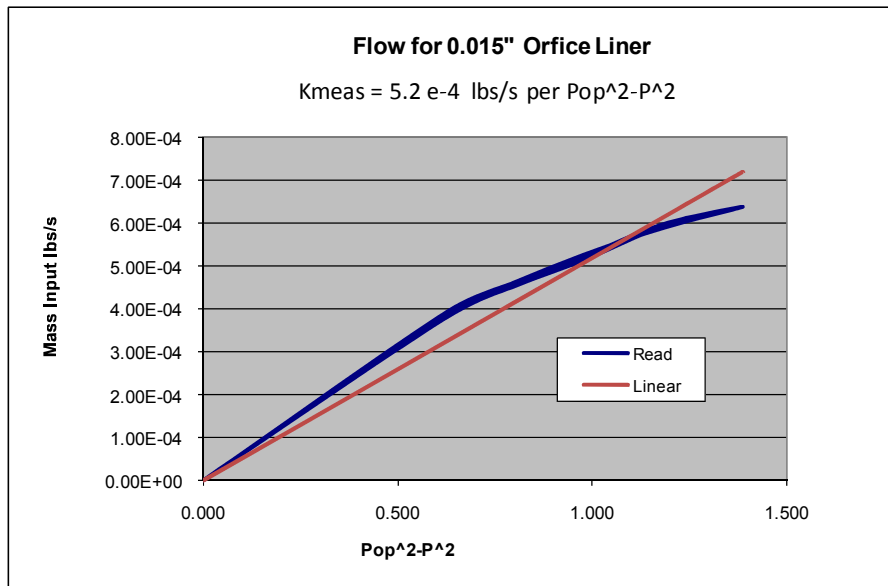
Pressure psig	Read flow in <sup>3</sup> /s	density lbs/in <sup>3</sup>	Mass in lbs/s	Kmeas 4.30E-04	
				Pop <sup>2</sup> -P <sup>1</sup>	lbs/s
0	0.013	4.40E-05	5.94E-07	0.000	0
5	6.933	5.90E-05	4.09E-04	0.796	3.42E-04
10	9.304	7.39E-05	6.88E-04	1.823	7.84E-04
5	6.867	5.90E-05	4.05E-04	0.796	3.42E-04
0	0.013	4.40E-05	5.94E-07	0.000	0.00E+00
4	6.275	5.60E-05	3.51E-04	0.618	2.66E-04
6	7.526	6.20E-05	4.66E-04	0.983	4.23E-04
8	8.514	6.79E-05	5.78E-04	1.385	5.95E-04
10	9.370	7.39E-05	6.93E-04	1.823	7.84E-04
8	8.580	6.79E-05	5.83E-04	1.385	5.95E-04
6	7.394	6.20E-05	4.58E-04	0.983	4.23E-04
4	6.736	5.60E-05	3.77E-04	0.618	2.66E-04
0	0.013	4.40E-05	5.94E-07	0.000	0.00E+00





D.6.7. 12 x 0.015" Feedhole Liner

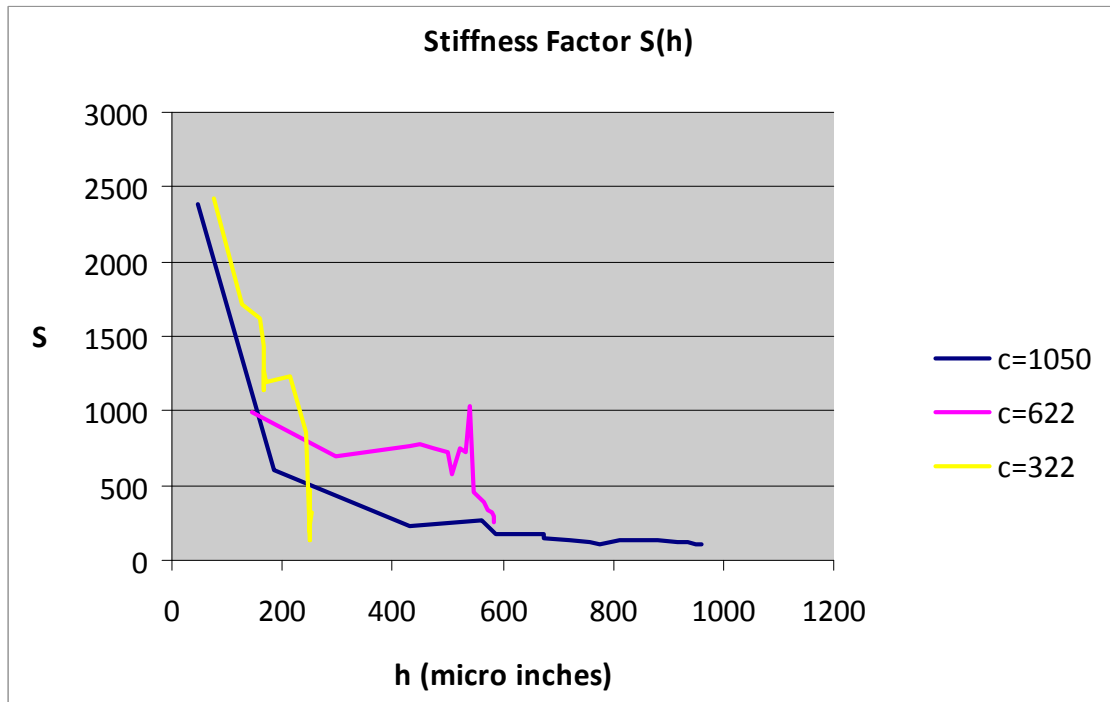
Pressure psig	Read flow in <sup>3</sup> /s	density lbs/in <sup>3</sup>	Mass in lbs/s	Kmeas 5.20E-04	
				Pop <sup>2</sup> -P <sup>1</sup>	lbs/s
0	0.013	4.40E-05	5.94E-07	0.000	0
4	6.802	5.60E-05	3.81E-04	0.618	3.21E-04
5	7.789	5.90E-05	4.59E-04	0.796	4.14E-04
6	8.448	6.20E-05	5.23E-04	0.983	5.11E-04
7	9.172	6.49E-05	5.96E-04	1.179	6.13E-04
8	9.370	6.79E-05	6.37E-04	1.385	7.20E-04
7	9.107	6.49E-05	5.91E-04	1.179	6.13E-04
6	8.382	6.20E-05	5.19E-04	0.983	5.11E-04
5	7.724	5.90E-05	4.55E-04	0.796	4.14E-04
4	6.736	5.60E-05	3.77E-04	0.618	3.21E-04
0	0.013	4.40E-05	5.94E-07	0.000	0.00E+00
4	6.736	5.60E-05	3.77E-04	0.618	3.21E-04
5	7.658	5.90E-05	4.52E-04	0.796	4.14E-04
6	8.316	6.20E-05	5.15E-04	0.983	5.11E-04
7	9.107	6.49E-05	5.91E-04	1.179	6.13E-04
8	9.370	6.79E-05	6.37E-04	1.385	7.20E-04
7	9.041	6.49E-05	5.87E-04	1.179	6.13E-04
6	8.514	6.20E-05	5.27E-04	0.983	5.11E-04
5	7.789	5.90E-05	4.59E-04	0.796	4.14E-04
4	6.933	5.60E-05	3.88E-04	0.618	3.21E-04
0	0.013	4.40E-05	5.94E-07	0.000	0.00E+00



D.7. Stiffness Factor  $s(h)$  vs  $h$

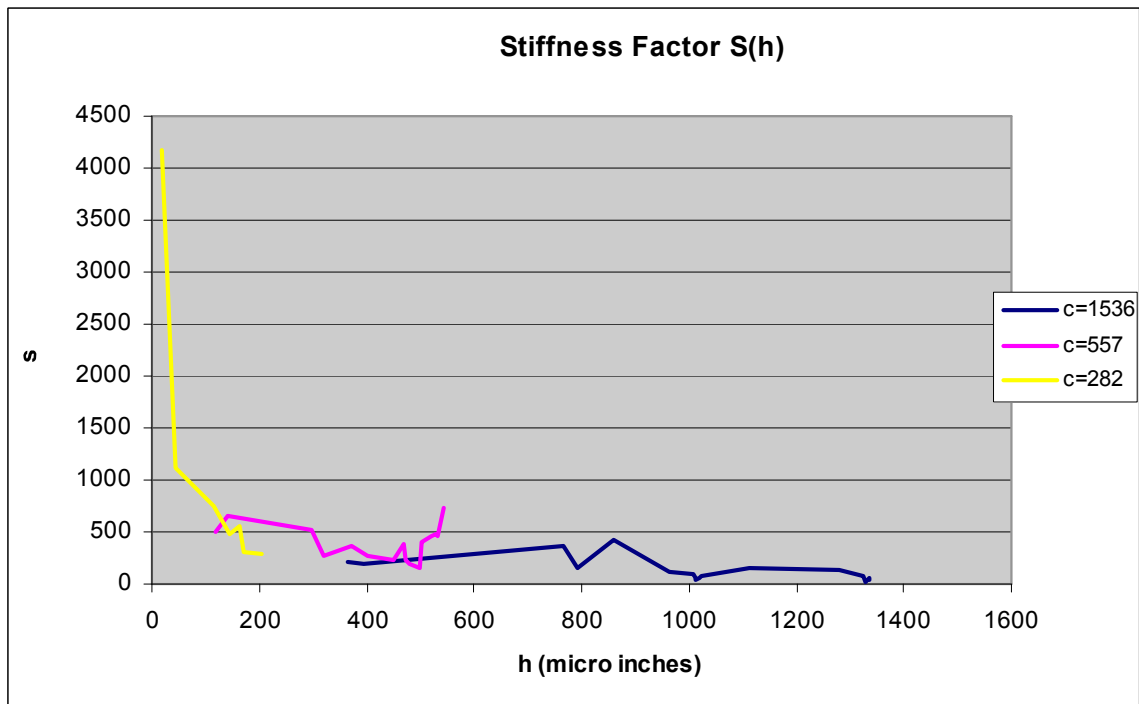
D.7.1. New Way Porous Graphite Liner

1050		622		322	
h	s	h	s	h	s
47	2380	146	997	78	2424
186	606	298	702	128	1709
430	234	430	762	159	1626
562	273	451	780	168	1434
586	178	477	753	168	1307
673	177	501	725	168	1135
674	151	507	581	168	1270
720	134	523	751	169	1190
757	119	532	717	213	1226
776	101	539	1030	245	860
811	140	548	449	250	153
881	131	564	383	250	131
917	125	573	338	251	468
935	116	581	327	251	188
950	111	585	298	251	236
960	106	585	257	253	320



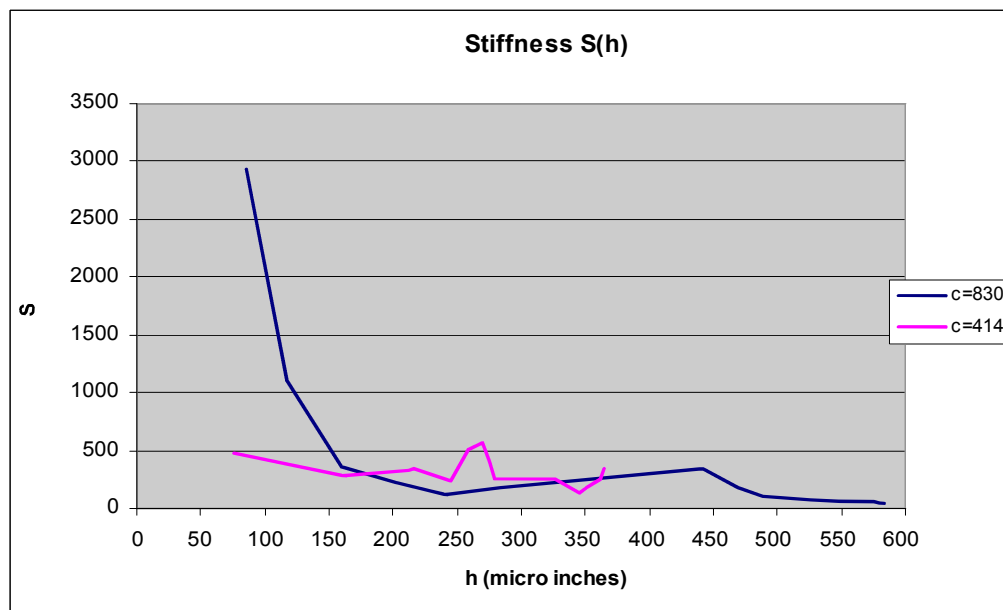
D.7.2. Porous Alumina Liner

1536		557		282	
h	s	h	s	h	s
364	207	119	496	18	4167
395	196	140	660	45	1111
768	358	298	515	115	741
793	146	322	271	146	490
858	415	372	360	165	556
966	110	404	261	171	300
1010	89	450	238	206	292
1013	51	470	383	228	1067
1013	44	472	236	231	327
1018	61	480	197	240	585
1022	73	500	155	251	705
1111	157	502	400	258	561
1278	129	521	460	266	673
1326	79	529	472	270	777
1329	23	533	458		
1329	27	544	733		
1331	33				
1335	55				
1336	42				



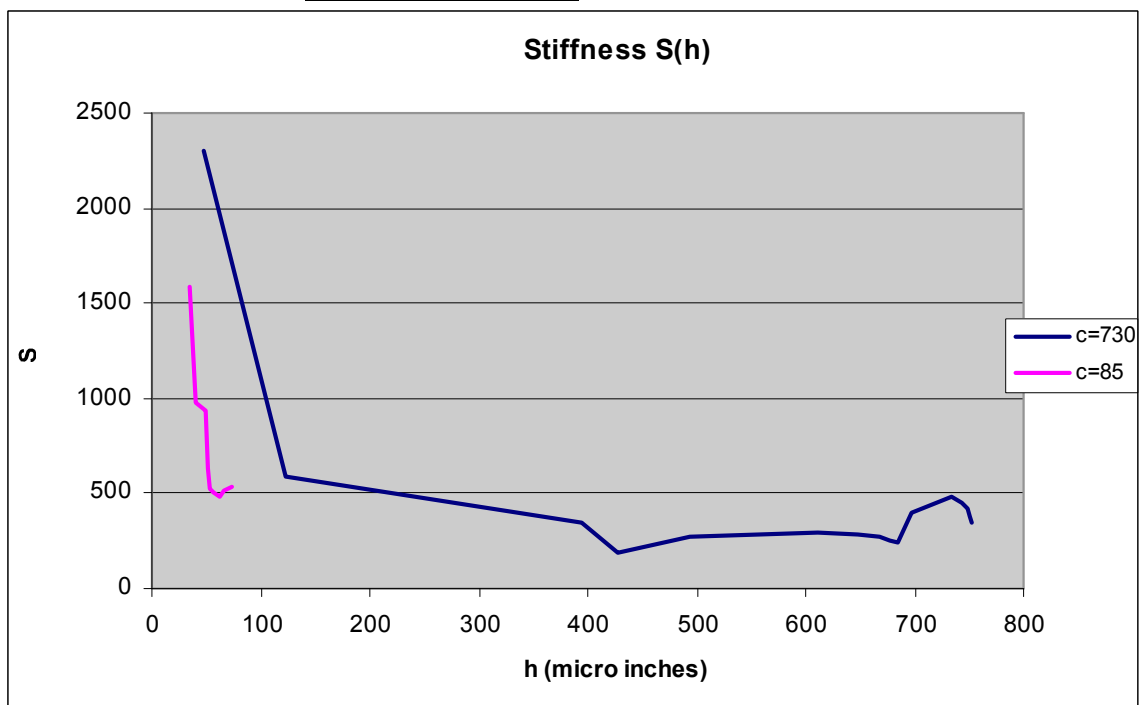
## D.7.3. 12 x 0.003" Feedhole Liner

830		414	
h	s	h	s
85	2930	75	476
117	1111	161	291
159	363	212	330
203	224	216	337
229	145	245	237
242	123	259	508
284	180	270	570
442	343	276	407
469	185	280	248
488	98	326	252
525	73	346	140
554	60	352	178
576	52	361	253
581	45	365	338
583	39		



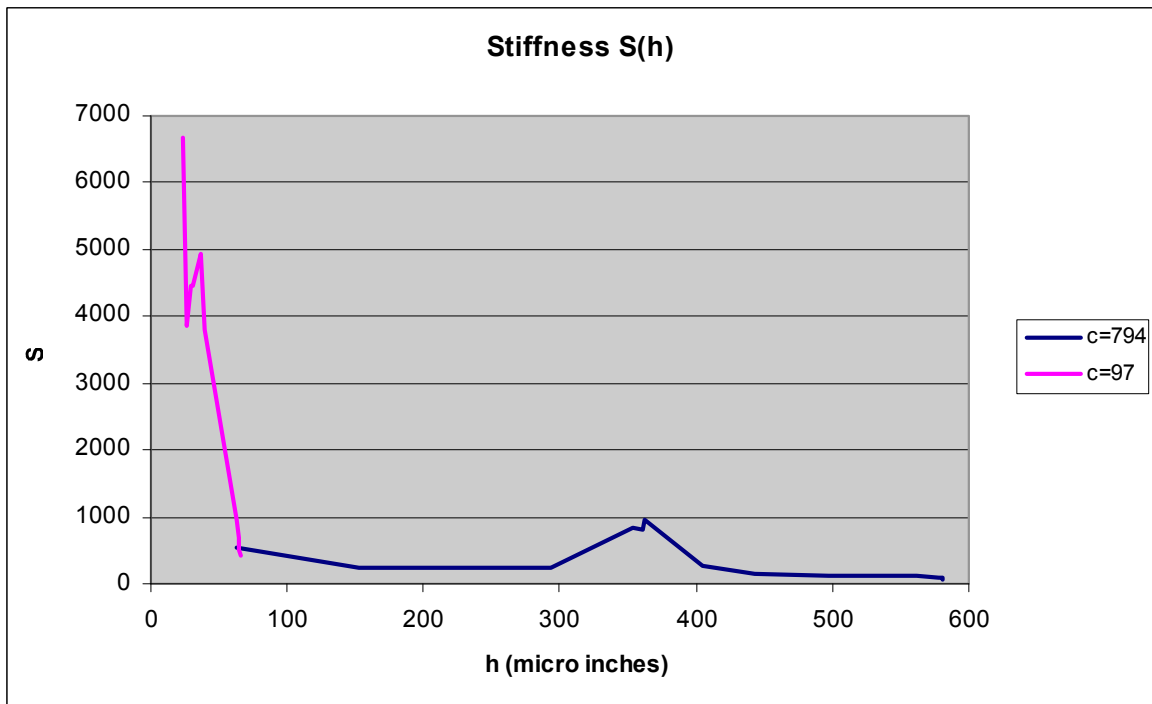
## D.7.4. 12 x 0.009" Feedhole Liner

730		85	
h	s	h	s
48	2299	35	1587
123	589	40	977
395	346	50	939
428	190	52	626
494	276	54	529
611	290	57	505
648	286	62	485
668	269	66	517
676	248	74	537
685	238		
698	404		
734	483		
743	450		
749	423		
751	377		
753	346		



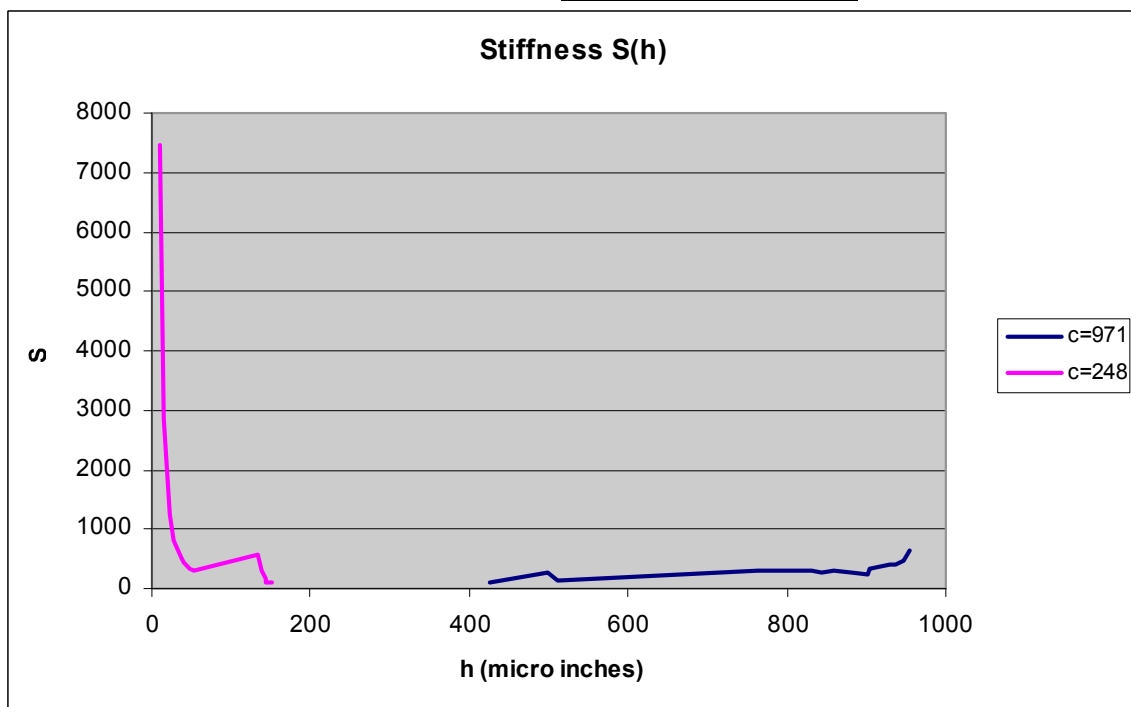
D.7.5. 12 x 0.015" Feedhole Liner

794		97	
h	s	h	s
63	551	23	6667
153	231	26	3865
293	225	29	4444
354	833	32	4444
361	794	36	4938
362	952	40	3810
405	257	63	966
444	143	64	679
497	112	65	517
562	108	66	423
578	93	68	380
581	78	70	346
581	67		



D.7.6. 12 x 0.018" Feedhole Liner

971		248	
h	s	h	s
425	114	11	7477
498	282	16	2857
510	145	24	1242
763	292	28	813
832	298	38	521
844	262	41	444
859	308	48	337
883	269	54	299
901	243	134	585
905	335	138	303
930	402	143	158
937	389	145	108
948	473	151	86
956	625	152	69
		156	60
		159	53



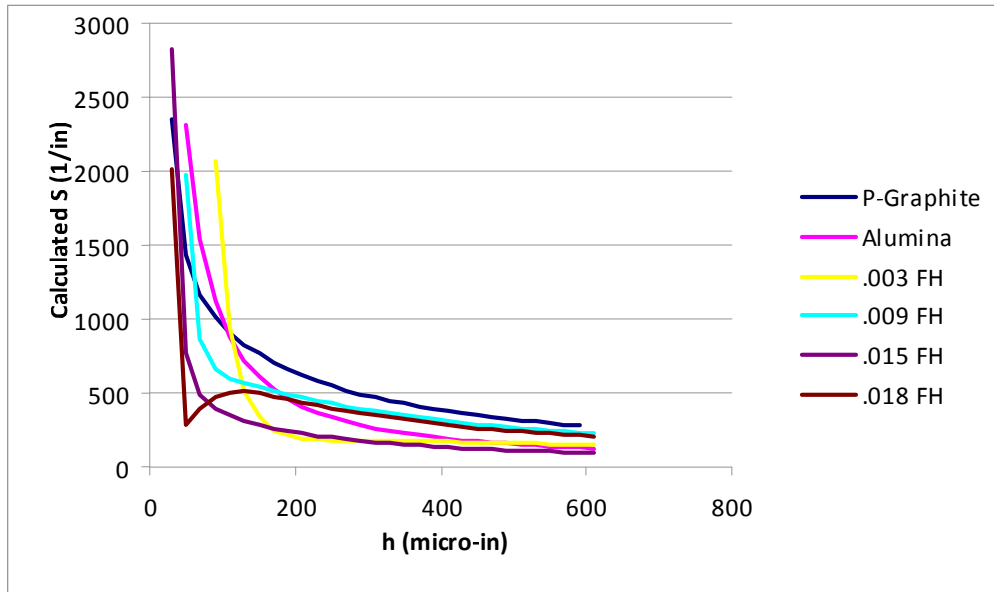
D.8. Curve Fitting of Stiffness Factor

Calculation of coefficients using Cramer's Rule

Bearing	h	s	a	b	c	d				
New Way	50	2400	0.02	0.0004	0.000008	2400	ad	-2.4142E-08	a=	188974.8809
D	220	650	0.004545455	2.06612E-05	9.39144E-08	650	bd	1.62952E-06	b=	-12755247.06
-1.27753E-13	570	300	0.001754386	3.07787E-06	5.39977E-09	300	cd	-5.87771E-05	c=	460085392.2
Bearing	h	s	a	b	c	d				
Alumina	18	4167	0.055555556	0.00308642	0.000171468	4167	ad	-7.49648E-07	a=	70685.43752
D	140	660	0.007142857	5.10204E-05	3.64431E-07	660	bd	-3.65439E-05	b=	3445781.018
-1.06054E-11	500	155	0.002	0.000004	0.000000008	155	cd	0.000643495	c=	-60676156.8
Bearing	h	s	a	b	c	d				
0.003	85	2930	0.011764706	0.000138408	1.62833E-06	2930	ad	-5.71896E-09	a=	147591.553
D	160	320	0.00625	3.90625E-05	2.44141E-07	320	bd	1.62459E-06	b=	-41926417.73
-3.87486E-14	469	185	0.002132196	4.54626E-06	9.69352E-09	185	cd	-0.000158478	c=	4089915643
Bearing	h	s	a	b	c	d				
0.009	48	2299	0.020833333	0.000434028	9.04225E-06	2299	ad	-8.4683E-08	a=	165516.0522
D	123	589	0.008130081	6.60982E-05	5.37384E-07	589	bd	8.86647E-06	b=	-17329836.84
-5.1163E-13	494	276	0.002024291	4.09776E-06	8.29505E-09	276	cd	-0.000357659	c=	699057775.2
Bearing	h	s	a	b	c	d				
0.015	23	6667	0.043478261	0.001890359	8.21895E-05	6667	ad	-1.39197E-06	a=	62924.42595
D	63	551	0.015873016	0.000251953	3.99925E-06	551	bd	8.85015E-05	b=	-4000751.638
-2.21212E-11	497	112	0.002012072	4.04844E-06	8.14575E-09	112	cd	-0.003086363	c=	139520445.2
Bearing	h	s	a	b	c	d				
0.018	41	444	0.024390244	0.000594884	1.45094E-05	444	ad	-2.93598E-07	a=	144723.6158
D	54	299	0.018518519	0.000342936	6.35066E-06	299	bd	2.54048E-05	b=	-12522804.44
-2.02868E-12	500	250	0.002	0.000004	0.000000008	250	cd	-0.00060809	c=	299746165

	P-Graphite	Alumina	.003 FH	.009 FH	.015 FH	.018 FH
30	9167				2820	2012
50	2358	2307	18901	1971	774	283
70	1438	1536	5476	866	489	386
90	1156	1128	2074	659	397	473
110	1009	882	950	598	346	506
130	908	720	516	566	311	509
150	829	606	332	540	283	497
170	764	523	250	516	260	479
190	708	459	212	493	241	459
210	660	408	194	471	224	438
230	618	367	185	449	209	417
250	581	334	181	430	197	398
270	548	306	179	411	185	379
290	519	282	178	393	175	362
310	492	262	177	377	166	347
330	468	244	176	362	158	332
350	447	229	175	348	150	318
370	427	215	173	335	144	306
390	408	203	172	322	137	294
410	392	192	170	311	132	283
430	376	182	168	300	126	273
450	362	173	166	290	122	263
470	349	165	164	280	117	254
490	336	158	161	272	113	246
510	325	151	159	263	109	238
530	314	145	157	255	105	230
550	304	140	154	248	102	224
570	295	134	152	241	99	217
590	286	129	150	234	96	211
610	278	125	147	228	93	205





## D.9. Summary Tables

## D.9.1. Flow rates

Feed Type	Shaft in	Clearance μ-in	Linked/Kinked	Linear Kma in <sup>5</sup> /s-lbf	Low Kma in <sup>5</sup> /s-lbf	Medium Kma in <sup>5</sup> /s-lbf	High Kma in <sup>5</sup> /s-lbf	High Pivot Pressure Psi	Low Pivot Pressure Psi
Porous Graphite	N/A	N/A	Linear	0.0470	N/A	N/A	N/A	N/A	N/A
	0.749	1050	Kinked (Single)	0.0426	0.0095	N/A	0.0517	9.5	N/A
	0.750	322	Kinked (Single)	0.0115	0.0037	N/A	0.0256	32.0	N/A
Porous Alumina	N/A	N/A	Linear	1.2750	N/A	N/A	N/A	N/A	N/A
	0.749	1536	Kinked (Single)	0.6950	0.8812	N/A	0.5516	4.9	N/A
	0.750	282	Linear	0.3120	N/A	N/A	N/A	N/A	N/A
12 x 0.003 Holes	N/A	N/A	Kinked (Single)	0.0040	0.0095	N/A	N/A	6.0	N/A
	0.749	830	Kinked (Double)	0.0034	0.0039	0.0016	0.0049	40.0	9.0
	0.750	414	Kinked (Double)	0.0014	0.0012	0.0020	0.0006	40.0	30.0
12 x 0.009 Holes	N/A	N/A	Kinked (Single)	0.1450	0.4299	N/A	0.0790	12.1	N/A
	0.749	730	Kinked (Single)	0.0885	0.1829	N/A	0.0362	16.5	N/A
	0.750	85	Linear	0.0141	N/A	N/A	N/A	N/A	N/A
12 x 0.018 Holes	N/A	N/A	N/A	N/A	N/A	N/A	N/A	N/A	N/A
	0.749	971	Kinked (Single)	0.2380	0.3955	N/A	0.1797	7.5	N/A
	0.750	248	Kinked (Single)	0.0225	0.0075	N/A	0.0346	20.0	N/A

## D.9.2. Stiffness

Feed Type	Shaft in	Clearance μ-in	S @ h=50 1/in	S @ h=100 1/in	S @ h=200 1/in	S @ h=300 1/in	S @ h=500 1/in	S @ h=750 1/in	S @ h=1000 1/in
Porous Graphite	0.7490	1050	2341	1703	584	432	251	121	n/a
	0.7494	622	n/a	n/a	892	702	726	n/a	n/a
	0.7500	322	n/a	2109	1246	n/a	n/a	n/a	n/a
Porous Alumina	0.7490	1536	n/a	n/a	n/a	n/a	241	350	93
	0.7494	557	n/a	n/a	604	494	155	n/a	n/a
	0.7500	282	1084	820	293	n/a	n/a	n/a	n/a
12 x 0.003 Holes	0.7490	830	n/a	2077	233	196	89	n/a	n/a
	0.7500	414	n/a	422	320	249	n/a	n/a	n/a
12 x 0.009 Holes	0.7490	730	2253	1113	518	429	276	400	n/a
	0.7500	85	939	n/a	n/a	n/a	n/a	n/a	n/a
12 x 0.015 Holes	0.7490	794	n/a	423	228	294	337	n/a	n/a
	0.7500	97	2573	n/a	n/a	n/a	n/a	n/a	n/a
12 x 0.018 Holes	0.7490	971	n/a	n/a	n/a	n/a	259	284	n/a
	0.7500	248	324	463	n/a	n/a	n/a	n/a	n/a

## Appendix E Literature Search Outline Of Gas Journal Bearing Progress

### E.1. Conformal gas journal bearings

1970 - [29] Barnett and Silber - Reports on AiResearch compliant face bearing with 1" diameter run to 240,000 RPM.

1978 - [30] Ruscitto et al. - Reports on NASA testing of hydresil™ (Chrysler foil bearing) at 60,000 RPM. Design details of the bearing are given.

1979 - [31] Gray - Reports development of Hydresil™ 1.5" diameter foil bearing for Chrysler automotive turbine engine program.

1979 - [32] Agrawal - Sites the advantages of foil bearings and reviews progress.

1979 - [33] Trippet - Reports on GM development program for an automotive gas turbine using a foil bearing at ~45,000 RPM.

1983 - [34] Heshmat et al. 1983 Mechanical Technology inc. - Presents Reynolds numerical solution for load, attitude angle and stiffness for a three spring supported compliant foil. The bearing gap is modified in the Reynolds equation to take in account spring deformation of the surface, small displacements from bearing equilibrium position ( $e, \theta_0$ ) are used to calculate cross-coupled spring coefficients.

1990 - [35] Murry of Allied signal/AiResearch - Reports on the use of penny size foil bearings in an extravehicular activity suit (EVA) fan to be operated at 146,000 RPM.

1992 - [36] Fukumoto et al. - Report Allied-Signal and Lockheed use of foil bearing for a device that operates up to 215,000 RPM and needs 90,000 RPM minimum for adequate stiffness.

1997 - [37] Dellacorte of Nasa Glenn - Reports the availability of a foil air bearing test for use to 700°C and 70,000 RPM.

2000 - [38] Valco and Dellacorte of NASA Glenn - Present a “rule of thumb” (ROT) method calculating the load capacity of foil bearings based on the body of published experimental work. The rule of thumb estimates that the load capacity is a linear function of a “bearing load capacity coefficient” multiplied by the nominal bearing area (L x D) and the surface speed of the shaft. The further need for ROTs for stiffness and damping coefficients is recognized. The bearing load capacity coefficient for 14 bearings ranging from 0.016 for early magnetic tape bearing to 1.4 for bump type w/multiple bump layers, which are split circumferentially and axially, are presented. This bearing carries US Pat. # 4,300,806.

2007 - [39] Salehi Heshmat, Walton and Tomarszewski, of Mohawk Innovative Technology Inc. (MiTi) - Recount the operation of MiTi micro-gas turbine ( $\mu$ GT) with a foil bearing up 700,000 RPM. Note that Heshmat was previously with Mechanical Technologies Inc.

2009 - [40] Howard of NASA Glenn - Reports using a to gas foil bearing supported rotor and a laser based shaft alignment system to investigate the misalignment tolerances of gas foil bearings. Concludes that they are at least an order of magnitude more tolerant than contact bearings that they are designed to replace.

2009 - Navy releases an SBIR topic for *Innovative concepts for HS rotating machines*. Foil hydrodynamic bearings are used in the F-18 environmental control systems and are reportedly suffering early failure due to contamination and overloading from impulses of carrier landings. Innovative oil-free bearing concepts are sought for components weighing 4-8 lbs and rotating between 60,000-80,000 rpm. Awards will eventually be given to Create Inc., Integran Technologies Inc., and Mohawk Innovative Technologies Inc.

## E.2. Hybrid, hydrodynamic , grooved, and noncircular gas journal bearings

1959 - [3] Ausman - Presents numerical results of pressure distributions, load capacity and attitude angle for a hydrodynamic gas journal bearing of finite length and compares results previously published experimental results.

1959 - [41] Whitley and Betts - Presents experimental results for hydrodynamic gas plain journal bearing and a bearing with a groove on top which are run in air, nitrogen, hydrogen, and neon. Results are compared with calculations of long bearings and bearings of finite length. Contains many good observations and concludes among other things that an isothermal model is more accurate than an adiabatic one and that when the groove is rotated relative to the load line, the whirl threshold speed shows a cyclic variation with the maximum speed being when the groove opposes the load.

1961 - [2] Raimondi - Reports on analysis of full gas journal bearings of finite length. Hand drawn circular diagrams are given of a cross section of the angular profile pressure wave at the center of the bearing showing a "pressure side" and a "suction side". Pressure wave angular profiles are drawn for the bearing center. The circular diagrams are drawn to illustrate the development of the pressure wave with increasing eccentricity ratio while the pressure profiles show the development with increasing speed. A contour map of a typical pressure wave is given. Load capacities and attitude angles for bearings with different L/D ratios are reported and compared to Ausman.

1970-[1] Powell - Writes a review a review of progress in gas lubrication in which some pressure distribution and design insights for cylindrical gas hydrodynamic and hybrid gas journals are given.

1973 - [42] Mori - Studies the performance of an externally pressurized porous-liner gas journal bearing and finds his analysis has “comparatively” good correlation to experimental results.

1977 - [43] Cohen - Presents hand drawn maps of stability regions in terms of speed, rotor mass, and eccentricity and compares his results of onset speed of half-speed whirl instability to other theoretical works.

1979 - [44] Gargiulo of Dupont - Reports an experimental investigation of a porous-liner gas journal bearing including onset speeds of vibrational instability. Concludes that the theoretical models adequately describe the test performance.

1979 - [27] Kamala - Performs analysis on 1, 2, and 3 rows of 8 feedholes for a hybrid bearing. Concludes that the radial component of the load force is large compared to the tangential component so that 70% of the load is “borne by aerostatic action” resulting in a small attitude angle and stable bearing operation. Also concludes for a fixed mass-addition parameter based on 0.5 mm feedhole diameter that each feedhole configuration has an optimum clearance also for a given clearance, orifice size and number of orifices per row there is an optimum L/D ratio.

1983 - [45] S. Wadwa et al. - Analyze a hybrid bearing externally pressurized by 2 rows of eight feedholes and concludes that the hybrid bearing has a larger load bearing capacity and is more dynamically stable.

1995 - [46], [47] Dimofte - The “wave” bearing concept, which is a slightly out of round 3-lobed hydrodynamic bearing, is analyzed and compared to a cylindrical journal bearing. A wave bearing with a groove is compared against a lobe bearing. The conclusions are that the wave bearing has load capability close to a cylindrical journal bearing but has better stability. Experimental results at a test

facility at NASA Lewis confirm the analysis. Dimofte was senior researcher at University of Toledo and developed the wave bearing concept under NASA Lewis. He will later join Nastec Inc, an advanced bearing company that seeks commercial applications for the wave bearing.

1999 - [48] Piekos - A simulation tool for journal bearings for the MIT microturbine using the orbit method is described. It is concluded that the method is flexible and computationally efficient.

2002 - [49] Saha and Mujumbar - Study an externally pressurized, two-layered porous gas journal bearing. They conclude that use of two-layered porous liner where a course (high permeability liner) has an inside liner with a thin, fine (low permeability) liner can give higher load bearing capacity than a single liner bearing.

2003 - [7] C-C Wang et al. of Far East College (Taiwan) - Studies the bifurcation of a porous liner hybrid gas journal bearing with a rigid rotor . The analysis reveals a complex periodic and quasi-periodic dynamic behavior.

2004 - [50] V. Grabovskii - Uses the methods of calculus of variations to determine that the optimum shape for the bearing base (of infinite length) is a discontinuous function with of several different types of curves. The optimization is in terms of maximum load capacity. The shape presented assumes a gravity orientation of the shaft bushing.

2004 - [23] C-C Wang et al. - Use a bifurcation method to study the stability of a loaded flexible shaft supported by 2 hydrodynamic bearings. He concludes that the system has a complex dynamic behavior that includes periodic and subharmonic responses and that the demonstrated technique can be used to optimize bearing design and operating conditions.



2004 - [51] Senatore and Popescu - Study the effect of wear pattern in out-of-round shapes on bearing stability for two bearings.

2004 - [52] Peirs et al. - Reports that a hybrid feedhole bearing designed for a turbine meant to be operated at 210,000 RPM was operated up to 96,000 RPM. Concludes that bearing speed is the main bottleneck to microgas turbines and intends further optimization to attain 500,000 RPM.

2005 - [9] C-C Wang et al. of Far East College (Taiwan) - Bifurcation analysis is done for a relatively short  $L/D=0.1$  hydrodynamic bearing with a flexible rotor supported by two bearings. A complex dynamic behavior is found and described and it is concluded that the techniques used can be applied to optimize design.

2005 - [15] Lee et al. - Analysis is made of a hydrodynamic journal bearing for a micro gas turbine that has local Knudsen numbers between 0.5 and 0.9. The Reynolds equation is modified to include slip flow effects and it is concluded that slip flow effects are significant for this bearing at increased temperatures (1600 K). The slip flow is found to affect the peak-to-peak pressure differential in the circumferential pressure wave near the angular location of the minimum flight height.

2006 - [10] C-C Wang of Far East College (Taiwan) - Uses bifurcation analysis to study the performance of a herringbone-grooved shaft in a cylindrical bushing and concludes "The techniques demonstrated in this article can be used to determine an optimal design configuration and ideal operating conditions for herringbone-grooved gas film rotor-bearing systems"

2006 - [11] C-C Wang - Uses the bifurcation method to study a porous-liner gas journal bearing and finds the existence of complex rotor dynamics with periodic

and quasi-periodic behavior. It concludes that techniques demonstrated can be used to optimize pressurized porous-liner gas journal bearings.

2006 - [18] Su and Lie - Analyzes feedhole hybrid bearing with 1,2,3,4, and 5 rows of 8 feedholes and porous liner hybrid bearing and concludes that the porous bearings are more stable at low speeds  $\Lambda < 1$  or high speeds  $\Lambda > 1$  with low mass feeding parameters. The 5 row feedhole bearing is more stable at moderate speeds  $0.3 < \Lambda < 0.6$  for lower mass feeding parameters. Increasing the mass feeding parameters increases the stability threshold up to point but further increases decrease the stability. This is because increasing the mass flow parameter increases the stiffness and decreases the damping.

2007 - [53] Liu and Spakovszky - Based on observations found in MIT microengines that ultrashort bearings  $L/D < 0.01$  running at surface speeds of 500 m/s exhibit whirl instability limits and a dynamic behavior much different from conventional hydrostatic gas bearings, design guidelines are developed for a novel axial-flow micro gas bearing concept that creates anisotropy in bearing stiffness.

2008 - [17] Teo, Spakovsky and Jacobson - As a part of MIT microgas turbine program the instability of ultra-short, axially fed, hybrid bearings is described in terms of unsteady vorticity impulses of the Lomakin effect.

2008 - [12] C-C Wang - Does bifurcation analysis of a short hydrodynamic gas journal bearing with stationary herringbone-grooves in the bushing. Stability is done for a rigid shaft supported by 2 bearings. He concludes that the shaft centers are stable when T-periodic but will be unstable when quasi-periodic motion appears. The ranges of stability for the specific bearing are given.

2008 - [54] Ruiz et al. - A feedhole fed three-lobed hybrid bearing is numerically analyzed and tested with a test rig that utilizes 2 magnetic bearings.

2008 - [55] Savoulides et al. - Fabrication methods are discussed for the bearing of a MEMS turbocharger for MIT's microscale gas turbine using a silicon rotor and silicon bushing, operated at 480,000 RPM with a tip speed of 200 m/s.

2009 - [5] Zhang and Xu - Study a feedhole hybrid gas journal with 2 rows of 8 feedholes. They conclude that the coupling effects of the aerodynamic and aerostatic effects greatly enhance the bearing performance and load capacity performance of the bearing compared to a purely hydrodynamic bearing. Some bearing gap pressure surfaces and profiles are given.

2009 - [56] V. Grabovskii - Shows that the gas dynamic seal efficiency is considerably higher for extremal step bearings than for eccentric bearings. With a decrease in  $\Delta/l$  and an increase in  $l$  these rapidly regain the advantage in load capacity which they have at infinite length.

2009 - [57] Ertas et al. - Report on a general purpose test facility at GE Global Research Center to test 70-120mm diameter bearings from 40,000-80,000 RPM to 1200 °F with dynamic and static load profiles up to 1000 lb.

2009 - [8] Ertas - Reports the development by GE Global of a combination hybrid and compliant bearing of 2.75" diameter for operation up to 40,000 RPM. Experimental and theoretical results are presented.

2009 - [13] Yang et al. - The stability of cylindrical hydrodynamic bearings for 3 cases using the orbit method is studied and it is concluded that the states of stable and unstable performance are separated by two thresholds rather than one.

2009 - [14] Zhou et al. - Bifurcation analysis is done for an ultrashort hydrodynamic bearing for MEMs devices with  $L/D=1$ . Results indicating complicated dynamic behavior are described.

2010 - [16] Zhang et al. - Analyze the performance and stability of an ultra-short hybrid gas bearing for use in a micro-turbine at 870,000 RPM which is fabricated with deep X-ray lithography and electroplating. Because the Knudsen ( $Kn$ ) number of the bearing operation varies from 0.5 to 0.9 they use a Reynolds equation modified for the slip-flow regime. They conclude that increases in  $Kn$  exponentially reduces the load carrying capacity and that the load capacity increases non-linearly with the bearing number (dimensionless speed). Use of the slip-flow boundary conditions increases the range of stability. Many other relationships are reported.

2011 - [58] Stolarski - Uses piezoelectric vibration of the bushing walls to create self-generating squeeze-film pressure that can be used for both circular and 3-lobed bearings to generate a self-lifting effect at low RPM similar to adding external pressurization to generate hydrostatic lift. It also appears to increase the instability thresholds.

### E.3. Hydrostatic bearings

1970 - [1] Powell - Shows a graph of load deflection tests for a hybrid gas journal bearing at 3 different speeds (7500, 5000, and 2500 RPM) and “aerostatic” (0 RPM). The aerostatic curve is shown as linear.

2002 - [59] Su of Far East College (Taiwan) - An approximate solution for hydrostatic-porous liner bearings is compared with numerical solutions. The approximate solution, which predicts a linear relationship between load bearing capacity and eccentricity ratio, is found to be applicable to short porous journal bearings ( $L/D < 0.5$ ) with low permeability, light load capacity, and low eccentricity ratio ( $\epsilon < 0.5$ ). Axial pressure profile lines are presented for angular positions of 0,  $\pi/2$ , and  $\pi$  along with power requirements to feed the mass flow through the porous liner.

2006 - [24] - New Way Bearings shows empirical, data-based flight height versus bearing load for flat bearings. These curves have increasing bearing stiffness as flight height is decreased to small values and falls off to zero as flight heights are increased over 0.001”. No curves are shown for journal bearings but these are sold based on bearing stiffness which implies a linear relationship.

2009 - [5] Liu et al. - Show hybrid numerical results for a feedhole bearing with 2 rows of 8 feedholes. They show graphical pressure distributions and compare the hybrid pressure wave development to the hydrodynamic pressure wave superimposed on the hydrostatic pressure wave. A graph is given of the load-carrying capacity versus eccentricity ratio of the bearing at eccentricity ratios varying from 0.1 to 0.9. The 0 RPM result (aerostatic line) shows a peak load capacity at an eccentricity ratio of about 0.8 and a decline in load capacity as it is raised to 0.9. The authors attribute “load capacity fall off” or “negative stiffness”

to being a phenomenon that occurs in what is termed the “static instability region”.

2010 - [6] Chen et al. - Experimental and theoretical computational data are shown for hydrostatic bearings with an external pressurization configuration of 2 rows of 8 feedholes. The study varies  $L/D$ , the operating pressure, and uses 2 geometries of feedholes (pocketed orifice and inherent orifices). It concludes that pocketed orifices have higher stiffness. Graphically it shows the dimensionless load capacity versus radial deflection to be virtually linear in appearance in all cases all the way to zero eccentricity ratio although it is not clear whether the zero eccentricity data is actual or an assumed extrapolation. The same dimensionless mass flow term is used for both types of feedholes so the difference must be assumed to be in the discharge coefficient used. Numerical results differ from experimental results by about 8%.

VITA

## VITA

Tom Marquis Lawrence

Education

B.A., Philosophy, Coe College, Cedar Rapids, Iowa  
B.S., Mechanical Engineering, Northwestern University, Evanston, Illinois  
M.S., Mechanical Engineering, Massachusetts Institute of Technology,  
Cambridge, Massachusetts  
M.B.A., Business, University of Wisconsin, Whitewater, Wisconsin  
Ph.D., Physics, Purdue University, Indianapolis, Indiana

Research Interests

Nanotechnology and MEMS  
Nanostructured materials  
High temperature small diameter wire  
Thermoelectric fiber  
Gas Bearings  
Continuous fiber coating processes  
High speed, low wear, low friction, ohmic conductivity

Professional Experience:

AeroQuest Research Group - Founder  
Aerodyn Engineering Inc. - Co-founder  
The Rockford Consulting Group - Senior Consultant  
Lawrence International LLC - Partner  
Lawrence Brothers Inc. - Executive Vice President and Treasurer  
Allied Signal - *Bendix Electric Power Division*, Director of Operations, *Amphenol C&I Division*, Director of Manufacturing Engineering, Plant Manager, Task Force Leader  
Division Relocation and Modernization, Manager of Division Process Improvement  
The Parker Pen Company - Project Principal, Continuation Engineer  
The French Oil Mill Machinery Company - Design Engineer  
Lawrence Brothers Inc. - Apprentice Tool and Die maker